

# **DISSERTATION**

## **Porphyrin-basierte Metall-Organische Gerüstverbindungen: Von Metall-Carboxylaten zu Metall-Phosphonaten**

Zur Erlangung des Doktorgrades  
der Mathematisch-Naturwissenschaftlichen Fakultät der  
Christian-Albrechts-Universität zu Kiel

vorgelegt von  
Timo Rhauderwiek

Institut für Anorganische Chemie  
Kiel, Juni 2018





Erster Gutachter: Prof. Dr. Norbert Stock

Zweiter Gutachter: Prof. Dr. Wolfgang Bensch

Tag der mündlichen Prüfung: 25.07.2018

Zum Druck genehmigt:

Gez. Prof. Dr. Natascha Oppelt Dekanin



## ***Meinen Eltern***



## Kurzzusammenfassung

Die vorliegende Arbeit beschäftigt sich mit der Synthese und Charakterisierung von Porphyrin-basierten Metall-Organischen Gerüstverbindungen (MOFs). Dabei wurden zwei verschiedene Linkermoleküle verwendet, zum einen die Porphyrin-basierte Carbonsäure Tetra(4-carboxyphenyl)porphyrin ( $H_6TCPP$ ) und die erstmalig in dieser Arbeit synthetisierte Ni-metallierte Porphyrin-basierte Tetrakisphosphonsäure Ni-Tetra(4-phosphonophenyl)porphyrin ( $Ni-H_8TPPP$ ).

Die Synthese der Metall-Carboxylate erfolgte dabei ausschließlich unter Einsatz von DMF/ $H_2O$  Gemischen bei  $120\text{ }^\circ\text{C}$  und die Synthese der Metall-Phosphonate in  $H_2O$  bei höheren Temperaturen von  $160\text{ -}180\text{ }^\circ\text{C}$ . Alle in dieser Arbeit synthetisierten MOFs wurden anfänglich unter Einsatz der Hochdurchsatz-Methode entdeckt. Diese wurde ebenfalls für die Syntheseoptimierung eingesetzt. Die Reaktionen wurden dabei oftmals im weiteren Verlauf der Temperatur-Zeit Optimierung auf Glasgefäße unter Rühren übertragen.

Mit dem  $H_6TCPP$  Linker konnten isostrukturelle Verbindungen zu dem bereits bekannten Al-PMOF [ $Al_2(OH)_2(H_2TCPP)$ ] mit  $Ga^{3+}$ ,  $In^{3+}$  und  $Ce^{3+}$  erhalten werden. Die Synthese des entsprechenden Ce-PMOFs [ $Ce_2(BA-NO_2)_2(H_2TCPP)$ ] ( $BA-NO_2^{2-} = 4\text{-Nitrobenzoat}$ ) gelang ausschließlich unter Verwendung von  $NH_4[Ce^{IV}(NO_3)_6]$  als Metallquelle sowie 4-Nitrobenzoesäure als Co-Ligand, wobei letztere ebenfalls in die Verbindung anstelle der üblicherweise gefundenen  $\mu\text{-OH}$  Gruppen eingebaut ist. Die Kristallstrukturbestimmung aller PMOFs erfolgte mittels Rietveld Verfeinerung. Ga- und In-PMOF sind porös gegenüber  $N_2$  bei  $77\text{ K}$  und es werden ähnliche spezifische Oberflächen zu dem bereits publizierten Al-PMOF ( $1400\text{ m}^2\text{ g}^{-1}$ ) von  $1150\text{-}1400\text{ m}^2\text{ g}^{-1}$  erhalten. Die Synthese des Ga- und In-PMOFs konnte des Weiteren in einem Flussreaktor und unter Ultraschallbehandlung durchgeführt werden. Dabei wurden in Abhängigkeit der Synthesemethode unterschiedliche Partikelgrößen im nanoskaligen Bereich zwischen  $65(18)$  und  $156(28)$  nm erhalten. Unter Einsatz von  $NH_4[Ce^{IV}(NO_3)_6]$  und dem  $H_6TCPP$  Linker wurden drei weitere MOFs entdeckt. Zum einen CAU-18 [ $Ce_4(H_2TCPP)_3(DMF)_2(H_2O)_4$ ], welches bei  $77\text{ K}$  nicht porös gegenüber  $N_2$  ist, jedoch durch thermische Behandlung für  $16\text{ h}$  bei  $250\text{ }^\circ\text{C}$  eine Phasenumwandlung in das poröse CAU-18a, [ $Ce_4(H_2TCPP)_3 \cdot 22\text{ H}_2\text{O}$ ] zeigt. Zum anderen gelang unter Verwendung unterschiedlich funktionalisierter Benzoessäuren ( $HBA\text{-X}$ ,  $X = H, 2\text{-Cl}, 3\text{-Cl}, 4\text{-Cl}, 3\text{-CO}_2\text{H}, 4\text{-NH}_2$ ,  $HBA = C_7H_4O_2$ ) die Synthese von CAU-19-X, [ $Ce_3(H_2TCPP)_2(BA\text{-X})(HBA\text{-X}/H_2O)_2 \cdot 2\text{ HBAX} \cdot n\text{ H}_2\text{O}$ ] (mit  $X = H, 2\text{-Cl}, 3\text{-Cl}, 4\text{-Cl}, 3\text{-CO}_2\text{H}, 4\text{-NH}_2$ ). In Abhängigkeit des enthaltenen Benzoensäurederivats wurden dabei unterschiedliche spezifische Oberflächen nach BET zwischen  $330$  und  $600\text{ m}^2\text{ g}^{-1}$  erhalten. Des Weiteren

konnte auch CAU-19-4NO<sub>2</sub> erhalten werden, jedoch nicht direkt durch Einsatz von 4-Nitrobenzoesäure, sondern nur als Produkt der Phasenumwandlung des Ce-PMOF in Aceton bei 70 °C. Die Strukturen von CAU-18 und CAU-19-H wurden anhand von Einkristalldaten bestimmt.

Mit dem Ni-H<sub>8</sub>TPPP Linker gelang die Synthese des ersten porösen Porphyrin-basierten Metall-Phosphonats M-CAU-29 [M(Ni-H<sub>6</sub>TPPP)(H<sub>2</sub>O)] (M= Mn, Co, Cd), dessen Struktur aus Einkristalldaten bestimmt wurde und für das spezifische Oberflächen nach BET von 0, 90, 145 und 180 m<sup>2</sup> g<sup>-1</sup> (Ni, Mn, Co, Cd) erhalten wurden. Unter Einsatz der vierwertigen Kationen Zr<sup>4+</sup> und Hf<sup>4+</sup> in Kombination mit NaF und NaOH gelang die Synthese eines weiteren Porphyrin-basierten Metall-Phosphonats [M<sub>2</sub>(Ni-H<sub>2</sub>TPPP)(OH/F)<sub>2</sub>] · x H<sub>2</sub>O (M= Zr, Hf) M-CAU-30, dessen Struktur durch Kombination von Elektronenbeugung und Rietveld Verfeinerung der Röntgenpulverdaten bestimmt wurde. CAU-30 ist das Metall-Phosphonat mit der bisher höchsten spezifischen Oberfläche nach BET von 1070 (Zr-) bzw. 1030 m<sup>2</sup> g<sup>-1</sup> (Hf-CAU-30) und weist Porendurchmesser von 1.3 x 2.0 nm auf. Des weiteren ist CAU-30 thermisch stabil bis 400 °C und chemisch stabil im kompletten pH Bereich von 0-12 sowie in 0.1 M Phosphatpuffer. Der Einsatz von DABCO (1,4-Diazabicyclo[2.2.2]octan) als Co-Ligand führte in Kombination mit Co<sup>2+</sup> und HCl zu einem dritten porösen Porphyrin-basierten Metall-Phosphonat dem Co-CAU-36 [Co<sub>2</sub>(Ni-H<sub>4</sub>TPPP)] · 2DABCO · 6H<sub>2</sub>O. Dessen Struktur wurde ausschließlich aus Elektronenbeugungsdaten bestimmt, wobei ebenfalls Protonen in der Differenz-Fourierkarte lokalisiert werden konnten und für Elektronenbeugungsdaten gute Gütefaktoren von 13.6 (R<sub>1</sub>) bzw. 33.4 % (wR<sub>2</sub>) erhalten wurden. CAU-36 ist ebenfalls porös gegenüber N<sub>2</sub> bei 77 K und weist eine spezifische Oberfläche nach BET von 700 m<sup>2</sup> g<sup>-1</sup> auf. M-CAU-30 und Co-CAU-36 sind strukturell verwandt, es werden annähernd gleiche Porengeometrien, jedoch unterschiedliche anorganische Baueinheiten in Form von Ketten trans-eckenverknüpfter MO<sub>6</sub> Oktaeder bei CAU-30 und Ketten von über Hydrogenphosphonatgruppen verknüpften CoO<sub>4</sub> Tetraedern erhalten. Die Poren in CAU-36 sind durch über Wasserstoffbrückenbindungen enthaltene DABCO Moleküle teilweise blockiert wodurch kleinere Porendurchmesser von 0.9 nm erhalten werden.

## Abstract

This thesis deals with the synthesis and characterization of porphyrin-based metal-organic frameworks (MOFs). Two different linker molecules were employed, the porphyrin-based carboxylic acid tetra(4-carboxyphenyl)porphyrin (H<sub>6</sub>TCPP) and the new Ni-metalated tetraphosphonic acid Ni-tetra(phosphonophenyl)porphyrin (Ni-H<sub>8</sub>TPPP), of which the latter was synthesized for the first time in this work.

The synthesis of metal-carboxylates was exclusively carried out using DMF/H<sub>2</sub>O solvent mixtures at 120 °C and for the synthesis of metal-phosphonates H<sub>2</sub>O was used at higher temperatures of 160-180 °C. All in this work synthesized MOFs were initially discovered and their synthesis parameters were optimized employing high-throughput methods. After further reaction-temperature and -time optimizations, most of the reactions could be transferred to glass vials under stirring.

Isostructural compounds to the already known Al-PMOF [Al<sub>2</sub>(OH)<sub>2</sub>(TCPP)] with Ga<sup>3+</sup>, In<sup>3+</sup> und Ce<sup>3+</sup> could be synthesized by using the H<sub>6</sub>TCPP linker. The synthesis of the respective Ce-PMOF [Ce<sub>2</sub>(BA-NO<sub>2</sub>)<sub>2</sub>(H<sub>2</sub>TCPP)] (BA-NO<sub>2</sub><sup>2-</sup>= 4-nitro benzoate) could only be carried out by usage of NH<sub>4</sub>[Ce<sup>IV</sup>(NO<sub>3</sub>)<sub>6</sub>] as the metal source and 4-nitrobenzoic acid as a co-ligand, the benzoic acid is also incorporated in the structure instead of the commonly observed μ-OH groups in other PMOFs. The structure determination of all mentioned PMOFs was achieved using the Rietveld method. Ga- and In-PMOF are porous toward N<sub>2</sub> at 77 K and exhibit similar specific surface areas compared to the published Al-PMOF (1400 m<sup>2</sup> g<sup>-1</sup>) of 1150-1400 m<sup>2</sup> g<sup>-1</sup>. Furthermore, the synthesis of Ga- and In-PMOF could be performed in a flow-reactor and in a sonication bath. Different nanosized particles, depending on the employed synthesis method, were found in a range between 65(18) and 156(28) nm. Three additional MOFs were discovered by employing NH<sub>4</sub>[Ce<sup>IV</sup>(NO<sub>3</sub>)<sub>6</sub>] and the H<sub>6</sub>TCPP linker. CAU-18 [Ce<sub>4</sub>(H<sub>2</sub>TCPP)<sub>3</sub>(DMF)<sub>2</sub>(H<sub>2</sub>O)<sub>4</sub>] is at 77 K not porous towards N<sub>2</sub>, but exhibits a phase transformation into the porous CAU-18a [Ce<sub>4</sub>(H<sub>2</sub>TCPP)<sub>3</sub>] · 22 H<sub>2</sub>O under thermal treatment over night at 250 °C. In addition by employing different benzoic acid derivatives (HBA-X, X= H, 2-Cl, 3-Cl, 4-Cl, 3-CO<sub>2</sub>H, 4-NH<sub>2</sub>, HBA = C<sub>7</sub>H<sub>4</sub>O<sub>2</sub>) in the synthesis of Ce-MOFs, CAU-19-X, [Ce<sub>3</sub>(H<sub>2</sub>TCPP)<sub>2</sub>(BA-X)(HBA-X/H<sub>2</sub>O)<sub>2</sub>] · 2 HBAX · n H<sub>2</sub>O (with X = H, 2-Cl, 3-Cl, 4-Cl, 3-CO<sub>2</sub>H, 4-NH<sub>2</sub>) was discovered. Depending on the incorporated benzoic acid derivative different specific surface areas according to BET between 330 and 600 m<sup>2</sup> g<sup>-1</sup> were achieved. CAU-19-4NO<sub>2</sub> was only obtained as transformation product of Ce-PMOF-4NO<sub>2</sub> in acetone at 70 °C. The structures of CAU-18 and CAU-19-H were determined by single crystal X-ray diffraction.

Employing the new Ni-H<sub>8</sub>TPPP linker for the synthesis of MOFs, the first porous porphyrin-based metal-phosphonate M-CAU-29 [M(Ni-H<sub>6</sub>TPPP)(H<sub>2</sub>O)] (M= Mn, Co, Cd) was discovered. Its structure was determined by single crystal X-ray diffraction and the compounds exhibit specific surface areas according to BET of 0, 90, 145 und 180 m<sup>2</sup> g<sup>-1</sup> (Ni, Mn, Co, Cd). Using the tetravalent cations Zr<sup>4+</sup> und Hf<sup>4+</sup> in combination with NaF and NaOH, further porphyrin-based metal-phosphonates [M<sub>2</sub>(Ni-H<sub>2</sub>TPPP)(OH/F)<sub>2</sub>] · x H<sub>2</sub>O (M= Zr, Hf) M-CAU-30 were synthesized. The structure of CAU-30 was determined by employing both electron diffraction data and Rietveld refinement of X-ray powder diffraction data. CAU-30 exhibits the highest specific surface area according to BET of all published metal-phosphonates of 1070 (Zr-) and 1030 m<sup>2</sup> g<sup>-1</sup> (Hf-CAU-30), while pore diameters of 1.3 x 2.0 nm are observed. Furthermore, CAU-30 is thermally stable up to 400 °C and chemically stable in the complete pH range between 0-12 as well as in a 0.1 M phosphate buffer. Employing DABCO (1,4-diazabicyclo[2.2.2]octan) as co-ligand in combination with Co<sup>2+</sup> and HCl, a third porous porphyrin-based metal-phosphonate Co-CAU-36 [Co<sub>2</sub>(Ni-H<sub>4</sub>TPPP)] · 2DABCO · 6H<sub>2</sub>O was synthesized. The structure of Co-CAU-36 was exclusively determined by electron diffraction and even protons could be localized in the difference Fourier map and good reliability factors of 13.6 (R<sub>1</sub>) and 33.4 % (wR<sub>2</sub>) were obtained. CAU-36 is porous towards N<sub>2</sub> at 77 K and exhibits a specific surface area according to BET of 700 m<sup>2</sup> g<sup>-1</sup>. M-CAU-30 and Co-CAU-36 are structurally related to each other and very similar pore geometries are observed, while different inorganic building units (chains of corner-sharing MO<sub>6</sub> octahedra in CAU-30 and chains of hydrogenphosphonate bridged CoO<sub>4</sub> tetrahedra in CAU-36) are observed. The pores in CAU-36 are partially blocked by hydrogen-bonded DABCO molecules, which reduce the accessible porediameter to 0.9 nm.



## Danksagung

An dieser Stelle möchte ich allen danken, ohne die diese Doktorarbeit nicht möglich gewesen wäre.

Mein erster Dank gilt Herrn Prof. Dr. Stock für das Thema, die Bereitstellung von Chemikalien und Ausrüstung, sowie der guten Betreuung, Unterstützung und Zusammenarbeit während der gesamten Promotionszeit.

Das effektive wissenschaftliche Arbeiten ist nicht möglich ohne ein angenehmes Arbeitsklima und der Zusammenarbeit mit Kolleginnen und Kollegen. Daher bedanke ich mich ebenfalls in großem Maße bei meinen Mitstreitern und zugleich Freunden für den Austausch, die Hilfe und viele schöne Zeiten innerhalb und außerhalb des Labors: Steve Waitschat, Martin Albat, Martin Lammert und Achim Fölster, sowie dem gesamten Arbeitskreis Stock.

Ein besonderer Dank gilt des weiteren Dr. Helge Reinsch, Dr. Ken Inge und Dr. Michael Wharmby für viele angeregte Diskussion und Erkenntnisse vor allem im Bereich der Kristallographie.

Neue wissenschaftliche Erkenntnisse sind ohne Kooperationen mit anderen Arbeitsgruppen in Deutschland und der Welt kaum möglich. Daher danke ich für die sehr gute Zusammenarbeit all meinen Kooperationspartnern und im Einzelnen: Dr. Stefan Wuttke (LMU München), Patrick Hirschle (LMU München), Bart Bueken (KU Leuven), Simon Smolders (KU Leuven), Sigurd Øien-Ødegaard (University of Oslo) und Konrad Wolkersdörfer (Universität Oldenburg).

Ebenfalls hausintern arbeiten viele Menschen, die täglich Messungen durchführen, ohne die die Publikation von Ergebnissen nicht möglich wäre. Daher gilt mein Dank der spektroskopischen Abteilung der anorganischen Chemie, dem Arbeitskreis Bensch für die thermogravimetrischen Messungen und der NMR Abteilung der organischen Chemie.

Während meiner Promotionszeit durfte ich ebenfalls einige F-Praktika und Bachelor-Arbeiten betreuen, bei denen eigentlich immer Ergebnisse erhalten wurden, die zum Gelingen meiner Arbeit beigetragen haben. Daher gilt mein Dank: Jan Thomas, Mana Mohammed, Bianca Pfalzgraf, Jonas Ströh, Hendrik Hansen, Melanie Walther und Harm Pewe.

An letzter Stelle kommt immer das wichtigste: Familie und Freunde. Der größte Dank gilt dabei meinen Eltern und meiner Freundin Meike für die Unterstützung, Liebe und Zuversicht während der gesamten Zeit. Außerdem zuletzt meinen besten Freunden Rene und Filip für eine großartige Zeit außerhalb der Universität und ein offenes Ohr für Probleme in jeder Lebenslage.



## Abkürzungsverzeichnis

CAU	Christian-Albrechts-Universität
CALF	Calgary Framework
DCM	Dichlormethan
DDQ	2,3-Dichlor-5,6-dicyano-1,4-benzochinon
DLS	Dynamische Lichtstreuung
DMF	<i>N,N</i> -Dimethylformamid
DMSO	Dimethylsulfoxid
EDX	Energiedispersive Röntgenfluoreszenzspektroskopie
H <sub>6</sub> TCPP	Tetracarboxyphenylporphyrin
Ni-H <sub>8</sub> TPPP	Ni-Tetraphosphonophenylporphyrin
IR	Infrarot
KZ	Koordinationszahl
MFM	Manchester Framework Material
MIL	Matériaux de l'Institut Lavoisier
MOF	Metal-Organic Framework (Metall-Organische Gerüstverbindung)
NMR	Nuclear magnetic resonance (Kernspinresonanz)
PCN	Porous coordination network
REM	Rasterelektronenmikroskopie
RT	Raumtemperatur
STA	St. Andrews porous material
SZ	Soochow University Zirconium Phosphonate
TEM	Transmissionselektronenmikroskopie
TG	Thermogravimetrie
UiO	Universitetet i Oslo
UPG	University of Perugia
XANES	X-ray absorption near edge spectroscopy (Röntgen-Nahkanten-Absorptionsspektroskopie)
XRD	X-ray diffraction (Röntgenbeugung)



# Inhaltsverzeichnis

KURZZUSAMMENFASSUNG .....	III
ABSTRACT.....	V
DANKSAGUNG .....	VII
ABKÜRZUNGSVERZEICHNIS .....	IX
<b>I ALLGEMEINER TEIL.....</b>	<b>- 1 -</b>
<b>1    EINLEITUNG .....</b>	<b>- 3 -</b>
<b>2    PRÄPARATIVE METHODEN .....</b>	<b>- 5 -</b>
2.1 <i>Solvothermal</i> synthese .....	- 5 -
2.2 <i>Hochdurchsatz</i> methoden .....	- 6 -
<b>3    CHARAKTERISIERUNGSMETHODEN.....</b>	<b>- 9 -</b>
3.1 <i>Einkristall</i> strukturanalyse.....	- 11 -
3.2 <i>Elektronen</i> beugung.....	- 19 -
<b>II KUMULATIVER TEIL .....</b>	<b>- 23 -</b>
<b>4 PORPHYRIN-BASIERTE METALL-ORGANISCHE GERÜSTVERBINDUNGEN: VON METALL-CARBOXYLATEN ZU METALL-PHOSPHONATEN.....</b>	<b>- 25 -</b>
4.1 <i>Porphyrine</i> .....	- 25 -
4.2 <i>Porphyrin-basierte MOFs</i> .....	- 27 -
4.3 <i>Porphyrin-basierte Phosphonsäuren</i> .....	- 31 -
4.4 <i>Poröse Metall-Phosphonate</i> .....	- 33 -
<b>4.5 <i>Ergebnisse</i> .....</b>	<b>- 41 -</b>
4.5.1 <i>Nanoscale Synthesis of Two Porphyrin-Based MOFs with Gallium and Indium</i> ....	- 41 -
4.5.2 <i>Co-Ligand Dependent Formation and Phase Transformation of Four Porphyrin-Based Cerium Metal–Organic Frameworks</i> .....	- 51 -
4.5.3 <i>Crystalline and permanently porous porphyrin-based metal tetrakisphosphonates</i> .-	- 67 -
4.5.4 <i>A porous cobalt tetrakisphosphonates metal-organic framework: structure determination by fast continuous rotation electron diffraction</i> .....	- 73 -
4.5.5 <i>Highly stable and porous porphyrin-based zirconium and hafnium phosphonates - Electron crystallography as an important tool for structure elucidation</i> .....	- 79 -
<b>5    ZUSAMMENFASSUNG.....</b>	<b>- 93 -</b>
5.1 <i>Poröse Metall-Carboxylate mit dem H<sub>6</sub>TCP</i> P Linker ( <i>Tetra(4-carboxyphenyl)porphyrin</i> ) .....	- 95 -
5.2 <i>Poröse Metall-Phosphonate mit dem Ni-H<sub>8</sub>T</i> PPP Linker ( <i>Ni-tetra(4-phosphonophenyl)porphyrin</i> ).....	- 98 -
<b>6    AUSBLICK .....</b>	<b>- 101 -</b>
<b>7 LITERATUR .....</b>	<b>- 105 -</b>
<b>III ANHANG .....</b>	<b>- 111 -</b>

8	SI ZU „NANOSCALE SYNTHESIS OF TWO PORPHYRIN-BASED MOFs WITH GALLIUM AND INDIUM” .....	113 -
9	SI ZU „CO-LIGAND DEPENDENT FORMATION AND PHASE TRANSFORMATION OF FOUR PORPHYRIN-BASED CERIUM METAL-ORGANIC FRAMEWORKS” .....	133 -
10	SI ZU „CRYSTALLINE AND PERMANENTLY POROUS PORPHYRIN-BASED METAL TETRAPHOSPHONATES” ..	187 -
11	SI ZU „A POROUS COBALT TETRAPHOSPHONATES METAL-ORGANIC FRAMEWORK: STRUCTURE DETERMINATION BY FAST CONTINUOUS ROTATION ELECTRON DIFFRACTION” .....	217 -
12	SI ZU „HIGHLY STABLE AND POROUS PORPHYRIN-BASED ZIRCONIUM AND HAFNIUM PHOSPHONATES - ELECTRON CRYSTALLOGRAPHY AS AN IMPORTANT TOOL FOR STRUCTURE ELUCIDATION” .....	235 -
	CURRICULUM VITAE.....	265 -
	TAGUNGSBEITRÄGE .....	266 -
	PUBLIKATIONEN .....	267 -
	EIDESSTÄTTLICHE ERKLÄRUNG .....	269 -

# **I Allgemeiner Teil**





## 1 Einleitung

Schon seit einiger Zeit stehen poröse Materialien wie metal-organic-frameworks (MOFs), zeolitic-imidazolate-frameworks (ZIFs) und Zeolithe im Fokus der Wissenschaft und Forschung,<sup>1, 2</sup> vor allem aufgrund der mannigfaltigen möglichen Anwendungsgebiete beruhend auf der porösen Natur dieser Materialien. Hierzu zählen heterogene Katalyse, Gasspeicherung und -trennung sowie der Einsatz als Ionentauscher oder in der Wirkstofffreisetzung.<sup>2-7</sup>

Bei MOFs handelt es sich laut der Empfehlung der IUPAC um Koordinationsnetzwerke mit organischen Liganden, welche potentielle Hohlräume aufweisen. Hierbei ist wiederum der Begriff Koordinationsnetzwerke definiert als Verbindungen, welche sich wiederholende Einheiten in einer bis drei Dimension aufweisen, wobei im Falle von 1D Wiederholungseinheiten Querverknüpfungen zu anderen Wiederholungseinheiten in mindestens einer weiteren Dimension vorliegen müssen.<sup>8</sup> Diese Definition beinhaltet dabei nicht die Eigenschaften, dass diese Verbindungen messbare Sorptionseigenschaften oder Kristallinität aufweisen müssen. Oftmals besitzen MOFs jedoch diese wichtigen und vorteilhaften Eigenschaften, um definierte Wirt-Gast Beziehungen in Hinblick auf verschiedene Anwendungsmöglichkeiten abzuleiten.<sup>4</sup> Die meisten MOFs sind dreidimensionale Koordinationspolymere, bei denen Metall-Sauerstoff-Cluster über polyfunktionelle organische Moleküle, sogenannte Linker, verbunden werden. Diese sind daher in den meisten Fällen kristalline Verbindungen mit definierter dreidimensionaler Netzwerkstruktur und Porengrößen.<sup>1</sup> Durch geeignete Wahl des Linkers und des Metalls ist es theoretisch möglich eine beliebige Porengröße und somit auch Materialeigenschaften wie das Sorptionsverhalten oder eine katalytische Aktivität durch bestimmte Metallionen einzustellen.<sup>9</sup> Geeignete Linkermoleküle als mögliche Verknüpfungsstellen zwischen den anorganischen Baueinheiten sind vor allem Carbonsäuren,<sup>2</sup> aber auch Phosphon-<sup>10-12</sup> und Sulfonsäuren.<sup>13</sup> Der modulare Aufbau von MOFs erlaubt oftmals sogar die Synthese isostruktureller oder isoretikulärer Verbindungen durch Veränderung des Metallkations, der Länge des Linkers oder des Linkergrundgerüsts. Dabei kann z.B.  $\text{Co}^{2+}$  gegen  $\text{Ni}^{2+}$  ausgetauscht werden<sup>14</sup> um isostrukturelle Verbindungen bzw. isoretikuläre Verbindungen durch Einsatz von Biphenyldicarbonsäure oder Fumarsäure anstatt von Terephthalsäure zu erhalten (Abb. 01).<sup>9, 15</sup>

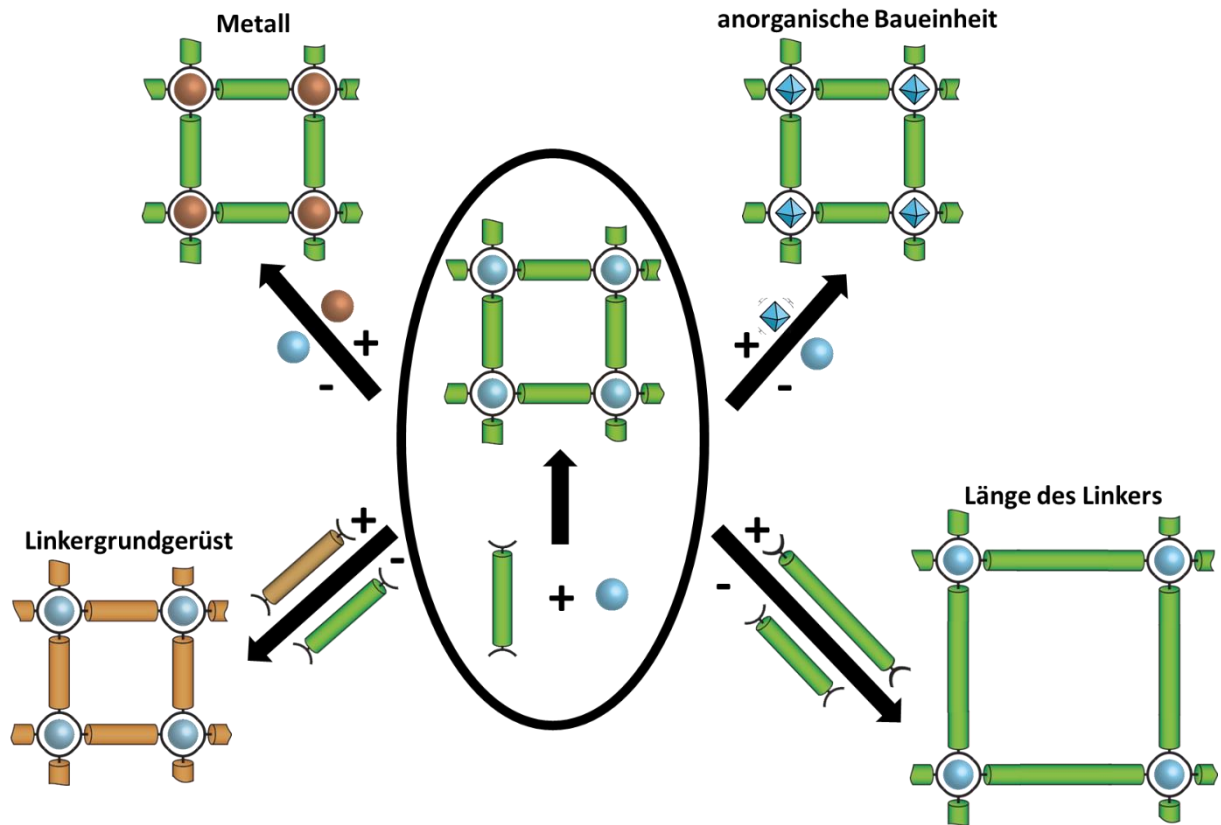


**Abbildung 01.** Schematische Darstellung des modularen Aufbaus von MOFs zur Darstellung isostruktureller und isoretikulärer Verbindungen anhand der Beispiele des Austauschs des Metalls, der anorganischen Baueinheit, des Linkergrundgerüsts und der Länge des Linkers.

## 2 Präparative Methoden

### 2.1 Solvothermalsynthese

Bei Metall-Organischen Gerüstverbindungen (MOFs) handelt es sich meistens um metastabile Reaktionsprodukte.<sup>16</sup> Im Vergleich zur konventionellen Hochtemperatursynthese, welche bei Temperaturen weit über 500 °C stattfindet und in der Regel thermodynamisch stabile Produkte liefert, wird die Synthese von MOFs häufig bei Temperaturen um den Siedepunkt des verwendeten Lösungsmittels durchgeführt.<sup>17</sup> Liegt die gewählte Reaktionstemperatur über dem Siedepunkt des Lösungsmittels wird von einer Solvothermalsynthese gesprochen, bei Wasser als Lösungsmittel entsprechend von einer Hydrothermalsynthese.<sup>16, 18</sup> Um ein Verdampfen des Lösungsmittels zu verhindern wird die Solvothermalsynthese dabei in dicht verschließbaren Reaktionsgefäßen, wie z.B. Stahlautoklaven durchgeführt (Abb. 02). Diese Stahlautoklaven beinhalten dabei Einsätze aus Teflon, welche die Reaktanden, Additive und Lösungsmittel enthalten.<sup>19</sup> Die Verwendung von Teflon als Reaktionsgefäß ist besonders geeignet, da es bis ca. 210 °C stabil ist ohne sich zu verformen und besonders inert gegenüber Säuren und Basen ist. Teflon hat zum anderen jedoch den Nachteil, dass es durch seine poröse Struktur Verunreinigungen wie z.B. Amine einlagert, welche dann in einer nachfolgenden Synthese diese stören oder zu Verunreinigungen des Reaktionsproduktes führen könnten.<sup>16</sup> Im Vergleich zu den Stahlautoklaven ist ebenfalls die Verwendung von Glasreaktoren möglich. Hierbei ist jedoch zu beachten, dass diese Gefäße bei zu hohem Druck bersten können und Reaktionen mit Fluoriden oder starken Basen das Glas zersetzen können. Durch das Erhitzen über den Siedepunkt des Lösungsmittels hinaus baut sich ein autogener Druck auf, welcher in Kombination mit der Temperatur einige physikalische und chemische Eigenschaften des Reaktionsgemisches beeinflusst.<sup>17</sup> Bei der Verwendung von Wasser als Lösungsmittel nimmt im Allgemeinen die Löslichkeit der Reaktanden und die Dielektrizitätskonstante zu sowie der pH Wert und die Viskosität ab.<sup>18</sup>



**Abbildung 02.** Lichtbild eines gebräuchlichen 30 mL Stahlautoklaven mit Tefloneinsatz (links) und 7 mL Glasgefäß (rechts) zur Durchführung von Solvothermalsynthesen.

## 2.2 Hochdurchsatzmethoden

Ein Problem bei der Verwendung von Solvothermalsynthesen ist die Nicht-Vorhersagbarkeit der sich bildenden Reaktionsprodukte. Dieses kann von kleinsten Änderungen wie z.B. Temperatur, Druck, pH Wert, Konzentration, Art und Größe des Reaktionsgefäßes aber auch den verwendeten Aufheiz- und Abkühlraten abhängen.<sup>16, 19</sup>

Um diese oftmals großen Phasenräume, in denen kristalline Produkte entstehen können, möglichst effizient abzusuchen eignen sich im besonderen Maße die Hochdurchsatzmethoden. Diese sind im Arbeitskreis Stock schon seit vielen Jahren etabliert und bieten mannigfaltige Vorteile gegenüber Einzelsynthesen.<sup>19</sup> Durch die Verwendung von Reaktoren, welche maximal 24 bzw. 48 Tefloneinsätze fassen können, ist es möglich nebeneinander während einer Reaktion mehrere Reaktionsparameter zu variieren. Diese Parallelisierung der Durchführung von Reaktionen ermöglicht es mit Hilfe der nachfolgenden röntgenographischen Analyse der Reaktionsprodukte etwaige Trends aufzudecken. Beispielsweise kann der Einfluss des pH-Wertes, der Reaktandenverhältnisse, der Konzentration oder des Lösungsmittels in nur wenigen Hochdurchsatzexperimenten vollständig untersucht werden.<sup>16</sup> Bei der Durchführung von Hochdurchsatzexperimenten im Arbeitskreis Stock werden anstatt der 30 mL Tefloneinsätze für Reaktoren sehr viel kleinere Einsätze von 0.3 (48er Reaktor) bzw. 2 mL (24er Reaktor) verwendet, was zu einer Miniaturisierung und somit zu Kostenersparnissen durch geringere Reaktandenmengen führt.<sup>19</sup> Nach dem Befüllen der Tefloneinsätze mit den Reaktanden, Additiven und Lösungsmitteln werden diese in einen Metallblock

eingesetzt und zwei Teflonfolien auf die Tefloneinsätze gelegt. Der Metallblock wird wiederum in den eigentlichen Reaktor eingesetzt, verschlossen und einem definierten Temperatur-Zeit-Programm unterworfen (Abb. 03, links). Die Abtrennung der Reaktionsprodukte erfolgt mittels eines entsprechenden Hochdurchsatz-Filtrierblocks (Abb. 03, Mitte) für 48 Proben. Aufgebaut ist dieser Filtrierblock zum einen aus einem Gehäuse, an dem sich ein Vakuum-Anschluss befindet, darüber befinden sich zwei Gummifolien, zwischen denen sich zwei Filterpapiere in einem Probenträger befinden. Wiederum darüber befindet sich ein Teflonblock mit Aussparungen für 48 Proben in den das Reaktionsprodukt hineinpipettiert wird. Zusammengehalten wird alles durch einen Rahmen aus Metall, welcher mittels Schrauben auf dem Gehäuse fixiert wird. Die Reaktionsprodukte werden beim Abfiltrieren aus der Teflonhülse in den Filtrierblock pipettiert und diese gegebenenfalls mit Lösungsmitteln gewaschen. Die röntgenographische Charakterisierung erfolgt wiederum mittels des in den Filtrierblock eingebauten Probenträgers (Abb. 03, rechts) an einem Hochdurchsatzdiffraktometer mit xy-Tisch, sodass die einzelnen Proben angesteuert werden können. Eine Automatisierung des gesamten Prozesses kann des weiteren durch Einsatz von Pipettier- oder Einwiegerobotern geschehen.

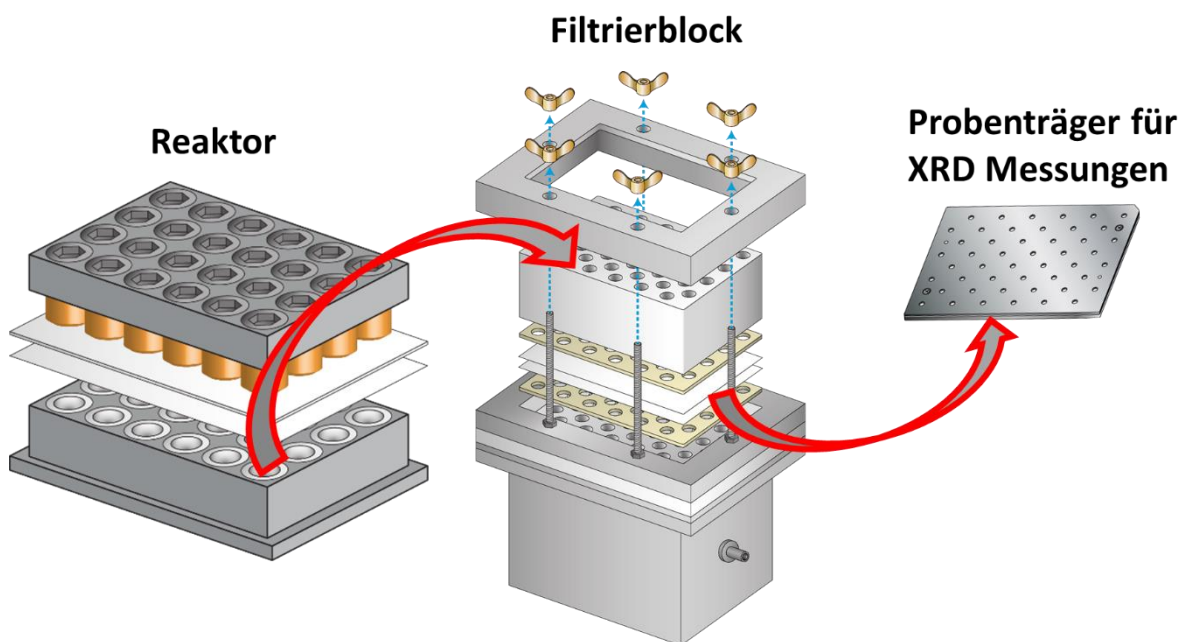


**Abbildung 03.** Schematische Skizze des Hochdurchsatzreaktors (links), des geöffneten Filtrierblocks (Mitte) und des Probenträger für röntgenographische Messungen am Hochdurchsatzdiffraktometer.



### 3 Charakterisierungsmethoden

In dieser Arbeit wurden eine Vielzahl von Charakterisierungsmethoden verwendet, um spezifische Stoffeigenschaften zu bestimmen. In Tabelle 01 sind die einzelnen Charakterisierungsmethoden und Geräte, sowie in Tabelle 02 die entsprechenden Auswertungsprogramme zur Datenanalyse aufgeführt. Detaillierter wird in diesem Abschnitt auf die Einkristallstrukturanalyse und die Strukturbestimmung mittels Elektronenbeugung eingegangen.

**Tabelle 01.** In dieser Arbeit verwendete Charakterisierungsmethoden mit Geräte-Typen.

Charakterisierungsmethode	Gerät	Bemerkung
Gassorption	Belsorp <sub>max</sub> von Bel Japan Inc.	Stickstoff, 77 K H <sub>2</sub> O, 298 K
Pulverdiffraktometrie	Stoe Stadi P/MP Mythen-Detektor	Transmissionsgeometrie Cu-K $\alpha_1$ ( $\lambda = 1.5406 \text{ \AA}$ ), xy-Proben Tisch
Einkristallstruktur-Analyse	Stoe IPDS II, Bruker D8 Venture	Mo-K $\alpha_1$ ( $\lambda = 0.7107 \text{ \AA}$ )
IR-Spektroskopie	Bruker Alpha-P, Thermo-Fischer NICOLET 6700	4000 - 400 cm <sup>-1</sup> Diamant ATR Einheit
UV-Spektroskopie	Spectroquant Pharo 300 M	250-800 nm
<sup>1</sup> H-NMR-Spektroskopie	Bruker Avance 200, Bruker ARX 300, Bruker DRX 500	Messungen in deuterierten Lösungsmitteln bei 300 K, Referenzierung: TMS, in D <sub>2</sub> O gegen Wasser
Elementaranalyse	HEKAtech Euro EA Elemental Analyzer	Elemente: CHNS referenziert auf Sulfanilamid
DTA-TG Analyse	Netzsch STA-409CD	Luftstrom: 75 ml/min Aufheizrate: 1K/min
SEM, EDX	Philips ESEM XL 30, JEOL JSM-7401F	Rasterelektronenmikroskop
TEM	TECNAI F30 S-TWIN, JEOL JEM-2100	300 kV
XANES	Rigaku R-XAS spectrometer	12 kV, 80 mA Johansson-type Ge (220) crystal

**Tabelle 02.** In dieser Arbeit verwendete Programme mit Verwendungsart.

<b>Programm</b>	<b>Verwendung</b>
Stoe WinXPow <sup>20</sup>	Graphische Darstellung von Pulverdiffraktogrammen und Konvertierung in andere Formate
Topas Academics 4.1 <sup>21</sup>	Indizierung, Verfeinerung von Zellparametern mit Pawley- und LeBail-Methoden, Strukturverfeinerung mit Rietveld-Methode
PowderCell <sup>22</sup>	Raumgruppenkonvertierung
Materials Studio 5.0 <sup>23</sup>	Erstellung von Strukturmodellen, Geometrieoptimierung mittels Kraftfeldberechnung, theoretische Berechnung von spezifischen Oberflächen
Diamond 3.1 <sup>24</sup>	Visualisierung von Strukturen
Platon <sup>25</sup>	Überprüfung von Einkristallstrukturen, Porenvolumina, voids, höhere Symmetrie, Verzwilligung
ADT3D software <sup>26, 27</sup>	Verarbeitung von Elektronenbeugungsdaten
SIR2014, <sup>28</sup> Shelx-s,-l, -xt <sup>29-31</sup> SAINT V9.32B, <sup>32</sup>	Strukturlösung, -verfeinerung



### 3.1 Einkristallstrukturanalyse

Die Ursprünge der Einkristallstrukturanalyse liegen in der Mitte des 19. Jahrhunderts mit der Theorie des Kristallgitters und den 14 möglichen Gittern nach Bravais (1850) sowie der Identifizierung der 230 Raumgruppen nach Fedorow und Schönflies (1891). Anfang des 20. Jahrhunderts entdeckte Laue (1912), dass Kristalle Röntgenstrahlen beugen können. Nur ein Jahr später konnten erstmals Vater und Sohn Bragg die Kristallstruktur von NaCl bestimmen. Durch diese Entdeckungen sowie die Arbeiten von Miller 1939 konnten ab diesem Zeitpunkt unzählige Kristallstrukturen aufgeklärt werden.<sup>33</sup>

Bei einem Kristall handelt es sich um einen homogenen, anisotropen und aus 3D translationsperiodisch angeordneten Struktureinheiten bestehenden Körper. Der Kristall ist dabei aus identischen Wiederholungseinheiten, der Elementarzelle aufgebaut, welche in alle drei Raumrichtungen vervielfacht, den Kristall ergibt. Somit kann die Gesamtinformation des Kristalls auf die der Elementarzelle reduziert werden, was die zu bestimmende Information bei einer Einkristallstrukturanalyse bereits stark reduziert. Eine Elementarzelle ist immer durch ihre Metrik, ihre drei Kantenlängen  $a$ ,  $b$ ,  $c$ , den Elementarzellen Vektoren und den Winkeln  $\alpha$ ,  $\beta$ ,  $\gamma$ , als Winkel zwischen diesen Vektoren, aufgebaut. Die Art und Weise wie einzelne Elementarzellen aneinander gesetzt sind, wird als Gitter beschrieben, wobei jeder Punkt dieses Gitters den Ursprung einer Elementarzelle darstellt. Jeder Punkt innerhalb einer Elementarzelle wiederum kann mittels seiner fraktionellen Koordinaten  $a/x$ ,  $b/y$ ,  $c/z$  als Bruchteile der Kantenlängen beschrieben werden.<sup>33, 34</sup>

Die Tatsache, dass Kristalle aus translationsperiodisch angeordneten Struktureinheiten aufgebaut sind, wird sich bei der Einkristallstrukturanalyse zunutze gemacht. Durch Streuung von Strahlung, welche sich im Wellenlängenbereich von atomaren Abständen befindet (Röntgenstrahlung), kann eben diese Periodizität sichtbar gemacht werden. Röntgenstrahlen wechselwirken mit Elektronen und werden elastisch an ihnen gestreut. Aus dieser Streuung an unterschiedlichen Streuzentren in einem Kristall können die resultierenden Strahlen entweder konstruktiv oder destruktiv miteinander interagieren (Abb. 04). Konstruktive Interferenz entsteht dabei, wenn der Gangunterschied  $2d \sin\theta$  zweier Wellen, mit  $\theta$  dem Beugungswinkel und  $d$  dem Abstand zweier Netzebenen, ein ganzzahliges Vielfaches  $n$  der Wellenlänge  $\lambda$  entspricht (Beugungsbedingung). Entspricht der Gangunterschied nicht einem Vielfachen der Wellenlänge führt dies zu destruktiver Interferenz und es werden keine Reflexe beobachtet. Dieser Sachverhalt wird durch die Bragg-Gleichung (01) beschrieben.<sup>33, 34</sup>

$$n \lambda = 2d \sin\theta$$

(01)

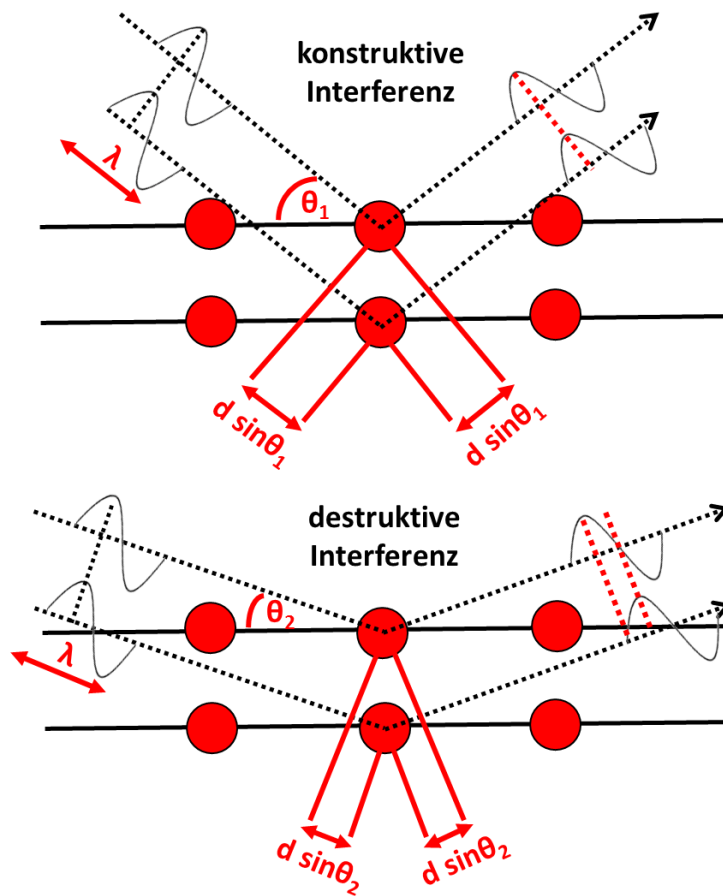


**Abbildung 04.** Schematische Darstellung für konstruktive und destruktive Interferenz nach Bragg. Oben: Der Gangunterschied  $d \sin\theta$  ist ein ganzzahliges Vielfaches  $n$  von der Wellenlänge  $\lambda$  resultierend in konstruktiver Interferenz  $2d \sin\theta = n \lambda$ . Unten: Destruktive Interferenz da  $2d \sin\theta \neq n \lambda$ .

Ein solches winkelabhängig gemessenes Beugungsexperiment, liefert ein sogenanntes Beugungsbild, wobei je nachdem, ob die Beugungsbedingung erfüllt ist oder nicht, Reflexe auftauchen. Die Erfüllung der Beugungsbedingung hängt von der vorhandenen Symmetrie im Realraum ab und die Abstände der Reflexe von der Zellmetrik.<sup>34</sup>

Im folgenden wird auf vorkommende Symmetrie in Kristallen näher eingegangen. Als mögliche Symmetrieeoperationen existieren Rotationsachsen (2, 3, 4 und 6), Spiegelebenen ( $m$ ), Inversionszentren ( $\bar{1}$ = Punktspiegelung) sowie die Kombinationen aus diesen, die Rotoinversionen ( $\bar{3}$ ,  $\bar{4}$ ,  $\bar{6}$ ), Schraubachsen (2, 3, 4 und 6-fach= Rotation+Translation) und Gleitspiegelebenen ( $a$ ,  $b$ ,  $c$ ,  $d$ ,  $n$ = Spiegelung+Translation).<sup>33</sup> Kristalle, welche Inversionssymmetrie aufweisen sind zentrosymmetrisch. Abgesehen von dem entsprechenden Symmetrieelement, dem Inversionszentrum, entsteht Inversionssymmetrie ebenfalls, wenn z.B. drei Spiegelebenen senkrecht aufeinander

stehen (Bsp. mmm), sowie wenn sich eine Rotationsachse senkrecht auf einer Spiegelebene (Bsp. 2/m) befindet.<sup>33, 35</sup>

Im dreidimensionalen Raum existieren sieben Kristallsysteme (Tab. 03), welche durch die Kantenlängen  $a$ ,  $b$ ,  $c$ , und den Winkeln  $\alpha$ ,  $\beta$ ,  $\gamma$  charakterisiert sind. Bei der Bestimmung des Kristallsystems ist zu beachten, dass immer die Symmetrie der Kristallstruktur das Kristallsystem bestimmt und nicht die Metrik der Zelle. Dies bedeutet z.B., dass bei kubischer Metrik nicht unbedingt ein kubisches Kristallsystem vorliegen muss, sondern dieses nur vorliegt wenn sich vier dreizählige Achsen unter einem Winkel von  $109.5^\circ$  schneiden (Tab. 03). Die minimalen Symmetriebedingungen sowie die Metrik der sieben Kristallsysteme sind in Tabelle 03 gezeigt.<sup>33, 36</sup>

**Tabelle 03.** Die sieben möglichen Kristallsysteme mit minimalen Symmetriebedingungen.<sup>35, 37, 38</sup>

Kristallsystem	Minimale Symmetriebedingung	Achsenlängen	Gitterwinkel
triklin	keine	$a \neq b \neq c$	$\alpha \neq \beta \neq \gamma \neq 90^\circ$
monoklin	eine zweizählige Achse oder eine Spiegelebene	$a \neq b \neq c$	$\alpha = \gamma = 90^\circ$ , $\beta \neq 90^\circ$
orthorhombisch	Kombination aus drei senkrecht aufeinander stehenden zweizähligen Achsen oder Spiegelebene	$a \neq b \neq c$	$\alpha = \beta = \gamma = 90^\circ$
tetragonal	eine vierzählige Achse oder vierzählige Inversionsachse	$a = b \neq c$	$\alpha = \beta = \gamma = 90^\circ$
hexagonal	eine sechszählige Achse oder sechszählige Inversionsachse	$a = b \neq c$	$\alpha = \beta = 90^\circ$ , $\gamma = 120^\circ$
trigonal	eine dreizählige Achse	$a = b \neq c$	$\alpha = \beta = 90^\circ$ , $\gamma = 120^\circ$
kubisch	vier dreizählige Achsen, welche sich unter einem Winkel von $109.5^\circ$ schneiden	$a = b = c$	$\alpha = \beta = \gamma = 90^\circ$

Unter Berücksichtigung von Zentrierungen ergeben sich anhand der sieben Kristallsysteme 14 Bravais-Gitter. Dabei existieren vier verschiedene Gittertypen: P= primitiv, C-, A- und B-zentriert (= c, a, b-Achse, senkrecht auf der Zentrierung), I= innenzentriert und F= flächenzentriert. Anhand der nicht-translationsabhängigen Symmetrieelemente ergeben sich 32 Punktgruppen und durch Kombination dieser mit den translationsabhängigen Symmetrieelementen (Zentrierungen, Schraubachsen und Gleitspiegelebenen) führt dies zu den 230 Raumgruppen.<sup>33, 34</sup>

Oftmals sind mehrere Elementarzellen anhand des Beugungsbildes möglich. Die Wahl der richtigen Elementarzelle ergibt sich daher, wenn die Aneinanderreihung von Elementarzellen ohne Rotation oder Spiegelung zum Kristall führt. Des Weiteren muss es von den übrigen möglichen Zellen, die kleinste mit höchster Symmetrie sein, sowie der Ursprung möglichst immer auf einem Inversionszentrum liegen.<sup>33, 34</sup>

Die Symmetrie im Realraum manifestiert sich, indem zwei oder mehr identische Gruppen von Atomen (Motive) durch die Symmetrieoperationen erzeugt werden und somit die Elementarzelle füllen. Dieses Motiv wird asymmetrische Einheit genannt. Somit existiert in einer Elementarzelle eine bestimmte Anzahl an symmetrie-äquivalenten Positionen an denen dieses Motiv in Abhängigkeit der Raumgruppe erscheint.<sup>33</sup>

Die Symmetrie eines Beugungsbildes im reziproken Raum hängt von der Symmetrie im Realraum ab, wobei sich die Symmetrie im reziproken Raum in den diskreten Gitterpunkten (Lage + Intensität) widerspiegelt. Das Beugungsmuster im reziproken Raum ist meistens zentrosymmetrisch (Friedelsches Gesetz), auch wenn die Symmetrie kein Inversionszentrum aufweist. Daher sind anhand des Beugungsbildes zentrosymmetrische und nicht-zentrosymmetrische Raumgruppen nicht zu unterscheiden. Dies gilt jedoch nicht streng, durch Effekte wie anomale Streuung ergeben sich leichte Intensitätsunterschiede zwischen  $I(hkl)$  und  $I(-h-k-l)$  und somit leichte Abweichungen von der Inversionssymmetrie, sodass die entsprechende Symmetrie oftmals doch richtig bestimmt werden kann. Die Symmetrie im reziproken Raum kann dabei durch die 11 Lauegruppen beschrieben werden. Die Lauegruppe reduziert die 32 möglichen Punktgruppen auf diejenigen, welche ein Inversionszentrum aufweisen. Im monoklinen Kristallsystem ergibt sich somit, dass die Punktgruppen  $2/m$ ,  $2$  und  $m$  alle der Lauegruppe  $2/m$  zuzuordnen sind. Dies führt dazu, dass in erster Näherung nur die 11 Lauegruppen ( $\bar{1}$ ,  $2/m$ ,  $mmm$ ,  $4/m$ ,  $4/mmm$ ,  $\bar{3}$ ,  $\bar{3}m$ ,  $6/m$ ,  $6/mmm$ ,  $m\bar{3}$  und  $m\bar{3}m$ ) aus dem Beugungsbild nicht aber die 32 Punktgruppen erhalten werden können.<sup>33-35</sup>

Jeder Gitterpunkt im reziproken Raum  $g_{hkl}$  kann beschrieben werden als  $g_{hkl} = ha + kb + lc$  wobei  $hkl$  als Millersche Indizes bezeichnet werden. Jeder reziproke Gitterpunkt  $hkl$  beschreibt eine Gruppe von parallelen Ebenen (Bragg-Ebenen, Netzebenen) im Realraum. Die Orientierung dieser Ebenen ist durch die Millerschen Indizes  $hkl$  definiert. Diese Ebenen schneiden die Zellachsen in ganzzahligen Bruchstücken in den drei Punkten  $a/h$ ,  $b/k$  und  $c/l$ , wobei somit auch die Elementarzelle in entsprechende Teile zerschnitten wird. Dieser Sachverhalt ist in Abbildung 05 für einige ausgewählte  $hkl$  Indizes in 2D Ansicht verdeutlicht.<sup>33</sup>

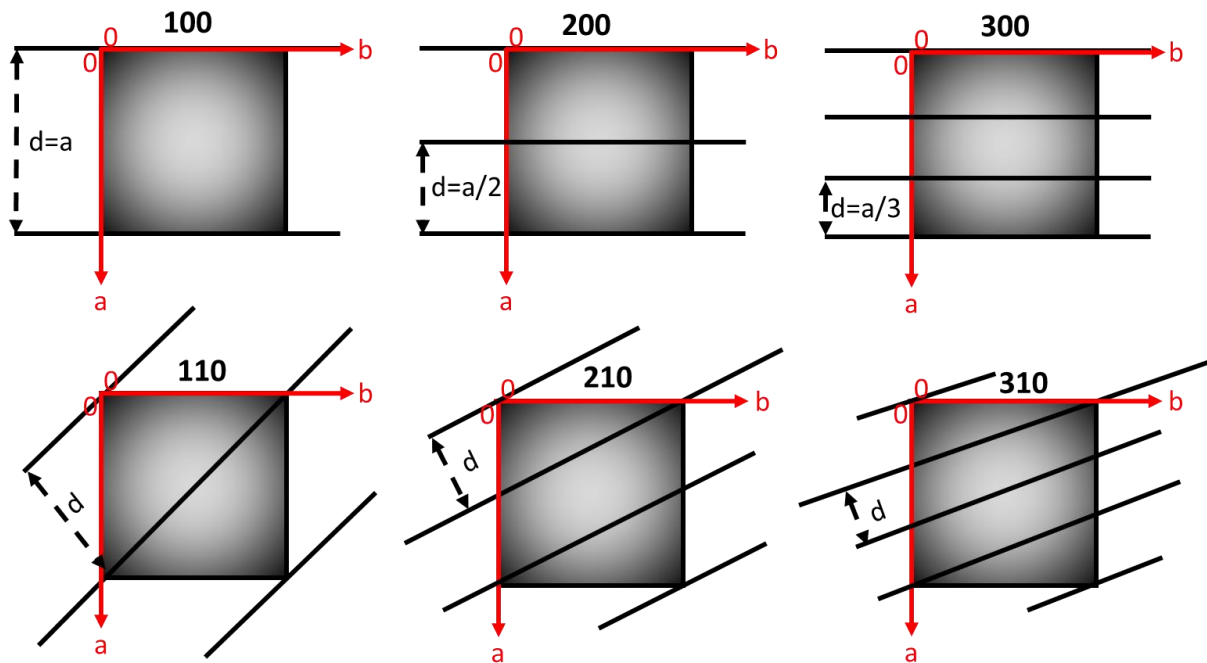


**Abbildung 05.** Schematische Darstellung einiger ausgewählter Netzebenen anhand der jeweiligen Millerschen Indizes in 2D Ansicht.

Der Abstand zweier Ebenen  $d$  ist dabei umgekehrt proportional zur Länge des reziproken Gittervektors  $g$ :  $d_{hkl}=1/|g_{hkl}|$ . Dies bedeutet, dass um so größer die Zellparameter im Realraum sind, desto kleiner sind die reziproken Gittervektoren und somit die Abstände zweier Reflexe im reziproken Raum. Zur Bestimmung der Zellparameter aus den gemessenen  $2\theta$  Werten wird die quadratische Braggsche Gleichung (Gl. 2) herangezogen. Im kubischen Kristallsystem kann diese Formel aufgrund der gleichen Kantenlängen und Winkel von  $90^\circ$  vereinfacht werden zu Gl.3, wobei wiederum  $\theta$  dem Beugungswinkel,  $a$ ,  $b$  und  $c$  den Achsenlängen der Elementarzelle,  $\alpha$ ,  $\beta$  und  $\gamma$  den Winkeln der Elementarzelle und  $\lambda$  der eingestrahlten Wellenlänge entspricht.<sup>33, 34</sup>

$$\begin{aligned} \sin^2(\theta) = & \frac{\lambda^2}{4} \left[ h^2 \frac{1}{V} bc \sin(\alpha) + k^2 \frac{1}{V} ca \sin(\beta) + l^2 \frac{1}{V} ab \sin(\gamma) \right. \\ & + 2kl \frac{1}{V} ca \sin(\beta) \frac{1}{V} ab \sin(\gamma) \frac{\cos(\beta) \cos(\gamma) - \cos(\alpha)}{\sin(\beta) \sin(\gamma)} \\ & + 2lh \frac{1}{V} ab \sin(\gamma) \frac{1}{V} bc \sin(\alpha) \frac{\cos(\gamma) \cos(\alpha) - \cos(\beta)}{\sin(\gamma) \sin(\alpha)} \\ & \left. + 2hk \frac{1}{V} bc \sin(\alpha) \frac{1}{V} ca \sin(\beta) \frac{\cos(\alpha) \cos(\beta) - \cos(\gamma)}{\sin(\alpha) \sin(\beta)} \right] \end{aligned} \quad (02)$$

$$\sin^2(\theta) = \frac{\lambda^2}{4a^2} [h^2 + k^2 + l^2] \quad (03)$$

Bei weiterer Begutachtung des Beugungsbildes fällt oftmals auf, dass in bestimmten Bereichen, oder in definierten Abständen Reflexe fehlen. Diese systematischen Auslöschungen werden durch die zuvor erwähnten translationsabhängigen Symmetrioperationen (Zentrierungen (integrale), Gleitspiegelebenen (zonale) und Schraubachsen (serielle)) erzeugt. Anhand dieses systematischen Fehlens von Reflexen kann die Raumgruppe bestimmt werden. Dennoch gibt es mehrere Raumgruppen, welche anhand ihrer translationsabhängigen Symmetrioperationen die gleichen Auslöschungsbedingungen aufweisen. Dies sei anhand des Beispiels der vier monoklinen Raumgruppen  $C_2$ ,  $C_m$ ,  $C_c$  und  $C_2/c$  verdeutlicht. In diesen vier Raumgruppen sind die translationsabhängigen Symmetrioperationen die C-Zentrierung und die c-Gleitspiegelebene. Dies bedeutet, dass die Paare  $C_2$  und  $C_m$  sowie  $C_c$  und  $C_2/c$  jeweils nicht zu unterscheiden sind, da sie dieselben translationsabhängigen Symmetrioperationen aufweisen und somit dieselben systematischen Auslöschungen im Beugungsbild verursachen. In Tabelle 04 sind einige Beugungsbedingungen und die entsprechenden Auslöschungsbedingungen für ausgewählte Symmetrioperationen gezeigt. Außer im hexagonalen und trigonalen Kristallsystem gilt, dass jeweils gerade Werte die Beugungsbedingung und ungerade Werte die Auslöschungsbedingung darstellen.<sup>33-35</sup>

**Tabelle 04.** Ausgewählte Symmetrieelemente mit Beugungs- und Auslöschungsbedingung, g=gerade und u=ungerade.<sup>39</sup>

Symmetrieelement (monoklin b-Achse)	Beugungsbedingung	Auslöschungsbedingung
C-Zentrierung	$h+k=2n=g$	$h+k=2n+1=u$
I-Zentrierung	$h+k+l=2n=g$	$h+k+l=2n+1=u$
F-Zentrierung	$h+k, h+l, k+l = 2n$ oder: $h, k, l$ g oder u	$h+k, h+l, k+l = 2n+1$
c-Gleitspiegelebene	$l=2n=g$	$l=2n+1=u$
n-Gleitspiegelebene	$l+h=2n=g$	$l+h=2n+1=u$
d-Gleitspiegelebene	$l+h=4n=g$	$l+h=4n+1=u$
$2_1, 4_2$ Schraubachse	$k=2n=g$	$k=2n+1=u$
$4_1, 4_3$ Schraubachse	$k=4n=g$	$k=4n+1=u$

Bisher wurde veranschaulicht, dass die Lage bzw. die Abwesenheit der Reflexe hkl die Bestimmung der Symmetrie und der Zellparameter einer Elementarzelle zulassen. Um die genaue Position und Sorte der Atome in einer Elementarzelle zu erhalten, müssen jedoch die Intensitäten I der Reflexe hkl herangezogen werden. Die Intensität I eines Reflexes hkl ist proportional zum Betragsquadrat des Strukturfaktors F (Gl. 04).<sup>33, 34</sup>

$$I \sim |F|^2 \quad (\text{Gl. 04})$$

Der Strukturfaktor  $F$  spiegelt die Fouriertransformierte der Elektronendichteverteilung innerhalb der Elementarzelle wieder. Der Strukturfaktor  $F(hkl)$  entspricht der Summe der sinusförmigen Wellen, welche untereinander verschoben sind. Die Information über die Phasenverschiebung geht bei der Messung verloren, da nur die Intensität  $I$  eines Reflexes detektiert wird.  $F(hkl)$  ist eine komplexe Zahl (Gl. 05), welche die Summe der einzelnen atomaren Streufaktoren (Atomformfaktor: Streukraft eines Atoms)  $f_j$  beinhaltet.<sup>33, 34</sup>

$$F(hkl) = \sum_{j=1}^N f_j(hkl) \cdot \exp[2\pi i(hx_j + ky_j + lz_j)] \quad (\text{Gl. 05})$$

Der atomare Streufaktor ist abhängig von der Strahlungsquelle (Röntgen-, Elektronen-, oder Neutronenstrahlung), dem Atomtyp, der thermischen Bewegung des Atoms und des Streuwinkels. Dabei ist zu beachten, dass bei Verwendung von Röntgenstrahlung der atomare Streufaktor mit steigendem Beugungswinkel abnimmt, dies bei Verwendung von Neutronenstrahlung jedoch nicht der Fall ist.<sup>33, 34</sup>

Der Strukturfaktor  $F(hkl)$  ist eine komplexe Zahl mit einem Amplituden Teil

$$|F(hkl)| = A(hkl) \quad (\text{Gl. 06})$$

und einem Phasen ( $\phi$ ) Teil

$$\exp[i\phi(hkl)] = iB(hkl). \quad (\text{Gl. 07})$$

Jeder einzelne Strukturfaktor  $F(hkl)$  kann als Funktion mit einem Sinus und einem Cosinus Teil mit gleicher Wellenlänge, durch Anwendung der Eulerschen Formel, beschrieben werden. Durch eine inverse Fouriertransformation kann der Strukturfaktor theoretisch in die resultierende Elektronendichte im Kristall überführt werden. Dieser Schritt wird in dieser Arbeit nicht näher diskutiert. Ein Problem dabei ist jedoch, dass die Phaseninformation  $\phi$  nicht erhalten wird (Phasenproblem).<sup>33, 34</sup> Um das Phasenproblem zu lösen werden unterschiedliche Methoden wie die Patterson- und die Direkte Methode herangezogen. Schwere Atome streuen stärker als leichtere, was zu höheren Intensitäten im Beugungsbild führt. Dies kann sich bei der Lösung des Phasenproblems mittels der Patterson-Methode als hilfreich herausstellen, da die Strukturfaktoren und dadurch die Phasen maßgeblich durch schwere Atome beeinflusst werden. Es werden hierbei die Phasen und Bindungsvektoren der Schweratome aus den Intensitäten extrahiert. Danach wird der Anteil der Schweratome an den Strukturfaktoren bestimmt und der restliche Anteil am Strukturfaktor resultiert somit aus den Leichtatomen.<sup>33, 34</sup>

Die Direkte Methode wurde 1953 von Hauptmann und Karle entwickelt. Bei der Direkten Methode werden (Start)-Phasen geschätzt und danach mittels statistischer Methoden die tatsächlichen Strukturfaktoren extrahiert. Dabei wird sich zunutze gemacht, dass die Phasen bestimmter Reflextripletts (hkl) korrelieren oder sogar gleich sind. Genauere mathematische Erläuterungen hierzu sind in dieser Arbeit nicht diskutiert. Trotzdem kann zur Illustration dargelegt werden, dass wenn wenige Reflexe betrachtet werden die Anzahl an möglichen Ergebnissen sehr groß ist. Je mehr Reflexe jedoch zu den statistischen Verfahren hinzugezogen werden, desto mehr reduziert sich die Anzahl an Möglichkeiten, wodurch das Phasenproblem in den meisten Fällen richtig gelöst wird.<sup>33, 34</sup>

Die anfängliche Strukturlösung liefert oftmals noch nicht die richtige Position der Elektronendichten in der Elementarzelle. Aus diesem Grund wird die Strukturlösung mittels least-squares Verfahren, wie sie in dem Programm shelxl enthalten sind, verfeinert. Dabei werden neue oder bestehende Elektronendichten jeweiligen Atomsorten zugeordnet, sowie z.B. Bindungslängen etc. verfeinert. Werden bei einer Verfeinerung zuerst die Elektronendichten der schwereren Atome bestimmt, können danach die Positionen von z.B. Nicht-Metall-Atomen verfeinert werden. Bei jedem Verfeinerungsschritt werden die Phasen und somit auch die Strukturfaktoren mitverfeinert. Die bereits zugeordneten Elektronendichten und daraus resultierende Strukturfaktoren dienen dabei als Anhaltspunkt, um die Strukturfaktoren der anderen Reflexe und somit die Positionen der weiteren Elektronendichten zu bestimmen. In jedem Verfeinerungsschritt wird sich somit der richtigen Struktur immer weiter angenähert.<sup>30, 33, 34</sup>

Eine weitere Fehlerquelle bei der Einkristallstrukturanalyse ist die thermische Bewegung der Atome. Um eben diese zu berücksichtigen wird eine anisotrope Verfeinerung der Atompositionen durchgeführt, bei der die Streurichtung verfeinert wird. Diese Verfeinerung resultiert dabei in Ellipsoiden. Ohne diese Verfeinerung liegt lediglich eine isotrope Verfeinerung vor, bei der die Atome als sphärische Kugeln beschrieben werden. Die anisotrope Verfeinerung ist von essentieller Wichtigkeit, da besonders bei leichten Atomen, durch die geringe Elektronendichte und höhere thermische Bewegung aber auch bei schweren Atomen, Abstände und Positionen falsch bestimmt werden, oder sogar zwei Atome gefunden werden, wo eigentlich nur ein einziges vorliegt.<sup>29, 30, 33, 34</sup>



### 3.2 Elektronenbeugung

Die Elektronenbeugung ist eine Methode zur Strukturbestimmung, bei der kleine Kristallite im nm- und kleinen  $\mu\text{m}$ -Bereich mittels Elektronen vermessen werden können. Die ersten Elektronenbeugungsexperimente wurden 1937 von Pinsker und Vainshtein durchgeführt. Bis zu diesem Zeitpunkt waren weder Techniken noch Theorien über Elektronenbeugung an Kristallen bekannt. Bereits zehn Jahre später wurde die erste Elektronendichtekarte von  $\text{BaCl}_2 \cdot \text{H}_2\text{O}$  aus Elektronenbeugungsdaten publiziert.<sup>40</sup>

Im folgenden wird auf einige Aspekte der Strukturbestimmung aus Elektronenbeugungsdaten eingegangen und vor allem Unterschiede zur Strukturbestimmung aus Röntgenbeugungsdaten herausgestellt.

Sowohl bei der Verwendung von Röntgenstrahlung als auch Elektronen wird das Phasenproblem beobachtet, es können zwar Intensitäten gemessen werden, aber nicht die korrekten Strukturformfaktoren bestimmt werden.  $I$  ist dabei ebenso proportional zum Betragsquadrat des Strukturformfaktors  $F$ :<sup>33</sup>

$$I \sim |F|^2$$

Auch bei der Elektronenbeugung müssen daher Methoden wie die Patterson oder die Direkte Methode angewendet werden, um die Struktur zu lösen. Die Direkte Methode wurde 1953 entwickelt und wurde bereits 1976 auf Elektronenbeugungsdaten angewendet. 1968 gelang es DeRosier und Klug erstmals Phase und Amplitude aus der Fouriertransformation elektronenmikroskopischer Beugungsdaten zu extrahieren. Bei der Aufnahme von HRTEM Beugungsbildern ist zu beachten, dass diese jeweils eine Überlappung aufweisen und daher Messungen in unterschiedlichen Orientierungen der Probe durchgeführt werden müssen. Ebenfalls durften die zu untersuchenden Proben dabei nur eine geringe Dicke aufweisen, um ein adäquates Beugungsbild zu erhalten. Dies führte jedoch wiederum in vielen Fällen zu einer höheren Strahlenempfindlichkeit der Proben. Wenk et al. zeigten dabei 1992 erstmals eine 3D Rekonstruktion aus mehreren kombinierten 2D Aufnahmen und seit 1995 wurden weitere Kristallstrukturen von Dorset et al. aus HRTEM Messungen bestimmt.<sup>33</sup>

Erste Elektronenbeugungsuntersuchungen wurden daher an Proben durchgeführt, die nur eine geringe Strahlenempfindlichkeit aufwiesen. Dabei handelte es sich um hochgeordnete anorganische Verbindungen mit kleinen Elementarzellen.<sup>33</sup>

Mittels Röntgenbeugungsuntersuchungen wurden bis 2010, ca. 500.000 organische, 135.000 anorganische und 70.000 Protein-basierte Kristallstrukturen bestimmt und im Vergleich dazu aber nur sehr wenige aus Elektronenbeugungsdaten. Die

Elektronenbeugung bietet jedoch einige Vorteile gegenüber der konventionellen Röntgenbeugung. Elektronen interagieren stärker mit Materie, was dazu führt, dass sehr kleine Kristalle vermessen werden können. Dabei liegt im Falle von Röntgenstrahlung die Grenze ungefähr bei  $50 \times 50 \times 50 \text{ } \mu\text{m}^3$ , während im Falle von Elektronenbeugung noch Kristalle von  $0.01 \times 0.1 \times 0.1 \text{ } \mu\text{m}^3$ , was ungefähr 10-20 Elementarzellen entspricht, vermessen werden können. Im Vergleich zu Röntgenstrahlung, können Elektronen fokussiert werden, was die Bildgebung erst möglich macht. Zudem ist die Interaktion der Elektronen mit den Kristallen anders als bei Röntgenstrahlung. Bei Röntgenbeugungsexperimenten wird die Elektronendichteverteilung detektiert und bei Elektronenbeugungsmessungen das elektrostatische Potential, welches durch die positiven Kerne und negativen Elektronen, erzeugt wird. Elektronen wechselwirken daher mit Elektronen und Kernen und nicht nur mit den Elektronen wie es bei der Röntgenbeugung der Fall ist. Auch bei Verwendung von Elektronen nimmt der Atomformfaktor mit steigendem Beugungswinkel ab, jedoch sind die einzelnen Streufaktoren für etwaige Atomsorten verschieden von denen bei Verwendung von Röntgenstrahlung. Es können bei Elektronenbeugungsexperimenten 10-100-fach mehr Reflexe erhalten werden und zudem Informationen über Defekte durch HRTEM Aufnahmen erhalten werden.<sup>33</sup>

Ein Problem der Wechselwirkung der Elektronen mit Materie stellt die Mehrfachstreuung dar, wodurch keine direkte Interpretation der HRTEM Aufnahmen möglich ist und ein sogenanntes image processing nötig wird. Dies macht oftmals hohe finanzielle Investitionen für Geräte und Programme notwendig, dennoch kann heutzutage bereits eine Auflösung  $\leq 1.5 \text{ } \text{Å}$  erreicht werden. Um die Mehrfachstreuung zu minimieren, ist es hilfreich wenn die zu vermessende Probe nur eine geringe Dicke aufweist. Zur Bestimmung von Einkristallstrukturen aus Röntgenbeugungsdaten werden heutzutage meistens Vierkreisdiffraktometer verwendet, wobei die Beugungsinformation aus vier Kreisen, durch Drehung der Probe mittels eines Goniometers, detektiert wird. Bei Elektronenbeugungsexperimenten wird die Probe in ein flaches Netz eingebracht, anhand dieses Aufbaus ist es lediglich möglich einen Teil des reziproken Raums zu untersuchen. Dies macht es nötig mehrere Messungen in verschiedenen Orientierungen des Netzes (bzw. an verschiedenen Kristallen) durchzuführen und diese danach zu kombinieren, um ein annähernd vollständiges Beugungsbild des kompletten Kristalls zu erhalten.<sup>33</sup>

Typische Elektronenmikroskope bestehen aus drei Hauptkomponenten dem Belichtungs-, dem Bildgebungs- und dem Aufnahmesystem. Das Belichtungssystem wiederum besteht aus Elektronenkanone und Kondensator, wobei die Elektronenkanone einen möglichst monochromatischen, hoch brillanten und wenig streuenden

Elektronenstrahl erzeugen soll. Das Filament einer solchen Elektronenquelle kann z.B. aus Wolfram oder LaB<sub>6</sub> bestehen. Der Kondensator besteht aus elektromagnetischen Linsen und Blenden und leitet die Elektronen weiter zur eigentlichen Probe, wobei der Strahl durch die Linsen fokussiert oder defokussiert und durch die Blenden die Anzahl der Elektronen, welche die Probe erreichen, begrenzt werden kann. Das Bildgebungssystem (Abb. 06) besteht ebenfalls aus elektromagnetischen Linsen und Blenden. Das Objektiv liegt direkt unterhalb der Probe und bestimmt die Auflösung, die Objektiv-Blende liegt hinter dem Brennpunkt des Objektivs, wo ein Beugungsbild erzeugt wird. Eine weitere Blende befindet sich wiederum dort, wo das Bild erzeugt wird und gestattet dem Nutzer die Auswahl eines bestimmten Bereichs. Außerdem sind weitere Zwischenlinsen unterhalb des Objektivs vorhanden, durch welche entweder ein Bild oder ein Beugungsbild vergrößert oder verkleinert werden kann. Des weiteren existiert noch eine Projektor-Linse, welche das endgültige (Beugungs)-Bild in das Aufnahmesystem projiziert.<sup>33</sup>

Zur Aufnahme der (Beugungs)-Bilder eignen sich verschiedene Systeme, wie einfache und günstige Fotofilme, CCD Kameras (charge-coupled device= ladungsgekoppeltes Bauteil) oder image plate Detektoren, wobei die beiden letzteren den Vorteil aufweisen, dass die erhaltenen Daten einfach digital gespeichert werden können.<sup>33</sup>

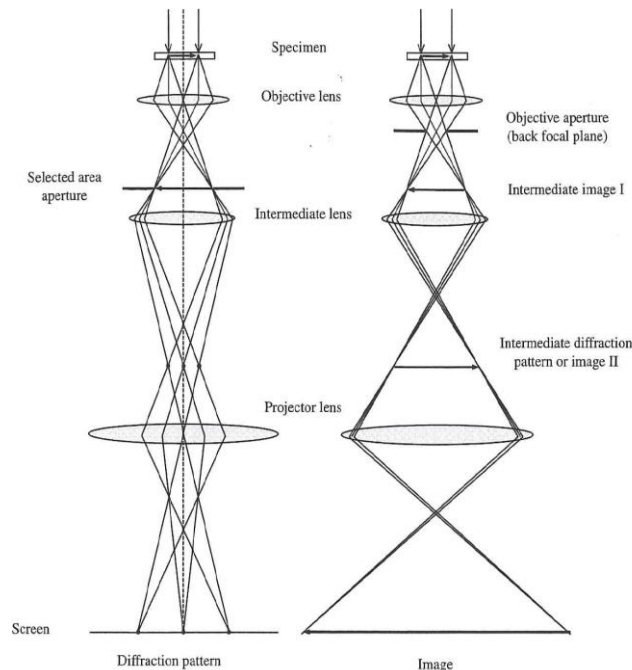


**Abbildung 06.** Schematische Darstellung des Aufbaus eines Elektronenmikroskops bei Erzeugung von Beugungsmustern oder Bildern.<sup>33</sup>

Wie zuvor beschrieben wechselwirken die eingestrahlteten Elektronen mit den Atomen der zu untersuchenden Probe. Die meisten Elektronen passieren die Probe ohne jegliche Interaktion (Primärstrahl), einige werden jedoch elastisch oder inelastisch

gestreut, wobei das Verhältnis bei ca. 50:50 liegt. Elastische Streuung tritt auf, wenn die Energie des Elektrons, welches auf die Probe trifft erhalten bleibt und nur die Richtung des Elektrons, durch Wechselwirkung mit dem elektrostatischen Potential der Probe, sich ändert. Elastisch gestreute Elektronen sind dabei diejenigen, welche zur Beugung und Bildgebung verwendet werden. Der atomare Streufaktor bei Elektronen beschreibt die Wahrscheinlichkeit, dass ein Elektron in eine bestimmte Richtung ( $2\theta$  in Relation zum einfallenden Strahl) gestreut wird. Bei niedrigen Streuwinkeln wird das Elektron hauptsächlich am Kernpotential, bei höheren Winkeln eher am außerhalb liegenden Elektronenpotential gestreut, was zu einer Phasenverschiebung mit steigendem Beugungswinkel führt, da das Elektron im Vergleich zur Streuung am Kernpotential einen längeren Weg zurück legen muss. Der Temperaturfaktor bzw. Debye-Waller Faktor beschreibt die thermische Schwingung von Atomen und lässt Atome somit größer erscheinen. Auch dieser Sachverhalt führt dazu, dass die Streukraft der Atome mit steigendem Beugungswinkel abfällt, da zusätzlich zu der Streuung am Kern- bzw. Elektronenpotential, die Bewegung der Atome dazu führt, dass immer weniger elektrostatisches Potential mit steigendem Beugungswinkel die Elektronen beeinflusst.<sup>33</sup>

Inelastische Streuung geht mit einem Energieübertrag auf die Atome der Probe einher. Es werden dabei oftmals Elektronen aus den Schalen der Atome geschlagen. Betrifft dies ein kernnahes Elektron, relaxiert ein Elektron aus einer höheren Schale in diese Lücke und emittiert die Energiedifferenz zwischen beiden Niveaus als charakteristische Röntgenstrahlung, welche spezifisch für jedes Element ist. Außerdem kann es zur Bildung sogenannter Auger-Elektronen kommen, wenn die Energiedifferenz nicht emittiert, sondern auf ein schwach gebundenes Elektron übertragen und dieses wiederum selbst emittiert wird. Herausgeschlagene Elektronen werden dabei als Sekundärelektronen bezeichnet und dienen zusammen mit den Rückstreuелеktronen bei der Rasterelektronenmikroskopie der Bildgebung. Außerdem tritt durch Wechselwirkung der eingestrahlten Elektronen mit dem Elektronenpotential Bremsstrahlung in Form von Röntgenstrahlung auf.<sup>33</sup>

## **II Kumulativer Teil**

Porphyrin-basierte Metall-Organische Gerüstverbindungen:  
Von Metall-Carboxylaten zu Metall-Phosphonaten

---

## 4 Porphyrin-basierte Metall-Organische Gerüstverbindungen: Von Metall-Carboxylaten zu Metall-Phosphonaten

### 4.1 Porphyrine

Das Porphyrin-Grundgerüst ist aus vier Pyrrol-Ringen aufgebaut, welche über ein weiteres Kohlenstoffatom miteinander verbrückt sind, an welchem sich oftmals weitere Reste wie funktionalisierte Aromaten befinden.<sup>41</sup> Porphyrine werden in den meisten Fällen durch Umsetzung von Pyrrol und einem Aldehyd hergestellt, die Synthese findet dabei z.B. in Propionsäure oder Essigsäure nach Adler<sup>41</sup> oder in DCM und DDQ mit  $\text{BF}_3$ -Ethanol nach Lindsey statt.<sup>42</sup> Die in dieser Arbeit verwendeten Porphyrine wurden dabei ausschließlich nach der Methode von Adler synthetisiert.<sup>41, 43</sup>

Durch die Amin-Gruppen der Pyrrol-Einheiten eines Porphyrins ist es ebenfalls möglich Metallkationen im Porphyrin-Zentrum zu komplexieren.<sup>44</sup> Die bekanntesten Vertreter der Porphyrine finden sich in der Natur in Form des Hämoglobins, einem Eisen-Porphyrin und dem roten Farbstoff des Blutes sowie des Chlorophylls, ein Magnesium-Porphyrin das in den Chloroplasten der Pflanzen vorliegt.<sup>45</sup> Hämoglobin ist in nahezu jedem Wirbeltier zu finden und dient dabei als Sauerstofftransporter durch den Körper. Sauerstoff bindet dabei an das aktive Eisen(II)-Zentrum des Porphyrins.<sup>46</sup> Chlorophyll in Pflanzen ist ein essentieller Bestandteil der Photosynthese und unterstützt die Photon-induzierte Exprimierung eines Elektrons zur Aktivierung der Photosynthese. Dabei absorbiert Chlorophyll das Licht und leitet es trichterförmig weiter, wobei es dann an zwei Chlorophyll-Einheiten zur Ladungstrennung kommt und ein Elektron freigesetzt wird.<sup>47</sup> Porphyrine kommen somit in nahezu jedem Lebewesen vor. Dadurch bedingt existieren biochemische Prozesse, wie z.B. der Bilirubin-Abbau des Hämoglobins (Abb. 07), um eben dieses abzubauen.<sup>48</sup>

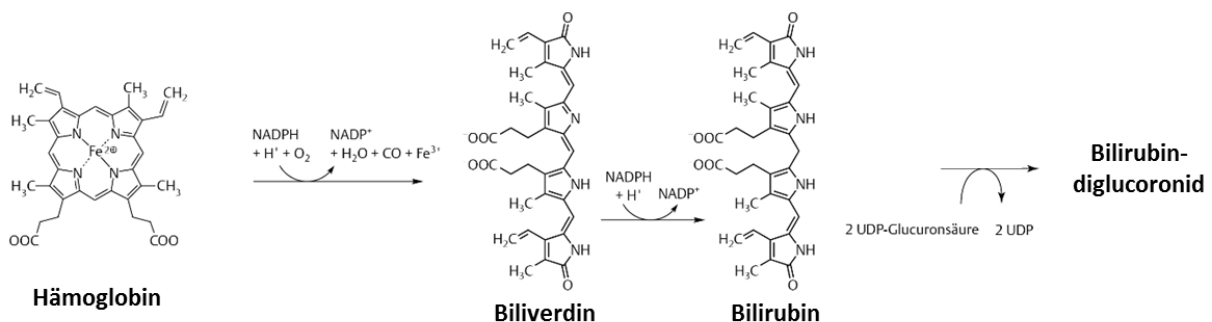


Abbildung 07. Schematische Darstellung des Hämoglobin Abbaus zu Bilirubin.<sup>48</sup>

Das Vorhandensein von natürlichen Abbaumechanismen lässt somit die Vermutung zu, dass Porphyrine oder zumindest bestimmte Porphyrine biokompatibel sind.<sup>45</sup>

Durch die mögliche Biokompatibilität ergeben sich eine Reihe von medizinischen Anwendungen. Porphyrine wurden z.B. in der Tumorbehandlung angewendet. Dabei wurden Haematoporphyrine oder Galactopyranosylcholesteryloxy-substituierte Porphyrine als Photosensitizer erforscht. Diese bilden unter Lichteinfluss zytotoxischen Singulett-Sauerstoff, wodurch sich mannigfaltige Anwendungsmöglichkeiten für Porphyrin-Photosensitizer im medizinischen Bereich, als antimikrobielle Agenzien in der Wasserbehandlung, Desinfektion oder zur Behandlung von Tumoren ergeben.<sup>49-51</sup> Durch ihr Vorkommen in der Natur eignen sich Porphyrine ebenfalls für die Nachahmung und Erforschung biologischer Prozesse wie z.B. der Photosynthese. Durch den Einsatz von Dendrimeren in Verbindung mit Zn-Porphyrinen wurde eine Nachahmung der Photosynthese durch das stark delokalisierte Elektronensystem des Moleküls erforscht. Es konnte dabei die benötigte Energie zur Erzeugung eines Elektrons aufgebracht werden. Die Lebenszeit des angeregten Zustands wird durch die dendritischen Baueinheiten verlängert. Somit können Rückschlüsse auf biochemische Prozesse, welche z.B. das Hämoglobin oder das Cytochrom-C in der Atmungskette beinhalten, nachvollzogen werden.<sup>52</sup>

Ein weiteres Feld in der Anwendung von Porphyrinen ergibt sich in der Sensorik, z.B. in der Detektion von gasförmigen Spezies. Insbesondere Metalloporphyrine zeigten dabei eine hohe Selektivität und wurden vielfältig untersucht. Gasförmige Spezies wie O<sub>2</sub>, CO, NO<sub>x</sub>, aber auch Amine binden dabei an das aktive Metallzentrum eines Porphyrins und verändern das Absorptionsspektrum. Dies kann optisch detektiert werden, was neben der Qualitativen auch eine Quantitative Gas-Detektion ermöglicht. Für die Sauerstoffdetektion wurde beispielsweise ein Pd-Tetracarboxyphenylporphyrin (Pd-H<sub>4</sub>T CPP)<sup>53, 54</sup> und für NO<sub>x</sub>- Spezies, sowie NH<sub>3</sub>-, CO-, und Triethylamin-Detektion Zn-Tetraphenylporphyrine (Zn-TPP) oder Fe-TPP-Cl Moleküle verwendet.<sup>55</sup> Aufgrund der besonderen Bedeutung von NO in der menschlichen Bioregulation konnte z.B. ein geeigneter Porphyrin-basierter Mikrosensor zur NO-Detektion im Körper entwickelt werden.<sup>56</sup>

Ein ebenfalls weit erforschtes Anwendungsgebiet für Porphyrine ist die Katalyse. Es wurden beispielsweise Porphyrin-basierte Katalysatoren für die Sauerstoff-Reduktion mittels Co-MTPP (Co-Tetramethoxyphenylporphyrin)<sup>57</sup> sowie Fe-TPP/TiO<sub>2</sub>/Graphit-Katalysatoren erforscht.<sup>58</sup> Weiterhin können derartige Metalloporphyrine als Katalysatoren für organische Synthesen verwendet werden. In der regioselektiven Epoxidierung von Dienen wurde beispielsweise ein Mn-TPP Katalysator verwendet,<sup>59</sup> sowie im photokatalytischen Abbau von Methylorange ein Fe-TPP/TiO<sub>2</sub>/Polystyrene-Katalysator.<sup>60</sup> Ebenfalls wurden Porphyrine in Halbleitermaterialien für organische Solarzellen eingesetzt oder zur Synthese neuer Plattformen genutzt, wobei dies durch



Adsorption von z.B. Fe-TPP, Ni-TPP oder Co-TPP auf C<sub>60</sub> Fullerenen in Form von SAMs (self assembled monolayers) gelang.<sup>61, 62</sup>

## 4.2 Porphyrin-basierte MOFs

Durch die Einbringung des Porphyrin-Motivs in die poröse Struktur von MOFs, können eine Vielzahl der bereits erwähnten Anwendungen auf die Porphyrin-basierten MOFs übertragen werden.<sup>63</sup> Die meisten Porphyrin-basierten MOFs enthalten das 4-Tetracarboxyphenylporphyrin (H<sub>6</sub>TCPP) als Linkermolekül, wobei ca. 40 Strukturen mit diesem Linker publiziert wurden und die meisten davon in den Übersichtsartikeln von Gao<sup>64</sup> und Huh<sup>65</sup> zusammengefasst sind.<sup>64-66</sup> Erste Arbeiten an Porphyrin-basierten MOFs mit dem H<sub>6</sub>TCPP Linker wurden dabei im Jahr 2000 und 2002 von Suslick et al. und Goldberg et al. durchgeführt und resultierten in mehreren porösen MOF Strukturen wie z.B. PIZA-1, [Co(Co-TCPP)<sub>1.5</sub>(C<sub>5</sub>H<sub>5</sub>N)<sub>3</sub>(H<sub>2</sub>O)]·11C<sub>5</sub>H<sub>5</sub>N.<sup>67, 68</sup>

Viele der publizierten Porphyrin-basierten MOFs enthalten zwei- oder vierwertige Kationen wie Zn<sup>2+</sup> oder Zr<sup>4+</sup>.<sup>64</sup> Eine Reihe von hochporösen Porphyrin-basierten Zr-MOFs konnten dabei von den Gruppen von Yaghi (MOF) und Zhou (PCN) erstmals hergestellt werden, darunter PCN-221,<sup>69</sup> MOF-545 (PCN-222<sup>94</sup>),<sup>70</sup> MOF-525,<sup>70</sup> PCN-223,<sup>71</sup> PCN-224<sup>72</sup> und PCN-225,<sup>73</sup> wobei einige der Verbindungen spezifische Oberflächen nach BET von weit über 2000 m<sup>2</sup> g<sup>-1</sup> aufweisen. Viele dieser MOFs konnten mit verschiedensten zwei- und dreiwertigen Kationen wie Cu<sup>2+</sup>, Co<sup>2+</sup>, Ni<sup>2+</sup>, Fe<sup>2+/3+</sup> oder Mn<sup>3+</sup> im Zentrum des Porphyrins synthetisiert werden.<sup>70, 72</sup> Ebenfalls wurden einige dieser Zr-MOFs bereits auf ihre katalytische Aktivität z.B. in der Oxidation von Cyclohexan (PCN-221)<sup>69</sup> oder der CO<sub>2</sub>/Propylenoxid Kupplung (PCN-224),<sup>72</sup> sowie die Einbringung von MOF-525 in Perowskit-Solar-Zellen resultierend in einer gesteigerten Zelleffizienz untersucht.<sup>74</sup> Weiterhin wurde die Verbindung PCN-222 als Cu(II) Sensor und Katalysator für die Heckreaktion (Abb. 08, oben)<sup>75</sup> sowie für die Photooxidation von Senfgas mittels Singulett-Sauerstoff (<sup>1</sup>O<sub>2</sub>)<sup>76</sup> oder für die Reduktion von Fe(III) zu Fe(II) im Porphyrinzentrum untersucht (Abb. 08, unten).<sup>77</sup>

Porphyrin-basierte Metall-Organische Gerüstverbindungen:  
 Von Metall-Carboxylaten zu Metall-Phosponaten

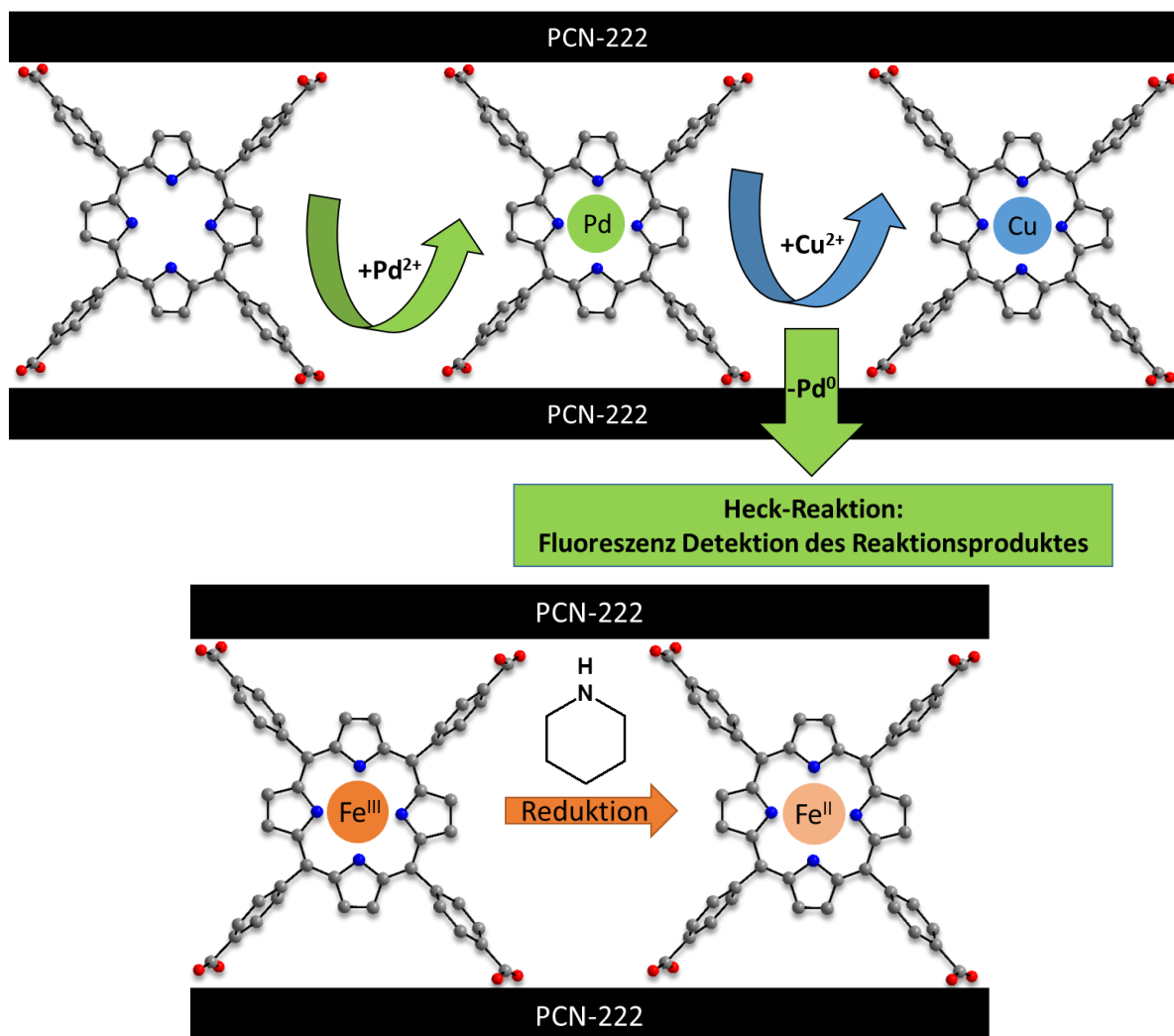


**Abbildung 08.** Anwendungsbeispiele für PCN-222 [ $\text{Zr}_6\text{O}_8(\text{H}_2\text{O})_8(\text{TCPP})_2$ ]; oben: Schematische Darstellung der  $\text{Cu}^{2+}$  Detektion durch Austausch mit  $\text{Pd}^{2+}$  (links), der Austausch von  $\text{Cu}^{2+}$  wurde durch die Fluoreszenz des Heck-Reaktionsproduktes (Pd als Katalysator) nachgewiesen<sup>75</sup> und unten: postsynthetische Reduktion von Fe(III) zu Fe(II) mittels Piperidin (Pip) im Porphyrinzentrum (Fe-PCN-222-Cl wird zu Fe-PCN-222-Pip<sub>2</sub>).<sup>77</sup>

Fe-MOF-525 wurde des weiteren als Katalysator für die elektrochemische  $\text{CO}_2$  Reduktion (Abb. 09),<sup>78</sup> Fe-PCN-223 für die Sauerstoffreduktion mit hoher  $\text{H}_2\text{O}/\text{H}_2\text{O}_2$  Selektivität<sup>79</sup> und Ni-PCN-224 für die Wasseroxidation untersucht.<sup>80</sup>

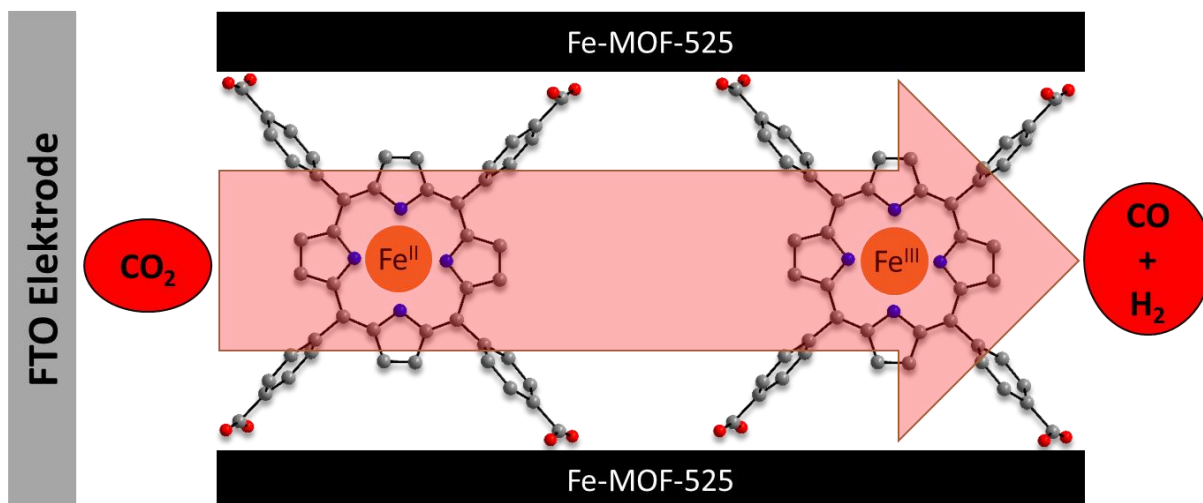


**Abbildung 09.** Schematische Darstellung der elektrochemischen  $\text{CO}_2$  Reduktion durch Fe-MOF-525  $[\text{Zr}_6\text{O}_4(\text{OH})_4(\text{Fe-TCPP})_3]$ .<sup>78</sup>

Des Weiteren wurde ein auf der fcu Topologie des bekannten UiO-66 basierender Hf-Porphyrin-MOF (DBC-UiO), welcher statt vier nur zwei Carbonsäuren trägt und somit die Geometrie des Terephthalsäure Moleküls nachahmt auf die Singulett-Sauerstoff ( $^1\text{O}_2$ ) Generierung zur effektiven Tumorbehandlung untersucht (Abb. 10).<sup>81</sup>

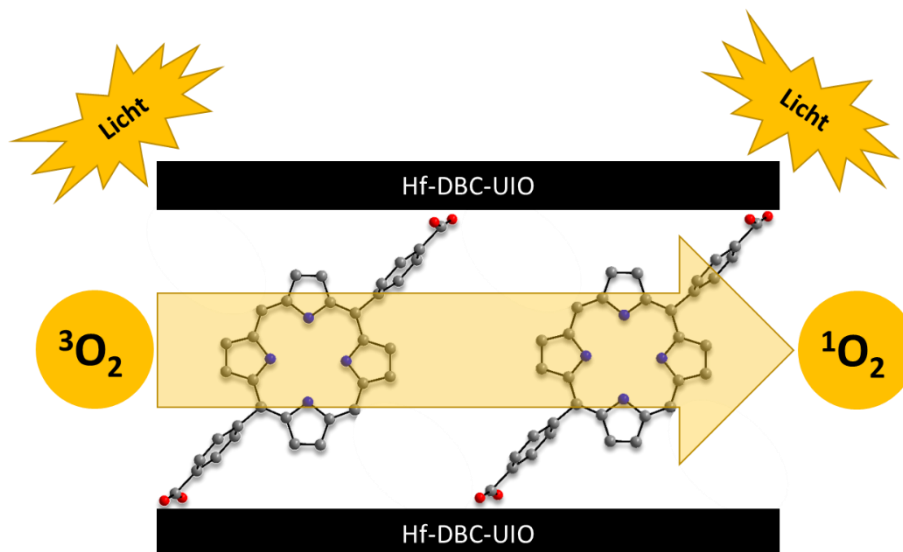


**Abbildung 10.** DBC-UiO  $[\text{Hf}_6(\text{O})_4(\text{OH})_4(\text{DBC})_6]$  (DBC=Dicarboxyphenylporphyrin) als photoaktiver MOF zur Singulett-Sauerstoff Generierung in der Tumorbehandlung.<sup>81</sup>

Außerdem sind auch einige Verbindungen mit dreiwertigen Kationen und dem  $\text{H}_6\text{TCPP}$  Linker bekannt. Darunter mit  $\text{Fe}^{3+}$  das PCN-600,<sup>82</sup> MIL-141  $[\text{NaFe}(\text{Ni-TCPP})]$ <sup>83</sup> und  $[\text{Fe}_2(\text{Fe-TCPP})(\text{C}_4\text{H}_4\text{N}_2)(\text{OH})_2]$  ( $\text{C}_4\text{H}_4\text{N}_2 = \text{Pyrazin}$ )<sup>84</sup> sowie mit den Gruppe 13 Kationen  $\text{Al}^{3+}$ ,  $\text{Ga}^{3+}$  und  $\text{In}^{3+}$  der Al-, Ga- und In-PMOF  $[\text{M}_2(\text{H}_2\text{TCPP})(\text{OH})_2] \cdot x \text{DMF} \cdot x \text{H}_2\text{O}$ .<sup>85, 86</sup> Der Al-PMOF wurde dabei für die photokatalytische  $\text{H}_2$ -Generierung an kolloidalem Platin untersucht.<sup>85</sup> Mit  $\text{Ga}^{3+}$  sind

neben dem PMOF keine und mit  $\text{In}^{3+}$  bis heute nur wenige Porphyrin-basierte In-MOFs bekannt (Linkermolekül in Klammern): Darunter MMPF-7,  $[\text{In}_{1.29}\text{O}_{0.57}(\text{T CPP})]$ ,<sup>87</sup> MMPF-8,  $[\text{In}(\text{In-T CBPP})] \cdot 12 \text{ DMF}$  ( $\text{H}_6\text{T CBPP}$ =Tetrakis-4-carboxybiphenylporphyrin)<sup>87</sup> und UNLPF-10,  $[\text{In}_3(\text{T BC PPP})]$  ( $\text{H}_{10}\text{T BC PPP}$ = Tetrakis-3,5-bis[4-carboxyphenyl]phenylporphyrin).<sup>88</sup> Der Vollständigkeit halber seien ebenfalls einige Lanthanoid MOFs mit dem  $\text{H}_6\text{T CPP}$  Linker und  $\text{Ce}$ ,<sup>89, 90</sup>  $\text{Nd}$ ,<sup>91</sup>  $\text{Sm}$ <sup>92</sup> und  $\text{Dy}$ <sup>91</sup> erwähnt, welche zwar alle kristallin sind aber ohne Physisorptionsmessungen veröffentlicht wurden.

Ein genauerer Blick auf die strukturelle Vielfalt in Porphyrin-basierten MOFs ergibt, dass fast alle publizierten MOFs in zwei Kategorien eingeteilt werden können (Abb. 11). Zum einen offene 3D Gerüste, wobei die potentiell metallierten Porphyrinzentren durch die Poren zugänglich sind. Hierbei existieren beispielsweise kubische Kristallstrukturen, bei der, wie in MOF-525,  $[\text{Zr}_6\text{O}_4(\text{OH})_4(\text{H}_2\text{T CPP})_3]$ , hexanukleare Zr-cluster auf den Ecken eines primitiven Gitters sitzen und sich durch Vernetzung mit den Linkern Käfige ausbilden.<sup>70</sup> Ein Ähnliches Motiv wird beispielsweise auch bei PCN-221 und PCN-224 beobachtet.<sup>69, 72</sup> Außerdem sind hexagonale Kristallstrukturen bekannt, welche ebenfalls hauptsächlich bei Zr-MOFs beobachtet werden und dabei oftmals große hexagonale Poren von mehreren Nanometern im Durchmesser wie in PCN-222  $[\text{Zr}_6\text{O}_8(\text{H}_2\text{O})_8(\text{T CPP})_2]$  aufweisen.<sup>94</sup> Weitere Beispiele für hexagonale Kristallstrukturen finden sich in MOF-545<sup>70</sup> und PCN-223.<sup>71</sup> Das zweite Strukturmotiv bei dem die Linkermoleküle parallel zueinander gestapelt sind und die anorganische Baueinheit oftmals aus eindimensionalen Baueinheiten besteht findet sich z.B. in der PMOF-Serie  $[\text{M}_2(\text{H}_2\text{T CPP})(\text{OH})_2]$  ( $\text{M} = \text{Fe}, \text{Al}, \text{Ga}, \text{In}$ ).<sup>84-86</sup> Hierbei sind die Porphyrinzentren durch die Stapelung der Porphyrin Linker meistens nicht zugänglich. Diese Verbindungen kristallisieren oftmals in tetragonaler Symmetrie, aber auch niedriger symmetrische wie monokline oder sogar trikline Kristallstrukturen wurden beobachtet. Diese Symmetrierniedrigung wird z.B. durch eine unsymmetrische anorganische Baueinheit in Form von Metallionen mit Koordinationszahlen größer sechs (MMPF-7  $[\text{In}_{1.29}\text{O}_{0.57}(\text{T CPP})]$ ,<sup>87</sup>  $[\text{Ce}_3(\text{T CPP})_2(\text{HCOO})(\text{H}_2\text{O})_3]$ <sup>90</sup>), nicht linearer Polyederverknüpfung  $[\text{Ce}_3(\text{T CPP})_2(\text{HCOO})(\text{H}_2\text{O})_3]$ <sup>90</sup>) oder aber der nicht exakten Stapelung der Linker  $[\text{Cd}_{1.25}(\text{Pd-H}_{1.5}\text{T CPP})(\text{H}_2\text{O})]$ <sup>93</sup> und  $[\text{Ce}_3(\text{T CPP})_2(\text{HCOO})(\text{H}_2\text{O})_3]$ <sup>90</sup>) hervorgerufen.

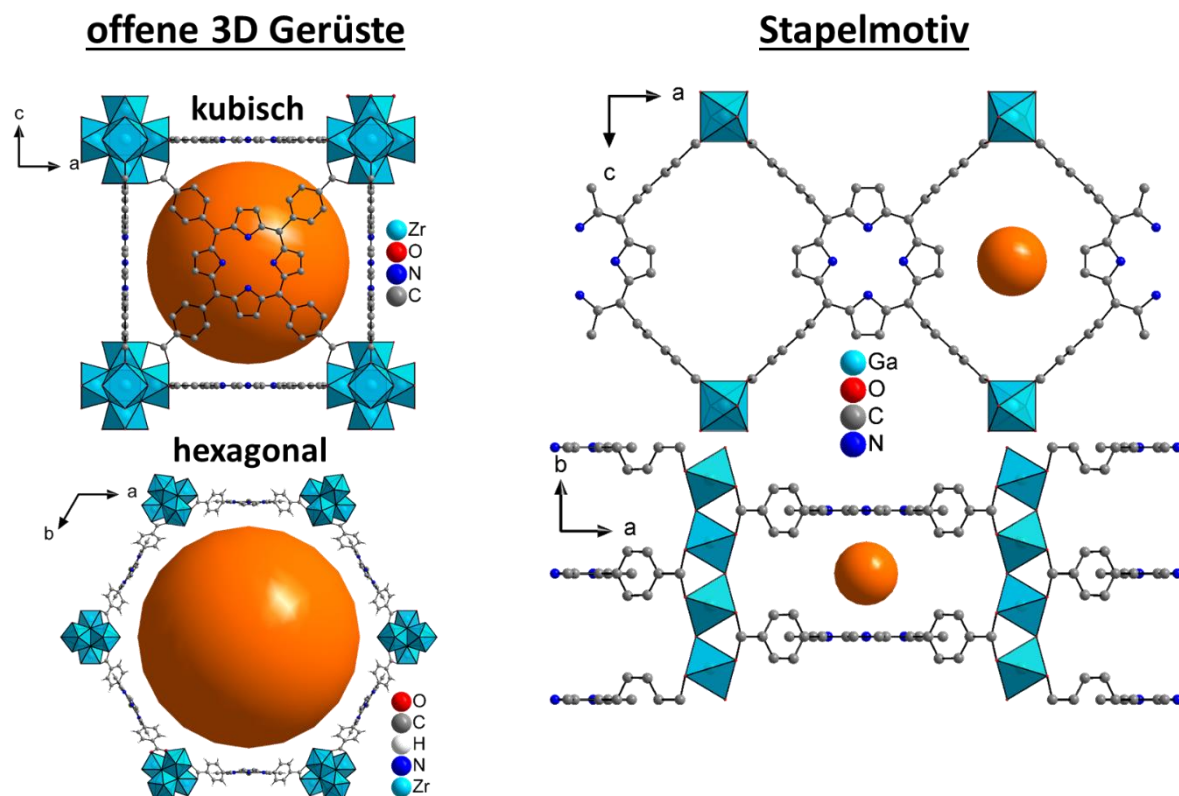


**Abbildung 11.** Exemplarische Darstellung der am häufigsten beobachteten Struktur motive in Porphyrin-basierten MOFs am Beispiel von MOF-525  $[\text{Zr}_6\text{O}_4(\text{OH})_4(\text{H}_2\text{TCPP})_3]$  (kubisch),<sup>70</sup> PCN-222  $[\text{Zr}_6\text{O}_8(\text{H}_2\text{O})_8(\text{TCPP})_2]$  (hexagonal)<sup>94</sup> und PMOF  $[\text{M}_2(\text{H}_2\text{TCPP})(\text{OH})_2]$  (Stapelmotiv, M= Fe, Al, Ga, In).<sup>84-86</sup>

### 4.3 Porphyrin-basierte Phosphonsäuren

Porphyrin-basierte Phosphonsäuren stellen in der Synthese von MOFs bisher noch eine sehr neue Linkerkategorie dar. Obwohl diese, zwei für die Anwendung von MOFs wichtige Eigenschaften kombinieren, nämlich die potentiell katalytischen Eigenschaften eines Porphyrin-Systems<sup>63, 64</sup> und die Stabilität von Metall-Phosphonaten,<sup>4, 95-97</sup> waren zu Beginn dieser Arbeit noch keine kristallinen und strukturell porösen Porphyrin-basierten Metall-Phosphonate bekannt.

4,4',4'',4'''-Tetraphosphonophenylporphyrin ( $\text{H}_{10}\text{TPPP}$ ) und seine mit verschiedenen Kationen metallierten Varianten könnte ein möglicher Linker sein, der diese Eigenschaften in sich vereint. Die Synthese des  $\text{H}_{10}\text{TPPP}$  Moleküls kann zum einen Pd-katalysiert mittels der Methode nach Hirao<sup>98</sup> bzw. über die Ni-katalysierte Methode nach Tavs,<sup>43</sup> bei der das entsprechende  $\text{Ni-H}_8\text{TPPP}$  erhalten wird, erfolgen.

$\text{H}_{10}\text{TPPP}$ , sowie metallierte<sup>99, 100</sup> als auch veresterte<sup>11</sup> Formen dieses Moleküls wurden in der Vergangenheit ausführlich bezüglich der elektrochemischen

Porphyrin-basierte Metall-Organische Gerüstverbindungen:  
Von Metall-Carboxylaten zu Metall-Phosphonaten

(Cyclovoltammetrie) <sup>101-103</sup> und photochemischen (UV/vis, Fluoreszenz-Spektroskopie) <sup>100-102</sup> Eigenschaften charakterisiert. Das Mn-H<sub>8</sub>TPPP-Cl Molekül wurde beispielsweise als Katalysator bei der Epoxidierung <sup>99, 100</sup> von z.B. Cycloocten untersucht. Weiterhin wurde dieses Molekül in der pH abhängigen Bindung von bovinem Albuminserum, <sup>104</sup> als Chemosensor für Nitroaromaten (Abb. 12) <sup>101</sup> und als Photosensitizer für TiO<sub>2</sub> Elektroden untersucht. <sup>105</sup> Außerdem wurde die Selbstaggregation in wässrigen Lösungen <sup>106, 107</sup> und die Interaktion mit Dendrimeren intensiv untersucht. <sup>108, 109</sup>

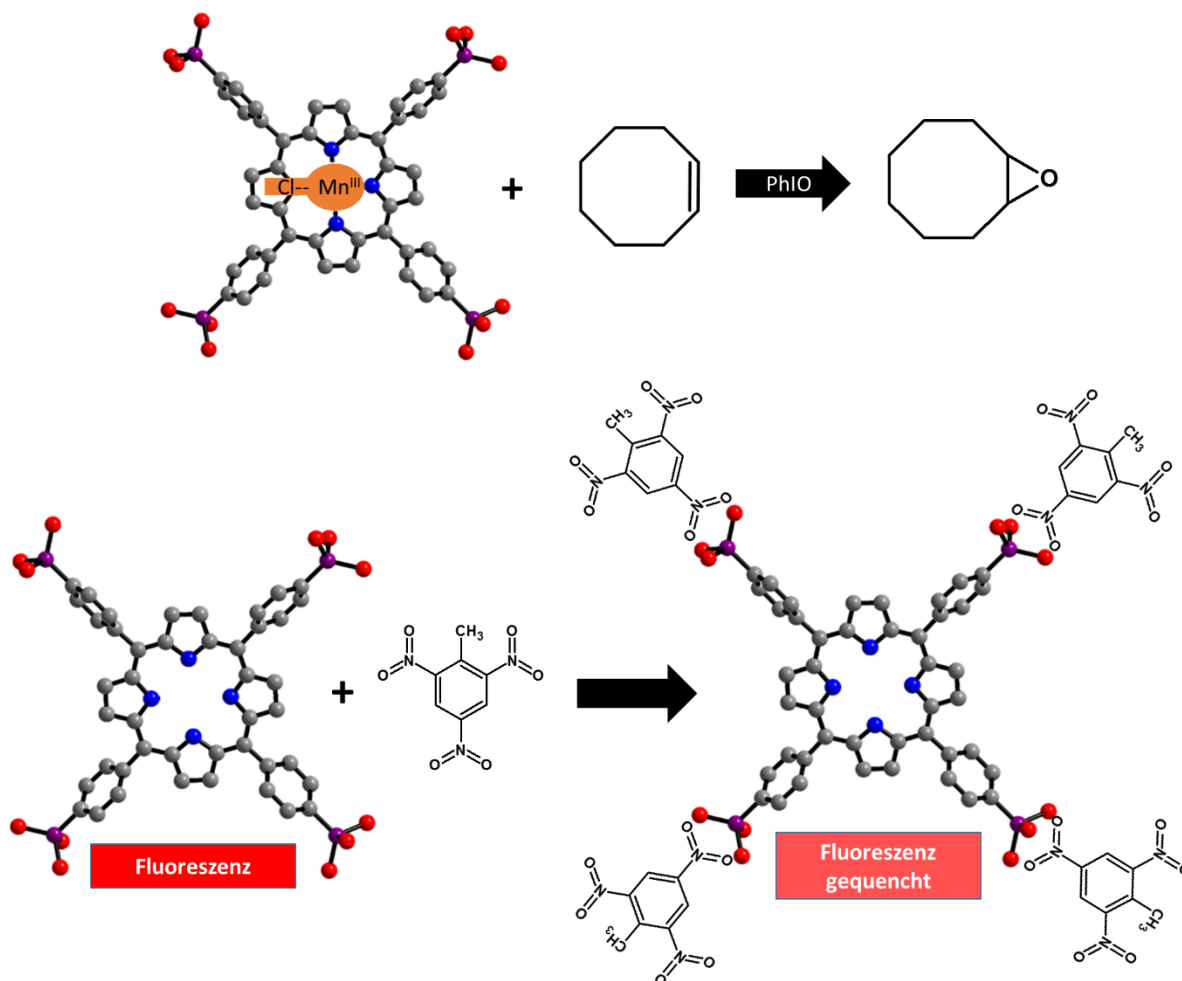
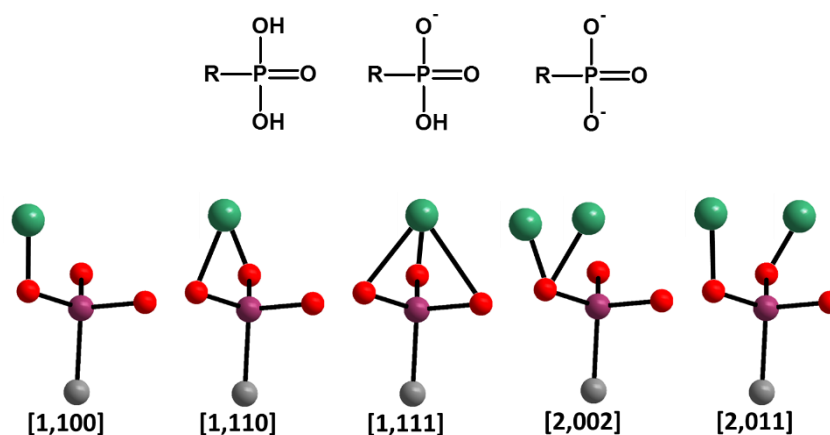


**Abbildung 12.** Schematische Darstellung der Epoxidierung von Cycloocten durch Mn-H<sub>8</sub>TPPP-Cl (oben)<sup>99</sup> und des Fluoreszenzquenchings von Nitroaromaten (TNT) durch H<sub>10</sub>TPPP.<sup>110</sup>

#### 4.4 Poröse Metall-Phosphonate

Auch die Anzahl an porösen Metall-Phosphonaten, welche auf anderen Linkermolekülen basieren, ist auf einige Duzend Strukturen beschränkt.<sup>11, 12, 111, 112</sup> Die Synthese von porösen Metall-Phosphonaten stellt oftmals eine große Herausforderung dar. Metalle in Verbindung mit Phosphonsäuren neigen meist zur Bildung dichter Schichtstrukturen oder weisen durch eine schnelle Präzipitation bedingt, geringe Fernordnung auf, was die Strukturaufklärung zu einer Herausforderung macht.<sup>113</sup> Weiterhin ist durch die unterschiedlichen Deprotonierungsstufen (Abb. 13, oben) und Koordinationsmodi (Abb. 13, Koordinationsmodi nach Harris) einer Phosphonsäure die Vorhersagbarkeit möglicher Strukturen im Vergleich zu Carbonsäuren erschwert.<sup>12, 113</sup> Für die Benennung von Koordinationsmodi eignet sich die Harris-Notation, welche das allgemeine Format [M,XYZ] hat. M stellt dabei die Anzahl an Metallionen dar, welche die entsprechende Phosphonatgruppe koordiniert und X, Y, Z die Anzahl an Bindungen, welche jedes Sauerstoff-Atom (X, Y, Z) zu den jeweiligen Metallionen ausbildet.<sup>114</sup> Anhand der Harris-Notation ergeben sich für bis zu drei koordinierende Metallionen pro Phosphonatgruppe bereits 25 unterschiedliche Koordinationsmodi (Abb. 13), während im Vergleich für eine Carbonsäure nur 10 unterschiedliche Koordinationsmodi existieren. Eine Struktur-Recherche in der CSD Datenbank ergab, dass Strukturen bekannt sind, bei denen an eine Phosphonatgruppe bis zu sieben Metallionen koordinieren können. Dennoch sind der Übersichtlichkeit halber in Abbildung 13 nur die Koordinationsmodi von bis zu drei Metallionen gezeigt. Die Variationsvielfalt an Koordinationsmodi bei mehr als drei Metallionen ist dabei nur begrenzt durch die maximale Anzahl an Bindungen (2, 3 und 3) zwischen Sauerstoff und Metallion, andernfalls würde mit steigender Anzahl an Metallionen pro Phosphonsäure die Anzahl an möglichen Koordinationsmodi exponentiell ansteigen.





Porphyrin-basierte Metall-Organische Gerüstverbindungen:  
 Von Metall-Carboxylaten zu Metall-Phosphonaten

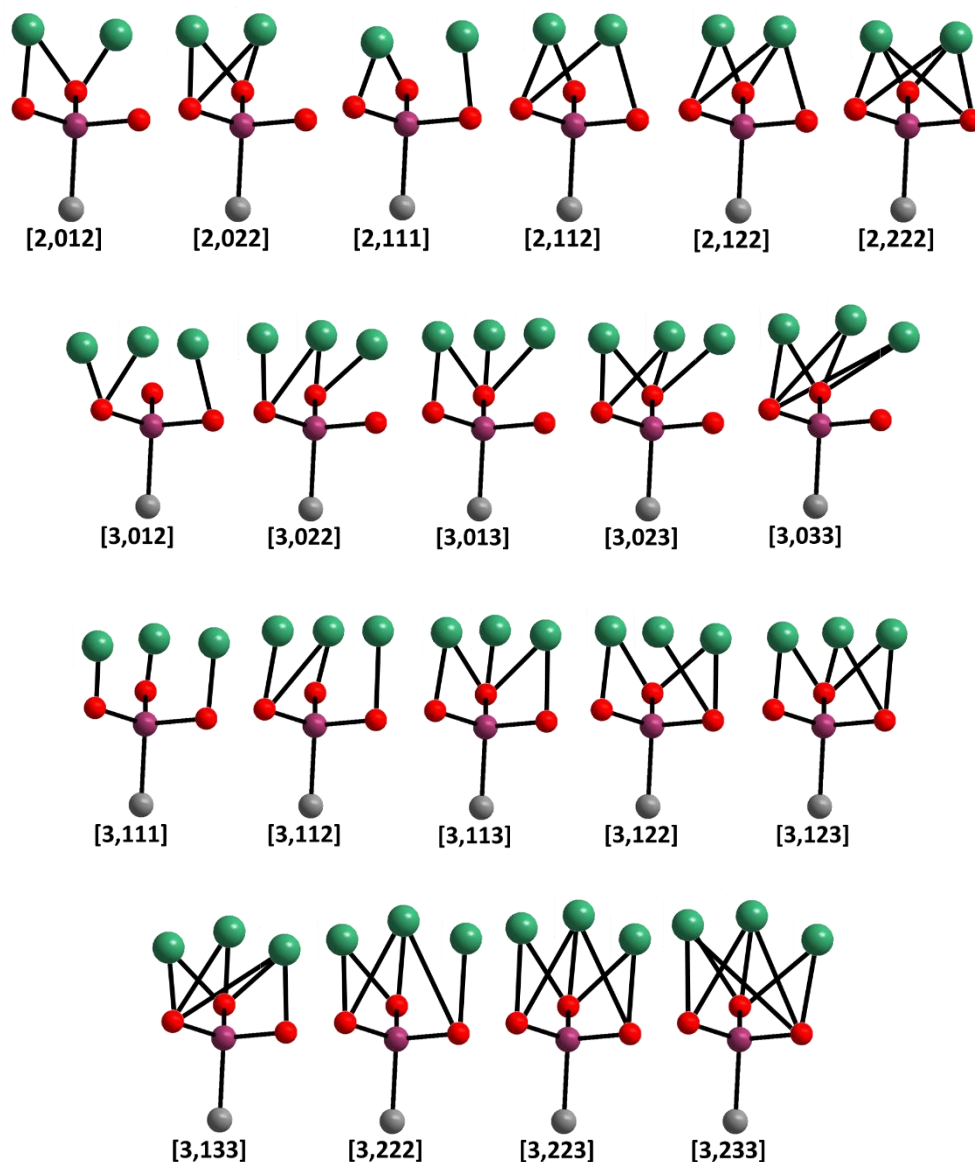


**Abbildung 13.** Alle möglichen Koordinationsmodi einer Phosphonsäure (nach Harris) zu eins bis drei Metallionen.<sup>114</sup>

Trotz der Probleme die bei der Synthese poröser Metall-Phosphonate auftreten können, ist diese Stoffklasse im Fokus der Wissenschaft, da Metall-Phosphonate im Vergleich zu Metall-Carboxylaten oftmals stabilere Gerüste ausbilden.<sup>111</sup> Diese Eigenschaft ist essentiell für die meisten Anwendungen wie Gasspeicherung und -trennung sowie Katalyse.<sup>12, 113</sup> Das Vorhandensein von Hydrogenphosphonat oder sogar Phosphonsäure Spezies in einem porösen Gerüst machen poröse Metall-Phosphonate des weiteren zu vielversprechenden Kandidaten in Bezug auf protonenleitfähige Materialien.<sup>113</sup>

Erste Arbeiten zu Metall-Phosphonaten wurden von Clearfield et al. 1964 mit der Synthese von  $Zr(HPO_4)_2 \cdot H_2O$ <sup>115</sup> und der darauffolgenden Strukturaufklärung im Jahre



Porphyrin-basierte Metall-Organische Gerüstverbindungen:  
Von Metall-Carboxylaten zu Metall-Phosphonaten

1969<sup>116</sup> ermöglicht.  $ZrO_6$  Oktaeder werden dabei über Hydrogenphosphonat-Gruppen zu Schichten verknüpft. Bereits 1978 wurde von Alberti et al. das erste Metall-Organische Zr-Phosphonat, ein Phenylphosphonat der Zusammensetzung,  $Zr(C_6H_5PO_3)_2$ , synthetisiert (Abb. 14, oben)<sup>117</sup> und daraufhin 1983 das erste poröse Zr-Phosphonat bei dem Zr-Phosphat Schichten von organischen Molekülen separiert wurden und sich statistisch angeordnete Poren ausbildeten (Abb. 14, unten).<sup>118</sup>

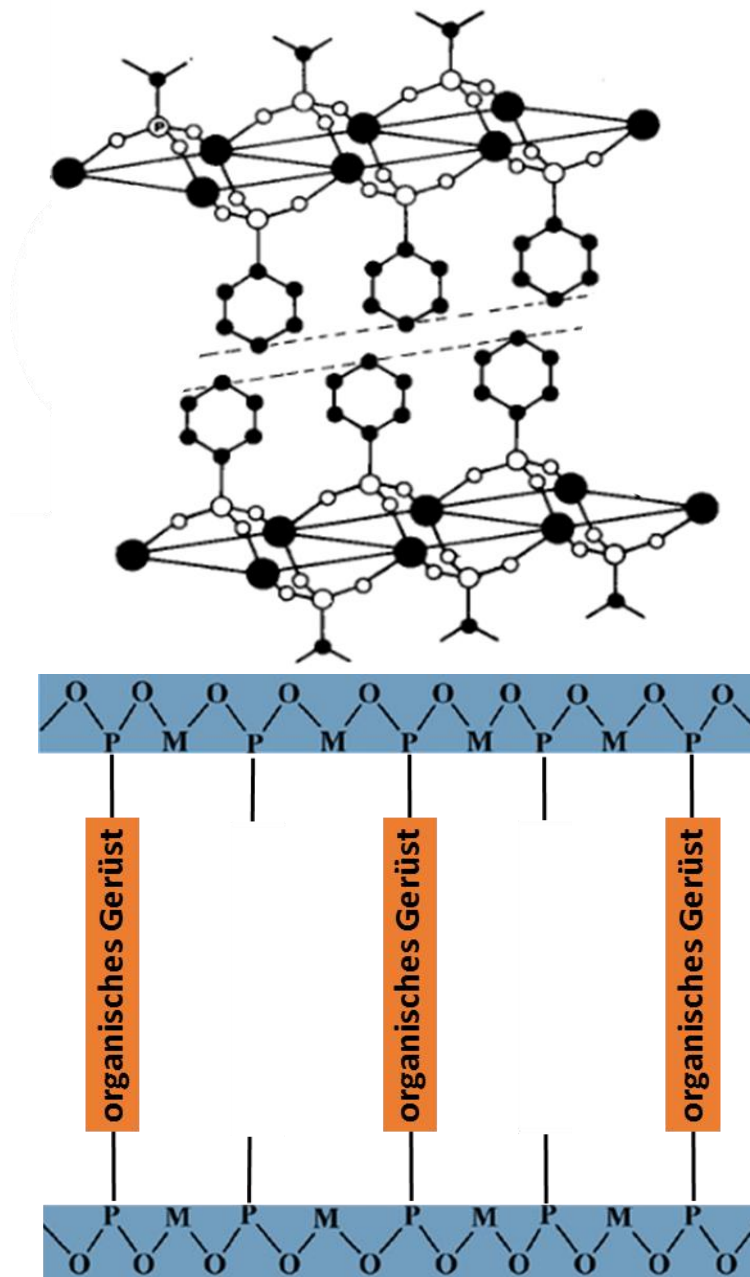


**Abbildung 14.** Das erste Metall-Organische Phosphonat,  $Zr(C_6H_5PO_3)_2$ , (oben)<sup>117</sup> und schematische Darstellung der statistischen Poren zwischen Metall-Phosphat Schichten durch organische Moleküle (unten).<sup>113</sup>

Porphyrin-basierte Metall-Organische Gerüstverbindungen:  
Von Metall-Carboxylaten zu Metall-Phosphonaten

Bis heute sind nur wenige poröse und kristalline Zr-Phosphonate bekannt (Tab. 05). Darunter UPG-1 (2,4,6-tris(4-(phosphonomethyl)phenyl)-1,3,5-triazin),<sup>97</sup> CALF-31 (1,3,5-tris(4-phosphonophenyl)benzene),<sup>96</sup> ZrH<sub>4</sub>L (H<sub>8</sub>L= tetra-phenylsilane tetrakis-4-phosphonsäure),<sup>119</sup> [Zr<sub>3</sub>(H<sub>3</sub>PPB)<sub>4</sub>] (1,3,5-*Tris*-(4-phosphonophenyl)benzol)<sup>95</sup> und SZ-1 bis 3 (1,3,5,7-tetrakis(4-phosphonophenyl)adamantan/methan))<sup>120</sup> mit spezifischen Oberflächen bis zu 793 m<sup>2</sup> g<sup>-1</sup> (CALF-31).<sup>96</sup> Der Vollständigkeit halber sei erwähnt, dass viele der von Clearfield et al. synthetisierten Zr-Phosphonate, bei denen Zr-Hydrogenphosphat Schichten durch organische Moleküle separiert sind, auch Poren aufweisen. Diese liegen dabei jedoch nur in geringem Maße geordnet vor, weshalb diese Verbindungen in dieser Arbeit nicht im Detail diskutiert werden.<sup>116, 121, 122</sup> Ebenfalls erwähnenswert ist die Tatsache, dass die anorganischen Baueinheiten aller bisher publizierten Zr-Phosphonate ZrO(F)<sub>6</sub> Oktaeder in isolierter (über (Hydrogen)-Phosphonate verbrückt) oder eckenverknüpfter Form aufweisen (Abb. 15). In den meisten Fällen werden dabei eindimensionale Ketten ausgebildet, im Falle von SZ-2 und -3 werden Tri-, Tetra- und Hexamere ausgebildet.<sup>97, 119, 120</sup> Alle anorganischen Baueinheiten, welche über (Hydrogen)-Phosphonat verbrückte ZrO<sub>6</sub> Oktaeder enthalten, lassen sich von der Struktur von Zr-Hydrogenphosphat, Zr(HPO<sub>4</sub>)<sub>2</sub>, nach Clearfield ableiten.<sup>116</sup> In dieser Struktur sind eben diese Ketten zu Schichten verknüpft, wobei es gelang wie in Abbildung 14 verdeutlicht diese Schichten durch organische Moleküle zu separieren um so Porosität zu erzeugen.<sup>112, 116, 117, 122</sup>

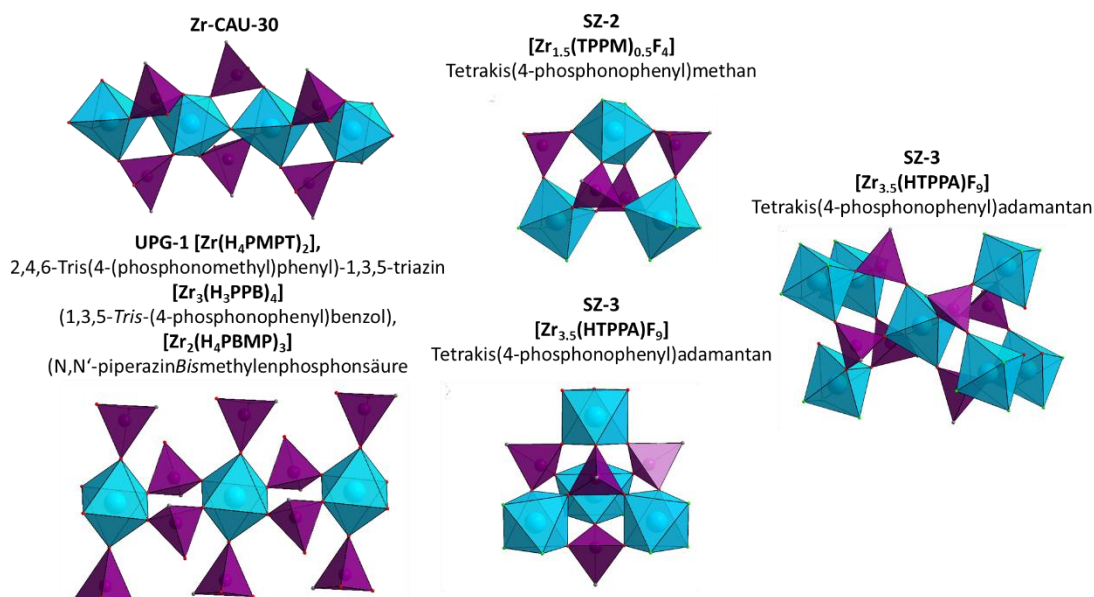


**Abbildung 15.** Darstellung der unterschiedlichen anorganischen Baueinheiten, welche in porösen Zr-Phosphonaten beobachtet werden.<sup>95, 97, 120, 123</sup>

Mit zweiwertigen Kationen wie Co<sup>2+</sup> oder Ni<sup>2+</sup> sind ebenfalls nur sehr wenige poröse Metall-Phosphonate bekannt. Darunter M-STA-12 (M= Mg, Ni, Co, Mn, Fe, Cd),<sup>14, 124,</sup>

Porphyrin-basierte Metall-Organische Gerüstverbindungen:  
Von Metall-Carboxylaten zu Metall-Phosphonaten

<sup>125</sup> M-STA-16 (M= Ni, Co),<sup>126</sup> M-MFM-500 (M= Ni, Co)<sup>127</sup> und  $[\text{Co}_4(\text{TPP})_3(\mu^3\text{-OH})(\text{H}_2\text{O})_3](\text{SO}_4)_{0.5}$  (TPP=4-(4H-1,2,4-triazol-4-yl)phenylphosphonsäure)<sup>128</sup> wobei maximale Porenvolumina von  $0.68 \text{ cm}^3 \text{ g}^{-1}$  im Falle von STA-16 erreicht wurden. Der Vergleich von STA-12 mit STA-16 stellt ebenfalls ein Beispiel für die Anwendung des modularen Aufbaus von MOFs dar, durch den Einsatz der entsprechend verlängerten Bipiperidinbismethylenphosphonsäure konnte die zu STA-12 isoretikuläre Verbindung mit doppelter Porengröße erhalten werden (Abb. 16).<sup>126</sup>

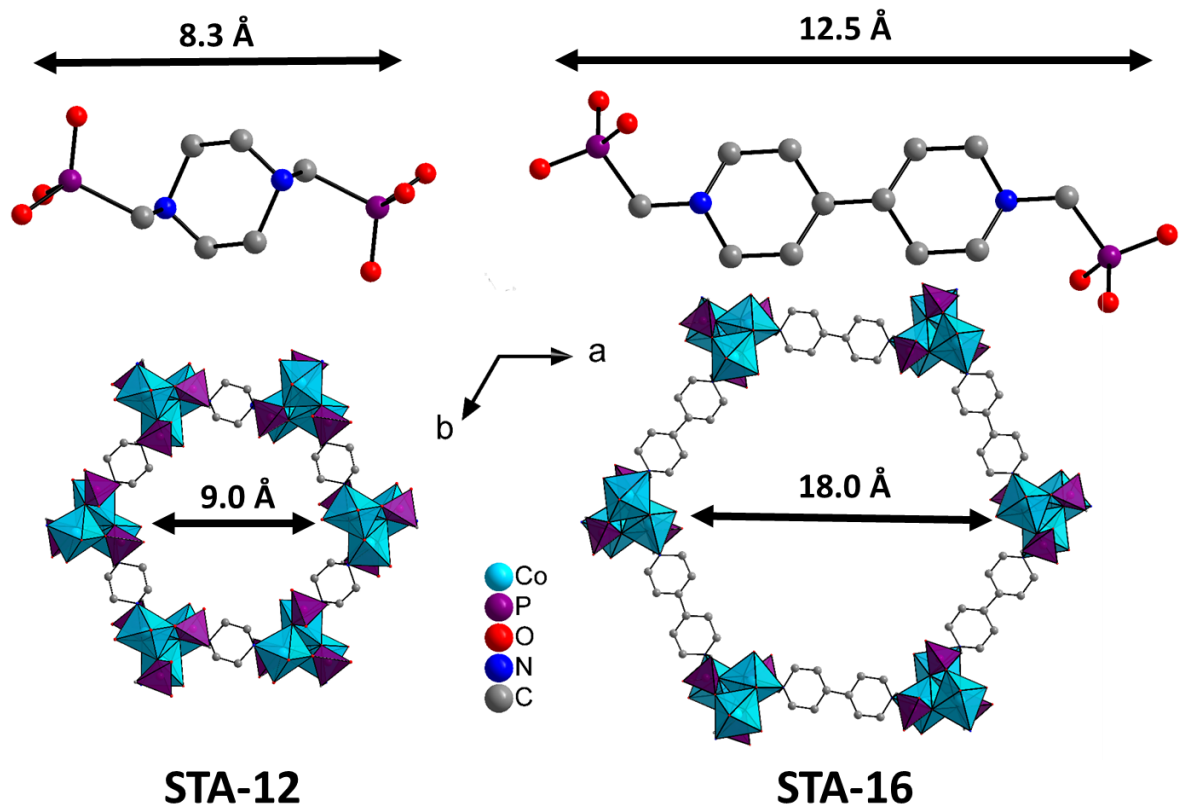


**Abbildung 16.** Schematische Darstellung der Kristallstrukturen von STA-12 (links) und STA-16 (rechts), wobei durch den Einsatz der Bipiperidinbismethylenphosphonsäure (STA-16) im Vergleich zur Piperazinbismethylenphosphonsäure (STA-12) die Porengröße in STA-16 verdoppelt werden konnte.<sup>126</sup>

Die Gesamtzahl an porösen und kristallinen Metall-Phosphonaten ist dabei auf einige Dutzend Strukturen begrenzt. Eine Auflistung der porösen und kristallinen Metall-Phosphonate sortiert nach der Wertigkeit der verwendeten Kationen, Sorptionseigenschaften und Raumgruppe ist in Tabelle 05 gegeben.<sup>11, 12, 111</sup> Die Abkürzungen der Linker mit L# ist in der darauffolgenden Abbildung 17 erklärt, in der die Lewis-Formeln der Linker, welche bisher in der Synthese poröser Metall-Phosphonate verwendet wurden, gezeigt sind.

Porphyrin-basierte Metall-Organische Gerüstverbindungen:  
Von Metall-Carboxylaten zu Metall-Phosphonaten

**Tabelle 05.** Übersicht über poröse und kristalline Metall-Phosphonate. Zum Vergleich sind der Name, die Summenformel, Sorptionseigenschaften (spezifische Oberfläche nach BET, Porenvolumen, Porendurchmesser oder CO<sub>2</sub>-Aufnahme) und Raumgruppe angegeben. Des weiteren ist die Tabelle unterteilt nach der Valenz der Metallkationen.

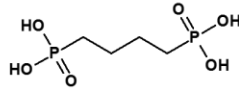
Name <sup>[Lit.]</sup>	Summenformel	Sorptions Eigenschaften	RG
<b>zweiwertig</b>			
M-STA-12 <sup>14, 124</sup> (M= Mg, Ni, Co, Mn, Fe)	[M <sub>2</sub> (H <sub>2</sub> O) <sub>2</sub> (L4)]	0.14- 0.27 cm <sup>3</sup> g <sup>-1</sup>	R $\bar{3}$
M-STA-16 <sup>126</sup> (M= Ni, Co)	[M <sub>2</sub> (H <sub>2</sub> O) <sub>2</sub> (L6)]	0.68 cm <sup>3</sup> g <sup>-1</sup>	R $\bar{3}$
SrL7 <sup>129</sup>	[Sr <sub>2</sub> (H <sub>2</sub> L7)(CH <sub>3</sub> OH)(H <sub>2</sub> O) <sub>4</sub> ]	3.1 mmol CO <sub>2</sub> g <sup>-1</sup>	P $\bar{1}$
CALF-33 <sup>130</sup>	[Cu <sub>3</sub> (L7-Et <sub>3</sub> ) <sub>2</sub> ]	895 m <sup>2</sup> g <sup>-1</sup>	P $\bar{1}$
CAU-25 <sup>131</sup>	[Zn <sub>2</sub> (H <sub>2</sub> L7)(H <sub>2</sub> O) <sub>2</sub> ]	7.3 mmol H <sub>2</sub> O g <sup>-1</sup>	C2/c
M-MFM-500 <sup>127</sup> (M= Ni, Co)	[M <sub>3</sub> (H <sub>3</sub> L7) <sub>2</sub> (H <sub>2</sub> O) <sub>9</sub> (C <sub>2</sub> H <sub>6</sub> SO) <sub>3</sub> ]	10 m <sup>2</sup> g <sup>-1</sup>	P6 <sub>3</sub> /m
CAU-14 <sup>132</sup>	[Cu <sub>3</sub> (L8)(H <sub>2</sub> O) <sub>3</sub> ]	739 m <sup>2</sup> g <sup>-1</sup>	Cm
CoL10 <sup>128</sup>	[Co <sub>4</sub> (L10) <sub>3</sub> (μ <sup>3</sup> -OH)(H <sub>2</sub> O) <sub>3</sub> ](SO <sub>4</sub> ) <sub>0.5</sub>	1.3 nm	P $\bar{6}2c$
CuL11 <sup>133</sup> ZnL11 <sup>134</sup>	[Cu(L11)(H <sub>2</sub> O)]	1.38- 2.80 mmol CO <sub>2</sub> g <sup>-1</sup>	C2/c
CALF-25 <sup>135</sup>	[Ba(H <sub>2</sub> L12)]	385 m <sup>2</sup> g <sup>-1</sup>	C2/c
CuL15 <sup>136</sup>	[Cu <sub>3</sub> (H <sub>3</sub> L15)(OH)(H <sub>2</sub> O) <sub>3</sub> ]	198 m <sup>2</sup> g <sup>-1</sup>	P2 <sub>1</sub> /n
<b>dreiwertig</b>			
AlMepO-α-β <sup>137, 138</sup>	[Al <sub>2</sub> (L1) <sub>3</sub> ]	297 m <sup>2</sup> g <sup>-1</sup>	P3 <sub>1</sub> c
Ln(H <sub>2</sub> L3) <sup>139</sup>	[Ln(H <sub>2</sub> L3) <sub>3</sub> ] Ln= Tb, Dy, Eu, Gd	81 m <sup>2</sup> g <sup>-1</sup>	P4 <sub>1</sub>
M-MIL-91 <sup>140</sup> (M= Al, Ga, Fe)	[Al(OH)(H <sub>2</sub> L4)]	500 m <sup>2</sup> g <sup>-1</sup>	C2/m
M-STA-13 <sup>141</sup> (M= Sc, Y, Yt-Gd)	[M <sub>2</sub> (H <sub>2</sub> L5) <sub>3</sub> ]	3.5 mmol g <sup>-1</sup>	P $\bar{3}$
HFeP-1-3 <sup>142</sup>	[Fe <sub>2.77</sub> (L7a)(OH) <sub>2.31</sub> ]	556 m <sup>2</sup> g <sup>-1</sup>	P $\bar{1}$
LaL10 <sup>143</sup>	[La <sub>3</sub> (L10) <sub>4</sub> (H <sub>2</sub> O) <sub>6</sub> ]Cl	1.9 nm	P $\bar{3}$
AlL13 <sup>144</sup>	[Al(H <sub>3</sub> L13)(H <sub>2</sub> O)]	687 m <sup>2</sup> g <sup>-1</sup>	R $\bar{3}$
<b>vierwertig</b>			
HSnP-1 <sup>145</sup>	[Sn(L2)]	338 m <sup>2</sup> g <sup>-1</sup>	tet.
Ti-MIL-91 <sup>140</sup>	[Ti(O)(H <sub>2</sub> L4)]	500 m <sup>2</sup> g <sup>-1</sup>	C2/m
CALF-28 <sup>146</sup>	[Sn(H <sub>2</sub> L7)]	500 m <sup>2</sup> g <sup>-1</sup>	P $\bar{1}$
HSnP-2 <sup>147</sup>	[Sn <sub>2.25</sub> (H <sub>4</sub> L7)]	380 m <sup>2</sup> g <sup>-1</sup>	hex.
CALF-31 <sup>96</sup>	[Zr(H <sub>2</sub> L7)]	793 m <sup>2</sup> g <sup>-1</sup>	Modell
ZrL7 <sup>95</sup>	[Zr <sub>3</sub> (H <sub>3</sub> L7) <sub>4</sub> ]	10 m <sup>2</sup> g <sup>-1</sup>	P $\bar{3}1c$
ZrL4 <sup>123</sup>	[Zr <sub>2</sub> (H <sub>4</sub> L4) <sub>3</sub> ]	-	R $\bar{3}$
UPG-1 <sup>97</sup>	[Zr(H <sub>4</sub> L9) <sub>2</sub> ]	410 m <sup>2</sup> g <sup>-1</sup>	R $\bar{3}$
SZ-1 <sup>120</sup>	[C <sub>4</sub> mpyr][Zr <sub>2.5</sub> (H <sub>3</sub> L14)F <sub>6</sub> ]	10 m <sup>2</sup> g <sup>-1</sup>	Pbca
SZ-2 <sup>120</sup>	[C <sub>4</sub> mpyr] <sub>2</sub> [Zr <sub>1.5</sub> (L14) <sub>0.5</sub> F <sub>4</sub> ]	225 m <sup>2</sup> g <sup>-1</sup>	I4/m
SZ-3 <sup>120</sup>	[C <sub>2</sub> py] <sub>2</sub> [Zr <sub>3.5</sub> (HL15)F <sub>9</sub> ]	594 m <sup>2</sup> g <sup>-1</sup>	P2 <sub>1</sub> /n

Porphyrin-basierte Metall-Organische Gerüstverbindungen:  
Von Metall-Carboxylaten zu Metall-Phosphonaten

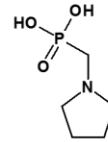
---



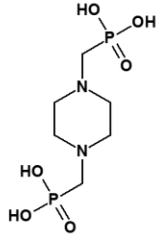
L1= Methylphosphonsäure  
(H<sub>2</sub>MeP)



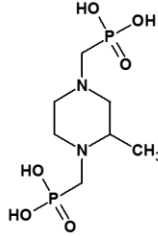
L2= Butyl-1,4,-diphosphonsäure  
(H<sub>4</sub>BuDP)



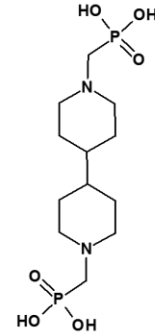
L3= N-phosphonomethylprolin  
(H<sub>2</sub>PMP)



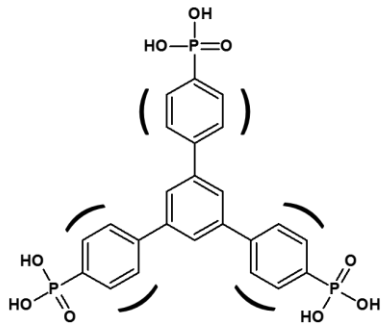
L4= N,N'-piperazin  
Bismethylenphosphonsäure  
(H<sub>4</sub>PBMP)



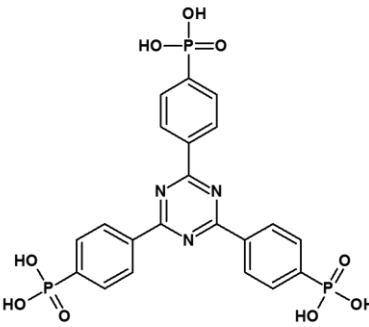
L5= N,N'-2-methylpiperazin  
Bismethylenphosphonsäure  
(H<sub>4</sub>MPBMP)



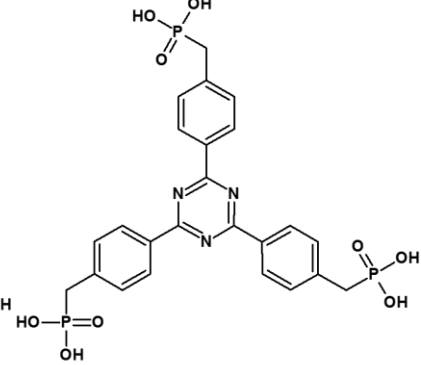
L6= N,N'-4,4'-bipiperidin  
Bismethylenphosphonsäure  
(H<sub>4</sub>BPBMP)



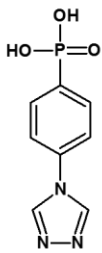
L7= 1,3,5-Tris-  
(4-phosphonophenyl)benzol (H<sub>6</sub>PPB)  
L7a= 1,3,5-Tris-4-phosphonobenzol (H<sub>6</sub>PB)



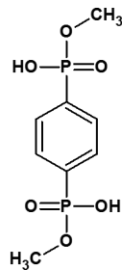
L8= 2,4,6-Tris-  
(4-phosphonophenyl)triazin (H<sub>6</sub>PPT)



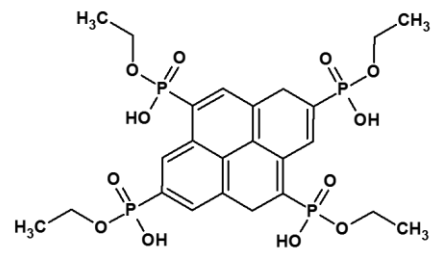
L9= 2,4,6-Tris(4-(phosphonomethyl)  
phenyl)-1,3,5-triazin (H<sub>6</sub>PMPT)



L10= 4-(4H-1,2,4-triazol-4-yl)  
Phenylphosphonsäure  
(H<sub>2</sub>TPP)

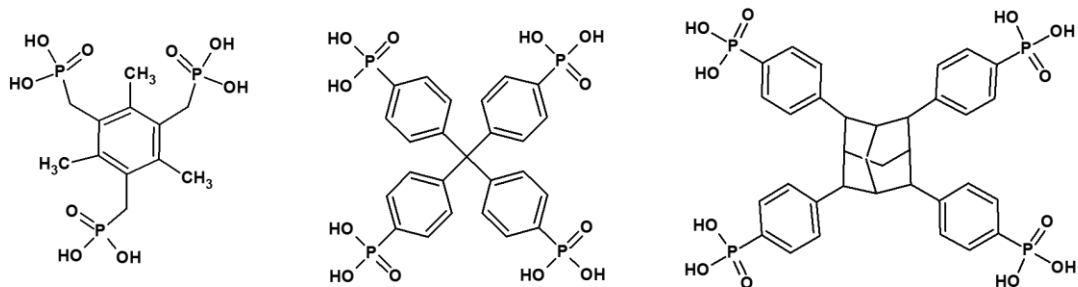


L11= 1,4-Benzoldiphosphonsäure  
bis(monomethylester) (H<sub>2</sub>BDPM)



L12= Tetraethyl-  
1,3,6,8-pyrenetetraphosphonsäure (H<sub>4</sub>PTPE)

Porphyrin-basierte Metall-Organische Gerüstverbindungen:  
 Von Metall-Carboxylaten zu Metall-Phosphonaten

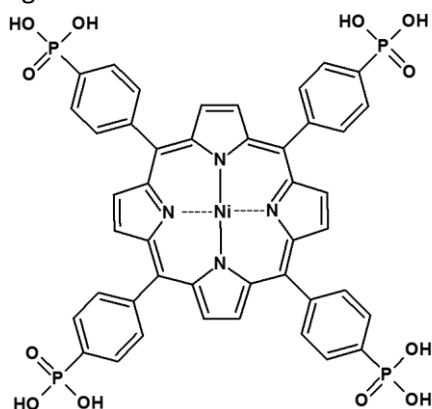


L13= 2,4,6-Trimethylbenzol  
 -1,3,5-triyl)tris(methylen)  
 Triphosphonsäure  
 ( $H_6TMBTMP$ )

L14= Tetrakis(4-phosphonophenyl)methan  
 ( $H_8TPPM$ )

L15= 1,3,5,7-Tetrakis(4-phosphonophenyl)  
 Adamantan ( $H_8TPPA$ )

**Abbildung 17.** Strukturformeln von Phosphonsäure basierten Linkern, welche zur Synthese von porösen Metall-Phosphonaten eingesetzt wurden.



L16= Ni-tetrakis(4-phosphonophenyl)porphyrin  
 ( $Ni-H_8TPPP$ )

**Abbildung 18.** Strukturformel von Ni-tetrakis(4-phosphonophenyl)porphyrin ( $Ni-H_8TPPP$ ).

## 4.5 Ergebnisse

### 4.5.1 Nanoscale Synthesis of Two Porphyrin-Based MOFs with Gallium and Indium

Der folgende Artikel wurde im Jahr 2016 in der Fachzeitschrift *Inorganic Chemistry*, ACS veröffentlicht. Der Wiederabdruck erfolgte mit freundlicher Genehmigung der ACS. Reproduced with permission from Timo Rhauderwiek, Steve Waitschat, Stefan Wuttke, Helge Reinsch, Thomas Bein and Norbert Stock, *Inorg. Chem.* **2016**, *55*, 5312-5319, DOI: 10.1021/acs.inorgchem.6b00221. Copyright 2016 American Chemical Society.

<http://pubs.acs.org/doi/abs/10.1021/acs.inorgchem.6b00221>

In diesem Artikel wurden zwei Porphyrin-basierte Metall-Organische Gerüstverbindungen (MOFs) synthetisiert und charakterisiert. Ga-PMOF  $[\text{Ga}_2(\text{OH})_2(\text{H}_2\text{TCPP})] \cdot 3 \text{ DMF} \cdot 3 \text{ H}_2\text{O}$  und In-PMOF  $[\text{In}_2(\text{OH})_2(\text{H}_2\text{TCPP})] \cdot 3 \text{ DMF} \cdot 4 \text{ H}_2\text{O}$  enthalten beide das 4-Tetracarboxyphenylporphyrin Anion als Linker und wurden unter Anwendung von Hochdurchsatzmethoden in Teflonreaktoren entdeckt. Die Synthesebedingungen wurden daraufhin ebenfalls mittels der Hochdurchsatzmethode optimiert. Die Kristallstruktur beider MOFs ist isostrukturell zu der von Al-PMOF, welche 2012 publiziert wurde.<sup>85</sup> Ausgehend von dem Strukturmodell von Al-PMOF konnten die Strukturen von Ga- und In-PMOF aus Röntgenpulverdaten durch Rietveld-Verfeinerung bestimmt werden. Alle PMOFs kristallisieren in der orthorhombischen Raumgruppe *Cmmm*. Ketten trans-eckenverknüpfter  $\text{MO}_6$  Oktaeder sind in der Kristallstruktur über deprotonierte Linkermoleküle  $\text{H}_2\text{TCPP}^{4-}$  verbrückt, wobei zwei Arten von eindimensionalen Kanälen entlang [010] und [001] von 5.0/11.8 Å und 3.4/11.8 Å (Ga-PMOF) sowie 5.0/11.8 Å und 4.0/12.6 Å (In-PMOF) ausgebildet werden. Ga- und In-PMOF sind porös gegenüber  $\text{N}_2$  (77 K) und  $\text{CO}_2$  (298 K) und weisen spezifische Oberflächen nach BET zwischen 1150 und 1400  $\text{m}^2 \text{ g}^{-1}$  auf. Beide MOFs sind des weiteren thermisch stabil bis 330 °C, zeigen jedoch begrenzte chemische Stabilität in Säuren und Basen. In  $\text{H}_2\text{O}$  nimmt die Fernordnung der Verbindungen ab, diese kann jedoch durch Waschen mit DMF wieder vollständig hergestellt werden. In allen getesteten organischen Lösungsmitteln wie Alkoholen, DCM, Diethylether und Aceton sind beide Verbindungen stabil. Partikelgrößenbestimmungen mittels DLS zeigten, dass beide MOFs im nanoskaligen Bereich (50-150 nm) erhalten wurden. Um die Partikelgröße beider MOFs in einem gewissen Bereich einzustellen, wurden unterschiedliche Syntheserouten versucht: batch-Synthese in Teflonreaktoren, Ultraschall unterstützte Synthese unter leichter Erwärmung (50 °C) in einem

Ultraschallbad und Synthese in einem Flussreaktor. Alle Synthesen, außer der im Ultraschallbad, wurden bei unterschiedlichen Reaktionstemperaturen durchgeführt. Die erhaltenen Produkte wurden mittels REM, TEM, DLS und Pulverdiffraktometrie auf ihre Partikelgröße untersucht. Für den Ga-PMOF ergaben sich im Flussreaktor die kleinsten Partikel mit einem Durchmesser von 65(18) nm. Höhere Reaktionstemperaturen im Flussreaktor führten dabei zur Bildung größerer Partikel. In Teflonreaktoren wurden Partikel mit einem Durchmesser von 92(25) nm erhalten. Im Falle vom In-PMOF wurden die kleinsten Partikel in einer Synthese im Ultraschallbad (74(21) nm) und etwas größere Partikel in Teflonreaktoren (132(25) nm) erhalten. Die Partikelgröße hatte ebenfalls einen Einfluss auf die Porosität, wobei kleinere Partikel zu einer größeren spezifischen Oberfläche führten.



## Nanoscale Synthesis of Two Porphyrin-Based MOFs with Gallium and Indium

Timo Rhauderwiek,<sup>†</sup> Steve Waitschat,<sup>†</sup> Stefan Wuttke,<sup>‡</sup> Helge Reinsch,<sup>§</sup> Thomas Bein,<sup>‡</sup> and Norbert Stock<sup>\*,†</sup>

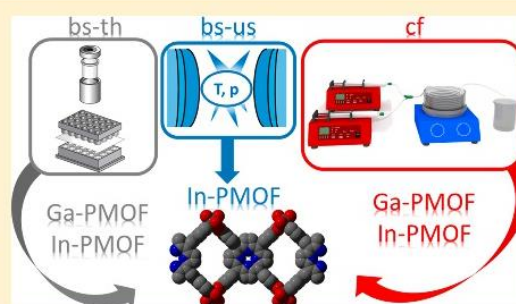
<sup>†</sup>Institute of Inorganic Chemistry, Christian-Albrechts-Universität, Max-Eyth Straße 2, D-24118 Kiel, Germany

<sup>‡</sup>Department of Chemistry and Center for NanoScience (CeNS), University of Munich (LMU), Butenandtstraße 5-13, D-81377 Munich, Germany

<sup>§</sup>Department of Chemistry, University of Oslo, N-0371 Oslo, Norway

**S** Supporting Information

**ABSTRACT:** Two porphyrin-based metal–organic frameworks (MOFs) containing gallium or indium,  $[\text{Ga}_2(\text{OH})_2(\text{H}_2\text{TCPP})] \cdot 3\text{DMF} \cdot 3\text{H}_2\text{O}$  (Ga-PMOF) and  $[\text{In}_2(\text{OH})_2(\text{H}_2\text{TCPP})] \cdot 3\text{DMF} \cdot 4\text{H}_2\text{O}$  (In-PMOF) ( $\text{H}_6\text{TCPP}$  = 4-tetracarboxyphenylporphyrin), were discovered using high-throughput methods. The structure was refined by the Rietveld-method starting from the structure model of Al-PMOF,  $[\text{Al}_2(\text{OH})_2(\text{H}_2\text{TCPP})]$ . The new PMOFs exhibit BET surface areas between 1150 and 1400  $\text{m}^2 \text{g}^{-1}$  and are also porous toward  $\text{CO}_2$  (Ga-PMOF, 15.2 wt %; In-PMOF, 12.9 wt %). They are thermally stable in air up to 330 °C, but show limited chemical stabilities toward acids and bases. In order to achieve size control, different synthesis routes were investigated, i.e., batch synthesis at different temperatures (yield: In-PMOF-bs-th 96%, Ga-PMOF-bs-th 87%), ultrasound-assisted synthesis (yield: In-PMOF-bs-us 85%), and continuous-flow synthesis (yield: Ga-PMOF-cf 71%). By using these different methods we could control the nucleation rate and the crystal size. The crystal sizes were found to vary about 60 to 160 nm and 70 to 130 nm for Ga- and In-PMOF, respectively, which was proven by dynamic light scattering (DLS), powder X-ray diffraction (PXRD), scanning electron microscopy (SEM), and transmission electron microscopy (TEM) measurements.



### INTRODUCTION

In the field of crystalline porous materials, metal–organic frameworks (MOFs) exhibit tunable pore sizes and surface chemistry, which in turn lead to a wide range of chemical and physical properties.<sup>1–3</sup> Hence MOFs are investigated in applications such as gas storage and separation, catalysis, and drug delivery.<sup>2,4–7</sup> An important challenge for the use of MOFs in drug delivery is to construct highly porous, nanoscaled, biocompatible materials consisting of nontoxic metals and linkers. Porphyrin-based linker molecules in combination with biocompatible metals like Ga and In, which have been shown to be toxic only in very high concentrations, could lead to MOFs suitable for applications in drug delivery.<sup>4,8–17</sup>

4-Tetracarboxyphenylporphyrin ( $\text{H}_6\text{TCPP}$ ) is the most intensively investigated linker for the synthesis of porphyrin-based MOFs, and nearly 30 compounds containing this linker are known.<sup>12</sup> In most cases, these MOFs are based on di- and tetravalent metal ions like  $\text{Zn}^{2+}$  and  $\text{Zr}^{4+}$ .<sup>12</sup> For zirconium the compounds PCN-221,<sup>18</sup> MOF-545,<sup>19</sup> MOF-525,<sup>19</sup> PCN-223,<sup>20</sup> PCN-224,<sup>21</sup> and PCN-225<sup>22</sup> have been reported. These porphyrin-based Zr-MOFs exhibit high specific surface areas and have been tested, for example, as heterogeneous catalysts

for the oxidation of cyclohexane (PCN-221),<sup>18</sup> or for the coupling reaction of  $\text{CO}_2$ /propylene oxide (PCN-224).<sup>21</sup> To date only a few compounds with trivalent metal ions such as iron (MIL-141,  $[\text{NaFe}(\text{Ni-TCPP})]$ <sup>23</sup> and  $[\text{Fe}_2(\text{Fe-TCPP})(\text{C}_4\text{H}_4\text{N}_2)(\text{OH}_2)]$  ( $\text{C}_4\text{H}_4\text{N}_2$  = pyrazine)<sup>24</sup>) and aluminum (Al-PMOF,  $[\text{Al}_2(\text{H}_2\text{TCPP})(\text{OH})_2] \cdot 3\text{DMF} \cdot 2\text{H}_2\text{O}$ )<sup>25</sup> have been described with the  $\text{H}_6\text{TCPP}$  linker.<sup>26</sup> Al-PMOF was investigated in the photocatalytic methyl viologen assisted  $\text{H}_2$ -generation on colloidal platinum.<sup>25</sup> With the homologues gallium and indium only In-MOFs containing porphyrin-based linkers have been reported (MMPF-7,  $[\text{In}_{1.29}\text{O}_{0.57}(\text{TCPP})]$ ,<sup>27</sup> MMPF-8  $[\text{In}(\text{In-TCBPP})] \cdot 12\text{DMF}$  ( $\text{H}_6\text{TCBPP}$  = tetrakis-4-carboxybiphenylporphyrin)<sup>27</sup> and UNLPF-10  $[\text{In}_3(\text{TBCPPP})]$  ( $\text{H}_{10}\text{TBCPPP}$  = tetrakis-3,5-bis[4-carboxyphenyl]phenyl porphyrin)<sup>28</sup>).

For the possible application of porphyrin-based MOFs, for example in catalysis or drug delivery, the control of particle size can be very important.<sup>3,10,29</sup> Various methods have been reported for the synthesis of nanoscale MOFs, such as batch

Received: February 3, 2016

Published: May 20, 2016



synthesis with thermal heating (bs-th),<sup>30–33</sup> ultrasound-assisted batch synthesis (bs-us),<sup>34</sup> and continuous-flow (cf) synthesis.<sup>35–37</sup> The latter has also been successfully employed for the synthesis of CdS nanoparticles.<sup>38</sup> In addition, this synthesis approach has been used for the continuous production of MOFs such as UiO-66,<sup>36</sup> Al-MIL-53,<sup>37</sup> or CAU-13<sup>35</sup> with high space–time yields of several hundred kilograms per cubic meter and day. Although synthetic strategies providing control of the particle size have been carried out for tetrapyrrolylporphyrin-based MOFs like Zn- and Cu-TPyP,<sup>39–41</sup> such studies have not been reported so far for tetracarboxyphenylporphyrin-based MOFs.

Herein, we present the synthesis and detailed characterization of two porphyrin-based MOFs containing Ga and In (Ga-PMOF and In-PMOF). Three synthesis methods, batch synthesis with thermal heating (bs-th), ultrasound-assisted batch synthesis (bs-us), and continuous-flow (cf) synthesis, were employed to study their influence on the purity and particle size of the MOFs.

## EXPERIMENTAL SECTION

**Materials.** Ga(NO<sub>3</sub>)<sub>3</sub>·H<sub>2</sub>O (99.99%, ABCR), In(NO<sub>3</sub>)<sub>3</sub>·H<sub>2</sub>O (99.99%, ABCR), DMF (99%, Grüssing), acetone (99%, Walther), and EtOH (99%, Walther) were used without further purification. The metal salts were dissolved in distilled H<sub>2</sub>O to achieve different concentrations. The linker 4,4',4'',4'''-(5,10,15,20-porphyrinetetrayl)-tetrabenzoic acid (H<sub>6</sub>TCPP) was synthesized according to literature procedures<sup>42–44</sup> starting with 4-formylbenzoic acid (98%, ABCR) and pyrrole (98%, ABCR) in propionic acid (99%, Grüssing). Details are given in the Supporting Information.

**Characterization.** For the optimization of synthesis conditions, our high-throughput (HT) methodology employing a 24-high-throughput reactor system was used.<sup>33,43,46</sup> The high-throughput PXRD measurements were carried out with a STOE HT diffractometer equipped with an *xy*-stage and an IPDS system (Cu K<sub>α</sub> radiation) in transmission geometry. High resolution PXRD patterns were measured on a STOE Stadi-P powder diffractometer equipped with a Mythen detector (Cu K<sub>α</sub> radiation). For the ultrasound-assisted syntheses the ultrasonication bath (Sonorex RK 100, 40 kHz, 80/160 W, Bandelin) and glass vials from Duran (*V*<sub>max</sub> = 7.0 mL, Pyrex) were used. IR spectra were recorded using a Bruker ALPHA-FT-IR A220/D-01 spectrometer equipped with an ATR unit. NMR data were measured on a Bruker DRX 500 spectrometer. For the quantitative analysis of occluded guest molecules, <sup>1</sup>H NMR spectroscopy was employed. The samples were dissolved in a mixture of 10% deuteriochloric acid (DCl) in D<sub>2</sub>O and deuterated dimethyl sulfoxide (*d*<sub>6</sub>-DMSO) (molar ratio = 1:7). Sorption experiments were performed with a BEL Japan Inc. BELSORP-max. Before sorption measurements all samples were activated at 140 °C under vacuum (10<sup>-2</sup> kPa) for 16 h. Thermogravimetric measurements were performed on a NETZSCH STA 409 CD analyzer under a flow of air (75 mL min<sup>-1</sup>) with a heating rate of 4 °C min<sup>-1</sup> over a temperature range between 25 and 700 °C in Al<sub>2</sub>O<sub>3</sub> crucibles. The data were corrected for buoyancy and current effects. Dynamic light scattering measurements were performed on a Delsa Nano C particle analyzer from Beckman Coulter with ethanol as solvent. Prior to the measurements, the samples which were stored in ethanol were redispersed. In the case of the reaction products Ga- and In-PMOF-bs-th as well as Ga-PMOF-cf the redispersion was accomplished by ultrasonication for 30 min. In-PMOF-bs-us formed a stable dispersion after washing with ethanol. For the measurement, 20 μL of the respective dispersion were added to a cuvette containing 4 mL of ethanol and measured subsequently. The particle sizes of all obtained samples were also determined from PXRD data using the program suite TOPAS academics V4.1. A LaB<sub>6</sub> standard was used to determine the instrumental line broadening, and the particle size was calculated employing the Scherrer equation.<sup>47,48</sup> For SEM imaging a Zeiss

NVision40 microscope was used. Secondary electron images were acquired using the inlense detector and a low acceleration voltage of 2.5 keV for all samples except for sample Ga-PMOF-cf (120 °C), which was imaged at an acceleration voltage of 5 keV. TEM studies were carried out with the In-PMOF-bs-us nanoparticles using a Titan-Themis 60-300 TEM (FEI Company) operating at 300 kV with a high-angle annular dark field detector. A droplet of the diluted nanoparticle dispersion in absolute ethanol was dried on a carbon-coated copper grid.

**Preparation.** Three different synthesis methods, i.e., batch synthesis with thermal heating in HT Teflon inserts = bs-th, ultrasound-assisted batch synthesis = bs-us, and continuous-flow synthesis = cf, for the formation of Ga- and In-PMOF were investigated (Figure 1).

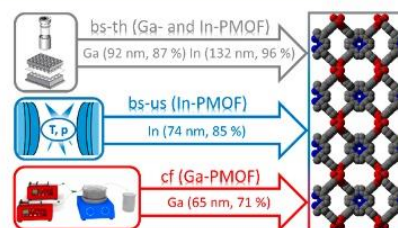


**Figure 1.** Schematic presentation of the different synthesis methods used in this study. The setups for the batch synthesis with thermal heating (bs-th), the ultrasound-assisted batch synthesis (bs-us), and the continuous-flow (cf) synthesis are shown in gray, blue, and red, respectively. Values in parentheses show the particle size measured by DLS and the yield of the individual reactions.

The synthesis of Ga- and In-PMOF-bs-th was studied using high-throughput methods (*V*<sub>max</sub> = 2.0 mL per Teflon insert, details see Figure S2). Different reaction temperatures between 80 and 160 °C in 20 °C steps, different molar ratios of reactants, additives like benzoic, formic, and acetic acid, and different volume ratios of H<sub>2</sub>O:DMF between 1:6 and 1:38 were tested. The results of the HT experiments leading to highly crystalline Ga- and In-PMOF-bs-th are shown in Figure S2, and the optimized synthesis conditions are described in the following paragraphs.

Optimized batch reactor synthesis of Ga-PMOF-bs-th: H<sub>6</sub>TCPP (15 mg, 1.9 × 10<sup>-2</sup> mmol), DMF (724 μL), and 1 M aqueous Ga(NO<sub>3</sub>)<sub>3</sub>·H<sub>2</sub>O solution (37.8 μL, 3.8 × 10<sup>-2</sup> mmol) were added to the 2.0 mL reactor. The reactor was heated for 48 h at 120 °C and cooled down to rt in 6 h. The resulting product was washed two times each with DMF and acetone. A yield of 220 mg, 87% (based on H<sub>6</sub>TCPP) was obtained for Ga-PMOF-bs-th, [Ga<sub>2</sub>(H<sub>2</sub>TCPP)(OH)<sub>2</sub>]<sub>2</sub>·3DMF·3H<sub>2</sub>O.

Optimized batch reactor synthesis of In-PMOF-bs-th: H<sub>6</sub>TCPP (15 mg, 1.9 × 10<sup>-2</sup> mmol), DMF (724 μL), and 0.5 M aqueous In(NO<sub>3</sub>)<sub>3</sub>·H<sub>2</sub>O solution (75.6 μL, 3.8 × 10<sup>-2</sup> mmol) were added to the 2.0 mL reactor. The reactor was heated for 48 h at 120 °C and cooled down to rt in 6 h. The resulting product was washed two times each with DMF and acetone. A yield of 292 mg, 96% (based on H<sub>6</sub>TCPP) was obtained for In-PMOF-bs-th [In<sub>2</sub>(H<sub>2</sub>TCPP)(OH)<sub>2</sub>]<sub>2</sub>·3DMF·4H<sub>2</sub>O. Both MOF syntheses can be scaled up in 30 mL Teflon reactors by using the 12-fold amount of all reactants, the same molar ratio of metal to linker (2:1), the same temperature–time program, and the same washing procedures.

Elemental analysis for Ga-PMOF-bs-th and In-PMOF-bs-th:



calcd (%) C 55.5, H 4.5, N 7.9; found (%) C 55.1, H 4.4, N 8.0



calcd (%) C 51.0, H 4.3, N 7.3; found (%) C 51.2, H 4.3, N 7.8



Ultrasound-assisted synthesis could only be achieved for the In-PMOF. In-PMOF-bs-us was synthesized in glass-vials ( $V_{\max} = 7.0$  mL) by mixing  $H_6TCPP$  (51 mg,  $6.5 \times 10^{-2}$  mmol), DMF (4 mL), and 0.5 M aqueous  $In(NO_3)_3 \cdot H_2O$  solution (257.0  $\mu L$ ,  $12.9 \times 10^{-2}$  mmol). The glass vial was ultrasonicated in a water bath for 7 h. The final temperature of the water bath was 50 °C. The resulting product was centrifuged for 30 min at 20000 rpm and washed three times with ethanol by subsequent centrifugation, each time for 30 min at 20000 rpm. A yield of 68 mg, 85% (based on  $H_6TCPP$ ) was obtained for In-PMOF-bs-us,  $[In_2(H_6TCPP)(OH)_2] \cdot 3DMF \cdot 4H_2O$ .

Continuous-flow synthesis of Ga-PMOF-cf and In-PMOF-cf was carried out using a two-syringe-pump flow reactor setup as previously described.<sup>35</sup> The MOFs were obtained using concentrations of 0.1 mol  $L^{-1}$  of  $Ga(NO_3)_3$  and  $H_6TCPP$  in a mixture of 94 vol % DMF and 6 vol % water. For the synthesis of In-PMOF-cf, corresponding solutions with a concentration of 0.05 mol  $L^{-1}$  were used. The solutions were injected into a flow reactor ( $V = 15$  mL) with flow rates of 0.167 mL  $min^{-1}$  for metal and 0.084 mL  $min^{-1}$  for the linker solution respectively, giving a total reaction time of 60 min. The different flow rates for metal and linker solution led to a molar metal-to-linker ratio of 2 to 1. During the reaction the flow reactor was kept at a temperature of 100 °C. In a second experiment a flow rate of 0.125 mL  $min^{-1}$  for both starting materials was used (molar ratio metal-to-linker 1:1) and the reaction temperature was raised to 120 °C. The products were collected and isolated by centrifugation for 15 min at 15000 rpm and washed three times with ethanol by subsequent centrifugation, each time for 15 min at 15000 rpm. The formation of Ga-PMOF-cf at 100 °C yielded 397 mg, 71% (based on  $H_6TCPP$ ) with a space-time yield of 648 kg  $m^{-3} d^{-1}$ . The corresponding synthesis of In-PMOF-cf at 100 °C was also carried out, but the reaction product contains X-ray amorphous impurities. Hence a detailed characterization of this product was not carried out. To confirm that In-PMOF-cf was obtained a Pawley fit was performed (Figure S5).

## RESULTS AND DISCUSSION

**Synthesis.** Three different synthesis settings (batch synthesis with thermal heating = bs-th, ultrasound-assisted batch synthesis = bs-us, continuous-flow synthesis = cf) were used to synthesize the two new porphyrin-based MOFs Ga- and In-PMOF. The two MOFs were investigated by high-throughput methods, and the resulting high-throughput experiment that led to the highly crystalline Ga- and In-PMOF-bs-th is shown in Figure S2. The optimized synthesis time and temperature was 48 h at 120 °C to achieve highly crystalline products with different particle sizes (92 (25) for Ga-PMOF and 132 (25) nm for In-PMOF). Using ultrasound-assisted and continuous-flow synthesis, it was possible to vary the resulting particle size of both MOFs in the range of 100 nm. In case of the ultrasound-assisted batch synthesis (bs-us) only In-PMOF-bs-us could be obtained. The synthesis was established in an ultrasonication bath within 7 h, which led to an increase of the reaction temperature to 50 °C. This synthesis led to particles sized at the order of 60 nm. Continuous-flow synthesis (cf) led to both MOFs, but In-PMOF-cf was only obtained with X-ray amorphous impurities. For the synthesis of Ga-PMOF-cf two different temperatures, 120 and 100 °C, were employed, which led to products with different particle sizes of about 65 nm (120 °C) and 156 nm (100 °C), respectively. Details regarding the particle size are given in the corresponding section below.

**Crystal Structure.** All compounds were obtained as microcrystalline powders. Initial powder X-ray diffraction (PXRD) measurements confirmed that Ga- and In-PMOF are isostructural to Al-PMOF.<sup>25</sup> For the structure refinement high resolution PXRD patterns of the batch synthesis products were used. Pawley fits of the high resolution data of Ga- and In-PMOF-bs-th with the program TOPAS academic V4.1<sup>48</sup> are in

good agreement with the cell parameters of Al-PMOF, corresponding to the different metal ion.<sup>25</sup> Using the structure of Al-PMOF<sup>25</sup> with the respective metal ion gallium or indium as starting model, their crystal structures were successfully refined by Rietveld methods with TOPAS academic V4.1.<sup>48</sup> The crystallographic data and the results of the Rietveld refinement are shown in Table 1 and Figures 2 and 3. Pawley

**Table 1.** Crystallographic Data of Al-, Ga-, and In-PMOF

	Al-PMOF <sup>25</sup>	Ga-PMOF-bs-th	In-PMOF-bs-th
SG	<i>Cmmm</i>	<i>Cmmm</i>	<i>Cmmm</i>
<i>a</i> [Å]	31.978(3)	32.950(4)	33.432(2)
<i>b</i> [Å]	6.5812(4)	6.700(2)	7.152(1)
<i>c</i> [Å]	16.862(2)	16.556(2)	16.718(1)
GOF	2.4	1.6	1.6
$R_{wp}$	4.0	6.5	5.7
$R_{Bragg}$		0.75	0.76

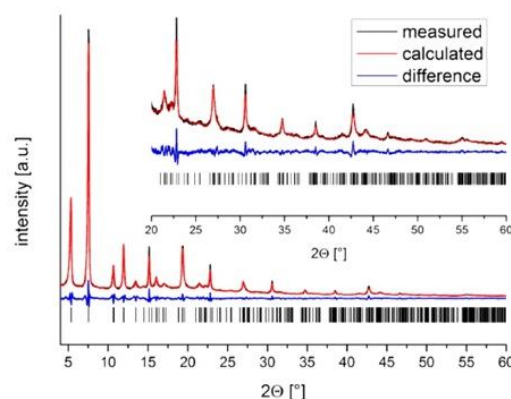


**Figure 2.** Result of the Rietveld refinement of Ga-PMOF-bs-th. Measured data are shown as a black line and calculated data as a red line, and the blue line gives the difference plot. Predicted peak positions are marked as vertical bars.

fits were also carried out for the products In-PMOF-bs-us, Ga-PMOF-cf, and In-PMOF-cf. The results of the Pawley fits and

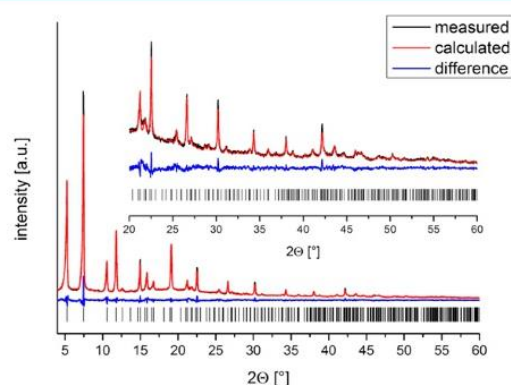


**Figure 3.** Result of the Rietveld-refinement of In-PMOF-bs-th. Measured data are shown as a black line, calculated data as a red line and the blue line gives the difference plot. Predicted peak positions are marked as vertical bars.



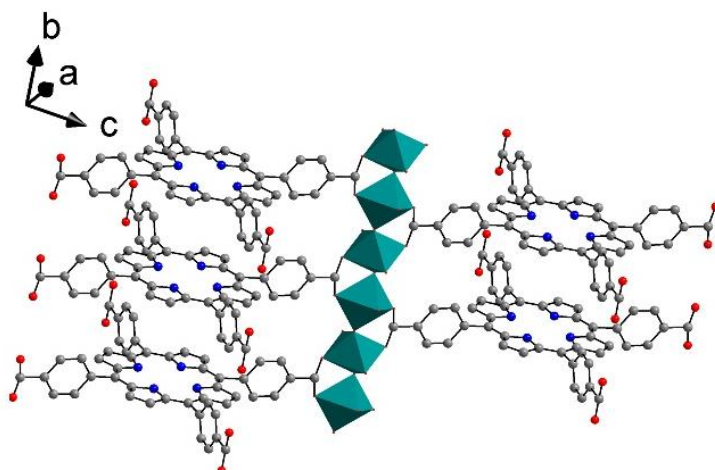


**Figure 4.** Chains of trans corner-sharing  $\text{GaO}_6$  and  $\text{InO}_6$  polyhedra in Ga- and In-PMOF with a few added linker molecules.

the refined cell parameters are shown in Figures S3, S4, and S5 and Table S1.<sup>48</sup>

The title compounds of framework composition  $[\text{Ga}_2(\text{H}_2\text{TCCP})(\text{OH})_2]$  and  $[\text{In}_2(\text{H}_2\text{TCCP})(\text{OH})_2]$  crystallize in the space group  $Cmnm$ . They are isostructural to the corresponding Al-PMOF<sup>25</sup> which contains the same linker, and therefore the structure is only briefly described.  $\text{GaO}_6$  and  $\text{InO}_6$  polyhedra are connected by  $\mu\text{-OH}$  groups and form chains of trans corner-sharing polyhedra (Figure 4). The other coordinating O atoms are from deprotonated carboxylate groups of the linker molecules. The chains are connected by  $\text{H}_2\text{TCCP}^{4-}$  molecules to form a three-dimensional framework. Two types of pores are formed each along  $[010]$  and  $[001]$ , with diameters of 5.0/11.8 Å and 3.4/11.8 Å respectively for Ga-PMOF (Figure 5) and 5.0/11.8 Å and 4.0/12.6 Å respectively for In-PMOF. The diameters were determined using DIAMOND V.3 taking the van der Waals radii of guest molecules into account.<sup>49,50</sup>

**Sorption Properties.** Sorption experiments using  $\text{N}_2$  and  $\text{CO}_2$  as adsorptives were performed. All samples were activated at 140 °C under vacuum ( $10^{-2}$  kPa) for 16 h.  $\text{N}_2$  sorption measurements at 77 K were measured for all the different reaction products obtained using the three synthesis methods (Table 2, Figure 6, and Figures S7 and S8). The micropore volumes  $V_m$  were determined by using the amount of adsorbed  $\text{N}_2$  at the relative pressure  $p/p_0 = 0.5$ .  $\text{CO}_2$  sorption measurements at 298 K were only performed for the samples obtained from the scale-up reaction using the batch synthesis, i.e., Ga- and In-PMOF-bs-th (Table 2, Figure S6). To verify the stability of all the investigated products, PXRD measurements were carried out after every sorption experiment. The data are shown in Figure S9 and confirm the stability of the compounds.

Depending on the synthesis method employed, the specific surface areas are in the range of 1150 to 1400  $\text{m}^2 \text{g}^{-1}$  and 1200 to 1250  $\text{m}^2 \text{g}^{-1}$  for the various Ga- and In-PMOFs, respectively. These values compare well with the reported one for Al-PMOF (1400  $\text{m}^2 \text{g}^{-1}$ ). Taking into account the different atomic masses of Al, Ga, and In, very similar specific surface areas in  $\text{m}^2 \text{mmol}^{-1}$  are found. The theoretical specific surface areas of Al-, Ga-, and In-PMOF were simulated using the program suite Materials Studio (v. 5.0)<sup>51</sup> and employing the strategy reported by Dören et al.<sup>52</sup> With this strategy the surface area is calculated

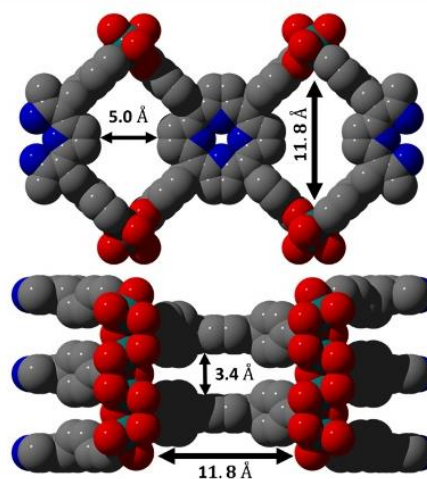


**Figure 5.** Space filling model of the crystal structure of Ga-PMOF; view along  $[010]$  (top) and along  $[001]$  (bottom). The pores along  $[010]$  have diameters of 5.0 and 11.8 Å, and along  $[001]$  pores with diameters of 3.4 and 11.8 Å are observed. Carbon is shown in gray, oxygen in red, nitrogen in blue, and gallium in turquoise. In the crystal structure of In-PMOF the pores along  $[010]$  have the same size as Ga-PMOF, and along  $[001]$  pores with diameters of 4.0 and 12.6 Å are observed.

from the center of a sphere with a diameter of 3.60 Å that rolls across the pore surface. The observed surface area values are slightly smaller by about 100–200  $\text{m}^2 \text{g}^{-1}$  compared to the calculated ones. The  $\text{CO}_2$  sorption measurements, which were only performed for the scaled-up products of Ga- and In-PMOF-bs-th, show an uptake of 15.2 and 12.9 wt % at 1 bar and 298.15 K for Ga- and In-PMOF-bs-th, respectively.

**Thermal and Chemical Stability.** To remove nonreacted linker molecules as well as solvent molecules and to investigate the chemical stability of the PMOFs, the samples were treated in different solvents ( $\text{H}_2\text{O}$ , EtOH, MeOH, acetone) at rt for 24 h under stirring followed by thermal activation between 120 and 180 °C for 12 h under vacuum ( $10^{-2}$  kPa). The results of these experiments (Figure 7) show that the crystallinity of the Ga- and In-PMOF correlates strongly with the presence of

# Porphyrin-basierte Metall-Organische Gerüstverbindungen: Von Metall-Carboxylaten zu Metall-Phosphonaten

**Table 2. Results of the Sorption Experiments ( $N_2$  at 77 K and  $CO_2$  at 298.15 K) of the Ga- and In-PMOFs Obtained Using Different Synthesis Methods: Ga-PMOF-bs-th (scaled up), In-PMOF-bs-th (scaled up), In-PMOF-bs-us, and Ga-PMOF-cf<sup>a</sup>**

	Al-PMOF <sup>25</sup>	Ga-PMOF-bs-th	In-PMOF-bs-th	In-PMOF-bs-us	Ga-PMOF-cf
$N_2$ (access.) [m <sup>2</sup> g <sup>-1</sup> ] [m <sup>2</sup> mmol <sup>-1</sup> ]	1400 1229	1150 1108	1200 1264	1250 1318	1400 1350
$N_2$ (access. surf.) [m <sup>2</sup> g <sup>-1</sup> ] <sup>b</sup>	1600	1550	1500	1500	1550
$N_2$ ( $V_m$ ) [cm <sup>3</sup> g <sup>-1</sup> ]	0.63	0.48	0.50	0.55	0.59
$CO_2$ (upt.) [mol mol <sup>-1</sup> ] [wt %]	-	3.8 15.2	3.2 12.9		

<sup>a</sup>These results are compared to the literature values of Al-PMOF.<sup>25</sup> The micropore volume was calculated at  $p/p_0 = 0.5$ . <sup>b</sup>The theoretically accessible surface areas were calculated using the strategy reported by Düren et al.<sup>52</sup>

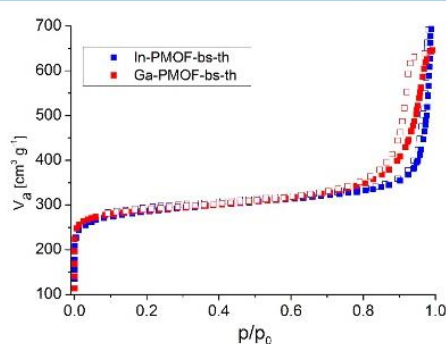


**Figure 6.**  $N_2$ -sorption isotherms of Ga- and In-PMOF-bs-th measured at 77 K. Filled squares represent adsorption and empty squares desorption, respectively.

DMF molecules in the pores, which was determined by <sup>1</sup>H NMR spectroscopy. Washing with water, 2 M HCl, or 2 M NaOH leads to a decrease or loss of long-range order (Figure 7). Corresponding stability tests at pH = 7 using a  $Na_2HPO_4/NaH_2PO_4$  buffer system were also carried out and led to the formation of X-ray amorphous products. Due to these experiments, the best activation procedure was determined as

washing with EtOH, MeOH, or acetone and activation at 140 °C under vacuum ( $10^{-2}$  kPa) for 16 h.

Samples treated with  $H_2O$  and HCl could be easily regenerated within a few seconds by impregnation with DMF at room temperature. Thermal activation above 145 °C at  $10^{-2}$  kPa leads to the removal of all DMF molecules and a strong decrease in crystallinity (Figure 7). These samples could also be regenerated in all cases by impregnation with DMF at room temperature within a few seconds. This indicates that loss of the long-range order is a reversible process.

The thermal stability was also investigated with thermogravimetric measurements (TG). For Ga- and In-PMOF-bs-th, TG measurements were carried out for the as-synthesized and the activated form, to determine the amount of solvent molecules in the pores. For all other compounds the TG data of the as-synthesized products are shown. The results of the TG investigations are summarized in Table 3, and the TG curves are presented in Figure 8 and Figures S10–S14. In the as-synthesized samples three characteristic steps of weight loss are observed. The loss up to 100 °C is assigned to the release of physisorbed water molecules and the one between 100 and 300 °C to the evaporation of DMF. Above 330 °C the decomposition of the PMOFs take place and the final products are  $In_2O_3$  and  $Ga_2O_3$  as confirmed by PXRD measurements

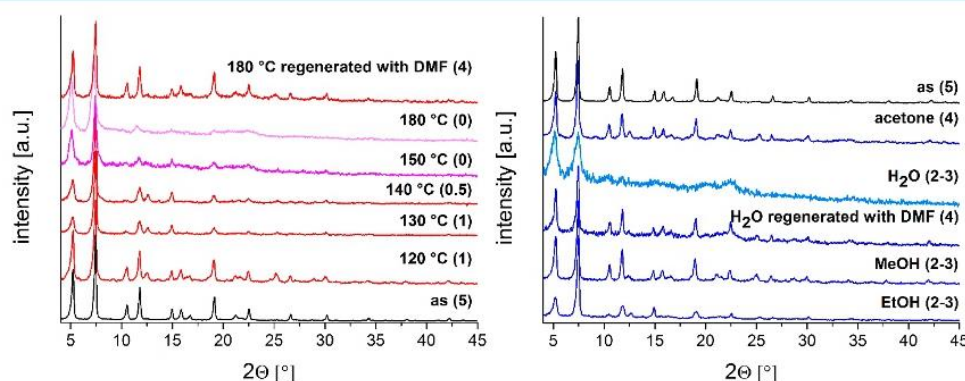


**Figure 7.** Thermal (left) and chemical stability (right) shown for In-PMOF-bs-th at activation temperatures between 120 and 180 °C and in different solvents (24 h, stirring at room temperature). The values in parentheses denote the number of DMF molecules per  $H_2TCPP^{4+}$  ion (as = as synthesized).



**Table 3. Results of the Thermogravimetric Measurements of All Obtained Compounds<sup>a</sup>**

	residual mass [%]	mass loss linker decompn [%]		mass loss physisorbed [%]	
		measd	calcd	H <sub>2</sub> O	DMF
Ga-PMOF-bs-th (as)	14.4	68.0 (1:1.8)	63.0 (1:2.0)	2.9 (1.9 H <sub>2</sub> O)	13.5 (2.2 DMF)
Ga-PMOF-bs-th (act)	19.1	76.4 (1:2.1)	80.6 (1:2.0)	4.6 (2.6 H <sub>2</sub> O)	
In-PMOF-bs-th (as)	19.4	53.8 (1:2.1)	57.3 (1:2.0)	3.0 (2.6 H <sub>2</sub> O)	24.9 (5.2 DMF)
In-PMOF-bs-th (act)	24.0	73.5 (1:1.9)	70.9 (1:2.0)	3.0 (1.9 H <sub>2</sub> O)	
In-PMOF-bs-us (as)	19.3	57.9 (1:2.0)	57.1 (1:2.0)	3.4 (2.6 H <sub>2</sub> O)	20.0 (3.9 DMF)
Ga-PMOF-cf (as)	14.2	59.9 (1:2.0)	62.2 (1:2.0)	5.5 (4.1 H <sub>2</sub> O)	10.3 (1.9 DMF)

<sup>a</sup>The number of solvent molecules per formula unit and resulting metal to linker ratios are shown in parentheses. The abbreviations “as” and “act” in parentheses denote as-synthesized and activated samples (solvent exchange and thermal activation at 140 °C and 10<sup>-2</sup> kPa for 16 h).

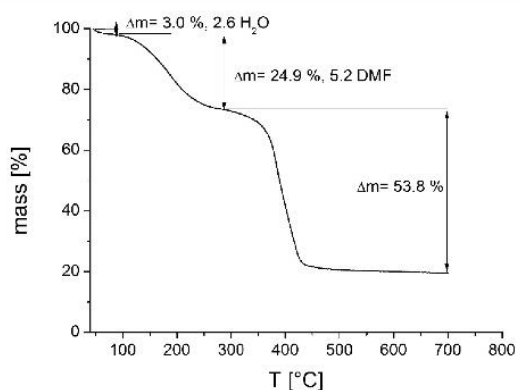


**Figure 8.** Thermogravimetric curve of an as-synthesized sample of In-PMOF-bs-th. Evaluation of the measurement reveals a molar ratio of linker:metal:H<sub>2</sub>O:DMF of 1:2.1:2.6:5.2 (Table 3).

(Figure S15). The results of the thermogravimetric analyses fit well with the elemental analyses given in the Experimental Section. Only the amounts of occluded solvent molecules differ slightly due to the storage conditions of the samples prior to the measurements. The TG curves of the activated samples of Ga- and In-PMOF-bs-th show a small mass loss of a few percent up to 100 °C, which is due to the release of 2 to 3 physisorbed H<sub>2</sub>O molecules per formula unit (Table 3).

**IR Spectroscopy.** IR spectra of as-synthesized samples of Ga- and In-PMOF-bs-th are shown in Figure S16, and the assignment of the bands is given in Table S2. Since the bands for the title compounds are observed at very similar wave numbers, only the IR spectrum of Ga-PMOF is briefly discussed. The stretching vibration of the N–H group is observed at 3320 cm<sup>-1</sup>. The asymmetric ( $\nu_{as}$ ) and symmetric ( $\nu_s$ ) stretching vibrations of the coordinating carboxylate groups are observed at 1590 and 1415 cm<sup>-1</sup>, respectively. The characteristic  $\nu(\text{C}=\text{C})$  valence vibration of the phenyl rings is observed at 1545 cm<sup>-1</sup>. Further characteristic vibrations such as the  $\nu(\text{C}-\text{N})$  valence vibration and  $\delta(\text{C}-\text{H}, \text{N}-\text{H})$  and  $\gamma(\text{C}-\text{H})$  deformation vibrations of the porphyrin moiety are found at 1362, 961, and 796 cm<sup>-1</sup>, respectively (Table S2). The vibration at 1710 cm<sup>-1</sup> is due to the presence of DMF molecules and can be assigned to the  $\nu(\text{C}=\text{O})$  stretching vibration.<sup>53,54</sup>

**Particle Size.** The influence of the synthesis method on the particle sizes of the resulting PMOFs was studied using dynamic light scattering (DLS), SEM, and TEM measurements. While the first method leads to quantitative information on the bulk properties and yields the hydrodynamic radius, the latter is used to get information about the particle shape. In addition

crystallographic details such as lattice parameters can be obtained for the PMOFs.

**DLS.** The results of the DLS measurements are shown in Figures S17 and S18. The observed particle sizes are between about 60 and 160 nm for Ga-PMOF and 70 and 130 nm for In-PMOF (Table 4). The synthesis of Ga-PMOF in the

**Table 4. Particle Sizes of Ga-PMOF-bs-th, In-PMOF-bs-th, In-PMOF-bs-us, and Ga-PMOF-cf as Obtained from DLS Measurements and the Evaluation of the PXRD Data Using the Scherrer Equation<sup>a</sup>**

	$r_H^b$ [nm]	PI <sup>c</sup>	particle size (PXRD) [nm]
Ga-PMOF-cf (120 °C)	65 (18)	0.19	38 (11)
Ga-PMOF-bs-th	92 (25)	0.12	64 (22)
Ga-PMOF-cf (100 °C)	156 (28)	0.30	
In-PMOF-bs-us	74 (21)	0.23	92 (30)
In-PMOF-bs-th	132 (25)	0.20	105 (70)

<sup>a</sup>Values in parentheses are the standard deviations. <sup>b</sup> $r_H$  = hydrodynamic radius. <sup>c</sup>PI = polydispersity index.

continuous-flow reactor using synthesis temperatures of 100 and 120 °C and molar ratios of reactants of metal-to-linker of 2:1 and 1:1 leads to different particle sizes of 65 nm (120 °C) and 156 nm (100 °C), respectively.

**PXRD.** The particle sizes of all obtained samples were also determined from PXRD data. They are in most cases consistent with the DLS measurements taking into account that the hydrodynamic radius is larger than the particle size (Table 4).<sup>55</sup> In one case the particle size determined from PXRD and DLS data is in the same range, but in this case high standard deviations are found.

**SEM.** The samples were also characterized by SEM measurements (Figures S19–S23). The micrographs reveal plate-shaped morphologies for all samples, and the edges of the plates are not very well-defined. Therefore, and because of particle agglomeration, the determination of a particle size distribution of the samples was not possible.<sup>55</sup> From the micrographs one can deduce that thermal heating leads to larger particles than the ones obtained under ultrasonication and that in the flow reactor at 120 °C the smallest particles are obtained. This is in agreement with the other characterization measurements.

The particle size and morphology of In-PMOF-bs-us nanoparticles were also investigated by TEM measurements (Figure 9). This sample was chosen due to its high crystallinity and the smallest particle size of the synthesized In-PMOFs, as shown with DLS measurements (Figure S18).

Figure 9 shows a typical TEM image of the In-PMOF-bs-us sample, in which the morphology and size of the crystalline

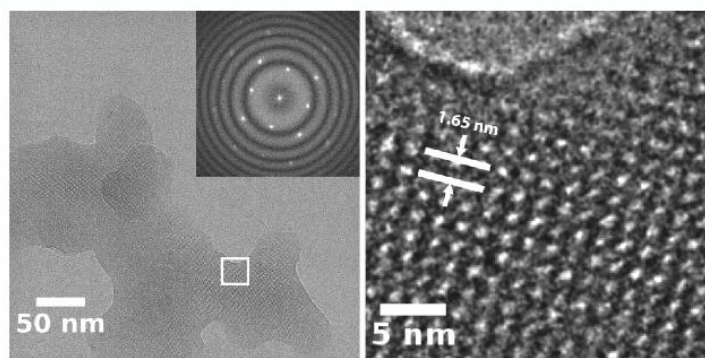


**Figure 9.** Left: TEM image of the as-synthesized In-PMOF-bs-us on a carbon support film. The inset shows the Fourier transform of the TEM image, in which the radial distance represents the lattice fringe distance. Right: Details of the TEM image shown on the left side with the lattice planes corresponding to the [001] reflection of In-PMOF-bs-us (1.65 nm).

particles are visible, in addition to individual sets of lattice planes. The particles exhibit different types of morphology and sizes and tend to agglomerate. Most of the particles appear almost circular in the projection, hinting at a spherical shape. Other particles are bounded by straight lines, indicating the formation of facets. The lateral size of the particles ranges from 25 to about 80 nm.

In order to determine the lattice parameters of the crystalline phase, the interplanar distances between the various sets of lattice planes were measured by means of digital image analysis. The inset in Figure 9 shows a Fourier transform (FT) of the TEM image. The radial distance of the apparent spots indicates the lattice distance in reciprocal space. A comparison with calculated values for the In-PMOF-bs-us sample shows very good agreement with the measured ones (Table 5).

**Table 5.** Measured Lattice Distances from TEM Micrographs Compared with the Calculated Ones from the Crystal Structure of In-PMOF<sup>a</sup>

measd lattice distance [nm]	calcd lattice distance from PXRD [nm]	corresponding lattice plane [hkl]
1.65	1.67	[001]
11.6	11.8	[201]
0.74	0.75	[202]

<sup>a</sup>The corresponding lattice planes are also shown.

## CONCLUSION

We demonstrated the successful synthesis and characterization of two new porphyrin based MOFs containing gallium and indium, i.e., Ga-PMOF [Ga<sub>2</sub>(H<sub>2</sub>TCPP)(OH)<sub>2</sub>·3DMF·3H<sub>2</sub>O] and In-PMOF [In<sub>2</sub>(H<sub>2</sub>TCPP)(OH)<sub>2</sub>·3DMF·4H<sub>2</sub>O], respectively. The synthesis of both MOFs was investigated by high-throughput methods,<sup>33</sup> and the structures were successfully refined by the Rietveld method. Three synthesis methods, i.e., batch synthesis, ultrasound-assisted, and continuous-flow synthesis were employed to vary the particle size of the resulting PMOFs. The resulting nanoparticles had diameters between about 60 and 160 nm for Ga-PMOF and 70 and 130 nm for In-PMOF as demonstrated by DLS, PXRD, SEM, and TEM measurements (for In-PMOF-bs-us). The TEM measurements show that In-PMOF-bs-us is obtained as nanoparticles of high crystallinity. The use of the continuous flow synthesis allows us to synthesize Ga-PMOF-cf at gram scale with a space-time

yield of 648 kg m<sup>-3</sup> d<sup>-1</sup>. Both MOFs show a high BET surface area between 1100 and 1400 m<sup>2</sup> g<sup>-1</sup> as determined from N<sub>2</sub> physisorption measurements at 77 K, and they are also porous toward CO<sub>2</sub> (uptake in Ga-PMOF is 15.2 and In-PMOF it is 12.9 wt % at 298.15 K and 1 bar).

Both MOFs show thermal stability up to about 145 °C and chemical stability in all tested organic solvents. The observed loss of long-range order after treatment with H<sub>2</sub>O or activation temperatures above 145 °C is reversible; impregnation with DMF at room temperature for a short time restores highly crystalline materials. The small particle size and the high crystallinity of the title compounds in combination with their porosity could make these porphyrin-based MOFs possible candidates in drug delivery applications or in catalysis.

## ASSOCIATED CONTENT

### Supporting Information

The Supporting Information is available free of charge on the ACS Publications website at DOI: 10.1021/acs.inorgchem.6b00221.

Synthesis and characterization of H<sub>6</sub>TCPP and other experimental details (PDF)

Crystallographic data of Ga-PMOF-bs-th (CIF)

Crystallographic data of In-PMOF-bs-th (CIF)

CCDC 1438646 and 1438647 also contain crystallographic data for this paper. These data can be obtained free of charge from The Cambridge Crystallographic Data Centre via [www.ccdc.cam.ac.uk/getstructures](http://www.ccdc.cam.ac.uk/getstructures).

## AUTHOR INFORMATION

### Corresponding Author

\*E-mail: [stock@ac.uni-kiel.de](mailto:stock@ac.uni-kiel.de).

### Notes

The authors declare no competing financial interest.

## ACKNOWLEDGMENTS

We appreciate support from the Deutsche Forschungsgemeinschaft (SPP-1362; STO 643/5-2), and we thank Achim Fölster for help in designing Figure 1. The authors thank Dr. Steffen Schmidt for assistance with TEM data acquisition and Ramona Hoffmann for measuring the SEM images.



■ REFERENCES

- (1) Yaghi, O. M.; O’Keeffe, M.; Ockwig, N. W.; Chae, H. K.; Eddaoudi, M.; Kim, J. *Nature* **2003**, *423*, 705–714.
- (2) Furukawa, H.; Cordova, K. E.; O’Keeffe, M.; Yaghi, O. M. *Science* **2013**, *341*, 1230444.
- (3) Stock, N.; Reinsch, H.; Schilling, L.-H. *Synthesis of MOFs. In Metal Organic Frameworks as Heterogeneous Catalysts*; The Royal Society of Chemistry: 2013; Chapter 2, pp 9–30.
- (4) Sun, C.-Y.; Qin, C.; Wang, X.-L.; Su, Z.-M. *Expert Opin. Drug Delivery* **2013**, *10*, 89–101.
- (5) Janiak, C.; Vieth, J. K. *New J. Chem.* **2010**, *34*, 2366–2388.
- (6) Mueller, U.; Schubert, M.; Teich, F.; Puetter, H.; Schierle-Arndt, K.; Pastre, J. J. *Mater. Chem.* **2006**, *16*, 626–636.
- (7) Zhou, H.-C.; Long, J. R.; Yaghi, O. M. *Chem. Rev.* **2012**, *112*, 673–674.
- (8) Bernini, M. C.; Fairen-Jimenez, D.; Pasinetti, M.; Ramirez-Pastor, A. J.; Snurr, R. Q. *J. Mater. Chem. B* **2014**, *2*, 766–774.
- (9) Horcajada, P.; Chalati, T.; Serre, C.; Gillet, B.; Sebrie, C.; Baati, T.; Eubank, J. F.; Heurtaux, D.; Clayette, P.; Kreuz, C.; Chang, J.-S.; Hwang, Y. K.; Marsaud, V.; Bories, P.-N.; Cynober, L.; Gil, S.; Férey, G.; Couvreur, P.; Gref, R. *Nat. Mater.* **2010**, *9*, 172–178.
- (10) Horcajada, P.; Gref, R.; Baati, T.; Allan, P. K.; Maurin, G.; Couvreur, P.; Férey, G.; Morris, R. E.; Serre, C. *Chem. Rev.* **2012**, *112*, 1232–1268.
- (11) Horcajada, P.; Serre, C.; Vallet-Regí, M.; Sebban, M.; Taulelle, F.; Férey, G. *Angew. Chem.* **2006**, *118*, 6120–6124.
- (12) Gao, W.-Y.; Chrzanowski, M.; Ma, S. *Chem. Soc. Rev.* **2014**, *43*, 5841–5866.
- (13) Harvey, R. A.; Ferrier, D. R. *Biochemistry*; Wolters Kluwer Health: 2011.
- (14) Martel, B.; Cassidy, K. *Chemical Risk Analysis: A Practical Handbook*; Taylor & Francis: 2000.
- (15) Nakajima, M.; Takahashi, H.; Sasaki, M.; Kobayashi, Y.; Ohno, Y.; Usami, M. *Teratog., Carcinog., Mutagen.* **2000**, *20*, 219–227.
- (16) Ungvary, G. J. *Toxicol. Environ. Health, Part A* **2000**, *59*, 27–42.
- (17) Ivanoff, C. S.; Ivanoff, A. E.; Hottel, T. L. *Food Chem. Toxicol.* **2012**, *50*, 212–215.
- (18) Feng, D.; Jiang, H.-L.; Chen, Y.-P.; Gu, Z.-Y.; Wei, Z.; Zhou, H.-C. *Inorg. Chem.* **2013**, *52*, 12661–12667.
- (19) Morris, W.; Voloskiy, B.; Demir, S.; Gándara, F.; McGrier, P. L.; Furukawa, H.; Cascio, D.; Stoddart, J. F.; Yaghi, O. M. *Inorg. Chem.* **2012**, *51*, 6443–6445.
- (20) Feng, D.; Gu, Z.-Y.; Chen, Y.-P.; Park, J.; Wei, Z.; Sun, Y.; Bosch, M.; Yuan, S.; Zhou, H.-C. *J. Am. Chem. Soc.* **2014**, *136*, 17714–17717.
- (21) Feng, D.; Chung, W.-C.; Wei, Z.; Gu, Z.-Y.; Jiang, H.-L.; Chen, Y.-P.; Daresbourg, D. J.; Zhou, H.-C. *J. Am. Chem. Soc.* **2013**, *135*, 17105–17110.
- (22) Jiang, H.-L.; Feng, D.; Wang, K.; Gu, Z.-Y.; Wei, Z.; Chen, Y.-P.; Zhou, H.-C. *J. Am. Chem. Soc.* **2013**, *135*, 13934–13938.
- (23) Fateeva, A.; Devautour-Vinot, S.; Heymans, N.; Devic, T.; Grenèche, J.-M.; Wuttke, S.; Miller, S.; Lago, A.; Serre, C.; De Weireld, G.; Maurin, G.; Vimont, A.; Férey, G. *Chem. Mater.* **2011**, *23*, 4641–4651.
- (24) Fateeva, A.; Clarisse, J.; Pilet, G.; Grenèche, J.-M.; Nouar, F.; Abeykoon, B. K.; Guegan, F.; Goutaudier, C.; Luneau, D.; Warren, J. E.; Rosseinsky, M. J.; Devic, T. *Cryst. Growth Des.* **2015**, *15*, 1819–1826.
- (25) Fateeva, A.; Chater, P. A.; Ireland, C. P.; Tahir, A. A.; Khimiyak, Y. Z.; Wiper, P. V.; Darwent, J. R.; Rosseinsky, M. J. *Angew. Chem.* **2012**, *124*, 7558–7562.
- (26) Huh, S.; Kim, S.-J.; Kim, Y. *CrystEngComm* **2016**, *18*, 345.
- (27) Gao, W.-Y.; Zhang, Z.; Cash, L.; Wojtas, L.; Chen, Y.-S.; Ma, S. *CrystEngComm* **2013**, *15*, 9320–9323.
- (28) Johnson, J. A.; Luo, J.; Zhang, X.; Chen, Y.-S.; Morton, M. D.; Echeverría, E.; Torres, F. E.; Zhang, J. *ACS Catal.* **2015**, *5*, 5283–5291.
- (29) He, C.; Liu, D.; Lin, W. *Chem. Rev.* **2015**, *115*, 11079–11108.
- (30) Rabenau, A. *Angew. Chem.* **1985**, *97*, 1017–1032.
- (31) Bauer, S.; Stock, N. *Chem. Unserer Zeit* **2007**, *41*, 390–398.
- (32) Sheldrick, W. S.; Wachhold, M. *Angew. Chem.* **1997**, *109*, 214–234.
- (33) Stock, N. *Microporous Mesoporous Mater.* **2010**, *129*, 287–295.
- (34) Safarifard, V.; Morsali, A. *Coord. Chem. Rev.* **2015**, *292*, 1–14.
- (35) Waitschat, S.; Wharmby, M. T.; Stock, N. *Dalton Trans.* **2015**, *44*, 11235.
- (36) Rubio-Martinez, M.; Batten, M. P.; Polyzos, A.; Carey, K.-C.; Mardel, J. I.; Lim, K.-S.; Hill, M. R. *Sci. Rep.* **2014**, DOI: 10.1038/srep05443.
- (37) Bayliss, P. A.; Ibarra, I. A.; Perez, E.; Yang, S.; Tang, C. C.; Poliakov, M.; Schroder, M. *Green Chem.* **2014**, *16*, 3796–3802.
- (38) Edel, J. B.; Fortt, R.; deMello, J. C.; deMello, A. J. *Chem. Commun.* **2002**, 1136–1137.
- (39) Shi, N.; Xie, L.; Sun, H.; Duan, J.; Yin, G.; Xu, Z.; Huang, W. *Chem. Commun.* **2011**, *47*, S055–S057.
- (40) Hu, J.-S.; Guo, Liang, H.-P.; Wan, L.-J.; Jiang, L. *J. Am. Chem. Soc.* **2005**, *127*, 17090–17095.
- (41) Shi, N.; Du, W.; Jin, X.; Zhang, Y.; Han, M.; Xu, Z.; Xie, L.; Huang, W. *Cryst. Growth Des.* **2014**, *14*, 1251–1257.
- (42) Jeong, E.-Y.; Ansari, M. B.; Mo, Y.-H.; Park, S.-E. *J. Hazard. Mater.* **2011**, *185*, 1311–1317.
- (43) Harada, A.; Yamaguchi, H.; Okamoto, K.; Fukushima, H.; Shiotsuki, K.; Kamachi, M. *Photochem. Photobiol.* **1999**, *70*, 298–302.
- (44) Garcia, G.; Sol, V.; Lamarche, F.; Granet, R.; Guillon, M.; Champavier, Y.; Krausz, P. *Bioorg. Med. Chem. Lett.* **2006**, *16*, 3188–3192.
- (45) Forster, P. M.; Stock, N.; Cheetham, A. K. *Angew. Chem., Int. Ed.* **2005**, *44*, 7608–7611.
- (46) Stock, N. *Chem. Ing. Tech.* **2010**, *82*, 1039–1047.
- (47) Balzar, D.; Audebrand, N.; Daymond, M. R.; Fitch, A.; Hewat, A.; Langford, J. I.; Le Bail, A.; Louer, D.; Masson, O.; McCowan, C. N.; Popa, N. C.; Stephens, P. W.; Toby, B. H. *J. Appl. Crystallogr.* **2004**, *37*, 911–924.
- (48) Coelho, A. *TOPAS-Academic V4.1*; Coelho Software: 2007.
- (49) Brandenburg, K. *Diamond Version 3*; Crystal Impact GbR: Bonn, 2012.
- (50) Pennington, W. J. *J. Appl. Crystallogr.* **1999**, *32*, 1028–1029.
- (51) *Materials Studio Version 5.0*; Accelrys Inc.: San Diego, CA, 2009.
- (52) Düren, T.; Millange, F.; Férey, G.; Walton, K. S.; Snurr, R. Q. *J. Phys. Chem. C* **2007**, *111*, 15350–15356.
- (53) Socrates, G. *Infrared and Raman Characteristic Group Frequencies: Tables and Charts*; Wiley: 2004.
- (54) Hesse, M.; Meier, H.; Zeeh, B. *Spektroskopische Methoden in der organischen Chemie*; Thieme: 2005.
- (55) Hirschle, P.; Preiß, Auras, F.; Pick, A.; Volkner, J.; Valdeperez, D.; Witte, G.; Parak, W. J.; Radler, J. O.; Wuttke, S. *CrystEngComm* **2016**, DOI: 10.1039/C6CE00198J.



#### 4.5.2 Co-Ligand Dependent Formation and Phase Transformation of Four Porphyrin-Based Cerium Metal–Organic Frameworks

Der folgende Artikel wurde im Jahr 2017 in der Fachzeitschrift *Crystal Growth & Design*, ACS veröffentlicht. Der Wiederabdruck erfolgte mit freundlicher Genehmigung der ACS. Reproduced with permission from Timo Rhauderwiek, Niclas Heidenreich, Helge Reinsch, Sigurd Øien-Ødegaard, Kirill A. Lomachenko, Uta Rütt, Alexander V. Soldatov, Karl Petter Lillerud and Norbert Stock, *Cryst. Growth Des.*, **2017**, *17*, 3462–3474, DOI: 10.1021/acs.cgd.7b00450. Copyright 2017 American Chemical Society.  
<http://pubs.acs.org/doi/abs/10.1021/acs.cgd.7b00450>

Der publizierte Artikel aus dem Jahr 2017 beschreibt die Synthese und Charakterisierung von vier Porphyrin-basierten Metall-Organischen Gerüstverbindungen (MOFs). Alle MOFs wurden unter Einsatz von 4-Tetracarboxyphenylporphyrin (H<sub>6</sub>TCPP) als Linker sowie Ce<sup>3+</sup> als Metallkation erhalten. In Anlehnung an die Arbeiten von Lammert et al.<sup>15</sup> wurden unter Einsatz von (NH<sub>4</sub>)<sub>2</sub>[Ce<sup>IV</sup>(NO<sub>3</sub>)<sub>6</sub>] und milden Reaktionsbedingungen versucht Porphyrin-basierte Ce(IV)-MOFs zu synthetisieren. Unter diesen Bedingungen fand jedoch eine Reduktion der Ce<sup>IV</sup>-Ionen (nachgewiesen mittels XANES Messungen an der Ce L<sub>3</sub>-Kante) statt und es wurden in Abhängigkeit des gewählten Co-Liganden, sowie der Aktivierungsmethode vier unterschiedliche MOF-Strukturen, resultierend in insgesamt zehn unterschiedlichen MOFs erhalten. In Abwesenheit eines Co-Liganden wurde der unporöse MOF CAU-18, [Ce<sub>4</sub>(H<sub>2</sub>TCPP)<sub>3</sub>(DMF)<sub>2</sub>(H<sub>2</sub>O)<sub>4</sub>], erhalten. Thermische Behandlung dieses MOFs für 16 h bei 250 °C führte zu CAU-18a, [Ce<sub>4</sub>(H<sub>2</sub>TCPP)<sub>3</sub>] · 22 H<sub>2</sub>O, welches eine spezifische Oberfläche nach BET von 550 m<sup>2</sup> g<sup>-1</sup> aufweist. Durch Einsatz unterschiedlich funktionalisierter Benzoesäuren (HBA-X, X= H, 2Cl, 3Cl, 4Cl, 3CO<sub>2</sub>H, 4NH<sub>2</sub> HBA = C<sub>7</sub>H<sub>4</sub>O<sub>2</sub>) wurde CAU-19-X, [Ce<sub>3</sub>(H<sub>2</sub>TCPP)<sub>2</sub>(BA-X)(HBA-X/H<sub>2</sub>O)<sub>2</sub>] · 2 HBAX · n H<sub>2</sub>O (mit X = H, 2Cl, 3Cl, 4Cl, 3CO<sub>2</sub>H, 4NH<sub>2</sub>), erhalten. In Abhängigkeit des enthaltenen Benzoesäure-Derivats wurden unterschiedliche spezifische Oberflächen nach BET zwischen 330 und 600 m<sup>2</sup> g<sup>-1</sup> erhalten. Der Einsatz von HBA-4NO<sub>2</sub> führte nicht zur Bildung von CAU-19-4NO<sub>2</sub>, statt dessen wird Ce-PMOF-4NO<sub>2</sub>, [Ce<sub>2</sub>(H<sub>2</sub>TCPP)(BA-4NO<sub>2</sub>)<sub>2</sub>] · 2 DMF unter diesen Synthesebedingungen erhalten. Ce-PMOF-4NO<sub>2</sub> kristallisiert isostrukturell zu den bereits publizierten Al-,<sup>85</sup> Ga- und In-PMOF,<sup>86</sup> wobei die CeO<sub>6</sub> Polyeder durch BA-4NO<sub>2</sub><sup>-</sup> Ionen und nicht durch μ-OH Gruppen verknüpft werden. Ce-PMOF-4NO<sub>2</sub> zeigt eine begrenzte Stabilität und wandelt sich in Aceton innerhalb von 72 h bei 70 °C in CAU-19-4NO<sub>2</sub> um, welches eine spezifische Oberfläche von 400 m<sup>2</sup> g<sup>-1</sup> aufweist. Die Kristallstrukturen von CAU-18 und CAU-19-H wurden anhand von Einkristallen und die von Ce-PMOF-4NO<sub>2</sub> mittels der

Rietveld-Verfeinerung aus Röntgenpulverdaten bestimmt. Alle Strukturen weisen unterschiedliche Ce-O Polyeder auf, die von CeO<sub>6</sub> (Ce-PMOF-4NO<sub>2</sub>) über CeO<sub>7</sub> und CeO<sub>9</sub> (CAU-18) bis CeO<sub>8</sub> und CeO<sub>12</sub> (CAU-19-X) variieren. In Ce-PMOF-4NO<sub>2</sub> und CAU-19-X bilden sich Ketten dieser Polyeder und in CAU-18 tetramere Baueinheiten aus, wobei die Polyeder untereinander unterschiedlich verknüpft sind. Der deprotonierte Linker H<sub>2</sub>TCP<sup>4-</sup> verbrückt diese anorganischen Baueinheiten und es werden eindimensionale Kanäle ausgebildet, welche teilweise von den jeweiligen Co-Liganden besetzt sind. CAU-18, CAU-18a und CAU-19-X sind thermisch bis zu 330 °C, sowie chemisch in H<sub>2</sub>O und allen getesteten Lösungsmitteln stabil. Aufgrund der kurzen Reaktionszeiten die zur Darstellung von CAU-18 und CAU-19-H nötig sind, wurde die Kristallisation *in situ* mittels Synchrotron-Pulverdiffraktometrie am DESY (beamline P09 und P07B) in Hamburg untersucht. Die Reaktionen wurden bei drei unterschiedlichen Reaktionstemperaturen (110, 120 und 130 °C) durchgeführt und die Reaktionskinetik mit der Methode nach Gualtieri ausgewertet. Die erhaltenen Arrhenius Aktivierungsenergien für die Nukleation ( $k_n$ ) und das Kristallwachstum ( $k_g$ ) lagen für CAU-18 und CAU-19-H bei 47(2) und 56(3) kJ mol<sup>-1</sup> (Nukleation) sowie 45(4) und 58(5) kJ mol<sup>-1</sup> (Kristallwachstum). Die Induktionszeit, sowie die Gesamtreaktionszeit sinken mit steigender Reaktionstemperatur. Das Maximum der Nukleationswahrscheinlichkeit ist mit steigenden Reaktionstemperaturen zu kürzeren Reaktionszeiten verschoben.

## Co-Ligand Dependent Formation and Phase Transformation of Four Porphyrin-Based Cerium Metal–Organic Frameworks

Timo Rhauderwiek,<sup>†</sup> Niclas Heidenreich,<sup>†,‡</sup> Helge Reinsch,<sup>†</sup> Sigurd Øien-Ødegaard,<sup>§</sup> Kirill A. Lomachenko,<sup>||,⊥</sup> Uta Rütt,<sup>‡</sup> Alexander V. Soldatov,<sup>||</sup> Karl Petter Lillerud,<sup>§</sup> and Norbert Stock<sup>\*,†,§,⊥</sup>

<sup>†</sup>Institut für Anorganische Chemie, Christian-Albrechts-Universität, Max-Eyth Straße 2, D-24118 Kiel, Germany

<sup>‡</sup>Deutsches-Elektronen-Synchrotron DESY, Notkestraße 85, 22607 Hamburg, Germany

<sup>§</sup>Department of Chemistry, University of Oslo, Sem Sælands vei 26, N-0371 Oslo, Norway

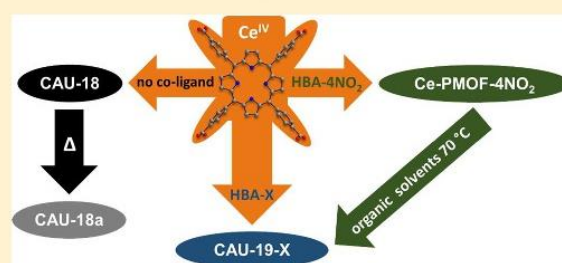
<sup>||</sup>International Research Center “Smart Materials”, Southern Federal University, Zorge Street 5, 344090 Rostov-on-Don, Russia

<sup>⊥</sup>European Synchrotron Radiation Facility, 71 avenue des Martyrs, CS 40220, 38043 Grenoble Cedex 9, France

### Supporting Information

**ABSTRACT:** The four porphyrin-based metal–organic frameworks (MOFs) containing Ce<sup>3+</sup> ions, [Ce<sub>4</sub>(H<sub>2</sub>TCPP)<sub>3</sub>·(DMF)<sub>2</sub>(H<sub>2</sub>O)<sub>4</sub>] (CAU-18), [Ce<sub>4</sub>(H<sub>2</sub>TCPP)<sub>3</sub>]·22H<sub>2</sub>O (CAU-18a), [Ce<sub>3</sub>(H<sub>2</sub>TCPP)<sub>2</sub>(BA-X)(HBA-X/H<sub>2</sub>O)<sub>2</sub>]·2HBA-X·nH<sub>2</sub>O (CAU-19-X with X = H, 2Cl, 3Cl, 4Cl, 3CO<sub>2</sub>H, 4NH<sub>2</sub>, 4NO<sub>2</sub>, HBA = C<sub>7</sub>H<sub>4</sub>O<sub>2</sub>), and [Ce<sub>2</sub>(H<sub>2</sub>TCPP)·(C<sub>7</sub>H<sub>4</sub>O<sub>2</sub>NO<sub>2</sub>)<sub>2</sub>]·2DMF (Ce-PMOF-4NO<sub>2</sub>) were synthesized using the linker 4-tetracarboxyphenylporphyrin (H<sub>2</sub>TCPP).

The formation of the respective MOFs depends mainly on the presence of a coligand in the synthesis mixture. CAU-18 was obtained in the absence of a coligand, while CAU-19-X was observed when the benzoic acid derivative HBA-X (X = H, 2Cl, 3Cl, 4Cl, 3CO<sub>2</sub>H, 4NH<sub>2</sub>) was added. In the case that HBA-4NO<sub>2</sub> was used as a coligand, yet another compound Ce-PMOF-4NO<sub>2</sub> is obtained. The structures of CAU-18 and CAU-19-H were determined from single crystal X-ray diffraction data, while the structure of Ce-PMOF-4NO<sub>2</sub> was refined from powder X-ray diffraction data by the Rietveld method. Activation of CAU-18 and Ce-PMOF-4NO<sub>2</sub> resulted in phase transformations. Thermal treatment of CAU-18 at 250 °C leads to CAU-18a, which is porous toward N<sub>2</sub> and H<sub>2</sub>O, while treatment of Ce-PMOF-4NO<sub>2</sub> in organic solvents at 70 °C leads to the formation of CAU-19-4NO<sub>2</sub>, which cannot be synthesized directly. All CAU-19-X compounds are porous toward N<sub>2</sub> and H<sub>2</sub>O, and the specific surface areas vary between 330 and 600 m<sup>2</sup> g<sup>-1</sup> depending on the size of the incorporated coligand. CAU-18, CAU-18a, and CAU-19-X are thermally stable in air up to 330 °C and chemically stable in H<sub>2</sub>O and all tested organic solvents. Ce L<sub>3</sub>-edge X-ray absorption near edge structure measurements revealed that exclusively Ce<sup>3+</sup> ions are present in the title compounds, despite the use of (NH<sub>4</sub>)<sub>2</sub>[Ce(NO<sub>3</sub>)<sub>6</sub>] in all syntheses. In addition, the crystallization of CAU-18 and CAU-19-H was investigated in situ by synchrotron powder X-ray diffraction at DESY, Hamburg, using reaction temperatures between 110 and 130 °C. The data were evaluated using the approach by Gualtieri to determine the probability of nucleation (*P<sub>n</sub>*) and the Arrhenius activation energy for nucleation (*k<sub>n</sub>*) and crystal growth (*k<sub>g</sub>*). The Arrhenius activation energies for the nucleation were determined as 47(2) and 56(3) kJ mol<sup>-1</sup> and for crystal growth 45(4) and 58(5) kJ mol<sup>-1</sup> for CAU-18 and CAU-19-H, respectively. The induction time (*t<sub>ind</sub>*), in which no crystalline products are detected, and the total reaction time to achieve full conversion (*t<sub>com</sub>*) are shortened at higher temperatures. Furthermore, the maximum of the probability of nucleation is shifted to earlier reaction times with increasing temperature.



### INTRODUCTION

The modular structure of metal–organic frameworks (MOFs) allows one to tune the pore size and pore surface properties, which in turn leads to a large range of chemical and physical properties.<sup>1–4</sup> Hence MOFs have been investigated in applications such as gas storage and separation, drug delivery, or catalysis.<sup>1,3,5–7</sup> In situ crystallization investigations were performed in recent years to study crystallization processes of MOFs in solution and to determine kinetic parameters. Examples comprise the formation of MIL-53<sup>8</sup> and MIL-100,<sup>9</sup> which are formed through an intermediate crystalline phase,

MOF-14,<sup>10</sup> which starts to decompose at longer reaction times, and CAU-1,<sup>11</sup> which was shown quantitatively to form within a few minutes.<sup>12</sup>

Porphyrin-based linker molecules have been intensively investigated in the synthesis of MOFs since the resulting porphyrin-based MOFs are often redox active. They have been used in catalysis<sup>13–21</sup> and were also tested for the singlet

Received: March 28, 2017

Revised: May 3, 2017

Published: May 8, 2017



oxygen production in biomedical and nonmedical applications as well as cancer therapy.<sup>22–24</sup> MOFs containing tri- or tetravalent cations are known for their high stability,<sup>25</sup> and in combination with 4-tetracarboxyphenylporphyrin ( $H_6TCPP$ ), which is the most intensively investigated porphyrin-linker in MOF synthesis,<sup>26–28</sup> various compounds exhibiting permanent porosity have been reported. First pioneering work in the field of porphyrin-based MOFs incorporating the  $H_6TCPP$  ligand were carried out by Suslick et al. and Goldberg et al. in 2000 and 2002.<sup>29,30</sup> More recent studies led to Zr-MOFs known as PCN-221 to -225,<sup>13,31,14,32</sup> MOF-545,<sup>33</sup> and MOF-525.<sup>33,34</sup> Some of these compounds have been tested in various catalytic reactions, such as the oxidation of cyclohexane,<sup>35</sup> the electrochemical reduction of  $CO_2$ ,<sup>16</sup> or the photooxidation of mustard gas.<sup>19</sup> A larger variety of porphyrin-based MOFs are known with trivalent ions. Thus, three isoreticular MOFs with the group 13 metal ions aluminum, gallium, and indium (Al-PMOF,<sup>36</sup> Ga-PMOF,<sup>37</sup> In-PMOF)<sup>37</sup> have been reported, and the Al-PMOF was investigated in the photocatalytic methyl viologen assisted  $H_2$ -generation on colloidal platinum.<sup>36</sup> In addition, porphyrin-based In-MOFs (MMPF-7,<sup>38</sup> MMPF-8,<sup>38</sup> and UNLPF-10<sup>39,40</sup>), Fe-MOFs (MIL-141,<sup>41</sup>  $[Fe_2(Fe-TCCP)(C_4H_4N_2)(OH_2)]$  ( $C_4H_4N_2$  = pyrazine),<sup>42</sup> and PCN-600)<sup>43</sup> and MOFs containing lanthanide ions like Ce,<sup>44,45</sup> Nd,<sup>46</sup> Sm,<sup>47</sup> and Dy<sup>46</sup> are also known. For the latter examples, only the crystal structures but no physisorption measurements were reported.

Herein we present the results of our systematic investigation on the synthesis of 12 trivalent Ce-MOFs using the porphyrin-based linker  $H_6TCPP$  in the absence and presence of various benzoic acid derivatives ( $HBA-X$ ,  $X = H, Cl, NH_2, NO_2, COOH$ ) that can act as a coligand (Figure 1), their structural transformation upon activation as well as the results of our in situ crystallization studies.



**Figure 1.** Graphical representation of the investigation of the system  $Ce^{IV}/H_6TCPP/DMF/H_2O$  in the absence or presence of benzoic acid derivatives ( $HBA-X$ ,  $X = H, Cl, NH_2, NO_2, COOH$ ) as coligands. The study led to the new porphyrin-based Ce-MOFs CAU-18, CAU-18a, CAU-19-X ( $X = H, 2Cl, 3Cl, 4Cl, 4NH_2, 4NO_2, 3CO_2H$ ) and Ce-PMOF-4NO<sub>2</sub>.

## EXPERIMENTAL SECTION

**Materials.** Cerium(IV) ammonium nitrate ( $(NH_4)_2[Ce(NO_3)_6]$ ) (98%, ABCR), benzoic acid (99.5%, ABCR), 2-chlorobenzoic acid (98%, ABCR), 3-chlorobenzoic acid (99%, Sigma-Aldrich), 4-chlorobenzoic acid (99%, Sigma Aldrich), 3-carboxybenzoic acid (trimellitic acid, 99%, Sigma-Aldrich), 4-aminobenzoic acid (99%, Sigma-Aldrich), 4-nitrobenzoic acid (99%, ABCR),  $ZnSO_4 \cdot H_2O$  (97%, Merck),  $CoCl_2 \cdot 6H_2O$  (98%, Fluka), dimethylformamide (DMF, 99%, Grüssing), acetone (99%, Walther), methanol (99%, Walther), dichloromethane (DCM, 99%, Walther), and ethanol (99%, Walther)

were used without further purification. The cerium(IV) ammonium nitrate was dissolved in distilled  $H_2O$  to achieve a 0.53 M solution. The linker 4,4',4'',4'''-(5,10,15,20-porphyrin-tetrayl)tetrabenzoic acid (4-tetracarboxyphenylporphyrin,  $H_6TCPP$ ) was synthesized according to reported procedures<sup>48–50</sup> starting with 4-formylbenzoic acid (98%, ABCR) and pyrrole (98%, ABCR) in propionic acid (99%, Grüssing). The metalated linker  $Co-H_4TCPP$  was synthesized according to reported procedures. First  $Co-TCCP-Me$ ,<sup>51</sup> was obtained by reaction of  $H_6TCPP$  with  $CoCl_2 \cdot 6H_2O$  in MeOH which was subsequently hydrolyzed.<sup>52</sup> Details are given in the Supporting Information.

**Characterization.** Single crystal X-ray diffraction data for CAU-18 and CAU-19-H were acquired at the beamline ID11 at ESRF (Grenoble, France). The reflections were indexed with the APEX3 suite, integrated with SAINT V9.32B,<sup>53</sup> solved with the program SHELXL,<sup>54</sup> and refined with the program SHELXL using Olex2 as GUI.<sup>55</sup> A radiation energy of 40 keV was used, corresponding to a wavelength of  $\lambda = 0.3112 \text{ \AA}$ . The nonstandard wavelength induced a checkcif warning due to mismatch of the determined and calculated absorption coefficient  $\mu$ . Only one full hemisphere ( $\phi$  scan) was collected for each sample, due to time constraints, resulting in incomplete data sets. Both crystals were very small and poorly diffracting, and in addition suffered from radiation damage during the measurements. Both structures contain stacked porphyrin rings, likely to cause stacking disorder in the crystals. This disorder is likely to have caused the poor precision on bond lengths and ADP values in the obtained crystal structures. Restraints forcing ADP tensor components to approximate to isotropic behavior (isor) and rigid body restraints (rigu) were used to prevent unphysical ADP values.

All Ce  $L_{3}$ -edge X-ray absorption near edge structure (XANES) measurements, except for  $Ce(NO_3)_3 \cdot 6H_2O$ , were performed at the Southern Federal University (Rostov-on-Don, Russia) using a Rigaku R-XAS spectrometer. The water-cooled X-ray tube with a fixed W anode was operating at 12 kV and 80 mA. The incident beam was monochromatized using a Johansson-type Ge (220) crystal, ensuring an energy resolution of around 1 eV at Ce  $L_{3}$ -edge (5730 eV). The measurements were conducted in transmission mode using an Ar-filled ionization chamber and a scintillation counter to monitor the intensity of incident ( $I_0$ ) and transmitted ( $I_t$ ) radiation, respectively. A He-filled bag was placed between the X-ray tube, the monochromator, and the  $I_0$  detector to reduce the X-rays absorption in air. The spectrum of  $Ce(NO_3)_3 \cdot 6H_2O$  was collected at the BM23 beamline of the European Synchrotron Radiation Facility (Grenoble, France) in transmission mode using a Si (111) crystal for monochromatization, Si mirrors for harmonics rejection and  $N_2/He$ -filled ionization chambers for photon detection, yielding resolution comparable with the laboratory measurement. In all cases the samples were measured in the form of self-supporting pellets mixed with boron nitride and pressed with a pressure below 400 kg/cm<sup>2</sup>. Mass of the samples was optimized by using the XAFSmass code<sup>56</sup> to obtain the best signal-to-noise ratio.

Powder X-ray diffraction (PXRD) measurements were carried out with a STOE HT diffractometer equipped with a xy-stage and an IPDS (Cu  $K_{\alpha 1}$  radiation) or Mythen (Mo  $K_{\alpha 1}$  radiation) detector system. High resolution PXRD patterns were measured on a STOE Stadi-P combi powder diffractometer equipped with a Mythen detector (Cu  $K_{\alpha 1}$  radiation). The structure of Ce-PMOF-4NO<sub>2</sub> was refined from PXRD data using the Rietveld method. Only an approximated structure model was obtained due to broad reflections with a low signal-to-noise ratio and the presence of small amounts of CAU-19-4NO<sub>2</sub>. An appropriate structure model for CAU-18a could not be set up due to limited long-range order in the sample. Nevertheless, the PXRD pattern of CAU-18a could be indexed using TOPAS academic V4.1,<sup>57</sup> and a unit cell similar to CAU-18 was found and confirmed by a Pawley fit (Table 2 and Figure S20). Pawley fits (Figures S22–S29) were carried out for all other CAU-19-X and M-CAU-19-H ( $M = Zn, Co$ ) derivatives to prove that they are isostructural to CAU-19-H. Pawley fits of CAU-18 and CAU-19-H (Figures S19 and S21) with the lattice parameters determined from the single crystal structure determination were carried out to prove the phase purity. Pawley fits and Rietveld-refinements were performed with the program



# Porphyrin-basierte Metall-Organische Gerüstverbindungen: Von Metall-Carboxylaten zu Metall-Phosphonaten

**Table 1. Summary and Comparison of the Synthesis Parameters of CAU-18, CAU-19-X (X = H, 2Cl, 3Cl, 4Cl, 3CO<sub>2</sub>H, 4NH<sub>2</sub>), and Ce-PMOF-4NO<sub>2</sub><sup>a</sup>**

CAU	-18	-19-H	-19-Cl <sup>b</sup>	-19-4NH <sub>2</sub>	-19-3CO <sub>2</sub>	Ce-PMOF
M/L/HBA-X <sup>c</sup>	1:2:0	1:2:180	1:2:150	1:2:200	1:2:140	9:18:450
H <sub>2</sub> O/DMF <sup>d</sup>	1:3	1:3	1:3	1:3	1:3	2.8:30
HBA-X [mg]		570	600	700	600	2000
T [°C]	100	120	120	120	120	120
t [h]	2	24	2	24	24	48
yield [%]	79	56	51, 30, 72 <sup>b</sup>	75	37	44

<sup>a</sup>All CAU-19-Cl derivatives were obtained using the same synthesis parameters. All syntheses were carried out in 7 mL glass vials except Ce-PMOF-4NO<sub>2</sub>, which was synthesized in a 30 mL Teflon reactor. <sup>b</sup>CAU-19-Cl indicates all CAU-19-Cl derivatives in following order 2Cl, 3Cl, 4Cl. <sup>c</sup>Molar ratio, the number 1 corresponds to 2.53 × 10<sup>-2</sup> (20 mg) mmol. <sup>d</sup>Volumetric ratio, the number 1 corresponds to 300 μL of H<sub>2</sub>O.

TOPAS academic V4.1.<sup>57</sup> The results of the refinement and crystallographic data of CAU-18, CAU-18a, CAU-19-H, and Ce-PMOF-4NO<sub>2</sub> is shown in Table 2. The refined cell parameters and results of the Pawley fits of the other CAU-19-X and M-CAU-19-H (M = Zn, Co) derivatives are shown in Tables S2 and S3 and Figures S19–S29. The diameters of all pores were determined using DIAMOND V.3.<sup>58</sup> taking the van-der-Waals radii of the atoms into account. The variable temperature PXRD (VT-PXRD) measurements were recorded on a STOE Stadi-P combi powder diffractometer (Cu Kα<sub>1</sub> radiation: CAU-18; Mo Kα<sub>1</sub> radiation: CAU-19-H) equipped with a capillary furnace. For the measurements 0.5 mm quartz capillaries were used. The samples were heated up in steps of 5 K to 500 and 600 °C for CAU-18 and CAU-19-H, respectively, and measured for 10 min each.

The in situ PXRD measurements were carried out at beamline P09<sup>59</sup> (λ = 0.53905 Å) and P07B<sup>60</sup> (λ = 0.14235 Å) at PETRA III, DESY, Hamburg. The sample-to-detector distance was 606.074 mm and 2682.568 mm at P09 and P07B, respectively. In both cases a PerkinElmer 1621 flat panel detector (2048 × 2048 pixel; 200 μm × 200 μm pixel size) was used. At beamline P09,<sup>59</sup> the experiments were executed with a beam size of 1 × 1 mm. At beamline P07B,<sup>60</sup> the beamsize was set to 0.5 × 0.5 mm. The reactions were carried out in a custom-built reactor that was developed at CAU Kiel in cooperation with the beamline staff of beamline P08, PETRA III, DESY.<sup>61</sup> The reactor was designed to enable the analysis of chemical reactions under solvothermal reaction conditions via synchrotron based techniques. The core of the reactor consists of an aluminum casing surrounded by copper-galvanized heating wires. Reaction vessels made from borosilicate glass (V<sub>max</sub> = 5 mL) can be inserted into the casing that is aligned in transmission geometry on the beamline. The temperature inside the reaction vessel was constantly monitored throughout the entire reaction by means of a PTFE-coated k-type thermocouple. Through a combination of resistive heating from the heating wires and direct cooling of the heating wires via compressed air the temperature inside, the glass vessel was precisely controlled with a deviation of ±0.5 °C. A stirring device under the base of the reactor allowed for homogenization of the sample during the reaction. The setup furthermore provides the option of adding solutions during the reaction by means of a remote-controlled syringe pump. The syringe pump system is connected to PTFE tubes that are embedded in the custom-built screw caps. In this study the syringe pump was used to start the reactions remotely that lead to the formation of CAU-19-H. To ensure a constant reaction temperature the linker solution was first heated to the target temperature followed by the injection of metal salt solution to start the reaction. A more detailed description of the experiment procedure is provided in the section discussing the in situ studies.

IR spectra were recorded using a Bruker ALPHA-FT-IR A220/D-01 spectrometer equipped with an ATR unit. UV/vis spectra were recorded at a Spectroquant Pharo 300 M. Prior to the measurements all samples were dissolved in 2 M NaOH and measured at once. <sup>1</sup>H NMR spectroscopy was employed for the quantitative analysis of occluded guest molecules and coligands. The NMR spectra were recorded on a Bruker DRX 500 spectrometer. The samples were dissolved in a mixture of 10% deuteriochloric acid (DCl) in D<sub>2</sub>O and

deuterated dimethyl sulfoxide (DMSO-*d*<sub>6</sub>) (molar ratio = 1:7). Sorption experiments were performed with a BEL Japan Inc. BELSORP-max. Before sorption measurements all samples were activated at 170 °C under reduced pressure (10<sup>-2</sup> kPa) for 16 h. Thermogravimetric measurements were performed on a NETZSCH STA 409 CD analyzer under a flow of air (75 mL min<sup>-1</sup>) with a heating rate of 4 °C min<sup>-1</sup> between 25 and 700 °C in Al<sub>2</sub>O<sub>3</sub>-crucibles. The data were corrected for buoyancy and current effects.

**Preparation.** The syntheses of CAU-18 and CAU-19-X (X = H, 2Cl, 3Cl, 4Cl, 3CO<sub>2</sub>H, 4NH<sub>2</sub>, 4NO<sub>2</sub>) were carried out in glass vials (V<sub>max</sub> = 7.0 mL, Pyrex) using a solvent mixture (volume ratio H<sub>2</sub>O to DMF of 1 to 3). Ce-PMOF-4NO<sub>2</sub> was obtained in 30 mL autoclaves with Teflon inserts using DMF as solvent and 4-nitrobenzoic acid as coligand. For the synthesis optimization reactions were carried out between 80 and 140 °C, at reaction times between 1 and 48 h using different molar ratios of metal/linker/HBA-X between 1:1:0 and 5:1:300 (HBA-X = C<sub>7</sub>H<sub>5</sub>O<sub>2</sub>-X, X = X = H, 2Cl, 3Cl, 4Cl, 3CO<sub>2</sub>H, 4NH<sub>2</sub>, 4NO<sub>2</sub>). The formation of the metalated compounds M-CAU-19-H (M = Zn, Co) was investigated starting from the synthesis conditions of CAU-19-H. In the case of Zn-CAU-19-H the addition of ZnSO<sub>4</sub>·H<sub>2</sub>O and a reaction time of 1 h resulted in the formation of Zn-CAU-19-H. Co-CAU-19-H was obtained by an increase of metal to linker ratio to 5:1 and a higher amount of DMF (2400 μL). Activation of the samples was carried out by thermal treatment or by a combination of solvent exchange at elevated temperatures followed by thermal treatment under reduced pressure.

The optimized synthesis parameters of all title compounds are summarized in Table 1, and the results of the elemental analyses are given in Table S1. The detailed synthesis procedures for CAU-18, CAU-18-HT, CAU-19-H, M-CAU-19-H (M = Zn, Co) and Ce-PMOF-4NO<sub>2</sub> are as follows.

**CAU-18.** H<sub>6</sub>TCPP (20 mg, 2.53 × 10<sup>-2</sup> mmol), DMF (1200 μL), H<sub>2</sub>O (300 μL), and 0.53 M aqueous (NH<sub>4</sub>)<sub>2</sub>[Ce(NO<sub>3</sub>)<sub>6</sub>] solution (94 μL, 5.06 × 10<sup>-2</sup> mmol) were added to a 7.0 mL glass vial. The glass vial was heated for 2 h at 100 °C. The resulting product was filtered off and washed two times each with DMF and acetone. A yield of 63 mg (79% based on H<sub>6</sub>TCPP) was obtained for CAU-18, [Ce<sub>4</sub>(H<sub>2</sub>TCPP)<sub>3</sub>·(DMF)<sub>2</sub>(H<sub>2</sub>O)<sub>4</sub>].

**CAU-18a.** CAU-18 (500 mg, 0.16 mmol) was placed in a crucible and heated for 24 h at 250 °C. A yield of 470 mg, 100% was obtained for CAU-18a, based on the composition [Ce<sub>4</sub>(H<sub>2</sub>TCPP)<sub>3</sub>]·22 H<sub>2</sub>O deduced from elemental analysis and thermogravimetric (TG) measurements.

**CAU-19-H.** H<sub>6</sub>TCPP (20 mg, 2.53 × 10<sup>-2</sup> mmol), benzoic acid (HBA-H) (570 mg, 4.67 mmol), DMF (1200 μL), H<sub>2</sub>O (300 μL), and 0.53 M aqueous (NH<sub>4</sub>)<sub>2</sub>[Ce(NO<sub>3</sub>)<sub>6</sub>] solution (94 μL, 5.06 × 10<sup>-2</sup> mmol) were added to a 7.0 mL glass vial. The glass vial was heated for 24 h at 120 °C. The resulting product was filtered off and washed two times each with DMF and acetone. A yield of 16 mg, 56% (based on H<sub>6</sub>TCPP) was obtained for CAU-19-H, [Ce<sub>3</sub>(H<sub>2</sub>TCPP)<sub>2</sub>(BA-H)(HBA-H/H<sub>2</sub>O)<sub>2</sub>]·2(HBA-H)·11H<sub>2</sub>O.

**Zn-CAU-19-H.** H<sub>6</sub>TCPP (20 mg, 2.53 × 10<sup>-2</sup> mmol), ZnSO<sub>4</sub> (5 mg, 3.10 × 10<sup>-2</sup> mmol), benzoic acid (HBA-H) (570 mg, 4.67 mmol), DMF (1200 μL), H<sub>2</sub>O (300 μL), and 0.53 M aqueous (NH<sub>4</sub>)<sub>2</sub>[Ce(NO<sub>3</sub>)<sub>6</sub>] solution (94 μL, 5.06 × 10<sup>-2</sup> mmol) were added to a 7.0 mL



**Table 2.** Crystallographic Data of CAU-18, CAU-18a, CAU-19-H, and Ce-PMOF-4NO<sub>2</sub>

	CAU-18	CAU-18a	CAU-19-H	Ce-PMOF-4NO <sub>2</sub>
formula	[Ce <sub>4</sub> (H <sub>2</sub> TCPP) <sub>3</sub> (DMF) <sub>2</sub> (H <sub>2</sub> O) <sub>4</sub> ]	[Ce <sub>4</sub> (H <sub>2</sub> TCPP) <sub>3</sub> ]	[Ce <sub>3</sub> (H <sub>2</sub> TCPP) <sub>2</sub> (C <sub>7</sub> H <sub>4</sub> O <sub>2</sub> H) <sub>2</sub> (H <sub>2</sub> O) <sub>2</sub> ]	[Ce <sub>2</sub> (H <sub>2</sub> TCPP)(C <sub>7</sub> H <sub>4</sub> O <sub>2</sub> NO <sub>2</sub> ) <sub>2</sub> ]
data determined by	single crystal	Pawley fit	single crystal	Rietveld refinement
crystal system	monoclinic	monoclinic	triclinic	orthorhombic
<i>a</i> [Å]	20.755(5), 23.572(6), 30.642(8)	22.420(3)	11.665(7)	33.077(3)
<i>b</i> [Å]		23.248(3)	13.915(8)	7.309(2)
<i>c</i> [Å]		34.419(5)	17.343(10)	16.539(2)
$\alpha$ [°]	90	90	95.514(4)	90
$\beta$ [°]	104.573 (2)	106.375(5)	99.792(4)	90
$\gamma$ [°]	90	90	101.313(5)	90
<i>V</i> [Å <sup>3</sup> ]	14509(7)	17212(4)	2696(3)	3998(1)
space group	C2/c	P2/c	P $\bar{1}$	Cmmm
tot., uniq. data, <i>R</i> <sub>int</sub>	21207, 12183, 0.073		10313, 9008 0.038	
observed data [ <i>I</i> > 2σ( <i>I</i> )]	6622		6710	
<i>R</i> <sub>1</sub> , <i>wR</i> <sub>2</sub> (gt) [%]	7.5, 18.0		7.8, 20.6	
GOF	0.97	1.19	1.04	1.24
<i>R</i> <sub>exp</sub>		2.03		4.46

glass vial. The glass vial was heated for 1 h at 120 °C under stirring. The resulting product was filtered off and washed two times each with DMF and acetone. A yield of 15 mg, 53% (based on H<sub>2</sub>TCPP) was obtained for Zn-CAU-19-H, [Ce<sub>3</sub>(Zn-TCPP)<sub>2</sub>(BA-H)(HBA-H/H<sub>2</sub>O)<sub>2</sub>]-2(HBA-H)-8H<sub>2</sub>O.

**Co-CAU-19-H.** Co-H<sub>2</sub>TCPP (20 mg, 2.53 × 10<sup>-2</sup> mmol), benzoic acid (HBA-H) (570 mg, 4.67 mmol), DMF (2400 μL), H<sub>2</sub>O (350 μL), and 0.53 M aqueous (NH<sub>4</sub>)<sub>2</sub>[Ce(NO<sub>3</sub>)<sub>6</sub>] solution (94 μL, 12.65 × 10<sup>-2</sup> mmol) were added to a 7.0 mL glass vial. The glass vial was heated for 2 h at 120 °C under stirring. The resulting product was filtered off and washed two times each with DMF and acetone. A yield of 12 mg, 42% (based on Co-H<sub>2</sub>TCPP) was obtained for Co-CAU-19-H, [Ce<sub>3</sub>(Co-TCPP)<sub>2</sub>(BA-H)(HBA-H/H<sub>2</sub>O)<sub>2</sub>]-2(HBA-H)-11H<sub>2</sub>O.

To prove that the porphyrin linker is still metalated after the MOF synthesis UV/vis spectra (Figure S4) were measured. Prior to the measurements all samples were dissolved in 2 M NaOH. The measurements reveal no significant loss of Co<sup>2+</sup> and Zn<sup>2+</sup> ions. The absorption maxima of the linker molecules incorporated in CAU-19-H, Zn-CAU-19-H, and Co-CAU-19-H after dissolution in 2 M aqueous NaOH solution were observed at 414, 422, and 430 nm, respectively, and correspond well to values reported in the literature (H<sub>2</sub>TCPP = 413,<sup>18,62</sup> Zn-H<sub>2</sub>TCPP = 424 nm,<sup>63</sup> Co-H<sub>2</sub>TCPP = 430 nm<sup>18</sup>).

To remove the noncoordinating solvent and HBA-X molecules from the as-synthesized samples, the materials were treated under reflux with acetone (CAU-19-X, with X = H, 2Cl, 4Cl, 4NH<sub>2</sub>, and M-CAU-19-H (M = Zn, Co)) or DMF (CAU-19-3Cl and CAU-19-3CO<sub>2</sub>H). This procedure was repeated until no further decrease of the amount of HBA-X was observed in the <sup>1</sup>H NMR spectra (Figures S5–S12).

**Ce-PMOF-4NO<sub>2</sub>.** H<sub>2</sub>TCPP (180 mg, 22.77 × 10<sup>-2</sup> mmol), 4-nitrobenzoic acid (HBA-4NO<sub>2</sub>) (2000 mg, 12.05 mmol), DMF (9000 μL), and 0.53 M aqueous (NH<sub>4</sub>)<sub>2</sub>[Ce(NO<sub>3</sub>)<sub>6</sub>] solution (850 μL, 45.54 × 10<sup>-2</sup> mmol) were added to a 30 mL Teflon vessel. The Teflon vessel was placed in an autoclave and was heated for 48 h at 120 °C. The resulting product was filtered off and washed with 100 mL DMF. A yield of 139 mg, 44% (based on H<sub>2</sub>TCPP) was obtained for Ce-PMOF-4NO<sub>2</sub>, [Ce<sub>2</sub>(H<sub>2</sub>TCPP)(BA-4NO<sub>2</sub>)<sub>2</sub>]-2DMF.

**CAU-19-4NO<sub>2</sub>.** Ce-PMOF-4NO<sub>2</sub> (500 mg, 0.36 mmol) and 30 mL of acetone were placed in a 50 mL glass vessel with screw cap and heated in an oven for 72 h at 70 °C. A yield of 427 mg, 100% was obtained for CAU-19-4NO<sub>2</sub> (yield calculated based on the linker molecule and corresponding to the formula [Ce<sub>3</sub>(H<sub>2</sub>TCPP)<sub>2</sub>(BA-NO<sub>2</sub>)(HBA-NO<sub>2</sub>/H<sub>2</sub>O)<sub>2</sub>]-2(HBA-NO<sub>2</sub>)-6H<sub>2</sub>O for CAU-19-4NO<sub>2</sub>).

## RESULTS AND DISCUSSION

The systematic study employing the linker molecule 4-tetracarboxyphenylporphyrine (H<sub>2</sub>TCPP) as well as coligands (HBA-X, with X = H, 2Cl, 3Cl, 4Cl, 3CO<sub>2</sub>H, 4NH<sub>2</sub>, 4NO<sub>2</sub>) led to 12 new porphyrin-based Ce-MOFs. In contrast to previous studies in the Goldberg group, we used coligands in our syntheses which have a strong influence on the product formation.<sup>45</sup>

The synthesis of the porphyrin-based Ce-MOFs was investigated starting from the reaction procedures recently reported for the synthesis of Ce-UiO-66 and an In-MOF containing the H<sub>2</sub>TCPP<sup>4-</sup> ion.<sup>21,37</sup> The title compounds CAU-18, [Ce<sub>4</sub>(H<sub>2</sub>TCPP)<sub>3</sub>(DMF)<sub>2</sub>(H<sub>2</sub>O)<sub>4</sub>] and CAU-19-X, [Ce<sub>3</sub>(H<sub>2</sub>TCPP)<sub>2</sub>(BA-X)(HBA-X/H<sub>2</sub>O)<sub>2</sub>]-2HBA-11H<sub>2</sub>O, were obtained under very similar reaction conditions as described for the formation of Ce-UiO-66.<sup>21</sup> Thus, (NH<sub>4</sub>)<sub>2</sub>[Ce(NO<sub>3</sub>)<sub>6</sub>] was used as the metal source, and the reaction was carried out using short reaction times (*T*<sub>max</sub> = 2 h), low reaction temperatures (100–120°), and a DMF/H<sub>2</sub>O solvent mixture (3:1). Although the formation of a hexanuclear {Ce<sub>6</sub>O<sub>8</sub>} cluster and therefore the crystallization of compounds isostructural to the known porphyrin-based Zr-MOFs<sup>34</sup> were anticipated, this approach resulted in the formation of new Ce-MOFs with dimeric and trimeric IBUs that are connected by the H<sub>2</sub>TCPP<sup>4-</sup> ions to form three-dimensional framework structures. CAU-18 is formed in the absence of a coligand, while CAU-19-H was obtained in the presence of benzoic acid (HBA). Subsequently, usage of different benzoic acid derivatives (HBA-X, with (X = H, 2Cl, 3Cl, 4Cl, 3CO<sub>2</sub>H, 4NH<sub>2</sub>)) resulted in the formation of a series of CAU-19 type compounds with the BA-X<sup>-</sup> ions incorporated into the crystal structure. While the molar ratio Ce<sup>4+</sup> to H<sub>2</sub>TCPP has the most pronounced impact on the product formation, the amount of coligand varies slightly (Table 1). Unexpectedly, the use of 4-nitrobenzoic acid (HBA-NO<sub>2</sub>) as a coligand and the increase of the DMF to H<sub>2</sub>O ratio from 3:1 to 9:1 result in the formation of the new Ce-MOF [Ce<sub>2</sub>(H<sub>2</sub>TCPP)(BA-4NO<sub>2</sub>)<sub>2</sub>]-2DMF (Ce-PMOF-4NO<sub>2</sub>).

**Activation of the Ce-MOFs.** Thermal activation and VT-PXRD measurements of the title compounds revealed several structural changes. Thus, the thermal treatment of CAU-18 at 250 °C leads to a desolvated compound denoted CAU-18a. Activation of Ce-PMOF-4NO<sub>2</sub> was carried out in a two-step

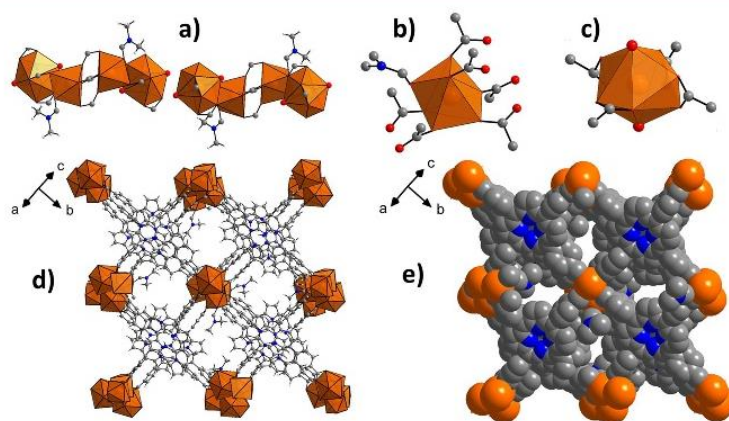


**Figure 2.** Structure of CAU-18. (a) IBUs composed of edge-sharing  $\text{CeO}_7$  and  $\text{CeO}_9$  polyhedra with bridging  $-\text{COO}^-$  groups and coordinated DMF and water molecules, (b)  $\text{CeO}_7$  polyhedron and coordination environment, (c)  $\text{CeO}_9$  polyhedron and coordination environment, (d) view of the framework structure, (e) space filling model of CAU-18. Carbon atoms are shown in gray, oxygen atoms in red, nitrogen atoms in blue, and cerium atoms/ $\text{CeO}$  polyhedra in orange.

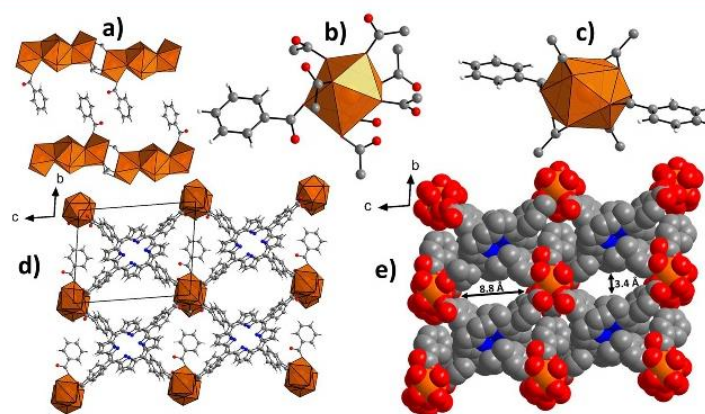


**Figure 3.** (a) IBU of CAU-19-H along  $[010]$ , (b)  $\text{CeO}_8$  polyhedron and coordination environment, (c)  $\text{CeO}_{12}$  polyhedron and coordination environment, (d) view along pores  $[100]$  with unit cell edges, and (e) space filling model along  $[100]$  of CAU-19-H with pore diameters of 3.4/8.8 Å. Carbon atoms are shown in gray, oxygen atoms in red, nitrogen atoms in blue, and cerium atoms/ $\text{CeO}$  polyhedra in orange.

process by treatment with an organic solvent at elevated temperatures, followed by thermal treatment under reduced pressure. The first step leads to the transformation of  $\text{Ce-PMOF-4NO}_2$  into  $\text{CAU-19-4NO}_2$  within 72 h at 70 °C. It is noteworthy that we have only been able to obtain  $\text{CAU-19-4NO}_2$  by this treatment.

**Crystal Structure.** The title compounds CAU-18 and CAU-19-H were obtained as single crystals (Figures S13 and S14), while all other MOFs were only synthesized as microcrystalline powders. Hence the structures of CAU-18 and CAU-19-H were determined from single crystal X-ray diffraction data, while the one of  $\text{Ce-PMOF-4NO}_2$  was refined from PXRD data (Figure 5, Table 2). In addition Pawley fits were carried out to determine the lattice parameters and to confirm phase purity of all title compounds (Figures S19–S29, Tables S2–S3).

CAU-18 is isostructural to  $[\text{Sm}_4(\text{H}_2\text{TCCP})_3(\text{DMF})_2(\text{H}_2\text{O})_4]$ .<sup>47</sup> The IBU consists of edge-sharing  $\text{CeO}_7$  and  $\text{CeO}_9$  polyhedra, in a monocapped trigonal prismatic and a distorted tricapped trigonal prismatic coordination environment (Figure 2). Each  $\text{CeO}_7$  polyhedron contains one DMF

molecule and each  $\text{CeO}_9$  polyhedron two water molecules, and the other oxygen atoms stem from carboxylate groups. The dimers are bridged to tetramers by carboxylate groups (Figure 2), and further interconnection by  $\text{H}_2\text{TCCP}^{4-}$  ions leads to a three-dimensional framework with very small pores of  $2.4 \times 5.0$  Å, which are too small to accommodate guest molecules (Figure 2). Adjacent tetramers approach each other along  $[101]$  to a distance of 3.13(3) Å, which hints at the presence of a weak H-bond interaction between a coordinated water molecule and an oxygen atom of a carboxylate group (Figure S15). The coordination modes of the carboxylate groups in CAU-18 are shown in Figure S16 using the Harris notation.<sup>64</sup> The Harris notation has the format  $[\text{A},\text{XY}]$ , the value A is the number of metal ions coordinated by the carboxylate group, and X, Y is the number of bonds every oxygen shares with a metal ion.<sup>64</sup> In the structure of CAU-18 the coordination modes  $[2,21]$ ,  $[2,11]$ ,  $[1,11]$ , and  $[1,10]$  are observed.

The bond lengths found in CAU-18 are in good agreement with the literature values. For the Ce–O bonds values between 2.296(10) (CN: 7) and 2.841(7) Å (CN: 9) were found which are in good agreement with the literature value of 2.386(8)



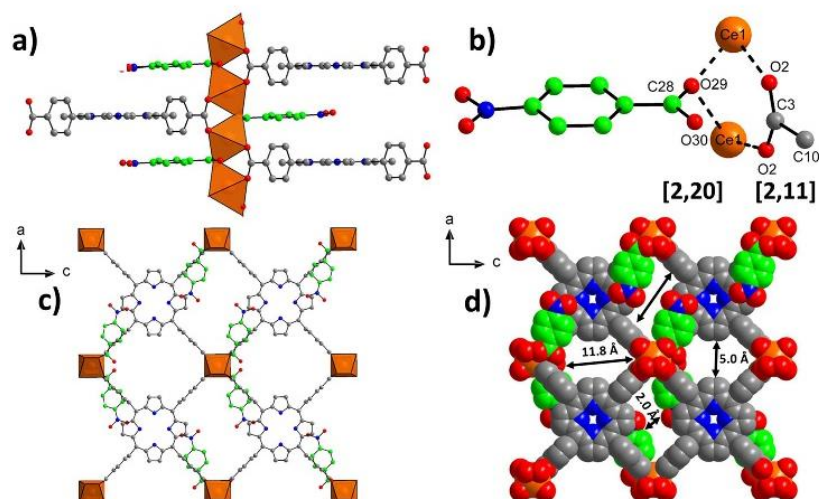


**Figure 4.** Structure of Ce-PMOF-4NO<sub>2</sub>. (a) IBU along [100] with BA-NO<sub>2</sub><sup>-</sup> ions as bridging groups between trans corner-sharing CeO<sub>6</sub> polyhedra (b) Harris notation in brackets for the carboxylate group of the coligand and the linker, (c) view along pores [010], and (d) space filling model along [010] with pore diameters of 5.0 × 11.8 Å and 2.0 × 11.8 Å, respectively. Carbon atoms are shown in gray, oxygen atoms in red, nitrogen atoms in blue, and cerium atoms/CeO polyhedra in orange; for clarity the carbon atoms of the BA-NO<sub>2</sub><sup>-</sup> ion are marked in green.

(CN:7) and 2.797(7) Å (CN:9).<sup>45,65</sup> The C=C double bond length varies between 1.319(14) (arom. phenyl) and 1.481(11) Å (arom. pyrrole) and the N=C double bond length between 1.323(12) and 1.349(10) Å, which are also in good agreement with the literature values of 1.303(9) to 1.508(6) Å and 1.358(6) to 1.383(6) Å, respectively.<sup>33,45</sup>

**CAU-19**, [Ce<sub>3</sub>(H<sub>2</sub>TCPP)<sub>2</sub>(BA-X)(HBA-X/H<sub>2</sub>O)], can be synthesized with different benzoic acid derivatives (HBA-X, X = H, 2Cl, 3Cl, 4Cl, 4NH<sub>2</sub>, 3CO<sub>2</sub>H) which are part of the structure (Figure 3). The IBU contains trimers which are formed by edge-sharing of two CeO<sub>8</sub> and one CeO<sub>12</sub> polyhedra, in a distorted square antiprismatic and a distorted icosahedral coordination environment.

The coligands are incorporated as the benzoic acid derivative ([1,10] mode) as well as the anion ([1,11] mode) (Figure 3b,c). The trimeric IBUs are connected to chains along [100] by H<sub>2</sub>TCPP<sup>4-</sup> ions (Figure 3), which also connect the chains to a three-dimensional framework structure with linear oval channels along [100]. These pores have diameters of 3.4 × 8.8 Å and are accessible to guest molecules (Figure 3). In the as-synthesized compounds the pores are occupied by HBA-X molecules, which are, based on the single crystal X-ray diffraction data, located in two positions with an occupancy of 0.5 each (Figure S17a, omitted for clarity in Figure 3e). The noncoordinating HBA-X molecules can be removed by solvent extraction followed by thermal activation. The coordination mode of the carboxylate groups of CAU-19-H are shown in Figure S17.<sup>64</sup>

The bond lengths found in CAU-19-H are in good agreement with the literature values. For Ce–O bonds, values between 2.374(8) and 2.730(6) Å were found, which are in good agreement with the literature values of 2.413(4) to 2.618(4) Å (CN: 8)<sup>45</sup> and 2.364(5) to 2.765(2) Å (CN: 12).<sup>45,65</sup> The C=C double bond length varies between 1.327(13) Å (arom. phenyl) and 1.512(11) Å (arom. pyrrole) and the N=C double bond length between 1.348(11) Å and 1.379(10) Å, which are also in good agreement with the

literature values of 1.303(9) Å to 1.508(6) Å and 1.358(6) Å to 1.383(6) Å, respectively.<sup>33,45</sup>

Only one other porphyrine-based Ce-MOF of composition [Ce<sub>3</sub>(H<sub>2</sub>TCPP)<sub>2</sub>(HCOO)(H<sub>2</sub>O)<sub>3</sub>] has been previously reported in the literature.<sup>45</sup> Its structure resembles some similarities to the one observed for CAU-19, but formate instead of benzoate ions are coordinated to the IBUs. In addition CeO<sub>10</sub> instead of CeO<sub>12</sub> polyhedra are incorporated in the trimeric IBUs which are interconnected by the linker molecules to form a framework similar to CAU-19.<sup>45</sup>

The structure of Ce-PMOF-4NO<sub>2</sub>, [Ce<sub>2</sub>(H<sub>2</sub>TCPP)(BA-4NO<sub>2</sub>)<sub>2</sub>·2DMF], consists of chains of trans corner-sharing CeO<sub>6</sub> polyhedra. The metal ions are bridged by the μ-oxygen atom of the carboxylate group of 4-nitrobenzoic acid (Figure 4). All other coordinating oxygen atoms stem from the carboxylate groups of the H<sub>2</sub>TCPP<sup>4-</sup> ions. The chains are connected by H<sub>2</sub>TCPP<sup>4-</sup> molecules to form a three-dimensional framework. Two types of pores are formed along [010], with pore diameters of 5.0 × 11.8 Å and 2.0 × 11.8 Å, respectively (Figure 4). This structure is similar to the ones of [M<sub>2</sub>(μ-OH)<sub>2</sub>(H<sub>2</sub>TCPP)], M = Al, Ga, and In<sup>36,37</sup> where the bridging of the M<sup>3+</sup> ions is accomplished through μ-OH groups. Since the BA-NO<sub>2</sub><sup>-</sup> ion is not located in a special position, the occupancy of the coligand was constrained to 0.25.

Thermal treatment of CAU-18 between 250 and 300 °C leads to a microcrystalline product, of composition [Ce<sub>4</sub>(H<sub>2</sub>TCPP)<sub>3</sub>], denoted CAU-18a, with low long-range order. At the activation temperature, removal of coordinating H<sub>2</sub>O and DMF molecules takes place and a permanently porous compound is formed which adsorbs 22 H<sub>2</sub>O molecules per formula unit. We anticipate condensation of the tetrameric units and formation of an open framework accessible for guest molecules. Thermogravimetric measurements confirm this hypothesis regarding the loss for DMF and H<sub>2</sub>O molecules at 250 °C (Figure 8). IR spectroscopy confirms the absence of DMF molecules in CAU-18a (Figure 11).

Since Ce(III) and Ce(IV) compounds exhibit very distinct Ce L<sub>3</sub>-edge XANES features, the corresponding measurements



were performed for all title compounds to probe the oxidation state of Ce ions, similarly to our previous Ce MOFs studies.<sup>21</sup> As demonstrated by comparison with the spectra of CeO<sub>2</sub> and Ce(NO<sub>3</sub>)<sub>3</sub>·6H<sub>2</sub>O reference compounds presented in Figure S18, all title compounds contain exclusively Ce<sup>3+</sup> ions, which were formed during the synthesis from the Ce(IV) precursor (NH<sub>4</sub>)<sub>2</sub>[Ce(NO<sub>3</sub>)<sub>6</sub>]. It is worth to note that in the synthesis of Ce-UiO-66<sup>21</sup> the same reaction conditions were employed, but the tetravalent oxidation state was preserved during the reaction. Hence redox-active linker molecules such as H<sub>6</sub>TCPHP lead to the reduction of the Ce<sup>4+</sup> ions during the reaction.

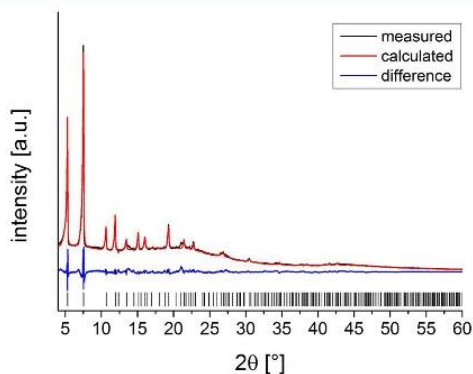


**Figure 5.** Result of the Rietveld-refinement of Ce-PMOF-4NO<sub>2</sub>. Measured data are shown as a black line, calculated data as a red line, and the blue line gives the difference plot. Predicted peak positions are marked as vertical bars.

**Sorption Properties.** Sorption experiments were only carried out for CAU-18a, CAU-19-X, and M-CAU-19-H (M = Zn, Co) since CAU-18 and Ce-PMOF-4NO<sub>2</sub> transform to CAU-18a and CAU-19-4NO<sub>2</sub> during the activation procedure. Prior to the sorption experiments all samples were activated at 170 °C under vacuum (10<sup>-2</sup> kPa) for 16 h. Subsequently sorption experiments using N<sub>2</sub> at 77 K (Figures 6, S30 and S31) and H<sub>2</sub>O at 298 K (Figure 7) as adsorptive were performed. The specific surface areas were determined using

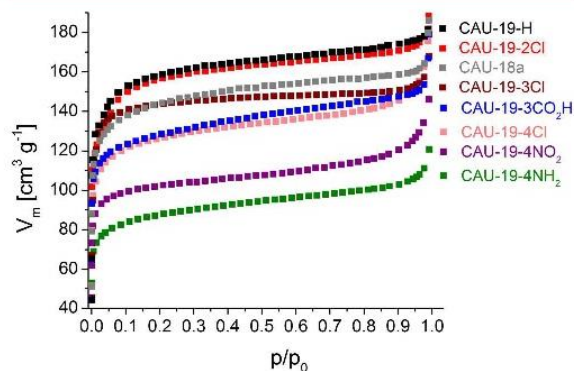


**Figure 6.** N<sub>2</sub>-sorption isotherms of CAU-18a and CAU-19-X (X = H, 2Cl, 3Cl, 4Cl, 3CO<sub>2</sub>H, 4NH<sub>2</sub>, 4NO<sub>2</sub>) measured at 77 K. Only the adsorption branch is shown; desorption is omitted for clarity. All N<sub>2</sub>-sorption isotherms including ad- and desorption are shown in the Supporting Information in Figure S30.

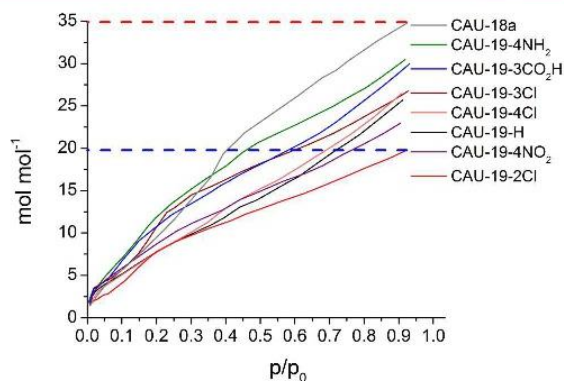


**Figure 7.** H<sub>2</sub>O sorption isotherms of CAU-18a and CAU-19-X (X = H, 2Cl, 3Cl, 4Cl, 3CO<sub>2</sub>H, 4NH<sub>2</sub>, 4NO<sub>2</sub>) measured at 298 K (mol mol<sup>-1</sup>). The red dashed line represents the sample with the highest uptake and the blue dashed line the sample with the lowest uptake, respectively.

the BET method and applying the method of Roquerol.<sup>66,67</sup> Micropore volumes  $V_m$  were determined by using the amount of adsorbed N<sub>2</sub> at the relative pressure  $p/p_0 = 0.5$  (Table 3). All compounds are stable toward activation and sorption measurements as proven by PXRD measurements (Figure S32). All N<sub>2</sub> measurements lead to a type-1a isotherm as expected for microporous materials with pore diameters  $\leq 1$  nm.<sup>67</sup> CAU-18a has a specific surface area of  $a_{\text{BET}} = 550$  m<sup>2</sup> g<sup>-1</sup> and the CAU-19-X derivatives have  $a_{\text{BET}}$  values between 330 and 600 m<sup>2</sup> g<sup>-1</sup> depending on the incorporated coligand. The metalated forms of CAU-19-H exhibit a specific surface area of 570 and 430 m<sup>2</sup> g<sup>-1</sup> for Zn-CAU-19-H and Co-CAU-19-H, respectively. If the specific surface areas per millimol are taken into account, the value of Zn-CAU-19-H is identical with the one of the nonmetalated form, while for Co-CAU-19-H a slightly lower value is observed (Table 3).

A direct correlation of the steric demand of the different functional groups in CAU-19-X on the  $a_{\text{BET}}$  values is not observed. A coligand with a functional group in 2-position seems to lead to higher specific surface areas than ligands with groups in 3- or 4-position (Table 3). CAU-19-4NH<sub>2</sub> has the smallest specific surface area of  $a_{\text{BET}} = 330$  m<sup>2</sup> g<sup>-1</sup> which is because not all HBA-NH<sub>2</sub> molecules could be removed from the pores during activation, as proven by NMR spectroscopy (Figure S10, one HBA-NH<sub>2</sub> molecule per formula unit remains in the pores). The rather low specific surface area of CAU-19-4NO<sub>2</sub> of 400 m<sup>2</sup> g<sup>-1</sup> is due to the low long-range order of the samples after the phase transformation.

The H<sub>2</sub>O sorption measurements at 298 K of all samples show an uptake between 10.7 and 21.3 wt % and CAU-18a exhibits the highest uptake of 21.3 wt %, followed by CAU-19-4NH<sub>2</sub> and CAU-19-3CO<sub>2</sub>H with values of 16.6 and 16.0 wt %. This result is remarkable since in the N<sub>2</sub> sorption experiments these latter MOFs showed the lowest N<sub>2</sub> uptake, but it is probably due to strong H-bond interactions between the amino- and the carboxy-group of the incorporated benzoic acid derivatives in the pores with the adsorptive water.

**Thermal and Chemical Stability.** To investigate the thermal stability TG measurements of all samples and VT-PXRD studies for CAU-18 and CAU-19-H were carried out.

The results of the TG measurements (Table S4, Figures 8 and 9 as well as Figures S33–S41) show two or three

**Table 3. Results of the Sorption Experiments (N<sub>2</sub> at 77 K and H<sub>2</sub>O at 298.15 K) of CAU-18a, CAU-19-X (X = H, 2Cl, 3Cl, 4Cl, 3CO<sub>2</sub>H, 4NH<sub>2</sub>, 4NO<sub>2</sub>) and M-CAU-19-H (M = Zn, Co)<sup>a</sup>**

	CAU-18a	H	Zn H	Co H	2Cl	3Cl	4Cl	3CO <sub>2</sub> H	4NH <sub>2</sub>	4NO <sub>2</sub>
N <sub>2</sub> ( <i>a</i> <sub>BET</sub> ) [m <sup>2</sup> g <sup>-1</sup> ]	550	600	570	430	590	580	480	490	330	400
[m <sup>2</sup> mmol <sup>-1</sup> ]	1620	1370	1374	1031	1390	1360	1130	1160	760	950
N <sub>2</sub> ( <i>V</i> <sub>m</sub> ) [cm <sup>3</sup> g <sup>-1</sup> ]	0.24	0.26	0.24	0.19	0.25	0.23	0.21	0.21	0.15	0.17
H <sub>2</sub> O (upt.) [mol mol <sup>-1</sup> ]	34.8	25.7			19.8	26.8	26.4	30.0	30.4	23.0
[wt %]	21.3	14.1			10.7	14.4	14.2	16.0	16.6	12.3

<sup>a</sup>The micropore volume was calculated at  $p/p_0 = 0.5$ .

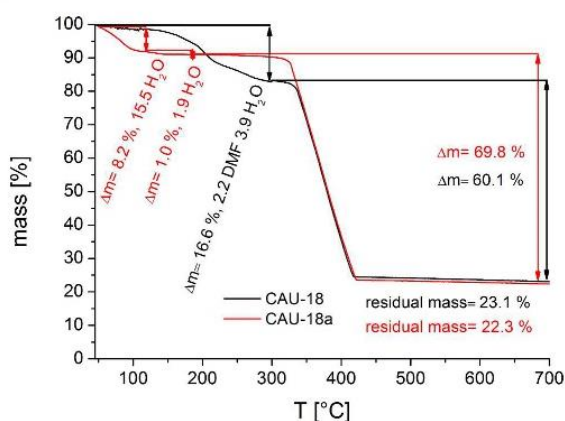


**Figure 8.** Thermogravimetric curve of CAU-18 ([Ce<sub>4</sub>(H<sub>2</sub>TCCP)<sub>3</sub>·(H<sub>2</sub>O)<sub>4</sub>(DMF)<sub>2</sub>) and CAU-18a ([Ce<sub>4</sub>(H<sub>2</sub>TCCP)<sub>3</sub>·17.4H<sub>2</sub>O (Table S4).

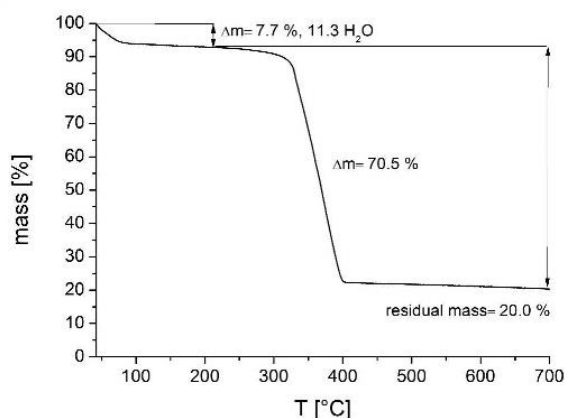


**Figure 9.** Thermogravimetric curve of CAU-19-H. Evaluation of the data reveals a molar ratio of metal/linker/benzoic acid/H<sub>2</sub>O of 3.1:2.4:11.3 (Table S4).

characteristic steps of weight loss, respectively. The loss up to 100 °C is assigned to the evaporation of physisorbed water molecules. In the case of CAU-18, the removal of the coordinated DMF and water molecules occurs between 100 and 250 °C. The weight loss between 100 and 250 °C for CAU-19-3CO<sub>2</sub>H is due to the evaporation of physisorbed DMF as confirmed by <sup>1</sup>H NMR spectroscopy (Figure S9). Above 330 °C the decomposition of the compounds take place, and CeO<sub>2</sub> is formed as the final product, as confirmed by PXRD measurements (Figure S42). In the TG curve of CAU-18a three steps of weight loss are observed. The first two steps

up to 150 °C can be assigned to the loss of water molecules. No further weight loss up to 330 °C is observed, when the framework starts to decompose. These results demonstrate that the DMF molecules have been quantitatively removed during the transformation of CAU-18 to CAU-18a, which was also confirmed by elemental analysis. In general, the results of the TG analysis fit well with the ones of the elemental analyses. Slight differences in the amounts of occluded solvent molecules are due to the storage of the samples prior to the measurements where guest molecules can be exchanged by atmospheric water molecules.

The results of the VT-PXRD studies of CAU-18 and CAU-19-H are shown in Figure 10. These measurements show for CAU-18 two phase transformations: one at 220 °C into an unknown intermediate and one at 300 °C into CAU-18a. Compared to the direct synthesis of CAU-18a (thermal treatment at 250 °C in air for 24 h) the phase transformation is delayed, probably because the VT-PXRD measurements are performed in the confinement of the quartz capillaries within 4 h instead of an open crucible within 24 h. The unknown intermediate was also sometimes observed in the direct synthesis at 250 °C but after shorter reaction times of 2 h. A first decrease of crystallinity is observed up to 380 °C, and the complete loss of crystallinity takes place at 490 °C. CAU-19-H shows a very similar behavior. Up to 380 °C, no remarkable loss of crystallinity is observable but a few reflections are shifted during the measurement. A decrease of crystallinity is observable at 385 °C, and the decomposition of the sample takes place at 480 °C. In comparison to the TG results, the measurements show higher decomposition temperatures (CAU-18: 450–500/330 °C, CAU-19-H: 450–550/330 °C), which is due to the confinement of the sample in a capillary during the VT-PXRD measurements.

To investigate the chemical stability, CAU-18a and CAU-19-H were exemplarily treated in different solvents (2 M HCl, 2 M NaOH, 100% acetic acid, H<sub>2</sub>O, MeOH, EtOH, acetone, dichloromethane) at RT for 24 h under stirring. After the treatment, the samples were isolated by filtration and measured by PXRD. The results of the chemical stability tests (Figure S43) reveal that both MOFs are stable in all tested organic solvents and water, but show a complete decomposition in 2 M HCl and 2 M NaOH and decrease of crystallinity in 100% acetic acid.

**In Situ X-ray Diffraction.** To learn more about the formation of CAU-18 and CAU-19-H in situ crystallization studies were carried out employing synchrotron radiation.<sup>68</sup> These MOFs are ideal candidates for such studies since they are formed within short reaction times of 1–2 h. In addition to the detection of possible crystalline intermediates X-ray diffraction (XRD) crystallization studies are a suitable method to determine kinetic parameters such as rate constants for nucleation ( $k_n$ ) and crystal growth ( $k_g$ ) as well as the respective



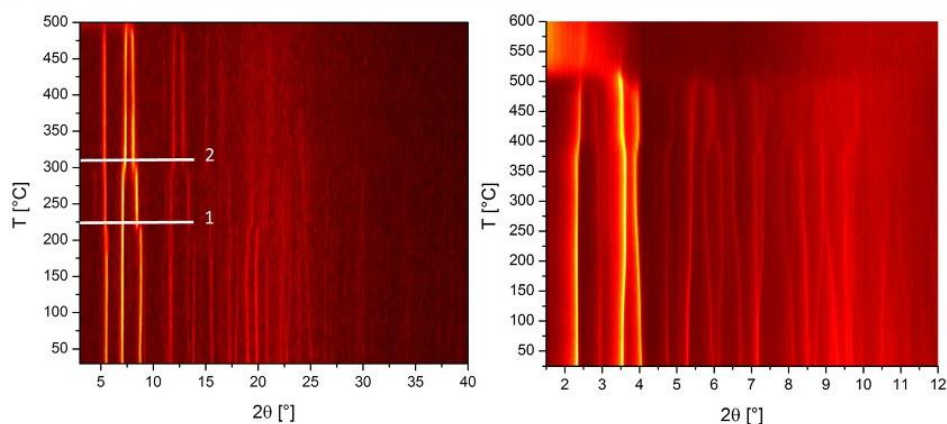


**Figure 10.** Results of the VT-PXRD studies of CAU-18 (left, Cu  $K\alpha_1$  radiation) and CAU-19-H (right, Mo  $K\alpha_1$  radiation) measured in open quartz capillaries (0.5 mm) under atmospheric conditions. The label 1 indicates the phase transformation into an unknown intermediate and the label 2 the phase transformation into CAU-18a.

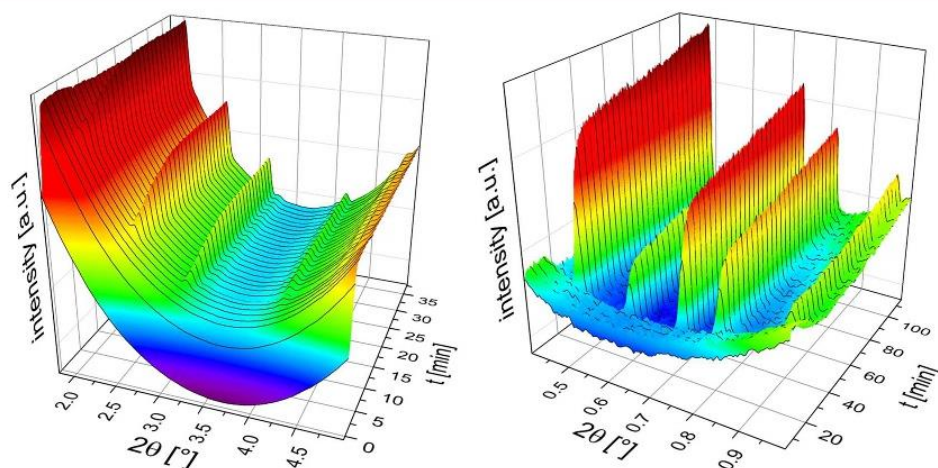


**Figure 11.** Results of the in situ XRD crystallization of CAU-18 (left) and CAU-19-H (right) at a reaction temperature of 120 °C. Measurements were carried out at beamlines P09 and P07B, PETRA III, DESY, Hamburg.

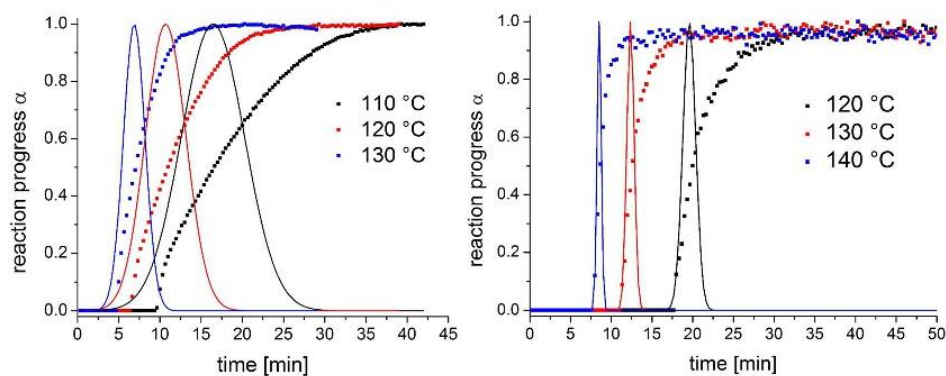


**Figure 12.** Reaction progress  $\alpha$  (filled squares) and probability of nucleation  $P_n$  (line) of CAU-18 (left) and CAU-19-H (right) as determined at the different reaction temperatures.

Arrhenius activation energies ( $E_A$ ) and the probability of nucleation ( $P_n$ ) and have been reported for several MOFs like

MIL-53,<sup>8</sup> MOF-14,<sup>10</sup> MIL-100,<sup>9</sup> and CAU-13.<sup>69</sup> Crystallization studies have also been reported for other compounds which are

**Table 4.** Rate Constants for Nucleation ( $k_n$ ) and Crystal Growth ( $k_g$ ), Nucleation Parameter  $b$ , Induction Time ( $t_{ind}$ ), Time to Reach Reaction Completeness ( $t_{com}$ ) and Maximum of Probability of Nucleation ( $P_n$ ) as Obtained Using the Method of Gualtieri<sup>12a</sup>

	$a = k_n^{-1}$	$k_g$	$b$	$t_{ind}$ [min]	$t_{com}$ [min]	$P_n$ (max) [min]
CAU-18 110 °C	16.43	0.09	5.43	9.7	37.0	16.3
CAU-18 120 °C	10.70	0.13	3.50	6.7	28.3	10.7
CAU-18 130 °C	6.89	0.19	1.86	5.0	17.7	7.0
CAU-19-H 120 °C	19.58	0.08	1.11	16.0 (13.0)	34.3 (31.3)	19.7
CAU-19-H 130 °C	12.36	0.13	0.63	9.7 (6.7)	22.3 (19.3)	12.3
CAU-19-H 140 °C	8.50	0.19	0.35	6.3 (3.3)	17.7 (14.7)	8.5

<sup>a</sup>Values in brackets represent the reduced values  $t_{ind}$  and  $t_{com}$  for injection of the metal salt solution after 3 min to initiate the formation of CAU-19-H.

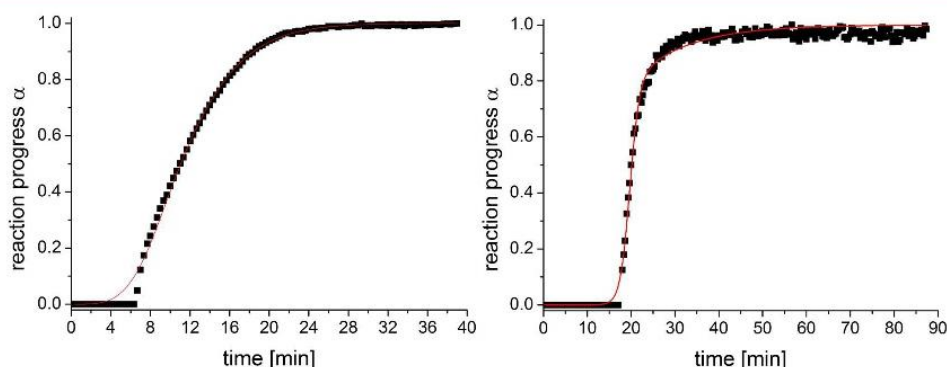


**Figure 13.** Gualtieri-fit of the reaction progress for the reactions carried out at 120 °C. Left, formation of CAU-18 and right, formation of CAU-19-H. The results of the fits are summarized in Figures S50 and S52.

obtained under solvothermal reaction conditions like zeolites,<sup>12</sup> polyoxovanadates,<sup>70</sup> and thioantimonates.<sup>71</sup>

The crystallization of CAU-18 was carried out at three different reaction temperatures (110, 120, and 130 °C). The linker ( $H_6$ TCPP, 20 mg,  $2.53 \times 10^{-2}$  mmol), 2400  $\mu$ L of *N,N*-dimethylformamide (DMF), 350  $\mu$ L of dist.  $H_2O$  and 94.5  $\mu$ L of a 0.53 mol/L solution of  $(NH_4)_2[Ce(NO_3)_6]$  in dist.  $H_2O$  were placed in a borosilicate glass vessel ( $V_{max} = 5$  mL). After homogenization by shaking, the glass vessel was immediately placed inside the reactor. The reaction mixture was heated to the target temperature within 3 min and stirred during the reaction while collecting powder diffraction data.

The ex situ crystallization study of CAU-19-H indicated a very fast formation. Hence the reactor was modified to include a syringe pump system which was employed to start the reaction remotely from the control hatch. The synthesis was carried out at three different reaction temperatures (120, 130, and 140 °C). A solution of  $H_6$ TCPP (20 mg,  $2.53 \times 10^{-2}$  mmol) and benzoic acid (550 mg, 4.5 mmol) in 2400  $\mu$ L of DMF and 200  $\mu$ L of  $H_2O$  was placed in a borosilicate glass vessel ( $V_{max} = 5$  mL) and heated to the target temperature (ca. 3 min) under stirring while continuously measuring XRD data. Subsequently 226  $\mu$ L of a 0.5333 mol/L solution of  $(NH_4)_2[Ce(NO_3)_6]$  in dist.  $H_2O$  was added via injection to initiate the reaction.

The results of the in situ crystallization of CAU-18 and CAU-19-H are shown for the reactions at 120 °C in Figure 11; further in situ crystallization plots are shown in Figures S44–S48. In order to investigate the kinetics of crystallization, the normalized peak areas at the different reaction times, which correspond to the reaction progress  $\alpha$ , were determined. For

CAU-18 the [020] and for CAU-19-H the [100] reflections were used, which are the ones with the highest intensity. The reaction progress  $\alpha$  at different reaction temperatures is shown in Figure 12. As expected, the induction time ( $t_{ind}$ ), in which no crystalline products are observed, and the total reaction time to achieve full conversion ( $t_{com}$ ) are shorter at higher temperatures (Figure 12 and Table 4).

The method of Gualtieri was employed to determine the kinetic constants of the crystallization process of CAU-18 and CAU-19-H.<sup>12</sup> In this model the nucleation and the crystal growth are taken into account and are considered as separate processes (eq 1).

$$\alpha = \frac{1}{1 + \exp\left[-\left(\frac{t-a}{b}\right)^n\right]} \{1 - \exp(-k_g t^n)\} \quad (1)$$

The reaction progress  $\alpha$  is a nonlinear function depending on the reaction time  $t$  and the parameters  $a = k_n^{-1}$  (reciprocal rate constant of nucleation),  $b$  (a constant related to nucleation),  $k_g$  (rate constant of crystal growth), and  $n$ , which represents the dimensionality of the crystal growth.<sup>12</sup> To find the right value for  $n$ , all dimensionalities were tested, and the best fit,  $n = 3$  for CAU-18 and  $n = 1$  for CAU-19-H was found, which was substantiated by the SEM measurements (Figures S13–S14). The results of the Gualtieri fits for the reaction at 120 °C for both compounds are shown in Figure 13, and the resulting parameters are listed in Table 4. The Gualtieri fits for the data obtained at the other reaction temperatures are shown in Figures S49–S54. The rate constants for nucleation and crystal growth increase with temperature and can be used to calculate the probability of nucleation  $P_n$  which is given in eq 2.



$$P_n = e^{-(t-a)^2/b^2} \quad (2)$$

$P_n$  is plotted versus time and depends on the Gualtieri constants  $a$  and  $b$ . The maximum of the probability of nucleation is shifted to smaller reaction times with increasing temperature (Figure 12 and Table 4). The Arrhenius activation energy for nucleation and crystal growth can be obtained by plotting  $\ln(k)$  vs  $1/T$  (Figures S55–S58). The Arrhenius activation energies were determined as 56(1) and 56(3) kJ mol<sup>-1</sup> for nucleation and 48(1) and 58(5) kJ mol<sup>-1</sup> for crystal growth for CAU-18 and CAU-19-H, respectively. The activation energies are in the same order of magnitude and in good agreement with other previous reported MOFs (Mn-MIL-100: 89.9/126.5 kJ mol<sup>-1</sup> (ref 9), MOF-14: 64–83 kJ mol<sup>-1</sup> (ref 10), CAU-13: 76–77 kJ mol<sup>-1</sup> (ref 69), and CAU-1: 131–136 kJ mol<sup>-1</sup> (ref 11)).

## CONCLUSION

We demonstrated the successful synthesis and characterization of four new porphyrin-based Ce-MOFs, CAU-18, [Ce<sub>4</sub>(H<sub>2</sub>TCPP)<sub>3</sub>(DMF)<sub>2</sub>(H<sub>2</sub>O)<sub>4</sub>], CAU-18a, [Ce<sub>4</sub>(H<sub>2</sub>TCPP)<sub>3</sub>·22 H<sub>2</sub>O], CAU-19-X, Ce<sub>3</sub>(H<sub>2</sub>TCPP)<sub>2</sub>(BA-X)(HBA-X/H<sub>2</sub>O)<sub>2</sub>·2 HBA·xH<sub>2</sub>O (X = H, 2Cl, 3Cl, 4Cl, 3CO<sub>2</sub>H, 4NH<sub>2</sub>, 4NO<sub>2</sub>), and Ce-PMOF-4NO<sub>2</sub>, [Ce<sub>2</sub>(H<sub>2</sub>TCPP)(C<sub>7</sub>H<sub>4</sub>O<sub>2</sub>NO<sub>2</sub>)<sub>2</sub>]<sub>2</sub>·2DMF (H<sub>6</sub>TCPP = 4-tetracarboxyphenylporphyrin).

Considering this observed structural diversity induced by the presence/nature of the coligand employed, it could be very interesting to evaluate the other lanthanide ions in a similar manner. Furthermore, the metalated form of CAU-19-H, M-CAU-19-H with M = Zn and Co were obtained. Despite the use of (NH<sub>4</sub>)<sub>2</sub>[Ce(NO<sub>3</sub>)<sub>6</sub>] as a source of Ce in all syntheses, all compounds contain exclusively Ce<sup>3+</sup> ions. The trivalent oxidation state was unequivocally confirmed by XANES measurements. Thermal treatment of CAU-18 at 250 °C leads to the removal of DMF molecules and the permanently porous compound CAU-18a formed. Phase transformation of Ce-PMOF-NO<sub>2</sub> to CAU-19-NO<sub>2</sub> is observed in organic solvents at 70 °C within 72 h. CAU-18a and all CAU-19-X derivatives are permanently porous with specific surface areas of 330–600 m<sup>2</sup> g<sup>-1</sup> as determined from N<sub>2</sub> physisorption measurements at 77 K, and they are also porous toward H<sub>2</sub>O with an uptake between 10.7 and 21.3 wt %. The in situ crystallization studies revealed the expected temperature dependent increase of the rate constants for the formation of CAU-18 and CAU-19-H.

In this context it could be very interesting to further investigate the formation of the title compounds by in situ XAS or EXAFS studies to gain insight into the reduction of the metal source and the relevance for the formation of Ce<sup>3+</sup>/Ce<sup>4+</sup> MOFs.

## ASSOCIATED CONTENT

### Supporting Information

The Supporting Information is available free of charge on the ACS Publications website at DOI: 10.1021/acs.cgd.7b00450.

Details of the synthesis and characterization of H<sub>6</sub>TCPP, Co–H<sub>4</sub>TCPP and information on the characterization of all obtained compounds, including <sup>1</sup>H NMR spectroscopy, Pawley fits, XANES spectra, structural representations, thermogravimetric measurements and IR-spectroscopy (PDF)

## Accession Codes

CCDC 1539771–1539772 contain the supplementary crystallographic data for this paper. These data can be obtained free of charge via [www.ccdc.cam.ac.uk/data\\_request/cif](http://www.ccdc.cam.ac.uk/data_request/cif), or by emailing [data\\_request@ccdc.cam.ac.uk](mailto:data_request@ccdc.cam.ac.uk), or by contacting The Cambridge Crystallographic Data Centre, 12 Union Road, Cambridge CB2 1EZ, UK; fax: +44 1223 336033.

## AUTHOR INFORMATION

### Corresponding Author

\*E-mail: [stock@ac.uni-kiel.de](mailto:stock@ac.uni-kiel.de).

### ORCID

Helge Reinsch: 0000-0001-5288-1135

Norbert Stock: 0000-0002-0339-7352

### Notes

The authors declare no competing financial interest.

## ACKNOWLEDGMENTS

We appreciate support from the Deutsche Forschungsgemeinschaft (SPP-1415; STO 643/6-2). We would like to acknowledge Milan Köppen for the development of software tools used for data treatment and DESY for the allocation of beamtime. Furthermore, we thank Jörg Stempfler and the beamline staff of beamline P07 and P09 for their support during the beamtime as well as HZG and Norbert Schell. This work has been supported by the MATsynCELL project through the Röntgen-Ångström Cluster, supported by the Swedish Research Council and the German Federal Ministry of Education and Research (BMBF). A.V.S. acknowledges the Mega-grant of the Russian Federation Government No. 14.Y26.31.0001. K.A.L. acknowledges the support from the Russian Foundation for Basic Research, Project No. 16-32-00572 mol\_a. Furthermore, we thank Simon Smolders from the KU Leuven for measuring the TG curves of Zn- and Co-CAU-19-H, Figures S40 and S41.

## REFERENCES

- (1) Furukawa, H.; Cordova, K. E.; O’Keeffe, M.; Yaghi, O. M. The Chemistry and Applications of Metal-Organic Frameworks. *Science* **2013**, *341*, 123044410.1126/science.1230444
- (2) Stock, N.; Reinsch, H.; Schilling, L.-H. CHAPTER 2 Synthesis of MOFs. *Metal Organic Frameworks as Heterogeneous Catalysts*; The Royal Society of Chemistry, 2013; pp 9–30.
- (3) Zhou, H.-C.; Long, J. R.; Yaghi, O. M. Introduction to Metal-Organic Frameworks. *Chem. Rev.* **2012**, *112*, 673–674.
- (4) Yaghi, O. M.; O’Keeffe, M.; Ockwig, N. W.; Chae, H. K.; Eddaoudi, M.; Kim, J. Reticular synthesis and the design of new materials. *Nature* **2003**, *423*, 705–714.
- (5) Sun, C.-Y.; Qin, C.; Wang, X.-L.; Su, Z.-M. Metal-organic frameworks as potential drug delivery systems. *Expert Opin. Drug Delivery* **2013**, *10*, 89–101.
- (6) Janiak, C.; Vieth, J. K. MOFs, MILs and more: concepts, properties and applications for porous coordination networks (PCNs). *New J. Chem.* **2010**, *34*, 2366–2388.
- (7) Mueller, U.; Schubert, M.; Teich, F.; Puetter, H.; Schierle-Arndt, K.; Pastre, J. Metal-organic frameworks-prospective industrial applications. *J. Mater. Chem.* **2006**, *16*, 626–636.
- (8) Millange, F.; Medina, M. I.; Guillou, N.; Férey, G.; Golden, K. M.; Walton, R. I. Time-Resolved In Situ Diffraction Study of the Solvothermal Crystallization of Some Prototypical Metal-Organic Frameworks. *Angew. Chem., Int. Ed.* **2010**, *49*, 763–766.
- (9) Reinsch, H.; Stock, N. Formation and characterisation of Mn-MIL-100. *CrystEngComm* **2013**, *15*, 544–550.
- (10) Millange, F.; El Osta, R.; Medina, M. E.; Walton, R. I. A time-resolved diffraction study of a window of stability in the synthesis of a



# Porphyrin-basierte Metall-Organische Gerüstverbindungen: Von Metall-Carboxylaten zu Metall-Phosphonaten

- copper carboxylate metal-organic framework. *CrystEngComm* **2011**, *13*, 103–108.
- (11) Ahnfeldt, T.; Moellmer, J.; Guillemin, V.; Staudt, R.; Serre, C.; Stock, N. High-Throughput and Time-Resolved Energy-Dispersive X-Ray Diffraction (EDXRD) Study of the Formation of CAU-1-(OH)2: Microwave and Conventional Heating. *Chem. - Eur. J.* **2011**, *17*, 6462–6468.
- (12) Gualtieri, F. A. Synthesis of sodium zeolites from a natural halloysite. *Phys. Chem. Miner.* **2001**, *28*, 719–728.
- (13) Feng, D.; Jiang, H.-L.; Chen, Y.-P.; Gu, Z.-Y.; Wei, Z.; Zhou, H.-C. Metal–Organic Frameworks Based on Previously Unknown Zr8/Hf8 Cubic Clusters. *Inorg. Chem.* **2013**, *52*, 12661–12667.
- (14) Feng, D.; Chung, W.-C.; Wei, Z.; Gu, Z.-Y.; Jiang, H.-L.; Chen, Y.-P.; Darensbourg, D. J.; Zhou, H.-C. Construction of Ultrastable Porphyrin Zr Metal–Organic Frameworks through Linker Elimination. *J. Am. Chem. Soc.* **2013**, *135*, 17105–17110.
- (15) Gallagher, A. T.; Keltly, M. L.; Park, J. G.; Anderson, J. S.; Mason, J. A.; Walsh, J. P. S.; Collins, S. L.; Harris, T. D. Dioxxygen binding at a four-coordinate cobaltous porphyrin site in a metal-organic framework: structural, EPR, and O2 adsorption analysis. *Inorg. Chem. Front.* **2016**, *3*, 536–540.
- (16) Hod, I.; Sampson, M. D.; Deria, P.; Kubiak, C. P.; Farha, O. K.; Hupp, J. T. Fe-Porphyrin-Based Metal–Organic Framework Films as High-Surface Concentration, Heterogeneous Catalysts for Electrochemical Reduction of CO<sub>2</sub>. *ACS Catal.* **2015**, *5*, 6302–6309.
- (17) Chang, T.-H.; Kung, C.-W.; Chen, H.-W.; Huang, T.-Y.; Kao, S.-Y.; Lu, H.-C.; Lee, M.-H.; Boopathi, K. M.; Chu, C.-W.; Ho, K.-C. Planar Heterojunction Perovskite Solar Cells Incorporating Metal–Organic Framework Nanocrystals. *Adv. Mater. (Weinheim, Ger.)* **2015**, *27*, 7229–7235.
- (18) Kung, C.-W.; Chang, T.-H.; Chou, L.-Y.; Hupp, J. T.; Farha, O. K.; Ho, K.-C. Post metalation of solvothermally grown electroactive porphyrin metal-organic framework thin films. *Chem. Commun.* **2015**, *51*, 2414–2417.
- (19) Liu, Y.; Howarth, A. J.; Hupp, J. T.; Farha, O. K. Selective Photooxidation of a Mustard-Gas Simulant Catalyzed by a Porphyrinic Metal–Organic Framework. *Angew. Chem., Int. Ed.* **2015**, *54*, 9001–9005.
- (20) Guo, Z.; Chen, B. Recent developments in metal-metalloporphyrin frameworks. *Dalton Trans* **2015**, *44*, 14574–14583.
- (21) Lammert, M.; Wharmby, M. T.; Smolders, S.; Bueken, B.; Lieb, A.; Lomachenko, K. A.; Vos, D. D.; Stock, N. Cerium-based metal organic frameworks with UiO-66 architecture: synthesis, properties and redox catalytic activity. *Chem. Commun.* **2015**, *51*, 12578–12581.
- (22) Alves, E.; Faustino, M. A. F.; Neves, M. G. P. M. S.; Cunha, Á.; Nadais, H.; Almeida, A. Potential applications of porphyrins in photodynamic inactivation beyond the medical scope. *J. Photochem. Photobiol., C* **2015**, *22*, 34–57.
- (23) Huang, H.; Song, W.; Rieffel, J.; Lovell, J. F. Emerging Applications of Porphyrins in Photomedicine. *Front. Phys.* **2015**, *3*, 10.3389/fphy.2015.00023
- (24) Lu, K.; He, C.; Lin, W. A Chlorin-Based Nanoscale Metal–Organic Framework for Photodynamic Therapy of Colon Cancers. *J. Am. Chem. Soc.* **2015**, *137*, 7600–7603.
- (25) Devic, T.; Serre, C. High valence 3p and transition metal based MOFs. *Chem. Soc. Rev.* **2014**, *43*, 6097–6115.
- (26) Gao, W.-Y.; Chrzanowski, M.; Ma, S. Metal-metalloporphyrin frameworks: a resurging class of functional materials. *Chem. Soc. Rev.* **2014**, *43*, 5841–5866.
- (27) Guo, Z.; Chen, B. Recent developments in metal-metalloporphyrin frameworks. *Dalton Trans* **2015**, *44*, 14574–14583.
- (28) Huh, S.; Kim, S.-J.; Kim, Y. Porphyrinic metal-organic frameworks from custom-designed porphyrins. *CrystEngComm* **2016**, *18*, 345.
- (29) Kosal, M. E.; Chou, J.-H.; Wilson, S. R.; Suslick, K. S. A functional zeolite analogue assembled from metalloporphyrins. *Nat. Mater.* **2002**, *1*, 118–121.
- (30) Goldberg, I. Metalloporphyrin Molecular Sieves. *Chem. - Eur. J.* **2000**, *6*, 3863–3870.
- (31) Feng, D.; Gu, Z.-Y.; Chen, Y.-P.; Park, J.; Wei, Z.; Sun, Y.; Bosch, M.; Yuan, S.; Zhou, H.-C. A Highly Stable Porphyrinic Zirconium Metal–Organic Framework with shp-a Topology. *J. Am. Chem. Soc.* **2014**, *136*, 17714–17717.
- (32) Jiang, H.-L.; Feng, D.; Wang, K.; Gu, Z.-Y.; Wei, Z.; Chen, Y.-P.; Zhou, H.-C. An Exceptionally Stable, Porphyrinic Zr Metal–Organic Framework Exhibiting pH-Dependent Fluorescence. *J. Am. Chem. Soc.* **2013**, *135*, 13934–13938.
- (33) Morris, W.; Voloskiy, B.; Demir, S.; Gándara, F.; McGrier, P. L.; Furukawa, H.; Cascio, D.; Stoddart, J. F.; Yaghi, O. M. Synthesis, Structure, and Metalation of Two New Highly Porous Zirconium Metal–Organic Frameworks. *Inorg. Chem.* **2012**, *51*, 6443–6445.
- (34) Bai, Y.; Dou, Y.; Xie, L.-H.; Rutledge, W.; Li, J.-R.; Zhou, H.-C. Zr-based metal-organic frameworks: design, synthesis, structure, and applications. *Chem. Soc. Rev.* **2016**, *45*, 2327–2367.
- (35) Feng, D.; Jiang, H.-L.; Chen, Y.-P.; Gu, Z.-Y.; Wei, Z.; Zhou, H.-C. Metal–Organic Frameworks Based on Previously Unknown Zr8/Hf8 Cubic Clusters. *Inorg. Chem.* **2013**, *52*, 12661–12667.
- (36) Fateeva, A.; Chater, P. A.; Ireland, C. P.; Tahir, A. A.; Khimiyak, Y. Z.; Wiper, P. V.; Darwent, J. R.; Rosseinsky, M. J. A Water-Stable Porphyrin-Based Metal–Organic Framework Active for Visible-Light Photocatalysis. *Angew. Chem.* **2012**, *124*, 7558–7562.
- (37) Rhauderwiek, T.; Waitschat, S.; Wuttke, S.; Reinsch, H.; Bein, T.; Stock, N. Nanoscale Synthesis of Two Porphyrin-Based MOFs with Gallium and Indium. *Inorg. Chem.* **2016**, *55*, 5312–5319.
- (38) Gao, W.-Y.; Zhang, Z.; Cash, L.; Wojtas, L.; Chen, Y.-S.; Ma, S. Two rare indium-based porous metal-metalloporphyrin frameworks exhibiting interesting CO<sub>2</sub> uptake. *CrystEngComm* **2013**, *15*, 9320–9323.
- (39) Johnson, J. A.; Luo, J.; Zhang, X.; Chen, Y.-S.; Morton, M. D.; Echeverría, E.; Torres, F. E.; Zhang, J. Porphyrin-Metalation-Mediated Tuning of Photoredox Catalytic Properties in Metal–Organic Frameworks. *ACS Catal.* **2015**, *5*, 5283–5291.
- (40) Johnson, J. A.; Zhang, X.; Reeson, T. C.; Chen, Y.-S.; Zhang, J. Facile Control of the Charge Density and Photocatalytic Activity of an Anionic Indium Porphyrin Framework via in Situ Metalation. *J. Am. Chem. Soc.* **2014**, *136*, 15881–15884.
- (41) Fateeva, A.; Devautour-Vinot, S.; Heymans, N.; Devic, T.; Grenèche, J.-M.; Wuttke, S.; Miller, S.; Lago, A.; Serre, C.; de Weireld, G.; et al. Series of Porous 3-D Coordination Polymers Based on Iron(III) and Porphyrin Derivatives. *Chem. Mater.* **2011**, *23*, 4641–4651.
- (42) Fateeva, A.; Clarisse, J.; Pilet, G.; Grenèche, J.-M.; Nouar, F.; Abeykoon, B. K.; Guegan, F.; Goutaudier, C.; Luneau, D.; Warren, J. E.; et al. Iron and Porphyrin Metal–Organic Frameworks: Insight into Structural Diversity, Stability, and Porosity. *Cryst. Growth Des.* **2015**, *15*, 1819–1826.
- (43) Wang, K.; Feng, D.; Liu, T.-F.; Su, J.; Yuan, S.; Chen, Y.-P.; Bosch, M.; Zou, X.; Zhou, H.-C. A Series of Highly Stable Mesoporous Metalloporphyrin Fe-MOFs. *J. Am. Chem. Soc.* **2014**, *136*, 13983–13986.
- (44) Yang, F.; Jing, L.; Ji, L.; Liu, Q.; Zhang, X. Design, fabrication and the relative catalytic properties of metal-organic framework complexes based on tetra(4-carboxyphenyl)porphyrin and cerium ions. *CrystEngComm* **2014**, *16*, 4274–4280.
- (45) Lipstman, S.; Goldberg, I. 2D and 3D coordination networks of tetra(carboxyphenyl)-porphyrins with cerium and thulium ions. *J. Mol. Struct.* **2008**, *890*, 101–106.
- (46) Muniappan, S.; Lipstman, S.; George, S.; Goldberg, I. Porphyrin Framework Solids. Synthesis and Structure of Hybrid Coordination Polymers of Tetra(carboxyphenyl)porphyrins and Lanthanide-Bridging Ions. *Inorg. Chem.* **2007**, *46*, 5544–5554.
- (47) Lipstman, S.; Muniappan, S.; George, S.; Goldberg, I. Framework coordination polymers of tetra(4-carboxyphenyl)-porphyrin and lanthanide ions in crystalline solids. *Dalton Trans* **2007**, 3273–3281.
- (48) Jeong, E.-Y.; Ansari, M. B.; Mo, Y.-H.; Park, S.-E. Removal of Cu(II) from water by tetrakis(4-carboxyphenyl) porphyrin-functionalized mesoporous silica. *J. Hazard. Mater.* **2011**, *185*, 1311–1317.

# Porphyrin-basierte Metall-Organische Gerüstverbindungen: Von Metall-Carboxylaten zu Metall-Phosphonaten

- (49) Harada, A.; Yamaguchi, H.; Okamoto, K.; Fukushima, H.; Shiotsuki, K.; Kamachi, M. Control of Photoinduced Electron Transfer from Zinc-Porphyrin to Methyl Viologen by Supramolecular Formation between Monoclonal Antibody and Zinc-Porphyrin. *Photochem. Photobiol.* **1999**, *70*, 298–302.
- (50) Garcia, G.; Sol, V.; Lamarche, F.; Granet, R.; Guilloton, M.; Champavier, Y.; Krausz, P. Synthesis and photocytotoxic activity of new chlorin–polyamine conjugates. *Bioorg. Med. Chem. Lett.* **2006**, *16*, 3188–3192.
- (51) Chen, W.; Fukuzumi, S. Change in Supramolecular Networks through In Situ Esterification of Porphyrins. *Eur. J. Inorg. Chem.* **2009**, *2009*, 5494–5505.
- (52) Feng, D.; Gu, Z.-Y.; Li, J.-R.; Jiang, H.-L.; Wei, Z.; Zhou, H.-C. Zirconium-Metalloporphyrin PCN-222: Mesoporous Metal–Organic Frameworks with Ultrahigh Stability as Biomimetic Catalysts. *Angew. Chem.* **2012**, *124*, 10453–10456.
- (53) SAINT V9.32B, Bruker AXS Inc.: Madison, Wisconsin, USA, 2012.
- (54) Sheldrick, G. A short history of SHELX. *Acta Crystallogr., Sect. A: Found. Crystallogr.* **2008**, *64*, 112–122.
- (55) Dolomanov, O. V.; Bourhis, L. J.; Gildea, R. J.; Howard, J. A. K.; Puschmann, H. OLEX2: a complete structure solution, refinement and analysis program. *J. Appl. Crystallogr.* **2009**, *42*, 339–341.
- (56) Klementiev, K.; Chernikov, R. XAFSmass: a program for calculating the optimal mass of XAFS samples. *J. Phys.: Conf. Ser.* **2016**, *712*, 12008.
- (57) Coelho, A. TOPAS-Academic V4.1; Coelho Software, 2007.
- (58) Brandenburg, K. Diamond Version 3; Crystal Impact GbR: Bonn, 2012.
- (59) Stempffer, J.; Francoual, S.; Reuther, D.; Shukla, D. K.; Skaugen, A.; Schulte-Schrepping, H.; Kracht, T.; Franz, H. Resonant scattering and diffraction beamline P09 at PETRA III. *J. Synchrotron Radiat.* **2013**, *20*, 541–549.
- (60) Brokmeier, H. G.; Müller, M.; Pranzas, P. K.; Schreyer, A.; Staron, P. The High Energy Materials Science Beamline (HEMS) at PETRA III. *Mater. Sci. Forum* **2014**, *772*, 57–61.
- (61) Heidenreich, N.; Rütt, U.; Köppen, M.; Inge, A. K.; Beier, S.; Dippel, A.-C.; Suren, R.; Stock, N. A multi-purpose reaction cell for the investigation of reactions under solvothermal conditions. *Rev. Sci. Instrum.* **2017**, submitted.
- (62) Afzal, S.; Daoud, W. A.; Langford, S. J. Self-cleaning cotton by porphyrin-sensitized visible-light photocatalysis. *J. Mater. Chem.* **2012**, *22*, 4083–4088.
- (63) Rochford, J.; Chu, D.; Hagfeldt, A.; Galoppini, E. Tetrachelate Porphyrin Chromophores for Metal Oxide Semiconductor Sensitization: Effect of the Spacer Length and Anchoring Group Position. *J. Am. Chem. Soc.* **2007**, *129*, 4655–4665.
- (64) Coxall, R. A.; Harris, S. G.; Henderson, D. K.; Parsons, S.; Tasker, P. A.; Winpenny, R. E. P. Inter-ligand reactions: in situ formation of new polydentate ligands. *J. Chem. Soc., Dalton Trans.* **2000**, 2349–2356.
- (65) Han, Y.; Li, X.; Li, L.; Ma, C.; Shen, Z.; Song, Y.; You, X. Structures and Properties of Porous Coordination Polymers Based on Lanthanide Carboxylate Building Units. *Inorg. Chem.* **2010**, *49*, 10781–10787.
- (66) Rouquerol, J.; Avnir, D.; Fairbridge, C. W.; Everett, D. H.; Haynes, J. M.; Pernicone, N.; Ramsay, J. D. F.; Sing, K. S. W.; Unger, K. K. Recommendations for the characterization of porous solids (Technical Report). *Pure Appl. Chem.* **1994**, *66*, 1739–1758.
- (67) Thommes, M.; Kaneko, K.; Neimark, A. V.; Olivier, J. P.; Rodriguez-Reinoso, F.; Rouquerol, J.; Sing, K. S. W. Physisorption of gases, with special reference to the evaluation of surface area and pore size distribution (IUPAC Technical Report). *Pure Appl. Chem.* **2015**, *87.10.1515/pac-2014-1117*
- (68) Pienack, N.; Bensch, W. In-Situ Monitoring of the Formation of Crystalline Solids. *Angew. Chem., Int. Ed.* **2011**, *50*, 2014–2034.
- (69) Niekel, F.; Ackermann, M.; Guerrier, P.; Rothkirch, A.; Stock, N. Aluminum-1,4-cyclohexanedicarboxylates: High-Throughput and Temperature-Dependent in Situ EDXRD Studies. *Inorg. Chem.* **2013**, *52*, 8699–8705.
- (70) Antonova, E.; Seidlhofer, B.; Wang, J.; Hinz, M.; Bensch, W. Controlling Nucleation and Crystal Growth of a Distinct Polyoxovanadate Cluster: An In Situ Energy Dispersive X-ray Diffraction Study under Solvothermal Conditions. *Chem. - Eur. J.* **2012**, *18*, 15316–15322.
- (71) Seidlhofer, B.; Antonova, E.; Wang, J.; Schinkel, D.; Bensch, W. On the Complexity of Crystallization of Thioantimonates: In-situ Energy Dispersive X-ray Diffraction (EDXRD) Studies of the Solvothermal Formation of the Isostructural Thioantimonates [TM-(tren)Sb4S7] (TM = Fe, Zn). *Z. Anorg. Allg. Chem.* **2012**, *638*, 2555–2564.

Porphyrin-basierte Metall-Organische Gerüstverbindungen:  
Von Metall-Carboxylaten zu Metall-Phosphonaten

---



### 4.5.3 Crystalline and permanently porous porphyrin-based metal tetraphosphonates

Der folgende Artikel wurde im Jahr 2018 in der Fachzeitschrift *Chemical Communications*, RSC veröffentlicht. Der Wiederabdruck erfolgte mit freundlicher Genehmigung der RSC. Reproduced from Timo Rhauderwiek, Konrad Wolkersdörfer, Sigurd Øien-Ødegaard, Karl Petter Lillerud, Michael Wark and Norbert Stock, *Chem. Commun.*, **2018**, 54, 389-392, DOI: 10.1039/C7CC07766A with permission from the Royal Society of Chemistry. Copyright 2017 Royal Society of Chemistry.  
<http://pubs.rsc.org/en/content/articlelanding/2018/cc/c7cc07766a#!divAbstract>

In diesem Artikel aus dem Jahr 2018 wird die Synthese einer neuartigen Porphyrin-basierten Tetraphosphonsäure (Ni-Tetraphosphonophenylporphyrin, Ni-H<sub>8</sub>TPPP) und deren erstmaligen Verwendung als Linker in der Synthese von MOFs beschrieben. Durch Umsetzung von Ni-H<sub>8</sub>TPPP mit zweiwertigen Kationen (M=Mn, Co, Ni, Cd) in Wasser wurde unter Einsatz von Hochdurchsatzmethoden die Verbindung M-CAU-29, [M(Ni-H<sub>6</sub>TPPP)(H<sub>2</sub>O)] entdeckt. Nach der Syntheseoptimierung, die ebenfalls unter Einsatz von Hochdurchsatzmethoden durchgeführt wurde, wurden alle Produkte vollständig charakterisiert. Die Strukturbestimmung von Ni-CAU-29 erfolgte anhand von Einkristallstrukturdaten, während die Kristallstruktur der anderen M-CAU-29 (M= Mn, Co, Cd) Derivate anhand von Röntgenpulverdaten bestätigt wurde. M-CAU-29 kristallisiert in der Raumgruppe  $P\bar{1}$  und weist eindimensionale Poren mit Durchmessern von 2.8 x 5.0 Å und 3.8 x 3.8 Å auf, welche durch Verbrückung des zweifach deprotonierten Linkers über Dimere von kantenverknüpften NiO<sub>6</sub> Oktaedern erfolgt. Ni-CAU-29 ist nicht porös gegenüber N<sub>2</sub> bei 77 K, wobei die anderen M-CAU-29 Derivate spezifische Oberflächen nach BET von 90, 145 und 180 m<sup>2</sup> g<sup>-1</sup> (Mn, Co, Cd) aufweisen. Des Weiteren sind die M-CAU-29 Verbindungen porös gegenüber H<sub>2</sub>O bei 298 K, wobei hier Ni-CAU-29 die höchste H<sub>2</sub>O-Aufnahme von 181 mg g<sup>-1</sup> zeigt, gefolgt von Co- (166 mg g<sup>-1</sup>), Mn- (140 mg g<sup>-1</sup>) und Cd-CAU-29 (116 mg g<sup>-1</sup>). Die Verbindungen sind bis 350 °C thermisch stabil, was durch thermogravimetrische und temperaturabhängige PXRD Messungen bestimmt wurde. Des Weiteren sind die M-CAU-29 MOFs stabil im pH Bereich zwischen 1 und 11 sowie in allen getesteten organischen Lösungsmitteln (MeOH, EtOH, DMF, Aceton, DCM, 100 % Essigsäure). Ni-CAU-29 wurde weiterhin auf seine Protonenleitfähigkeit aufgrund der Anwesenheit von -PO<sub>3</sub>H<sup>-</sup> Gruppen, welche in die Poren zeigen mittels Impedanz-Spektroskopie untersucht. Messungen wurden bei drei verschiedenen relativen Luftfeuchtigkeitswerten (rh) von 50, 75 und 90 %, sowie bei den Temperaturen von 80,

100, 120 und 140 °C durchgeführt. Die Protonenleitfähigkeit wurde danach mittels Bode Plots bestimmt und ein Maximalwert von  $7.8 \cdot 10^{-6} \text{ S} \cdot \text{cm}^{-1}$  bei 140 °C und 90 % rh erhalten. Die gemessene Protonenleitfähigkeit hängt bei allen gemessenen relativen Luftfeuchten linear von der Temperatur ab, wodurch eine Arrhenius Auftragung durchgeführt werden konnte und die Aktivierungsenergien zwischen 0.1 und 0.4 eV aus der Steigung erhalten wurden. Die Aktivierungsenergie sinkt bei steigender relativer Luftfeuchtigkeit und weiterhin legen die berechneten Aktivierungsenergien den Grotthus-Mechanismus als dominierenden Protonentransportmechanismus in Ni-CAU-29 nahe.



## Crystalline and permanently porous porphyrin-based metal tetraphosphonates†

Cite this: *Chem. Commun.*, 2018, 54, 389

Received 7th October 2017,  
Accepted 8th December 2017

DOI: 10.1039/c7cc07766a

rsc.li/chemcomm

Timo Rhauderwiek,<sup>a</sup> Konrad Wolkersdörfer,<sup>b</sup> Sigurd Øien-Ødegaard,<sup>c</sup> Karl-Petter Lillerud,<sup>c</sup> Michael Wark<sup>b</sup> and Norbert Stock<sup>b,\*</sup>

The new porphyrin-based tetraphosphonic acid (Ni-H<sub>8</sub>TPPP) was employed in the synthesis of four isostructural MOFs of composition [M(Ni-H<sub>6</sub>TPPP)(H<sub>2</sub>O)], denoted CAU-29 (M = Mn, Co, Ni, Cd). Ni-CAU-29 was thoroughly characterized regarding its thermal and chemical stability as well as for proton conductivity.

Metal phosphonates are often highly stable which can be explained by the higher charge and the larger number of donor atoms of the –PO<sub>3</sub><sup>2-</sup> in comparison to the –CO<sub>2</sub><sup>-</sup> group.<sup>1</sup> They are therefore promising candidates for applications in gas separation and catalysis.<sup>2,3</sup> Metal phosphonates containing –PO<sub>3</sub>H<sup>-</sup> groups are also studied for their proton conductivity.<sup>2</sup> Only a relatively small number of porous metal phosphonates has been reported to date due to the higher coordination flexibility of the phosphonate groups.<sup>3,4</sup> Taddei *et al.* have recently demonstrated that the use of non-linear large and rigid tritopic phosphonic acids leads to the formation of porous metal phosphonates.<sup>5</sup> Accordingly tetratopic ligands with tetrahedral geometry like adamantane or methane based tetraphosphonic acids resulted in four porous metal phosphonates.<sup>6,7</sup>

In recent years numerous metal organic frameworks (MOFs) were obtained using tetra(4-carboxyphenyl)porphyrin (H<sub>4</sub>TCPP) as the organic building unit.<sup>8,9</sup> Especially Zr-MOFs containing the H<sub>2</sub>TCPP<sup>4-</sup> ion are highly porous and stable.<sup>8,10</sup> The presence of the porphyrin moiety leads to selective redox properties.<sup>9</sup> The analogous linker containing –PO<sub>3</sub>H<sub>2</sub> instead of –COOH groups, *i.e.* tetra(4-phosphonophenyl)porphyrin (H<sub>10</sub>TPPP) has been already reported in 1992,<sup>11</sup> but it has not been employed for the synthesis of MOFs yet. In addition to the free-base linker H<sub>10</sub>TPPP,

its esterified form<sup>12,13</sup> as well as the Mn-metalated linker (Mn-H<sub>8</sub>TPPP)<sup>14,15</sup> have been reported. These molecular compounds were characterized regarding their electrochemical<sup>12,13,16</sup> and photochemical<sup>13,16,17</sup> properties as well as in catalytic<sup>14,15</sup> and self assembling<sup>18–21</sup> processes.

Here we present the synthesis of a new planar porphyrin-based tetraphosphonic acid (Ni-H<sub>8</sub>TPPP) and its use in the synthesis of MOFs. The linker with a Ni<sup>2+</sup> ion coordinated in the centre of the porphyrin ring (Ni-H<sub>8</sub>TPPP) was obtained in a three step synthesis (Fig. S1, ESI†) starting from 4-bromobenzaldehyde.<sup>22,23</sup> In the second step the resulting 4-bromophenylporphyrin (H<sub>2</sub>TBrPP) was phosphorylated using NiCl<sub>2</sub> as the catalyst.<sup>24,25</sup> With a yield of 75% this approach is by far more efficient compared to the Pd-catalysed reaction leading to H<sub>10</sub>TPPP (yield: 28%).<sup>26,27</sup> Acid catalyzed (conc. HCl) hydrolysis leads in the last step to the metalated linker Ni-H<sub>8</sub>TPPP. The resulting product was obtained in high purity with an overall yield of 23%.

High-throughput methods were employed in the screening of synthesis parameters such as molar ratio of metal to linker, pH and reaction temperature (details see ESI†). The use of the divalent metal ions Mn<sup>2+</sup>, Co<sup>2+</sup>, Ni<sup>2+</sup> and Cd<sup>2+</sup> in hydrothermal syntheses resulted in the formation of a series of four isostructural, highly crystalline and porous MOFs (Fig. 1) of composition [M(Ni-H<sub>6</sub>TPPP)(H<sub>2</sub>O)] (M = Mn, Co, Ni, Cd), which were denoted as M-CAU-29. The use of molar metal to linker ratios of

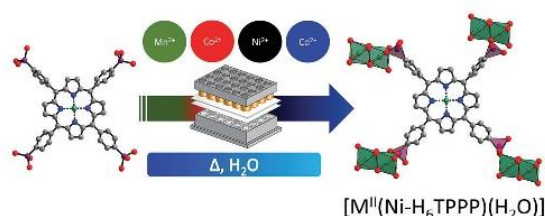


Fig. 1 Scheme of the high-throughput investigation of M-CAU-29 (M = Mn, Co, Ni, Mn) using Ni-H<sub>8</sub>TPPP (left) and MCl<sub>2</sub> salts in H<sub>2</sub>O as solvent.

<sup>a</sup> Institut für Anorganische Chemie, Christian-Albrechts-Universität, Max-Eyth Straße 2, D-24118 Kiel, Germany. E-mail: stock@ac.uni-kiel.de

<sup>b</sup> Chemical Technology 1, Carl von Ossietzky University Oldenburg, Carl-von-Ossietzky Str. 9-11, D-26129 Oldenburg, Germany

<sup>c</sup> Department of Chemistry, University of Oslo, Sem Sælands vei 26, N-0371 Oslo, Norway

† Electronic supplementary information (ESI) available: Experimental procedures, analytical data including NMR-spectroscopy, Pawley-fits, TG, IR, UV/vis and sorption measurements. CCDC 1566851. See DOI: 10.1039/c7cc07766a



1 to 1 resulted in CAU-29 with low crystallinity, while higher ratios up to 5 to 1 and the 3-fold concentration of metal and linker led to highly crystalline CAU-29 (Fig. S5, ESI†).

Despite the harsh reaction conditions of 180 °C and a reaction time of 48 h, no leaching of Ni<sup>2+</sup> ions from the porphyrin center was observed, as proven by UV/vis spectroscopy (Fig. S28, ESI†) as well as thermogravimetric (TG) and elemental analysis (see ESI†).

Mn-, Co- and Cd-CAU-29 were obtained as microcrystalline powders while for Ni-CAU-29 very small single crystals were obtained (Fig. S6, ESI†). The crystal structure of CAU-29 was elucidated by single crystal X-ray diffraction using a crystal of 5 × 10 × 20 μm<sup>3</sup> (Table S1, ESI†).<sup>28</sup> High resolution PXRD measurements of M-CAU-29 (M = Mn, Co, Ni, Cd) were performed (Fig. 3) and Rietveld refinements (Co-, Ni-CAU-29) and Pawley fits (Mn-, Cd-CAU-29, Fig. S8–S11 and Table S2, ESI†) were carried out using the single crystal X-ray diffraction data of Ni-CAU-29 as a starting model. Thus, phase purity was proven and lattice parameters of the isostructural compounds were determined. Ni-CAU-29 crystallizes in a triclinic crystal system in the space group *P* $\bar{1}$  (*a* = 9.561(5) Å, *b* = 15.086(9) Å, *c* = 16.722(9) Å and  $\alpha$  = 94.723(9)°,  $\beta$  = 97.602(9)°,  $\gamma$  = 7.880(9)°, Table S1, ESI†). $\ddagger$  The inorganic building unit of Ni-CAU-29, [Ni(Ni-H<sub>6</sub>TPPP)(H<sub>2</sub>O)]·11H<sub>2</sub>O, consists of two isolated edge-sharing NiO<sub>6</sub> polyhedra, which are bridged by the linker Ni-H<sub>6</sub>TPPP<sup>2-</sup> to a three dimensional porous network (Fig. 2). Thus two kinds of 1D pores with the dimensions 2.8 × 5.0 Å and 3.8 × 3.8 Å are formed, taking the van-der-Waals radii into account. The coordination modes [2,002] and [1,001] of the (di)hydrogen phosphonate groups in Ni-CAU-29 are shown in Fig. S7 (ESI†).<sup>29</sup> The bond lengths found in Ni-CAU-29 are in

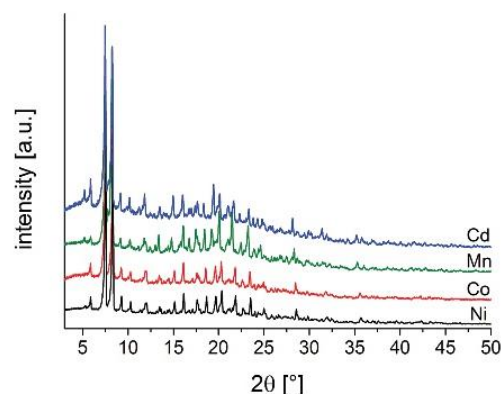


Fig. 3 High resolution PXRD pattern of M-CAU-29 (M = Mn, Co, Ni, Cd).

good agreement with literature values (selected bond lengths are shown in Table S1a, ESI†). Ni–O distances between 2.04(2) and 2.14(2) Å were observed (lit.: 2.008(15)–2.114(16) Å).<sup>30,31</sup> The P–O bond lengths vary between 1.48(2) and 1.57(2) Å, which agrees well with the presence of P=O, P–OH and P–O<sup>-</sup> groups. In literature P=O and P–OH/ P–O<sup>-</sup> distances are reported in ranges of 1.486(3)<sup>32</sup> to 1.491(6) Å<sup>30</sup> and 1.529(3)<sup>32</sup> to 1.581(6) Å,<sup>30</sup> respectively.

The sorption properties of M-CAU-29 were studied employing N<sub>2</sub> (Fig. 4) and H<sub>2</sub>O (Fig. S12, ESI†) at 77 and 298 K, respectively. Prior to the measurements the samples were activated at 170 °C under reduced pressure of 10<sup>-2</sup> kPa for 16 h. Ni-CAU-29 shows no uptake of N<sub>2</sub> at 77 K but the highest water uptake of 181 mg g<sup>-1</sup>. Mn-, Co- and Cd-CAU-29 exhibit N<sub>2</sub> uptakes of 90, 145 and

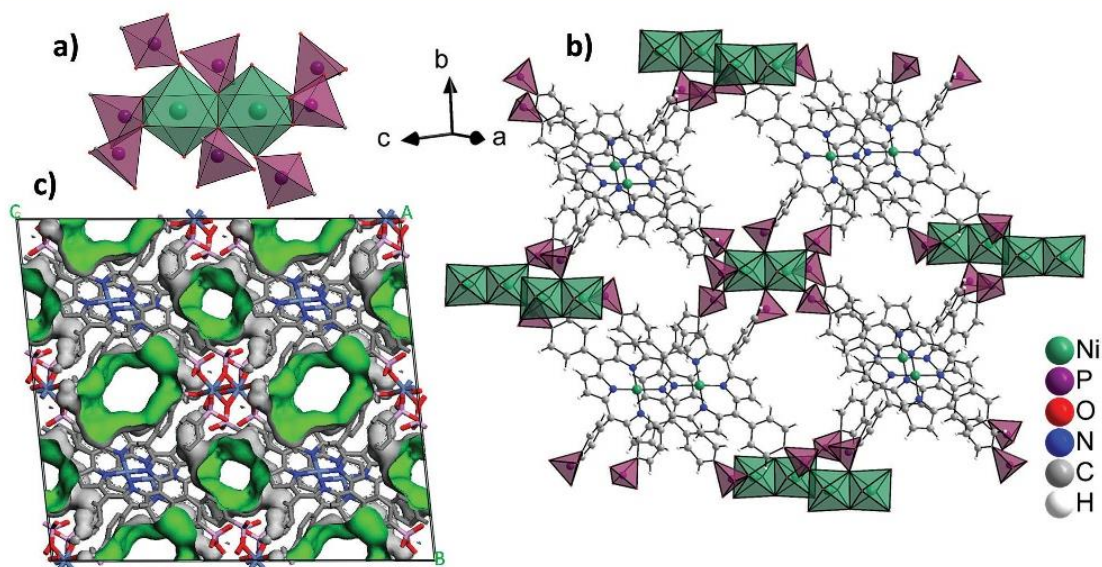


Fig. 2 Crystal structure of Ni-CAU-29: (a) inorganic building unit (IBU), formed by two edge sharing NiO<sub>6</sub> polyhedra, and next coordination environment, (b) stick-and-ball model showing the interconnection of the IBUs and the formation of 1D pores (2.8 × 5.0 Å and 3.8 × 3.8 Å) with PO<sub>3</sub>C and NiO<sub>6</sub> polyhedra shown in purple and green, respectively, and (c) Connolly surface of the pores (green, probe radius of 1.8 Å, view along [101]).



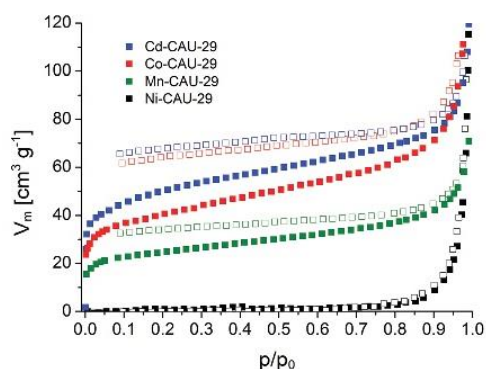


Fig. 4 Results of the  $N_2$ -sorption experiments of M-CAU-29 (M = Mn, Ni, Co, Cd) at 77 K (activated prior the measurement at 170 °C, overnight at reduced pressure of  $10^{-1}$  kPa).

$180 \text{ m}^2 \text{ g}^{-1}$  and  $H_2O$  uptakes of 140, 166 and  $116 \text{ mg g}^{-1}$ , respectively. These differences in adsorption properties are probably due to the presence of the small micropores in combination with slight metal-dependent structural changes upon thermal activation (dehydration) as confirmed by variable temperature PXRD as well as differences in the kinetic diameters of  $N_2$  and  $H_2O$  ( $3.64$  and  $2.65 \text{ \AA}$ )<sup>33</sup> and the different temperatures during sorption measurements ( $77$  vs.  $298 \text{ K}$ ). Such differences are not unusual and have been reported for example for STA-12.<sup>34</sup> Similar pore volumes were determined at  $p/p_0 = 0.5$  for Mn-, Co- and Cd-CAU-29 as  $0.05$ ,  $0.08$  and  $0.09 \text{ cm}^3 \text{ g}^{-1}$ . PXRD measurements after the sorption experiments prove the stability of CAU-29 after activation and the sorption experiment (Fig. S13, ESI†). Due to the strong hysteresis observed in all samples, which is probably due to kinetic effects, well known for samples containing ultramicropores ( $< 0.7 \text{ nm}$ ), the desorption measurement was aborted at  $p/p_0 = 0.1$ .<sup>35</sup>

The thermal stability of all title compounds was proven by TG (Fig. S14–S18 and Table S3, ESI†) and variable temperature (VT-) PXRD measurements (Fig. S20–S23, ESI†). In the TG curves of all compounds two broad steps of weight loss are observed at nearly identical temperatures. The first step up to a temperature of  $300 \text{ °C}$  indicates the loss of crystal water and the second step; the collapse of the frameworks is observed above  $350 \text{ °C}$ . An increase in weight just before the collapse of the framework is only observed in an air atmosphere. Since this increase has not been observed in  $N_2$  (Fig. S17, ESI†), we assume the formation of *e.g.* NiO before the collapse of the framework. The results of the VT-PXRD measurements are in good agreement with those of the TG measurements. The complete loss of crystallinity due to the collapse of the framework is observed around  $350 \text{ °C}$ . Prior to the complete loss of crystallinity in case of Ni- and Cd-CAU-29 a small decrease of crystallinity is observed above  $250 \text{ °C}$ . In case of Mn- and Co-CAU-29 a phase transformation above  $200 \text{ °C}$  followed by the complete loss of crystallinity is observed. PXRD of the remaining products of the TG measurements (Fig. S19, ESI†) reveal the formation of different Ni-M- pyro- and metaphosphates (M = Mn, Co, Cd).

The chemical stability of Ni-CAU-29 was proven for Ni-CAU-29 by stirring the compound in different solvents for 24 h and subsequent PXRD analysis (Fig. S24, ESI†). Ni-CAU-29 is stable in a pH range (HCl or NaOH) between 1 and 11 as well as in all tested organic solvents (DCM, EtOH, DMF, acetone) and in 100% acetic acid. At pH = 0 a loss of crystallinity is observed and above pH 11 and in phosphate buffer ( $0.1 \text{ M}$ , pH = 7) the complete decomposition of the framework takes place.

UV/vis spectroscopy was employed to prove the metalation of the porphyrin moiety after the solvothermal reaction. The pure linker Ni- $H_8$ TPPP as well as the MOFs exhibited nearly identical positions for the Soret- and Q1- band at  $412/413$  and  $526/527 \text{ nm}$ , respectively (Fig. S28, ESI†).

The proton conductivity of Ni-CAU-29 was tested due to the presence of  $-PO_3H^-$  groups protruding into the pores. The impedance spectroscopic measurements were carried out at 50, 75, 90% relative humidity (%rh) and temperatures in the range of  $80$  to  $140 \text{ °C}$ . The ionic resistance  $Z_{\text{ionic}}$  was extracted from Bode plots (Fig. S25, ESI†). The ionic conductance  $\sigma_{\text{ionic}}$  was then calculated according to:  $\sigma_{\text{ionic}} = l(A \times Z_{\text{ionic}})$ , with  $l$  being the sample thickness and  $A$  the electrode surface, respectively.

The relative humidity controls the proton conductivity of Ni-CAU-29. At  $80 \text{ °C}$  a change in relative humidity from 50 to 90% rh increases the proton conductivity from  $2.4 \times 10^{-7}$  to  $5.6 \times 10^{-6} \text{ S cm}^{-1}$  (Table 1). The  $-PO_3H^-$  groups pointing into the pores of the CAU-29 could facilitate the formation of an H-bond network which is in line with a strong influence of humidity on the proton conduction. The activation energy of the ionic conductance can be extracted from the slope of the straight line of an Arrhenius plot.<sup>36</sup> An increase in humidity induces a decrease in the activation energy (Fig. 5). The values of the activation energy range from  $0.1$  to  $0.34 \text{ eV}$ . Accordingly, these values support that Grotthus mechanism<sup>36</sup> is the dominant pathway for proton conductivity in Ni-CAU-29.

Moreover, the structure is unaffected by the humidified atmosphere at elevated temperature during the proton conductivity measurements as proven by PXRD pattern recorded after the experiment (S26, ESI†).

In summary, we have demonstrated the successful synthesis and characterization of a series of isostructural MOFs containing a new Ni-metalated porphyrin-based phosphonic acid as linker molecule. To the best of our knowledge to date only four other porous and crystalline metal phosphonates with the in this work discussed cations  $Mn^{2+}$ ,  $Co^{2+}$ ,  $Ni^{2+}$  and  $Cd^{2+}$  have been reported.<sup>2,31,34,37,38</sup> M-CAU-29 [M(Ni- $H_8$ TPPP)( $H_2O$ )] (M = Mn, Co, Ni, Cd) exhibit different sorption properties towards  $N_2$  and

Table 1 Proton conductivity at different temperatures between  $80$  and  $140 \text{ °C}$  and Arrhenius activation energies  $E_A$  of Ni-CAU-29 at different relative humidities (%rh) of 50, 75 and 90%

Relative humidity [%rh]	50	75	90
Conductivity [ $S \text{ cm}^{-1}$ ]			
80 °C	$2.41 \times 10^{-7}$	$1.35 \times 10^{-6}$	$5.62 \times 10^{-6}$
100 °C	$3.46 \times 10^{-7}$	$1.78 \times 10^{-6}$	$5.80 \times 10^{-6}$
120 °C	$6.02 \times 10^{-7}$	$2.60 \times 10^{-6}$	$6.85 \times 10^{-6}$
140 °C	$1.04 \times 10^{-6}$	$3.42 \times 10^{-6}$	$7.82 \times 10^{-6}$
$E_A$ [eV]	0.34	0.23	0.10



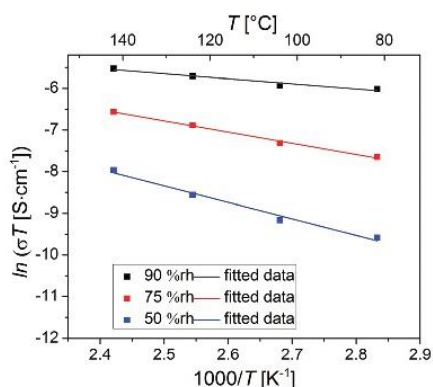


Fig. 5 Arrhenius plot of the ionic conductance of Ni-CAU-29.

H<sub>2</sub>O at 77 and 298 K, respectively. The thermal and chemical stability of M-CAU-29 was tested and reveals a thermal stability up to 400 °C and chemical stability in a pH-range between 1 and 11 in aqueous solutions. Furthermore Ni-CAU-29 was tested regarding the proton conductivity by electrochemical impedance spectroscopy; at 80 °C and 90% relative humidity a value of  $5.62 \times 10^{-6}$  S cm<sup>-1</sup> was achieved. The new linker Ni-H<sub>8</sub>TPPP opens a new field in the synthesis of porous MOFs in which e.g. the catalytic properties of the porphyrin moiety could potentially be combined with the stability of metal phosphonates. Thus future work will focus on the use of tri- and tetravalent ions for the synthesis of new MOFs using Ni-H<sub>8</sub>TPPP as the linker.

We appreciate support from the Deutsche Forschungsgemeinschaft (SPP 1928, COORNETs, STO 643/11-1, WA 1116/30-1).

## Conflicts of interest

There are no conflicts to declare.

## References

‡ Crystal data. C<sub>45.50</sub>H<sub>24</sub>N<sub>4</sub>Ni<sub>2</sub>O<sub>14</sub>P<sub>4</sub>, *M* = 1091.95 g mol<sup>-1</sup>, triclinic, *a* = 9.561(5) Å, *b* = 15.086(9) Å, *c* = 16.722(9) Å and  $\alpha$  = 94.723(9)°,  $\beta$  = 97.602(9)°,  $\gamma$  = 97.880(9)°, *V* = 2356(2) Å<sup>3</sup>, *T* = 100 K, space group *P*1 (no. 2), *Z* = 2, 6040 reflections measured, 1832 unique (*R*<sub>int</sub> = 0.118), 1180 observed (*I* > 2σ(*I*)). The final *R*<sub>1</sub> was 9.97% and the *wR*<sub>2</sub> 23.46% (*I* > 2σ(*I*)). CCDC 1566851 contains the crystallographic data for the structural analysis.

- G. K. H. Shimizu, R. Vaidyanathan and J. M. Taylor, *Chem. Soc. Rev.*, 2009, **38**, 1430–1449.
- S. Pili, S. P. Argent, C. G. Morris, P. Rought, V. Garcia-Sakai, I. P. Silverwood, T. L. Easun, M. Li, M. R. Warren, C. A. Murray, C. C. Tang, S. Yang and M. Schröder, *J. Am. Chem. Soc.*, 2016, **138**, 6352–6355.
- A. Clearfield and K. Demadis, *Buch Metallphosphonate Metal Phosphonate Chemistry: From Synthesis to Applications*, Royal Society of Chemistry, 2011.
- K. J. Gagnon, H. P. Perry and A. Clearfield, *Chem. Rev.*, 2012, **112**, 1034–1054.
- M. Taddei, F. Costantino and R. Vivani, *Eur. J. Inorg. Chem.*, 2016, 4300–4309.
- J. M. Taylor, A. H. Mahmoudkhani and G. K. H. Shimizu, *Angew. Chem., Int. Ed.*, 2007, **46**, 795–798.

- T. Zheng, Z. Yang, D. Gui, Z. Liu, X. Wang, X. Dai, S. Liu, L. Zhang, Y. Gao, L. Chen, D. Sheng, Y. Wang, J. Diwu, J. Wang, R. Zhou, Z. Chai, T. E. Albrecht-Schmitt and S. Wang, *Nat. Commun.*, 2017, **8**, 15369.
- Y. Bai, Y. Dou, L.-H. Xie, W. Rutledge, J.-R. Li and H.-C. Zhou, *Chem. Soc. Rev.*, 2016, **45**, 2327–2367.
- Z. Guo and B. Chen, *Dalton Trans.*, 2015, **44**, 14574–14583.
- D. Feng, Z.-Y. Gu, J.-R. Li, H.-L. Jiang, Z. Wei and H.-C. Zhou, *Angew. Chem.*, 2012, **124**, 10453–10456.
- S. B. Ungashe, W. L. Wilson, H. E. Katz, G. R. Scheller and T. M. Putvinski, *J. Am. Chem. Soc.*, 1992, **114**, 8717–8719.
- Y. Fang, Y. G. Gorbunova, P. Chen, X. Jiang, M. Manowong, A. A. Sinelshchikova, Y. Y. Enakieva, A. G. Martynov, A. Y. Tsvadze, A. Bessmertnykh-Lemeune, C. Stern, R. Guillard and K. M. Kadish, *Inorg. Chem.*, 2015, **54**, 3501–3512.
- K. M. Kadish, P. Chen, Y. Y. Enakieva, S. E. Nefedov, Y. G. Gorbunova, A. Y. Tsvadze, A. Bessmertnykh-Lemeune, C. Stern and R. Guillard, *J. Electroanal. Chem.*, 2011, **656**, 61–71.
- D. Deniaud, B. Schollorn, D. Mansuy, J. Rouxel, P. Battioni and B. Bujoli, *Chem. Mater.*, 1995, **7**, 995–1000.
- D. Deniaud, G. A. Spyroulias, J.-F. Bartoli, P. Battioni, D. Mansuy, C. Pinel, F. Odobel and B. Bujoli, *New J. Chem.*, 1998, **22**, 901–905.
- N. Venkatramiah, C. F. Pereira, R. F. Mendes, F. A. A. Paz and J. P. C. Tomé, *Anal. Chem.*, 2015, **87**, 4515–4522.
- F. Odobel, E. Blart, M. Lagree, M. Villieras, H. Boujtita, N. El Murr, S. Caramori and C. Alberto Bignozzi, *J. Mater. Chem.*, 2003, **13**, 502–510.
- M. De Napoli, S. Nardis, R. Paolesse, M. G. H. Vicente, R. Lauceri and R. Purrello, *J. Am. Chem. Soc.*, 2004, **126**, 5934–5935.
- R. Lauceri, M. De Napoli, A. Mammanna, S. Nardis, A. Romeo and R. Purrello, *Synth. Met.*, 2004, **147**, 49–55.
- P. Kubát, K. Lang, P. Janda and P. Anzenbacher, *Langmuir*, 2005, **21**, 9714–9720.
- P. Kubát, K. Lang and Z. Zelinger, *J. Mol. Liq.*, 2007, **131–132**, 200–205.
- A. D. Adler, F. R. Longo, F. Kampas and J. Kim, *J. Inorg. Nucl. Chem.*, 1970, **32**, 2443–2445.
- A. D. Adler, F. R. Longo, J. D. Finarelli, J. Goldmacher, J. Assour and L. Korsakoff, *J. Org. Chem.*, 1967, **32**, 476.
- G. G. Rajeshwaran, M. Nandakumar, R. Sureshbabu and A. K. Mohanakrishnan, *Org. Lett.*, 2011, **13**, 1270–1273.
- P. Tavs, *Chem. Ber.*, 1970, **103**, 2428–2436.
- T. Hirao, T. Masunaga, Y. Ohshiro and T. Agawa, *Synthesis*, 1981, 56–57.
- P. Kubát, K. Lang and P. Anzenbacher, *Biochim. Biophys. Acta, Gen. Subj.*, 2004, **1670**, 40–48.
- G. Sheldrick, *Acta Crystallogr., Sect. A: Found. Adv.*, 2015, **71**, 3–8.
- R. A. Coxall, S. G. Harris, D. K. Henderson, S. Parsons, P. A. Tasker and R. E. P. Winpenny, *J. Chem. Soc., Dalton Trans.*, 2000, 2349–2356, DOI: 10.1039/B001404O.
- F. Zhai, Q. Zheng, Z. Chen, Y. Ling, X. Liu, L. Weng and Y. Zhou, *CrystEngComm*, 2013, **15**, 2040–2043.
- J. A. Groves, S. R. Miller, S. J. Warrender, C. Mellot-Draznieks, P. Lightfoot and P. A. Wright, *Chem. Commun.*, 2006, 3305–3307, DOI: 10.1039/B0605400E.
- A. Clearfield and K. Demadis, *Metal Phosphonate Chemistry: From Synthesis to Applications*, Royal Society of Chemistry, 2011.
- A. F. Ismail, K. C. Khulbe and T. Matsuura, *Gas Separation Membranes: Polymeric and Inorganic*, Springer International Publishing, 2015.
- M. T. Wharmby, G. M. Pearce, J. P. S. Mowat, J. M. Griffin, S. E. Ashbrook, P. A. Wright, L.-H. Schilling, A. Lieb, N. Stock, S. Chavan, S. Bordiga, E. Garcia, G. D. Pirngruber, M. Vreeke and L. Gora, *Microporous Mesoporous Mater.*, 2012, **157**, 3–17.
- M. Thommes, K. Kaneko, V. Neimark Alexander, P. Olivier James, F. Rodriguez-Reinoso, J. Rouquerol and S. W. Sing Kenneth, *Pure Appl. Chem.*, 2015, **87**, 1051–1069.
- P. Ramaswamy, N. E. Wong and G. K. H. Shimizu, *Chem. Soc. Rev.*, 2014, **43**, 5913–5932.
- M. T. Wharmby, J. P. S. Mowat, S. P. Thompson and P. A. Wright, *J. Am. Chem. Soc.*, 2011, **133**, 1266–1269.
- S. Begum, S. Horike, S. Kitagawa and H. Krautscheid, *Dalton Trans.*, 2015, **44**, 18727–18730.

#### **4.5.4 A porous cobalt tetrakisphosphonates metal-organic framework: structure determination by fast continuous rotation electron diffraction**

Der folgende Artikel wurde im Jahr 2018 zur Begutachtung in der Fachzeitschrift *CrystEngComm*, RSC eingereicht. Der Wiederabdruck erfolgte mit freundlicher Genehmigung der RSC. Reproduced from Bin Wang,<sup>†</sup> Timo Rhauderwiek,<sup>†</sup> A. Ken Inge, Hongyi Xu, Taimin Yang, Zhehao Huang, Norbert Stock\* and Xiaodong Zou\*, *CrystEngComm.*, **2018**, submitted, with permission from the Royal Society of Chemistry. Copyright 2017 Royal Society of Chemistry.

Der zur Begutachtung eingereichte Artikel aus dem Jahr 2018 beschreibt die Synthese, Charakterisierung und Strukturbestimmung eines porösen Co-Tetrakisphosphonates Co-CAU-36 [Co<sub>2</sub>(Ni-H<sub>4</sub>TTPP)]·2DABCO·6H<sub>2</sub>O. Als Linkermolekül wurde die kurz zuvor erstmals in der Synthese von MOFs eingesetzte Porphyrin-basierte Tetrakisphosphonsäure (Ni-Tetrakisphosphonophenylporphyrin, Ni-H<sub>8</sub>TTPP) verwendet. Durch Umsetzung von Ni-H<sub>8</sub>TTPP mit Co<sup>2+</sup> in Wasser und unter Zuhilfenahme des Diamins DABCO (1,4-Diazabicyclo[2.2.2]octan) sowie Salzsäure wurde mittels Hochdurchsatzmethoden Co-CAU-36 entdeckt. Die Strukturbestimmung von Co-CAU-36 erfolgte unter Einsatz der von der Arbeitsgruppe von Xiaodong Zou entwickelten cRED (continuous rotation electron diffraction) Methode. Hierbei war es aufgrund der hohen Kristallinität der Probe und sehr guten Datenqualität ebenfalls möglich Gastmoleküle in den Poren zu lokalisieren, wodurch eine Strukturverfeinerung aus Pulverdaten nicht mehr notwendig war. Der komplette Datensatz wurde bereits nach neun Stunden erhalten und dabei Gütekriterien von 13.6 (R<sub>1</sub>) und 33.4 % (wR<sub>2</sub>) bestimmt. Co-CAU-36 kristallisiert in der Raumgruppe  $P\bar{4}c2$  und weist eindimensionale Poren von 9 Å Durchmesser auf. Die anorganische Baueinheit besteht aus CoO<sub>4</sub> Tetraedern, welche über die Hydrogenphosphonatgruppen zu eindimensionalen Ketten verbrückt sind, der vierfach deprotonierte Linker wiederum verknüpft vier dieser Ketten zu einem dreidimensionalen Netzwerk. DABCO Moleküle sind in den Poren lokalisiert und Formen mit den Hydrogenphosphonatgruppen Wasserstoffbrückenbindungen PO···H···N-C mit Donor-Akzeptor Abständen von 2.82 und 3.36 Å. Co-CAU-36 ist porös gegenüber N<sub>2</sub> bei 77 K und weist eine spezifische Oberfläche nach BET von 700 m<sup>2</sup> g<sup>-1</sup> auf. Co-CAU-36 ist thermisch stabil bis 350 °C, was durch thermogravimetrische und temperaturabhängige PXRD Messungen bestimmt wurde. Co-CAU-36 ist stabil in organischen Lösungsmitteln wie Aceton, weist jedoch eine begrenzte Stabilität in Wasser auf.



Journal Name

ARTICLE

Received 00th January 20xx,  
Accepted 00th January 20xx

DOI: 10.1039/x0xx00000x

www.rsc.org/

## A porous cobalt tetrakisphosphate metal-organic framework: structure determination by fast continuous rotation electron diffraction

Bin Wang,<sup>a, †</sup> Timo Rhauderwiek,<sup>b, ‡</sup> A. Ken Inge,<sup>a</sup> Hongyi Xu,<sup>a</sup> Taimin Yang,<sup>a</sup> Zhehao Huang,<sup>a</sup> Norbert Stock<sup>b</sup> and Xiaodong Zou<sup>a</sup>

**A novel porous cobalt metal-organic framework with 1D channels, [Co<sub>2</sub>(Ni-H<sub>8</sub>TPPP)]·2DABCO·6H<sub>2</sub>O (denoted Co-CAU-36) was synthesized. Its structure was determined by continuous rotation electron diffraction. We show that for the first time not only the framework positions, but also the solvent DABCO and water molecules in the pores can be refined to high precision.**

Metal-organic frameworks (MOFs) are an intensively investigated class of materials. Due to their modular structures, the pore size and pore surface properties can be tuned, which in turn leads to a large range of chemical and physical properties.<sup>1–4</sup> MOFs have shown wide applications such as gas storage and separation, drug delivery and catalysis.<sup>1,3,5–7</sup> While most porphyrin-based MOFs have been obtained using tetracarboxyphthalate (H<sub>4</sub>TCP) as the linker, only one with the Ni-(4-tetrakisphosphonatophenylporphyrin) (Ni-H<sub>8</sub>TPPP) linker has been reported.<sup>8</sup> This observation is in line with the fewer number of known porous metal phosphonates in comparison to porous metal carboxylates.<sup>9,10</sup> In terms of cobalt MOFs, only four porous cobalt phosphonate-based MOFs are currently known.<sup>11–15</sup>

In order to establish structure-property relationships, structure determination of new MOFs is of paramount importance. The most conventional technique, single crystal X-ray diffraction, is not applicable to many MOFs because they are only obtained as nano- or micrometre-sized crystals. Electron crystallog-

raphy, especially the recent emergence of the rotation method in electron diffraction, such as Automated Diffraction Tomography (ADT)<sup>16</sup> and Rotation Electron Diffraction (RED),<sup>17,18</sup> has shown to be powerful for structure solution of such small crystallites.<sup>19</sup> One major drawback of electron crystallography on MOFs has been electron beam damage of the crystals. The beam damage often results in a reduction of data resolution and data completeness, which prevents determination of accurate structural models and location of guest molecules in the pores. It is often necessary to perform Rietveld refinement using powder X-ray diffraction (PXRD) in order to obtain the detailed structural information.<sup>20,21</sup> However, it is not always possible to obtain high quality PXRD data needed for Rietveld refinement, especially for MOFs, which may lose crystallinity upon the removal of guest species in the pores. Therefore, it is of significant interest to minimize electron beam damage in the data collection so that high quality electron diffraction data can be obtained for accurate structure determination.

The data collection in the original ADT and RED methods was performed in a stepwise manner, where the crystal is rotated in discrete steps to given angles before ED frames are taken.<sup>16–18</sup> A complete data collection normally takes 1–2 hours. A much faster data collection can be achieved by continuous crystal rotation.<sup>22,23</sup> Unlike the stepwise RED (sRED), each ED frame in the continuous rotation electron diffraction (cRED) data records integrated intensities of reflections within a given rotation interval (Fig. 1). Using a recently installed fast and noise-free electron counting detector, the data collection time can be shortened to 0.5–4 min for a typical cRED dataset. In combination with sample cooling (< 100 K), beam damage is greatly reduced and data resolution is enhanced.<sup>24</sup> In addition, the low background of the detector makes it possible to detect weak reflections at short exposure times.

Here we report the synthesis and *ab initio* structure determination of a new cobalt phosphonate with permanent porosity, denoted Co-CAU-36. We show that cRED data can be used for a complete structure determination, of not only framework atoms, but also guest species in the pores. Precise structural

<sup>a</sup> Berzelii Center EXSELENT on Porous Materials, Department of Materials and Environmental Chemistry, Stockholm University, SE-106 91 Stockholm, Sweden. E-mail: xaou@mmk.su.se

<sup>b</sup> Institut für Anorganische Chemie, Christian-Albrechts-Universität zu Kiel, DE-24118 Kiel, Germany. E-mail: stock@ac.uni-kiel.de

<sup>†</sup> Electronic Supplementary Information (ESI) available: Materials and characterization, Synthesis of the Ni-H<sub>8</sub>TPPP and Co-CAU-36, Crystal structure analysis, N<sub>2</sub> sorption properties, TGA and chemical stability tests, FT-IR and UV/vis spectroscopy. CCDC 1824409. For ESI and crystallographic data in CIF or other electronic format, see DOI: 10.1039/x0xx00000x.

<sup>‡</sup> These authors contributed equally to this work.



models can be obtained, which is confirmed by the good agreements of the eight structural models refined using different cRED datasets from different crystals.

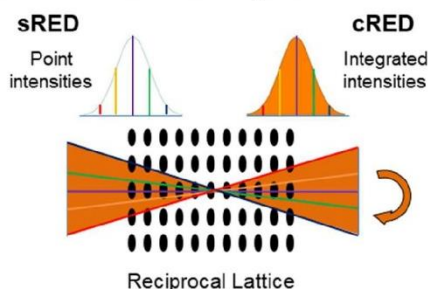


**Figure 1.** Difference between stepwise rotation electron diffraction (sRED) and continuous rotation electron diffraction (cRED). In sRED, reflections are sampled as discrete points in reciprocal space, and point intensities are recorded. In cRED, intensities are integrated with regard to the recording period, and thus are more accurate.

The synthesis and characterization of the linker Ni-H<sub>8</sub>TPPP are given in the Electronic Supporting Information (Figs. S1-S4, †ESI). Co-CAU-36 was synthesized in the system Co<sup>2+</sup>/Ni-H<sub>8</sub>TPPP/DABCO/HCl in water at 140°C. A systematic investigation for optimization of the synthesis parameters was carried out using high-throughput (HT) methods.<sup>25–27</sup> The results of the HT investigation are illustrated in Figure S5. The product formation depends mainly on the amount of DABCO and the linker to metal ratio. A highly crystalline product of Co-CAU-36 was obtained using the molar ratios of Co<sup>2+</sup> : Ni-H<sub>8</sub>TPPP : DABCO : HCl = 1 : 1 : 50 : 4.

SEM images show that crystals of Co-CAU-36 have a rod-like morphology with diameters of less than 1 μm (Fig. S6, †ESI). Due to the small crystal sizes, the structure determination of Co-CAU-36 was conducted using continuous rotation electron diffraction (cRED) data. Eight individual datasets were collected at 96 K using a cooling sample holder. Unit cell parameters were first determined from one single cRED dataset to be  $a = 22.17$ ,  $b = 21.91$ ,  $c = 9.06$  Å,  $\alpha = 90.05$ ,  $\beta = 90.66$  and  $\gamma = 91.58^\circ$ , which were reasonably close to a tetragonal cell. The cRED data was further processed and intensities extracted using the software XDS.<sup>28</sup> The unit cell parameters were refined in a tetragonal cell both against the cRED data using XDS ( $a = 21.980(5)$ ,  $c = 8.960(2)$  Å) and against the PXRD data by a Pawley refinement ( $a = 21.642(1)$ ,  $c = 9.0166(8)$  Å) (Fig. 3a). The systematic absences could be obtained from the 2D slices cut from the 3D reciprocal lattice (Fig. 2) to be  $0kl: l = 2n+1$ ;  $00l: l = 2n+1$ , which led to three possible space groups:  $P4_2cm$  (No. 101),  $P4c2$  (No. 116),  $P4_2/mcm$  (No. 132).

*Ab initio* structure solution was performed with each of the three space groups by direct methods using SIR-2014.<sup>29</sup> The space group  $P4c2$  gave significantly lower initial  $R_1$  value (0.213) than the other two (0.277 for  $P4_2cm$  and 0.397 for  $P4_2/mcm$ ). Thus the initial structural model with the space group  $P4c2$  was chosen for the subsequent structure refinement. All the metal Co and Ni ions and the linker Ni-H<sub>4</sub>TPPP<sup>4-</sup> positions could be directly located from the initial structure solution. One solvent DABCO and two H<sub>2</sub>O molecules could also be located in the pores from the difference Fourier map.

Structure refinement was subsequently performed against the cRED data using SHELXL<sup>30</sup> assuming kinematical intensities. All non-hydrogen framework atoms and water molecules were refined without applying any restraints. Soft restraints were applied to the DABCO molecule. The final  $R_1$  value converged to 0.1356 for 1978 unique reflections with  $F^2 > 2\sigma(F^2)$  and 0.2133 for all 4008 unique reflections. The relatively high  $R$ -values compared to those in X-ray crystallography are due to the presence of dynamical effects and other errors in electron diffraction intensities. The data collection, crystal data and refinement details are given in Table 1 and Section S3, †ESI. Due to the fast data collection and high data quality, the entire structure determination process was accomplished within 9 hours, including TEM sample preparation, data collection, structure solution and refinement. The final refined chemical formula of Co-CAU-36 is [Co<sub>2</sub>(Ni-H<sub>4</sub>TPPP)]·2DABCO·6H<sub>2</sub>O.

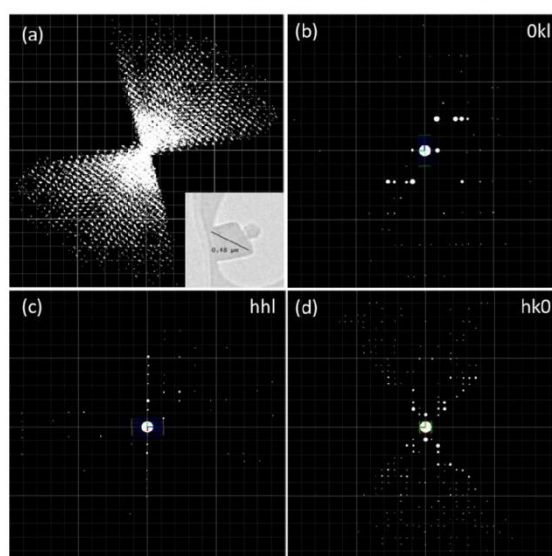


**Figure 2.** (a) Reconstructed 3D reciprocal lattice of Co-CAU-36 from cRED data processed using the REDp software.<sup>31</sup> Inset shows the corresponding crystal (ca 480 nm in size) from which the cRED data was collected. Some extra diffraction spots from the nearby tiny crystal were also observed, and excluded in the unit cell determination and indexing step. (b-d) Three 2D slices ( $0kl$ ), ( $hhl$ ), ( $hk0$ ) cut from the 3D reciprocal lattice, showing the systematic absence  $0kl: l = 2n+1$ . The unit cell axes  $a$ ,  $b$  and  $c$  are shown in red, green and blue, respectively.

**Table 1.** Crystallographic data and structure refinement details of Co-CAU-36.

Sample	Co-CAU-36
Chemical formula	[Co <sub>2</sub> (Ni-H <sub>4</sub> TPPP)]·2DABCO·6H <sub>2</sub> O
Temperature /K	96
Wavelength/Å	0.0251
Space Group	$P4c2$
Lattice Parameters/Å	$a=b=21.980(5)$ , $c=8.960(2)$
Resolution/Å	0.83
Completeness/%	96.7
$R_{int}$	0.2269
$R_1$ , $wR_2$ , GoF for $F^2 > 2\sigma(F^2)$	0.1356, 0.3364, 1.045
# Reflections (observed)	4008 (1978)
# Parameters (restraints)	192 (84)

The crystal structure of Co-CAU-36 is shown in Figure 3b-d. The framework structure contains one cobalt, one nickel, one phosphorus, and three oxygen atoms in the asymmetric unit.

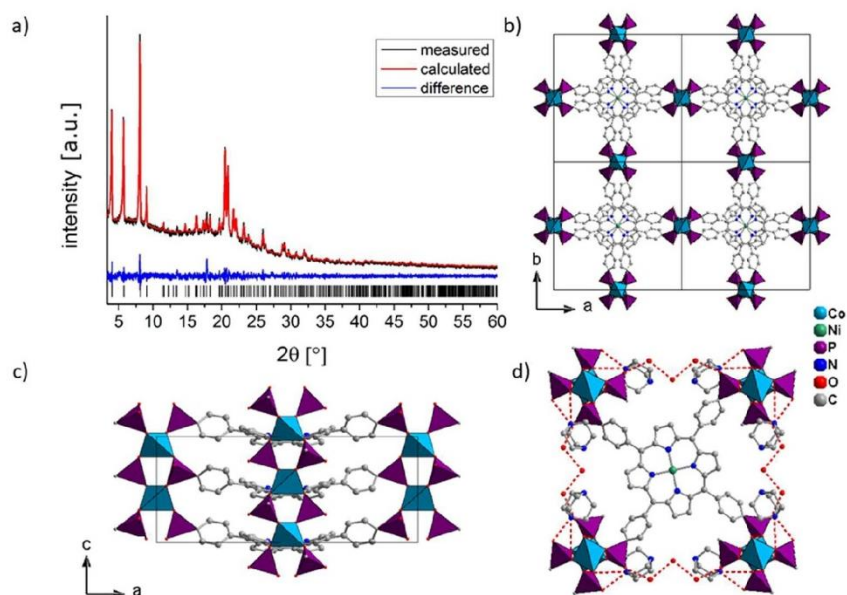


**Figure 3.** (a) PXRD pattern (Cu  $K\alpha_1$ ,  $\lambda = 1.5406 \text{ \AA}$ ) of Co-CAU-36 together with the Pawley fitting profile ( $R_{wp} = 0.0279$ ,  $GOF = 1.15$ ). (b-c) The framework structure of Co-CAU-36 viewed along [001] (b) and [010] (c). The inorganic building unit consisting of corner-sharing  $\text{CoO}_4$  and  $\text{PO}_3\text{C}$  tetrahedra, which forms 1D chains along [001]. (d) The hydrogen bonding networks between the solvent molecules and the framework in Co-CAU-36, represented as dashed red lines.

The cobalt atom is coordinated to four oxygen atoms from four different phosphonate groups, one from each  $\text{Ni-H}_4\text{TPPP}^{4-}$  moiety, to form 1D chain along [001] with alternating  $\text{CoO}_4$  and  $\text{PO}_3\text{C}$  tetrahedra (Fig. 3c). The chains are connected through the porphyrin  $\text{Ni-H}_4\text{TPPP}^{4-}$  moieties to form a 3D framework containing 1D channels with a pore diameter of  $12.5 \text{ \AA}$  without the solvents and ca.  $9 \text{ \AA}$  with the solvent molecules (Fig. 3a, Fig. S7,  $^\dagger$ ESI). The distance between the Ni ions in the porphyrin centres is  $4.48 \text{ \AA}$ . The water molecules (Ow1 and Ow2), together the terminal hydroxyl group of the  $\text{PO}_3\text{C}$  tetrahedra (O3), form a strong H-bonding network (see Fig. 3d, O3...Ow1 =  $2.60 \text{ \AA}$  and Ow1...Ow2 =  $2.81 \text{ \AA}$ ). The DABCO molecule forms two H-bonds with the framework (N3...O3 =  $2.82 \text{ \AA}$ , N3...O1 =  $3.36 \text{ \AA}$ ).

The PXRD pattern simulated from the structural model agrees well with the experimental one (Fig. S8,  $^\dagger$ ESI). Because of the continuous change of the peak positions and significant loss of the crystallinity upon the removal of the guest species (Figs. S10-12,  $^\dagger$ ESI), Rietveld refinement against PXRD data could not be conducted. Therefore, we carried out independent structure refinements against eight individual dataset in order to verify the structural model. The structure refinements converged to  $R1$  values of  $0.136$ - $0.189$  for reflections with  $F^2 > 2\sigma(F^2)$  and  $0.164$ - $0.241$  for all reflections (Table S1,  $^\dagger$ ESI). The atomic positions refined against the different datasets were compared to the corresponding positions averaged from the eight models. For the non-H atoms, the average deviation is  $0.031(17) \text{ \AA}$  for the framework atoms (maximum deviation  $0.083 \text{ \AA}$ ),  $0.098(65) \text{ \AA}$  for the DABCO molecule and  $0.16(12) \text{ \AA}$  for the water molecules (Table S2,  $^\dagger$ ESI). The small deviations in the positions of the framework atoms from the different cRED datasets confirm that the structural models obtained from each of the single datasets are all correct, despite the

relatively high  $R1$  values compared to those in X-ray diffraction (see Table S1,  $^\dagger$ ESI). We have for the first time been able to locate and refine the solvent molecules in the pores using the cRED data. The somehow larger deviations in the positions of DABCO and water molecules could be due to their slightly different locations in different crystals. Figure S9 shows a superposition of the eight refined structures, where the framework atoms almost perfectly overlap. We also investigated the effects of data merging on the final structural model, by comparing the refined structural model using the cRED data merged from four datasets with those refined against the four individual datasets. Compared to the averaged positions from the four individual models, the atomic positions from the merged data deviate by  $0.022(7) \text{ \AA}$  for the framework atoms,  $0.078(14) \text{ \AA}$  for DABCO and  $0.14(2) \text{ \AA}$  for water (Table S3,  $^\dagger$ ESI).

Thermogravimetric analysis (TGA) and variable temperature (VT)-PXRD show that Co-CAU-36 is stable above  $350 \text{ }^\circ\text{C}$  upon the removal of solvent molecules (Figs. S11-12), although the crystallinity decreased significantly. The higher solvent content given by TGA compared to that from the structure refinement can be due to the presence of disordered solvent molecules.  $\text{N}_2$  sorption isotherm (Fig. 4) shows that Co-CAU-36 is porous with a BET specific surface area of  $700 \text{ m}^2 \text{ g}^{-1}$  and a micropore volume of  $V_m = 0.31 \text{ cm}^3 \text{ g}^{-1}$ . FT-IR spectroscopy shows a NH vibration band at  $3670 \text{ cm}^{-1}$ , indicating the presence of H-DABCO species, which suggests that the proton is located at the DABCO molecule instead of at the phosphonate group (Fig. S13, Table S4,  $^\dagger$ ESI). This agrees with the structural model in which one N in the DABCO acts as an H-donor to form an H-bond with a bridging framework oxygen (O1). UV/Vis spectroscopy confirms that Ni is coordinated to the porphyrins (Fig. S13 and S14).



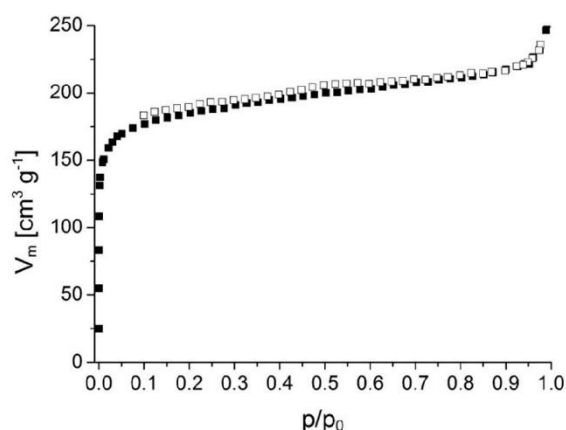


**Figure 4.**  $N_2$ -sorption isotherm of Co-CAU-36 measured at 77 K. A specific surface area of  $a_{\text{BET}} = 700 \text{ m}^2 \text{ g}^{-1}$  ( $V_m = 0.31 \text{ cm}^3 \text{ g}^{-1}$ ) was obtained. Prior to the measurement the sample was activated at 170 °C under vacuum ( $10^{-2}$  kPa) for 16 h.

In conclusion, a new and porous cobalt tetraphosphonophenylporphyrin metal-organic framework  $[\text{Co}_2(\text{Ni}-\text{H}_4\text{TTPPP})] \cdot 2\text{DABCO} \cdot 6\text{H}_2\text{O}$ , denoted Co-CAU-36, was synthesized. The crystal structure was determined using the cRED data collected at low temperature (96 K). Co-CAU-36 is built from 1D inorganic chains of alternating  $\text{CoO}_4$  and  $\text{PO}_3\text{C}$  tetrahedra from the phosphonate groups to form a 3D framework with 1D channel. We show that not only the framework atoms, but also solvent molecules in the pores, could be located and refined. Accurate structural models can be obtained from each of the eight datasets collected from different crystals. The atomic positions deviated by less than 0.03(2) Å for the framework atoms, 0.10(6) Å for DABCO and 0.16(11) Å for water molecules. The entire structure determination process, from TEM sample preparation, data collection and processing, to the final structure solution and refinement, was conducted within 9 hours. This shows that electron diffraction can be used as a stand-alone method for fast structure determination of unknown structures.

### Conflicts of interest

There are no conflicts to declare.

### Acknowledgements

The authors thank the Swedish Research Council (VR), Swedish Governmental Agency for Innovation Systems (VINNOVA) through the Berzelii Center EXSELENT on Porous Materials, and the Knut and Alice Wallenberg Foundation (KAW) for financial supports. AKI is supported by the Swedish Foundation for Strategic Research (SSF) and also a scholarship from KAW.

### Notes and references

1 H. Furukawa, K. E. Cordova, M. O’Keeffe and O. M. Yaghi, *Science*, 2013, 341, 1230444.

- 2 N. Stock, H. Reinsch and L.-H., in *Metal Organic Frameworks as Heterogeneous Catalysts*, The Royal Society of Chemistry, Cambridge, 2013, pp. 9–30.
- 3 H.-C. Zhou, J. R. Long and O. M. Yaghi, *Chem. Rev.*, 2012, **112**, 673–674.
- 4 O. M. Yaghi, M. O’Keeffe, N. W. Ockwig, H. K. Chae, M. Eddaoudi and J. Kim, *Nature*, 2003, **423**, 705–714.
- 5 C.-Y. Sun, C. Qin, X.-L. Wang and Z.-M. Su, *Expert Opin. Drug Deliv.*, 2013, **10**, 89–101.
- 6 C. Janiak and J. K. Vieth, *New J. Chem.*, 2010, **34**, 2366–2388.
- 7 U. Mueller, M. Schubert, F. Teich, H. Puetter, K. Schierle-Arndt and J. Pastre, *J. Mater. Chem.*, 2006, **16**, 626–636.
- 8 T. Rhauderwiek, K. Wolkersdörfer, S. Øien-Ødegaard, K.-P. Lillerud, M. Wark and N. Stock, *Chem. Commun.*, 2018, **54**, 389–392.
- 9 K. J. Gagnon, H. P. Perry and A. Clearfield, *Chem. Rev.*, 2012, **112**, 1034–1054.
- 10 M. Taddei, F. Costantino and R. Vivani, *Eur. J. Inorg. Chem.*, 2016, **2016**, 4300–4309.
- 11 J. A. Groves, S. R. Miller, S. J. Warrender, C. Mellot-Draznieks, P. Lightfoot and P. A. Wright, *Chem. Commun.*, 2006, 3305–3307.
- 12 M. T. Wharmby, G. M. Pearce, J. P. S. Mowat, J. M. Griffin, S. E. Ashbrook, P. A. Wright, L.-H. Schilling, A. Lieb, N. Stock, S. Chavan, S. Bordiga, E. Garcia, G. D. Pirngruber, M. Vreeke and L. Gora, *Microporous Mesoporous Mater.*, 2012, **157**, 3–17.
- 13 M. T. Wharmby, J. P. S. Mowat, S. P. Thompson and P. A. Wright, *J. Am. Chem. Soc.*, 2011, **133**, 1266–1269.
- 14 S. Pili, S. P. Argent, C. G. Morris, P. Rought, V. García-Sakai, I. P. Silverwood, T. L. Easun, M. Li, M. R. Warren, C. A. Murray, C. C. Tang, S. Yang and M. Schröder, *J. Am. Chem. Soc.*, 2016, **138**, 6352–6355.
- 15 S. Begum, S. Horike, S. Kitagawa and H. Krautscheid, *Dalton Trans.*, 2015, **44**, 18727–18730.
- 16 U. Kolb, T. Gorelik, C. Kübel, M. T. Otten and D. Hubert, *Ultramicroscopy*, 2007, **107**, 507–513.
- 17 D. Zhang, P. Oleynikov, S. Hovmöller and X. Zou, *Z. Kristallogr.* 2010, **225**, 94–102.
- 18 W. Wan, J. Sun, J. Su, S. Hovmöller and X. Zou, *J. Appl. Cryst.*, 2013, **46**, 1863–1873.
- 19 T. Willhammar, Y. Yun and X. Zou, *Adv. Func. Mater.* 2014, **24**, 182–199.
- 20 M. Feyand, E. Mugnaioli, F. Vermoortele, B. Bueken, J.M. Dieterich, T. Reimer, U. Kolb, D. de Vos, and N. Stock, *Angew. Chem. Int. Ed.*, 2012, **51**, 10373–10376.
- 21 Y. Yun, X. Zou, S. Hovmöller and W. Wan, *IUCrJ*, 2015, **2**, 267–282.
- 22 M. Gemmi, M. G. I. L. Placa, A. S. Galanis, E. F. Rauch and S. Nicolopoulos, *J. Appl. Cryst.*, 2015, **48**, 718–727.
- 23 B.L. Nannenga, D. Shi, A.G.W. Leslie and T. Gonen, *Nat. Methods*, 2014, **11**, 927–930.
- 24 Y. Wang, S. Takki, O. Cheung, H. Xu, W. Wan, L. Öhrström, A.K. Inge, *Chem. Commun.*, 2017, **53**, 7018–7021.
- 25 N. Stock, *Microporous Mesoporous Mater.*, 2010, **129**, 287–295.
- 26 P. M. Forster, N. Stock and A. K. Cheetham, *Angew. Chem. Int. Ed.*, 2005, **44**, 7608–7611.
- 27 N. Stock, *Chem. Ing. Tech.*, 2010, **82**, 1039–1047.
- 28 W. Kabsch, *Acta Cryst.*, 2010, **D66**, 125–132.
- 29 M. C. Burla, R. Caliendo, B. Carrozzini, G. L. Cascarano, C. Cuocci, C. Giacovazzo, M. Mallamo, A. Mazzone and G. Polidori, *J. Appl. Cryst.*, 2015, **48**, 306–309.
- 30 G. M. Sheldrick, *Acta Cryst.*, 2008, **A64**, 112–122.

Porphyrin-basierte Metall-Organische Gerüstverbindungen:  
Von Metall-Carboxylaten zu Metall-Phosphonaten

---

#### 4.5.5 Highly stable and porous porphyrin-based zirconium and hafnium phosphonates - Electron crystallography as an important tool for structure elucidation

Der folgende Artikel wurde im Jahr 2018 in der Fachzeitschrift Chemical Science, RSC veröffentlicht. Der Wiederabdruck erfolgte mit freundlicher Genehmigung der RSC. Reproduced from Timo Rhauderwiek, Haishuang Zhao, Patrick Hirschle, Markus Döblinger, Bart Bueken, Helge Reinsch, Dirk de Vos, Stefan Wuttke, Ute Kolb and Norbert Stock, *Chem. Sci.*, **2018**, 10.1039/C8SC01533C with permission from the Royal Society of Chemistry. Copyright 2017 Royal Society of Chemistry.

Dieser Artikel aus dem Jahr 2018 beschreibt die Synthese und Charakterisierung von zwei thermisch und chemisch sehr stabilen und porösen Metall-Tetraphosphonaten M-CAU-30  $[M_2(Ni-H_2TPPP)(OH/F)_2] \cdot x H_2O$  (M= Zr, Hf). Als Linkermolekül wurde die kurz zuvor erstmals in der Synthese von MOFs eingesetzte Porphyrin-basierte Tetraphosphonsäure (Ni-Tetraphosphonophenylporphyrin, Ni-H<sub>8</sub>TPPP) verwendet. Durch Einsatz von Hochdurchsatzmethoden konnte M-CAU-30 in dem chemischen System M<sup>4+</sup>/Ni-H<sub>8</sub>TPPP/NaF/NaOH in H<sub>2</sub>O entdeckt werden. Die Synthese konnte anschließend ebenfalls durch Einsatz von Hochdurchsatzmethoden optimiert werden. Des Weiteren konnte durch Einsatz von Glasgefäßen unter Rühren die Reaktionszeit von 48 h auf 3 h und die Reaktionstemperatur von 180 auf 160 °C reduziert werden. Die Strukturbestimmung von Zr-CAU-30 erfolgte durch Kombination von Elektronenbeugung (automated diffraction tomography) zur Strukturlösung und der Rietveld-Methode zur Strukturverfeinerung aus Pulverdaten. M-CAU-30 kristallisiert in der Raumgruppe *I4<sub>1</sub>cd*, wobei die anfängliche Strukturlösung eine höhere Symmetrie von *I41/acd* suggerierte. Anhand von zusätzlichen Reflexen im Pulverdiffraktogramm, welche reversibel durch Aktivierung bei Temperaturen von 250 °C auftauchen, konnte die Struktur mittels der Rietveld-Methode in der Raumgruppe *I4<sub>1</sub>cd* verfeinert werden. Diese Symmetrierniedrigung wird maßgeblich durch das Entfernen von Wassermolekülen aus den Poren hervorgerufen. Die anorganische Baueinheit besteht aus eckenverknüpften ZrO<sub>6</sub> Oktaedern, welche zusätzlich über Hydrogenphosphonatgruppen zu eindimensionalen Ketten verknüpft werden. Über den teilweise deprotonierten Linker Ni-H<sub>2</sub>TPPP<sup>6-</sup> werden diese Ketten zu einem dreidimensionalen Netzwerk verknüpft, wobei eindimensionale Poren von 1.3 x 2 nm Durchmesser ausgebildet werden. Beide CAU-30 Verbindungen sind porös gegenüber N<sub>2</sub> bei 77 K und H<sub>2</sub>O bei 298 K und es wurden dabei spezifische Oberflächen nach BET von 1070 bzw. 1030 m<sup>2</sup> g<sup>-1</sup> und Wasseraufnahmen von 250 bzw. 340 mg g<sup>-1</sup> für Zr- und Hf-CAU-30 erhalten. Beide MOFs sind thermisch stabil bis 400 °C, was durch



thermogravimetrische und temperaturabhängige PXRD Messungen bestimmt wurde. Des Weiteren weisen die M-CAU-30 Verbindungen eine außerordentlich hohe chemische Stabilität in Säuren und Basen in einem pH Bereich von 0-12 (HCl, NaOH), in 100 % Essigsäure, Phosphatpuffer (pH 7), sowie in allen getesteten organischen Lösungsmitteln auf. Die Partikelgröße und Morphologie von M-CAU-30 wurde mittels REM und TEM Messungen untersucht. Es wurden dabei Nadeln von bis zu 500 nm Länge mit hoher Ordnung beobachtet, sowie kleinere Mengen an Verunreinigungen von 10 % MO<sub>2</sub> (M= Zr, Hf) die als Nanopartikel auf diesen Nadeln haften. Die Struktur der MO<sub>2</sub> Verunreinigungen wurde ebenfalls mittels Elektronenbeugungsmessungen überprüft.



Cite this: DOI: 10.1039/c8sc01533c

## Highly stable and porous porphyrin-based zirconium and hafnium phosphonates – electron crystallography as an important tool for structure elucidation†

Timo Rhauderwiek,<sup>a</sup> Haishuang Zhao,<sup>b</sup> Patrick Hirschle,<sup>c</sup> Markus Döblinger,<sup>c</sup> Bart Bueken,<sup>d</sup> Helge Reinsch,<sup>a</sup> Dirk De Vos,<sup>d</sup> Stefan Wuttke,<sup>c</sup> Ute Kolb<sup>\*a</sup> and Norbert Stock<sup>†\*a</sup>

The Ni-metallated porphyrin-based tetraphosphonic acid (Ni-tetra(4-phosphonophenyl)porphyrin, Ni-H<sub>8</sub>TPPP) was used for the synthesis of highly porous metal phosphonates containing the tetravalent cations Zr<sup>4+</sup> and Hf<sup>4+</sup>. The compounds were thoroughly characterized regarding their sorption properties towards N<sub>2</sub> and H<sub>2</sub>O as well as thermal and chemical stability. During the synthesis optimization the reaction time could be substantially decreased under stirring from 24 to 3 h in glass vials. M-CAU-30, [M<sub>2</sub>(Ni-H<sub>2</sub>TPPP)(OH/F)<sub>2</sub>]·H<sub>2</sub>O (M = Zr, Hf) shows exceptionally high specific surface areas for metal phosphonates of  $a_{\text{BET}} = 1070$  and  $1030 \text{ m}^2 \text{ g}^{-1}$  for Zr- and Hf-CAU-30, respectively, which are very close/correspond to the theoretical values of  $1180$  and  $1030 \text{ m}^2 \text{ g}^{-1}$ . CAU-30 is always obtained as mixtures with one mol ZrO<sub>2</sub>/HfO<sub>2</sub> per formula unit as proven by TEM, electron diffraction, TG and elemental analysis. Hence experimentally derived specific surface areas are  $970$  and  $910 \text{ m}^2 \text{ g}^{-1}$ , respectively. M-CAU-30 is chemically stable in the pH range 0 to 12 in HCl/NaOH and thermally up to  $420 \text{ }^\circ\text{C}$  in air as determined by variable-temperature powder X-ray diffraction (VT-PXRD). The crystal structure of M-CAU-30 was determined by combining electron diffraction tomography for structure solution and powder X-ray diffraction data for the structure refinement. The crystal structure consists of chains of corner sharing MO<sub>6</sub> octahedra interconnected by the partly deprotonated linker molecules Ni-H<sub>2</sub>TPPP<sup>6-</sup>. Thus 1D channels with pore diameters of  $1.3 \times 2.0 \text{ nm}$  are formed. The redox activity of Zr-CAU-30 was investigated by cyclic voltammetry resulting in a reversible redox process at a half-wave potential of  $E_{1/2} = -0.649 \text{ V}$ .

Received 4th April 2018  
Accepted 27th May 2018

DOI: 10.1039/c8sc01533c

rsc.li/chemical-science

## Introduction

Metal organic frameworks (MOFs) are an intensively investigated class of materials. Due to their modular structure they allow one to tune their pore size and pore surface properties, which in turn leads to a large range of chemical and physical properties.<sup>1–4</sup> Although MOFs have been intensively investigated

in applications such as gas storage and separation, drug delivery or catalysis<sup>1,3,5–7</sup> their stability is often a limitation for most applications.<sup>8</sup>

The use of tri- and tetravalent cations often leads, especially for the metals Al, Cr and Zr to highly thermally and chemically stable MOFs.<sup>9–13</sup> The investigation of these compounds is frequently hampered by the challenging structure determination since only microcrystalline products are obtained. Electron diffraction, *i.e.* automated diffraction tomography (ADT)<sup>14,15</sup> and rotation electron diffraction (RED),<sup>16</sup> has been established as a powerful tool to elucidate crystal structures of nano crystalline materials within the last decade.<sup>17–21</sup> For beam sensitive materials like organic compounds and MOFs,<sup>20</sup> data acquisition under cryogenic conditions at liquid nitrogen temperature, is important to reduce electron beam damage.

The combination of tetracarboxylic acids with Zr<sup>4+</sup> and Hf<sup>4+</sup> ions has been shown to yield highly interesting and functional compounds such as NU-1000,<sup>22</sup> PCN-222 (MOF-545)<sup>23,24</sup> or Zr-

<sup>a</sup>Institut für Anorganische Chemie, Christian-Albrechts-Universität, Max-Eyth Straße 2, D-24118 Kiel, Germany. E-mail: nstock@ac.uni-kiel.de

<sup>b</sup>Institute of Inorganic Chemistry and Analytical Chemistry, Johannes Gutenberg-University Mainz, Duesbergweg 10-14, D-55128 Mainz, Germany. E-mail: kolb@uni-mainz.de

<sup>c</sup>Department of Chemistry and Center for NanoScience (CeNS), University of Munich (LMU), Butenandtstraße 5-13, D-81377 Munich, Germany

<sup>d</sup>Centre for Surface Chemistry and Catalysis, KU Leuven, Celestijnenlaan 200f Box 2461, B-3001 Leuven, Belgium

† Electronic supplementary information (ESI) available: Experimental procedures, analytical data including NMR spectroscopy, Pawley fits, TG, IR, microscopy and sorption measurements. CCDC 1831844. For ESI and crystallographic data in CIF or other electronic format see DOI: 10.1039/c8sc01533c

PPn.<sup>25</sup> The latter two materials are porphyrin-based Zr-MOFs exhibiting carboxylate and phenolate groups respectively and they are active as catalysts in Fe<sup>III</sup>/Fe<sup>II</sup> reduction<sup>13</sup> in the Heck-reaction<sup>26</sup> or CO<sub>2</sub> reduction.<sup>25</sup> The stability of those MOFs can be explained by the high oxophilicity of the tetravalent cations.<sup>9</sup> According to the HSAB theory,<sup>11,27</sup> hard acids like Zr<sup>4+</sup> and hard bases like carboxylate or phosphonate groups result in stable Zr–O bonds.<sup>27</sup> Comparing metal carboxylates to metal phosphonates, the latter are often more stable due to the higher charge and the increased number of donor atoms.<sup>28</sup> This is in line with the larger number of coordination modes observed in metal phosphonates, which often leads to dense, layered structures.<sup>29,30</sup>

First studies in the field of Zr-phosphates were carried out by Clearfield *et al.* in 1964 by the preparation of Zr(HPO<sub>4</sub>)<sub>2</sub>·H<sub>2</sub>O<sup>31</sup> and the structural characterisation in 1969.<sup>32</sup> The work on porous Zr-phosphonates began with the investigation of organically pillared Zr-phosphonates in 1983, which are structurally related to Zr(HPO<sub>4</sub>)<sub>2</sub>·H<sub>2</sub>O. In these compounds the pores are statistically distributed, formed due to separation of the Zr–P–O layers by organic molecules.<sup>33</sup>

The total number of porous metal phosphonates is limited to only a few dozen structures<sup>28,34–37</sup> and up to now only eight porous, crystalline Zr-phosphonate and no Hf-phosphonate MOFs have been reported (Table S1†): [Zr<sub>2</sub>H<sub>4</sub>(O<sub>3</sub>PCH<sub>2</sub>)<sub>2</sub>·(N<sub>2</sub>C<sub>4</sub>H<sub>8</sub>)<sub>3</sub>],<sup>38</sup> UPG-1,<sup>39</sup> Zrbtbp,<sup>40</sup> CALF-31,<sup>41</sup> ZrH<sub>4</sub>L<sup>42</sup> and most recently SZ-1 to 3.<sup>43</sup> The specific surface areas of the known Zr-phosphonate MOFs range between 10 and 793 m<sup>2</sup> g<sup>−1</sup> (CALF-31).<sup>41</sup>

In contrast to numerous porphyrin-based MOFs bearing carboxylate groups<sup>44,45</sup> to date only one such MOF (CAU-29) containing phosphonate groups has been reported.<sup>46</sup> After the first report of tetra(4-phosphonoethylphenyl)porphyrin, H<sub>10</sub>TPPP in 1995 (ref. 49) (Fig. 1) molecular structures such as the ester<sup>47,48</sup> and different metalated compounds with di- and trivalent cations (Mn<sup>3+</sup>,<sup>49,50</sup> Ni<sup>2+</sup>,<sup>46</sup> Zn<sup>2+</sup>)<sup>48,51</sup> have been reported. These molecules have been characterized in literature regarding their electrochemical<sup>47,48,52</sup> and photochemical<sup>48,52,53</sup> properties as well as in catalytic<sup>49,50</sup> and self-assembling<sup>54,55</sup> or -aggregation<sup>56,57</sup> processes.

Comparison of porous Zr-phosphonates reveals preferred formation of linear inorganic building units (IBU) consisting of ZrO<sub>6</sub> octahedra.<sup>38–40</sup> In combination with rigid tritopic phosphonic acids, which turned out to suppress the layer motive, “honeycomb” like pores were mostly observed in porous Zr-phosphonates (Fig. 1).<sup>39,40</sup> Applying this information to rigid tetratopic phosphonic acids two types of structures exhibiting pores of different size can be envisioned (Fig. 1). Therefore the combination of tetravalent cations with geometrically demanding phosphonic acids could lead to highly porous and exceptionally stable MOFs.<sup>43</sup>

Here we present our results which are based on the previously mentioned considerations. We have carried out a systematic investigation on Zr- and Hf-phosphonates using the square planar tetraphosphonic linker Ni-H<sub>8</sub>TPPP in hydrothermal reactions.

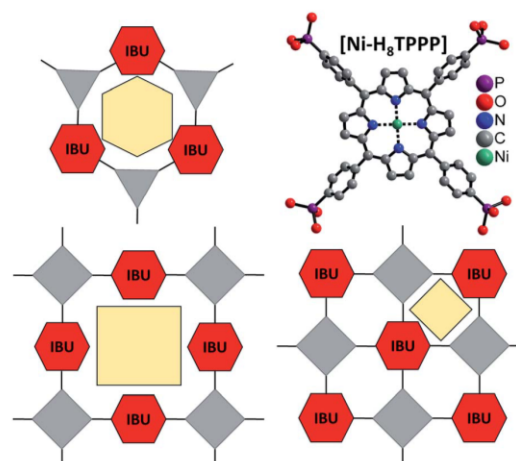


Fig. 1 Concept for the design of porous Zr and Hf phosphonates with 1D IBUs (red hexagons) using rigid and planar tetraphosphonic acid as linker molecule (top, right). Top, left: scheme of known porous Zr triphosphonates with honeycomb structure and a 1D IBU (red hexagons).<sup>39,40</sup> Bottom: possible connection of the 1D IBUs by planar tetraphosphonic ions which should lead to the formation of porous metal phosphonates. Grey triangles and squares represent tri- and tetraphosphonic acids and yellow polygons the schematic pore space.

## Results and discussion

### Synthesis

The systematic study of the system Ni-H<sub>8</sub>TPPP/M<sup>4+</sup>/NaF/NaOH (M = Zr<sup>4+</sup>, Hf<sup>4+</sup>) using high-throughput (HT) methods resulted in highly porous and stable metal phosphonates (Fig. S5a†). The product formation depends mainly on the presence of F<sup>−</sup> ions and the pH value of the reaction mixture (pH<sub>start</sub> = 7). In case of Zr- and Hf-CAU-30 a molar linker : metal : NaF : NaOH ratio of 1 : 2 : 60 : 8 resulted in highly crystalline products (1 equivalent corresponds to 5.3 × 10<sup>−3</sup> mmol). The syntheses can be scaled up by at least to a factor of 12. The initially used reaction time and temperature can be reduced from 24 to 3 h and 180 °C to 160 °C, respectively, when a glass reactor is employed and the reaction mixture is stirred (Fig. S5b†). Although F<sup>−</sup> ions are present in the reaction mixture no reaction with the glass reactor was observed.

### Crystal structure

Zr- and Hf-CAU-30 were obtained as microcrystalline powders. Therefore the structure of Zr-CAU-30 was solved employing automated electron diffraction tomography (ADT), while the structure was refined from the PXRD data of an activated (-act) sample, *i.e.* Zr-CAU-30-act (Fig. S7b,† Table 1). The PXRD patterns of the as-synthesized (-as) form Zr- and Hf-CAU-30-as are compared with the one of Zr-CAU-30-act in Fig. 2. Activation was carried out at 250 °C under reduced pressure of 10<sup>−2</sup> kPa in a 0.5 mm glass capillary. The differences in the relative intensities of Zr-CAU-30-as and -act are due to the loss of H<sub>2</sub>O molecules from the pores.



**Table 1** Results of the Rietveld refinement of Zr-CAU-30-act (activated at 250 °C for 2 h under reduced pressure of  $10^{-2}$  kPa) and the Pawley refinements of M-CAU-30-as (M = Zr, Hf)

	Zr-CAU-30-act	Zr-CAU-30-as	Hf-CAU-30-as
Method	Rietveld	Pawley	Pawley
Crystal system	Tetragonal	Tetragonal	Tetragonal
<i>a</i> [Å]	44.778(6)	45.121(5)	45.040(5)
<i>b</i> [Å]	44.778(6)	45.121(5)	45.040(5)
<i>c</i> [Å]	7.658(4)	8.090(2)	8.049(3)
$\alpha$ [°]	90	90	90
$\beta$ [°]	90	90	90
$\gamma$ [°]	90	90	90
<i>V</i> [Å <sup>3</sup> ]	15 354(8)	16 470(5)	16 329(8)
Space group	<i>I</i> <sub>4</sub> <i>cd</i>	<i>I</i> <sub>4</sub> <i>/acd</i>	<i>I</i> <sub>4</sub> <i>/acd</i>
GoF	2.0	0.72	0.94
<i>R</i> <sub>wp</sub> , <i>R</i> <sub>bragg</sub> [%]	3.8, 0.5	3.3	3.8

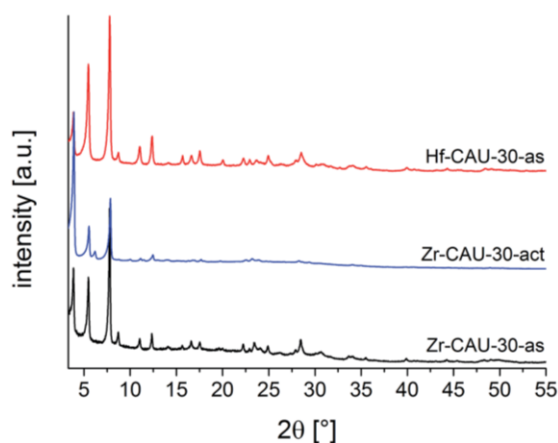


**Fig. 2** PXRD patterns of Zr-CAU-30-as, Zr-CAU-30-act and Hf-CAU-30-as.

The tetragonal cell indexed from the PXRD pattern of Zr-CAU-30-act is in line with the unit cell parameters of the as-synthesized form obtained from reconstruction of 3D electron diffraction data (Table 1). However, the extinction conditions indicate a lower symmetry for the activated compound. The amount of water in the pores has a strong influence on the relative intensities hence the activated sample was chosen for the structure refinement in *I*<sub>4</sub>*cd* symmetry (Fig. S7b†). To prove the reversibility of the transformation from the activated (*I*<sub>4</sub>*cd*) into the as-synthesized (*I*<sub>4</sub>*/acd*) form, PXRD patterns of the activated form in an open capillary were recorded every five minutes over five days (Fig. S7d†). The changes in relative intensities upon hydration is best detected monitoring the 130 reflection. While in the as-synthesized compound only reflections *hk0* with *h* = 2*n* are observed indicating the presence of an *a*-glide plane, additional reflection such as the 130 reflections are clearly seen in the PXRD pattern of the activated sample (Fig. S7d†).

### Structure solution by electron diffraction tomography

Needle-like crystals with different sizes (Fig. S6a†) could be observed for Zr-CAU-30-as. The diameters of the nanorods range from a few tens up to about 500 nm, and are therefore suitable for TEM experiments. The crystals are stable under cooling conditions using low beam illumination. Nano electron diffraction experiments show that the nanorods are highly crystalline.

Aggregates of spherical nanoparticles smaller than 5 nm with partial crystallinity were also observed by TEM as a minor secondary phase (Tables S5 and S6†). Crystals with a diameter of some hundred nanometres were selected for TEM experiments.

Cell parameters extracted from three-dimensional electron diffraction data describe a unit cell with *a* = 46.09 Å, *b* = 45.74 Å, *c* = 7.81 Å (Fig. S6b†), which are in line with the results obtained from PXRD (Fig. S7a† and Table 1). Systematic extinctions conditions with *h* + *k* + *l* = 2*n* for the *hkl* reflections indicated an *I*-centred Bravais lattice. The reflection conditions can be observed from 2D-cuts from the reconstructed lattice (Fig. S6c†) as following *h* = 2*n* and *k* = 2*n* for *hk0*; *k* = 2*n* and *l* = 2*n* for *0kl*; 2*h* + *l* = 4*n* for *hkl* delivering the extinction rule *Iacd* associated with the tetragonal space group *I*<sub>4</sub>*/acd* (no. 142). An ADT dataset collected in combination with electron beam precession from a single nanocrystal with a tilt range from −65 to +58 (Table 2) was used for crystal structure solution employing direct methods.

The *ab initio* structure solution converged with a final residual *R* value of 0.173. The structure solution delivered a well-resolved Fourier potential map (Fig. S6d†), accompanying some extra potentials, which probably correspond to residual water molecules in the pores. The two strongest maxima (2.24 and 1.63 e<sup>−</sup> Å<sup>−3</sup>) correspond to the two metal atoms Zr and Ni, respectively. The next maximum with 1.24 e<sup>−</sup> Å<sup>−3</sup> is consistent with the position of the P atom. The following peaks for O, N and C atoms were detected with a scattering potential range of 0.98 down to 0.49 e<sup>−</sup> Å<sup>−3</sup>. One missing O atom located at P could only be detected from the difference Fourier map.

Structure refinement was accomplished from PXRD data of the activated compound (Zr-CAU-30-act).‡ Starting with the structure model of the framework as determined from electron diffraction data, we set up a model by first converting the space group symmetry from *I*<sub>4</sub>*/acd* to *I*<sub>4</sub>*cd* using Powdercell<sup>88</sup> and subsequent optimisation of the structure using the universal force field as implemented in Materials Studio.<sup>89</sup> Due to the low

**Table 2** Experimental parameters of electron diffraction dataset for structure solution of Zr-CAU-30-as in space group *I*<sub>4</sub>*/acd*

Tilt range (°)	−65/+58
No. of total reflections	18 149
No. of independent reflections	2021
Reflection coverage (%)	99
Resolution (Å)	1.0
<i>R</i> <sub>int</sub>	0.344
Overall <i>U</i> (Å <sup>2</sup> )	0.023
Residual <i>R</i> (SIR2014)	0.173

# Porphyrin-basierte Metall-Organische Gerüstverbindungen: Von Metall-Carboxylaten zu Metall-Phosphonaten

View Article Online

Chemical Science

Edge Article

number of reflections in combination with the very large unit cell only a partial Rietveld refinement could be carried out. Hence, for example the position of the porphyrin moiety was fixed and the phenylphosphonate fragments were treated as rigid bodies. The Zr–O bond lengths were restrained to literature values. More details are given in the Experimental section.

## Structure description

The asymmetric unit of Zr-CAU-30,  $[\text{Zr}_2(\text{Ni-H}_2\text{TPPP})(\text{OH}/\text{F})_2] \cdot 23\text{H}_2\text{O}$ , is shown in Fig. 3a and consists of one  $\text{Zr}^{4+}$  and one  $(\text{OH}^-/\text{F}^-)$  ion as well as a linker located on an centre of inversion. In addition water guest molecules are shown. The inorganic building unit (IBU) of Zr-CAU-30 consists of chains of trans corner sharing  $\text{ZrO}_6/\text{ZrO}_4\text{F}_2$  octahedra (Fig. 3b) where bridging is accomplished through  $\mu\text{-OH}^-/\text{F}^-$  ions. Each chain is interconnected to six other chains by the  $\text{Ni-H}_4\text{TPPP}^{4-}$  linker ions and a 3D framework with 1D channels exhibiting pore diameters of 1.3 along the edge and 2.0 nm along the diagonal of the pore (Fig. 3d) are formed (Connolly surface Fig. S6e†). Furthermore each linker molecule is coordinated to eight  $\text{Zr}^{4+}$  ions (Fig. S6f†).

One of the two symmetry independent phosphonate groups is probably protonated and based on the donor–acceptor distance of 2.6(2) Å to a guest molecule in the pores a hydrogen bond can be anticipated. The presence of P–OH and  $\mu\text{-OH}$

groups was further proven by IR spectroscopy. The coordination mode of the phosphonate and the hydrogenphosphonate group is each [2,110] employing the Harris notation.<sup>29</sup> The Harris notation has the format [A,XYZ], the value A being the number of metal ions coordinated by the hydrogenphosphonate group and X, Y, Z the number of bonds each oxygen atom shares with a metal ion.<sup>29</sup>

The use of  $\text{F}^-$  ions in the synthesis of crystalline Zr-phosphonates has been previously shown to be highly beneficial.<sup>39,41</sup> However the quantitative determination is often challenging. In this work, the fluoride content was determined by means of a fluoride-sensitive electrode. Before the analysis, the samples were digested by fusion with  $\text{Na}_2\text{CO}_3/\text{K}_2\text{CO}_3$ :  $[\text{Zr}_2(\text{H}_2\text{-TPPP})\text{F}_2] \cdot 23\text{H}_2\text{O} \cdot \text{ZrO}_2$  calc.: 2.2%, found: 3.5% and  $[\text{Hf}_2(\text{H}_2\text{-TPPP})\text{F}_2] \cdot 30\text{H}_2\text{O} \cdot \text{HfO}_2$  calc.: 1.8%, found: 3.9%. Considering a large standard deviation due to the low content of  $\text{F}^-$  in CAU-30 the values are in a reasonable range.

To further confirm the crystal structure additional high-resolution transmission electron microscopy (HRTEM) measurements were carried out to visualize structural details of Zr-CAU-30-as. Fig. 4 shows a reconstructed phase image based on the analysis of a focal series of 20 images, the sections of the crystal structure with Zr, Ni, P and O atoms, and the intensity profile. A direct comparison with the crystal structure of Zr-CAU-30 viewed along [010] reveals already a high resemblance. The crystal structure viewed along the crystallographic

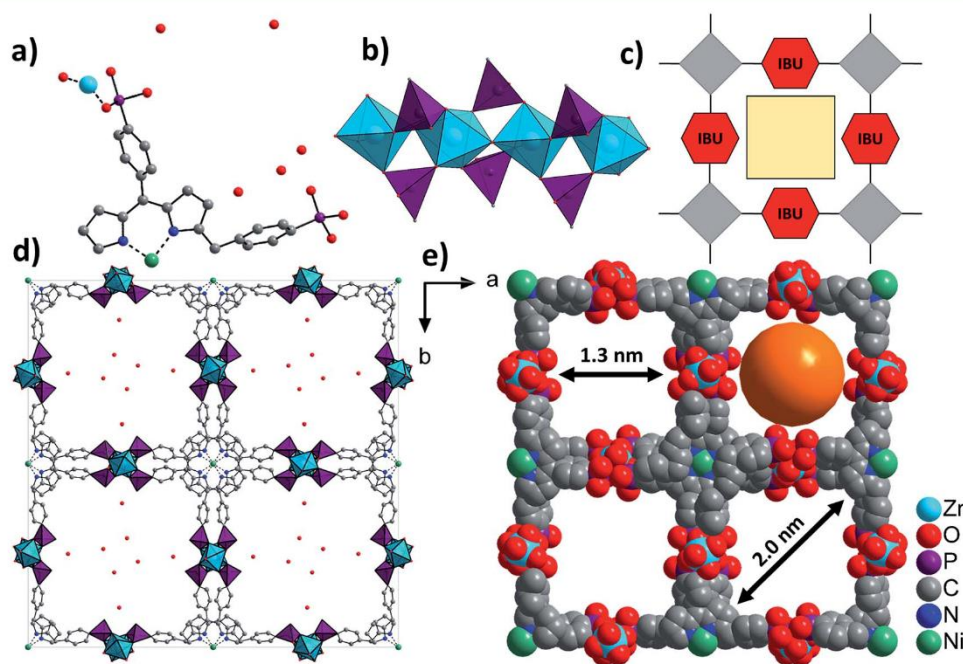


Fig. 3 Structural representation of Zr-CAU-30, (a) the asymmetric unit, (b) the IBU consisting of chains of trans corner sharing  $\text{ZrO}_6/\text{ZrO}_4\text{F}_2$  octahedra further connected by  $\text{PO}_3\text{C}$  tetrahedra to form 1D chains, view along [100], (c) schematic representation of a porous structure composed of square planar tetratopic linker and a 1D IBU according to Fig. 1, (d) the network structure of Zr-CAU-30 along [001] with  $\text{H}_2\text{O}$  molecules in the pores and (e) space filling view along [001] and pore diameters of 1.3 and 2.0 nm, respectively, measured by taking the van der Waals radius of the atoms lining the pores into account (water molecules are omitted for clarity).



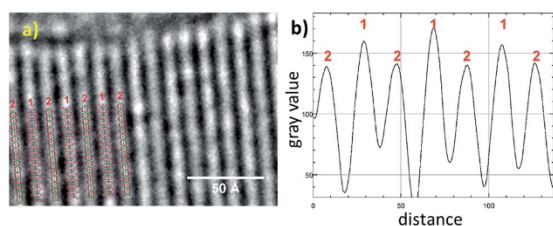


Fig. 4 (a) High resolution TEM: reconstructed phase image of Zr-CAU-30-as recorded along [010] zone axis (red); (b) intensity profiles of the electron density 1 and 2 in (a).

*b* axis shows two columns, one containing Zr and Ni clusters (marked as 1) and another only with Zr clusters (marked as 2). The enhanced density of column 1 is evident in the extracted intensity profile.

#### Particle morphology and composition by SEM and TEM

To determine the morphology of the Zr-CAU-30 crystals, SEM measurements were performed. The results are depicted in micrograph (a) in Fig. 5. The MOF crystallizes in form of needles that are up to 6  $\mu\text{m}$  long and 200 nm broad. In subsequent TEM measurements shown in the micrographs (b) and (c) the crystallinity of the sample was confirmed: the needles in micrograph (c) depict a visible periodicity perpendicular to the growth direction of the needles. The Fourier-transform of a diffraction pattern was used to determine the lattice parameters of the respective crystals (Fig. S6g<sup>†</sup>). The resulting spots in the reciprocal space correspond to lattice distances of 2.35 nm, 1.18 nm and 0.77 nm respectively and are well in agreement with the first (020 at  $d = 2.24$  nm), fourth (040 at  $d = 1.12$  nm) and eleventh (0.75 nm, 060) reflection of the PXRD pattern. As seen in (b), there is a secondary phase present in the sample in form of very small spherical particles (3–5 nm) on the surface of the needles. Further characterization revealed that this phase consist of monoclinic  $\text{ZrO}_2$  (details are shown in the ESI Section 6<sup>†</sup>). The SEM, TEM and EDX results for M-CAU-30 (M = Zr, Hf) are accordingly given in the ESI Section 6.†

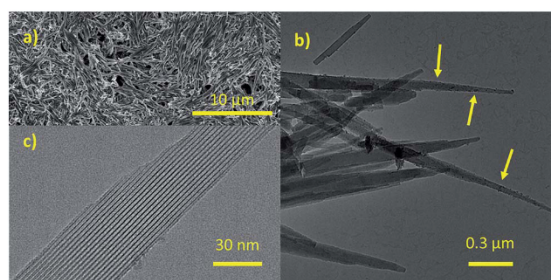


Fig. 5 Results of the SEM and TEM measurements performed on Zr-CAU-30. (a) SEM image of Zr-CAU-30, (b) TEM image of needles of Zr-CAU-30 with small spherical particles of  $\text{ZrO}_2$  on the surface of the needles (marked with arrows), (c) a detailed TEM image of one needle.

#### Sorption properties

Sorption experiments were carried out for both title compounds. Prior to the measurements all samples were activated at 170  $^{\circ}\text{C}$  under vacuum ( $10^{-2}$  kPa) for 16 h. Subsequently sorption experiments using  $\text{N}_2$  at 77 K (Fig. 6) and  $\text{H}_2\text{O}$  at 298 K (Fig. S8<sup>†</sup>) as adsorptives were performed. The specific surface areas were determined using the BET method and applying the method of Rouquerol.<sup>60,61</sup> Thus, the BET equation has been fitted between  $p/p_0 = 5.223 \times 10^{-6} - 0.103$  and  $6.740 \times 10^{-5} - 0.078$  for Zr- and Hf-CAU-30, respectively. Micropore volumes  $V_m$  were determined by using the amount of adsorbed  $\text{N}_2$  at the relative pressure  $p/p_0 = 0.5$  (Table 3). Both compounds are stable towards activation and sorption experiments as proven by PXRD measurements (Fig. S9<sup>†</sup>). The  $\text{N}_2$  measurements led to a Type-1 isotherm as expected for microporous materials.<sup>61</sup> Experimental specific surface areas of  $a_{\text{BET}} = 970$  (Zr) and 910 (Hf)  $\text{m}^2 \text{g}^{-1}$  were obtained (Table 3). The  $\text{H}_2\text{O}$  sorption measurements at 298 K (Fig. S8<sup>†</sup>) show uptakes of 250 (Zr) and 340 (Hf)  $\text{mg g}^{-1}$ .

The theoretical specific surface area of Zr-CAU-30 was calculated using the program Materials Studio V5.<sup>59</sup> Employing a probe molecule of 1.8 Å radius the maximum specific surface area was calculated to be 1180  $\text{m}^2 \text{g}^{-1}$ . The difference of ca. 200  $\text{m}^2 \text{g}^{-1}$  to the measured specific surface area is reasonable due to the presence of crystalline  $\text{ZrO}_2$  species (ESI, Section 6<sup>†</sup>) on the particles of Zr-CAU-30. Taking the impurity of one  $\text{ZrO}_2$  per formula unit, as determined from the TG and elemental analysis, into account the specific surface area of the single phase CAU-30 amounts to 1070 and 1030  $\text{m}^2 \text{g}^{-1}$ .

#### Thermal and chemical stability

To investigate the thermal stability thermogravimetric (TG) measurements of all samples and variable temperature (VT) PXRD studies were carried out.

The results of the TG measurements (Fig. 7 and S10, Table S3<sup>†</sup>) show two characteristic steps of weight loss, respectively. The loss up to 120  $^{\circ}\text{C}$  is assigned to the evaporation of

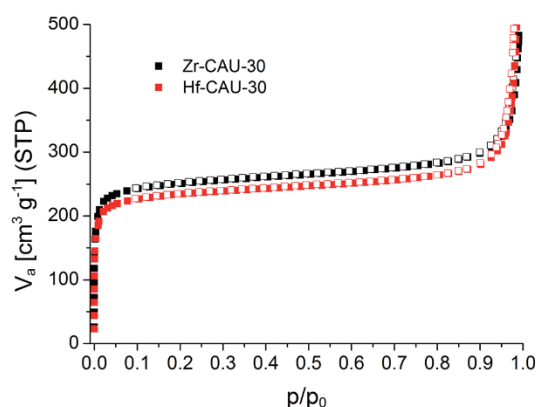


Fig. 6  $\text{N}_2$ -sorption isotherms of M-CAU-30 (M = Zr (black), Hf (red)) measured at 77 K.

# Porphyrin-basierte Metall-Organische Gerüstverbindungen: Von Metall-Carboxylaten zu Metall-Phosphonaten

View Article Online

Chemical Science

Edge Article

**Table 3** Results of the N<sub>2</sub> sorption experiments at 77 K of M-CAU-30 (M = Zr, Hf). The micropore volume was calculated at  $p/p_0 = 0.5$ . The theoretical specific surface areas were calculated using the program Materials Studio V5 and were each calculated for the pure framework and the framework with one mol MO<sub>2</sub> per formula unit (framework + MO<sub>2</sub>)

	Zr-CAU-30 framework + ZrO <sub>2</sub>	Zr-CAU-30 pure framework	Hf-CAU-30 framework + HfO <sub>2</sub>	Hf-CAU-30 pure framework
N <sub>2</sub> ( $a_{\text{BET}}$ ), [m <sup>2</sup> g <sup>-1</sup> ]	970	1070	910	1030
$a_{\text{BET}}$ (theory)	980	1180	890	1030
N <sub>2</sub> ( $V_{\text{m}}$ ), [cm <sup>3</sup> g <sup>-1</sup> ]	0.41		0.38	
H <sub>2</sub> O (upt.), [mg g <sup>-1</sup> ]	250		340	

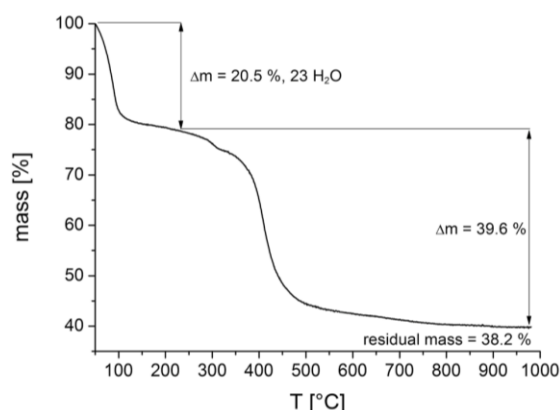


**Fig. 7** Thermogravimetric curve of a sample of Zr-CAU-30 (Table 3). Comparison of calculated and theoretical weight losses in combination with the results of the SEM and TEM measurements allow to quantify the amount of ZrO<sub>2</sub> in the reaction product as one ZrO<sub>2</sub> per formula unit.

physisorbed water molecules. Above 400 °C the decomposition of the compounds take place and different M<sup>IV</sup>Ni<sup>II</sup>-phosphates (M = Zr, Hf) are formed as the final product, which could partially be identified by PXRD measurements (Fig. S11†). In general, the results of the TG analysis fit well with the ones of the elemental analyses. Slight differences in the amounts of occluded solvent molecules are due to the storage of the samples prior to the measurements. The comparison of the calculated and the measured residual mass of the title compounds confirm the presence of inorganic impurities as identified by TEM and EDX measurements to be the monoclinic phases of ZrO<sub>2</sub> and HfO<sub>2</sub>, respectively (Tables S5 and S6†). The sample contains one mol ZrO<sub>2</sub> per formula unit of CAU-30.

The results of the VT-PXRD studies of Zr-CAU-30 (Fig. 8) and Hf-CAU-30 (Fig. S12†) fit well to the results of the TG measurement. Apart from the decomposition of the framework at 400 °C, no phase transformations are observed. Up to 150 °C, the relative reflection intensities change strongly which is in line with the loss of physisorbed water molecules and the activated form, *i.e.* Zr-CAU-30-act is formed. Identical results were observed for Hf-CAU-30 (Fig. S12†). The small differences compared to the TG measurements are due to the confinement of the sample in a capillary during the VT-PXRD measurement.

To investigate the chemical stability, M-CAU-30 (M = Zr, Hf) was exposed to different solvents (HCl (pH 0–7), NaOH (pH 7–14), 100% acetic acid, H<sub>2</sub>O, MeOH, EtOH, acetone, DMF, dichloromethane and 0.1 M phosphate buffer) at RT for 24 h under stirring. After the treatment the samples were isolated by filtration and measured by PXRD. The results of the chemical stability tests (Fig. 9 and S13†) reveal that M-CAU-30 is stable in all tested organic solvents as well as in a pH range between 0 and 12 (aqueous HCl/NaOH solutions). Remarkably, M-CAU-30 is also stable in 0.1 M phosphate buffer (pH 7).

## Spectroscopy

IR spectra of the title compounds and the Ni-H<sub>8</sub>TPPP linker are shown in Fig. S14a.† The assignment of the bands are given in Table S4† in detail. The characteristic bands for M-CAU-30 (M = Zr, Hf) are identical and compared with the ones of the free linker Ni-H<sub>8</sub>TPPP.

In the following discussion the position of the bands of the free linker Ni-H<sub>8</sub>TPPP are given in brackets, behind the ones of the MOF material. Vibrations of the porphyrin moiety like the  $\nu(\text{C}=\text{C})$ ,  $\delta(\text{C}=\text{C}, \text{C}=\text{N})$ ,  $\nu(\text{C}=\text{N})$ ,  $\gamma(\text{C}-\text{H})$  and  $\delta(\text{C}-\text{H}, \text{N}-\text{H})$  are observed at 1560, 1390, 1350, 800 and 737 cm<sup>-1</sup>, respectively.<sup>62</sup> Characteristic bands of the hydrogenphosphonate (phosphonic

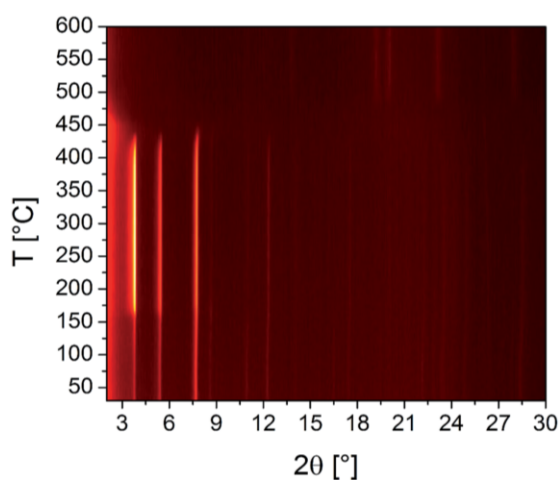


**Fig. 8** Results of the VT-PXRD study of Zr-CAU-30 (Cu-K $\alpha_1$  radiation) measured in an open quartz capillary (0.5 mm).

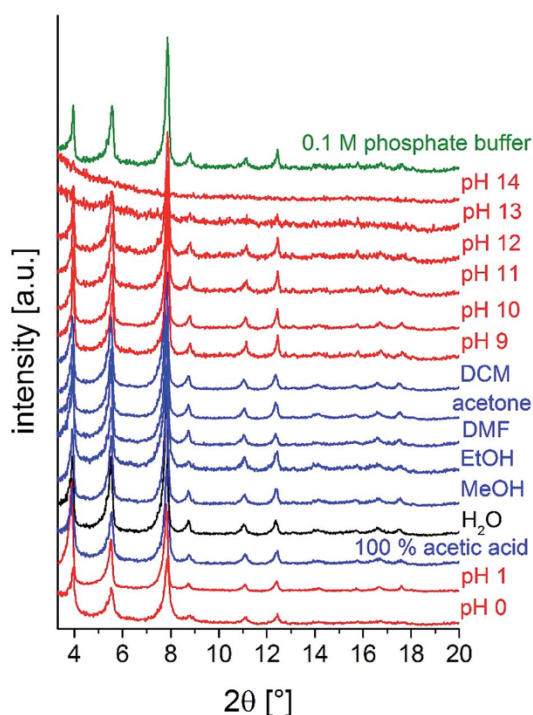


Fig. 9 Chemical stability of Zr-CAU-30 in different solvents (24 h, stirring at room temperature).

acid) group are for example the  $\nu(\text{P}-\text{O}(\text{OH}))$  and  $\nu(\text{P}-\text{C})$  vibrations at  $1634$  ( $1606$ ) and  $1501$  ( $1480$ )  $\text{cm}^{-1}$ ,<sup>63</sup> but the band at  $1634$   $\text{cm}^{-1}$  is mainly due to the presence of water molecules ( $\delta_s$  vibration) in the non-activated sample. The  $\nu(\text{P}=\text{O})$  and  $\nu(\text{P}-\text{O})$  bands are observed at  $1234$  ( $1223$ ),  $1141$  ( $1136$ ) and  $966$  ( $921$ )  $\text{cm}^{-1}$ . Furthermore  $\gamma(\text{P}-\text{C})$  and  $\delta(\text{P}(\text{OR})_3)$  deformation vibrations are observed at  $717$  ( $704$ ) and  $588$  ( $567$ )  $\text{cm}^{-1}$ .<sup>10,11,64</sup>

More insight into the proton topology of Zr-CAU-30 was gathered from FTIR spectra recorded after an *in situ* thermal evacuation ( $200$  °C) of the material (Fig. 10). Two samples were investigated, the pure Zr-CAU-30 material, and the same diluted as 2.5 wt% in dry KBr. The spectrum of the latter corresponds well with that of the non-evacuated sample, featuring multiple prominent bands corresponding to  $\nu(\text{P}-\text{O})$  ( $1143$   $\text{cm}^{-1}$ ;  $997$   $\text{cm}^{-1}$ ),  $\gamma(\text{P}-\text{C})$  ( $715$   $\text{cm}^{-1}$ ) and  $\delta(\text{P}(\text{OR})_3)$  ( $590$   $\text{cm}^{-1}$ ). Other bands attributable to vibrational modes in the linker are found at  $734$   $\text{cm}^{-1}$ ,  $799$   $\text{cm}^{-1}$ ,  $1350$   $\text{cm}^{-1}$ ,  $1390$   $\text{cm}^{-1}$  and  $1560$   $\text{cm}^{-1}$ . The broad band centered at  $3400$   $\text{cm}^{-1}$  in the non-evacuated sample, attributable to water and hydrogen-bonded  $\mu\text{-OH}$ -groups, fully disappears upon activation. In its place, a small OH-band at approximately  $3640$   $\text{cm}^{-1}$  is observed (Fig. 10, blue), which correspond to the  $\mu\text{-OH}$  groups bridging the metal ions. In the spectrum of the pure Zr-CAU-30 sample (Fig. 10, black), this band is clearly pronounced, and in fact three distinct vibrations, a prominent one at  $3650$   $\text{cm}^{-1}$ , are observed. Additionally, a broad band in the  $2240$ – $2440$   $\text{cm}^{-1}$  region can be

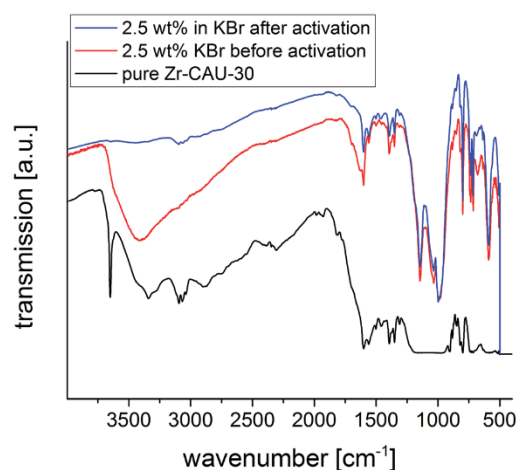


Fig. 10 IR spectra of Zr-CAU-30 with 2.5 wt% KBr before (red) and after (blue) activation at  $200$  °C as well as the pure sample (black).

observed. The presence of both vibrational modes is indicative of P-OH groups in the material. Nevertheless, it cannot be excluded that the much weaker  $\nu(\text{O}-\text{H})$  bands originate from  $\mu\text{-OH}$  groups connecting the  $\text{ZrO}_6$ -octahedra.

UV/vis spectroscopy was employed to prove the metalation of the porphyrin moiety after the hydrothermal reaction. The pure linker Ni- $\text{H}_8$ TPPP as well as the two MOFs exhibited nearly identical positions for the Soret- and Q1-band at  $413$  and  $526$  nm, respectively (Fig. 11). Thus the high stability of the metalated porphyrin linker under hydrothermal conditions at  $180$  °C for 48 h is confirmed.

#### Redox activity

Cyclic voltammograms (CVs) of Zr-CAU-30 were measured on a fluorine doped tin oxide (FTO) electrode in 0.1 M phosphate

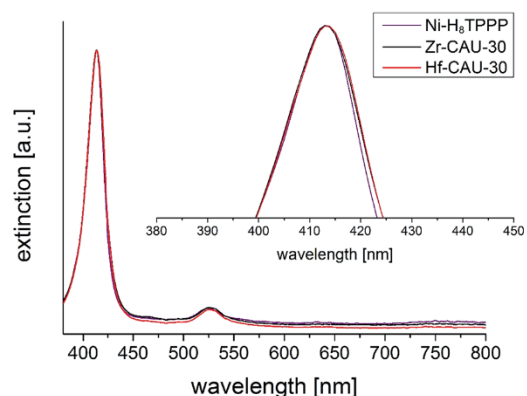


Fig. 11 UV/vis spectra of M-CAU-30 ( $M = \text{Zr}, \text{Hf}$ ) compared with the UV/vis spectrum of the free linker Ni- $\text{H}_8$ TPPP. The absorption maximum (Soret-band) of the Ni- $\text{H}_8$ TPPP linker was in all cases found at  $413$  nm, furthermore the Q1-band was found at  $526$  nm.



buffer (pH 7) with a Ag/AgCl type reference electrode and Pt as counter electrode. The complete CV between  $-1$  and  $1$  V of Zr-CAU-30 (on FTO) in comparison with the pure FTO electrode is shown in Fig. 12. In this CV a reversible redox process at a half-wave potential of  $E_{1/2} = -0.649$  V is observed which demonstrates the redox activity of Zr-CAU-30 under these conditions. In comparison to literature values of Ni-metalated<sup>65,66</sup> and phosphonate groups bearing porphyrin derivatives<sup>48,53</sup> this redox process at  $-0.649$  V can likely be assigned to the reversible reduction of the porphyrin moiety. Furthermore, the cyclic stability was demonstrated by measuring 50 cycles (scan rate =  $250$   $\text{mV s}^{-1}$ ); the first and the 50<sup>th</sup> CV is shown in Fig. S22.† Applying different scan rates between  $50$  and  $1000$   $\text{mV s}^{-1}$  reveals the expected behaviour of increasing currents with the scan rate (Fig. S23†).

## Conclusions

In summary, we have demonstrated the successful synthesis and thorough characterization of two new isostructural highly porous metal phosphonates of composition  $[\text{M}(\text{Ni-H}_2\text{-TTPPP})(\text{OH}/\text{F})_2]$  ( $\text{M} = \text{Zr}, \text{Hf}$ ) (M-CAU-30) containing a Ni-metalated porphyrin-based phosphonate as linker molecule. Although both compounds are only obtained with  $\text{ZrO}_2$  and  $\text{HfO}_2$  as impurities, respectively, sorption measurements result in high specific surface areas of  $970$  and  $910$   $\text{m}^2 \text{g}^{-1}$  for the reaction products which corresponds to values of  $1080$  and  $1030$   $\text{m}^2 \text{g}^{-1}$  for the phase pure materials. Thus they exhibit to the best of our knowledge the highest specific area for porous metal phosphonates ever reported. Furthermore CAU-30 reveals remarkably high thermal and chemical stability of  $400$   $^\circ\text{C}$  and in a pH range between  $0$  and  $12$  as well as in phosphate buffer. The redox activity of Zr-CAU-30 was investigated by cyclic voltammetry resulting in a reversible redox process at a half-wave potential of  $E_{1/2} = -0.649$  V. CAU-30 stands out due to its thermal and chemical stability which makes CAU-30 a promising candidate for many applications discussed in the context of MOFs, from conventional gas-separation to storage over

catalysis or proton conductivity. The fact that a  $\text{Ni}^{2+}$  ion is connected to the centre of the porphyrin ring opens applications in catalysis due to the catalytic activity of the free Ni metal sites. In addition free  $-\text{OH}$  groups of the linker reside in the pores, which makes CAU-30 a possible candidate for proton conductivity where stability in a large pH range is required.

## Experimental

### Materials

$\text{ZrOCl}_2 \cdot 8\text{H}_2\text{O}$  (99.5%, Sigma Aldrich),  $\text{HfCl}_4$  (98%, Sigma Aldrich),  $\text{NiCl}_2 \cdot 6\text{H}_2\text{O}$  (97%, Merck),  $\text{EtOH}$  (99% + 1% MEK, Walther), dichloromethane (Walther), *N,N*-dimethylformamide (99%, Grüssing), acetone (99%, Walther), 100% acetic acid (VWR chemicals),  $\text{NaH}_2\text{PO}_4$  (99%, Sigma-Aldrich) and  $\text{Na}_2\text{HPO}_4$  (99%, Sigma-Aldrich) were used without further purification. The linker Ni-4,4',4'',4'''-(5,10,15,20-porphyrin-tetrayl)-tetraphosphonobenzoic acid (Ni-tetra(4-phosphonophenyl)porphyrin, Ni-H<sub>8</sub>TTPPP) was synthesized according to reported procedures<sup>67–69</sup> starting with 4-bromobenzaldehyde (99%, Sigma Aldrich) and pyrrole (98%, ABCR) in propionic acid (99%, Grüssing) with following  $\text{NiCl}_2$ -catalyzed (97%, Merck) phosphorylation in 1,3-diisopropylbenzene (96%, Sigma-Aldrich) using triethyl phosphite (98%, Sigma-Aldrich) with following hydrolysis in conc.  $\text{HCl}$  (35%, VWR chemicals). Details are given in the ESI.†

### Preparation

The synthesis of M-CAU-30 ( $\text{M} = \text{Zr}, \text{Hf}$ ) was studied using high-throughput methods ( $V_{\text{max}} = 2.0$  mL per Teflon insert) with  $\text{H}_2\text{O}$  as solvent.<sup>70</sup> Reaction temperatures between  $120$  and  $180$   $^\circ\text{C}$ , reaction times between  $6$  and  $48$  h and different molar ratios of metal to linker to NaF to NaOH in a range between  $1 : 1 : 10 : 1$  and  $5 : 1 : 120 : 16$  were employed (1 equivalent corresponds to  $5.3 \times 10^{-3}$  mmol). Various additives like  $\text{HCl}$ , formic or acetic acid were employed, but only the use of NaF in combination with NaOH resulted in highly porous compounds. The influence of fluoride ions in the synthesis of porous Zr-phosphonates has been previously discussed in the literature.<sup>35,41</sup> Furthermore an upscaling of the synthesis of M-CAU-30 in  $30$  mL reactors was successfully carried out by using the 12-fold amounts of all reactants. Reactions under stirring using the 3-fold amounts were carried out in  $5$  mL glass vials. Under these conditions the highly crystalline compounds were already obtained at a reaction temperature of  $160$   $^\circ\text{C}$  within  $3$  h.

The optimized synthesis conditions for both title compounds in  $5$  mL glass vials are given in the following paragraphs.

**Zr-CAU-30.** Ni-H<sub>8</sub>TTPPP ( $15.0$  mg,  $15.9 \times 10^{-3}$  mmol),  $\text{ZrOCl}_2 \cdot 8\text{H}_2\text{O}$  ( $9.8$  mg,  $33.0 \times 10^{-3}$  mmol), NaF ( $38.2$  mg,  $9.6 \times 10^{-1}$  mmol),  $\text{H}_2\text{O}$  ( $3000$   $\mu\text{L}$ ),  $2$  M aqueous solution NaOH ( $60.6$   $\mu\text{L}$ ,  $12.9 \times 10^{-2}$  mmol) were added to a  $5$  mL glass vial and placed in a reaction block on a heating plate. The block was heated for  $3$  h at  $160$   $^\circ\text{C}$  under stirring. The resulting product was centrifuged at  $6000$  rpm for  $10$  min and washed once with  $\text{H}_2\text{O}$  and acetone each. A yield of  $6.7$  mg was obtained which

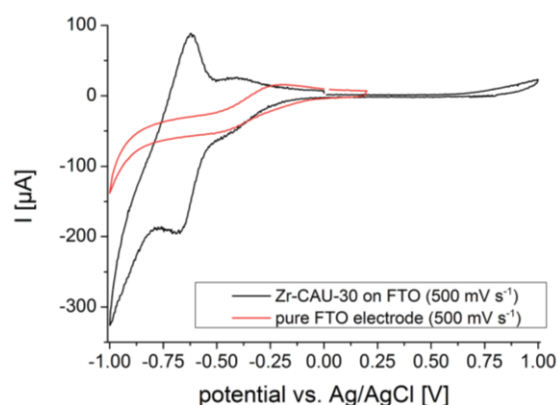


Fig. 12 CV curves of Zr-CAU-30 on FTO (black) and the pure FTO electrode (red) between  $-1$  and  $1$  V and a scan rate of  $500$   $\text{mV s}^{-1}$ .



# Porphyrin-basierte Metall-Organische Gerüstverbindungen: Von Metall-Carboxylaten zu Metall-Phosphonaten

View Article Online

Edge Article

Chemical Science

consist of a mixture of  $ZrO_2$  and Zr-CAU-30,  $[Zr_2(Ni-H_2TPPP)(OH/F)_2] \cdot 23H_2O$ .

Elemental analysis of Zr-CAU-30  $[Zr_2(Ni-H_2TPPP)(OH/F)_2] \cdot 23H_2O$ : calc. (%): C 30.1, H 5.9, N 3.2, found (%): C 28.5, H 3.3, N 3.0. Elemental analysis of a one to one mixture of  $ZrO_2$  and  $[Zr_2(Ni-H_2TPPP)(OH/F)_2] \cdot 23H_2O$ : calc. (%): C 28.9, H 5.0, N 3.1, found (%): C 28.5, H 3.3, N 3.0.

**Hf-CAU-30.** Ni- $H_8$ TPPP (15.0 mg,  $15.9 \times 10^{-3}$  mmol),  $HfCl_4$  (9.7 mg,  $3.3 \times 10^{-2}$  mmol), NaF (38.2 mg,  $9.6 \times 10^{-1}$  mmol),  $H_2O$  (3000  $\mu$ L), 2 M aqueous solution NaOH (60.6  $\mu$ L,  $12.9 \times 10^{-2}$  mmol) were added to a 5 mL glass vial and placed in a reaction block on a heating plate. The block was heated for 3 h at 160 °C under stirring. The resulting product was centrifuged at 6000 rpm for 10 min and washed once with  $H_2O$  and acetone each. A yield of 7.0 mg was obtained which consist of a mixture of  $HfO_2$  and Hf-CAU-30,  $[Hf_2(Ni-H_2TPPP)(OH/F)_2] \cdot 30H_2O$ .

Elemental analysis of Hf-CAU-30  $[Hf_2(Ni-H_2TPPP)(OH/F)_2] \cdot 30H_2O$ : calc. (%): C 29.0, H 5.0, N 3.1, found (%): C 24.9, H 3.5, N 2.6.

Elemental analysis of a one to one mixture of  $HfO_2$  and  $[Hf_2(Ni-H_2TPPP)(OH/F)_2] \cdot 30H_2O$ : calc. (%): C 24.3, H 4.2, N 2.6, found (%): C 24.9, H 3.5, N 2.6.

To activate the samples and to remove X-ray amorphous side-products as observed in form of  $Na^+$  impurities in the EDX analysis the samples were stirred for 24 h in 0.1 M aqueous HCl solution, followed by washing with acetone and activation under reduced pressure of  $10^{-2}$  kPa at 170 °C for 16 h.

## Characterization

The crystal structure of Zr-CAU-30 was investigated by combining electron diffraction tomography with powder diffraction data.

For the TEM experiments (TEM, STEM, ADT, HRTEM), a small quantity of Zr-CAU-30-as was dispersed in ethanol using an ultrasonic bath. The dispersion was transferred into a caved tip with a pipette and then sprayed onto standard 300 mesh Cu TEM grids with a thin amorphous carbon film, using an ultrasonic vaporizer. Phase contrast TEM, scanning TEM (STEM), and automated diffraction tomography (ADT) measurements were carried out using a TECNAI F30 S-TWIN transmission electron microscope equipped with a field emission gun and operating at 300 kV. STEM images were collected using a Fischione high-angle annular dark field (HAADF) detector. TEM images and nano electron diffraction (NED) patterns were acquired with a  $4k \times 4k$  Gatan US4000 CCD camera (Gatan, Pleasanton, USA). In order to increase the stability of the sample under the electron beam, it was cooled down to about 97 K using a cryo-transfer holder filled with liquid  $N_2$  after insertion into TEM. Electron diffraction data were collected with an automated acquisition module developed for FEI microscopes.<sup>14</sup> A Gatan cryotransfer tomography holder (model 914) with a tilt range of  $\pm 70^\circ$  was used for electron diffraction data acquisition. A small condenser aperture of 10  $\mu$ m, weak gun lens and large condenser spot size were used in order to reduce the electron dose rate on the sample. The crystal position was tracked in microprobe STEM mode and electron diffraction

patterns were collected using the above settings. The beam size was set to 100 nm in diameter. In order to integrate reflection intensities over the full tilt wedge, ADT was coupled with precession electron diffraction (PED),<sup>71,72</sup> which was performed using a NanoMEGAS DigStar unit. The precession angle of the beam was kept at 1°. ADT tilt series were collected sequentially in a fixed tilt step of 1°. The exposure time for each frame was set to 3 seconds. TEM in-line holography<sup>73</sup> was realized by focal series reconstruction from image series collected using a TECNAI F30 ST operating at 300 kV, without aberration corrector, under suitable TEM conditions. 20 images were recorded at a primary magnification of 390 000 with 10 nm focal increment, thus covering a focal range of 190 nm including Gaussian focus. The accumulated dose per focal series was about  $90 e^- \text{ \AA}^{-2}$ . The images were hardware-binned by 2 resulting in  $2k \times 2k$  images with a physical pixel size of 0.057 nm. After image alignment, a  $320 \times 320$  pixel region was chosen for exit wave reconstruction, employing a Gerchberg-Saxton algorithm programmed in Python. Residual axial aberrations were corrected by an automated minimization routine implemented in Python.

Further TEM investigations, standard ED and energy dispersive X-ray (EDX) spectroscopy were performed on a Tecnai G2 20 S-TWIN (FEI) at 200 kV and on a Titan Themis 60-300 (FEI) equipped with a SuperX EDX detector, operated at 300 kV.

Crystal structure solution of Zr-CAU-30-as was carried out from ADT data. The ADT3D software<sup>15,72</sup> was used for processing the three-dimensional electron diffraction data yielding unit-cell parameters, symmetry information and reflection intensities. The unit-cell parameters were refined with a Pawley fit against PXRD data. The *ab initio* structure solution using direct methods as implemented in SIR2014 (ref. 74) was based on the reflection intensities derived from electron diffraction data.

IR spectra were recorded using a Bruker ALPHA-FT-IR A220/D-01 spectrometer equipped with an ATR-unit. Additional FTIR spectra of an *in situ* activated sample of Zr-CAU-30 were recorded on a Thermo-Fischer NICOLET 6700 spectrometer featuring a DTGS detector. The material was pressed into both a self-supporting pellet and a KBr pellet containing 2.5 wt% Zr-CAU-30. Prior to measurements, adsorbed water was removed *in situ* by heating the pellets at 200 °C for 2 h under vacuum. Spectra of 128 scans were recorded at 25 °C in the 500–4000  $cm^{-1}$  range, with a 2  $cm^{-1}$  resolution. UV/vis spectra were recorded on a Spectroquant Pharo 300 M spectrometer. For the measurement 0.1 mg of the respective sample was dissolved in 1 mL 2 M aqueous NaOH solution and diluted with water to a total volume of 5 mL. Afterwards a 4 mL cuvette was filled with 3 mL water and 120  $\mu$ L of the porphyrin containing solution was added to the cuvette and subsequently measured. The  $^1H$ - and  $^{31}P$ -NMR spectra of the Ni- $H_8$ TPPP linker were recorded on a Bruker DRX 500 spectrometer after digestion in  $DMSO-d_6$ . Sorption experiments were performed with a BEL Japan Inc. BELSORP-max. Before sorption measurements all samples were activated at 170 °C under reduced pressure ( $10^{-2}$  kPa) for 16 h. Thermogravimetric measurements were performed on a NETZSCH STA 409 CD analyser under a flow of air (75  $mL \text{ min}^{-1}$ ) with a heating rate of 4 °C  $\text{min}^{-1}$  between 25 and 1000 °C in  $Al_2O_3$  crucibles. The data were corrected for buoyancy



and current effects. Cyclic voltammograms (CV) were measured on a EG&G Princeton Applied Research/Model 273A with Ag/AgCl 207 mV vs. NHE type reference electrode and Pt as counter electrode. As electrolyte 0.1 M phosphate buffer (pH 7) and as working electrode FTO (fluorine doped tin oxide) on glass (Sigma) 100 nm thickness, surface resistivity 7 ohm per cm<sup>2</sup> was employed. For the preparation of the FTO electrode 5 mg Zr-CAU-30, 30 μL Nafion (5% in lower aliphatic alcohols and water) and 143 μL EtOH were added to 857 μL H<sub>2</sub>O followed by ultrasonication for 30 min. The mixture was dropcasted on a 1 cm<sup>2</sup> area of the FTO electrode and dried overnight under atmospheric conditions.

### Structure refinement

The PXRD pattern of the activated compound matches well with a tetragonal unit cell related to the one observed by electron diffraction methods. In comparison to the PXRD pattern of Zr-CAU-30-as additional reflections are observed in the PXRD pattern of Zr-CAU-30-act which indicates a change of symmetry upon thermal treatment. The detailed analysis of the extinction conditions indicate the space group *I*<sub>4</sub>*cd* (no. 110) for CAU-30-act with a lower symmetry than observed for Zr-CAU-30-as (*I*<sub>4</sub>/*acd* no. 142) from electron diffraction data. Starting with the crystal structure of the framework as determined from electron diffraction data, we set up a model by first converting the space group symmetry from *I*<sub>4</sub>/*acd* to *I*<sub>4</sub>*cd* using Powdercell<sup>58</sup> and subsequent optimisation of the structure using the universal force field as implemented in Materials Studio.<sup>59</sup> While the small number of reflections in combination with the very large unit cell prevented a full refinement, the crystal structure could still be approximated by Rietveld methods using TOPAS.<sup>75</sup> Hence, the position of the porphyrin moiety was kept fixed and the phenylphosphonate fragments were treated as rigid bodies while the remaining zirconium and oxygen atom were only refined along their *x* and *y* coordinates. Moreover the intensities can be only fitted when considering a preferred orientation along (110) and taking into account some residual electron density, represented by partially occupied oxygen atoms (designated as *Gn*). The electron density of *G1* is positioned in chemically unreasonable distance to the linker molecules (1.7(3) Å) and therefore we assume that this rather indicates further positional disorder of the linker molecules in the crystal structure. However, further modelling of this disorder is beyond the capability of the method, also taking into account the quality of the PXRD data. Residual electron density in the pores were refined as oxygen atoms of water molecules. This fact indicates that a complete removal of all solvent molecules is not possible by activation at elevated temperatures in vacuum. Some relevant final parameters and the final plot for the Rietveld-based approximation are given in Table 1 and Fig. S7b.†

High resolution PXRD patterns were measured on a STOE Stadi-P combi powder diffractometer equipped with a Mythen detector (Cu K $\alpha_1$  radiation). Pawley fits (Fig. S7a, c†) were carried out for M-CAU-30 (M = Zr, Hf) to confirm phase purity. Pawley fits were performed with the program TOPAS Academic

V4.1.<sup>75</sup> The results of the refinements and crystallographic data of M-CAU-30 are shown in Table 1. The diameters of all pores were determined using DIAMOND V.3 (ref. 76) taking the van der Waals radii of the atoms into account. The variable temperature (VT) PXRD measurements were recorded on a STOE Stadi-P combi powder diffractometer (Mo K $\alpha_1$  radiation) equipped with a capillary furnace. For the measurements 0.5 mm quartz capillaries were used. The samples were heated up in steps of 5 K between 250 and 450 °C and measured for 10 minutes each.

### Conflicts of interest

There are no conflicts to declare.

### Acknowledgements

Haishuang Zhao gratefully acknowledges the financial support by Carl Zeiss Stiftung. We thank Dr B. Barton, University of Mainz, for the help with the acquisition of HRTEM data. Prof. E. Kemnitz (HU Berlin) is kindly acknowledged for determining the F contents of the samples.

### Notes and references

† Crystal data: Zr<sub>2</sub>O<sub>21.1</sub>P<sub>4</sub>C<sub>44</sub>N<sub>4</sub>Ni<sub>1</sub>, *M* = 1285.5 g mol<sup>-1</sup>, tetragonal, *a* = *b* = 44.7776(58), *b* = 15, *c* = 7.6581(39) Å and  $\alpha = \beta = \gamma = 90^\circ$ , *U* = 15 354(8) Å<sup>3</sup>, *T* = 298 K, space group *I*<sub>4</sub>*cd* (no. 110), *Z* = 8. The final *R*<sub>w</sub>p was 3.8% and the *g* of 2.0%.

- H. Furukawa, K. E. Cordova, M. O'Keeffe and O. M. Yaghi, *Science*, 2013, **341**, 1–12.
- N. Stock, H. Reinsch and L.-H. Schilling, in *Metal Organic Frameworks as Heterogeneous Catalysts*, The Royal Society of Chemistry, 2013, pp. 9–30, DOI: 10.1039/9781849737586-00009.
- H.-C. Zhou, J. R. Long and O. M. Yaghi, *Chem. Rev.*, 2012, **112**, 673–674.
- O. M. Yaghi, M. O'Keeffe, N. W. Ockwig, H. K. Chae, M. Eddaoudi and J. Kim, *Nature*, 2003, **423**, 705–714.
- C.-Y. Sun, C. Qin, X.-L. Wang and Z.-M. Su, *Expert Opin. Drug Delivery*, 2013, **10**, 89–101.
- C. Janiak and J. K. Vieth, *New J. Chem.*, 2010, **34**, 2366–2388.
- U. Mueller, M. Schubert, F. Teich, H. Puetter, K. Schierle-Arndt and J. Pastre, *J. Mater. Chem.*, 2006, **16**, 626–636.
- M. Bosch, M. Zhang and H.-C. Zhou, *Adv. Chem.*, 2014, **2014**, 8.
- M. Kim and S. M. Cohen, *CrystEngComm*, 2012, **14**, 4096–4104.
- Y. Bai, Y. Dou, L.-H. Xie, W. Rutledge, J.-R. Li and H.-C. Zhou, *Chem. Soc. Rev.*, 2016, **45**, 2327–2367.
- T. Devic and C. Serre, *Chem. Soc. Rev.*, 2014, **43**, 6097–6115.
- J. H. Cavka, S. Jakobsen, U. Olsbye, N. Guillou, C. Lamberti, S. Bordiga and K. P. Lillerud, *J. Am. Chem. Soc.*, 2008, **130**, 13850–13851.
- O. I. Lebedev, F. Millange, C. Serre, G. Van Tendeloo and G. Férey, *Chem. Mater.*, 2005, **17**, 6525–6527.

# Porphyrin-basierte Metall-Organische Gerüstverbindungen: Von Metall-Carboxylaten zu Metall-Phosphonaten

View Article Online

Edge Article

Chemical Science

- 14 U. Kolb, T. Gorelik, C. Kübel, M. T. Otten and D. Hubert, *Ultramicroscopy*, 2007, **107**, 507–513.
- 15 U. Kolb, T. Gorelik and M. T. Otten, *Ultramicroscopy*, 2008, **108**, 763–772.
- 16 B. Ravnsbæk Dorthe, Y. Filinchuk, R. Cerný and R. Jensen Torben, *Z. Kristallogr.*, 2010, **225**, 557.
- 17 J. Jiang, J. L. Jorda, J. Yu, L. A. Baumes, E. Mugnaioli, M. J. Diaz-Cabanas, U. Kolb and A. Corma, *Science*, 2011, **333**, 1131–1134.
- 18 H. Zhao, Y. Krysiak, K. Hoffmann, B. Barton, L. Molina-Luna, R. B. Neder, H.-J. Kleebe, T. M. Gesing, H. Schneider, R. X. Fischer and U. Kolb, *J. Solid State Chem.*, 2017, **249**, 114–123.
- 19 M. B. Mesch, K. Bärwinkel, Y. Krysiak, C. Martineau, F. Taulelle, R. B. Neder, U. Kolb and J. Senker, *Chem.–Eur. J.*, 2016, **22**, 16878–16890.
- 20 M. Feyand, E. Mugnaioli, F. Vermoortele, B. Bueken, J. M. Dieterich, T. Reimer, U. Kolb, D. De Vos and N. Stock, *Angew. Chem., Int. Ed.*, 2012, **51**, 10373–10376.
- 21 J. Hynek, P. Brázda, J. Rohlíček, G. S. Londesborough Michael and J. Demel, *Angew. Chem., Int. Ed.*, 2018, **57**, 5016–5019.
- 22 T. C. Wang, N. A. Vermeulen, I. S. Kim, A. B. F. Martinson, J. F. Stoddart, J. T. Hupp and O. K. Farha, *Nat. Protoc.*, 2016, **11**, 149–162.
- 23 D. Feng, Z.-Y. Gu, J.-R. Li, H.-L. Jiang, Z. Wei and H.-C. Zhou, *Angew. Chem.*, 2012, **124**, 10453–10456.
- 24 W. Morris, B. Voloskiy, S. Demir, F. Gándara, P. L. McGrier, H. Furukawa, D. Cascio, J. F. Stoddart and O. M. Yaghi, *Inorg. Chem.*, 2012, **51**, 6443–6445.
- 25 E.-X. Chen, M. Qiu, Y.-F. Zhang, Y.-S. Zhu, L.-Y. Liu, Y.-Y. Sun, X. Bu, J. Zhang and Q. Lin, *Adv. Mater.*, 2018, **30**, 1704388.
- 26 Y.-Z. Chen and H.-L. Jiang, *Chem. Mater.*, 2016, **28**, 6698–6704.
- 27 R. G. Pearson, *J. Am. Chem. Soc.*, 1963, **85**, 3533–3539.
- 28 G. K. H. Shimizu, R. Vaidhyanathan and J. M. Taylor, *Chem. Soc. Rev.*, 2009, **38**, 1430–1449.
- 29 R. A. Coxall, S. G. Harris, D. K. Henderson, S. Parsons, P. A. Tasker and R. E. P. Winpenny, *J. Chem. Soc., Dalton Trans.*, 2000, 2349–2356, DOI: 10.1039/B001404O.
- 30 Y.-P. Zhu, T.-Y. Ma, Y.-L. Liu, T.-Z. Ren and Z.-Y. Yuan, *Inorg. Chem. Front.*, 2014, **1**, 360–383.
- 31 A. Clearfield and J. A. Stynes, *J. Inorg. Nucl. Chem.*, 1964, **26**, 117–129.
- 32 A. Clearfield and G. D. Smith, *Inorg. Chem.*, 1969, **8**, 431–436.
- 33 M. B. Dines, R. E. Cooksey, P. C. Griffith and R. H. Lane, *Inorg. Chem.*, 1983, **22**, 1003–1004.
- 34 M. Taddei, F. Costantino and R. Vivani, *Eur. J. Inorg. Chem.*, 2016, **2016**, 4300–4309.
- 35 K. J. Gagnon, H. P. Perry and A. Clearfield, *Chem. Rev.*, 2012, **112**, 1034–1054.
- 36 S. Bauer, H. Müller, T. Bein and N. Stock, *Inorg. Chem.*, 2005, **44**, 9464–9470.
- 37 N. Stock, A. Stoll and T. Bein, *Microporous Mesoporous Mater.*, 2004, **69**, 65–69.
- 38 M. Taddei, F. Costantino and R. Vivani, *Inorg. Chem.*, 2010, **49**, 9664–9670.
- 39 M. Taddei, F. Costantino, F. Marmottini, A. Comotti, P. Sozzani and R. Vivani, *Chem. Commun.*, 2014, **50**, 14831–14834.
- 40 M. Taddei, F. Costantino, R. Vivani, S. Sabatini, S.-H. Lim and S. M. Cohen, *Chem. Commun.*, 2014, **50**, 5737–5740.
- 41 R. K. Mah, B. S. Gelfand, J. M. Taylor and G. K. H. Shimizu, *Inorg. Chem. Front.*, 2015, **2**, 273–277.
- 42 C.-Y. Gao, J. Ai, H.-R. Tian, D. Wu and Z.-M. Sun, *Chem. Commun.*, 2017, **53**, 1293–1296.
- 43 T. Zheng, Z. Yang, D. Gui, Z. Liu, X. Wang, X. Dai, S. Liu, L. Zhang, Y. Gao, L. Chen, D. Sheng, Y. Wang, J. Diwu, J. Wang, R. Zhou, Z. Chai, T. E. Albrecht-Schmitt and S. Wang, *Nat. Commun.*, 2017, **8**, 15369.
- 44 S. Huh, S.-J. Kim and Y. Kim, *CrystEngComm*, 2016, **18**, 345–368.
- 45 W.-Y. Gao, M. Chrzanowski and S. Ma, *Chem. Soc. Rev.*, 2014, **43**, 5841–5866.
- 46 T. Rhauderwiek, K. Wolkersdorfer, S. Oien-Odegaard, K.-P. Lillerud, M. Wark and N. Stock, *Chem. Commun.*, 2018, **54**, 389–392.
- 47 Y. Fang, Y. G. Gorbunova, P. Chen, X. Jiang, M. Manowong, A. A. Sinelshchikova, Y. Y. Enakieva, A. G. Martynov, A. Y. Tsivadze, A. Bessmertnykh-Lemeune, C. Stern, R. Guilard and K. M. Kadish, *Inorg. Chem.*, 2015, **54**, 3501–3512.
- 48 K. M. Kadish, P. Chen, Y. Y. Enakieva, S. E. Nefedov, Y. G. Gorbunova, A. Y. Tsivadze, A. Bessmertnykh-Lemeune, C. Stern and R. Guilard, *J. Electroanal. Chem.*, 2011, **656**, 61–71.
- 49 D. Deniaud, B. Schollorn, D. Mansuy, J. Rouxel, P. Battioni and B. Bujoli, *Chem. Mater.*, 1995, **7**, 995–1000.
- 50 D. Deniaud, G. A. Spyroulias, J.-F. Bartoli, P. Battioni, D. Mansuy, C. Pinel, F. Odobel and B. Bujoli, *New J. Chem.*, 1998, **22**, 901–905.
- 51 N. Venkatramaiah, C. F. Pereira, R. F. Mendes, F. A. A. Paz and J. P. C. Tomé, *Anal. Chem.*, 2015, **87**, 4515–4522.
- 52 N. Venkatramaiah, C. F. Pereira, R. F. Mendes, F. A. A. Paz and J. P. C. Tomé, *Anal. Chem.*, 2015, **87**, 4515–4522.
- 53 F. Odobel, E. Blart, M. Lagree, M. Villieras, H. Boujtita, N. El Murr, S. Caramori and C. Alberto Bignozzi, *J. Mater. Chem.*, 2003, **13**, 502–510.
- 54 M. De Napoli, S. Nardis, R. Paolesse, M. G. H. Vicente, R. Lauceri and R. Purrello, *J. Am. Chem. Soc.*, 2004, **126**, 5934–5935.
- 55 R. Lauceri, M. De Napoli, A. Mammanna, S. Nardis, A. Romeo and R. Purrello, *Synth. Met.*, 2004, **147**, 49–55.
- 56 P. Kubát, K. Lang, P. Janda and P. Anzenbacher, *Langmuir*, 2005, **21**, 9714–9720.
- 57 P. Kubát, K. Lang and Z. Zelinger, *J. Mol. Liq.*, 2007, **131–132**, 200–205.
- 58 W. Kraus and G. Nolze, *J. Appl. Crystallogr.*, 1996, **29**, 301–303.
- 59 *Materials Studio Version 5.0*, Accelrys Inc., San Diego, CA, 2009.

# Porphyrin-basierte Metall-Organische Gerüstverbindungen: Von Metall-Carboxylaten zu Metall-Phosphonaten

[View Article Online](#)

Chemical Science

[Edge Article](#)

- 60 J. Rouquerol, D. Avnir, C. W. Fairbridge, D. H. Everett, J. M. Haynes, N. Pernicone, J. D. F. Ramsay, K. S. W. Sing and K. K. Unger, *Pure Appl. Chem.*, 1994, **66**, 1739–1758.
- 61 M. Thommes, K. Kaneko, V. Neimark Alexander, P. Olivier James, F. Rodriguez-Reinoso, J. Rouquerol and S. W. Sing Kenneth, *Pure Appl. Chem.*, 2015, **87**, 1051–1069.
- 62 J. O. Alben, S. S. Choi, A. D. Adler and W. S. Caughey, *Ann. N. Y. Acad. Sci.*, 1973, **206**, 278–295.
- 63 K. D. Demadis and S. D. Katarachia, *Phosphorus, Sulfur Silicon Relat. Elem.*, 2004, **179**, 627–648.
- 64 L. D. Quin, *A Guide to Organophosphorus Chemistry*, Wiley, 2000.
- 65 J. M. a. Pedrosa, M. a. T. Martín, J. J. Ruiz and L. Camacho, *J. Electroanal. Chem.*, 2002, **523**, 160–168.
- 66 K. M. Kadish, M. Lin, E. V. Caemelbecke, G. De Stefano, C. J. Medforth, D. J. Nurco, N. Y. Nelson, B. Krattinger, C. M. Muzzi, L. Jaquinod, Y. Xu, D. C. Shyr, K. M. Smith and J. A. Shelnutt, *Inorg. Chem.*, 2002, **41**, 6673–6687.
- 67 A. D. Adler, F. R. Longo, F. Kampas and J. Kim, *J. Inorg. Nucl. Chem.*, 1970, **32**, 2443–2445.
- 68 A. D. Adler, F. R. Longo, J. D. Finarelli, J. Goldmacher, J. Assour and L. Korsakoff, *J. Org. Chem.*, 1967, **32**, 476.
- 69 P. Tavs, *Chem. Ber.*, 1970, **103**, 2428–2436.
- 70 N. Stock, *Chem. Ing. Tech.*, 2010, **82**, 1039–1047.
- 71 R. Vincent and P. A. Midgley, *Ultramicroscopy*, 1994, **53**, 271–282.
- 72 E. Mugnaioli, T. Gorelik and U. Kolb, *Ultramicroscopy*, 2009, **109**, 758–765.
- 73 F.-R. Chen, C. Kisielowski and D. Van Dyck, *Adv. Struct. Chem. Imaging*, 2017, **3**, 8.
- 74 M. C. Burla, R. Caliandro, B. Carrozzini, G. L. Cascarano, C. Cuocci, C. Giacovazzo, M. Mallamo, A. Mazzone and G. Polidori, *J. Appl. Crystallogr.*, 2015, **48**, 306–309.
- 75 A. Coelho, *Topas Academic 4.1*, 2007.
- 76 K. Brandenburg, *Diamond Version 3*, Crystal Impact GbR, Bonn, 2012.



## 5 Zusammenfassung

Die Ergebnisse dieser Arbeit lassen sich in zwei Bereiche einteilen:

1. Poröse Metall-Carboxylate mit dem  $H_6$ TCP P Linker (Tetra(4-carboxyphenyl)porphyrin)
2. Poröse Metall-Phosphonate mit dem  $Ni-H_8$ T P P P Linker (Ni-tetra(4-phosphonophenyl)porphyrin)

In dieser Arbeit wurden mit dem  $H_6$ TCP P Linker (Abb. 19) drei isostrukturelle Verbindungen zu dem bereits publizierten Al-PMOF<sup>85</sup> mit  $Ga^{3+}$ ,<sup>86</sup>  $In^{3+}$ <sup>86</sup> und  $Ce^{3+}$ <sup>148</sup> erhalten. Des weiteren wurden zwei neue Ce-MOFs, CAU-18 und CAU-19-X entdeckt, wobei CAU-19-X mit sieben unterschiedlichen Benzoesäurederivaten (HBA-X, X= H, 2Cl, 3Cl, 4Cl, 3CO<sub>2</sub>H, 4NH<sub>2</sub>, 4NO<sub>2</sub>) als Co-Liganden synthetisiert werden konnte.

Ebenfalls wurde der neue  $Ni-H_8$ T P P P Linker (Ni-tetra(4-phosphonophenyl)porphyrin, Abb. 19) erhalten und in der Synthese von drei neuen MOFs eingesetzt. M-CAU-29 (M= Mn, Co, Ni, Cd), M-CAU-30 (M= Zr, Hf) und Co-CAU-36 sind alle (außer Ni-CAU-29) porös gegenüber N<sub>2</sub> bei 77 K und Zr-CAU-30 ist das Metall-Phosphonat mit der bisher höchsten Porosität aller publizierten Metall-Phosphonate.

Insgesamt wurden in dieser Arbeit 19 Porphyrin-basierte MOFs synthetisiert und dabei sechs neue MOF-Strukturen entdeckt, welche in Tabelle 07 mit Summenformeln, kristallographischen Parametern sowie Sorptionseigenschaften zusammengefasst sind.

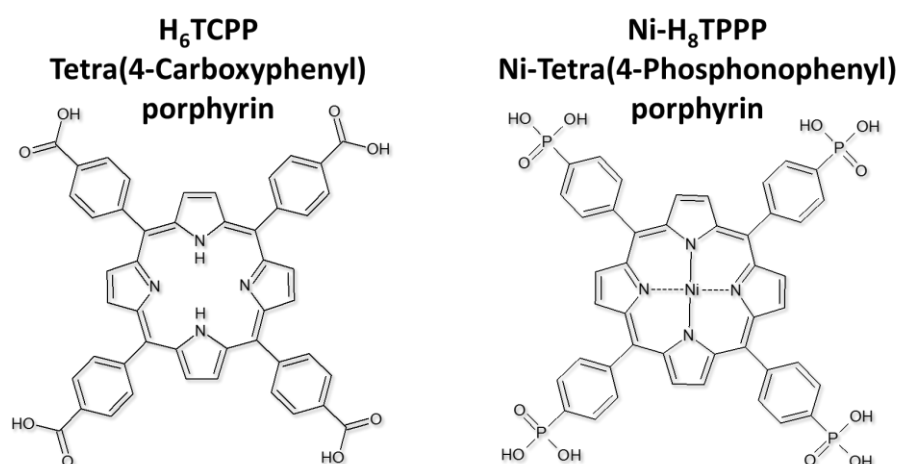


**Abbildung 19.** Die zwei in dieser Arbeit verwendeten Linkermoleküle  $H_6$ TCP P und  $Ni-H_8$ T P P P.

## Zusammenfassung

**Tabelle 07.** Übersicht über die in dieser Arbeit synthetisierten MOFs. Es sind der Name, die Summenformel, Sorptionseigenschaften (spezifische Oberfläche nach BET in  $\text{m}^2 \text{g}^{-1}$ ,  $\text{N}_2$  bei 77 K) und die kristallographischen Parameter (Raumgruppe,  $a$ ,  $b$ ,  $c$ , [ $\text{\AA}$ ]  $\alpha$ ,  $\beta$ ,  $\gamma$  [ $^\circ$ ]) angegeben. HBA-X= Benzoesäure-X =  $\text{C}_7\text{H}_5\text{O}_2\text{-X}$  (X= H, 2Cl, 3Cl, 4Cl,  $3\text{CO}_2\text{H}$ ,  $4\text{NH}_2$ ,  $4\text{NO}_2$ )

Name	Summenformel	Sorptions Eigenschaften	RG + Zelle
<b>H<sub>6</sub>TCPP</b>			
Ga-PMOF	$[\text{Ga}_2(\text{OH})_2(\text{H}_2\text{TCPP}) \cdot 3\text{DMF} \cdot 3\text{H}_2\text{O}]$	1150	<i>Cmmm</i> 32.950(4), 6.700(2), 16.556(2) $\text{\AA}$
In-PMOF	$[\text{In}_2(\text{OH})_2(\text{H}_2\text{TCPP}) \cdot 3\text{DMF} \cdot 4\text{H}_2\text{O}]$	1200	<i>Cmmm</i> 33.432(2), 7.152(1), 16.718(1) $\text{\AA}$
Ce-PMOF-4NO <sub>2</sub>	$[\text{Ce}_2(\text{BA-4NO}_2)_2(\text{H}_2\text{TCPP}) \cdot 2\text{DMF}]$	nicht stabil	<i>Cmmm</i> 33.077(3), 7.309(2), 16.539(2) $\text{\AA}$
Ce-CAU-18	$[\text{Ce}_4(\text{H}_2\text{TCPP})_3(\text{DMF})_2(\text{H}_2\text{O})_4]$	nicht porös	<i>C2/c</i> 20.755(5), 23.572(6), 30.642(8) $\text{\AA}$ ; 104.573(2) $^\circ$
Ce-CAU-18a	$[\text{Ce}_4(\text{H}_2\text{TCPP})_3 \cdot 22\text{H}_2\text{O}]$	550	<i>P2/c</i> 22.420(3), 23.248(3), 34.419(5) $\text{\AA}$ ; 106.375(5) $^\circ$
Ce-CAU-19-X	$[\text{Ce}_3(\text{H}_2\text{TCPP})_2(\text{BA-X})(\text{HBA-X}/\text{H}_2\text{O})_2] \cdot 2 \text{HBA-X} \cdot n \text{H}_2\text{O}$	600 (H) 590 (2Cl) 580 (3Cl) 480 (4Cl) 490 (3CO <sub>2</sub> H) 330 (4NH <sub>2</sub> ) 400 (4NO <sub>2</sub> )	für X=H: <i>P<math>\bar{1}</math></i> 11.665(7), 13.915(8), 17.343(10) $\text{\AA}$ ; 95.514(4), 99.792(4), 101.313(5) $^\circ$
<b>Ni-H<sub>8</sub>TPPP</b>			
Mn-CAU-29	$[\text{Mn}(\text{Ni-H}_6\text{TPPP})(\text{H}_2\text{O}) \cdot 9 \text{H}_2\text{O}]$	90	<i>P<math>\bar{1}</math></i> 9.761(2), 15.055(5), 17.022(6) $\text{\AA}$ ; 94.168(7), 96.809(20), 97.057(17) $^\circ$
Co-CAU-29	$[\text{Co}(\text{Ni-H}_6\text{TPPP})(\text{H}_2\text{O}) \cdot 11 \text{H}_2\text{O}]$	145	<i>P<math>\bar{1}</math></i> 9.6860(7), 15.1223(18), 16.7747(22) $\text{\AA}$ ; 94.751(3), 97.412(8), 97.288(8) $^\circ$
Ni-CAU-29	$[\text{Ni}(\text{Ni-H}_6\text{TPPP})(\text{H}_2\text{O}) \cdot 11 \text{H}_2\text{O}]$	0	<i>P<math>\bar{1}</math></i> 9.561(5), 15.086(9), 16.722(9) $\text{\AA}$ ; 94.723(9), 97.602(9), 7.880(9) $^\circ$
Cd-CAU-29	$[\text{Cd}(\text{Ni-H}_6\text{TPPP})(\text{H}_2\text{O}) \cdot 8 \text{H}_2\text{O}]$	180	<i>P<math>\bar{1}</math></i> 9.691(3), 15.067(7), 16.722(9) $\text{\AA}$ ; 94.638(10), 97.158(35), 97.489(29) $^\circ$
Zr-CAU-30	$[\text{Zr}_2(\text{Ni-H}_2\text{TPPP})(\text{OH}/\text{F})_2 \cdot 23 \text{H}_2\text{O}]$	1070	<i>I4<sub>1</sub>cd</i> 44.778(6), 44.778(6), 7.658(4) $\text{\AA}$
Hf-CAU-30	$[\text{Hf}_2(\text{Ni-H}_2\text{TPPP})(\text{OH}/\text{F})_2 \cdot 30 \text{H}_2\text{O}]$	1030	<i>I4<sub>1</sub>cd</i> 45.040(5), 45.040(5), 8.049(3) $\text{\AA}$
Co-CAU-36	$[\text{Co}_2(\text{Ni-H}_4\text{TPPP}) \cdot 2\text{DABCO} \cdot 6\text{H}_2\text{O}]$	700	<i>P<math>\bar{4}c2</math></i> 21.980(5), 21.980(5), 8.960(2) $\text{\AA}$

## 5.1 Poröse Metall-Carboxylate mit dem H<sub>6</sub>TCP Porphyrin Linker (Tetra(4-carboxyphenyl)porphyrin)

Die porösen Metall-Carboxylate mit dem H<sub>6</sub>TCP Porphyrin Linker, welche in dieser Arbeit synthetisiert wurden enthalten ausschließlich dreiwertige Kationen (Ga<sup>3+</sup>, In<sup>3+</sup>, Ce<sup>3+</sup>), wobei in der Synthese der Ce-MOFs die Verbindung NH<sub>4</sub>[Ce<sup>IV</sup>(NO<sub>3</sub>)<sub>6</sub>] als Edukt eingesetzt und das Ce<sup>4+</sup>- Ion während der Reaktion zu Ce<sup>3+</sup> reduziert wurde.

1. Alle erhaltenen Porphyrin-basierten Metall-Carboxylate wurden unter ähnlichen Synthesebedingungen (molares Linker : Metall Verhältnis von 1 : 2) erhalten. Bei 120 °C Reaktionstemperatur sowie der Verwendung von DMF/ Wasser Gemischen (3 : 1 – 20 : 1) konnten kristalline und poröse Verbindungen erhalten werden.
2. Alle erhaltenen Porphyrin-basierten Metall-Carboxylate weisen untereinander ebenfalls strukturelle Ähnlichkeit auf. Es werden in allen Fällen (außer für CAU-18) eindimensionale anorganische Baueinheiten erhalten, welche durch den Linker verknüpft werden. Ebenfalls liegen die Linker Moleküle in allen Verbindungen hintereinander gestapelt vor (Abb. 20).

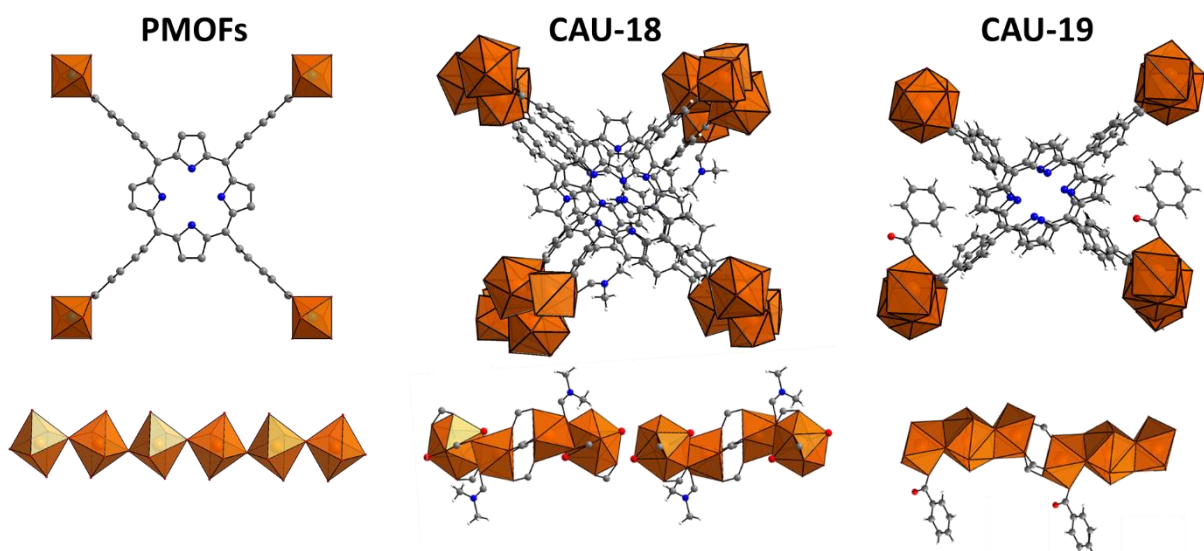


**Abbildung 20.** Vergleich der anorganischen Baueinheiten sowie der Stapelung der Porphyrine in den in dieser Arbeit synthetisierten Metall-Carboxylaten.

3. Ga-, In- und Ce-PMOF sind alle isostrukturell zu dem bereits publizierten Al-PMOF  $[\text{Al}_2(\text{H}_2\text{TCPP})(\text{OH})_2]$ , wobei im Falle des Ce-PMOFs die 4-Nitro-Benzoationen die  $\mu\text{-OH}$  Gruppen, welche in der anorganischen Baueinheit der anderen PMOFs zu finden sind, ersetzen (Abb. 21). Während Ce-PMOF-4NO<sub>2</sub> nicht porös gegenüber N<sub>2</sub> bei 77 K ist, zeigen Ga- und In-PMOF ähnliche spezifische Oberflächen nach BET zum publizierten Al-PMOF von 1150-1400 m<sup>2</sup> g<sup>-1</sup>.

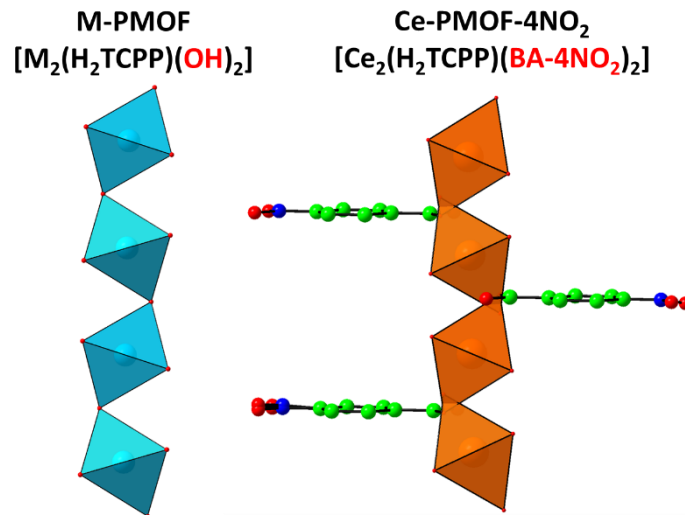


**Abbildung 21.** Vergleich der anorganischen Baueinheiten von M-PMOF (links, M=Al, Ga, In) und Ce-PMOF-4NO<sub>2</sub> (rechts). Die Kohlenstoffatome der 4-Nitro-Benzoensäure sind der Übersichtlichkeit halber grün dargestellt.

4. Für die Darstellung von Ga- und In-PMOF wurde ebenfalls der Einfluss der Synthesemethode auf die Partikelgröße untersucht. Dabei wurde festgestellt, dass durch Einsatz von Ultraschall bzw. der Synthese in einem Flussreaktor kleinere Partikel erhalten werden, als bei dem Einsatz von Hochdurchsatzreaktoren. Die Partikelgrößen lagen dabei in Abhängigkeit der Synthesemethode zwischen 65(18) und 132(25) nm, was mittels REM, TEM und DLS untersucht wurde. Je kleiner die Partikel waren, desto höhere spezifische Oberflächen nach BET wurden erhalten.
5. Bei dem Versuch Ce(IV) Analoga zu den bekannten Porphyrin-basierten Zr-MOFs zu erhalten, wurden unter Einsatz von  $\text{NH}_4[\text{Ce}^{\text{IV}}(\text{NO}_3)_6]$  und verschiedenen Co-Liganden drei neue MOF-Strukturen entdeckt, wobei das Ce(IV)-Ion während der Synthese zu Ce(III) reduziert wurde.



- a. CAU-18,  $[\text{Ce}_4(\text{H}_2\text{TCP})_3(\text{DMF})_2(\text{H}_2\text{O})_4]$ , wird in Abwesenheit eines Co-Liganden erhalten und ist nicht porös gegenüber  $\text{N}_2$  bei 77 K, zeigt jedoch eine Phasenumwandlung zu dem porösen CAU-18a,  $[\text{Ce}_4(\text{H}_2\text{TCP})_3]$  ( $a_{\text{BET}}=550 \text{ m}^2 \text{ g}^{-1}$ ), durch thermische Behandlung für 24 h bei 250 °C. Die Struktur von CAU-18 konnte aus Einkristallen bestimmt werden, wobei für die Struktur von CAU-18a lediglich ein Strukturmodell entwickelt werden konnte, da die Verbindung nur eine geringe strukturelle Fernordnung aufwies.
- b. CAU-19-X,  $[\text{Ce}_3(\text{H}_2\text{TCP})_2(\text{BA-X})(\text{HBA-X}/\text{H}_2\text{O})_2] \cdot 2 \text{ HBA-X} \cdot n \text{ H}_2\text{O}$  (HBA-X= X-Benzoesäure, X= H, 2Cl, 3Cl, 4Cl, 3CO<sub>2</sub>H, 4NH<sub>2</sub>), kann mit verschiedenen Benzoessäurederivaten synthetisiert werden. Alle Derivate sind porös gegenüber  $\text{N}_2$  bei 77 K, wobei spezifische Oberflächen nach BET zwischen 330 und 600  $\text{m}^2 \text{ g}^{-1}$  ermittelt wurden. Die Struktur von CAU-19-H wurde aus Röntgenbeugungsdaten an Einkristallen bestimmt, wobei die Zellparameter der anderen CAU-19-X Derivate durch Pawley-Verfeinerungen bestimmt wurden.
- c. Ausgehend von der Synthese von CAU-19-H und dem Einsatz von 4-Nitro-Benzoesäure wurde Ce-PMOF-4NO<sub>2</sub> erhalten. Diese Verbindung ist jedoch nicht stabil und wandelt sich langsam an Luft bzw. innerhalb von 72 h in Aceton bei 70 °C in CAU-19-4NO<sub>2</sub> um, welches wiederum stabil ist und vollständig charakterisiert werden konnte.
- d. Aufgrund der kurzen Reaktionszeiten die zur Darstellung von CAU-18 und CAU-19-H nötig sind, wurde die Kristallisation beider Verbindungen mittels *in situ* Synchrotron Pulverdiffraktometrie an den Beamlines P09 und P07B, DESY, Hamburg untersucht. Dabei wurden die Messungen bei drei verschiedenen Reaktionstemperaturen (110-130 °C) durchgeführt und anschließend eine quantitative Auswertung der Kristallisation nach Gualtieri und eine Arrhenius Auftragung vorgenommen. Dabei wurden die Aktivierungsenergien für die Nukleation  $k_n$  und das Kristallwachstum  $k_g$  zu 47(2) und 56(3)  $\text{kJ mol}^{-1}$  (Nukleation) sowie 45(4) und 58(5)  $\text{kJ mol}^{-1}$  (Kristallwachstum) entsprechend für CAU-18 und CAU-19-H bestimmt.

## 5.2 Poröse Metall-Phosphonate mit dem Ni-H<sub>8</sub>TPPP Linker (Ni-tetra(4-phosphonophenyl)porphyrin)

In dieser Arbeit konnte erstmals der Linker Ni-H<sub>8</sub>TPPP (Ni-tetra(4-phosphonophenyl)porphyrin) synthetisiert und in der Synthese von porösen Metall-Phosphonaten eingesetzt werden. Dabei wurden mit den zweiwertigen Kationen Mn<sup>2+</sup>, Co<sup>2+</sup>, Ni<sup>2+</sup> und Cd<sup>2+</sup> sowie den vierwertigen Kationen Zr<sup>4+</sup> und Hf<sup>4+</sup> poröse Verbindungen erhalten.

1. Alle erhaltenen Metall-Phosphonate wurden unter ähnlichen Synthesebedingungen erhalten. Es war immer eine Reaktionstemperatur zwischen 140 und 180 °C nötig, sowie beim Arbeiten in Teflon Gefäßen, ohne Rühren eine Reaktionszeit von mindestens 12 h. Außerdem wurden nur kristalline Produkte bei Verwendung von H<sub>2</sub>O als Lösungsmittel erhalten.
2. Alle erhaltenen Porphyrin-basierten Metall-Phosphonate weisen untereinander ebenfalls strukturelle Ähnlichkeit auf. Der quadratisch planare Linker verknüpft die anorganische Baueinheit so, dass in allen Fällen eindimensionale Poren ausgebildet werden. Des weiteren sind die Linkermoleküle in allen Kristallstrukturen parallel zueinander angeordnet.
3. Unter Einsatz des Ni-H<sub>8</sub>TPPP Linkers und den zweiwertigen Kationen Mn<sup>2+</sup>, Co<sup>2+</sup>, Ni<sup>2+</sup> und Cd<sup>2+</sup> konnte unter hydrothermalen Synthesebedingungen unter Einsatz von Hochdurchsatzmethoden bei 180 °C die Verbindung M-CAU-29, [M(Ni-H<sub>6</sub>TPPP)(H<sub>2</sub>O)] · x H<sub>2</sub>O, entdeckt und die Synthesebedingungen optimiert werden.
  - a. Die Verbindungen CAU-29 stellen die ersten porösen und kristallinen Porphyrin-basierten Metall-Phosphonate dar.
  - b. Alle vier M-CAU-29 Derivate sind porös gegenüber H<sub>2</sub>O bei 298 K und N<sub>2</sub> bei 77 K, außer Ni-CAU-29, welches keine Stickstoffaufnahme unter diesen Bedingungen zeigt. H<sub>2</sub>O-Aufnahmen: 181 (Ni-), 166 (Co-), 140 (Mn-), 116 mg g<sup>-1</sup> (Cd-CAU-29). Spezifische Oberflächen nach BET: 0 (Ni-), 145 (Co-), 90 (Mn-), 180 m<sup>2</sup> g<sup>-1</sup> (Cd-CAU-29).

- c. Die Kristallstruktur von Ni-CAU-29 wurde aus Röntgenbeugungsdaten an Einkristallen bestimmt und die Zellparameter der anderen M-CAU-29 Derivate mittels der Pawley Methode verfeinert (Tab. 07).
4. Unter Einsatz von Hochdurchsatzmethoden konnten im chemischen System Ni-H<sub>8</sub>TPPP/NaF/NaOH/M<sup>4+</sup> (M= Zr<sup>4+</sup>, Hf<sup>4+</sup>) unter hydrothermalen Reaktionsbedingungen bei 180 °C die neuen Metall-Phosphonate M-CAU-30, [M<sub>2</sub>(Ni-H<sub>2</sub>TPPP)(OH/F)<sub>2</sub>] · x H<sub>2</sub>O, synthetisiert und deren Synthese optimiert werden.
- a. CAU-30 entsteht in einem sehr engen Bereich des Phasenraums. Die Verbindung bildet sich nur unter Einsatz von 40-100 eq. NaF. Bei Zugabe von mehr als 8 eq. NaOH wird kein festes Reaktionsprodukt erhalten und unterhalb von 6 eq. NaOH entstehen nur röntgenamorphe Reaktionsprodukte. Das optimierte Reaktandenverhältnis liegt daher bei Ni-H<sub>8</sub>TPPP : NaF : NaOH : M<sup>4+</sup> = 1 : 60 : 8 : 2.
- b. Die MOFs M-CAU-30 sind die Metall-Phosphonate mit den bisher höchsten spezifischen Oberfläche nach BET. Es wurden dabei Werte von a<sub>BET</sub>= 1070 und 1030 m<sup>2</sup> g<sup>-1</sup> für Zr- und Hf-CAU-30 erhalten. Beide Verbindungen adsorbieren ebenfalls H<sub>2</sub>O bei 298 K, wobei Werte von 250 (Zr-CAU-30) und 340 mg g<sup>-1</sup> (Hf-CAU-30) ermittelt wurden.
- c. Die Struktur von Zr-CAU-30 wurde durch Kombination von Elektronenbeugung zur Strukturlösung und der Rietveld-Methode zur Strukturverfeinerung aus Röntgenpulverdaten bestimmt. Die Zellparameter von Hf-CAU-30 wurden mittels der Pawley-Methode verfeinert (Tab. 07).
- d. Die Verbindungen M-CAU-30 sind außergewöhnlich stabil in Säuren und Basen in einem pH-Bereich von 0-12 (HCl, NaOH), sowie in Phosphatpuffer (pH 7), 100 % Essigsäure und allen getesteten organischen Lösungsmitteln. Die thermische Stabilität beträgt 400 °C.

- e. Die Reaktionsprodukte, die bei der Darstellung von M-CAU-30 erhalten wurden, weisen Verunreinigungen von ca. 10 gew.%  $\text{MO}_2$  auf, was ebenfalls mittels Elektronenbeugung ermittelt und anhand der anderen Charakterisierungsmethoden (REM, TEM, TG, CHNS) bestätigt wurde.
- f. Die TEM Aufnahmen von M-CAU-30 zeigen, dass die Verbindungen in Form von Nadeln von bis zu 500 nm Länge kristallisieren und die Kristalle eine sehr hohe Ordnung (Abb. 21) aufweisen.

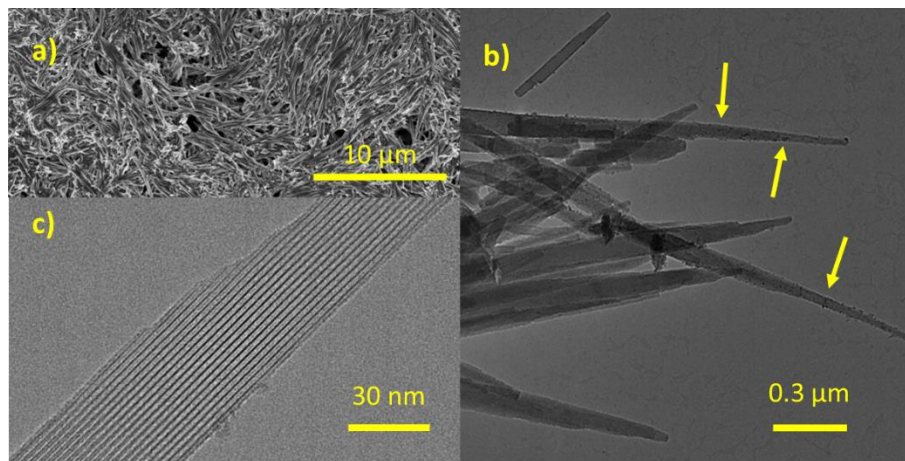


**Abbildung 21.** Ergebnisse der SEM und TEM Messungen von Zr-CAU-30. a) SEM Aufnahmen, b) TEM Aufnahmen von Nadeln von Zr-CAU-30 mit kleinen sphärischen Verunreinigungen von  $\text{ZrO}_2$  auf der Oberfläche (gelbe Pfeile), c) detaillierte TEM Aufnahme einer Nadel.

- 5. Unter Einsatz von Hochdurchsatzmethoden im chemischen System  $\text{Ni-H}_8\text{TPPP/DABCO/HCl/Co}^{2+}$  konnte unter hydrothermalen Synthesebedingungen bei 160 °C das neue Co-Phosphonat Co-CAU-36,  $[\text{Co}_2(\text{Ni-H}_4\text{TPPP})] \cdot 2 \text{ DABCO} \cdot 6 \text{ H}_2\text{O}$ , entdeckt und die Synthese optimiert werden.
  - a. Co-CAU-36 ist porös gegenüber  $\text{N}_2$  bei 77 K und weist eine spezifische Oberfläche nach BET von  $700 \text{ m}^2 \text{ g}^{-1}$  auf.
  - b. Die Struktur von Co-CAU-36 konnte aufgrund seiner hohen Kristallinität vollständig aus Elektronenbeugungsdaten (cRED-Methode) gelöst und verfeinert werden, wobei für diese Methode außerordentlich gute Gütekriterien von 13.6 ( $R_1$ ) und 33.4 % ( $wR_2$ ) erhalten wurden.



## 6 Ausblick

Alle in dieser Arbeit synthetisierten Metall-Carboxylate und Metall-Phosphonate weisen eine Stapelung der Porphyrin-Linker auf. Durch Unterdrücken dieses Motivs vor allem in der Synthese von Metall-Phosphonaten könnten offenere Netzwerke mit höherer Porosität erhalten werden. Beispielsweise könnte dies durch Einsatz anderer Metallionen, welche tendenziell andere anorganische Baueinheiten ausbilden gelingen. Beispielsweise können  $\text{Zn}^{2+}$  und  $\text{Cu}^{2+}$  die sogenannte Paddle-Wheel-Einheit ausbilden und so zu anderen Verknüpfungsmustern der Linker führen (Abb. 22, links).<sup>150</sup> Des weiteren könnte die Verwendung von entsprechenden Phosphonsäureestern, welche ähnliche Koordinationseigenschaften wie Carboxylationen aufweisen, zu den entsprechenden offenen Netzwerken führen (Abb. 22, Mitte). Auch die Verwendung von Co-Liganden wie 4,4-Bipyridin, welche beispielweise an die Metallzentren im Porphyrinring koordinieren, könnte zu einer Aufweitung der Porphyrin-Porphyrin Abstände und somit zu größeren Poren führen (Abb. 22, rechts).

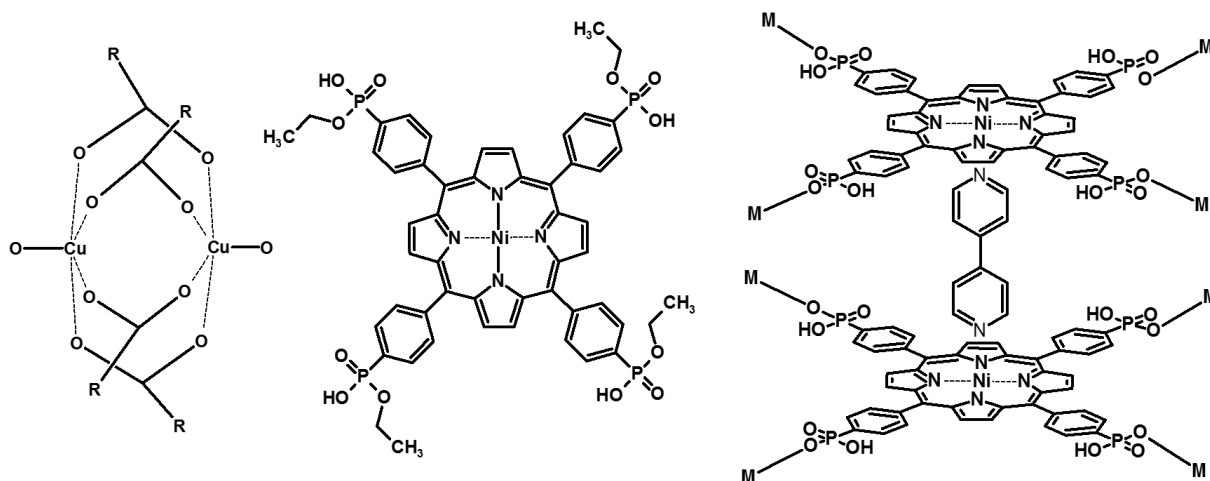


**Abbildung 22.** Schematische Darstellung einiger Möglichkeiten zur Unterdrückung der Linkerstapelung bei Porphyrin-basierten Metall-Phosphonaten. Links: Paddle-Wheel-Einheit als Beispiel für eine andere anorganische Baueinheit, Mitte: die Verwendung von Phosphonsäureestern in der Synthese von Metall-Phosphonaten und rechts: die Verwendung von Co-Liganden wie 4,4-Bipyridin zur Aufweitung der Porphyrin-Porphyrin Abstände im Stapelmotiv.

CAU-30 könnte sich durch seine hohe Porosität und Stabilität für viele Anwendungen eignen, welche im Kontext mit MOFs diskutiert wurden. Bisher wurden jedoch noch kaum Experimente hierzu durchgeführt. CAU-30 könnte durch seine freien Hydrogenphosphonatgruppen sehr gut Protonen leiten, des weiteren könnte das Ni-Porphyrin katalytisch oder elektrochemisch aktiv sein. Ebenfalls wären medizinische

Anwendungen durch die hohe Unempfindlichkeit dieser Verbindung gegenüber Säuren und Basen denkbar.

In dieser Arbeit wurden drei neue Strukturen mit dem Ni-H<sub>8</sub>TPPP Linker entdeckt, im Vergleich zu der Vielzahl an Verbindungen, welche mit der entsprechenden Carbonsäure H<sub>6</sub>TCPD entdeckt wurden,<sup>65</sup> ist diese Zahl sehr gering. Daher würde es sich lohnen weitere Metalle wie Cu, Zn, Ti, Fe oder Al in Kombination mit anderen Lösungsmitteln wie Acetonitril, organischen Säuren oder DMF in der Synthese neuer Metall-Phosphonate auszuprobieren, um möglicherweise neue poröse Verbindungen zu erhalten.

Neben der in dieser Arbeit synthetisierten quadratisch planaren Tetrakisphosphonsäure Ni-Tetra(phosphonphenyl)porphyrin (Ni-H<sub>8</sub>TPPP) könnten sich weitere Tetrakisphosphonsäuren für die Synthese neuer hochporöser Metall-Phosphonate eignen. In Abbildung 23 sind einige Tetrakisphosphonsäuren gezeigt, die zur Synthese von MOFs eingesetzt werden sollten. Mit den Methan- und Adamantan-basierten Linkern, die eine tetraedrische Geometrie aufweisen, wurden bereits poröse Metall-Phosphonate erhalten.<sup>120, 136</sup> Mit den quadratisch planaren Tetracarbonsäuren welche auf Benzol, Ethylen und Pyren basieren (Abb. 23) sind vor allem MOFs mit zweiwertigen Kationen wie Co<sup>2+</sup>,<sup>151</sup> Ni<sup>2+</sup>,<sup>152-154</sup> Zn<sup>2+</sup>,<sup>151, 155-157</sup> und Cd<sup>2+</sup>,<sup>151, 158, 159</sup> sowie mit Zr<sup>4+</sup> zwei poröse Metall-Carboxylate mit dem Pyren-<sup>160</sup> und Benzol-basierten Linker<sup>161</sup> bekannt. Die Synthese der entsprechenden Phosphonsäuren könnte dabei analog zu der in dieser Arbeit durchgeführten Phosphonylierung nach Tavs<sup>43</sup> aus den entsprechenden Brom-Derivaten gelingen.

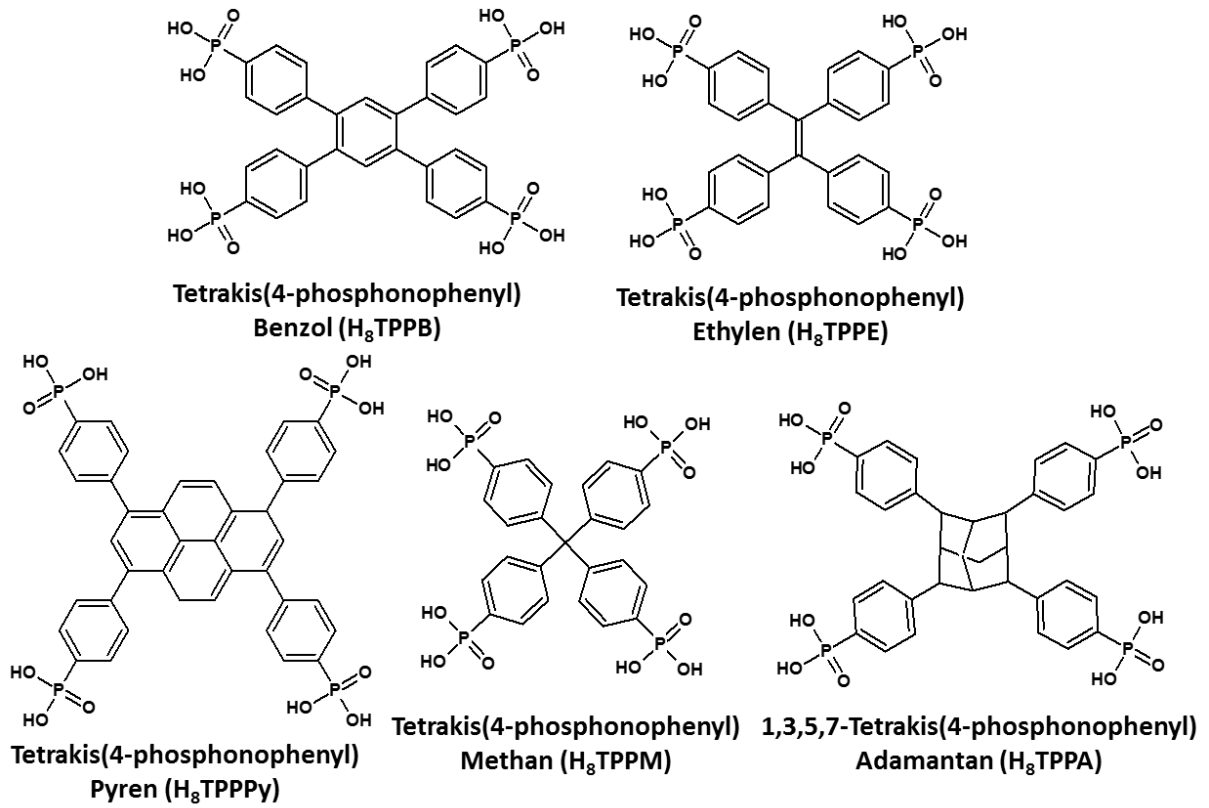


**Abbildung 23.** Strukturformeln von Tetraphosphonsäuren, die für die Synthese neuer hochporöser und stabiler Metall-Phosphonate untersucht werden sollten.





## 7 Literatur

1. S. Bauer and N. Stock, *Chem. unserer Zeit*, 2008, **42**, 12-19.
2. H.-C. Zhou, J. R. Long and O. M. Yaghi, *Chem. Rev.*, 2012, **112**, 673-674.
3. P. A. Wright and J. A. Connor, *Microporous Framework Solids*, Royal Society of Chemistry, 2007.
4. H. Furukawa, K. E. Cordova, M. O'Keeffe and O. M. Yaghi, *Science*, 2013, **341**, 1-12.
5. C.-Y. Sun, C. Qin, X.-L. Wang and Z.-M. Su, *Expert. Opin. Drug. Deliv.*, 2013, **10**, 89-101.
6. C. Janiak and J. K. Vieth, *New J. Chem.*, 2010, **34**, 2366-2388.
7. U. Mueller, M. Schubert, F. Teich, H. Puetter, K. Schierle-Arndt and J. Pastre, *J. Mater. Chem.*, 2006, **16**, 626-636.
8. R. Batten Stuart, R. Champness Neil, X.-M. Chen, J. Garcia-Martinez, S. Kitagawa, L. Öhrström, M. O'Keeffe, M. Paik Suh and J. Reedijk, *Pure Appl. Chem.*, 2013, **85**, 1715.
9. M. Eddaoudi, J. Kim, N. Rosi, D. Vodak, J. Wachter, M. O'Keeffe and O. M. Yaghi, *Science*, 2002, **295**, 469-472.
10. N. Stock and T. Bein, *Angew. Chem. Int. Ed.*, 2004, **43**, 749-752.
11. M. Taddei, F. Costantino and R. Vivani, *Eur. J. Inorg. Chem.*, 2016, **2016**, 4300-4309.
12. K. J. Gagnon, H. P. Perry and A. Clearfield, *Chem. Rev.*, 2012, **112**, 1034-1054.
13. G. K. H. Shimizu, R. Vaidyanathan and J. M. Taylor, *Chem. Soc. Rev.*, 2009, **38**, 1430-1449.
14. M. T. Wharmby, G. M. Pearce, J. P. S. Mowat, J. M. Griffin, S. E. Ashbrook, P. A. Wright, L.-H. Schilling, A. Lieb, N. Stock, S. Chavan, S. Bordiga, E. Garcia, G. D. Pirngruber, M. Vreeke and L. Gora, *Micropor. Mesopor. Mater.*, 2012, **157**, 3-17.
15. M. Lammert, M. T. Wharmby, S. Smolders, B. Bueken, A. Lieb, K. A. Lomachenko, D. D. Vos and N. Stock, *Chem. Commun.*, 2015, **51**, 12578-12581.
16. S. Bauer and N. Stock, *Chem. unserer Zeit*, 2007, **41**, 390-398.
17. W. S. Sheldrick and M. Wachhold, *Angew. Chem.*, 1997, **109**, 214-234.
18. A. Rabenau, *Angew. Chem.*, 1985, **97**, 1017-1032.
19. N. Stock, *Chem. Ing. Tech.*, 2010, **82**, 1039-1047.
20. *Stoe & Cie GmbH; WinXPow*, Darmstadt, Germany, 2011.
21. A. Coelho, *TOPAS-Academic V4.1*, Coelho Software, 2007.
22. W. Kraus and G. Nolze, *J. Appl. Crystallogr.*, 1996, **29**, 301-303.
23. *Materials Studio Version 5.0*, Accelrys Inc., San Diego, CA, 2009.
24. K. Brandenburg, *Diamond Version 3*, Crystal Impact GbR, Bonn, 2012.
25. A. Spek, *Acta Crystallographica Section D*, 2009, **65**, 148-155.
26. U. Kolb, T. Gorelik and M. T. Otten, *Ultramicroscopy*, 2008, **108**, 763-772.
27. E. Mugnaioli, T. Gorelik and U. Kolb, *Ultramicroscopy*, 2009, **109**, 758-765.
28. M. C. Burla, R. Caliandro, B. Carrozzini, G. L. Casciarano, C. Cuocci, C. Giacovazzo, M. Mallamo, A. Mazzone and G. Polidori, *J. Appl. Crystallogr.*, 2015, **48**, 306-309.
29. G. Sheldrick, *Acta Crystallogr. Sect. A*, 2008, **64**, 112-122.
30. G. Sheldrick, *Acta Crystallographica Section C*, 2015, **71**, 3-8.
31. G. Sheldrick, *Acta Crystallogr. Sect. A*, 2015, **71**, 3-8.
32. Bruker, *SAINT V9.32B*, Bruker AXS Inc., Madison, Wisconsin, USA, 2012.
33. X. Zou, S. Hovmöller and P. Oleynikov, *Electron Crystallography: Electron Microscopy and Electron Diffraction*, OUP Oxford, 2011.
34. W. Massa, *Kristallstrukturbestimmung*, Vieweg+Teubner Verlag, 2011.
35. L. Spieß, G. Teichert, R. Schwarzer, H. Behnken and C. Genzel, *Moderne Röntgenbeugung: Röntgendiffraktometrie für Materialwissenschaftler, Physiker und Chemiker*, Vieweg+Teubner Verlag, 2013.
36. R. Allmann and A. Kern, *Röntgenpulverdiffraktometrie: Rechnergestützte Auswertung, Phasenanalyse und Strukturbestimmung*, Springer, 2002.

37. E. Wiberg, A. F. Holleman and N. Wiberg, *Lehrbuch Der Anorganischen Chemie*, Walter de Gruyter, 2007.
38. L. Smart and E. Moore, *Einführung in die Festkörperchemie*, Vieweg, 1997.
39. P. Paufler, *Acta Crystallogr. Sect. A*, 2007, **63**, 483.
40. B. K. Vainshtein, E. Feigl and J. A. Spink, *Structure Analysis by Electron Diffraction*, Elsevier Science, 2013.
41. A. D. Adler, F. R. Longo, J. D. Finarelli, J. Goldmacher, J. Assour and L. Korsakoff, *The Journal of Organic Chemistry*, 1967, **32**, 476-476.
42. J. S. Lindsey and R. W. Wagner, *The Journal of Organic Chemistry*, 1989, **54**, 828-836.
43. P. Tavs, *Chem. Ber.*, 1970, **103**, 2428-2436.
44. A. D. Adler, F. R. Longo, F. Kampas and J. Kim, *J. Inorg. Nucl. Chem.*, 1970, **32**, 2443-2445.
45. M. Königshoff and T. Brandenburger, *Kurzlehrbuch Biochemie*, Thieme, 2012.
46. G. S. Adair and J. H. Field, *J. Biol. Chem.*, 1925, **63**, 529-545.
47. H. W. Heldt and B. Piechulla, *Pflanzenbiochemie*, Spektrum Akademischer Verlag, 2008.
48. J. Rassow, K. Hauser, R. Netzker and R. Deutzmann, *Duale Reihe Biochemie*, Thieme, 2016.
49. R. Bonnett, *Chem. Soc. Rev.*, 1995, **24**, 19-33.
50. E. Alves, M. A. F. Faustino, M. G. P. M. S. Neves, Â. Cunha, H. Nadais and A. Almeida, *Journal of Photochemistry and Photobiology C: Photochemistry Reviews*, 2015, **22**, 34-57.
51. H. Huang, W. Song, J. Rieffel and J. F. Lovell, *Frontiers in Physics*, 2015, **3**.
52. S. Hecht and J. M. J. Fréchet, *Angew. Chem.*, 2001, **113**, 76-94.
53. M. Sinaasappel and C. Ince, *Journal of Applied Physiology*, 1996, **81**, 2297-2303.
54. E. G. Mik, T. G. van Leeuwen, N. J. Raat and C. Ince, *Journal of Applied Physiology*, 2004, **97**, 1962-1969.
55. D. Filippini, A. Alimelli, C. Di Natale, R. Paolesse, A. D'Amico and I. Lundström, *Angew. Chem. Int. Ed.*, 2006, **45**, 3800-3803.
56. T. Malinski and Z. Taha, *Nature*, 1992, **358**, 676-678.
57. P. Bogdanoff, I. Herrmann, M. Hilgendorff, I. Dorbandt, S. Fiechter and H. Tributsch, *J. New. Mat. Electrochem. Systems*, 2004, **7**, 85-92.
58. X. Li, C. Liu, W. Xing and T. Lu, *J. Power Sources*, 2009, **193**, 470-476.
59. K. S. Suslick and B. R. Cook, *J. Chem. Soc., Chem. Commun.*, 1987, 200-202.
60. L. Shao, B. Hu, P. Dong, W. Ji and C. Qi, *J. Porphyrins Phthalocyanines*, 2010, **14**, 993-999.
61. M. Bassiouk, E. Álvarez-Zauco and V. A. Basiuk, *Appl. Surf. Sci.*, DOI: 10.1016/j.apsusc.2012.07.161, 24116-24126.
62. D. V. Konarev, S. S. Khasanov, M. A. Faraonov and R. N. Lyubovskaya, *Cryst. Eng. Comm.*, 2012, **14**, 4350-4356.
63. Z. Guo and B. Chen, *Dalton Trans.*, 2015, **44**, 14574-14583.
64. W.-Y. Gao, M. Chrzanowski and S. Ma, *Chem. Soc. Rev.*, 2014, **43**, 5841-5866.
65. S. Huh, S.-J. Kim and Y. Kim, *Cryst. Eng. Comm.*, 2016, DOI: 10.1039/C5CE02106E.
66. Z. Guo and B. Chen, *Dalton Trans.*, 2015, **44**, 14574-14583.
67. M. E. Kosal, J.-H. Chou, S. R. Wilson and K. S. Suslick, *Nat. Mater.*, 2002, **1**, 118-121.
68. I. Goldberg, *Chem. Eur. J.*, 2000, **6**, 3863-3870.
69. D. Feng, H.-L. Jiang, Y.-P. Chen, Z.-Y. Gu, Z. Wei and H.-C. Zhou, *Inorg. Chem.*, 2013, **52**, 12661-12667.
70. W. Morris, B. Voloskiy, S. Demir, F. Gándara, P. L. McGrier, H. Furukawa, D. Cascio, J. F. Stoddart and O. M. Yaghi, *Inorg. Chem.*, 2012, **51**, 6443-6445.
71. D. Feng, Z.-Y. Gu, Y.-P. Chen, J. Park, Z. Wei, Y. Sun, M. Bosch, S. Yuan and H.-C. Zhou, *J. Am. Chem. Soc.*, 2014, **136**, 17714-17717.
72. D. Feng, W.-C. Chung, Z. Wei, Z.-Y. Gu, H.-L. Jiang, Y.-P. Chen, D. J. Darensbourg and H.-C. Zhou, *J. Am. Chem. Soc.*, 2013, **135**, 17105-17110.
73. H.-L. Jiang, D. Feng, K. Wang, Z.-Y. Gu, Z. Wei, Y.-P. Chen and H.-C. Zhou, *J. Am. Chem. Soc.*, 2013, **135**, 13934-13938.

74. T.-H. Chang, C.-W. Kung, H.-W. Chen, T.-Y. Huang, S.-Y. Kao, H.-C. Lu, M.-H. Lee, K. M. Boopathi, C.-W. Chu and K.-C. Ho, *Adv. Mater.*, 2015, **27**, 7229-7235.
75. Y.-Z. Chen and H.-L. Jiang, *Chem. Mater.*, 2016, **28**, 6698-6704.
76. Y. Liu, A. J. Howarth, J. T. Hupp and O. K. Farha, *Angew. Chem. Int. Ed.*, 2015, **54**, 9001-9005.
77. P. Kucheryavy, N. Lahanas, E. Velasco, C.-J. Sun and J. V. Lockard, *The Journal of Physical Chemistry Letters*, 2016, **7**, 1109-1115.
78. I. Hod, M. D. Sampson, P. Deria, C. P. Kubiak, O. K. Farha and J. T. Hupp, *ACS Catalysis*, 2015, **5**, 6302-6309.
79. P. M. Usov, B. Huffman, C. C. Epley, M. C. Kessinger, J. Zhu, W. A. Maza and A. J. Morris, *ACS Applied Materials & Interfaces*, 2017, DOI: 10.1021/acsami.7b01547.
80. P. M. Usov, S. R. Ahrenholtz, W. A. Maza, B. Stratakes, C. C. Epley, M. C. Kessinger, J. Zhu and A. J. Morris, *Journal of Materials Chemistry A*, 2016, **4**, 16818-16823.
81. K. Lu, C. He and W. Lin, *J. Am. Chem. Soc.*, 2015, **137**, 7600-7603.
82. K. Wang, D. Feng, T.-F. Liu, J. Su, S. Yuan, Y.-P. Chen, M. Bosch, X. Zou and H.-C. Zhou, *J. Am. Chem. Soc.*, 2014, **136**, 13983-13986.
83. A. Fateeva, S. Devautour-Vinot, N. Heymans, T. Devic, J.-M. Grenèche, S. Wuttke, S. Miller, A. Lago, C. Serre, G. De Weireld, G. Maurin, A. Vimont and G. Férey, *Chem. Mater.*, 2011, **23**, 4641-4651.
84. A. Fateeva, J. Clarisse, G. Pilet, J.-M. Grenèche, F. Nouar, B. K. Abeykoon, F. Guegan, C. Goutaudier, D. Luneau, J. E. Warren, M. J. Rosseinsky and T. Devic, *Cryst. Growth Des.*, 2015, **15**, 1819-1826.
85. A. Fateeva, P. A. Chater, C. P. Ireland, A. A. Tahir, Y. Z. Khimyak, P. V. Wiper, J. R. Darwent and M. J. Rosseinsky, *Angew. Chem.*, 2012, **124**, 7558-7562.
86. T. Rhauderwiek, S. Waitschat, S. Wuttke, H. Reinsch, T. Bein and N. Stock, *Inorg. Chem.*, 2016, **55**, 5312-5319.
87. W.-Y. Gao, Z. Zhang, L. Cash, L. Wojtas, Y.-S. Chen and S. Ma, *Cryst. Eng. Comm.*, 2013, **15**, 9320-9323.
88. J. A. Johnson, J. Luo, X. Zhang, Y.-S. Chen, M. D. Morton, E. Echeverría, F. E. Torres and J. Zhang, *ACS Catalysis*, 2015, **5**, 5283-5291.
89. F. Yang, L. Jing, L. Ji, Q. Liu and X. Zhang, *Cryst. Eng. Comm.*, 2014, **16**, 4274-4280.
90. S. Lipstman and I. Goldberg, *J. Mol. Struct.*, 2008, **890**, 101-106.
91. S. Muniappan, S. Lipstman, S. George and I. Goldberg, *Inorg. Chem.*, 2007, **46**, 5544-5554.
92. S. Lipstman, S. Muniappan, S. George and I. Goldberg, *Dalton Trans.*, 2007, DOI: 10.1039/b703698a, 3273-3281.
93. M.-H. Xie, X.-L. Yang and C.-D. Wu, *Chem. Commun.*, 2011, **47**, 5521-5523.
94. D. Feng, Z.-Y. Gu, J.-R. Li, H.-L. Jiang, Z. Wei and H.-C. Zhou, *Angew. Chem.*, 2012, **124**, 10453-10456.
95. M. Taddei, F. Costantino, R. Vivani, S. Sabatini, S.-H. Lim and S. M. Cohen, *Chem. Commun.*, 2014, **50**, 5737-5740.
96. R. K. Mah, B. S. Gelfand, J. M. Taylor and G. K. H. Shimizu, *Inorganic Chemistry Frontiers*, 2015, **2**, 273-277.
97. M. Taddei, F. Costantino, F. Marmottini, A. Comotti, P. Sozzani and R. Vivani, *Chem. Commun.*, 2014, **50**, 14831-14834.
98. T. Hirao, T. Masunaga, Y. Ohshiro and T. Agawa, *Synthesis*, 1981, **1981**, 56-57.
99. D. Deniaud, B. Schollorn, D. Mansuy, J. Rouxel, P. Battioni and B. Bujoli, *Chem. Mater.*, 1995, **7**, 995-1000.
100. D. Deniaud, G. A. Spyroulias, J.-F. Bartoli, P. Battioni, D. Mansuy, C. Pinel, F. Odobel and B. Bujoli, *New J. Chem.*, 1998, **22**, 901-905.
101. N. Venkatramiah, C. F. Pereira, R. F. Mendes, F. A. A. Paz and J. P. C. Tomé, *Anal. Chem.*, 2015, **87**, 4515-4522.

102. K. M. Kadish, P. Chen, Y. Y. Enakieva, S. E. Nefedov, Y. G. Gorbunova, A. Y. Tsivadze, A. Bessmertnykh-Lemeune, C. Stern and R. Guilard, *J. Electroanal. Chem.*, 2011, **656**, 61-71.
103. Y. Fang, Y. G. Gorbunova, P. Chen, X. Jiang, M. Manowong, A. A. Sinelshchikova, Y. Y. Enakieva, A. G. Martynov, A. Y. Tsivadze, A. Bessmertnykh-Lemeune, C. Stern, R. Guilard and K. M. Kadish, *Inorg. Chem.*, 2015, **54**, 3501-3512.
104. P. Kubát, K. Lang and P. Anzenbacher Jr, *Biochimica et Biophysica Acta (BBA) - General Subjects*, 2004, **1670**, 40-48.
105. F. Odobel, E. Blart, M. Lagree, M. Villieras, H. Boujtita, N. El Murr, S. Caramori and C. Alberto Bignozzi, *J. Mater. Chem.*, 2003, **13**, 502-510.
106. M. De Napoli, S. Nardis, R. Paolesse, M. G. H. Vicente, R. Lauceri and R. Purrello, *J. Am. Chem. Soc.*, 2004, **126**, 5934-5935.
107. R. Lauceri, M. De Napoli, A. Mammana, S. Nardis, A. Romeo and R. Purrello, *Synth. Met.*, 2004, **147**, 49-55.
108. P. Kubát, K. Lang, P. Janda and P. Anzenbacher, *Langmuir*, 2005, **21**, 9714-9720.
109. P. Kubát, K. Lang and Z. Zelinger, *J. Mol. Liq.*, 2007, **131-132**, 200-205.
110. N. Venkatramaiah, C. F. Pereira, R. F. Mendes, F. A. A. Paz and J. P. C. Tomé, *Anal. Chem.*, 2015, **87**, 4515-4522.
111. G. K. H. Shimizu, R. Vaidhyanathan and J. M. Taylor, *Chem. Soc. Rev.*, 2009, **38**, 1430-1449.
112. A. Clearfield and K. Demadis, *Metallphosphonate Metal Phosphonate Chemistry: From Synthesis to Applications*, Royal Society of Chemistry, 2011.
113. Y.-P. Zhu, T.-Y. Ma, Y.-L. Liu, T.-Z. Ren and Z.-Y. Yuan, *Inorganic Chemistry Frontiers*, 2014, **1**, 360-383.
114. R. A. Coxall, S. G. Harris, D. K. Henderson, S. Parsons, P. A. Tasker and R. E. P. Winpenny, *J. Chem. Soc., Dalton Trans.*, 2000, DOI: 10.1039/B001404O, 2349-2356.
115. A. Clearfield and J. A. Stynes, *J. Inorg. Nucl. Chem.*, 1964, **26**, 117-129.
116. A. Clearfield and G. D. Smith, *Inorg. Chem.*, 1969, **8**, 431-436.
117. G. Alberti, U. Costantino, S. Allulli and N. Tomassini, *J. Inorg. Nucl. Chem.*, 1978, **40**, 1113-1117.
118. M. B. Dines, R. E. Cooksey, P. C. Griffith and R. H. Lane, *Inorg. Chem.*, 1983, **22**, 1003-1004.
119. C.-Y. Gao, J. Ai, H.-R. Tian, D. Wu and Z.-M. Sun, *Chem. Commun.*, 2017, **53**, 1293-1296.
120. T. Zheng, Z. Yang, D. Gui, Z. Liu, X. Wang, X. Dai, S. Liu, L. Zhang, Y. Gao, L. Chen, D. Sheng, Y. Wang, J. Diwu, J. Wang, R. Zhou, Z. Chai, T. E. Albrecht-Schmitt and S. Wang, *Nat Commun.*, 2017, **8**, 15369.
121. A. Clearfield and K. Demadis, *Metal Phosphonate Chemistry: From Synthesis to Applications*, Royal Society of Chemistry, 2011.
122. A. Clearfield and Z. Wang, *J. Chem. Soc., Dalton Trans.*, 2002, DOI: 10.1039/B202371G, 2937-2947.
123. M. Taddei, F. Costantino and R. Vivani, *Inorg. Chem.*, 2010, **49**, 9664-9670.
124. J. A. Groves, S. R. Miller, S. J. Warrender, C. Mellot-Draznieks, P. Lightfoot and P. A. Wright, *Chem. Commun.*, 2006, DOI: 10.1039/B605400E, 3305-3307.
125. S. Waitschat, M. T. Wharmby and N. Stock, *Dalton Trans.*, 2015, **44**, 11235-11240.
126. M. T. Wharmby, J. P. S. Mowat, S. P. Thompson and P. A. Wright, *J. Am. Chem. Soc.*, 2011, **133**, 1266-1269.
127. S. Pili, S. P. Argent, C. G. Morris, P. Rought, V. García-Sakai, I. P. Silverwood, T. L. Easun, M. Li, M. R. Warren, C. A. Murray, C. C. Tang, S. Yang and M. Schröder, *J. Am. Chem. Soc.*, 2016, **138**, 6352-6355.
128. S. Begum, S. Horike, S. Kitagawa and H. Krautscheid, *Dalton Trans.*, 2015, **44**, 18727-18730.
129. R. Vaidhyanathan, A. H. Mahmoudkhani and G. K. H. Shimizu, *Can. J. Chem.*, 2009, **87**, 247-253.
130. B. S. Gelfand, R. P. S. Huynh, S. P. Collins, T. K. Woo and G. K. H. Shimizu, *Chem. Mater.*, 2017, **29**, 10469-10477.
131. N. Hermer, H. Reinsch, P. Mayer and N. Stock, *Cryst. Eng. Comm.*, 2016, **18**, 8147-8150.
132. N. Hermer and N. Stock, *Dalton Trans.*, 2015, **44**, 3720-3723.

133. S. S. Iremonger, J. Liang, R. Vaidhyanathan, I. Martens, G. K. H. Shimizu, T. D. Daff, M. Z. Aghaji, S. Yeganegi and T. K. Woo, *J. Am. Chem. Soc.*, 2011, **133**, 20048-20051.
134. S. S. Iremonger, J. Liang, R. Vaidhyanathan and G. K. H. Shimizu, *Chem. Commun.*, 2011, **47**, 4430-4432.
135. J. M. Taylor, R. Vaidhyanathan, S. S. Iremonger and G. K. H. Shimizu, *J. Am. Chem. Soc.*, 2012, **134**, 14338-14340.
136. J. M. Taylor, A. H. Mahmoudkhani and G. K. H. Shimizu, *Angew. Chem. Int. Ed.*, 2007, **46**, 795-798.
137. K. Maeda, Y. Kiyozumi and F. Mizukami, *Angewandte Chemie International Edition in English*, 1994, **33**, 2335-2337.
138. K. Maeda, J. Akimoto, Y. Kiyozumi and F. Mizukami, *Angewandte Chemie International Edition in English*, 1995, **34**, 1199-1201.
139. Q. Yue, J. Yang, G.-H. Li, G.-D. Li and J.-S. Chen, *Inorg. Chem.*, 2006, **45**, 4431-4439.
140. C. Serre, J. A. Groves, P. Lightfoot, A. M. Z. Slawin, P. A. Wright, N. Stock, T. Bein, M. Haouas, F. Taulelle and G. Férey, *Chem. Mater.*, 2006, **18**, 1451-1457.
141. M. T. Wharmby, S. R. Miller, J. A. Groves, I. Margiolaki, S. E. Ashbrook and P. A. Wright, *Dalton Trans.*, 2010, **39**, 6389-6391.
142. M. Pramanik and A. Bhaumik, *Chem. Eur. J.*, 2013, **19**, 8507-8514.
143. S. Begum, Z. Wang, A. Donnadio, F. Costantino, M. Casciola, R. Valiullin, C. Chmelik, M. Bertmer, J. Kärger, J. Haase and H. Krautscheid, *Chem. Eur. J.*, 2014, **20**, 8862-8866.
144. S.-F. Tang, J.-J. Cai, L.-J. Li, X.-X. Lv, C. Wang and X.-B. Zhao, *Dalton Trans.*, 2014, **43**, 5970-5973.
145. M. Pramanik, M. Nandi, H. Uyama and A. Bhaumik, *Catalysis Science & Technology*, 2012, **2**, 613-620.
146. R. K. Mah, M. W. Lui and G. K. H. Shimizu, *Inorg. Chem.*, 2013, **52**, 7311-7313.
147. M. Pramanik and A. Bhaumik, *Journal of Materials Chemistry A*, 2013, **1**, 11210-11220.
148. T. Rhauderwiek, N. Heidenreich, H. Reinsch, S. Øien-Ødegaard, K. A. Lomachenko, U. Rütt, A. V. Soldatov, K. P. Lillerud and N. Stock, *Cryst. Growth Des.*, 2017, **17**, 3462-3474.
149. T. Rhauderwiek, K. Wolkersdorfer, S. Oien-Odegaard, K.-P. Lillerud, M. Wark and N. Stock, *Chem. Commun.*, 2018, **54**, 389-392.
150. M. K. Bhunia, J. T. Hughes, J. C. Fettinger and A. Navrotsky, *Langmuir*, 2013, **29**, 8140-8145.
151. J. R. Karra, H. Jasuja, Y.-G. Huang and K. S. Walton, *Journal of Materials Chemistry A*, 2015, **3**, 1624-1631.
152. Z. Zhou, C. He, J. Xiu, L. Yang and C. Duan, *J. Am. Chem. Soc.*, 2015, **137**, 15066-15069.
153. K. C. Stylianou, J. Bacsá, D. Bradshaw and M. J. Rosseinsky, *Z. Anorg. Allg. Chem.*, 2014, **640**, 2123-2131.
154. Z. Zhou, L. Yang, Y. Wang, C. He, T. Liu and C. Duan, *RSC Advances*, 2016, **6**, 108010-108016.
155. W. Cheng, T. Wang, W. Xu, Y. Zhang, J. Zhang and M. Fang, *J. Coord. Chem.*, 2016, **69**, 2220-2230.
156. O. Karagiari, W. Bury, D. Fairen-Jimenez, C. E. Wilmer, A. A. Sarjeant, J. T. Hupp and O. K. Farha, *Inorg. Chem.*, 2014, **53**, 10432-10436.
157. K. C. Stylianou, J. Rabone, S. Y. Chong, R. Heck, J. Armstrong, P. V. Wiper, K. E. Jelfs, S. Zlatogorsky, J. Bacsá, A. G. McLennan, C. P. Ireland, Y. Z. Khimiyak, K. M. Thomas, D. Bradshaw and M. J. Rosseinsky, *J. Am. Chem. Soc.*, 2012, **134**, 20466-20478.
158. F. Yuan, C.-M. Yuan, H.-M. Hu, T.-T. Wang and C.-S. Zhou, *Polyhedron*, 2018, **139**, 257-261.
159. R.-J. Li, M. Li, X.-P. Zhou, S. W. Ng, M. O'Keeffe and D. Li, *Cryst. Eng. Comm.*, 2014, **16**, 6291-6295.
160. J. E. Mondloch, W. Bury, D. Fairen-Jimenez, S. Kwon, E. J. DeMarco, M. H. Weston, A. A. Sarjeant, S. T. Nguyen, P. C. Stair, R. Q. Snurr, O. K. Farha and J. T. Hupp, *J. Am. Chem. Soc.*, 2013, **135**, 10294-10297.
161. M. Lammert, H. Reinsch, C. A. Murray, M. T. Wharmby, H. Terraschke and N. Stock, *Dalton Trans.*, 2016, **45**, 18822-18826.





## **III Anhang**



## **8 SI zu „Nanoscale Synthesis of Two Porphyrin-Based MOFs with Gallium and Indium“**

### **Supporting Information**

# **Nanoscale Synthesis of two Porphyrin-based MOFs with Gallium and Indium**

*Timo Rhauderwiek,<sup>a</sup> Steve Waitschat,<sup>a</sup> Stefan Wuttke,<sup>b</sup> Helge Reinsch,<sup>c</sup> Thomas Bein,<sup>b</sup> Norbert Stock<sup>a,\*</sup>*

<sup>a</sup> Institute of Inorganic Chemistry, Christian-Albrechts-Universität, Max-Eyth Straße 2, D-24118 Kiel, Germany

<sup>b</sup> Department of Chemistry and Center for NanoScience (CeNS), University of Munich (LMU), Butenandtstraße 5-13, D-81377 Munich, Germany

<sup>c</sup> Department of Chemistry, University of Oslo, N-0371 Oslo, Norway

- 1. Synthesis of H<sub>6</sub>TCPP**
- 2. High-throughput investigation of Ga- and In-PMOF**
- 3. Pawley-fits and crystallographic data of Ga-PMOF-cf, In-PMOF-cf and In-PMOF-bs-us**
- 4. Sorption properties and PXRD patterns of the activated samples**
- 5. TG investigations and PXRD patterns of the decomposition products**
- 6. IR spectroscopy of Ga- and In-PMOF-bs-th**
- 7. DLS and SEM investigations**
- 8. Literature**

**1. Synthesis of H<sub>6</sub>TCPP.** The synthesis of H<sub>6</sub>TCPP was carried out following the procedures described in the literature.<sup>1-3</sup> Pyrrole (14.01 mL, 202.5 mmol) and 4-formylbenzoic acid (30.40 g, 202.5 mmol) in 750 mL propionic acid were heated under reflux for 2 h. Afterwards the reaction mixture was cooled down to RT and poured into 1000 mL of MeOH and stirred for 30 min in an ice bath. The resulting precipitate was filtered and washed several times with MeOH until the filtrate was clear. Subsequently, the product was washed with 200 mL warm distilled water and dried at 70 °C in a drying oven.

Elemental analysis of H<sub>6</sub>TCPP: calc (%): C 72.9, H 3.8, N 7.1, found (%): C 71.3, H 4.3, N 6.9. The small difference between the calculated and observed values is due to impurities caused by solvent molecules used in the synthesis. These impurities were also observed in the <sup>1</sup>H-NMR measurements.

<sup>1</sup>H-NMR (Figure S1), (500 MHz, DMSO-d<sub>6</sub>): δ= 8.86 (s, 8H, H-1); 8.39 (d, 8H, H-2); 8.33 (d, 8H, H-3); 3.35 (s, 2H, H<sub>2</sub>O); 2.50 (s, 6H, DMSO); 2.22 (q, 2H, propionic acid); 1.00 (t, 3H, propionic acid) ppm.



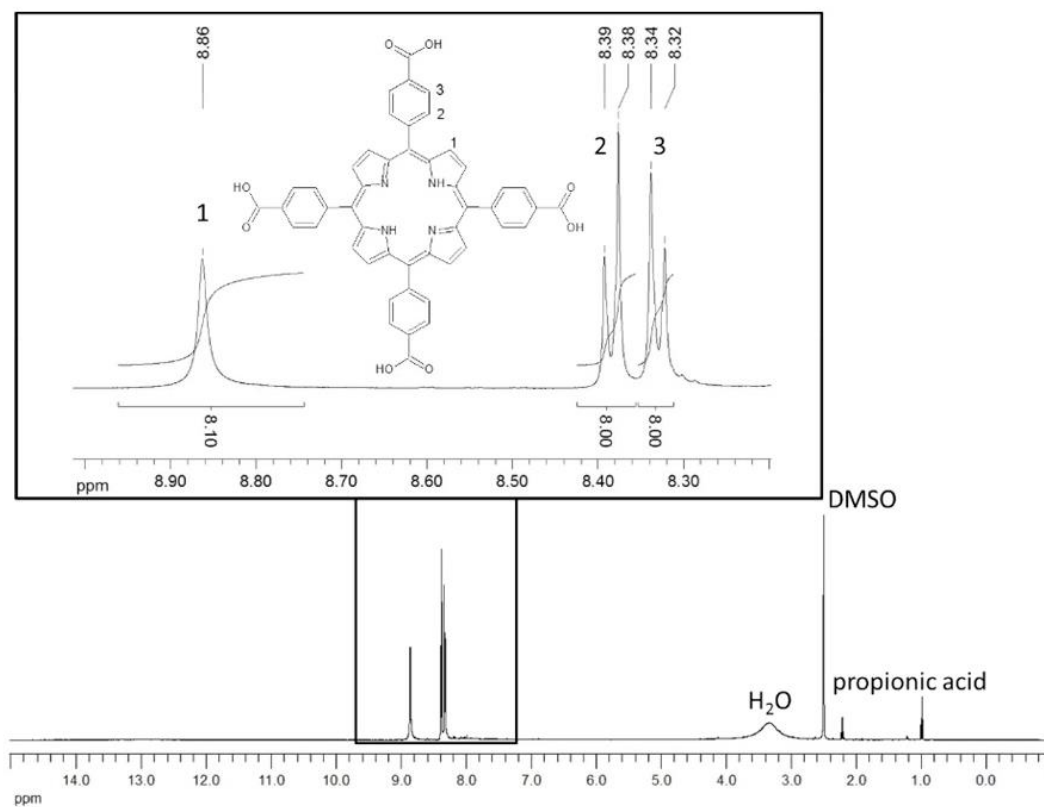


**Figure S1.**  $^1\text{H-NMR}$  spectrum of the synthesized  $\text{H}_6\text{T CPP}$  linker.

## 2. High-throughput investigation of Ga- and In-PMOF-bs-th

The crystallinity of Ga- and In-PMOF depends strongly on the water : DMF ratio. With a large amount of water or linker : metal ratios  $> 1 : 5$ , no crystalline products are observed.

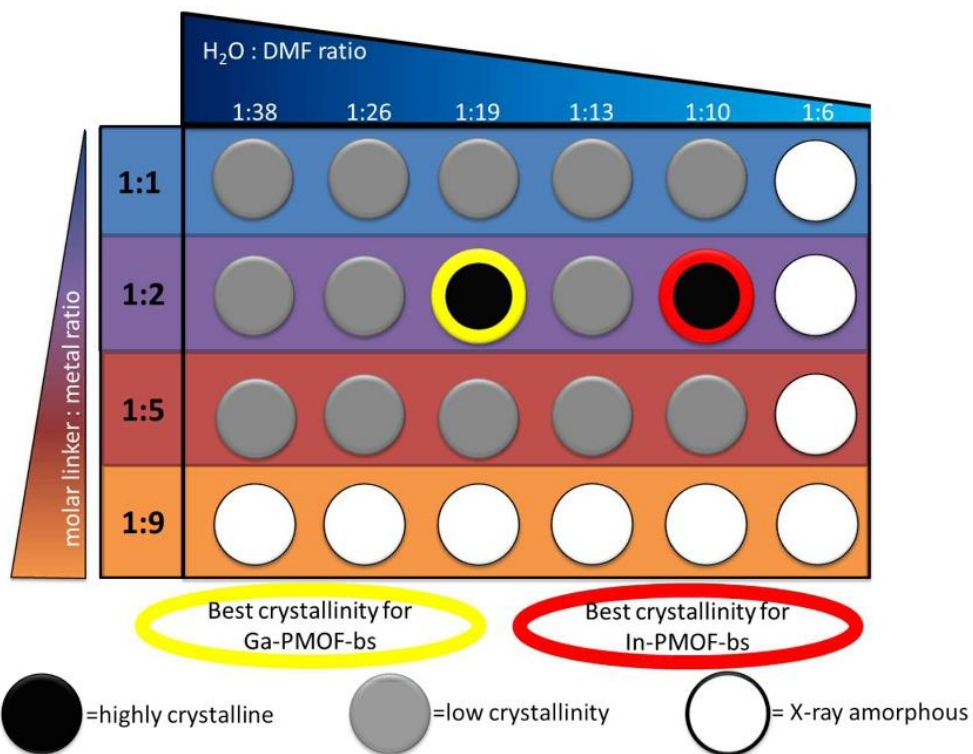


**Figure S2.** Schematic illustration of HT-experiments that led to the resulting Ga- and In-PMOF-bs-th. Water : DMF ratios are given in vol %.

### 3. Pawley fits and crystallographic data of In-PMOF-bs-us, Ga-PMOF-cf and In-PMOF-cf

The Pawley fits show that all measured samples show no additional crystalline impurities.

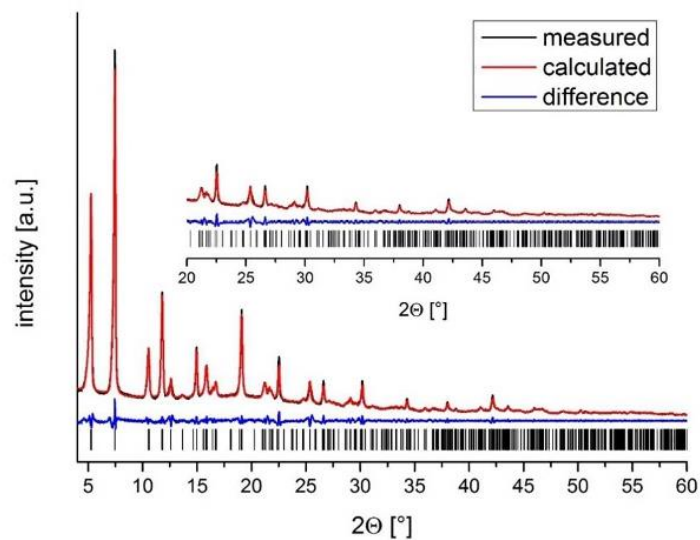


**Figure S3.** Result of the Pawley fit of In-PMOF-bs-us.

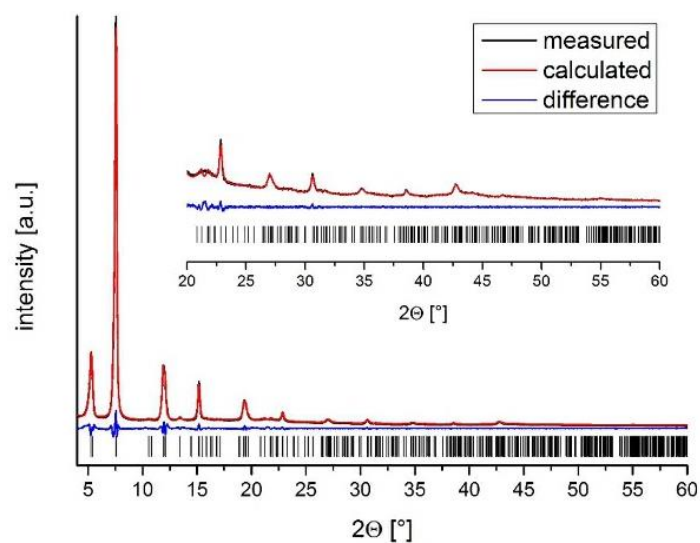


**Figure S4.** Result of the Pawley fit of Ga-PMOF-cf.

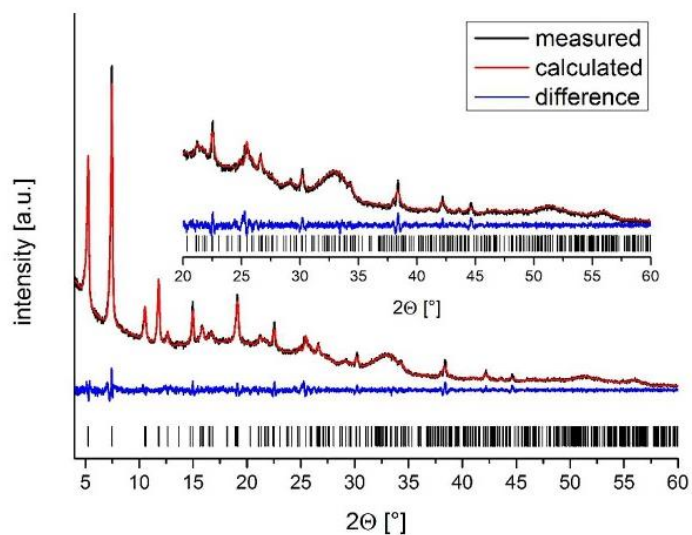


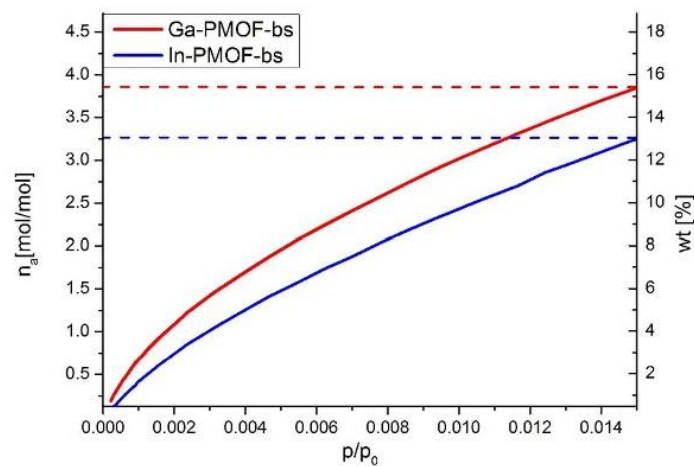
**Figure S5.** Result of the Pawley fit of In-PMOF-cf.

**Table S1.** Refined crystallographic parameters of In-PMOF-bs-th, -bs-us and -cf and Ga-PMOF-bs-th, -bs-us in comparison.

	SG	<i>a</i> [Å]	<i>b</i> [Å]	<i>c</i> [Å]	GOF	$R_{wp}$
In-PMOF-bs-th	<i>Cmmm</i>	33.432(2)	7.152(1)	16.7181(9)	1.6	5.7
In-PMOF-bs-us	<i>Cmmm</i>	33.351(2)	7.1742(5)	16.786(1)	1.0	5.0
In-PMOF-cf	<i>Cmmm</i>	33.283(8)	7.151(2)	16.793(4)	1.1	3.6
Ga-PMOF-bs-th	<i>Cmmm</i>	32.950(4)	6.700(2)	16.556(2)	2.4	6.5
Ga-PMOF-cf	<i>Cmmm</i>	32.652(8)	6.716(4)	16.739(4)	2.1	5.5

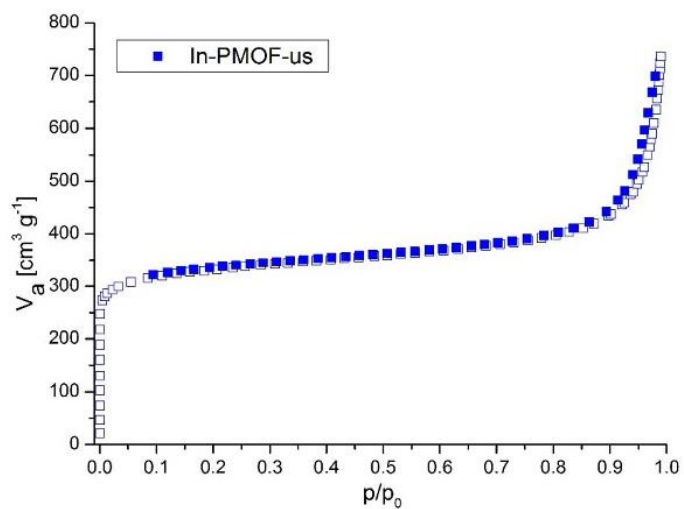
#### 4. Sorption properties and PXRD patterns of the activated samples

Figure S6 shows the CO<sub>2</sub>-sorption isotherm (298.15 K,  $p_{\max} = 1$  bar) of Ga- and In-PMOF-bs-th in mol mol<sup>-1</sup> and wt%. Figure S7 and S8 show the N<sub>2</sub>-Sorpton isothermes of In-PMOF-bs-us and Ga-PMOF-cf (120 °C). The hysteresis at  $p/p_0$  of 0.8 is due to the small particle size of this samples of about 65 nm and indicates textural porosity between the nanoparticles.

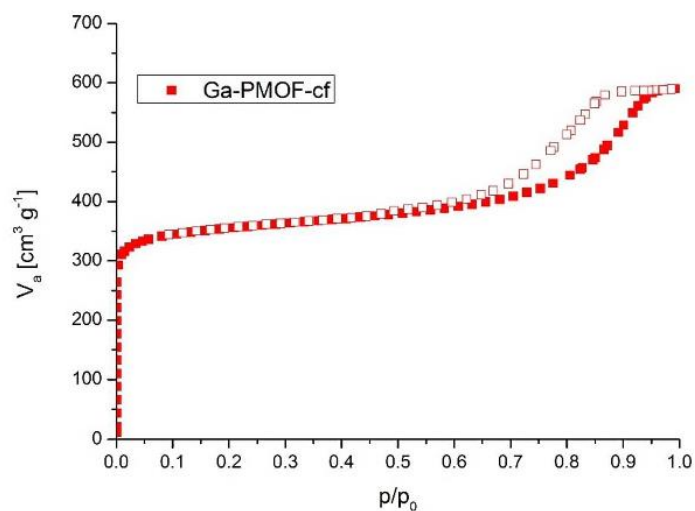


**Figure S6.** CO<sub>2</sub>-sorption isotherm of Ga- and In-PMOF obtained from the batch synthesis measured at 298.15 K up to 1 bar.

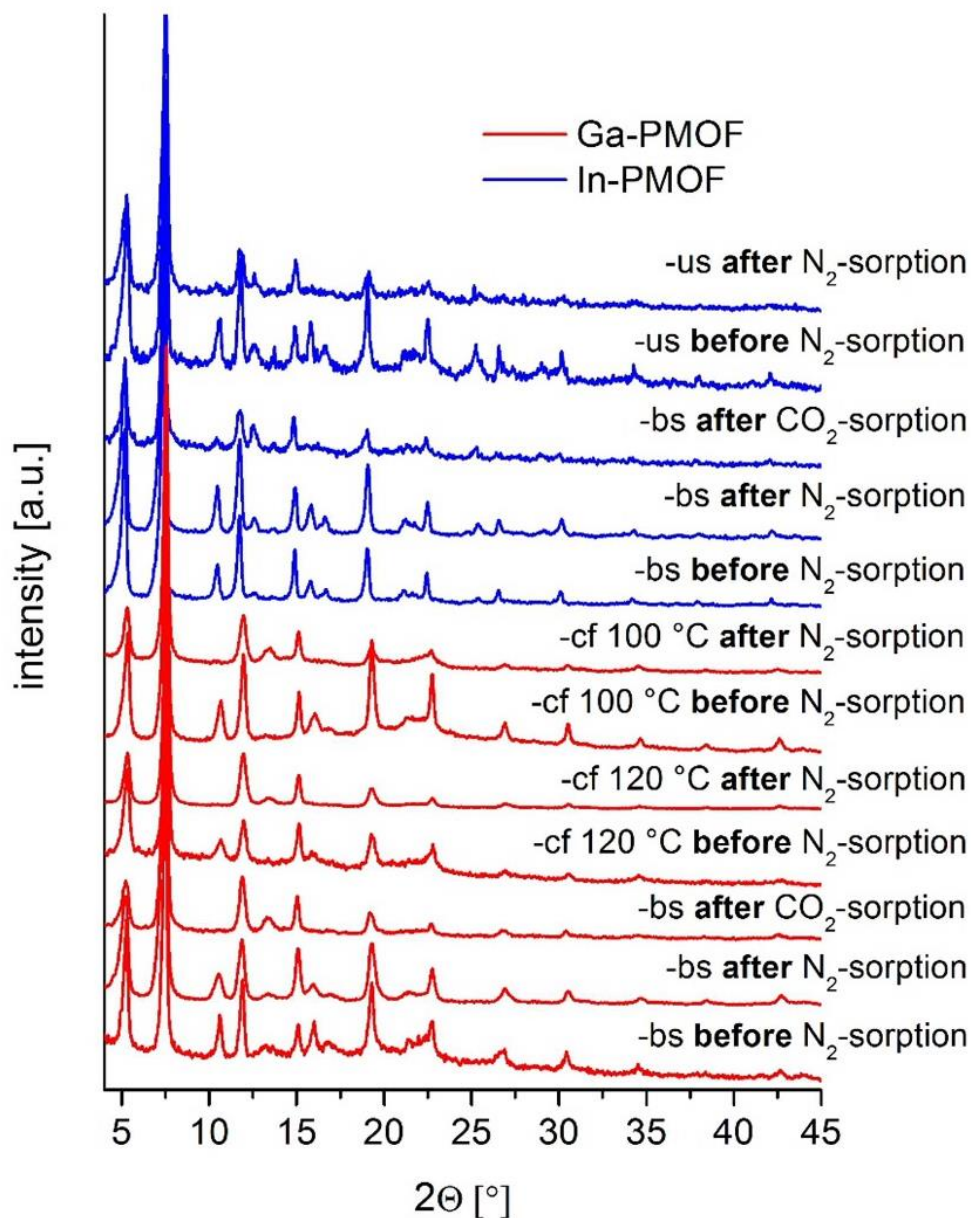




**Figure S7.**  $\text{N}_2$ -sorption isotherm of In-PMOF-bs-us measured at 77 K. Filled squares represent the adsorption and empty squares show desorption.



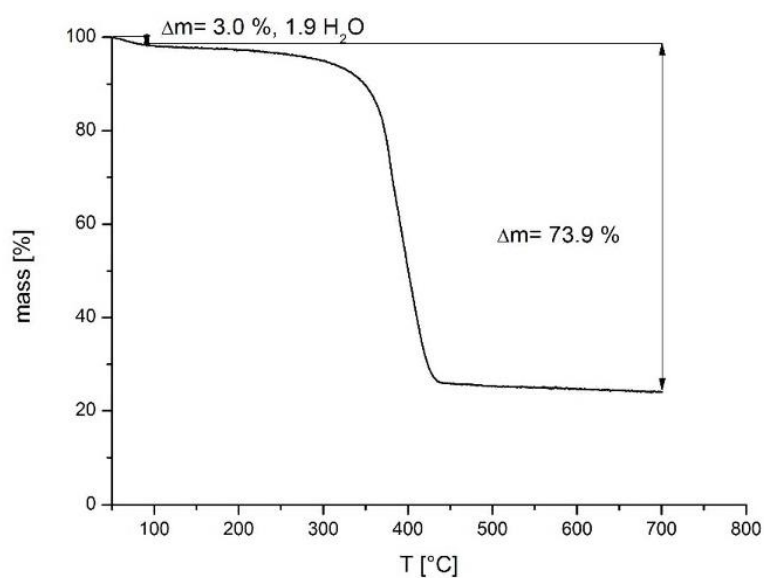
**Figure S8.**  $\text{N}_2$ -sorption isotherm of Ga-PMOF-cf (120 °C) measured at 77 K. Filled squares represent the adsorption and empty squares show desorption.



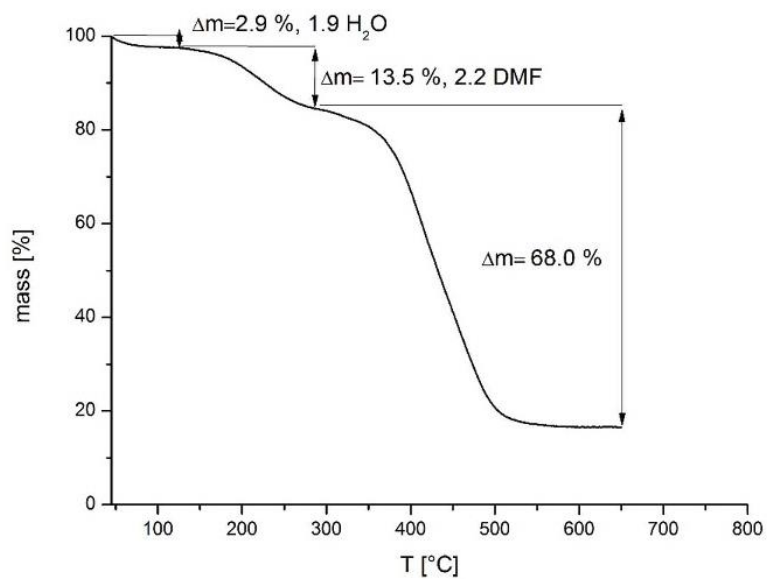
**Figure S9.** PXRD patterns of all measured samples before and after the individual sorption experiments.

## 5. TG investigations and PXRD patterns of the decomposition products

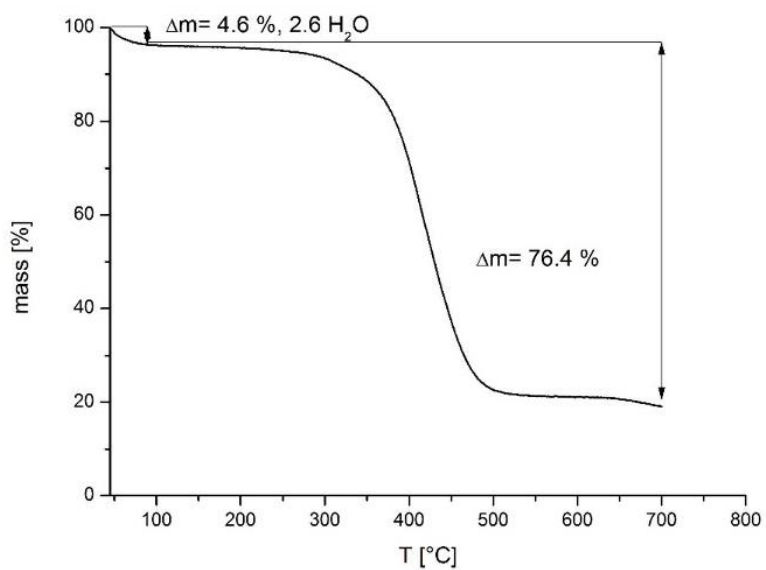
The TG measurements of the as-synthesized samples show slightly different amounts of solvent molecules in the pores (Figs. S11, S13, S14). After activation at 140 °C at  $10^{-2}$  kPa the DMF molecules can be removed and just small amounts of physisorbed water remains in the pores (Fig. S10 and S12). The decomposition products of the Ga- and In-PMOFs are  $\text{Ga}_2\text{O}_3$  and  $\text{In}_2\text{O}_3$ , which was shown by PXRD measurements (Fig. S15).



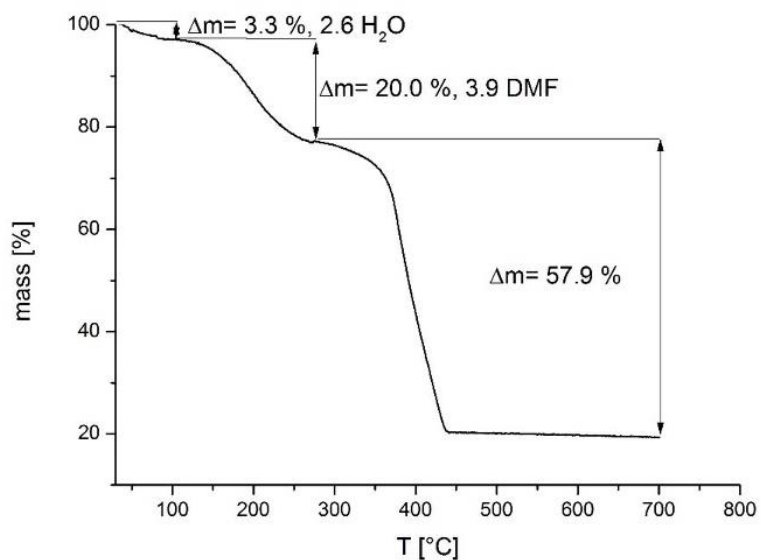
**Figure S10.** Thermogravimetric curve of an activated sample of In-PMOF-bs-th (140 °C,  $10^{-2}$  kPa). The measurement reveals a molar linker : metal :  $\text{H}_2\text{O}$  ratio of 1 : 1.9 : 1.9.



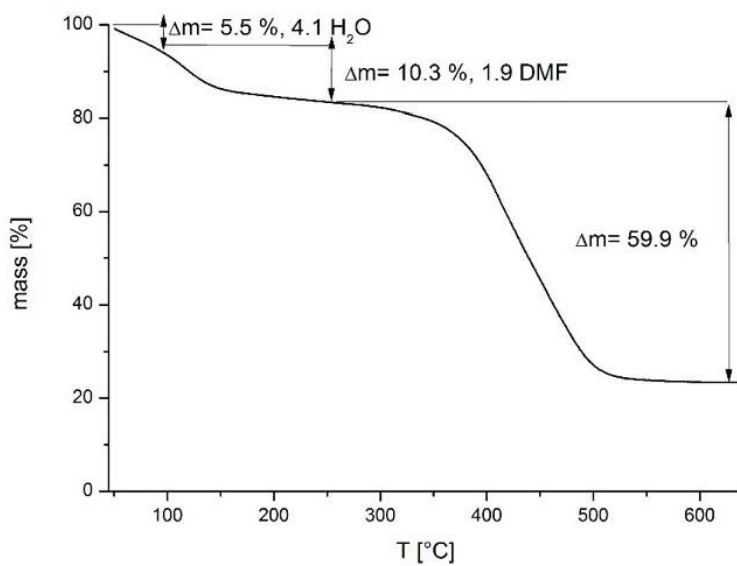
**Figure S11.** Thermogravimetric curve of an as-synthesized sample of Ga-PMOF-bs-th. The measurement reveals a molar linker : metal : H<sub>2</sub>O : DMF ratio of 1 : 1.8 : 1.9 : 2.2.



**Figure S12.** Thermogravimetric curve of an activated samples of Ga-PMOF-bs-th (140 °C, 10<sup>-2</sup> kPa). The measurement reveals a molar linker : metal : H<sub>2</sub>O ratio of 1 : 2.1 : 2.6.

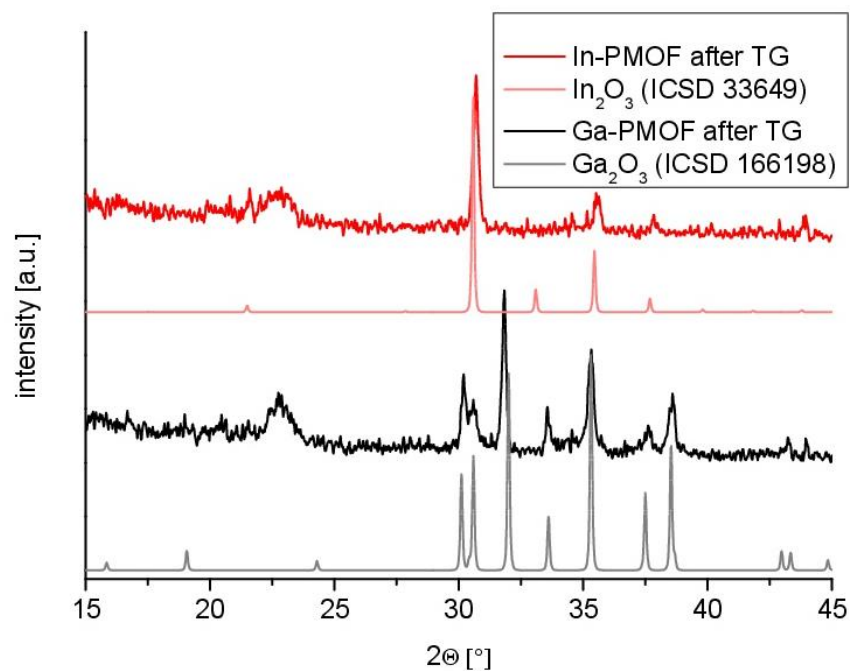


**Figure S13.** Thermogravimetric curve of an as-synthesized sample of In-PMOF-bs-us. The measurement reveals a molar linker : metal : H<sub>2</sub>O : DMF ratio of 1 : 2.0 : 2.6 : 3.9.

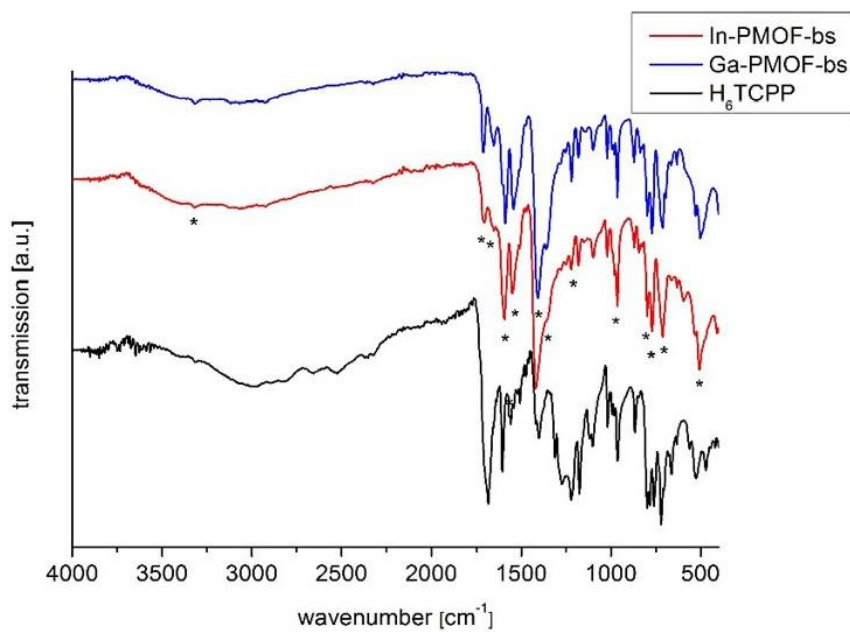


**Figure S14.** Thermogravimetric curve of an as-synthesized sample of Ga-PMOF-cf (120 °C). The measurement reveals a molar linker : metal : H<sub>2</sub>O : DMF ratio of 1 : 2.0 : 1.9 : 4.1.





**Figure S15.** PXRD patterns of the decomposition products of Ga-PMOF (black) and In-PMOF (red) after thermogravimetric measurements up to 700 °C. The simulated PXRD patterns of In<sub>2</sub>O<sub>3</sub> and Ga<sub>2</sub>O<sub>3</sub> are also presented for comparison.

**6. IR spectroscopy of Ga- and In-PMOF-bs-th**

**Figure S16.** IR-spectra of as-synthesized samples of Ga- (blue) and In-PMOF-bs-th (red). For comparison the IR-spectrum of the linker H<sub>6</sub>TCPP (black) is also presented. The black stars mark the selected bands commented in Table S2.

**Table S2.** Assignment of the vibrations in the IR-spectra of Ga- and In-PMOF-bs-th as-synthesized. Red numbers indicate slight impurities with DMF or linker, black numbers represent vibrations of the corresponding MOF.<sup>4,5</sup>

Vibration	Ga-PMOF-bs-th $\tilde{\nu}$ IR [cm <sup>-1</sup> ]	In-PMOF-bs-th $\tilde{\nu}$ IR [cm <sup>-1</sup> ]	H <sub>6</sub> TCPP $\tilde{\nu}$ IR [cm <sup>-1</sup> ] <sup>1-3</sup>
$\nu$ NH (pyrrole)	3320	3318	3315
$\nu$ CO (DMF)	1709	1711	
$\nu_{as}$ CO (COOH (H <sub>6</sub> TCPP))	1652	1652	1684
$\nu_{as}$ CO (COO)	1594	1587	
$\nu$ C=C (arom.)	1550	1542	1558
$\nu_s$ CO (COO)	1417	1409	
$\nu$ C-N (pyrrole)	1362	1362	1399
$\delta$ O-H (COOH (H <sub>6</sub> TCPP))	1222	1219	1222/ 1173
$\delta$ C-H, N-H (pyrrole), neighboring H	961	964	962
$\gamma$ C-H (1,4-subst.)	796	799	798
$\delta$ C-H, N-H (pyrrole), neighboring H	766	768	757
$\gamma$ C-H (out of plane)	708	714	717
$\delta$ C=C (skeleton)	504	506	525

## 7. DLS and SEM measurements

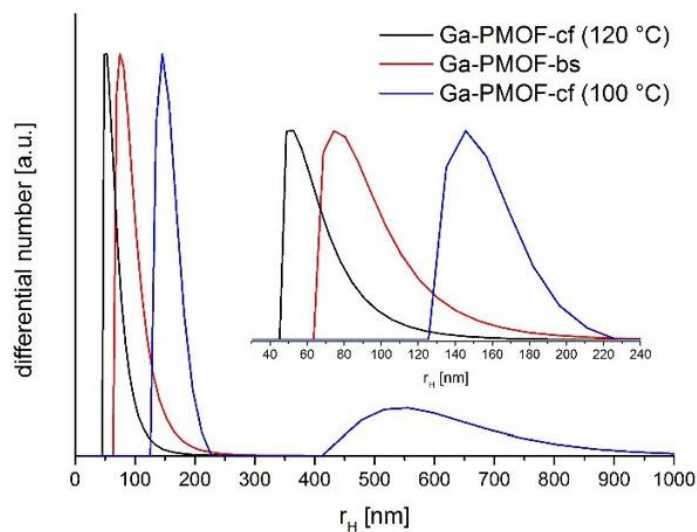


**Figure S17.** Results of the DLS measurements of as-synthesized samples of the Ga-PMOFs by number distribution. Ga-PMOF-cf (120 °C) is shown in black, Ga-PMOF-bs-th in red and Ga-PMOF-cf (100 °C) in blue. The small fraction of larger particle sizes of Ga-PMOF-cf (100 °C) is caused by agglomeration during the DLS measurement.

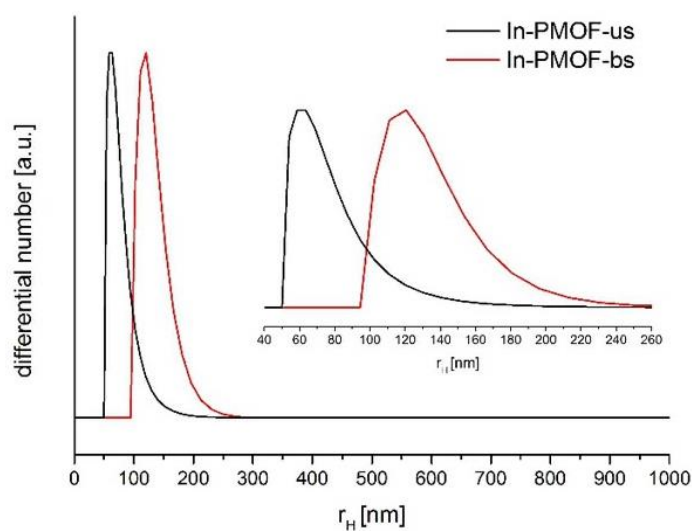


**Figure S18.** Results of the DLS measurements of as-synthesized samples of the In-PMOFs by number distribution. In-PMOF-bs-us is shown in black and In-PMOF-bs-th in red.

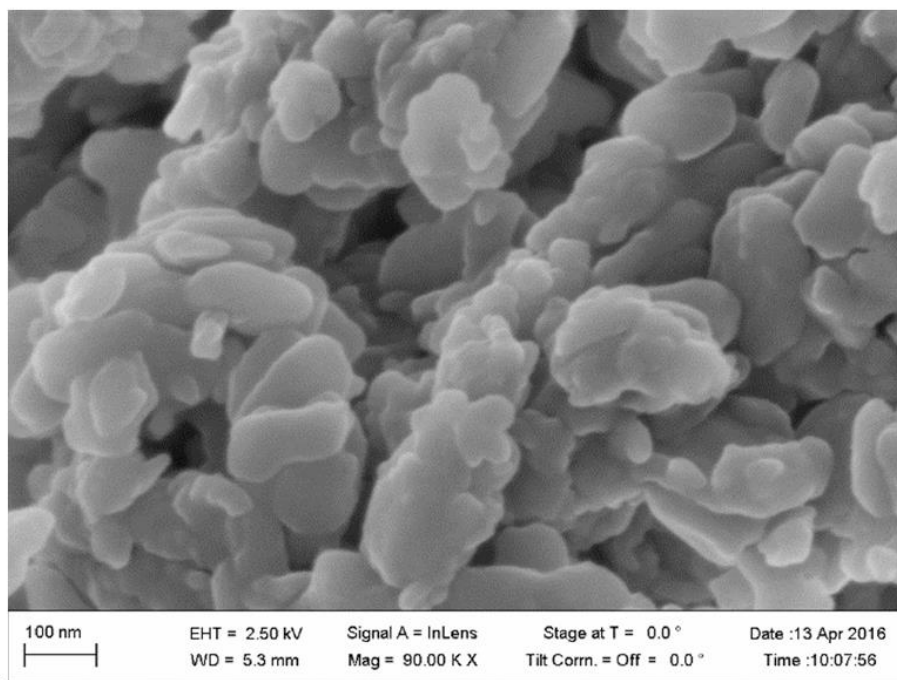


**Figure S19.** SEM image of Ga-PMOF-bs-th.

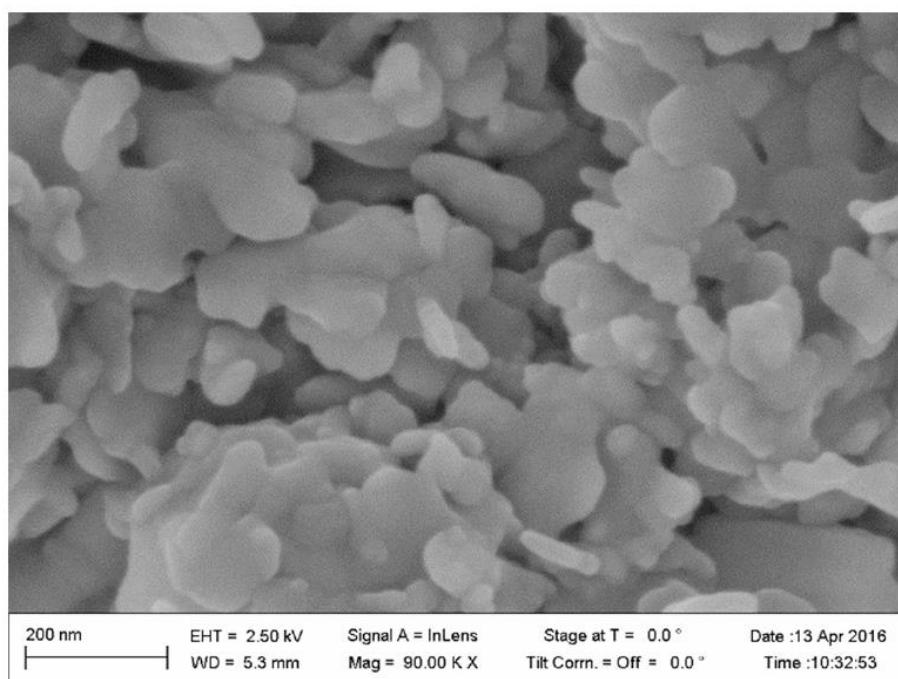


**Figure S20.** SEM image of In-PMOF-bs-th.



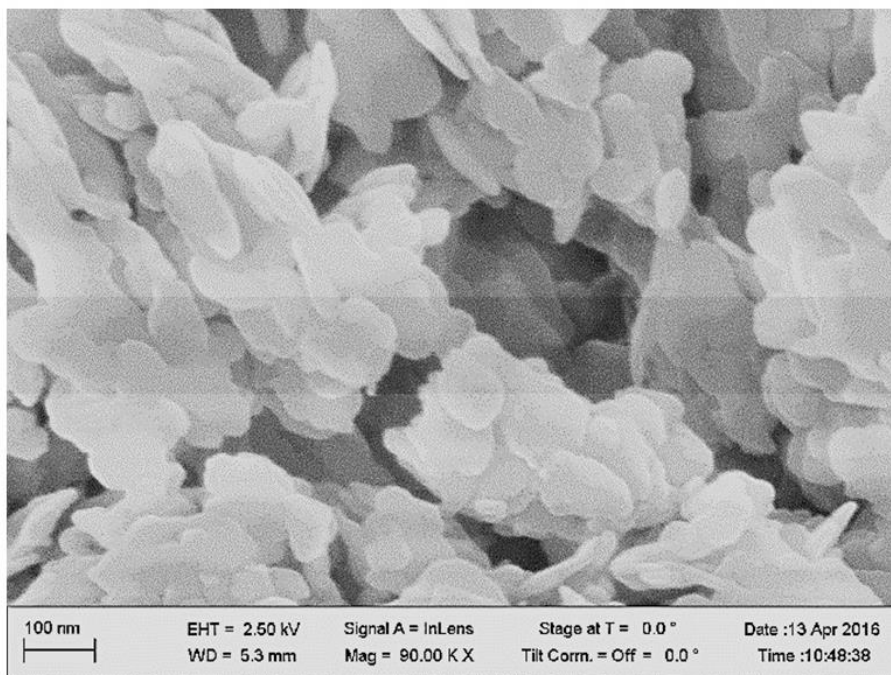


**Figure S21.** SEM image of In-PMOF-bs-us.

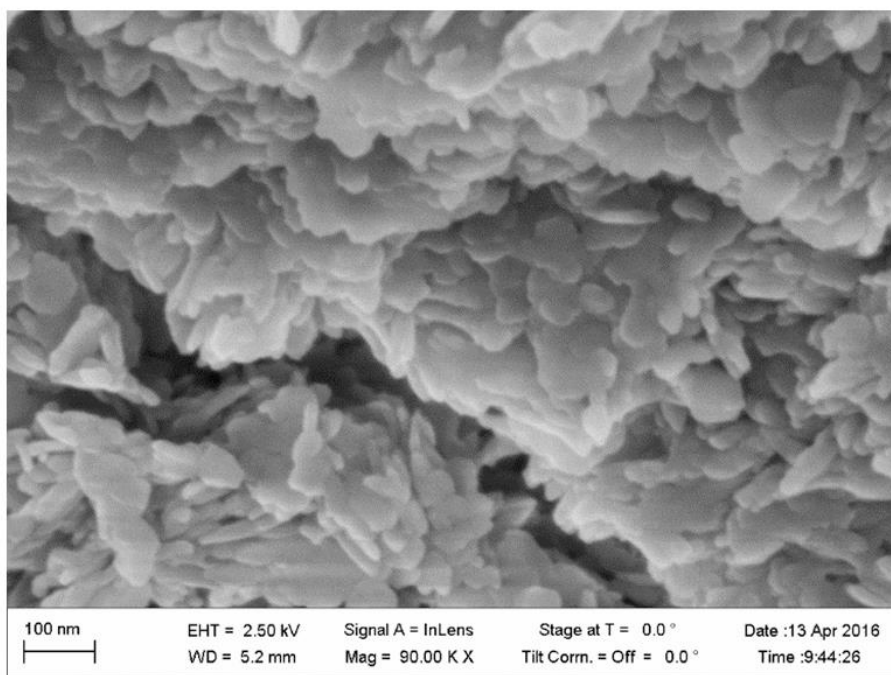


**Figure S22.** SEM image of Ga-PMOF-cf(100 °C).

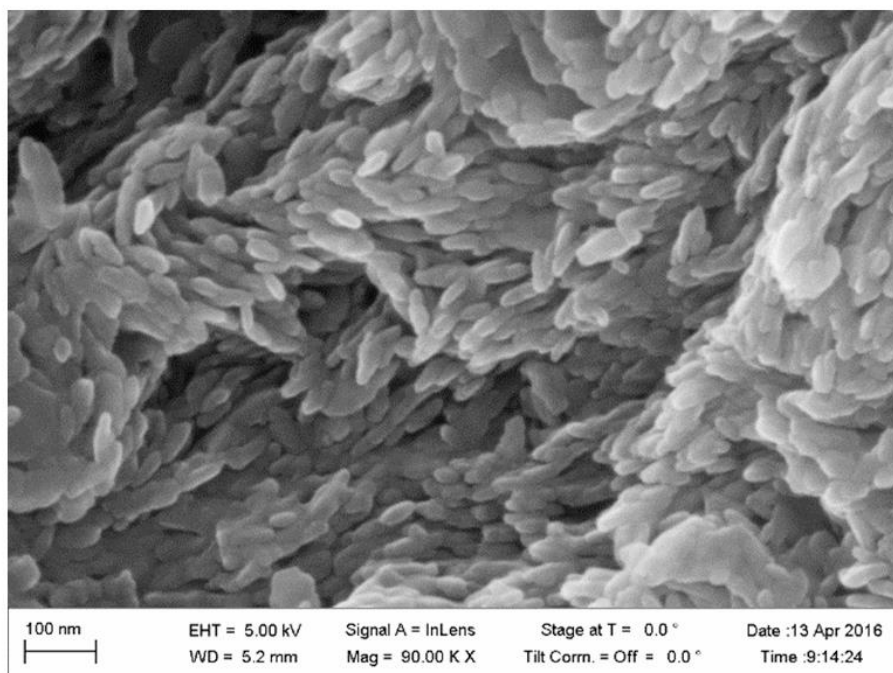


**Figure S23.** SEM image of Ga-PMOF-cf. (120 °C).

## 8. Literature

- (1) Jeong, E.-Y.; Ansari, M. B.; Mo, Y.-H.; Park, S.-E., *J. Hazard. Mater.* **2011**, *185*, 1311-1317.
- (2) Harada, A.; Yamaguchi, H.; Okamoto, K.; Fukushima, H.; Shiotsuki, K.; Kamachi, M., *Photochem. Photobiol.* **1999**, *70*, 298-302.
- (3) Garcia, G.; Sol, V.; Lamarche, F.; Granet, R.; Guilloton, M.; Champavier, Y.; Krausz, P., *Bioorg. Med. Chem. Lett.* **2006**, *16*, 3188-3192.
- (4) Socrates, G., *Infrared and Raman Characteristic Group Frequencies: Tables and Charts*. Wiley: **2004**.
- (5) Hesse, M.; Meier, H.; Zeeh, B., *Spektroskopische Methoden in der organischen Chemie*. Thieme: **2005**.



**9 SI zu „Co-Ligand Dependent Formation and Phase Transformation of Four Porphyrin-Based Cerium Metal–Organic Frameworks”  
Supporting Information**

**Co-ligand dependent Formation and Phase  
Transformation of Four Porphyrin-based Cerium  
MOFs**

*Timo Rhauderwiek,<sup>a</sup> Niclas Heidenreich,<sup>a,b</sup> Helge Reinsch,<sup>a</sup> Sigurd Øien-Ødegaard,<sup>c</sup> Kirill A. Lomachenko,<sup>d,e</sup> Uta Rütt,<sup>b</sup> Alexander V. Soldatov,<sup>d</sup> Karl Petter Lillerud,<sup>c</sup> Norbert Stock<sup>a,c,\*</sup>*

<sup>a</sup> Institute of Inorganic Chemistry, Christian-Albrechts-Universität, Max-Eyth Straße 2, D-241 18 Kiel, Germany

<sup>b</sup> Deutsches-Elektronen-Synchrotron DESY, Notkestraße 85, 22607 Hamburg

<sup>c</sup> Department of Chemistry, University of Oslo, Sem Sælands vei 26, N-0371 Oslo, Norway

<sup>d</sup> International Research Center “Smart Materials”, Southern Federal University, Zorge Street 5, 344090 Rostov-on-Don, Russia

<sup>e</sup> European Synchrotron Radiation Facility, 71 avenue des Martyrs, CS 40220, 38043 Grenoble Cedex 9, France

<b>1. Synthesis of H<sub>6</sub>TCPP (<sup>1</sup>H-NMR spectrum) and Co-H<sub>4</sub>TCPP (PXRD, UV/vis).....</b>	<b>3-</b>
	<b>7</b>
<b>2. <sup>1</sup>H-NMR spectroscopy and elemental analysis (title compounds) .....</b>	<b>8-</b>
	<b>17</b>
<b>3. SEM images of single crystals of CAU-18 and CAU-19-H, structural representations of CAU-18 and CAU-19-H, Ce L<sub>3</sub>-edge XANES spectra (title compounds).....</b>	<b>17-</b>
	<b>21</b>
<b>4. Crystallographic data and Pawley-fits of M-CAU-19-X.....</b>	<b>22-</b>
	<b>29</b>
<b>5. Sorption properties and PXRD patterns of the activated samples.....</b>	<b>30-</b>
	<b>31</b>
<b>6. TG investigations and PXRD patterns of the decomposition products.....</b>	<b>32-</b>
	<b>38</b>
<b>7. <i>In situ</i> XRD studies of CAU-18 and CAU-19-H.....</b>	<b>39-</b>
	<b>46</b>
<b>8. IR spectroscopy of CAU-18, CAU-18a, Ce-PMOF-4NO<sub>2</sub> and CAU-19-X.....</b>	<b>47-52</b>
<b>9. References.....</b>	<b>53</b>



**1. Synthesis of H<sub>6</sub>TCPP (<sup>1</sup>H-NMR spectrum) and Co-H<sub>4</sub>TCPP (PXRD, UV/vis)**

**Synthesis of H<sub>6</sub>TCPP.** The synthesis of H<sub>6</sub>TCPP was carried out following the procedures described in the literature.<sup>1-3</sup> Pyrrole (14.01 mL, 202.5 mmol) and 4-formylbenzoic acid (30.40 g, 202.5 mmol) in 750 mL propionic acid were heated under reflux for 2 h. Afterwards the reaction mixture was cooled down to room temperature and poured into 1000 mL of MeOH and stirred for 30 min in an ice bath. The resulting precipitate was filtered off and washed several times with MeOH until the filtrate was clear. Subsequently, the product was washed with 200 mL warm distilled water and dried at 70 °C in a drying oven over night.

Elemental analysis of H<sub>6</sub>TCPP: calc (%): C 72.9, H 3.8, N 7.1, found (%): C 71.3, H 4.3, N 6.9. The small difference between the calculated and observed values is due to impurities caused by solvent molecules used in the synthesis. These impurities were also observed in the <sup>1</sup>H-NMR measurements.

<sup>1</sup>H-NMR (Figure S1), (500 MHz, DMSO-d<sub>6</sub>): δ= 8.86 (s, 8H, H-1); 8.39 (d, 8H, H-2); 8.33 (d, 8H, H-3); 3.35 (s, 2H, H<sub>2</sub>O); 2.50 (s, 6H, DMSO); 2.22 (q, 2H, propionic acid); 1.00 (t, 3H, propionic acid) ppm.

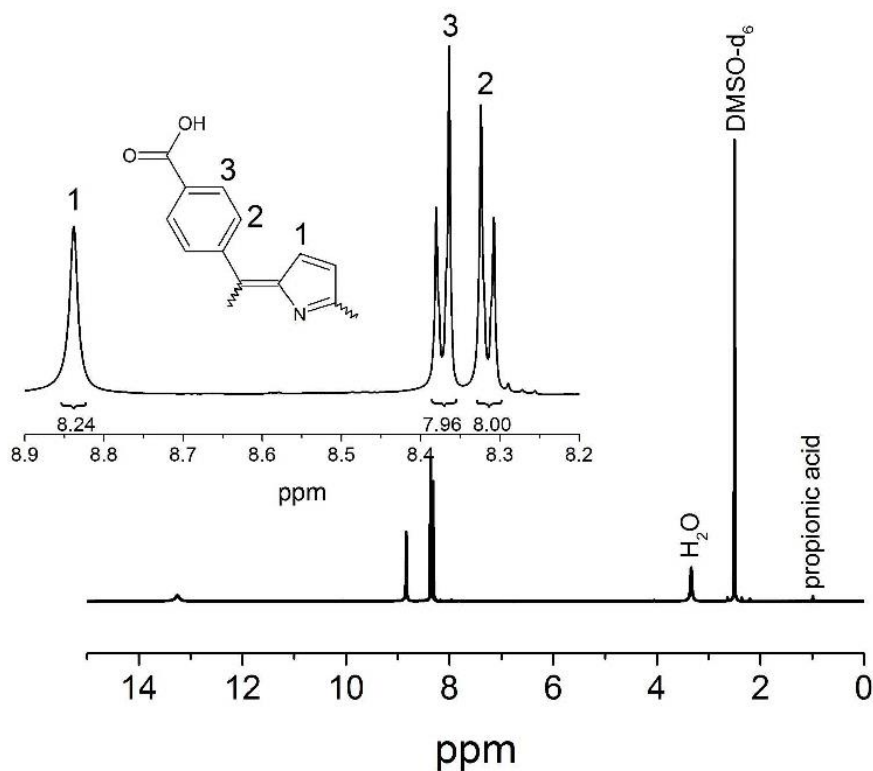


**Figure S1.** <sup>1</sup>H-NMR spectrum of the synthesized H<sub>6</sub>TCPP linker.

**Synthesis of Co-H<sub>4</sub>TCPP.** The synthesis of Co-H<sub>4</sub>TCPP was accomplished by hydrolysis of the metalated methyl ester Co-TCPP-Me<sub>4</sub>,<sup>5</sup> which was obtained according to a literature procedure.<sup>4</sup>

Co-TCPP-Me<sub>4</sub>: H<sub>6</sub>TCPP (79 mg, 0.1 mmol), CoCl<sub>2</sub> · 6 H<sub>2</sub>O (23.8 mg, 0.1 mmol) and 10 mL MeOH were sealed in a 30 mL Teflon-lined steel autoclave and heated for 24 h at 180 °C and cooled down to room temperature over 30 h. The precipitate was filtered off and washed several times with MeOH to achieve 55 mg (61 %, Lit.<sup>4</sup>: 63 %) of black crystals. To proof that Co-TCPP-Me<sub>4</sub> was successfully synthesized PXRD measurements (Fig. S2) were carried out.

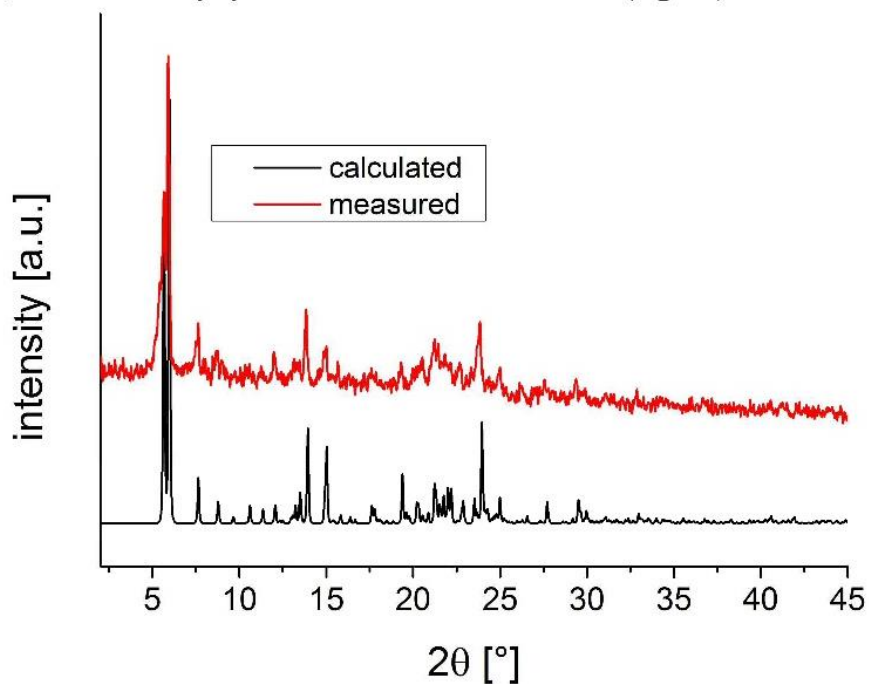


**Figure S2.** PXRD pattern of Co-TCPP-Me<sub>4</sub> compared with the calculated PXRD pattern.<sup>4</sup>

The UV/vis spectra of the metallated free linker molecules and the dissolved MOFs show no significant decrease in metalation (Fig. S4). The cobalt and zinc ions are still in the porphyrin centre after the MOF synthesis.

Co-H<sub>4</sub>TCPP: Co-TCPP-Me<sub>4</sub> (250 mg, 0.29 mmol), 25 mL THF, 25 mL MeOH and KOH (2.63g, 46,95 mmol) in 25 mL H<sub>2</sub>O were heated under reflux for 19 h at 80 °C. The resulting product was filtered off, washed several times with MeOH and dried at 70 °C to achieve a quantitative amount of the hydrolysed Co-H<sub>4</sub>TCPP. To proof quantitative metalation UV/vis spectra were measured (Fig. S3).

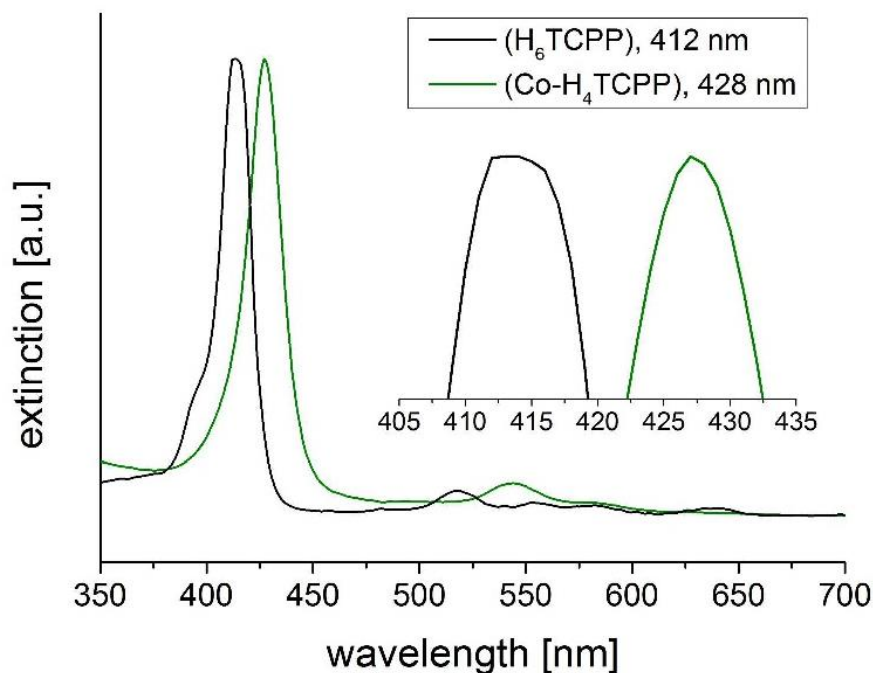


**Figure S3.** UV/vis spectra of H<sub>6</sub>TCPP and Co-H<sub>4</sub>TCPP dissolved in 2M NaOH. Both absorption maxima are well separated. The absorption maximum of H<sub>6</sub>TCPP is found at 412 and the absorption maximum of Co-H<sub>4</sub>TCPP at 428 nm (Lit.: H<sub>6</sub>TCPP = 413,<sup>6, 7</sup> Co-H<sub>4</sub>TCPP = 430 nm<sup>6</sup>).

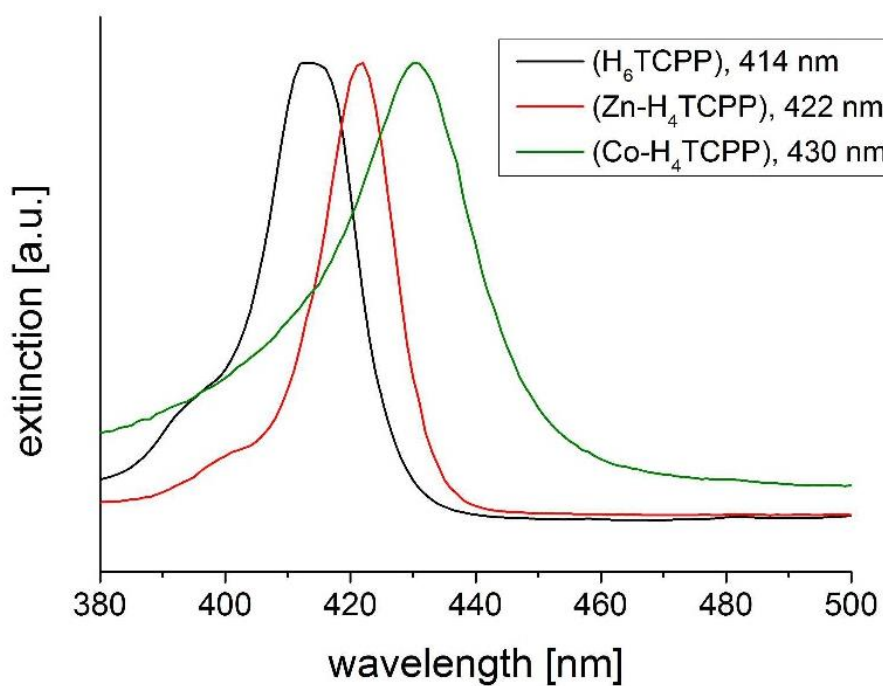


**Figure S4.** UV/vis spectra of CAU-19-H, Zn-CAU-19-H and Co-CAU-19-H dissolved in 2M NaOH. All absorption maxima are well separated from each other. The absorption maximum of the  $H_6TCPP$ ,  $Zn-H_4TCPP$  and  $Co-H_4TCPP$  is found at 414, 422 and 430 nm, respectively (Lit.:  $H_6TCPP=413$ ,<sup>6,7</sup>  $Zn-H_4TCPP=424$  nm,<sup>8</sup>  $Co-H_4TCPP=430$  nm<sup>6</sup>).



## 2. $^1\text{H-NMR}$ spectroscopy and elemental analysis (title compounds)

The  $^1\text{H-NMR}$  spectra (Fig. S5-S12) of all measured compounds show no further impurities except solvent molecules and small amounts of formic acid, which is explainable as decomposition product of DMF. The MOFs were dissolved and subsequently measured in  $\text{DMSO-d}_6+5\% \text{ DCl}$  in  $\text{D}_2\text{O}$ .

### CAU-19-H: ( $\text{H}_6\text{TCPP}$ and benzoic acid (HBA-H))

$^1\text{H-NMR}$  (Figure S5), (500 MHz,  $\text{DMSO-d}_6+5\% \text{ DCl}$  in  $\text{D}_2\text{O}$  (7:1):  $\delta= 8.76$  (d, 8H, H-3); 8.74 (s, 8H, H-1); 8.60 (d, 8H, H-2); 8.10 (s, 1H, formic acid); 8.01 (s, 1H, DMF); 7.90 (d, 2H, H-6); 7.59 (t, 1H, H-4); 7.47 (t, 2H, H-5) 4.06 (s, 2H,  $\text{H}_2\text{O}$ ); 2.86 (s, 3H, DMF); 2.70 (s, 3H, DMF); 2.50 (s, 6H,  $\text{DMSO-d}_6$ ); 2.05 (s, 6H, acetone) ppm.

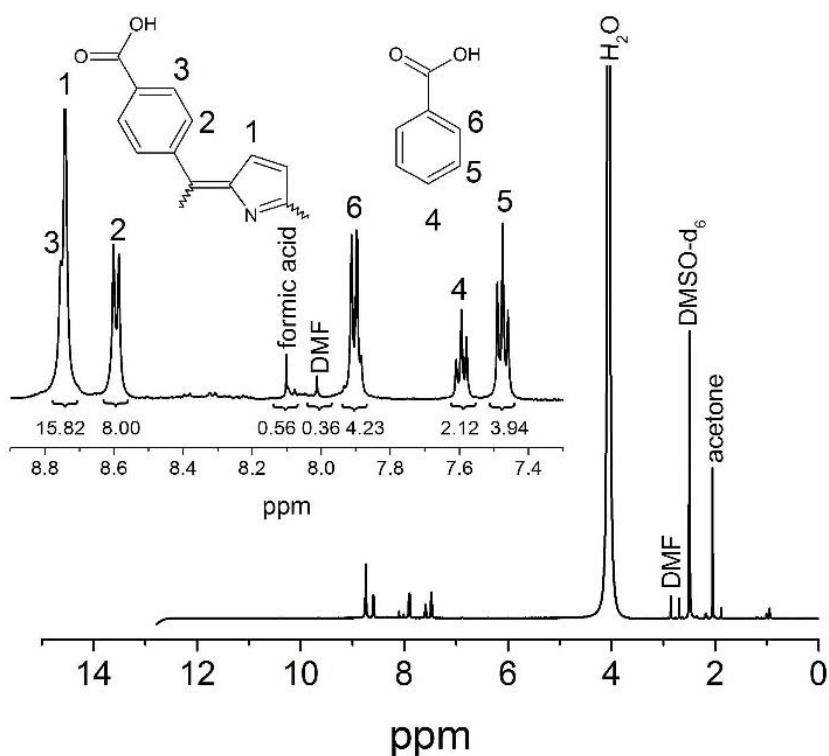


**Figure S5.**  $^1\text{H-NMR}$  spectrum of CAU-19-H digested in a mixture of  $\text{DMSO}$  and  $\text{DCl}$ .

**CAU-19-2Cl: (H<sub>6</sub>TCPP and 2-chlorobenzoic acid (HBA-2Cl))**

<sup>1</sup>H-NMR (Figure S6), (500 MHz, DMSO-d<sub>6</sub>+5% DCl in D<sub>2</sub>O (7:1): δ= 8.78 (d, 8H, H-3); 8.74 (s, 8H, H-1); 8.62 (d, 8H, H-2); 8.11 (s, 1H, formic acid); 7.90 (s, 1H, DMF); 7.75 (d, 1H, H-4); 7.52 (m, 2H, H-5,6); 7.41 (m, 1H, H-7); 4.05 (s, 2H, H<sub>2</sub>O); 2.87 (s, 3H, DMF); 2.70 (s, 3H, DMF); 2.50 (s, 6H, DMSO-d<sub>6</sub>); 2.06 (s, 6H, acetone) ppm.

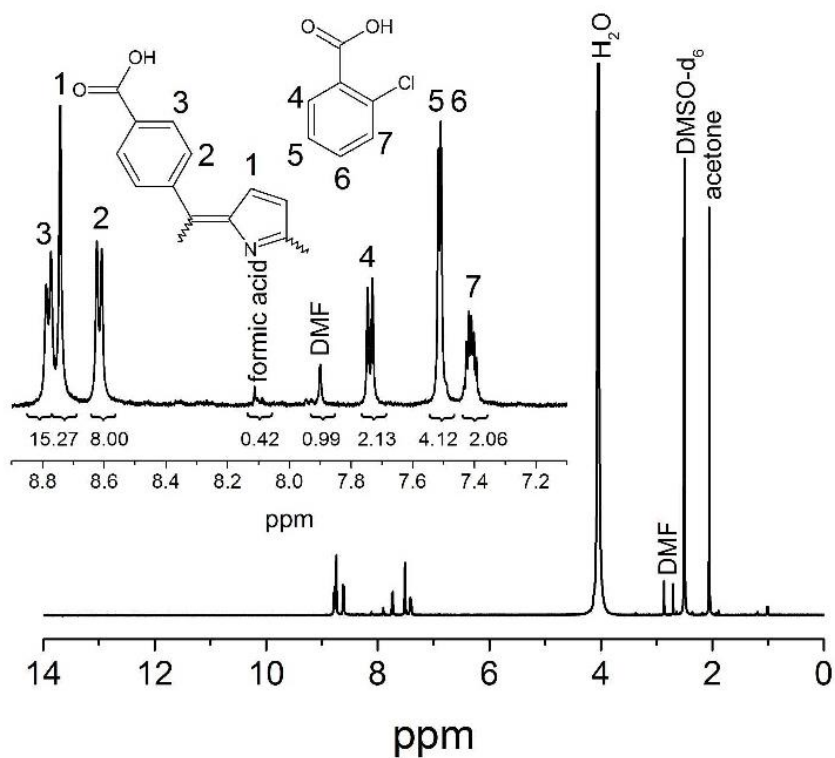


**Figure S6.** <sup>1</sup>H-NMR spectrum of CAU-19-2Cl digested in a mixture of DMSO and DCl.

**CAU-19-3Cl: (H<sub>6</sub>TCPP and 3-chlorobenzoic acid (HBA-3Cl))**

<sup>1</sup>H-NMR (Figure S7), (500 MHz, DMSO-d<sub>6</sub>+5% DCl in D<sub>2</sub>O (7:1): δ= 8.76 (d, 8H, H-3); 8.75 (s, 8H, H-1); 8.61 (d, 8H, H-2); 8.35 (d, 1H, H-4); 8.27 (d, 1H, H-6); 8.11 (s, 1H, formic acid); 7.86 (s, 1H, DMF); 7.67 (d, 1H, H-7); 7.54 (t, 1H, H-5); 4.03 (s, 2H, H<sub>2</sub>O); 2.50 (s, 6H, DMSO-d<sub>6</sub>) ppm.

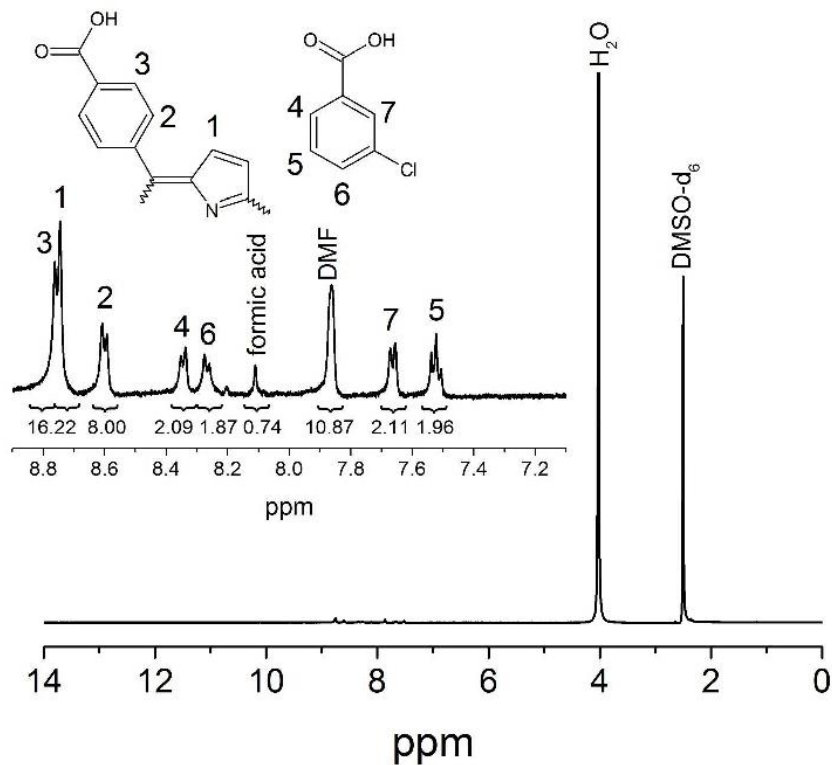


**Figure S7.** <sup>1</sup>H-NMR spectrum of CAU-19-3Cl digested in a mixture of DMSO and DCl.

**CAU-19-4Cl: (H<sub>6</sub>TCPP and 4-chlorobenzoic acid (HBA-4Cl))**

<sup>1</sup>H-NMR (Figure S8), (500 MHz, DMSO-d<sub>6</sub>+5% DCl in D<sub>2</sub>O (7:1): δ= 8.75 (d, 8H, H-3); 8.70 (s, 8H, H-1); 8.63 (d, 8H, H-2); 8.13 (s, 1H, formic acid); 7.91 (d, 2H, H-4); 7.57 (d, 2H, H-5); 4.15 (s, 2H, H<sub>2</sub>O); 2.88 (s, 3H, DMF); 2.72 (s, 3H, DMF); 2.50 (s, 6H, DMSO-d<sub>6</sub>) ppm.

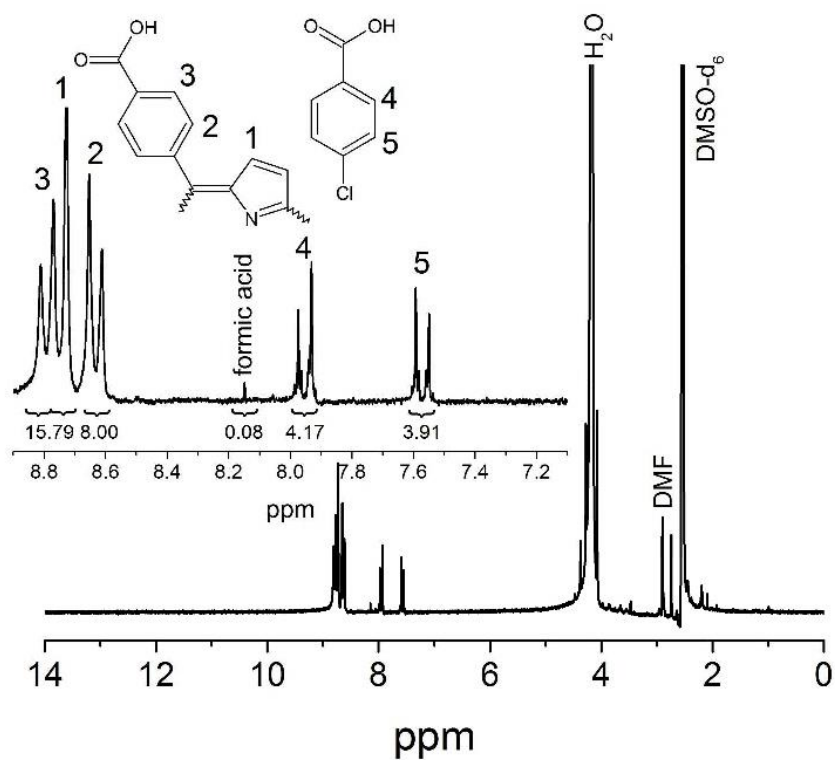


**Figure S8.** <sup>1</sup>H-NMR spectrum of CAU-19-4Cl digested in a mixture of DMSO and DCl.

**CAU-19-3CO<sub>2</sub>H: (H<sub>6</sub>TCPP and 3-carboxybenzoic acid, HBA-COOH)**

<sup>1</sup>H-NMR (Figure S9), (500 MHz, DMSO-d<sub>6</sub>+5% DCl in D<sub>2</sub>O (7:1): δ= 8.79 (d, 8H, H-3); 8.75 (s, 8H, H-1); 8.63 (d, 8H, H-2); 8.44 (s, 1H, H-4); 8.16 (d, 2H, H-5); 8.11 (s, 1H, formic acid); 7.90 (s, 1H, DMF); 7.64 (t, 1H, H-6); 4.08 (s, 2H, H<sub>2</sub>O); 2.87 (s, 3H, DMF); 2.70 (s, 3H, DMF); 2.50 (s, 6H, DMSO-d<sub>6</sub>) ppm.

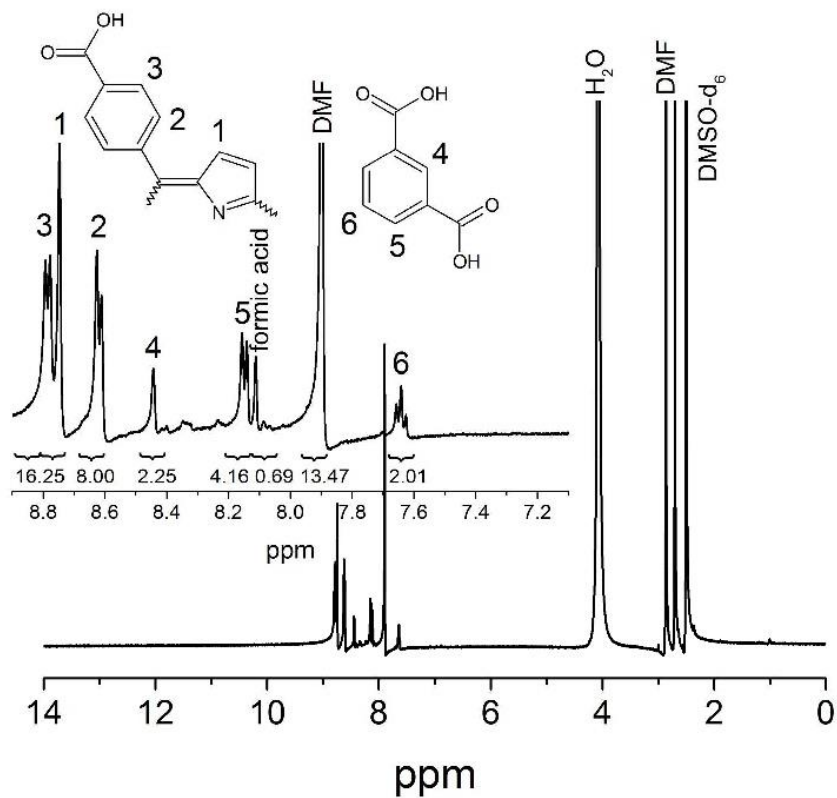


**Figure S9.** <sup>1</sup>H-NMR spectrum of CAU-19-3CO<sub>2</sub>H digested in a mixture of DMSO and DCl.



**CAU-19-4NH<sub>2</sub>: (H<sub>6</sub>TCPP and 4-aminobenzoic acid, HBA-NH<sub>2</sub>)**

<sup>1</sup>H-NMR (Figure S10), (500 MHz, DMSO-d<sub>6</sub>+5% DCl in D<sub>2</sub>O (7:1): δ= 8.75 (d, 8H, H-3); 8.75 (s, 8H, H-1); 8.61 (d, 8H, H-2); 8.11 (s, 1H, formic acid); 7.90 (s, 1H, DMF); 7.87 (d, 2H, H-4); 7.13 (d, 2H, H-5); 4.02 (s, 2H, H<sub>2</sub>O); 2.87 (s, 3H, DMF); 2.70 (s, 3H, DMF); 2.50 (s, 6H, DMSO-d<sub>6</sub>); 2.05 (s, 6H, acetone); 1.00 (d, 3H, ethanol) ppm.

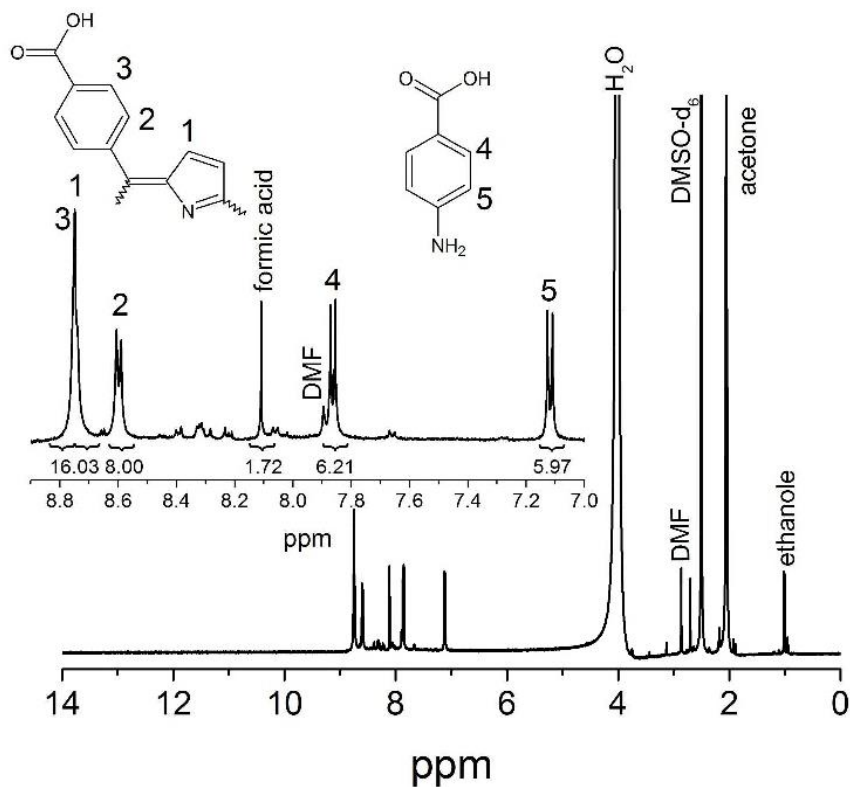


**Figure S10.** <sup>1</sup>H-NMR spectrum of CAU-19-4NH<sub>2</sub> digested in a mixture of DMSO and DCl.

**CAU-19-4NO<sub>2</sub>: (H<sub>6</sub>TCPP and 4-nitrobenzoic acid (HBA-4NO<sub>2</sub>))**

<sup>1</sup>H-NMR (Figure S11), (500 MHz, DMSO-d<sub>6</sub>+5% DCl in D<sub>2</sub>O (7:1): δ= 8.79 (d, 8H, H-3); 8.73 (s, 8H, H-1); 8.62 (d, 8H, H-2); 8.29 (d, 2H, H-4); 8.15 (d, 2H, H-5); 8.11 (s, 1H, formic acid); 7.89 (s, 1H, DMF); 4.13 (s, 2H, H<sub>2</sub>O); 2.87 (s, 3H, DMF); 2.70 (s, 3H, DMF); 2.50 (s, 6H, DMSO-d<sub>6</sub>) ppm.

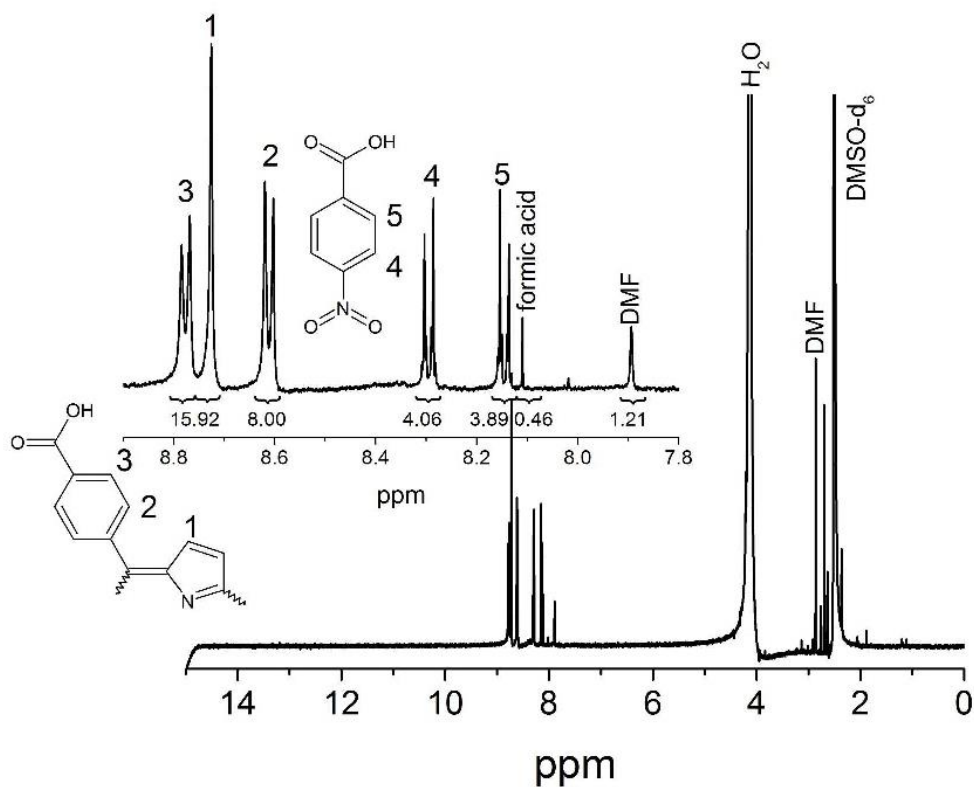


**Figure S11.** <sup>1</sup>H-NMR spectrum of CAU-19-4NO<sub>2</sub> digested in a mixture of DMSO and DCl.

**Ce-PMOF-4NO<sub>2</sub>: (H<sub>6</sub>TCPP and 4-nitrobenzoic acid (HBA-4NO<sub>2</sub>))**

<sup>1</sup>H-NMR (Figure S12), (500 MHz, DMSO-d<sub>6</sub>+5% DCl in D<sub>2</sub>O (7:1):  $\delta$ = 8.79 (d, 8H, H-3); 8.73 (s, 8H, H-1); 8.62 (d, 8H, H-2); 8.29 (d, 2H, H-4); 8.15 (d, 2H, H-5); 4.13 (s, 2H, H<sub>2</sub>O); 2.50 (s, 6H, DMSO-d<sub>6</sub>); 2.05 (s, 6H, acetone) ppm.

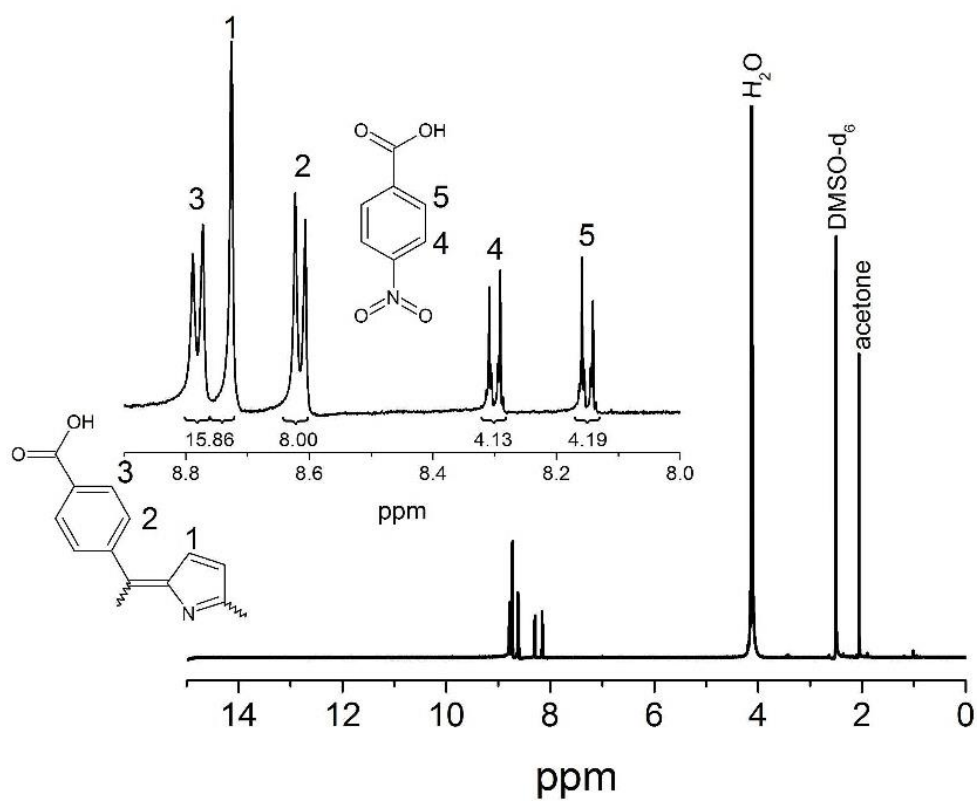


**Figure S12.** <sup>1</sup>H-NMR spectrum of Ce-PMOF-4NO<sub>2</sub> digested in a mixture of DMSO and DCl.

**Table S1.** Results of the elemental analyses of CAU-18, CAU-18a, CAU-19-X (X=H, 2Cl, 3Cl, 4Cl, 3CO<sub>2</sub>H, 4NH<sub>2</sub>, 4NO<sub>2</sub>) and Ce-PMOF-4NO<sub>2</sub>.

sample	physisorbed solvents	calculated			found		
		C [%]	H [%]	N [%]	C [%]	H [%]	N [%]
<b>CAU-18</b>		55.6	3.3	6.1	55.6	3.8	7.5
<b>CAU-18a</b>	22 H <sub>2</sub> O	50.6	3.8	4.9	49.4	3.0	4.9
<b>CAU-19-H</b>	11 H <sub>2</sub> O	52.8	3.5	4.5	53.1	3.1	4.9
<b>Zn-CAU-19-H</b>	16 H <sub>2</sub> O	48.5	3.6	4.1	48.3	2.4	4.7
<b>Co-CAU-19-H</b>	16 H <sub>2</sub> O	48.7	3.6	4.1	48.2	2.6	4.2
<b>CAU-19-2Cl</b>	13 H <sub>2</sub> O	52.1	3.6	4.4	52.2	2.6	4.9
<b>CAU-19-3Cl</b>	9 H <sub>2</sub> O	54.4	3.2	4.6	54.5	2.7	5.4
<b>CAU-19-4Cl</b>	8 H <sub>2</sub> O	52.8	3.5	4.5	52.5	3.0	5.7
<b>CAU-19-3CO<sub>2</sub></b>	3 DMF 10 H <sub>2</sub> O	52.1	3.9	5.5	51.3	2.9	5.3
<b>CAU-19-4NH<sub>2</sub></b>	11 H <sub>2</sub> O	52.2	3.6	5.5	52.3	3.3	5.4
<b>CAU-19-4NO<sub>2</sub></b>	6 H <sub>2</sub> O	52.8	3.1	5.6	52.9	2.8	5.8
<b>Ce-PMOF-4NO<sub>2</sub></b>	2 DMF	51.7	3.2	7.1	53.0	4.0	7.2

### 3. SEM images of single crystals of CAU-18 and CAU-19-H, structural representations of CAU-18 and CAU-19-H, Ce L<sub>3</sub>-edge XANES spectra (title compounds)

The SEM images of CAU-18 and CAU-19-H are shown in Figure S13 and S14. Single crystals and intergrown crystals in the range of 100 to 200  $\mu\text{m}$  can be found in the reaction products.

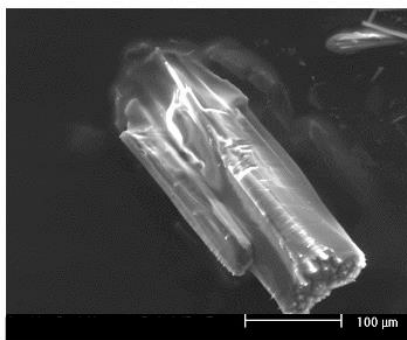


**Figure S13.** SEM image of CAU-18. The SEM measurements reveal a crystal size of ca. 200 x 100  $\mu\text{m}$ .

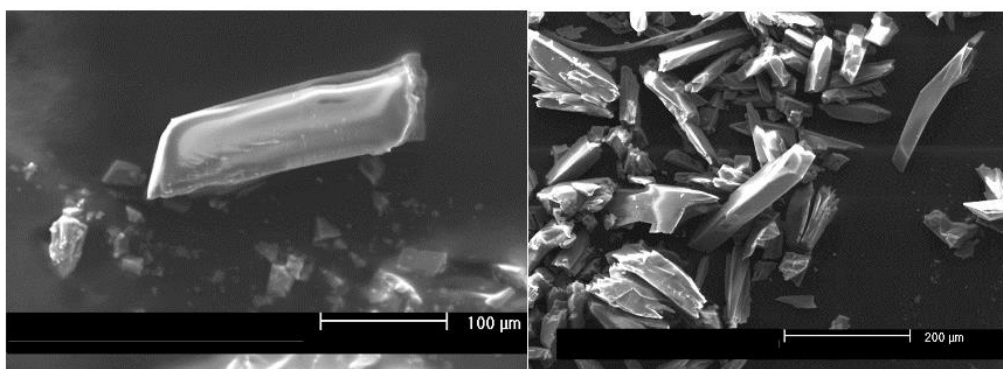


**Figure S14.** SEM image of CAU-19-H. The SEM measurements reveal a crystal size of ca. 200 x 50  $\mu\text{m}$ .



**Crystal structure of CAU-18 and CAU-19:**

In CAU-18 tetrameric IBUs are observed that are connected to a three-dimensional framework structure. Between adjacent tetrameric IBUs (Figure S15) contacts ( $\text{O}\cdots\text{O}$  distance = 3.13(3) Å) between a coordinating water molecule and a coordinating  $-\text{COO}^-$  group is observed which indicates the presence of hydrogen bonds.

To illustrate the coordination of the carboxylate groups to the cerium ions the Harris-notation was chosen.<sup>9</sup> The Harris-notation has the format  $[\text{A},\text{XY}]$ , the value A is the number of metal ions coordinated to the carboxylic group and X, Y is the number of bonds every oxygen shares with a metal ion.<sup>9</sup> The coordination of the carboxylate groups in CAU-18 and CAU-19 are shown in Fig. S16 and S17.

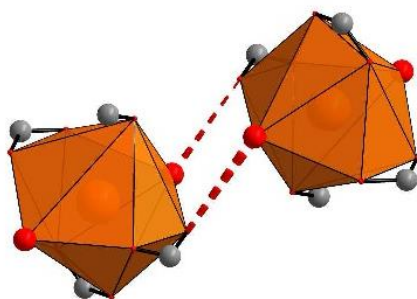


**Figure S15.** Structural representation of two adjacent  $\text{CeO}_9$  polyhedra in CAU-18 ( $\text{O}\cdots\text{O}$  distance = 3.13(3) Å) indication H-bond interactions between a coordinating water molecule and an oxygen atom of a carboxylate group of a coordinating  $\text{H}_2\text{T CPP}^{4+}$  ion.

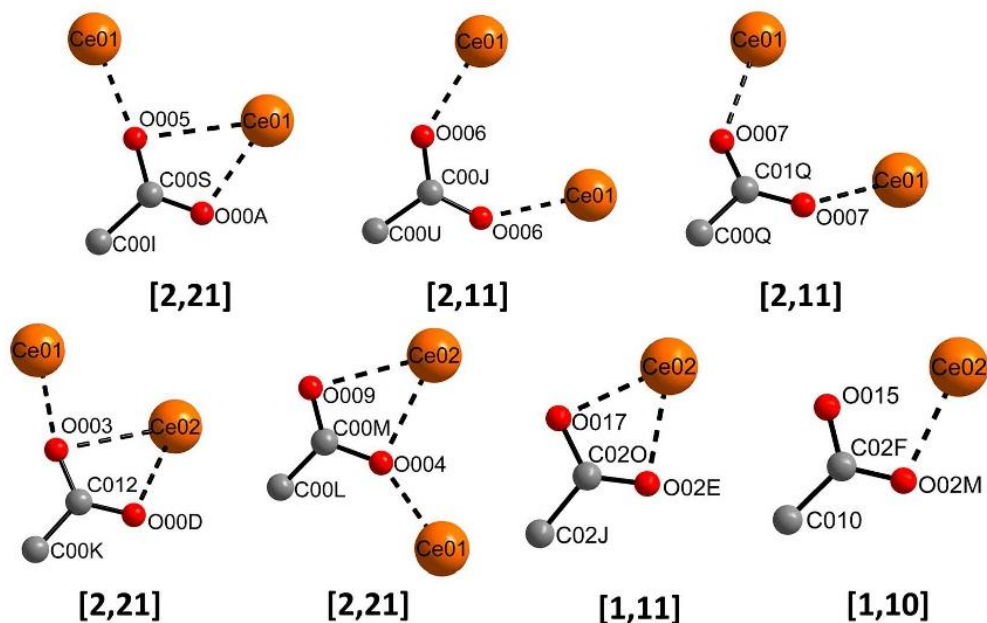


**Figure S16.** Graphical illustration of all coordination modes of carboxylate groups in CAU-18. Numbers in brackets represent the Harris-notation.

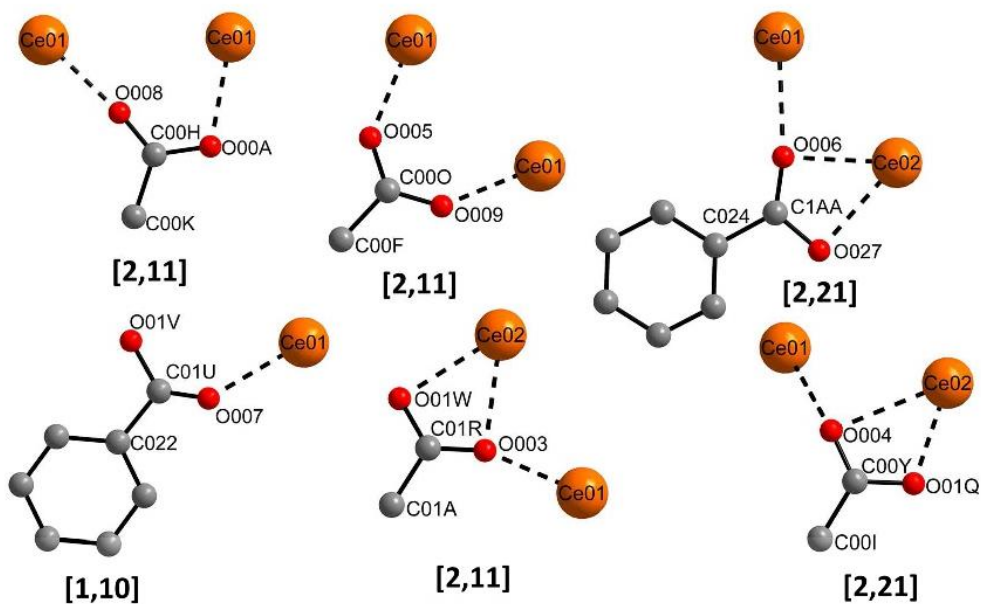


**Figure S17.** Graphical illustration of all coordination modes of carboxylate groups in CAU-19-H. Numbers in brackets represent the Harris-notation.

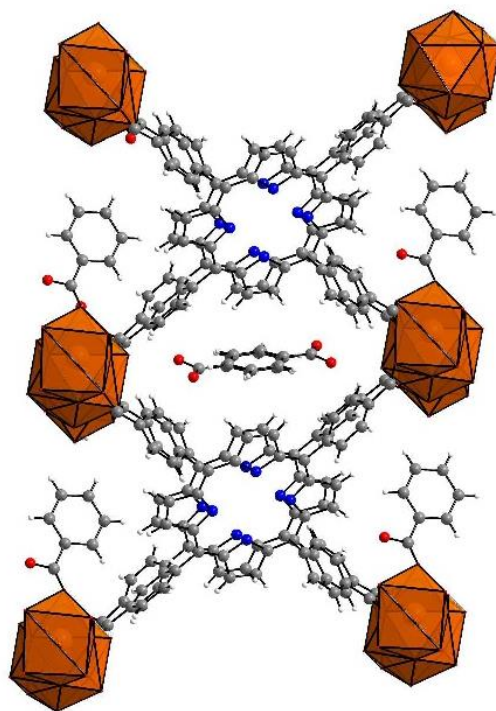


**Figure S17a.** View on the framework structure of CAU-19-H with HBA-H molecules in the pores located in two positions with an occupancy of 0.5 each.

The Ce L<sub>3</sub>-edge spectra of the title compounds compared with [CeO<sub>2</sub>] and [Ce(NO<sub>3</sub>)<sub>3</sub>] are shown in Figure S18, demonstrating the Ce<sup>3+</sup> oxidation state in all studied MOFs.

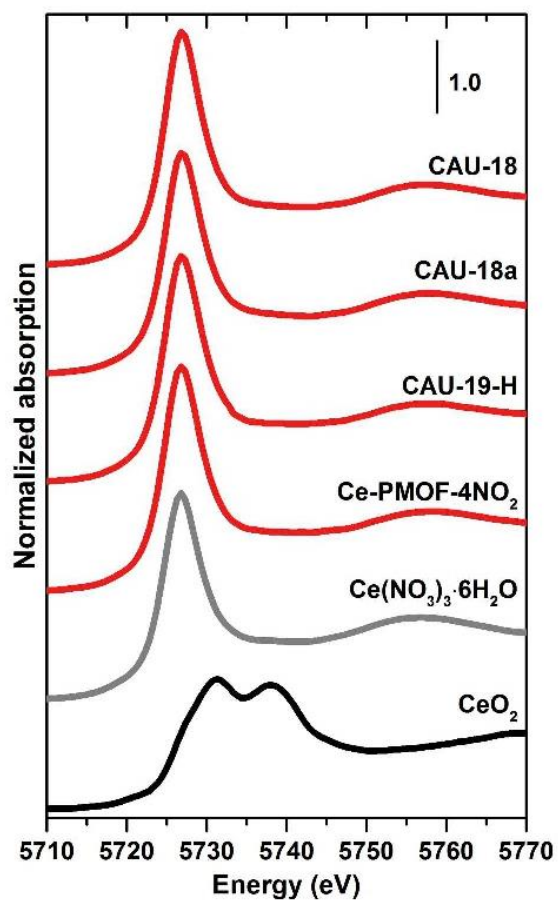


**Figure S18.** Ce L<sub>3</sub>-edge XANES spectra of the synthesized MOFs in comparison with Ce(NO<sub>3</sub>)<sub>3</sub>·6H<sub>2</sub>O and CeO<sub>2</sub> reference compounds, proving that all title MOFs contain the dominant fraction of trivalent cerium ions.

#### 4. Crystallographic data and Pawley fits of M-CAU-19-X

The crystallographic data of all activated CAU-19-X and M-CAU-19-H (M=Zn, Co) derivatives reveal very similar cell parameters and the resulting Pawley-fits show no further impurities in the samples (Tab. S2 and S3). The Pawley-fit of CAU-18 shows no further impurities.

**Table S2.** Results of the Pawley refinements of the crystallographic data of CAU-19-X (X= H, 2Cl, 3Cl, 4Cl, 3CO<sub>2</sub>H, 4NH<sub>2</sub>, 4NO<sub>2</sub>).

	<b>H</b>	<b>2Cl</b>	<b>3Cl</b>	<b>4Cl</b>	<b>4NH<sub>2</sub></b>	<b>4NO<sub>2</sub></b>	<b>3CO<sub>2</sub>H</b>
<b>M</b> [g mol <sup>-1</sup> ]	2284	2353	2353	2353	2314	2374	2370
<b>SG</b>	<i>P</i> $\bar{1}$	<i>P</i> $\bar{1}$	<i>P</i> $\bar{1}$	<i>P</i> $\bar{1}$	<i>P</i> $\bar{1}$	<i>P</i> $\bar{1}$	<i>P</i> $\bar{1}$
<b><i>a</i></b> [Å]	11.696(3)	13.0667(7)	13.571(34)	13.43(8)	11.37(1)	12.53(2)	14.460(6)
<b><i>b</i></b> [Å]	13.822(3)	13.5805(6)	13.705(9)	13.94(4)	13.59(2)	13.98(2)	13.616(4)
<b><i>c</i></b> [Å]	17.080(5)	17.7205(9)	17.459(11)	17.28(4)	17.90(4)	17.23(3)	17.470(6)
<b><math>\alpha</math></b> [°]	95.04(2)	94.543(3)	94.506(48)	94.36(19)	96.37(12)	95.44(5)	93.87(1)
<b><math>\beta</math></b> [°]	98.05(4)	98.386(4)	99.382(14)	99.01(32)	98.03(10)	99.16(17)	96.23(4)
<b><math>\gamma</math></b> [°]	102.40(2)	100.576(5)	99.090(22)	101.08(73)	100.93(12)	100.08(15)	101.36(7)
<b>V</b> [Å <sup>3</sup> ]	2650(1)	3039.9(3)	3145(9)	3109(24)	2661(8)	2911(8)	3338(2)
<b><i>r</i><sub>wp</sub></b>	4.89	4.26	5.17	3.72	3.72	2.90	3.85
<b>GOF</b>	2.12	0.96	2.41	1.95	1.64	1.34	1.64



**Table S3.** Results of the Pawley refinements of CAU-19-H, Zn-CAU-19-H and Co-CAU-19-H.

	<b>CAU-19-H</b>	<b>Zn-CAU-19-H</b>	<b>Co-CAU-19-H</b>
<b>M [g mol<sup>-1</sup>]</b>	2284	2411	2398
<b>SG</b>	$P\bar{1}$	$P\bar{1}$	$P\bar{1}$
<b><i>a</i> [Å]</b>	11.696(3)	12.866(7)	12.86(2)
<b><i>b</i> [Å]</b>	13.822(3)	13.656(8)	13.71(2)
<b><i>c</i> [Å]</b>	17.080(5)	17.386(12)	17.38(4)
<b><math>\alpha</math> [°]</b>	95.04(2)	92.94(4)	93.84(6)
<b><math>\beta</math> [°]</b>	98.05(4)	97.49(6)	96.08(17)
<b><math>\gamma</math> [°]</b>	102.40(2)	102.01(4)	102.84(11)
<b>V [Å<sup>3</sup>]</b>	2650(1)	2952(3)	2957(9)
<b><i>r</i><sub>wp</sub></b>	4.89	3.86	2.42
<b>GOF</b>	2.12	2.11	1.93

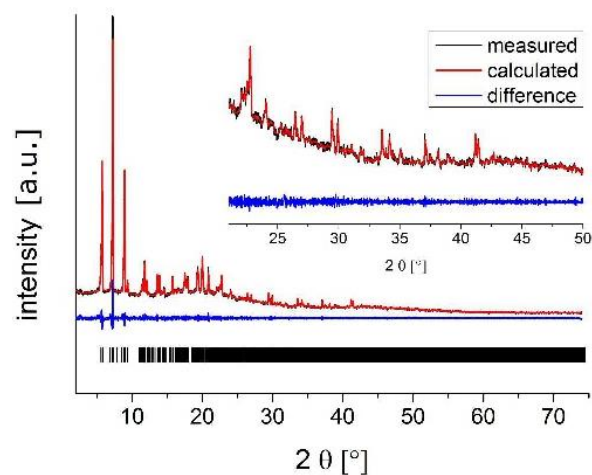


**Figure S19.** Result of the Pawley fit of CAU-18 (powder) using crystallographic data of the single crystal structure determination. Measured data are shown as a black line, calculated data as a red line and the blue line gives the difference plot. Predicted peak positions are marked as vertical bars.

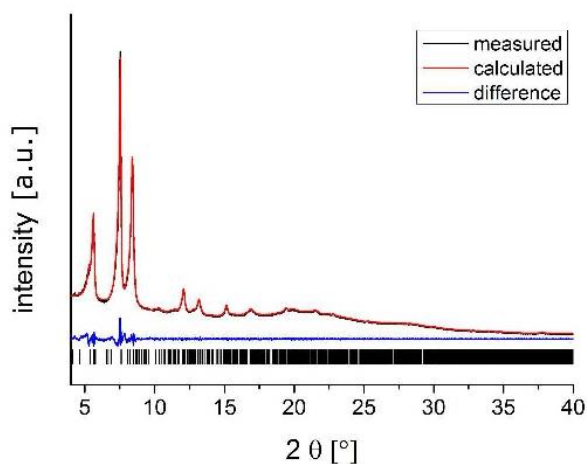


**Figure S20.** Result of the Pawley-fit with the indexed crystallographic parameters of CAU-18a. Measured data are shown as a black line, calculated data as a red line and the blue line gives the difference plot. Predicted peak positions are marked as vertical bars.

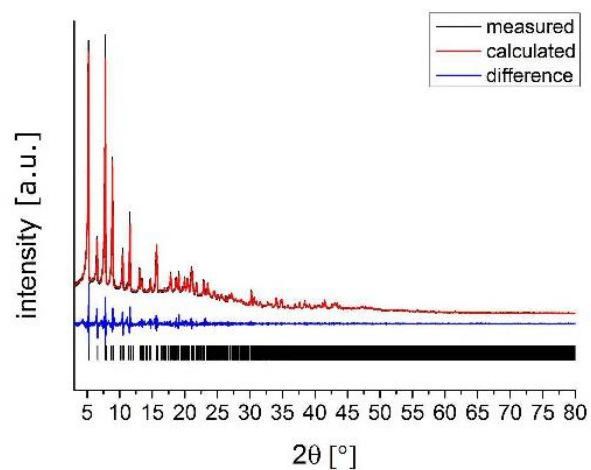


**Figure S21.** Result of the Pawley-fit of CAU-19-H (powder, as synthesized sample) using crystallographic data of the single crystal structure determination. Measured data are shown as a black line, calculated data as a red line and the blue line gives the difference plot. Predicted peak positions are marked as vertical bars.

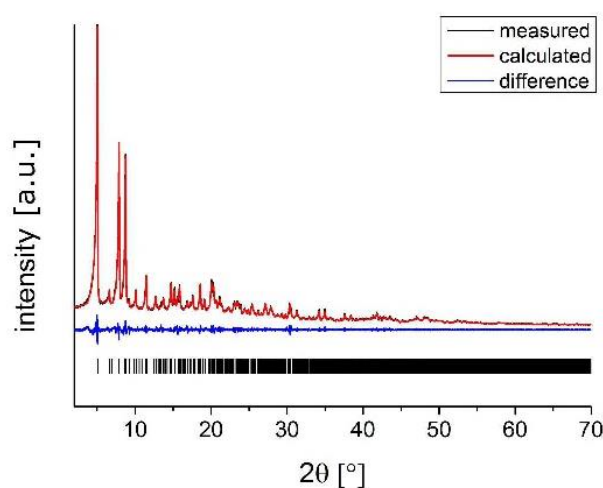


**Figure S22.** Result of the Pawley-fit of CAU-19-2Cl (powder, activated sample) using crystallographic data of the single crystal structure determination of CAU-19-H. Measured data are shown as a black line, calculated data as a red line and the blue line gives the difference plot. Predicted peak positions are marked as vertical bars.

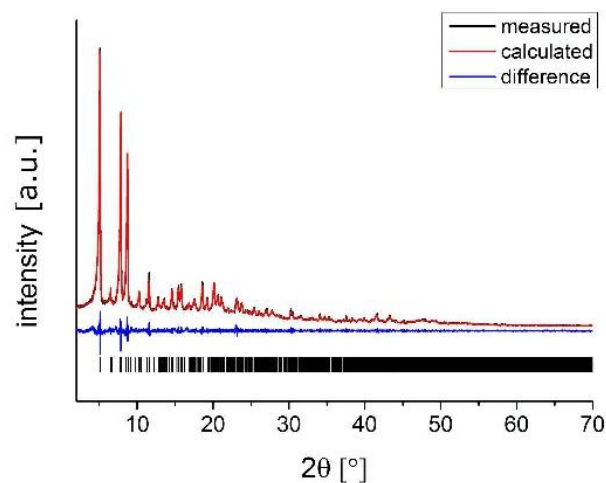


**Figure S23.** Result of the Pawley-fit of CAU-19-3Cl (powder, activated sample) using crystallographic data of the single crystal structure determination of CAU-19-H. Measured data are shown as a black line, calculated data as a red line and the blue line gives the difference plot. Predicted peak positions are marked as vertical bars.

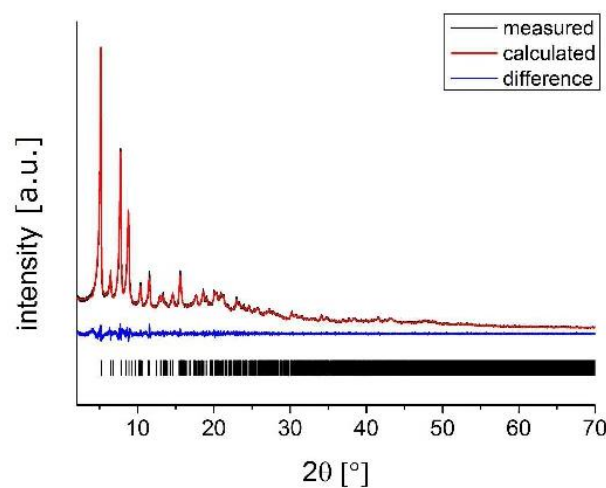


**Figure S24.** Result of the Pawley-fit of CAU-19-4Cl (powder, activated sample) using crystallographic data of the single crystal structure determination of CAU-19-H. Measured data are shown as a black line, calculated data as a red line and the blue line gives the difference plot. Predicted peak positions are marked as vertical bars.

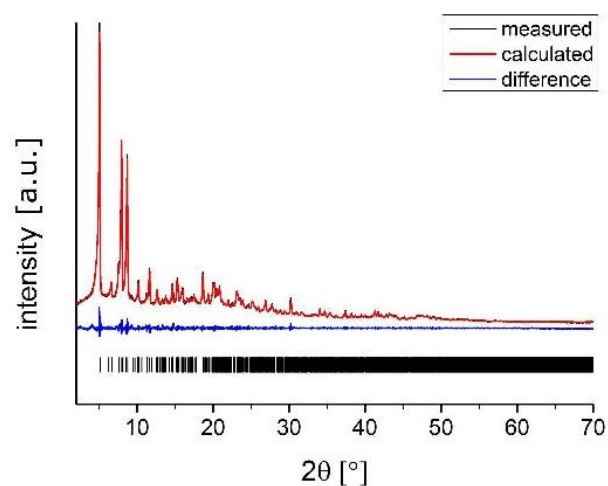


**Figure S25.** Result of the Pawley-fit of CAU-19-3CO<sub>2</sub>H (powder, activated sample) using crystallographic data of the single crystal structure determination of CAU-19-H. Measured data are shown as a black line, calculated data as a red line and the blue line gives the difference plot. Predicted peak positions are marked as vertical bars.

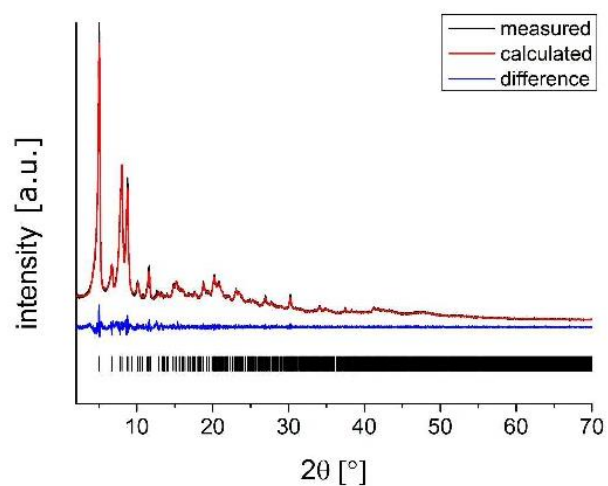


**Figure S26.** Result of the Pawley-fit of CAU-19-4NH<sub>2</sub> (powder, activated sample) using crystallographic data of the single crystal structure determination of CAU-19-H. Measured data are shown as a black line, calculated data as a red line and the blue line gives the difference plot. Predicted peak positions are marked as vertical bars.



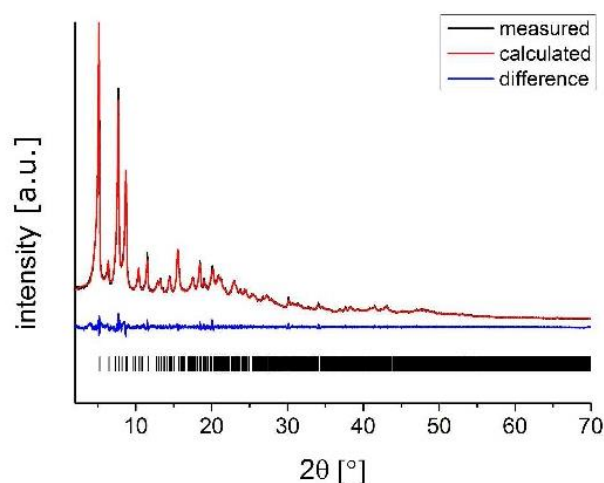


**Figure S27.** Result of the Pawley-fit of CAU-19-4NO<sub>2</sub> (powder, activated sample) using crystallographic data of the single crystal structure determination of CAU-19-H. Measured data are shown as a black line, calculated data as a red line and the blue line gives the difference plot. Predicted peak positions are marked as vertical bars.

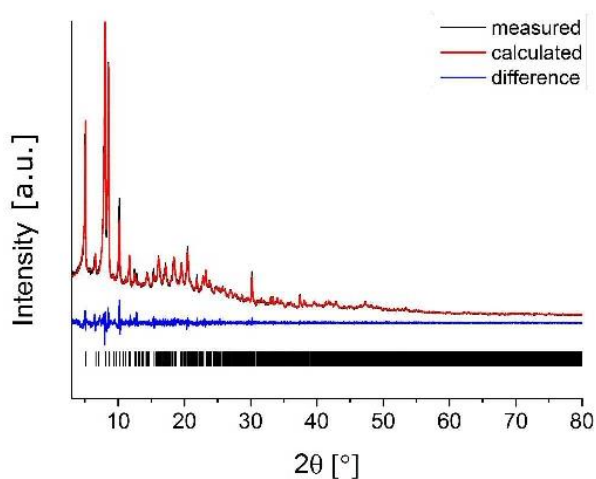


**Figure S28.** Result of the Pawley-fit of Zn-CAU-19-H (powder, activated sample) using crystallographic data of the single crystal structure determination of CAU-19-H. Measured data are shown as a black line, calculated data as a red line and the blue line gives the difference plot. Predicted peak positions are marked as vertical bars.

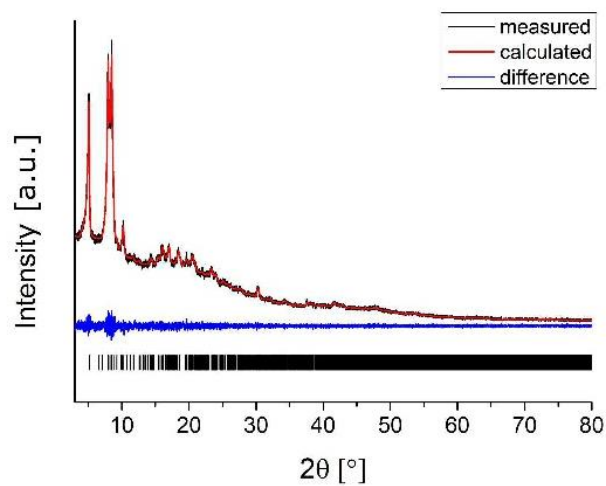


**Figure S29.** Result of the Pawley-fit of Co-CAU-19-H (powder, activated sample using crystallographic data of the single crystal structure determination of CAU-19-H). Measured data are shown as a black line, calculated data as a red line and the blue line gives the difference plot. Predicted peak positions are marked as vertical bars.

### 5. Sorption properties and PXRD patterns of the activated samples

$N_2$ -sorption isotherms of all measured samples (Figure S34 and S35) and PXRD patterns of the samples after the sorption experiment compared with the PXRD pattern before the measurement (Figure S36). For clarity the CAU-19-X derivatives were only compared with the CAU-19-H PXRD pattern.

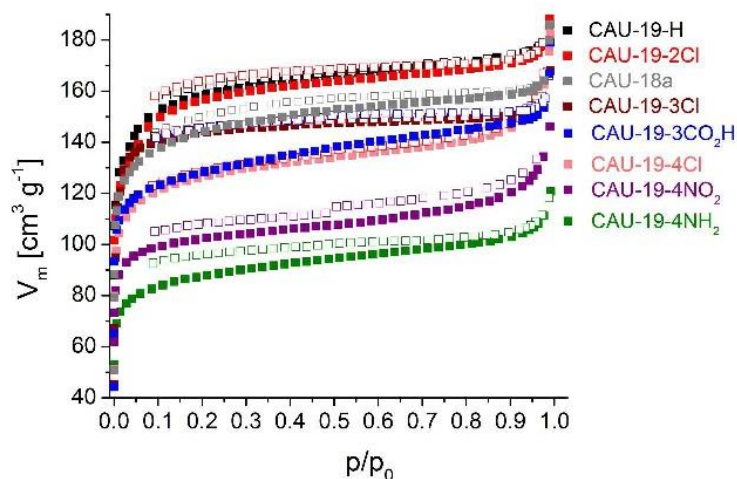


**Figure S30.**  $N_2$ -sorption isotherms of CAU-18a and CAU-19-X (X=H, 2Cl, 3Cl, 4Cl, 3CO<sub>2</sub>H, 4NH<sub>2</sub>, 4NO<sub>2</sub>) measured at 77 K. Filled squares represent adsorption, empty squares represent desorption.

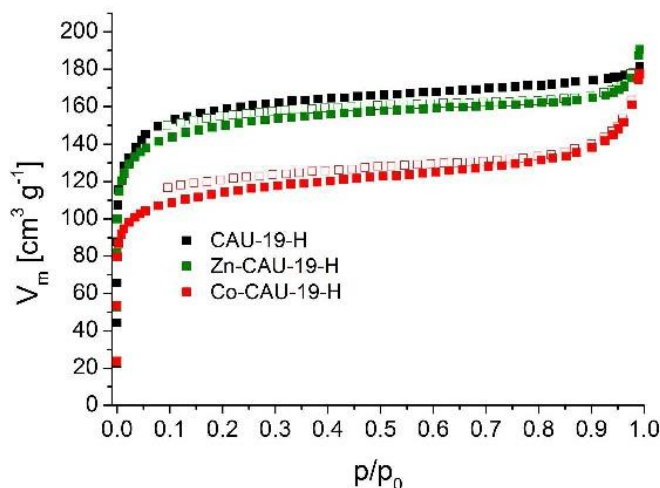


**Figure S31.**  $N_2$ -sorption isotherms of CAU-19-H, Zn-CAU-19-H and Co-CAU-19-H measured at 77 K. Filled squares represent adsorption, empty squares represent desorption.

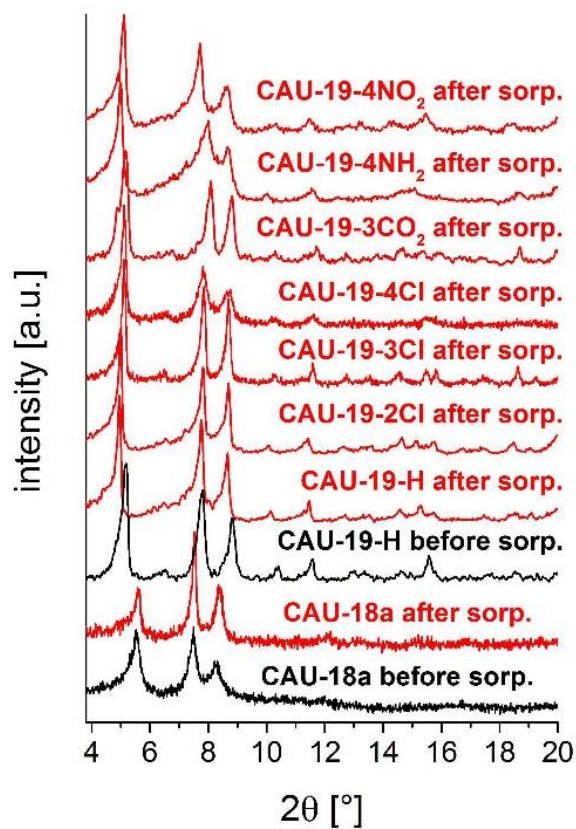


**Figure S32.** PXRD patterns (red) of CAU-18 and CAU-19-X after the sorption experiments (activation 170 °C, 10<sup>-2</sup> kPa). For comparison the patterns of CAU-18a and CAU-19-H before the sorption experiment are also presented (black).

## 6. TG investigations, PXRD patterns of the decomposition products and chemical stability

The results of all TG measurements are shown in Fig. S37-S45 and Tab. S4. The decomposition products of all measured samples is CeO<sub>2</sub> (icsd 262755) which was shown exemplary for CAU-18a, Ce-PMOF-4NO<sub>2</sub> and CAU-19-H by PXRD measurements (Fig. S46).

The results of the chemical stability test in different solvents as well as 2 M HCl and NaOH solutions are shown in Fig. S47.

**Table S4.** Results of the thermogravimetric measurements of all title compounds. The numbers in red correspond to coordinating solvent molecules per formula unit. Resulting metal to linker ratios are shown in brackets.

	<b>residual mass [%]</b>	mass loss organic decomposition <b>meas. [%]</b>	mass loss organic decomposition <b>calc. [%]</b>	<b>mass loss H<sub>2</sub>O [%]</b>	<b>mass loss DMF [%]</b>
<b>CAU-18</b>	23.1	70.1 (4.5:3)	75.6 (4.0:3)	<b>2.1 (4.0 H<sub>2</sub>O)</b>	<b>4.7 (2.2 DMF)</b>
<b>CAU-18a</b>	22.3	69.7 (4.6:3)	73.0 (4.0:3)	9.2 (17.4 H <sub>2</sub> O)	
<b>CAU-19-H</b>	20.0	70.5 (3.1:2)	68.3 (3.0:2)	7.7 (11.3 H <sub>2</sub> O)	
<b>Zn-CAU-19-H</b>	26.9	67.7 (5.5:2)	61.5 (5.0:2)	5.4 (8.2 H <sub>2</sub> O)	
<b>Co-CAU-19-H</b>	26.1	66.7 (5.5:2)	60.6 (5.0:2)	7.2 (11.1 H <sub>2</sub> O)	
<b>CAU-19-2Cl</b>	21.6	72.0 (3.4:2)	77.0 (3.0:2)	7.1 (10.6 H <sub>2</sub> O)	
<b>CAU-19-3Cl</b>	21.1	74.2 (3.2:2)	74.9 (3.0:2)	6.0 (8.7 H <sub>2</sub> O)	
<b>CAU-19-4Cl</b>	19.6	72.5 (3.0:2)	69.7 (3.0:2)	8.7 (12.7 H <sub>2</sub> O)	
<b>CAU-19-3CO<sub>2</sub>H</b>	20.4	69.8 (3.3:2)	73.3 (3.0:2)	2.5 (3.8 H <sub>2</sub> O)	7.9 (3.0 DMF)
<b>CAU-19-4NH<sub>2</sub></b>	20.8	71.5 (2:3.2)	72.5 (2:3.0)	8.6 (12.6 H <sub>2</sub> O)	
<b>CAU-19-4NO<sub>2</sub></b>	22.5	73.2 (3.5:2)	80.8 (3.0:2)	4.8 (7.1 H <sub>2</sub> O)	
<b>Ce-PMOF-4NO<sub>2</sub></b>	22.4	73.5 (2.0:1)	69.1 (2.0:1)	4.4 (3.7 H <sub>2</sub> O)	



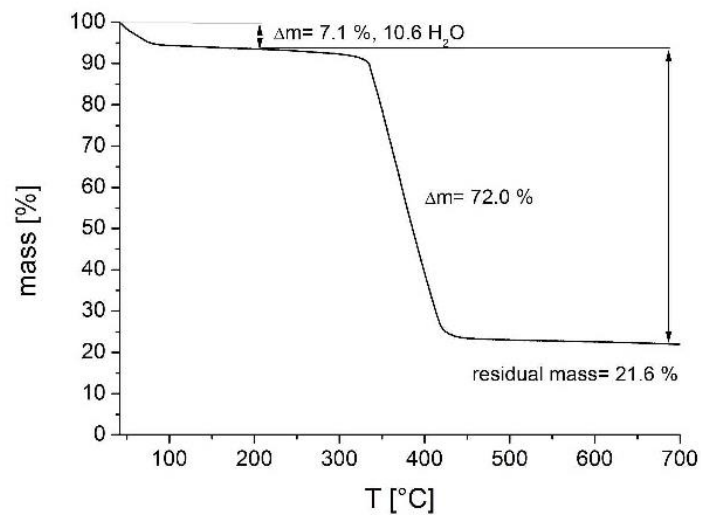


**Figure S33.** Thermogravimetric curve of CAU-19-2Cl. Evaluation of the measurement reveals a molar ratio of linker : metal : 2Cl-benzoic acid : H<sub>2</sub>O of 2 : 3.4 : 4 : 10.6 (Table S4).

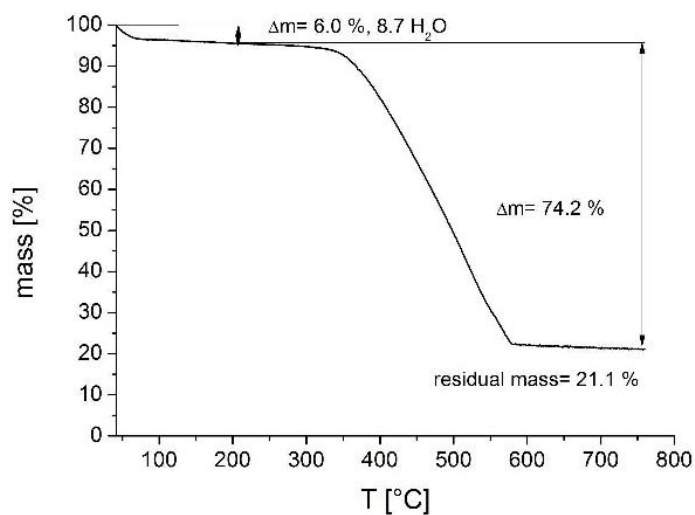


**Figure S34.** Thermogravimetric curve of CAU-19-3Cl. Evaluation of the measurement reveals a molar ratio of linker : metal : 3Cl-benzoic acid : H<sub>2</sub>O of 2 : 3.2 : 4 : 8.7 (Table S4).

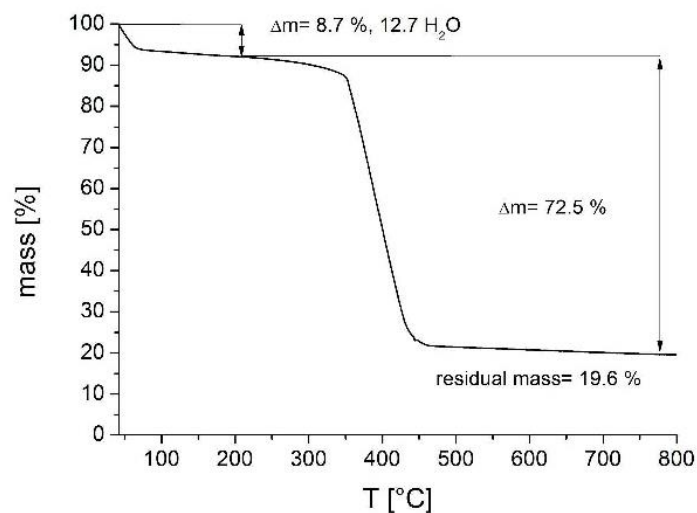


**Figure S35.** Thermogravimetric curve of CAU-19-4Cl. Evaluation of the measurement reveals a molar ratio of linker : metal : 4Cl-benzoic acid : H<sub>2</sub>O of 2 : 3.0 : 4 : 12.7 (Table S4).

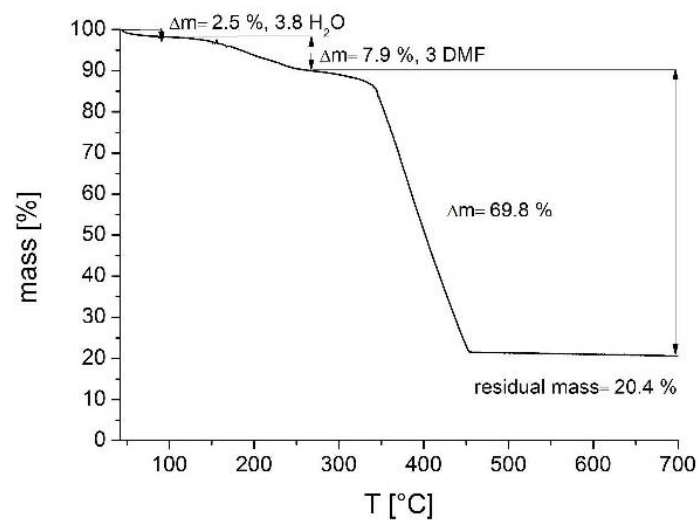


**Figure S36.** Thermogravimetric curve of CAU-19-3CO<sub>2</sub>H. Evaluation of the measurement reveals a molar ratio of linker : metal : 3CO<sub>2</sub>H-benzoic acid : DMF : H<sub>2</sub>O of 2 : 3.3 : 4 : 3.0 : 3.8 (Table S4).

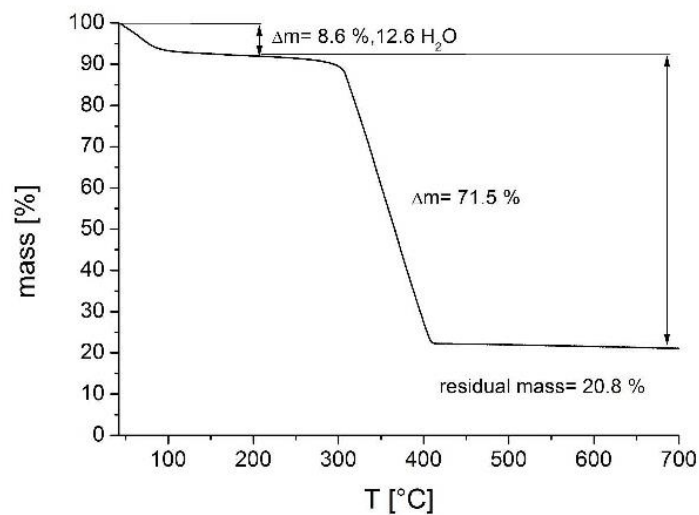


**Figure S37.** Thermogravimetric curve of CAU-19-4NH<sub>2</sub>. Evaluation of the measurement reveals a molar ratio of linker : metal : 4NH<sub>2</sub>-benzoic acid : H<sub>2</sub>O of 2 : 3.2 : 4 : 12.6 (Table S4).

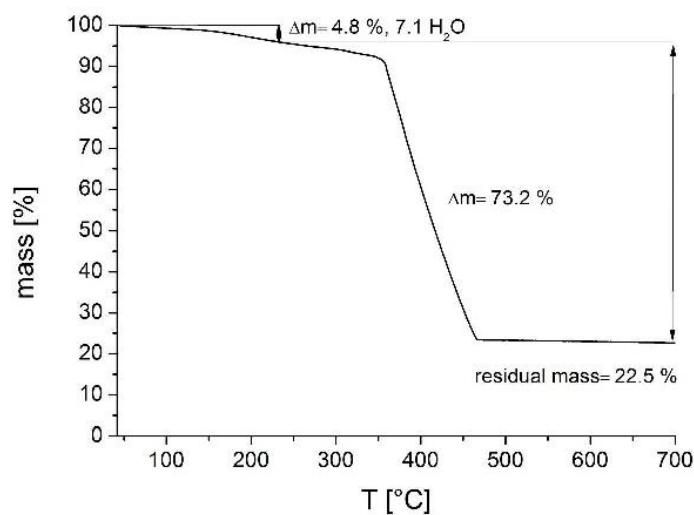


**Figure S38.** Thermogravimetric curve of CAU-19-4NO<sub>2</sub>. Evaluation of the measurement reveals a molar ratio of linker : metal : 4NO<sub>2</sub>-benzoic acid : H<sub>2</sub>O of 2 : 3.5 : 4 : 7.1 (Table S4).

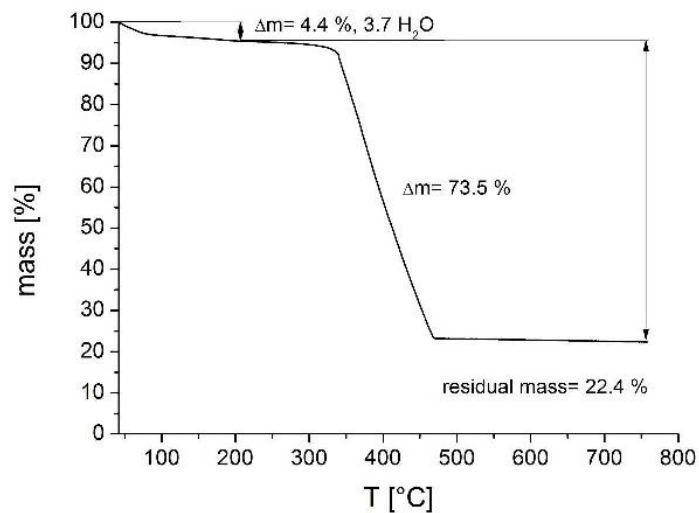


**Figure S39.** Thermogravimetric curve of Ce-PMOF-4NO<sub>2</sub>. Evaluation of the measurement reveals a molar ratio of linker : metal : 4NO<sub>2</sub>-benzoic acid : H<sub>2</sub>O of 1 : 2 : 2 : 3.7 (Table S4).

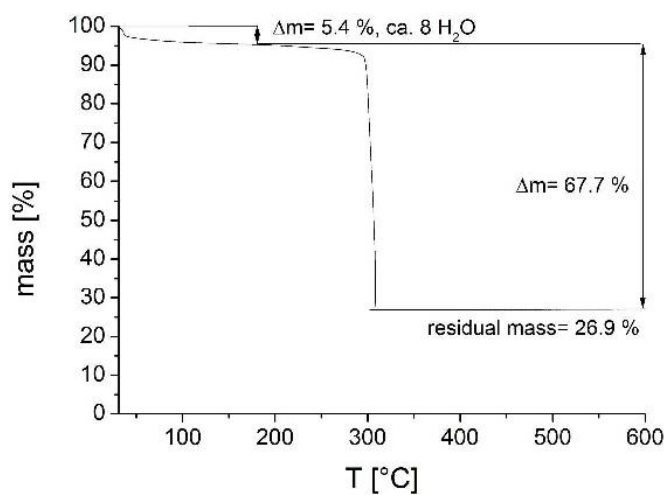


**Figure S40.** Thermogravimetric curve of Zn-CAU-19-H. Evaluation of the measurement reveals a molar ratio of linker : cerium : zinc : benzoic acid : H<sub>2</sub>O of 2 : 3 : 2 : 2 : 8 (Table S4).

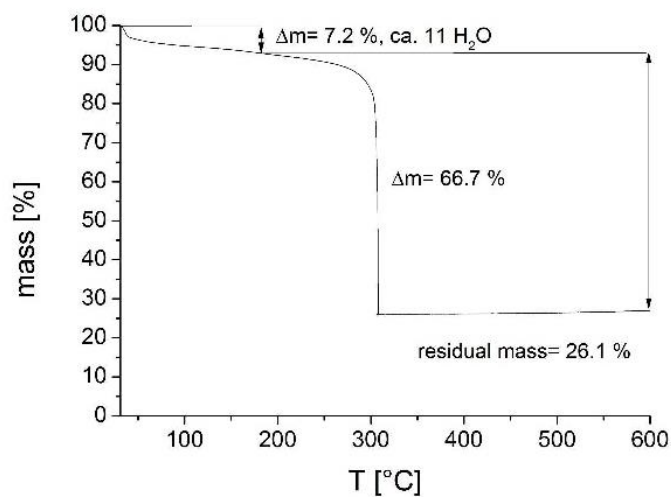


**Figure S41.** Thermogravimetric curve of Co-CAU-19-H. Evaluation of the measurement reveals a molar ratio of linker : cerium : cobalt : benzoic acid : H<sub>2</sub>O of 2 : 3 : 2 : 2 : 11 (Table S4).

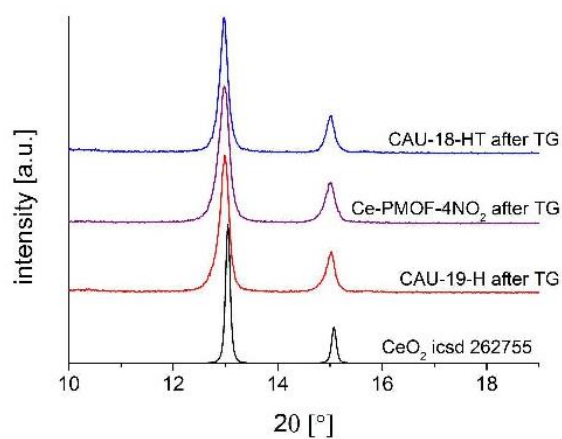


**Figure S42.** PXRD pattern of CeO<sub>2</sub> (icsd 262755) compared with the remaining products of the thermogravimetric experiments exemplarily shown for CAU-18a, Ce-PMOF-4NO<sub>2</sub> and CAU-19-H.



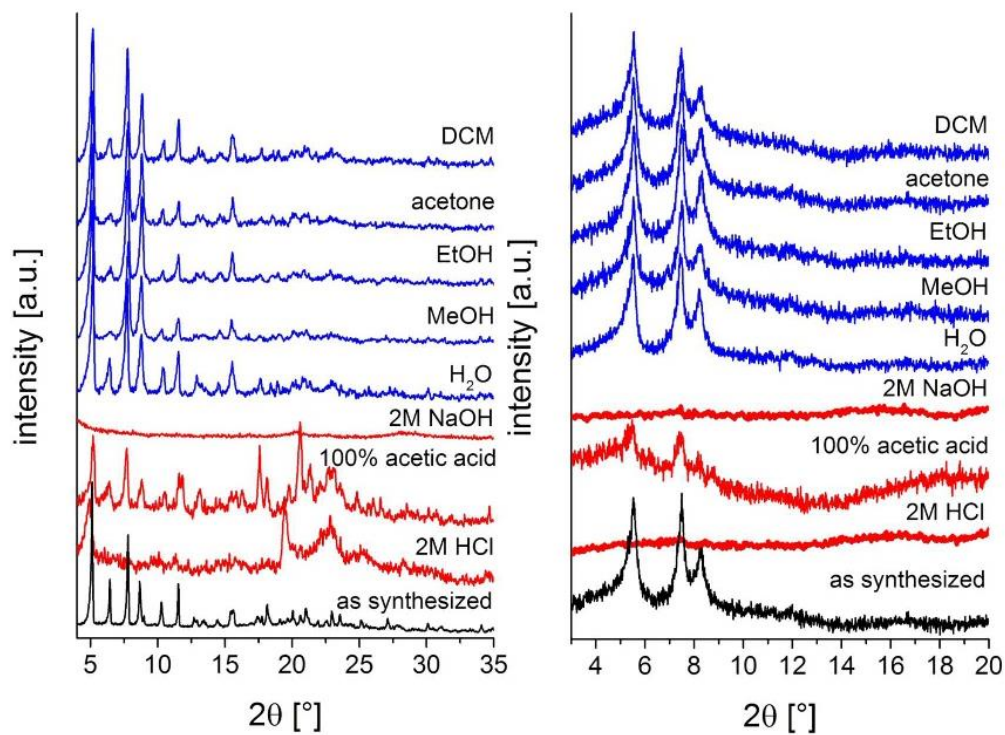


**Figure S43.** Chemical stability of CAU-19-H (left) and CAU-18a (right) in different solvents (24 h, stirring at room temperature).

### 7. *In situ* PXRD studies of CAU-18 and CAU-19-H

The contour diagrams of the two samples synthesized at various different reaction temperatures are shown in Figure S48-S51. The PXRD patterns of the *in situ* measurement and the in house data of CAU-18 and CAU-19-H are compared in Figure S52. The Gualtieri-fits are shown in Figures S53-S58 and the Arrhenius-plots are shown in Figures S59-S62.

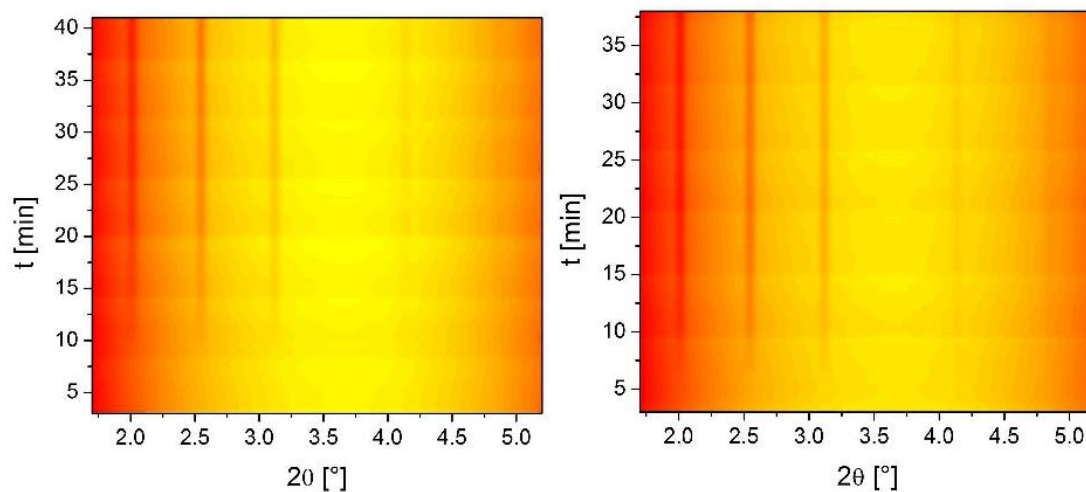


**Figure S44.** Contour diagram of the *in situ* data of CAU-18 synthesized at 110 (left) and 120 °C (right).

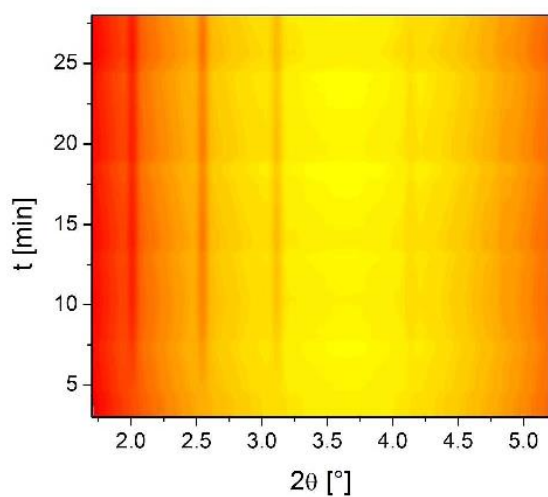


**Figure S45.** Contour diagram of the *in situ* data of CAU-18 synthesized at 130 °C.

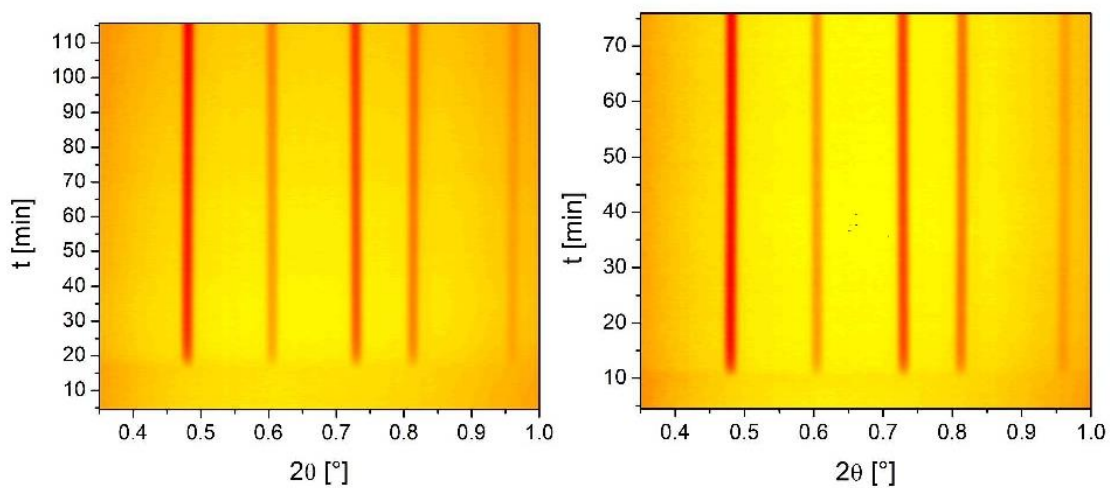


**Figure S46.** Contour diagram of the *in situ* data of CAU-19-H synthesized at 120 (left) and 130 °C (right).

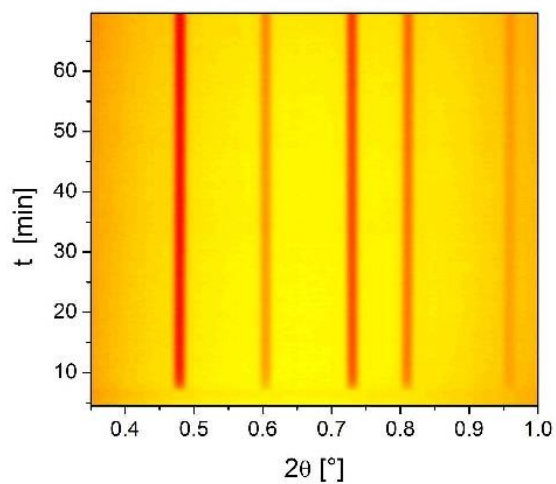


**Figure S47.** Contour diagram of the *in situ* data of CAU-19-H synthesized at 140 °C.

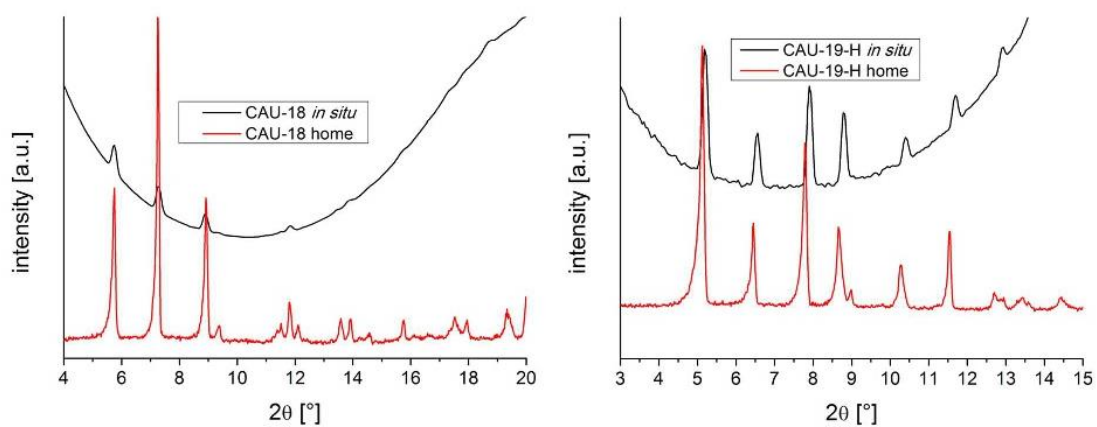


**Figure S48.** PXRD pattern of the *in situ* data (black) compared with the in house data (red) of CAU-18 (left) and CAU-19-H (right).

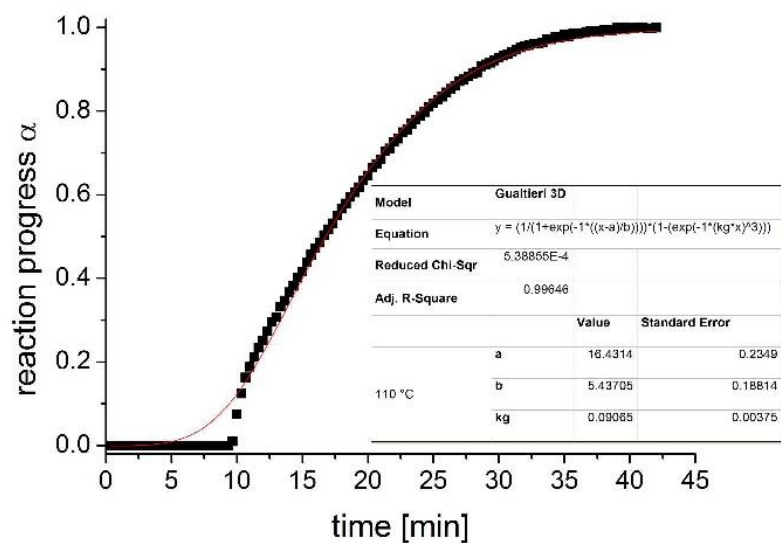


**Figure S49.** Gualtieri-fit for the synthesis of CAU-18 at 110 °C. The standard deviations, used equations and results of the fitting are shown in the included table.

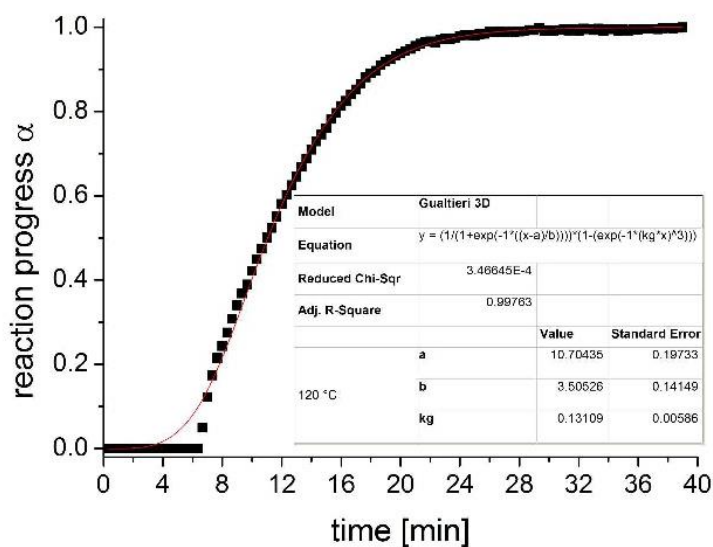


**Figure S50.** Gualtieri-fit for the synthesis of CAU-18 at 120 °C. The standard deviations, used equations and results of the fitting are shown in the included table.

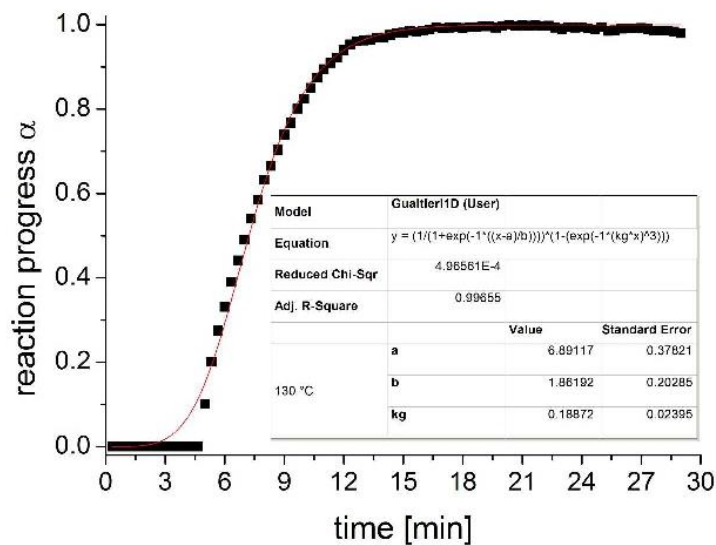


**Figure S51.** Gualtieri-fit for the synthesis of CAU-18 at 130 °C. The standard deviations, used equations and results of the fitting are shown in the included table.

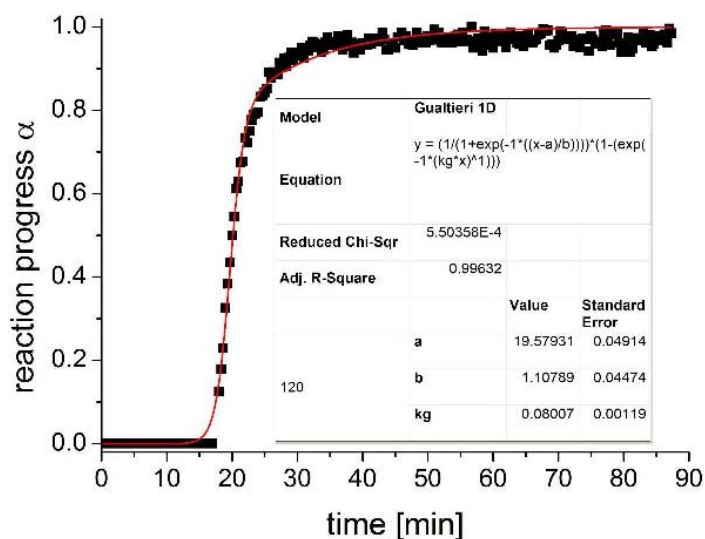


**Figure S52.** Gualtieri-fit for the synthesis of CAU-19-H at 120 °C. The standard deviations, used equations and results of the fitting are shown in the included table.



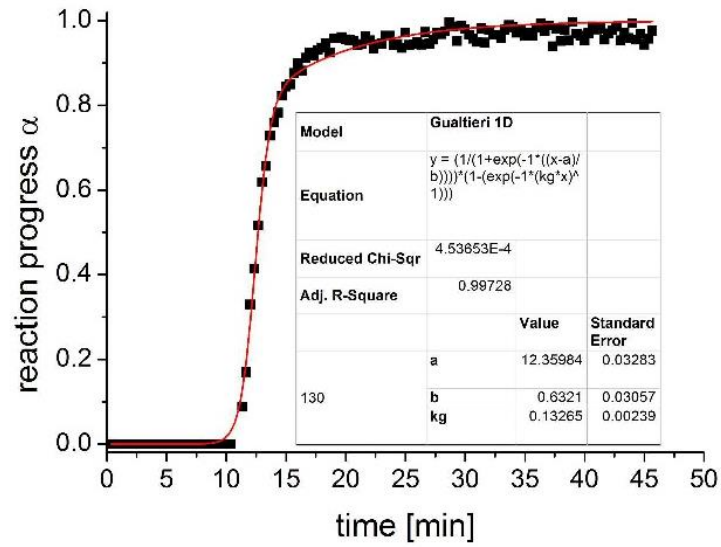


**Figure S53.** Gualtieri-fit for the the synthesis of CAU-19-H at 130 °C. The standard deviations, used equations and results of the fitting are shown in the included table.

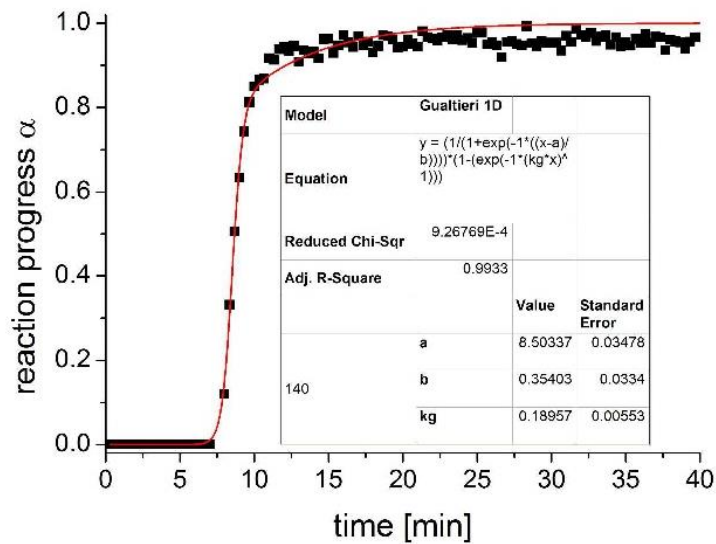


**Figure S54.** Gualtieri-fit for the the synthesis of CAU-19-H at 140 °C. The standard deviations, used equations and results of the fitting are shown in the included table.

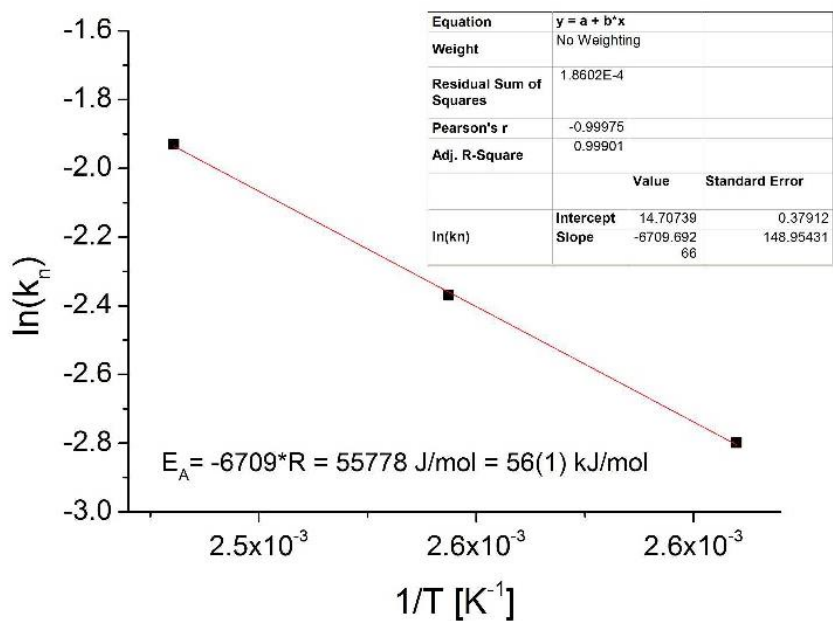


Figure S55. Arrhenius plot for the nucleation of CAU-18 between 110 and 130 °C.

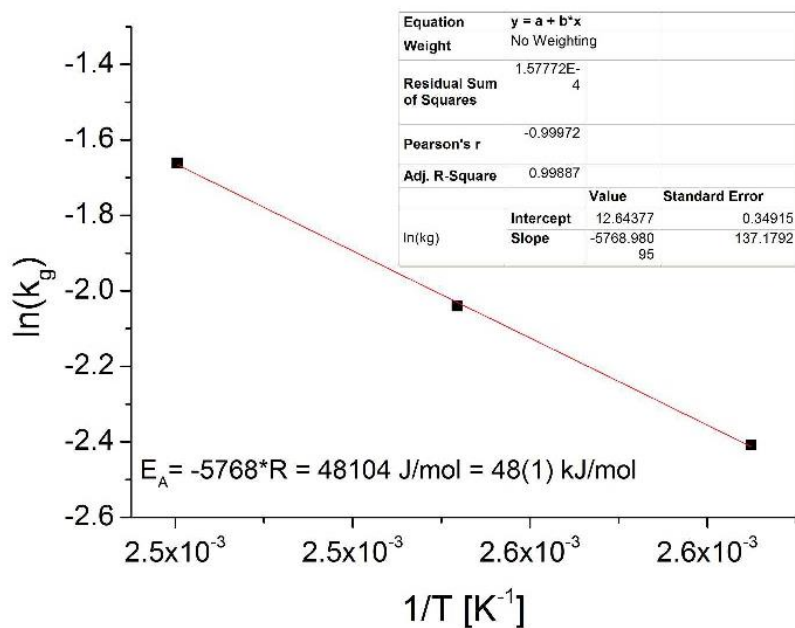
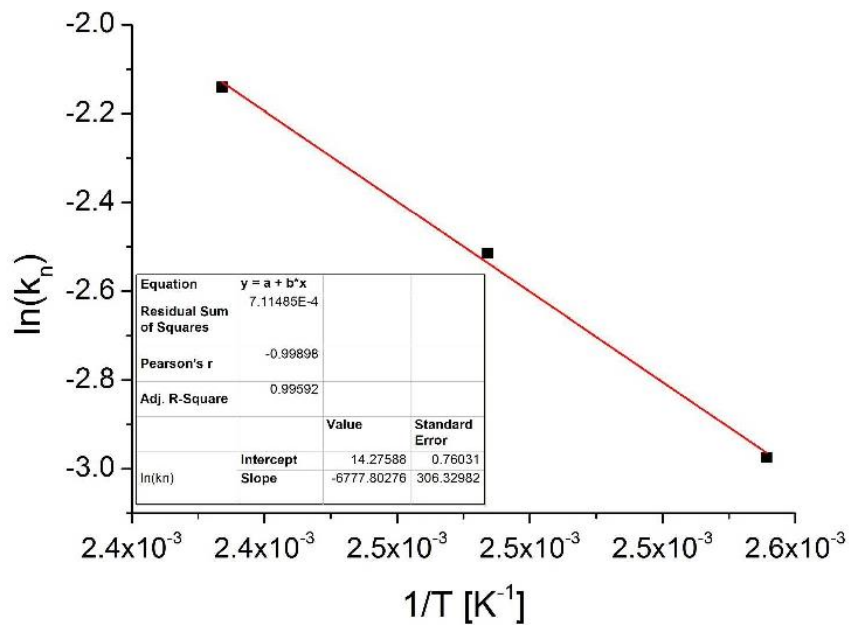
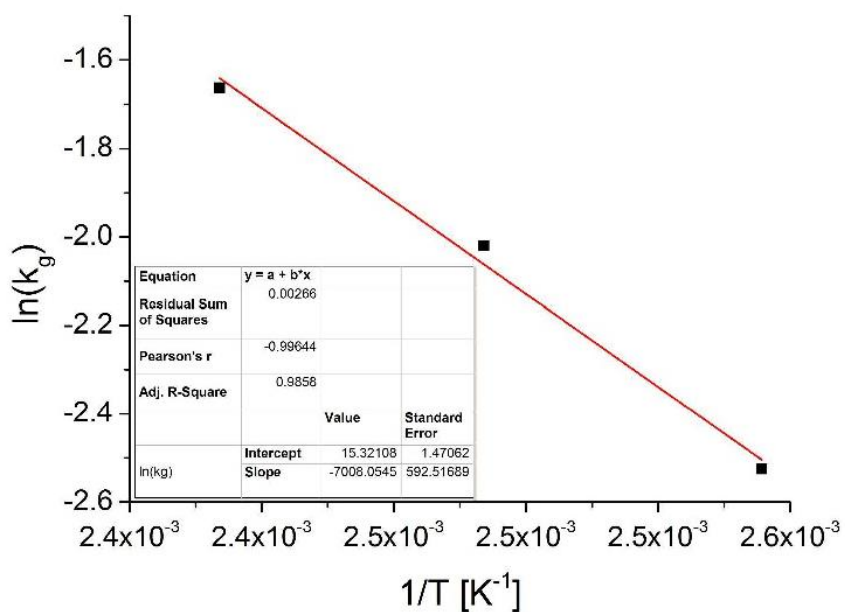


Figure S56. Arrhenius plot for the crystal growth of CAU-18 between 110 and 130 °C.



**Figure S57.** Arrhenius plot for the nucleation of CAU-19-H between 120 and 140 °C.



**Figure S58.** Arrhenius plot for the crystal growth of CAU-19-H between 120 and 140 °C.

## 8. IR spectroscopy of CAU-18, CAU-18a, Ce-PMOF-4NO<sub>2</sub> and CAU-19-X (X=H, 2Cl, 3Cl, 4Cl, 3CO<sub>2</sub>H, 4NH<sub>2</sub>, 4NO<sub>2</sub>)

IR spectra of all title compounds and the H<sub>6</sub>TCPPI linker are shown in Figures S59-S61. The assignment of the bands are given in Tables S5 and S6, respectively.

In the following, first the characteristic bands of the coordinating linker is discussed followed by the ones due to the presence of co-ligands. The position of bands of the porphyrin linker are almost identical in all IR spectra. The stretching vibration of the N-H group is observed around 3320 cm<sup>-1</sup>. The asymmetric ( $\nu_{as}$ ) and symmetric ( $\nu_s$ ) stretching vibration of the coordinating carboxylate groups are observed at 1585 and 1402 cm<sup>-1</sup>, respectively. The characteristic  $\nu(C=C)$  valence vibration of the phenyl rings are observed at 1525 cm<sup>-1</sup>. Further characteristic vibrations such as the  $\nu(C-N)$  valence vibration and  $\delta(C-H, N-H)$  and  $\gamma(C-H)$  deformation vibrations of the porphyrin moiety are found at 1348, 968 and 798 cm<sup>-1</sup>, respectively (Table S5).

The asymmetric ( $\nu_{as}$ ) and symmetric ( $\nu_s$ ) stretching vibration of the coordinating carboxylate and the  $\nu(C=C)$  valence vibration of the phenyl rings of the benzoic acid derivative cannot be clearly distinguished from the corresponding bands of the porphyrin linker. The  $\nu(C=O)$  stretching vibration of the coordinated DMF molecule in CAU-18 is found at 1674 cm<sup>-1</sup> and is not observed in the IR spectrum of CAU-18a, confirming that DMF was fully removed upon thermal activation. The presence of the co-ligands in CAU-19-X can only be unequivocally demonstrated for CAU-19-CO<sub>2</sub>H and CAU-19-2(3,4)Cl due to strong overlap with bands of the porphyrin linker. The  $\nu(C=O)$  stretching vibration of the non-coordinating -COOH group of the 3-carboxybenzoic acid is observed at 1658 cm<sup>-1</sup> for CAU-19-CO<sub>2</sub>H. The characteristic  $\delta(C-Cl)$  deformation vibrations of the 2 (3, 4)-chlorobenzoic acid in CAU-19-2Cl (-3Cl, -4Cl) are observed at 1053 (1070, 1056) cm<sup>-1</sup>. The  $\nu(C=O)$  stretching vibration at 1712 cm<sup>-1</sup> is due to

small impurities with DMF molecules (Tab. S6).<sup>67, 68</sup> In case of M-CAU-19-H (M= Zn, Co, Fig. S61) the position of characteristic bands of the porphyrin moiety are almost identical with the ones of the non-metalated compound CAU-19-H. The only difference between the metalated and the unmetalated form of CAU-19-H is the missing stretching vibration of the N-H group observed at  $3320\text{ cm}^{-1}$  (Fig. S61, black arrow).<sup>67, 68</sup>

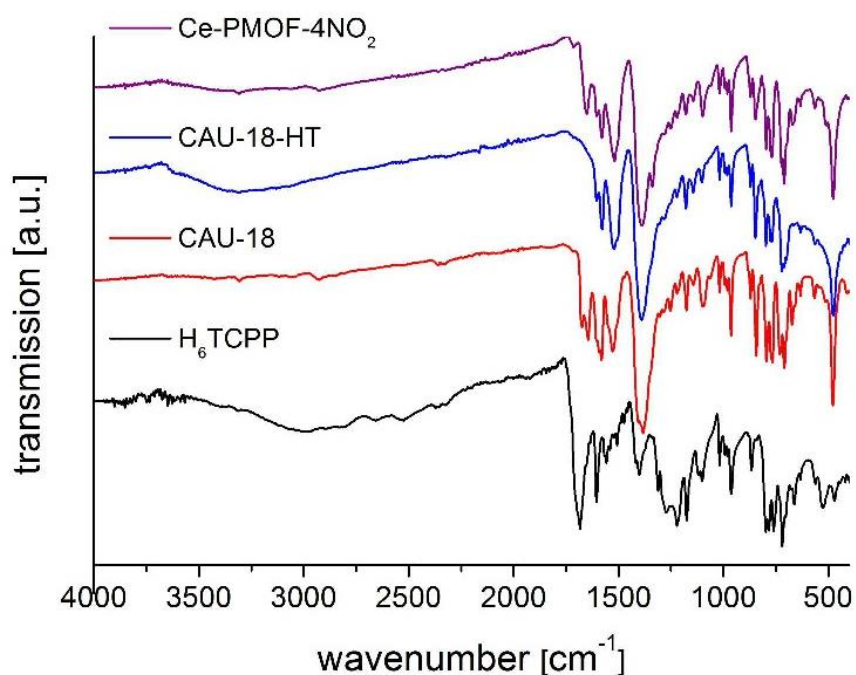


**Figure S59.** IR-spectra of CAU-18 (red), CAU-18a (blue) and Ce-PMOF-4NO<sub>2</sub> (purple). For comparison the IR-spectrum of the linker H<sub>6</sub>TCPP (black) is also presented.

**Table S5.** Assignment of the vibrations in the IR-spectra of CAU-18, CAU-18a and Ce-PMOF-4NO<sub>2</sub>. Red numbers indicate slight impurities with DMF or linker, black numbers represent vibrations of the porphyrin moiety and blue numbers represent vibrations of the incorporated co-ligands DMF and 4-nitrobenzoic acid.<sup>10, 11</sup>

Vibration $\tilde{\nu}$ IR [cm <sup>-1</sup> ]	CAU-18	CAU-18a	Ce-PMOF-4NO <sub>2</sub>	H <sub>6</sub> TCPP
$\nu$ NH (pyrrole)	3317	3317	3317	3315
$\nu$ CH (DMF)	2921		2921	
$\nu$ CO (DMF)	1712/1674		1712	
$\nu_{as}$ CO (COOH (H <sub>6</sub> TCPP))	1652		1652	1684
$\nu_{as}$ CO (COO)	1585	1585	1585	
$\nu_{as}$ NO (NO <sub>2</sub> )			1585	
$\nu$ C=C (arom.)	1525	1515	1515	1558
$\nu_s$ CO (COO)	1402	1402	1402	
$\nu_s$ NO (NO <sub>2</sub> )			1383	
$\nu$ C-N (pyrrole)	1335	1335	1335	1399
$\delta$ O-H (COOH (H <sub>6</sub> TCPP))	1222	1222	1222	1222/ 1173
$\delta$ C-H (in plane)	1178	1178	1178	
$\delta$ C-H, N-H (pyrrole), <sub>3 neighboring H</sub>	1100	1100	1100	1106
$\delta$ C-H (in plane)	1022	1022	1022	
$\delta$ C-H, N-H (pyrrole), <sub>neighboring H</sub>	968	968	968	962
$\gamma$ C-H (out of plane)	843	843	843	
$\gamma$ C-H (1,4-subst.)	798	798	798	798
$\delta$ C-H, N-H (pyrrole), <sub>neighboring H</sub>	768	768	768	757
$\gamma$ C-H (out of plane)	725	725	725	717
$\delta$ C=C (skeleton)	482	482	482	525



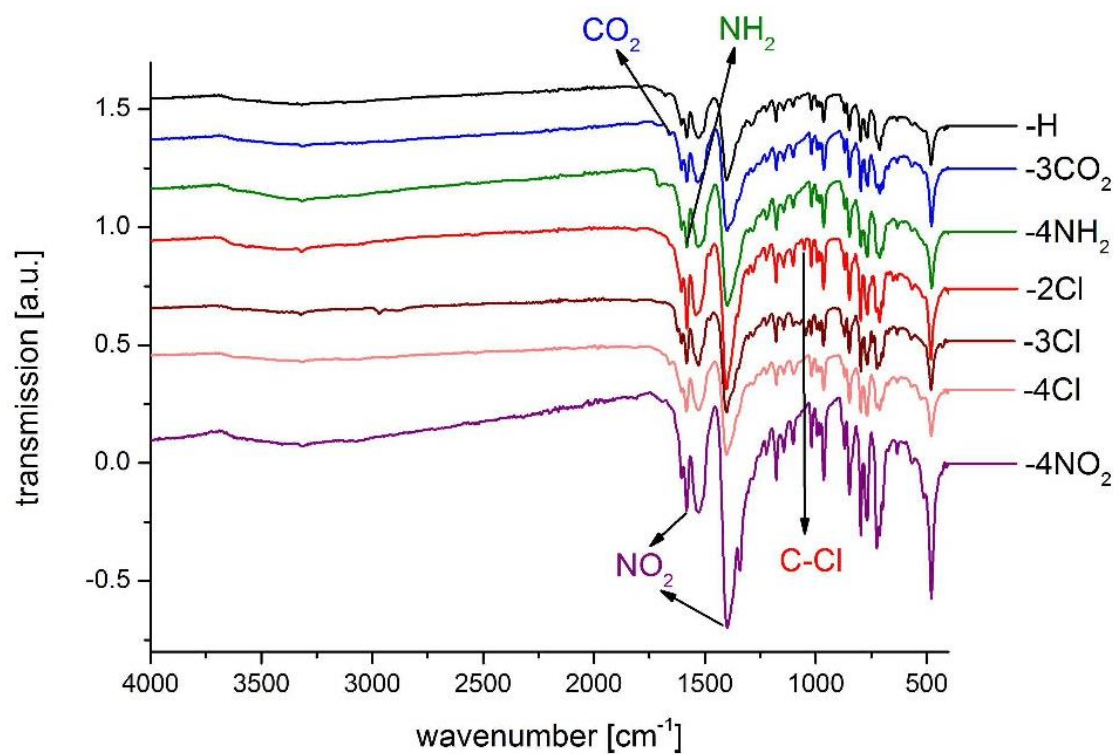


**Figure S60.** IR-spectra of CAU-19-X (X=H (black), 3CO<sub>2</sub>H (blue), 4NH<sub>2</sub> (green), 2Cl (bright red), 3Cl (dark red), 4Cl (pale red), 4NO<sub>2</sub> (purple)). Characteristic bands of the incorporated co-ligands are marked with black arrows.

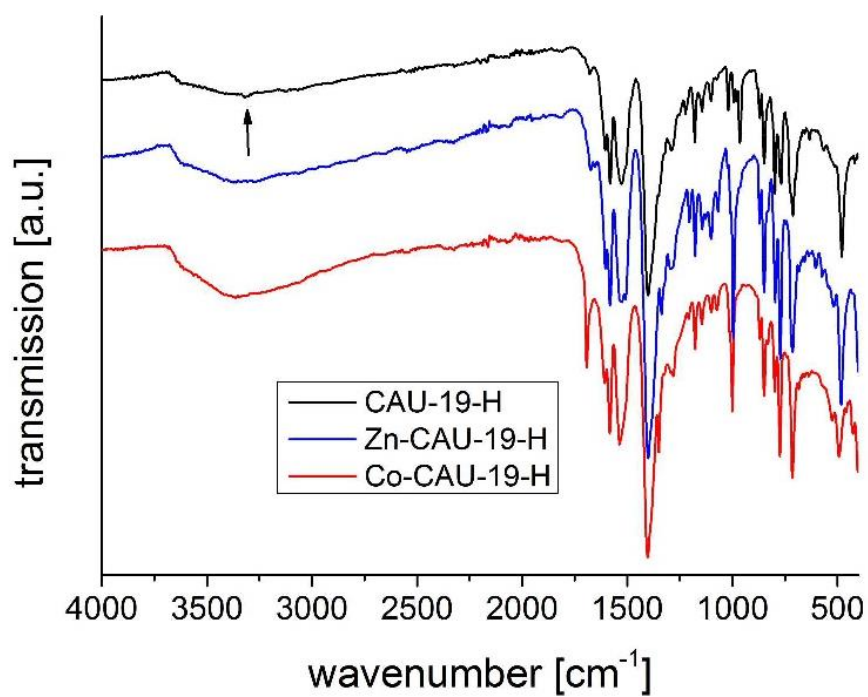


**Figure S61.** IR-spectra of CAU-19-H (black), Zn-CAU-19-H (blue) and Co-CAU-19-H (red). Characteristic NH stretching vibration is indicated by a black arrow.

**Table S6.** Assignment of the vibrations in the IR-spectra of CAU-19-X (X=H, 2Cl, 3Cl, 4Cl, 3CO<sub>2</sub>H, 4NO<sub>2</sub>, 4NH<sub>2</sub>). Red numbers indicate slight impurities with DMF or linker, black numbers represent vibrations of the incorporated linker molecule and blue numbers represent vibrations of the incorporated co-ligand.<sup>10,11</sup>

Vibration $\tilde{\nu}$ IR [cm <sup>-1</sup> ]	H	3CO <sub>2</sub> H	4NH <sub>2</sub>	2Cl	3Cl	4Cl	4NO <sub>2</sub>	H <sub>6</sub> TCPP
$\nu$ NH (pyrrole)	3317	3317	3317	3317	3317	3317	3317	3315
$\nu$ CO (DMF)		1712	1712					
$\nu_{as}$ CO (COOH (H <sub>6</sub> TCPP))	1677	1660		1660		1660		1684
$\nu_{as}$ CO (COOH)		1658						
$\nu_{as}$ CO (COO)	1580	1580	1580	1580	1580	1585	1585	
$\nu_{as}$ NO (NO <sub>2</sub> )							1585	
$\nu$ C=C (arom.)	1528	1528	1528	1528	1528	1528	1528	1558
$\delta$ N-H (NH <sub>2</sub> )			1580					
$\nu_s$ CO (COO)							1402	
$\nu_s$ CO (COO)	1402	1402	1402	1402	1402	1402	1402	
$\nu_s$ NO (NO <sub>2</sub> )							1402	
$\nu$ C-N (pyrrole)	1348	1348	1348	1348	1348	1348	1338	1399
$\delta$ O-H (COOH (H <sub>6</sub> TCPP))	1225	1225	1225	1225	1225	1225	1225	1222/ 1173
$\delta$ C-H (in plane)	1178	1178	1178	1178	1178	1178	1178	
$\delta$ C-H, N-H (pyrrole)	1100	1100	1100	1100	1100	1100	1100	1106
$\delta$ C-Cl				1053	1070	1056		
$\delta$ C-H (in plane)	1022	1022	1022	1022	1022	1022	1022	
$\delta$ C-H, N-H (pyrrole)	968	968	968	968	968	968	968	962
$\gamma$ C-H (out of plane)	843	843	843	843	843	843	843	
$\gamma$ C-H (1,4-subst.)	798	798	798	798	798	798	798	798
$\delta$ C-H, N-H (pyrrole)	768	768	768	768	768	768	768	757
$\gamma$ C-H (out of plane)	715	715	715	715	725	725	725	717
$\delta$ C=C (skeleton)	482	482	482	482	482	482	482	525

**9. References**

- (1) Jeong, E.-Y.; Ansari, M. B.; Mo, Y.-H.; Park, S.-E., *J. Hazard. Mater.* **2011**, *185*, 1311-1317.
- (2) Harada, A.; Yamaguchi, H.; Okamoto, K.; Fukushima, H.; Shiotsuki, K.; Kamachi, M., *Photochem. Photobiol.* **1999**, *70*, 298-302.
- (3) Garcia, G.; Sol, V.; Lamarche, F.; Granet, R.; Guilloton, M.; Champavier, Y.; Krausz, P., *Bioorg. Med. Chem. Lett.* **2006**, *16*, 3188-3192.
- (4) Chen, W.; Fukuzumi, S., *Eur. J. Inorg. Chem.* **2009**, *2009*, 5494-5505.
- (5) Feng, D.; Gu, Z.-Y.; Li, J.-R.; Jiang, H.-L.; Wei, Z.; Zhou, H.-C., *Angew. Chem.* **2012**, *124*, 10453-10456.
- (6) Kung, C.-W.; Chang, T.-H.; Chou, L.-Y.; Hupp, J. T.; Farha, O. K.; Ho, K.-C., *Chem. Commun.* **2015**, *51*, 2414-2417.
- (7) Afzal, S.; Daoud, W. A.; Langford, S. J., *J. Mater. Chem.* **2012**, *22*, 4083-4088.
- (8) Rochford, J.; Chu, D.; Hagfeldt, A.; Galoppini, E., *J. Am. Chem. Soc.* **2007**, *129*, 4655-4665.
- (9) Coxall, R. A.; Harris, S. G.; Henderson, D. K.; Parsons, S.; Tasker, P. A.; Winpenny, R. E. P., *J. Chem. Soc., Dalton Trans.* **2000**, 2349-2356.
- (10) Socrates, G., *Infrared and Raman Characteristic Group Frequencies: Tables and Charts*. Wiley: **2004**.
- (11) Hesse, M.; Meier, H.; Zeeh, B., *Spektroskopische Methoden in der organischen Chemie*. Thieme: **2005**.



**10 SI zu „Crystalline and permanently porous porphyrin-based metal tetraphosphonates“**

Supporting Information

**Crystalline and permanently porous porphyrin-based metal tetraphosphonates**

*Timo Rhauderwiek,<sup>a</sup> Konrad Wolkersdörfer,<sup>b</sup> Sigurd Oien-Odegaard,<sup>c</sup> Karl-Petter Lillerud,<sup>c</sup> Michael Wark<sup>b</sup> and Norbert Stock<sup>a,c</sup>*

<sup>a</sup> Institute of Inorganic Chemistry, Christian-Albrechts-Universität, Max-Eyth Straße 2, D-24118 Kiel, Germany.

<sup>b</sup> Chemical Technology 1, Carl von Ossietzky University Oldenburg, Carl-von-Ossietzky Str. 9-11, D-26129 Oldenburg, Germany.

<sup>c</sup> Department of Chemistry, University of Oslo, Sem Sælands vei 26, N-0371 Oslo, Norway.

<b>1. Materials and Characterization.....</b>	<b>2-3</b>
<b>2. Synthesis of Ni-H<sub>5</sub>TPPP and M-CAU-29 (M= Mn, Co, Ni, Cd). ....</b>	<b>4-8</b>
<b>3. SEM image of Ni-CAU-29, coordination mode, crystallographic parameters, bond distances and results of the Rietveld- and Pawley refinement of M-CAU-29.....</b>	<b>9-14</b>
<b>4. H<sub>2</sub>O Sorption properties and PXRD patterns of the activated samples .....</b>	<b>15</b>
<b>5. TG investigations, PXRD patterns of the decomposition products, VT-PXRD studies and chemical stability.....</b>	<b>16-21</b>
<b>6. Proton conductivity.....</b>	<b>22-27</b>
<b>7. IR and UV/vis spectroscopy .....</b>	<b>28-29</b>
<b>8. References.....</b>	<b>30</b>



## 1 Materials and Characterization

### 1.1 Materials.

MnCl<sub>2</sub> · 4 H<sub>2</sub>O (99 %, Merck), CoCl<sub>2</sub> · 6 H<sub>2</sub>O (98 %, Fluka), NiCl<sub>2</sub> · 6 H<sub>2</sub>O (97 %, Merck), CdCl<sub>2</sub> · H<sub>2</sub>O (98 %, Merck), EtOH (99 % + 1 % MEK, Walther), dichloromethane (Walther), N,N-dimethylformamide (99 %, Grüssing), acetone (99 %, Walther), 100 % acetic acid (VWR chemicals), NaH<sub>2</sub>PO<sub>4</sub> (99 %, Sigma-Aldrich) and Na<sub>2</sub>HPO<sub>4</sub> (99 %, Sigma-Aldrich) were used without further purification. The linker Ni-4,4',4'',4'''-(5,10,15,20-porphyrinotetrayl)tetraphosphonobenzoic acid Ni-(4-tetraphosphonophenylporphyrin, Ni-H<sub>8</sub>TPPP) was synthesized according to reported procedures<sup>1-3</sup> starting with 4-bromobenzaldehyd (98 %, ABCR) and pyrrole (98 %, ABCR) in propionic acid (99 %, Grüssing) with following NiCl<sub>2</sub>-catalyzed (97 %, Merck) phosphorylation in 1,3-Diisopropylbenzene (96 %, Sigma-Aldrich) using triethyl phosphite (98 %, Sigma-Aldrich) with following hydrolysis in conc. HCl (35 %, VWR chemicals). Details are given in the Supporting Information.

### 1.2 Characterization.

Single crystal X-ray diffraction data for Ni-CAU-29 were acquired using a Bruker D8 Venture diffractometer equipped with a Photon 100 CMOS area detector and a Mo K $\alpha$  microsource ( $\lambda$  = 0.71073 Å). The reflections were indexed with the APEX3 suite, integrated with SAINT V9.32B,<sup>4</sup> solved with the program SHELXT,<sup>5</sup> and refined with the program SHELXL using Olex2 as GUI.<sup>6</sup> The crystal was very small (5 x 20  $\mu$ m) and poorly diffracting, limiting the resolution to a (sin  $\theta$ )/ $\lambda$  value of 0.36 which corresponds to a d spacing of 1.4 Å. The data also showed poor consistency ( $R_{\text{int}}$  = 0.186). The poor diffraction at higher angles resulted in a low number of unique reflections and thus limited accuracy of determined bond lengths. Geometric constraints were used on the 6-membered rings in the structure refinement to improve the data-to-parameter ratio, although the structure refines just as well without.

The structure contains sheets of stacked porphyrin rings, likely to cause stacking disorder in the crystals. This disorder is likely to have caused the poor diffraction quality, thus resulting in low precision on bond lengths and ADP values in the obtained crystal structures. Only Ni and P atoms were refined anisotropically to avoid overparametrization.

The crystal structure contains 1-dimensional channels along [1 0 0] that are partly filled with an unknown adsorbate. The data quality is not sufficient to use solvent masking. Instead, dummy atoms (C47, C48, O14) were used to emulate adsorbed species at the points of highest electron density in the pores (obtained from the Fourier difference map).

High resolution PXRD patterns were measured on a STOE Stadi-P combi powder diffractometer equipped with a Mythen detector (Cu K $\alpha$ <sub>1</sub> radiation). Rietveld-refinements and Pawley-fits (Fig. S8 – S11) were carried out for all M-CAU-29 (M= Mn, Co, Ni, Cd) derivatives to proof that they are phase pure and isostructural to Ni-CAU-29. Pawley-fits were performed with the program TOPAS academic V4.1.<sup>7</sup> The results of the refinement and crystallographic data of M-CAU-29 is shown in Table S2. The diameters of all pores were determined using DIAMOND V.3<sup>8</sup> taking the van-der-Waals radii of the atoms into account as well as Material Studio V5<sup>9</sup> to determine the Connolly surface. The VT-PXRD measurements were recorded on a STOE Stadi-P combi powder diffractometer (Mo K $\alpha$ <sub>1</sub> radiation) equipped with a capillary furnace. For the measurements 0.5 mm quartz capillaries were used. The samples were heated up in steps of 5 K between 25 and 450 °C and measured for 10 minutes each.

IR-spectra were recorded using a Bruker ALPHA-FT-IR A220/D-01 spectrometer equipped with an ATR-unit. UV/vis spectra were recorded at a Spectroquant Pharo 300 M. Prior to the measurements all samples were dissolved in 2M NaOH and measured at once. The <sup>1</sup>H- and <sup>31</sup>P-

NMR spectra of the Ni-H<sub>8</sub>TPPP linker were recorded on a Bruker DRX 500 spectrometer. Sorption experiments were performed with a BEL Japan Inc. BELSORP-max. Before sorption measurements all samples were activated at 170 °C under reduced pressure (10<sup>-2</sup> kPa) for 16 h. Thermogravimetric measurements were performed on a NETZSCH STA 409 CD analyzer under a flow of air (75 ml min<sup>-1</sup>) with a heating rate of 4 °C min<sup>-1</sup> between 25 and 700 °C in Al<sub>2</sub>O<sub>3</sub>-crucibles. The data were corrected for buoyancy and current effects.

## 2. Synthesis of Ni-H<sub>8</sub>TPPP and M-CAU-29 (M= Mn, Co, Ni, Cd).

The three step synthesis route of Ni-H<sub>8</sub>TCP (Fig. S1) was carried out employing in the first step the Adler method<sup>1, 2</sup> in the synthesis of 4-Bromophenylporphyrin (H<sub>2</sub>TBrPP). The second step, the phosphorylation of H<sub>2</sub>TBrPP was achieved by using a Ni-catalyzed variation of the Arbuzov reaction,<sup>3, 10</sup> with the following third step, the hydrolysis of the -PO(OEt)<sub>2</sub> groups in conc. HCl.

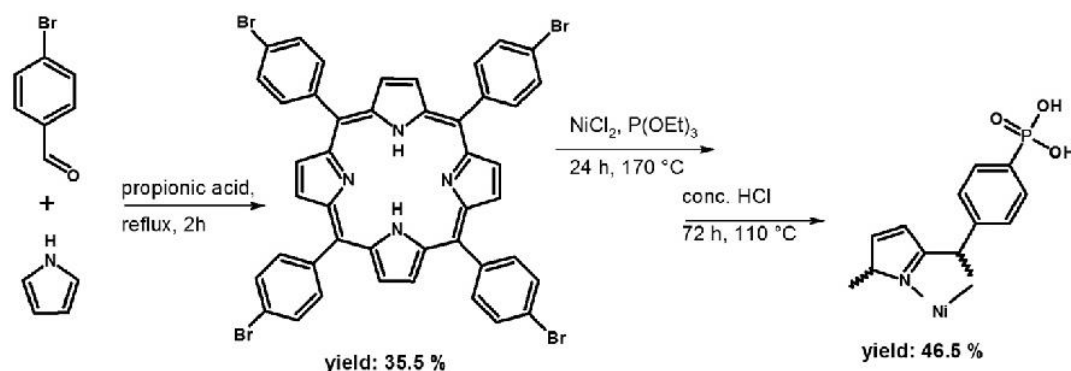


**Figure S1.** Schematic representation of the synthesis route of Ni-H<sub>8</sub>TPPP.

**H<sub>2</sub>TBrPP:** Pyrrole (7.47 mL, 108 mmol) and 4-bromobenzaldehyde (20.0 g, 108 mmol) in 400 mL propionic acid were heated under reflux for 2 h. Afterwards the reaction mixture was cooled down to room temperature and poured into 500 mL of MeOH and stirred for 30 min in an ice bath. The resulting precipitate was filtered off and washed several times with MeOH until the filtrate was clear. Subsequently, the product was washed with 100 mL warm distilled water and dried at 70 °C in a drying oven over night. A blue powder of H<sub>2</sub>TBrPP 7.63 g (8.2 mmol, 30.4 %) was obtained.

Elemental analysis of H<sub>2</sub>TBrPP (Br<sub>4</sub>C<sub>44</sub>H<sub>26</sub>N<sub>4</sub>): calc (%): C 56.8, H 2.6, N 6.0, found (%): C 59.7, H 3.2, N 6.2. The small difference between the calculated and observed values is due to impurities caused by propionic acid used in the synthesis. Propionic acid was also observed in the <sup>1</sup>H-NMR measurements, but not in the <sup>1</sup>H-NMR spectra of the products in the next synthesis steps. The low intensity peaks between 8.5 and 8.0 ppm are due to interactions of the H<sub>2</sub>TBrPP with propionic acid, indicated by the different chemical shift and have no influence on the purity of the products in the next synthesis steps.

**$^1\text{H-NMR}$  (Fig. S2),  $\text{H}_2\text{TBrPP}$  (500 MHz  $\text{CDCl}_3$ ):**  $\delta = 8.76$  (s, 8H, H-1); 7.99 (d, 8H, H-2); 7.82 (d, 8H, H-3); 7.18 (s, 1H,  $\text{CDCl}_3$ ); 2.30 (q, 2H, propionic acid); 1.08 (t, 3H, propionic acid) ppm. Additional peaks between 7 and 9 ppm are due to low impurities with higher condensed porphyrines.

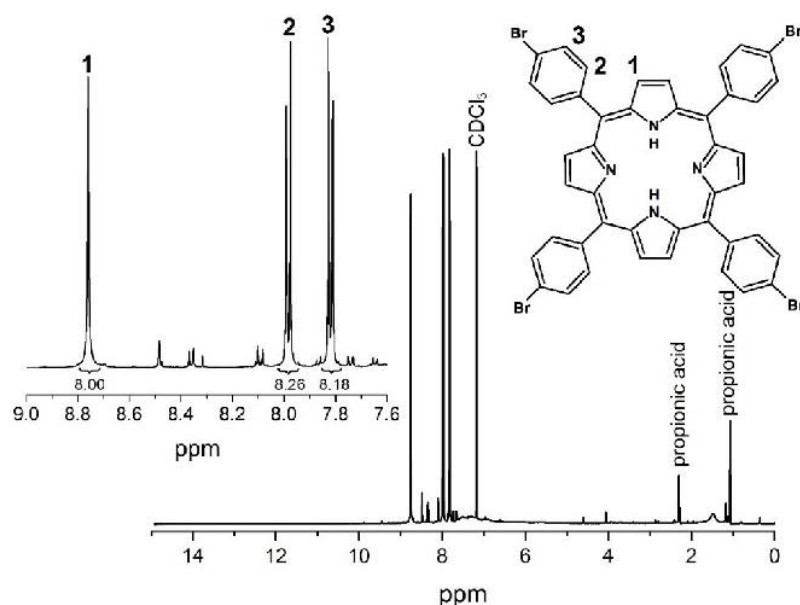


**Figure S2.**  $^1\text{H-NMR}$  spectrum of  $\text{H}_2\text{TBrPP}$  digested in DMSO.

**$\text{Ni-H}_8\text{TPPP}$ :**  $\text{H}_2\text{TBrPP}$  (3.42 g, 3.7 mmol) and anhydrous  $\text{NiCl}_2$  (1.79 g, 13.8 mmol) in 70 mL 1,3-diisopropylbenzene (prior the reaction for 30 min with  $\text{N}_2$  degassed) were heated up to exactly  $170\text{ }^\circ\text{C}$  under  $\text{N}_2$  atmosphere. Afterwards triethylphosphite (7.05 mL, 43.7 mmol) as added slowly (30 min) and dropwise to the reaction mixture and heated for further 24 h at  $170\text{ }^\circ\text{C}$ . The reaction mixture was cooled down to room temperature and the resulting precipitate was filtered off and washed with 250 mL DCM. The resulting organic phase was washed 2 times each with 100 mL  $\text{H}_2\text{O}$ . The organic solvents were evaporated under reduced pressure and the resulting precipitate was hydrolyzed with 80 mL conc.  $\text{HCl}$  at  $110\text{ }^\circ\text{C}$  over 72 h. The resulting product was filtered off, washed with 100 mL cooled water and afterwards stirred in 100 mL DCM for 24 h. The resulting clean product was filtered off and dried at  $70\text{ }^\circ\text{C}$  in a drying oven over night. A red powder of  $\text{Ni-H}_8\text{TPPP}$  2.74 g (2.76 mmol, 75 %) was obtained.

Elemental analysis of  $\text{Ni-H}_8\text{TPPP}$  ( $\text{C}_{44}\text{H}_{32}\text{N}_4\text{NiO}_{12}$ )  $\cdot 4\text{H}_2\text{O}$ : calc (%): C 49.8, H 3.6, N 5.3, found (%): C 49.1, H 3.6, N 5.1.

**$^1\text{H-NMR}$  (Abb. S3),  $\text{Ni-H}_8\text{TPPP}$  (500 MHz  $\text{DMSO-d}_6$ ):**  $\delta = 8.74$  (s, 8H, H-1); 8.11 (dd, 8H, H-2); 8.06 (dd, 8H, H-3); 2.50 (s, 6H,  $\text{DMSO-d}_6$ ); 2.09 (s, 6H, acetone) ppm.

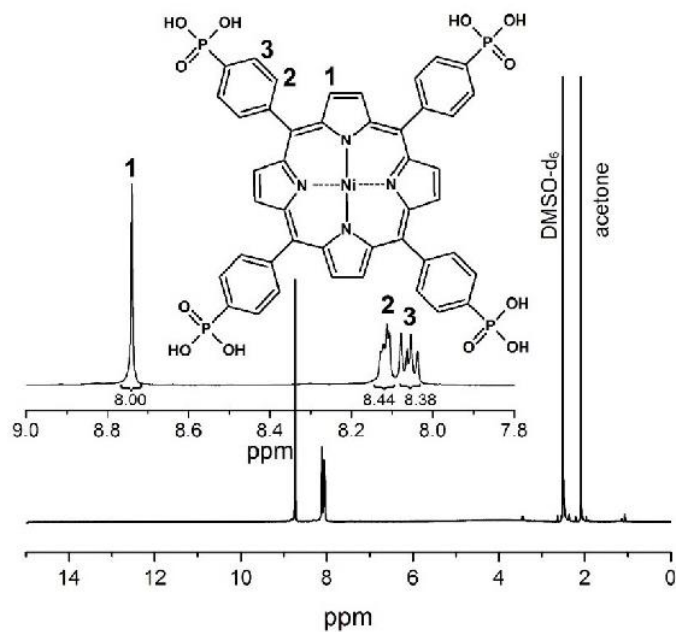


**Figure S3.**  $^1\text{H-NMR}$  spectrum of  $\text{Ni-H}_8\text{TPPP}$  digested in  $\text{DMSO}$ .

**$^{31}\text{P-NMR}$  (Abb. S4),  $\text{Ni-H}_8\text{TPPP}$  (500 MHz  $\text{DMSO-d}_6$ ):**  $\delta = 12.04$  (s, 4P,  $-\text{PO}(\text{OH})_2$ ) ppm.

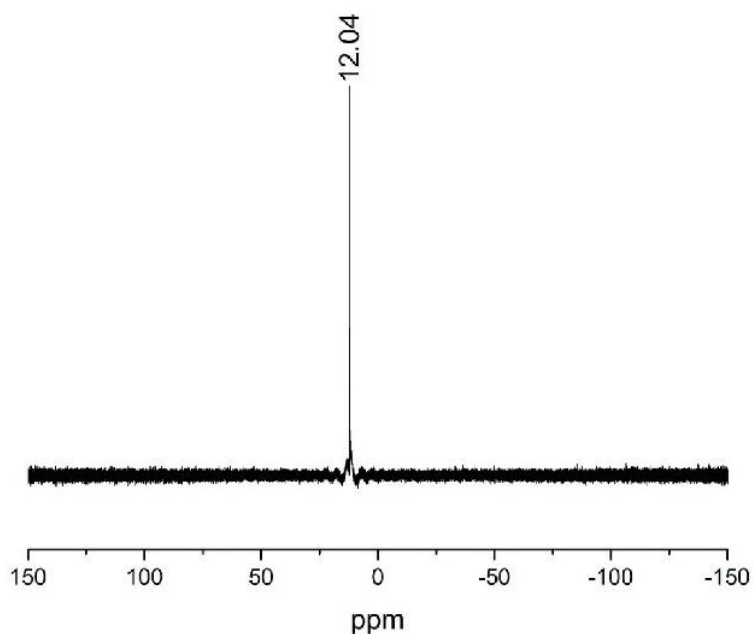


**Figure S4.**  $^{31}\text{P-NMR}$  spectrum of  $\text{Ni-H}_8\text{TPPP}$  digested in  $\text{DMSO}$ .

**Synthesis of M-CAU-29.**

High-throughput methods (2 mL teflon inserts) were employed in the screening of synthesis parameters such as molar ratio of metal to linker, pH and reaction temperature. The usage of molar linker to metal ratios of 1 : 1 resulted in CAU-29 with low crystallinity, while higher ratios up to a five times excess of metal (1 : 1 in the structure) and the 3-fold concentration of the reactants led to highly crystalline CAU-29 (Fig. S5). Furthermore an upscaling in 30 mL teflon inserts of CAU-29 was possible using the 12 fold amount of all reactants. In the following the optimized and upscaled synthesis parameters of M-CAU-29 (M= Mn, Co, Ni, Cd) are given. The usage of other divalent cations like  $Mg^{2+}$ ,  $Ca^{2+}$ ,  $Fe^{2+}$ ,  $Cu^{2+}$  and  $Zn^{2+}$  under this synthesis conditions led in most cases either to X-ray amorphous or products of low crystallinity.

**Synthesis of Mn-CAU-29:** Ni- $H_8$ TPPP (180 mg,  $18.3 \times 10^{-5}$  mmol),  $MnCl_2 \cdot 4 H_2O$  (190.5 mg,  $91.5 \times 10^{-5}$  mmol) and  $H_2O$  (12 mL) were added to a 30 mL Teflon insert and placed in a steel reactor. The reactor was heated for 48 h at 180 °C and cooled down to room temperature in 6 h. The resulting product was filtered off and washed with  $H_2O$  and acetone. A yield of 162 mg, (84 % based on Ni- $H_8$ TPPP) was obtained for Mn-CAU-29,  $[Mn(Ni-H_6TPPP)(H_2O)] \cdot 7 H_2O$ . Elemental analysis of Mn-CAU-29: calc (%): C 50.4, H 4.2, N 5.4, found (%): C 50.1, H 3.4, N 5.2.

**Synthesis of Co-CAU-29:** Ni- $H_8$ TPPP (180 mg,  $18.3 \times 10^{-5}$  mmol),  $CoCl_2 \cdot 6 H_2O$  (229.2 mg,  $91.5 \times 10^{-5}$  mmol) and  $H_2O$  (12 mL) were added to a 30 mL Teflon insert and placed in a steel reactor. The reactor was heated for 48 h at 180 °C and cooled down to room temperature in 6 h. The resulting product was filtered off and washed with  $H_2O$  and acetone. A yield of 156 mg, (81 % based on Ni- $H_8$ TPPP) was obtained for Co-CAU-29,  $[Co(Ni-H_6TPPP)(H_2O)] \cdot 5 H_2O$ . Elemental analysis of Co-CAU-29: calc (%): C 49.2, H 3.8, N 5.2, found (%): C 49.3, H 3.3, N 5.1.

**Synthesis of Ni-CAU-29:** Ni- $H_8$ TPPP (180 mg,  $18.3 \times 10^{-5}$  mmol),  $NiCl_2 \cdot 6 H_2O$  (228.9 mg,  $91.5 \times 10^{-5}$  mmol) and  $H_2O$  (12 mL) were added to a 30 mL Teflon insert and placed in a steel reactor. The reactor was heated for 48 h at 180 °C and cooled down to room temperature in 6 h. The resulting product was filtered off and washed with  $H_2O$  and acetone. A yield of 165 mg, (86 % based on Ni- $H_8$ TPPP) was obtained for Ni-CAU-29,  $[Ni(Ni-H_6TPPP)(H_2O)] \cdot 5 H_2O$ . Elemental analysis of Ni-CAU-29: calc (%): C 49.2, H 3.8, N 5.2, found (%): C 49.3, H 3.4, N 5.1.

**Synthesis of Cd-CAU-29:** Ni- $H_8$ TPPP (180 mg,  $18.3 \times 10^{-5}$  mmol),  $CdCl_2 \cdot H_2O$  (193.8 mg,  $91.5 \times 10^{-5}$  mmol) and  $H_2O$  (12 mL) were added to a 30 mL Teflon insert and placed in a steel reactor. The reactor was heated for 48 h at 180 °C and cooled down to room temperature in 6 h. The resulting product was filtered off and washed with  $H_2O$  and acetone. A yield of 180 mg, (89 % based on Ni- $H_8$ TPPP) was obtained for Cd-CAU-29,  $[Cd(Ni-H_6TPPP)(H_2O)] \cdot 7 H_2O$ . Elemental analysis of Ni-CAU-29: calc (%): C 47.8, H 4.0, N 5.1, found (%): C 47.7, H 3.2, N 4.9.



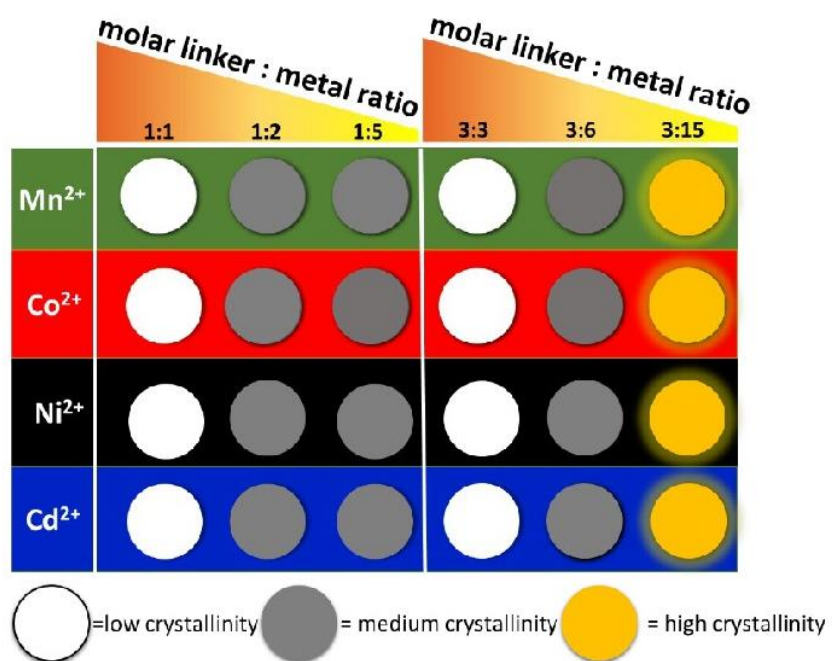


**Figure S5.** Results of the high-throughput investigation of CAU-29.

### 3. SEM image of Ni-CAU-29, coordination mode, crystallographic parameters, bond distances and results of the Rietveld- and Pawley-refinement of M-CAU-29

The SEM image of Ni-CAU-29 reveals small needles and block shaped crystals in a range of 10-50  $\mu\text{m}$ .

The coordination mode of the (di)hydrogen phosphonate groups (P003-P006) in Ni-CAU-29 is given in Figure S7 using the Harris notation. The Harris-notation has the format [A,XYZ], the value A is the number of metal ions coordinated by the (di)hydrogen phosphonate group and X, Y, Z is the number of bonds every oxygen shares with a metal ion.<sup>11</sup>

The crystallographic data and results of the single crystal X-ray diffraction analysis of Ni-CAU-29 (Tab. S1, selected bond lengths Tab. S1a) and all M-CAU-29 derivatives (Tab. S2) reveal very similar cell parameters and the resulting Rietveld- and Pawley-refinements prove all M-CAU-29 (M=Mn, Co, Ni, Cd) derivatives are isostructural and show no further impurities in the samples (Fig. S8 – S11).

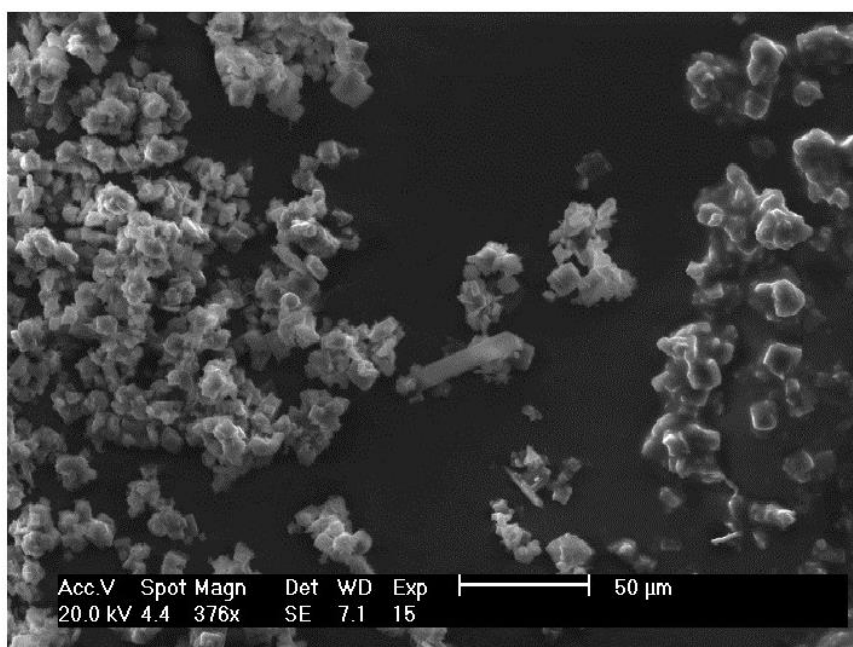


**Figure S6.** SEM image of Ni-CAU-29. The SEM measurements reveal crystal sizes between 10 and 50  $\mu\text{m}$ .

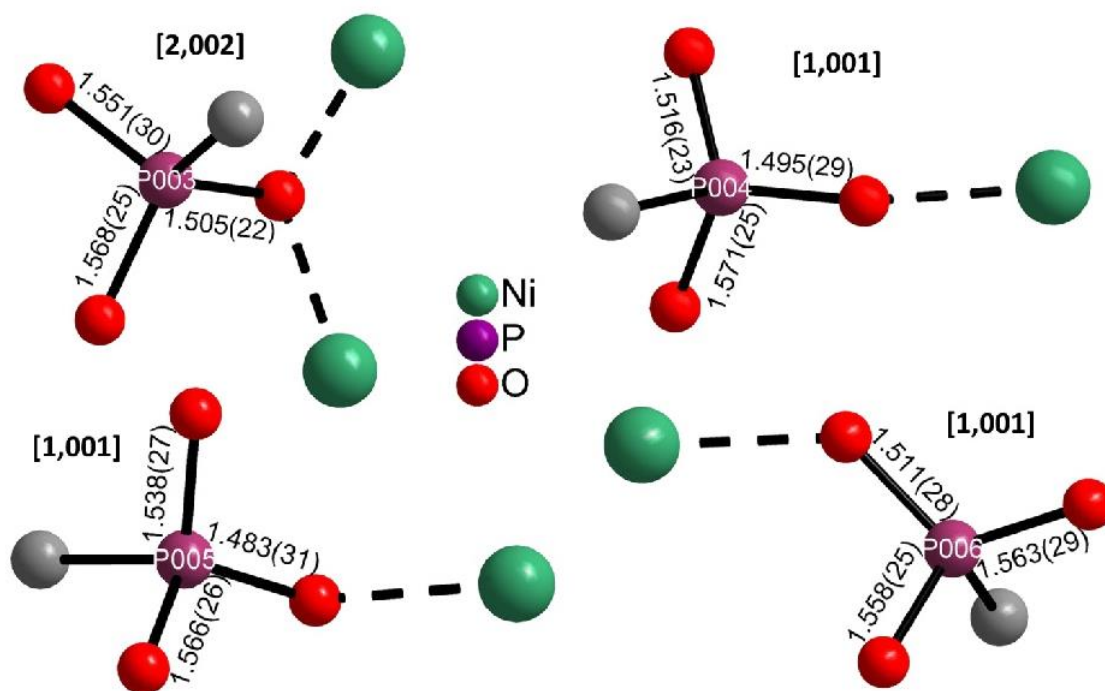


**Figure S7.** Graphical representation of the coordination mode of the (di)hydrogen phosphonate groups (P003-P006) in Ni-CAU-29. Numbers in brackets represent the Harris notation.

**Table S1.** Results of the single crystal X-ray diffraction analysis of Ni-CAU-29.

<b>Ni-CAU-29</b>	
<b>Crystal system</b>	<i>triclinic</i>
<i>a</i> [Å]	9.561(5)
<i>b</i> [Å]	15.086(9)
<i>c</i> [Å]	16.722(9)
$\alpha$ [°]	94.723(9)
$\beta$ [°]	97.602(9)
$\gamma$ [°]	97.880(9)
<i>V</i> [Å <sup>3</sup> ]	2356(2)
<i>Z</i>	2
<b>space group</b>	<i>P</i> $\bar{1}$
<b>total data</b>	6040
<b>unique data</b>	1832
<b><i>R</i><sub>int</sub></b>	0.118
<b>Observed data [<i>I</i> &gt; 2σ(<i>I</i>)]</b>	1180
<b><i>R</i><sub>1</sub> [<i>I</i> &gt; 2σ(<i>I</i>)] [%]</b>	9.97
<b>w<i>R</i><sub>2</sub> [<i>I</i> &gt; 2σ(<i>I</i>)] [%]</b>	23.46
<b>GOF</b>	1.13

**Table S1a.** Selected bond lengths in Ni-CAU-29.

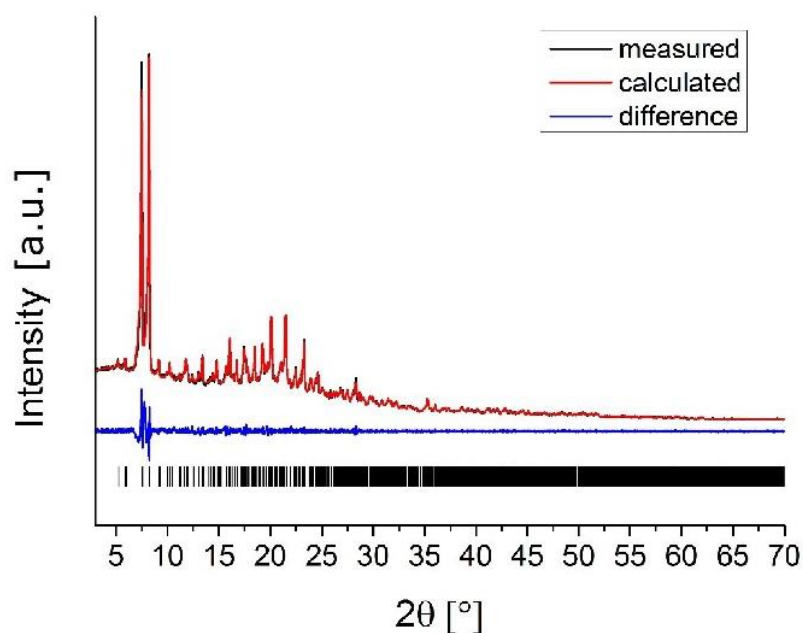
	<b>bond distance [Å]</b>		<b>bond distance [Å]</b>
Ni01—O007	2.11 (2)	P003—C00P	1.794 (18)
Ni01—O007	2.14 (2)	P004—O009	1.50 (2)
Ni01—O008	2.05 (2)	P004—O00A	1.57 (2)
Ni01—O009	2.13 (2)	P004—O00B	1.52 (2)
Ni01—O00E	2.10 (2)	P004—C01B	1.86 (2)
Ni01—O00F	2.04 (2)	P005—O008	1.48 (2)
Ni02—N00H	1.90 (2)	P005—O00G	1.57 (2)
Ni02—N00L	1.95 (3)	P005—O00J	1.54 (2)
Ni02—N00M	1.94 (3)	P005—C01E	1.78 (2)
Ni02—N00N	1.93 (3)	P006—O00F	1.51 (2)
P003—O007	1.50 (2)	P006—O00I	1.56 (3)
P003—O00C	1.55 (2)	P006—O00K	1.56 (2)
P003—O00D	1.57 (2)	P006—C01G	1.83 (2)

**Rietveld refinements of Co- and Ni-CAU-29.**

To further confirm the crystal structures of Ni- and Co-CAU-29, structure refinements by the Rietveld method were carried out using TOPAS academics V4.1.<sup>7</sup> The structure as determined from single crystal X-ray diffraction was used as a starting point. The hydrogen atoms, guest atoms and atoms resulting from disorder were removed from the structure after inserting cobalt atoms into the inorganic building unit. The Ni-tetra(4-phosphonophenyl)porphyrin moiety was refined as rigid body while the positions of all other atoms were freely refined. Residual electron density was identified by Fourier synthesis and considered as two independent oxygen atoms, representing any kind of guest molecules, although the interatomic distances are in a reasonable range for strong hydrogen bonding. The temperature factors of the rigid body and all other atoms, respectively, were refined as general coefficients. In addition preferred orientation along the *c* axis was also taken into account. The structure obtained after convergence was further used as starting point for the Rietveld refinement of Ni-CAU-29 which was refined in the same manner. The final plots are shown below in Figure S9 and S10 and some relevant parameters are summarized in Table S2.

**Table S2.** Results of the Rietveld refinements of Co- and Ni-CAU-29 and Pawley refinements of Mn- and Cd-CAU-29 of the crystallographic data of M-CAU-29 (M= Mn, Co, Ni, Cd).

	<b>Mn</b>	<b>Co</b>	<b>Ni</b>	<b>Cd</b>
<b>SG</b>	$P\bar{1}$	$P\bar{1}$	$P\bar{1}$	$P\bar{1}$
<b>a</b> [Å]	9.761(2)	9.6860(7)	9.6473(6)	9.691(3)
<b>b</b> [Å]	15.055(5)	15.1223(18)	15.1046(15)	15.067(7)
<b>c</b> [Å]	17.022(6)	16.7747(22)	16.7115(19)	16.722(9)
<b><math>\alpha</math></b> [°]	94.168(7)	94.751(3)	94.662(4)	94.638(10)
<b><math>\beta</math></b> [°]	96.809(20)	97.412(8)	97.263(8)	97.158(35)
<b><math>\gamma</math></b> [°]	97.057(17)	97.288(8)	97.309(7)	97.489(29)
<b>V</b> [Å <sup>3</sup> ]	2455(1)	2404.5(5)	2384.3(4)	2390(2)
<b>GoF</b>	1.65	1.1	1.5	1.75
<b>R<sub>wp</sub></b> [%]	3.51	3.1	6.7	3.42
<b>R<sub>Bragg</sub></b> [%]		0.7	2.5	

**Figure S8.** Result of the Pawley fit of Mn-CAU-29 (as-synthesized). Measured data are shown as a black line, calculated data as a red line and the blue line gives the difference plot. Predicted peak positions are marked as vertical bars.

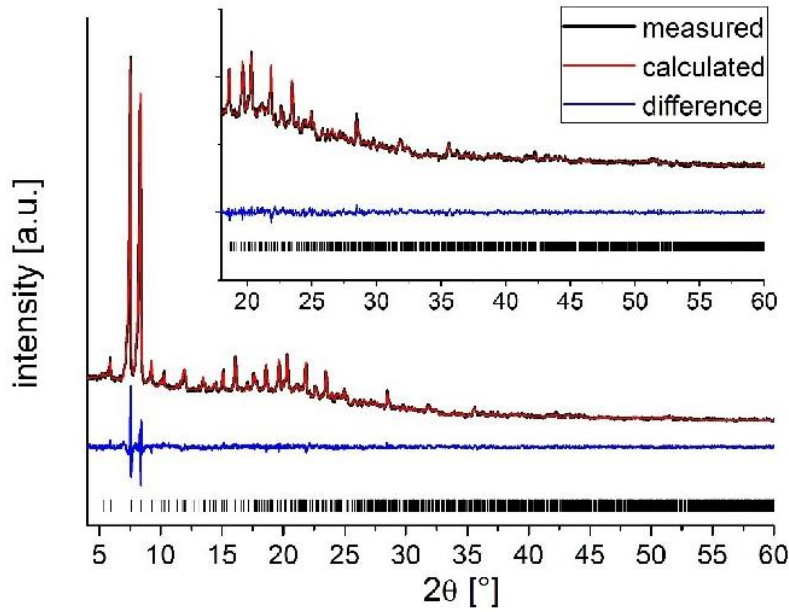


**Figure 9:** Result of the Rietveld refinement of Co-CAU-29. The black line gives the measured data, the red line gives the fit and the blue line is the difference curve. Black vertical bars indicate allowed peak positions.

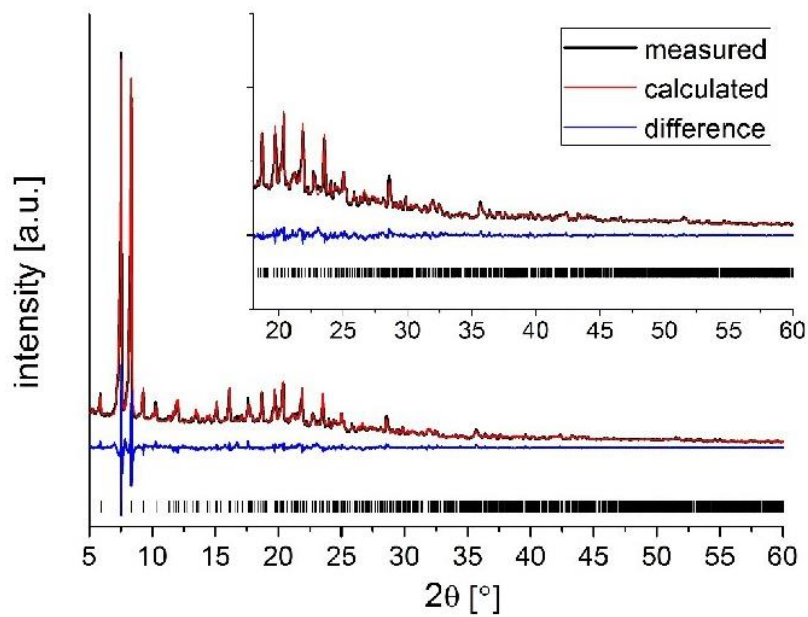


**Figure 10:** Result of the Rietveld refinement of Ni-CAU-29. The black line gives the measured data, the red line gives the fit and the blue line is the difference curve. Black vertical bars indicate allowed peak positions.



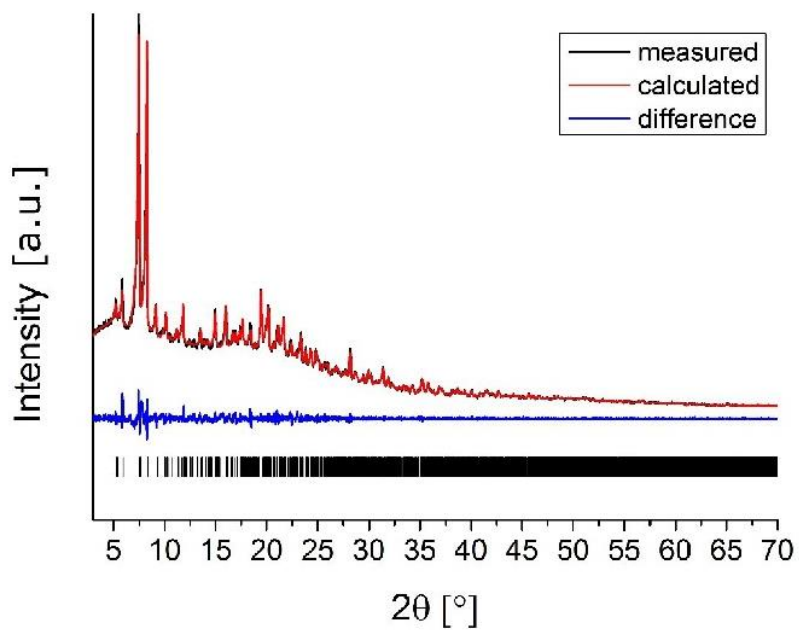


**Figure S11.** Result of the Pawley fit of Cd-CAU-29 (as-synthesized). Measured data are shown as a black line, calculated data as a red line and the blue line gives the difference plot. Predicted peak positions are marked as vertical bars.

#### 4. H<sub>2</sub>O Sorption properties and PXRD patterns of the activated samples

H<sub>2</sub>O-sorption isotherms of M-CAU-29 (M= Mn, Co, Ni, Cd) (Figure S12) and PXRD patterns of the samples after the sorption experiment compared with the PXRD pattern before the measurement (Figure S13).

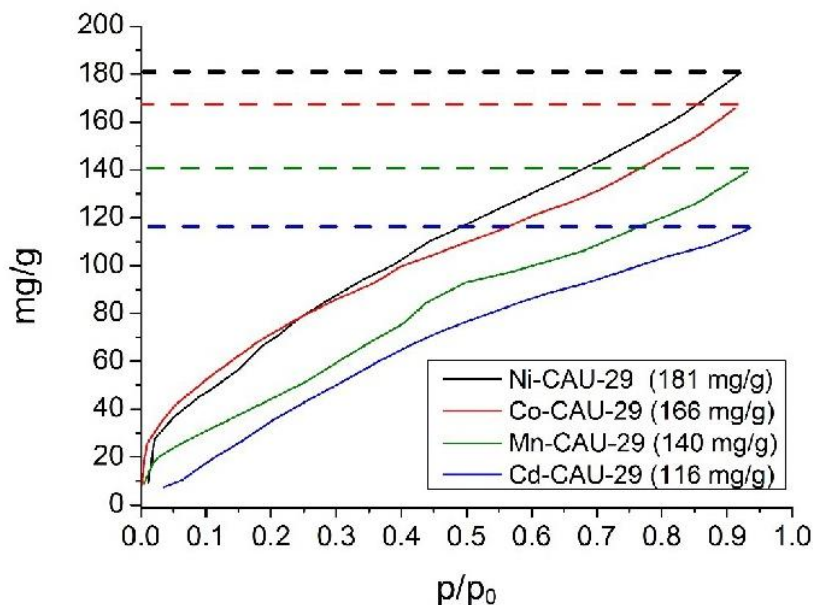


**Figure S12.** Results of the H<sub>2</sub>O sorption experiments at 298 K (activated prior measurement at 170 °C, overnight under reduced pressure of 10<sup>-2</sup> kPa). The uptake corresponds to the amount of physisorbed water in the pores (Mn- : 9 H<sub>2</sub>O, Co- : 11 H<sub>2</sub>O, Ni- : 11 H<sub>2</sub>O, Cd- : 8 H<sub>2</sub>O).

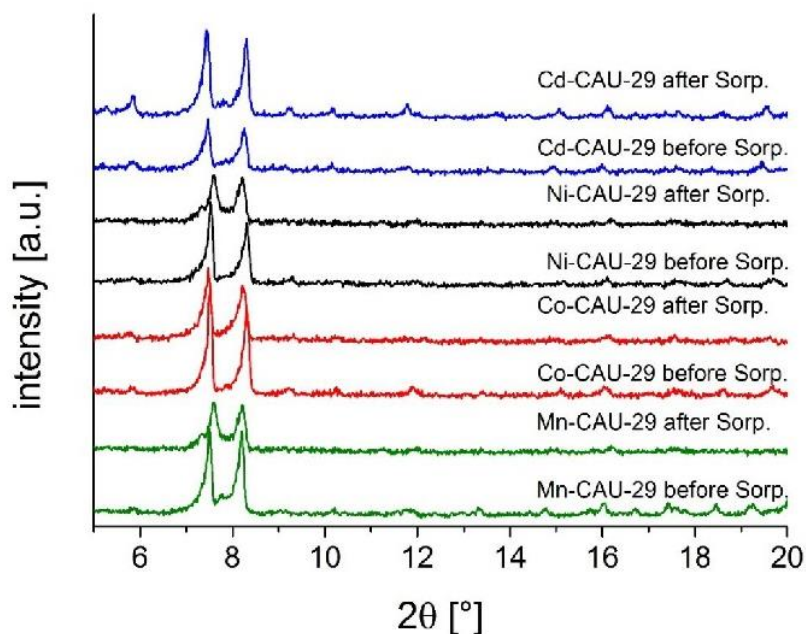


**Figure S13.** PXRD patterns of M-CAU-29 (M= Mn, Co, Ni, Cd) after the sorption experiments (activation 170 °C, 10<sup>-2</sup> kPa). For comparison the patterns of M-CAU-29 before the sorption experiment are also presented below the ones after the sorption experiments each.

### 5. TG investigations, PXRD patterns of the decomposition products, VT-PXRD studies and chemical stability.

The results of all TG measurements are shown in Fig. S14-S18 and Tab. S3. The decomposition products of M-CAU-29 (M= Mn, Co, Ni, Cd) are Ni-M-pyro- and metaphosphates (M= Mn, Co, Cd) which was shown by PXRD measurements (Fig. S19). The results of VT-PXRD studies (Fig. S20- S23) confirm the results obtained from the TG measurements. Complete collapse of the frameworks takes place above ca. 350 °C.

The results of the chemical stability test in different solvents as well as in a pH range between 0 and 14 and phosphate buffer (pH 7) are shown for Ni-CAU-29 in Fig. S24.

**Table S3.** Results of the TG measurements of M-CAU-29 (M=Mn, Co, Ni, Cd). Number in brackets represents the amount of H<sub>2</sub>O taken up during H<sub>2</sub>O sorption experiments.

sum formula	residual mass		mass loss linker decomposition		mass loss H <sub>2</sub> O	
	meas. [%]	calc. [%]	meas. [%]	calc. [%]	meas. [%]	calc. [%]
[Mn(Ni-H <sub>6</sub> TPPP)(H <sub>2</sub> O)] · 6.7 H <sub>2</sub> O (9.0 H <sub>2</sub> O)	31.1		58.9		8.8	
		31.8		59.4		8.8
[Co(Ni-H <sub>6</sub> TPPP)(H <sub>2</sub> O)] · 6.4 H <sub>2</sub> O (11.2 H <sub>2</sub> O)	35.5		55.5		8.0	
		32.1		59.4		8.0
[Ni(Ni-H <sub>6</sub> TPPP)(H <sub>2</sub> O)] · 9.0 H <sub>2</sub> O (10.8 H <sub>2</sub> O)	34.8		56.0		11.3	
		31.0		57.4		11.3
[Cd(Ni-H <sub>6</sub> TPPP)(H <sub>2</sub> O)] · 8.2 H <sub>2</sub> O (7.9 H <sub>2</sub> O)	34.4		58.2		8.2	
		34.7		57.2		8.2

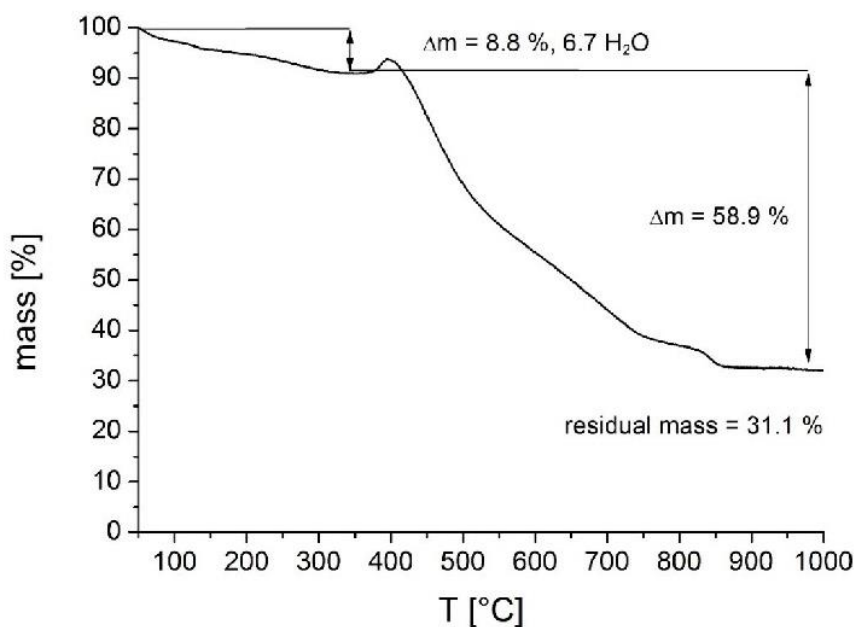


**Figure S14.** Thermogravimetric curve of Mn-CAU-29 (under air). Evaluation of the data reveals a molar ratio of metal : linker : H<sub>2</sub>O of 1 : 2.0 : 6.7 (Tab. S3). The weight gain before

the collapse of the framework indicates a reaction for example between the  $\text{Ni}^{2+}$  ions with oxygen, since it was not observed in the TG measurement under  $\text{N}_2$  atmosphere.

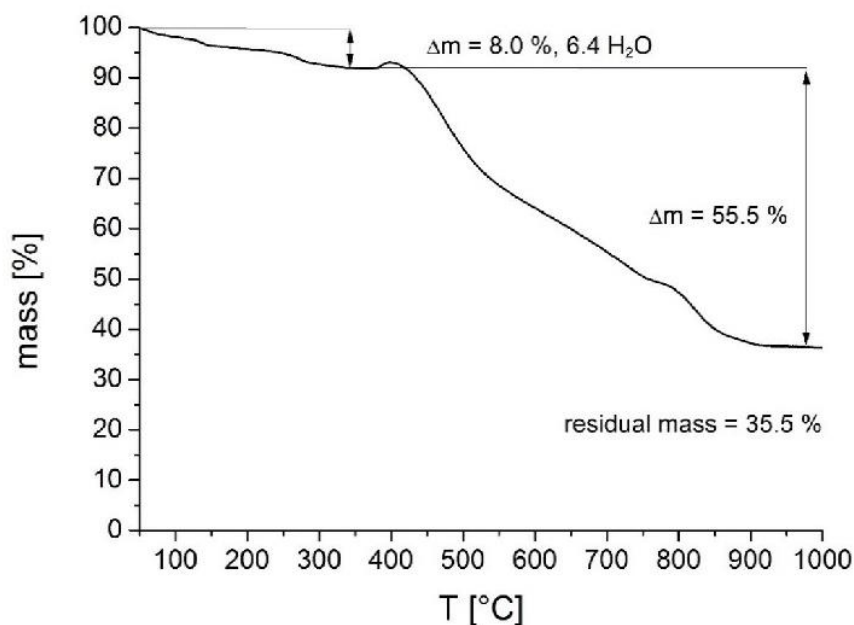


**Figure S15.** Thermogravimetric curve of Co-CAU-29 (under air). Evaluation of the data reveals a molar ratio of metal : linker :  $\text{H}_2\text{O}$  of 1 : 2.4 : 6.4 (Tab. S3). The weight gain before the collapse of the framework indicates a reaction for example between the  $\text{Ni}^{2+}$  ions with oxygen, since it was not observed in the TG measurement under  $\text{N}_2$  atmosphere.

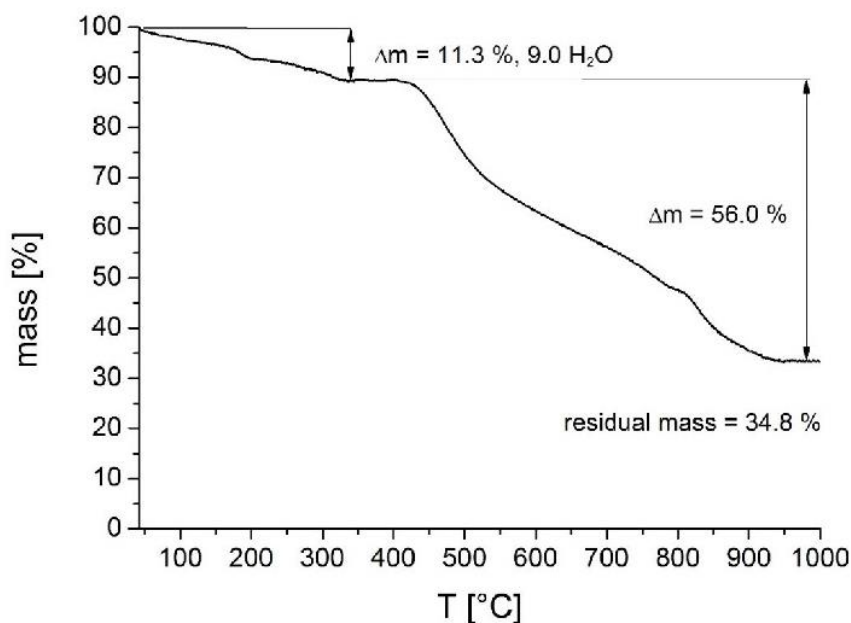


**Figure S16.** Thermogravimetric curve of Ni-CAU-29 (under air). Evaluation of the data reveals a molar ratio of metal : linker :  $\text{H}_2\text{O}$  of 1 : 2.3 : 9.0 (Tab. S3). The weight gain before the collapse of the framework indicates a reaction for example between the  $\text{Ni}^{2+}$  ions with oxygen, since it was not observed in the TG measurement under  $\text{N}_2$  atmosphere.

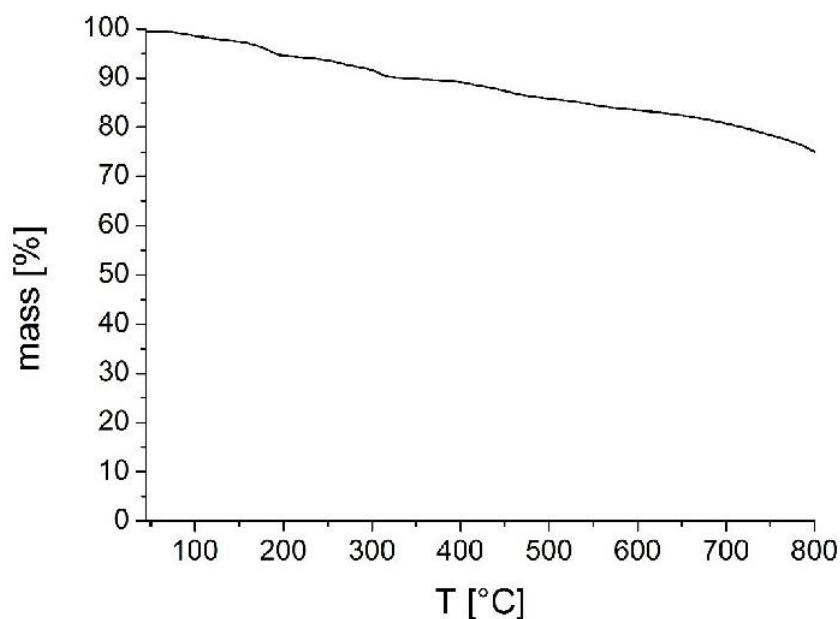


**Figure S17.** Thermogravimetric curve of Ni-CAU-29 (under N<sub>2</sub>). Measurement under N<sub>2</sub> could only be carried out up to a temperature of 800 °C. The whole curve is shifted to higher temperatures compared to the measurement under air, though the observed weight gain before the collapse of the framework is not observed anymore.

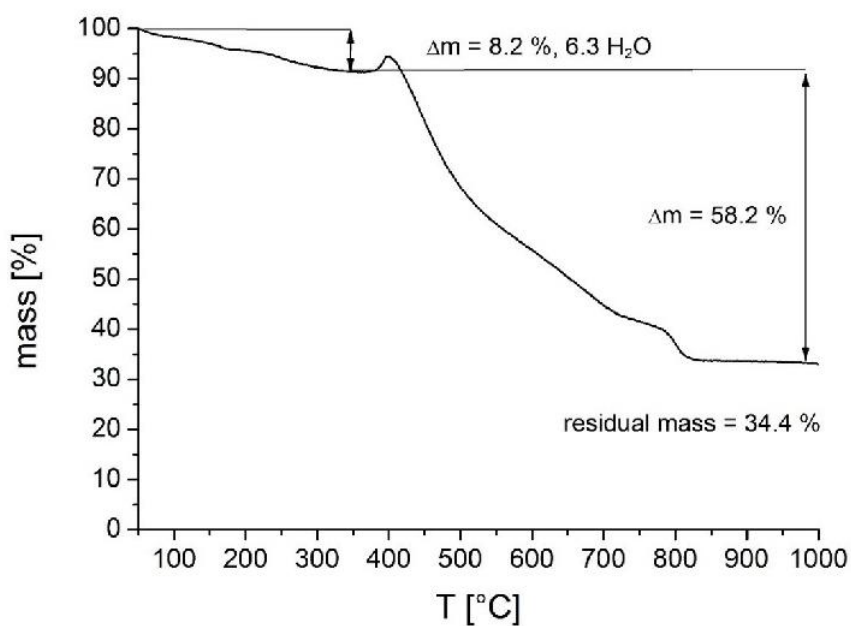


**Figure S18.** Thermogravimetric curve of Cd-CAU-29 (under air). Evaluation of the data reveals a molar ratio of metal : linker : H<sub>2</sub>O of 1.9 : 1 : 6.3 (Tab. S3). The weight gain before the collapse of the framework indicates a reaction for example between the Ni<sup>2+</sup> ions with oxygen, since it was not observed in the TG measurement under N<sub>2</sub> atmosphere.



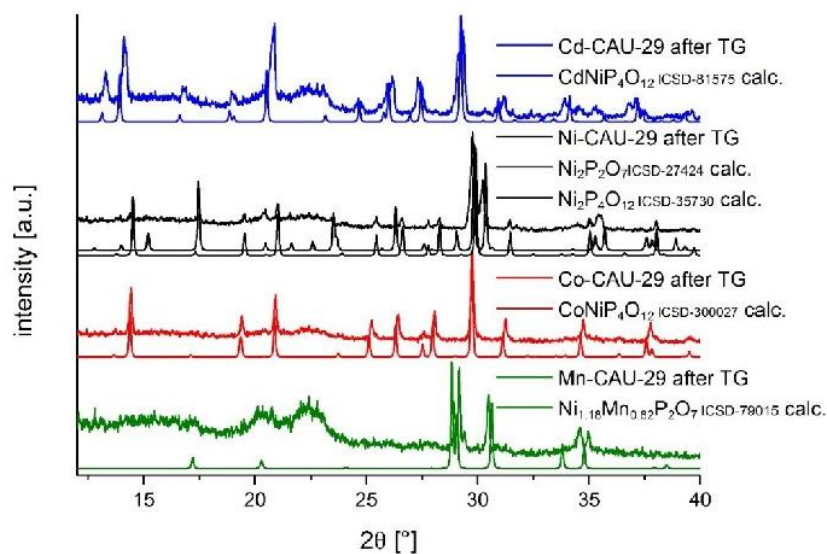


**Figure S19.** PXRD pattern of M-Ni-phosphates (M=Mn, Co, Ni, Cd) (ICSD-79015, 3000027, 27424, 35730, 81575) compared with the remaining products of the thermogravimetric experiments of M-CAU-29 (M= Mn, Co, Ni, Cd).

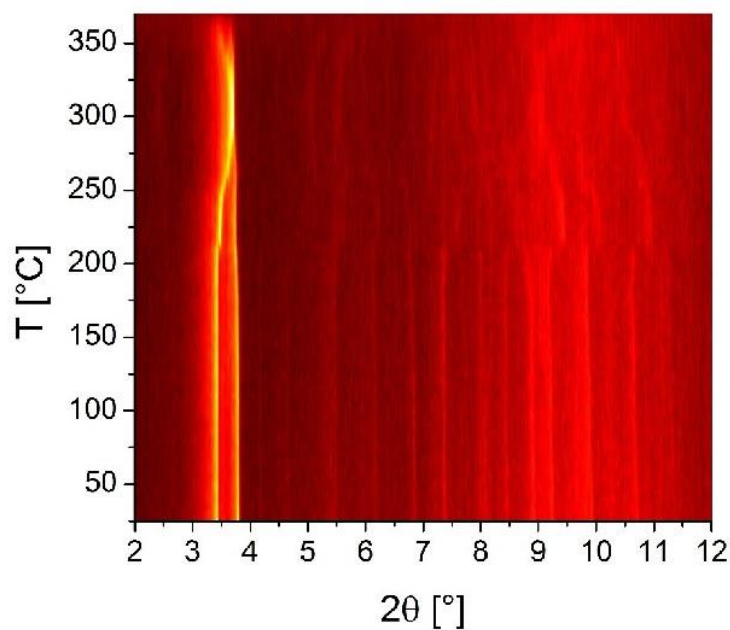


**Figure 20.** Results of the VT-PXRD studies of Mn-CAU-29 measured in open quartz capillaries (0.5 mm) under atmospheric conditions.



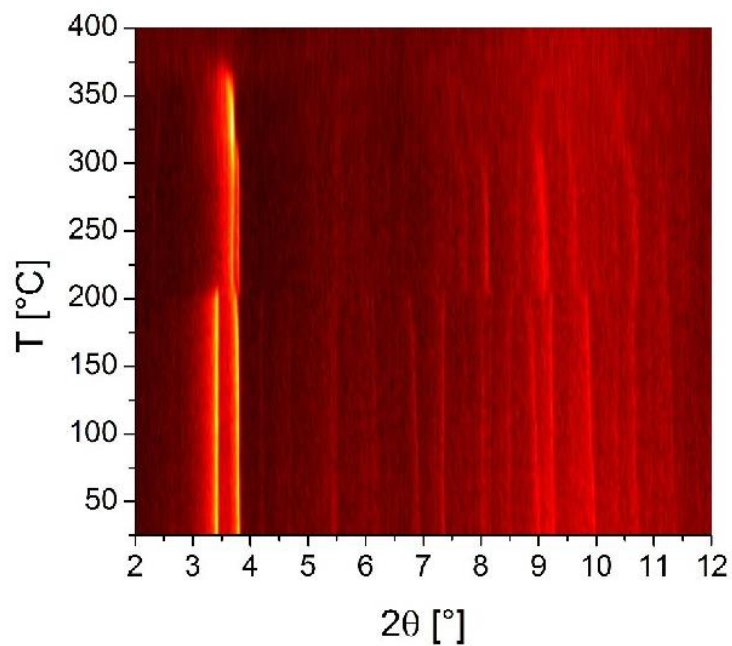


**Figure 21.** Results of the VT-PXRD studies of Co-CAU-29 measured in open quartz capillaries (0.5 mm) under atmospheric conditions.

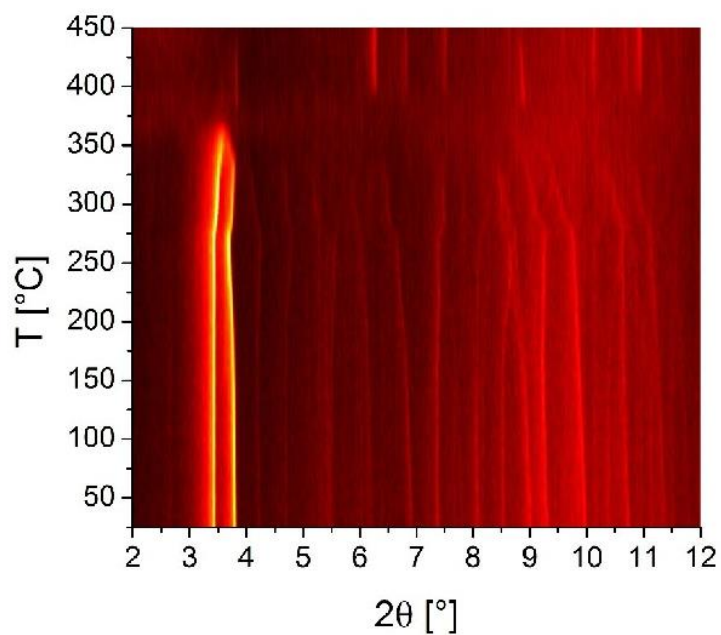


**Figure 22.** Results of the VT-PXRD studies of Ni-CAU-29 measured in open quartz capillaries (0.5 mm) under atmospheric conditions.

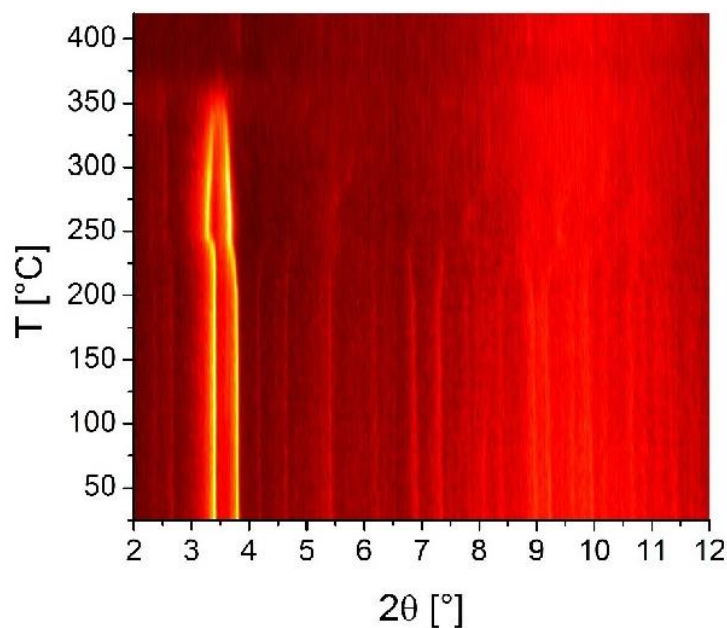


**Figure 23.** Results of the VT-PXRD studies of Cd-CAU-29 measured in open quartz capillaries (0.5 mm) under atmospheric conditions.

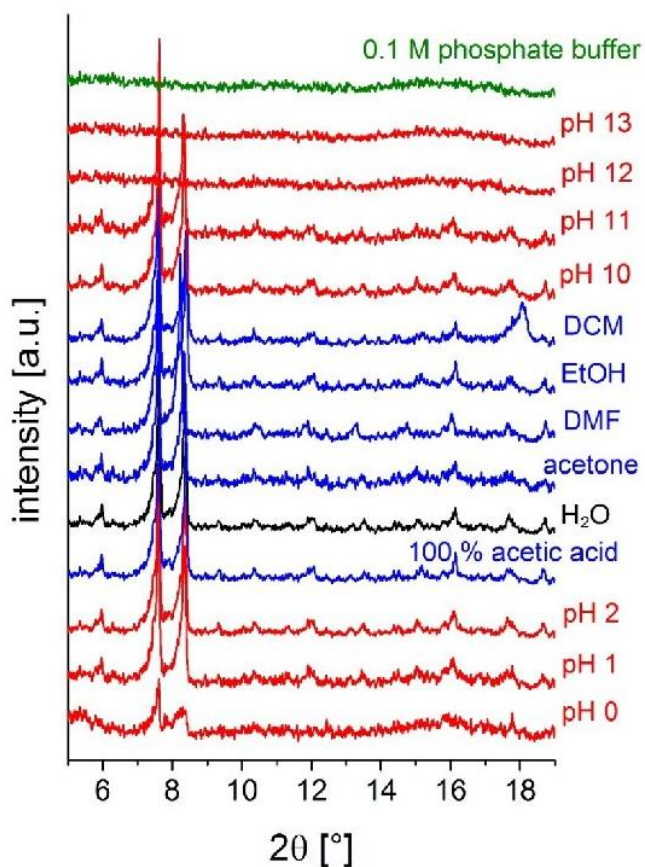


**Figure S24.** Chemical stability of Ni-CAU-29 in different solvents (24 h, stirring at room temperature).

## 6. Proton conductivity

The proton conductivity of Ni-CAU-29 was determined by electrochemical impedance spectroscopy (EIS). Powder samples were compressed between two porous stainless steel electrodes by a torque of 40 cN·m to purchase pellets of 82 mm in diameter and approx. 0.53 mm thickness. GDL 25 BC (SGL) graphite felt ensures the connection of the pellet and the electrode surface. The Teflon sample holder was placed in a previously described custom-made measuring cell which was connected to a ZahnerZennium electrochemical workstation.<sup>12</sup> In the EIS measurements an alternating voltage of 10 mV was employed in the frequency range from 1 Hz to 1 MHz. The relative humidity was adjusted by means of the temperature difference between sample chamber and water reservoir.

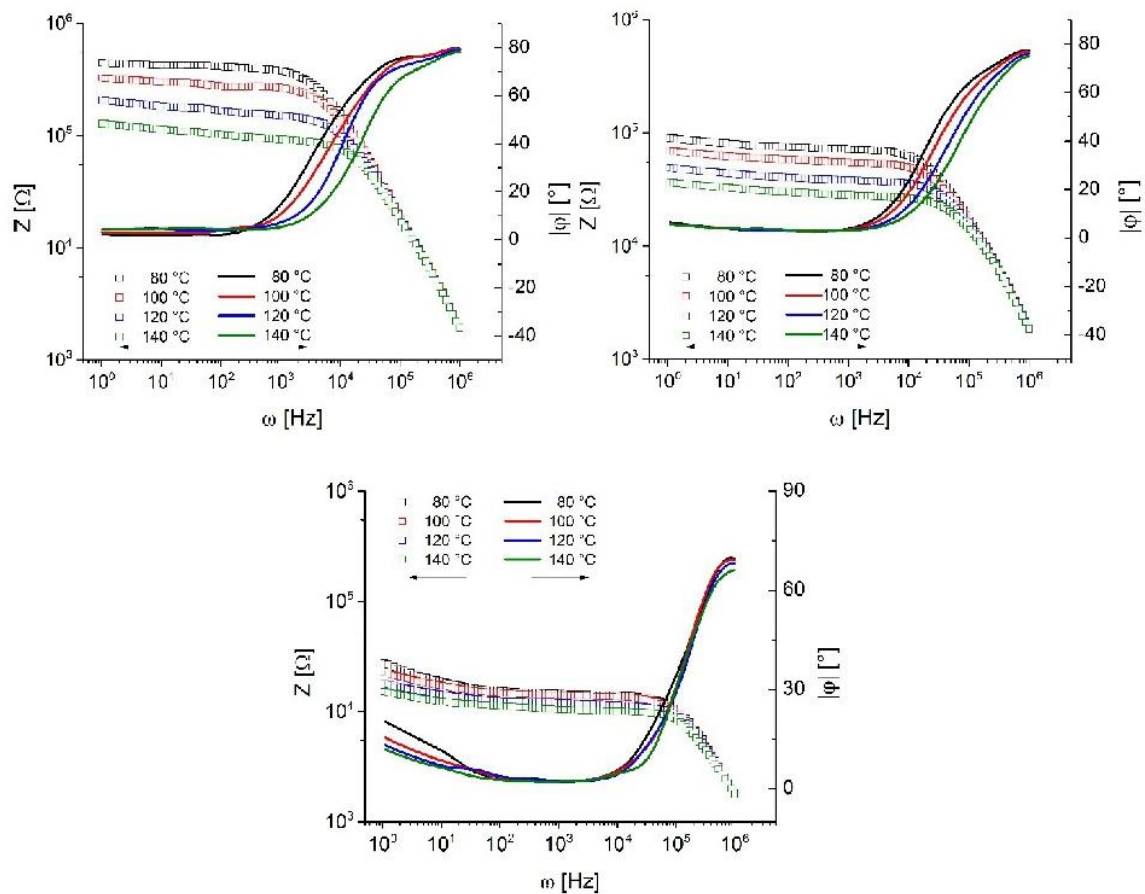


**Figure S25a.** Bode plots, top left: 50 % relative humidity, top right: 75 % relative humidity, bottom: 90 % relative humidity. Square symbols: ionic resistance, triangle symbols: phase shift.

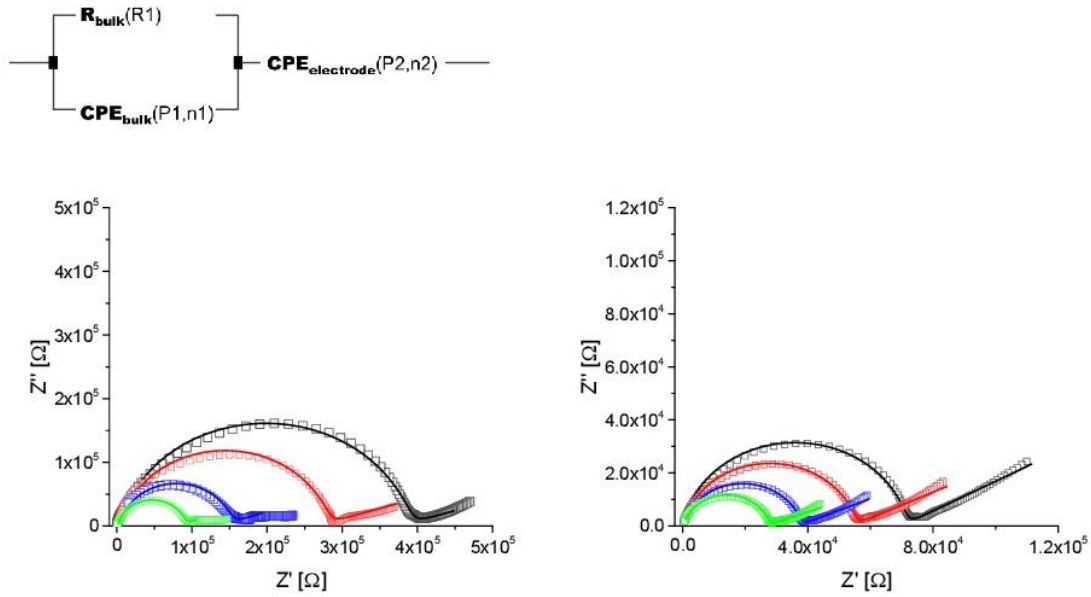


**Figure S25b.** Nyquist plots and equivalent circuit, top: equivalent circuit; bottom left: 50 % relative humidity, bottom right: 75 % relative humidity. *Black:* 80 °C, *red:* 100 °C, *blue:* 120 °C, *green:* 140 °C; *square symbols:* measured data, *straight line:* fits for the depicted equivalent circuit. The fits were computed with the program EIS Analyser 1.0.<sup>13</sup>

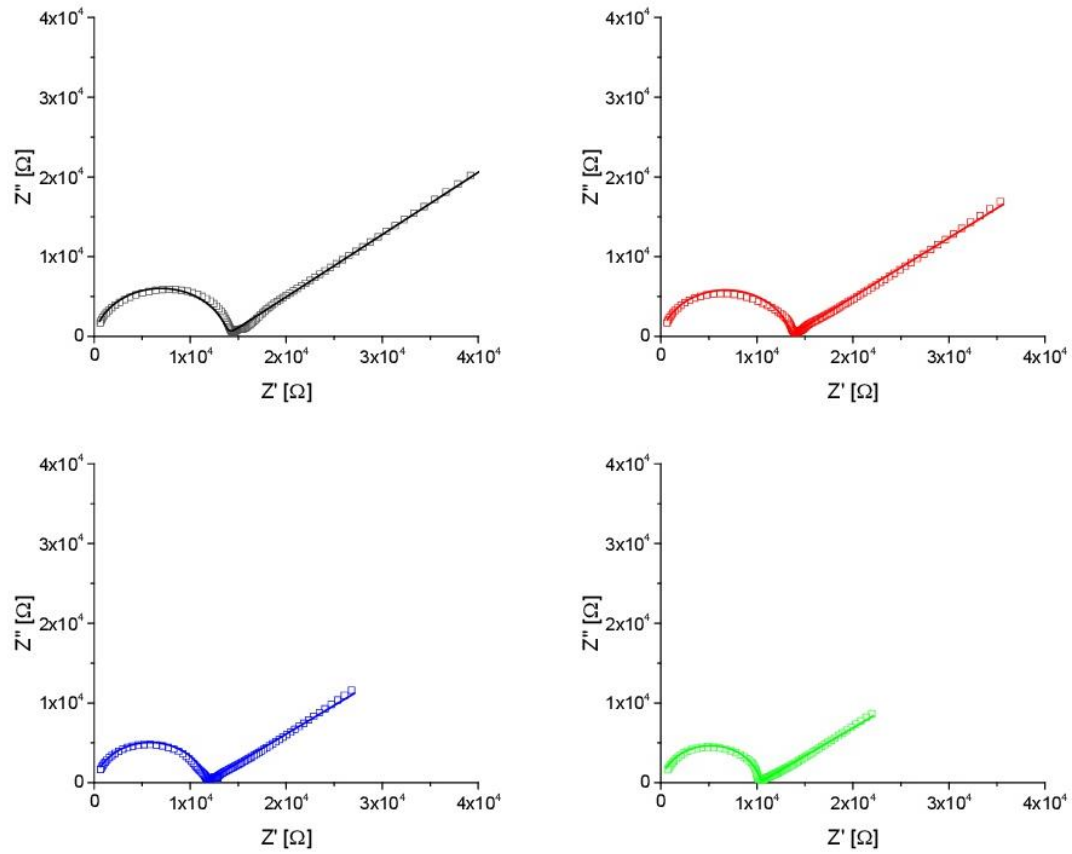


**Figure S25c.** Representative Nyquist plots for measurements at 90 %RH; *square symbols*: measured data, *straight lines*: fitted data. Clockwise: 80 °C, 100 °C, 120 °C, 140 °C.

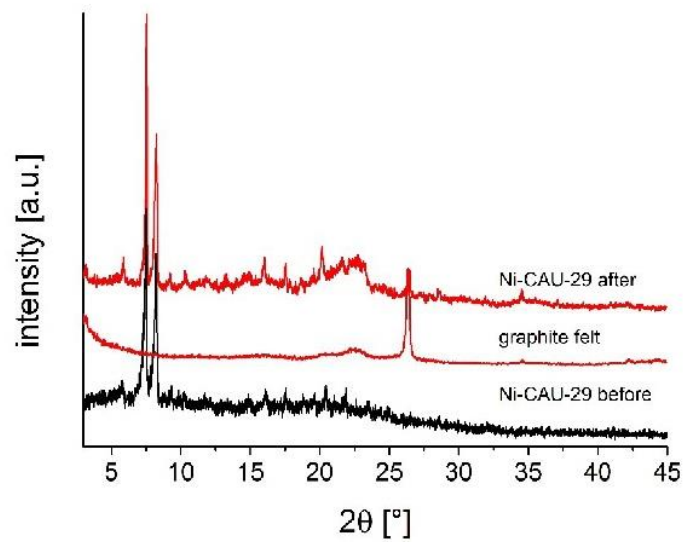


**Figure S26.** Comparison of the PXRD pattern of Ni-CAU-29 before and after the EIS measurements. Furthermore the PXRD pattern of the graphite felt in which the sample was embedded for the measurement is shown.

**Table S4.** Fit parameter.

relative humidity [% RH]	temperature [°C]	Parameters	Values of the Parameters	Errors [%]
50	80	R1	3.76E+05	0.16777
		P1	2.96E-10	0.84572
		n1	0.89067	0.10521
		P2	1.31E-05	2.4697
		n2	0.202	6.1721
	100	R1	2.67E+05	0.8445
		P1	2.62E-10	2.0489
		n1	0.90695	0.21599
		P2	1.14E-05	1.6027
		n2	0.20381	1.7565
	120	R1	1.39E+05	0.55092
		P1	1.99E-10	5.6562
		n1	0.94104	0.52788
		P2	8.29E-06	5.9269
		n2	0.22955	4.8118
	140	R1	84191	0.41542
		P1	1.87E-10	2.797
		n1	0.94889	0.24101
		P2	8.67E-06	3.5874
		n2	0.27614	1.7075



Anhang

Relative humidity [%RH]	temperature [°C]	Parameters	Values of the Parameters	Errors [%]
75	80	R1	70073	1.7805
		P1	2.46E-10	2.6283
		n1	0.92295	0.18929
		P2	2.45E-05	2.886
		n2	0.32653	2.6006
	100	R1	53828	0.28282
		P1	2.99E-10	1.4666
		n1	0.90685	0.13069
		P2	3.36E-05	1.1611
		n2	0.28825	1.5418
	120	R1	36602	0.30357
		P1	3.25E-10	1.6097
		n1	0.90064	0.13954
		P2	4.54E-05	1.1269
		n2	0.26445	1.5289
	140	R1	26467	0.4174
		P1	3.07E-10	2.2488
		n1	0.90746	0.18776
		P2	5.86E-05	1.4152
		n2	0.23732	1.9669
90	80	R1	13661	3.0103
		P1	3.14E-10	1.2919
		n1	0.91296	0.10124
		P2	2.93E-05	1.1463
		n2	0.42224	1.5035
	100	R1	13359	0.19722
		P1	3.09E-10	3.377
		n1	0.90613	0.28191
		P2	4.35E-05	0.83672
		n2	0.40667	0.44136
	120	R1	11512	1.2678
		P1	2.88E-10	4.8049
		n1	0.91297	0.36949
		P2	6.26E-05	1.2923
		n2	0.39673	0.69649
	140	R1	10246	0.33638
		P1	2.31E-10	3.4176
		n1	0.93387	0.24437
		P2	8.25E-05	1.3766
		n2	0.39097	0.87166



**Figure S26.** Comparison of the PXRD pattern of Ni-CAU-29 before and after the EIS measurements. Furthermore the PXRD pattern of the graphite felt in which the sample was embedded for the measurement is shown.

## 7. IR and UV/vis spectroscopy

IR spectra of M-CAU-29 (M= Mn, Co, Ni, Cd) and the Ni-H<sub>8</sub>TPPP linker are shown in Figures S27. The assignment of the bands are given in Table S4.

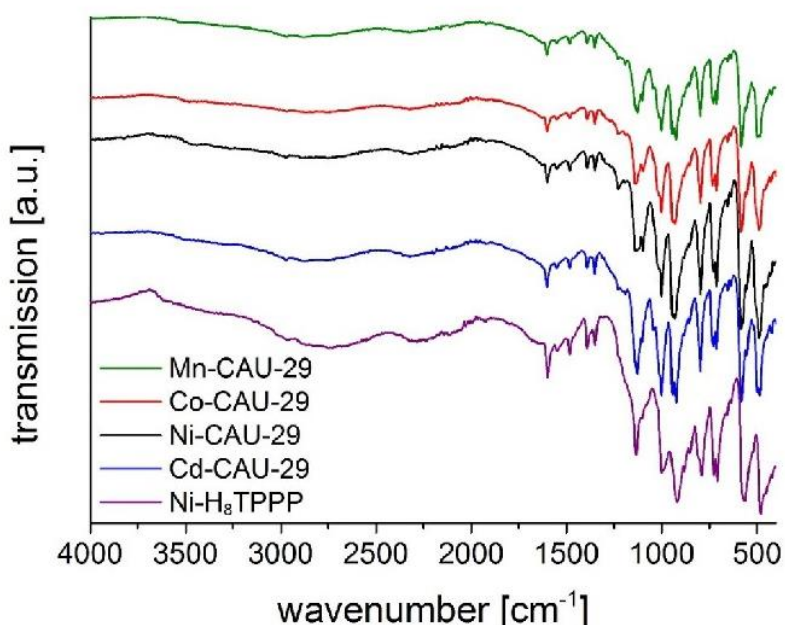


**Figure S27.** IR-spectra of M-CAU-29 (M= Mn, Co, Ni, Cd). For comparison the IR-spectrum of the linker Ni-H<sub>8</sub>TPPP (purple) is also presented.

**Table S5.** Assignment of the vibrations in the IR-spectra of M-CAU-29 (M= Mn, Co, Ni, Cd) and the free linker Ni-H<sub>8</sub>TPPP.<sup>14, 15</sup>

Vibration $\tilde{\nu}_{\text{IR}}$ [cm <sup>-1</sup> ]	Mn	Co	Ni	Cd	Ni-H <sub>8</sub> TPPP
$\nu$ CH (phenyl, pyrrole)	2970	2970	2970	2970	2970
$\nu$ P-OH	1606	1606	1606	1606	1606
$\nu$ C=C (arom.)	1549	1549	1549	1549	1519
$\nu$ P-C (phenyl)	1480	1480	1480	1480	1480
$\delta$ C=C, N=C (in plane)	1389	1389	1389	1389	1389
$\nu$ C-N (pyrrole)	1352	1352	1352	1352	1352
$\nu$ P=O (stretching)	1223	1223	1223	1223	1223
$\nu$ P-O (stretching)	1136	1136	1136	1136	1136
$\delta$ C-H, N-H (pyrrole)	1100	1100	1100	1100	1100
$\delta$ C-H (in plane)	1005	1005	1005	1005	1005
$\nu$ P=O (stretching)	944	944	944	944	921
$\gamma$ C-H (1,4-subst.)	793	793	793	793	793
$\delta$ C-H, N-H (pyrrole)	730	730	730	730	730
$\gamma$ P-C	704	704	704	704	704
$\delta$ P(OR) <sub>3</sub>	578	578	578	578	567
$\delta$ C=C (skeleton)	499	499	499	499	484

UV/vis spectra were recorded to prove the metalation of the porphyrin after the synthesis of the MOF (Fig. 28). For the measurement 0.1 mg sample was dissolved in 1 mL 2 M aqueous NaOH solution and filled up with water to a total volume of 5 mL. Afterwards a 4 mL cuvette was filled with 3 mL water and 5 drops of the porphyrin containing solution was added to the cuvette and subsequently measured.

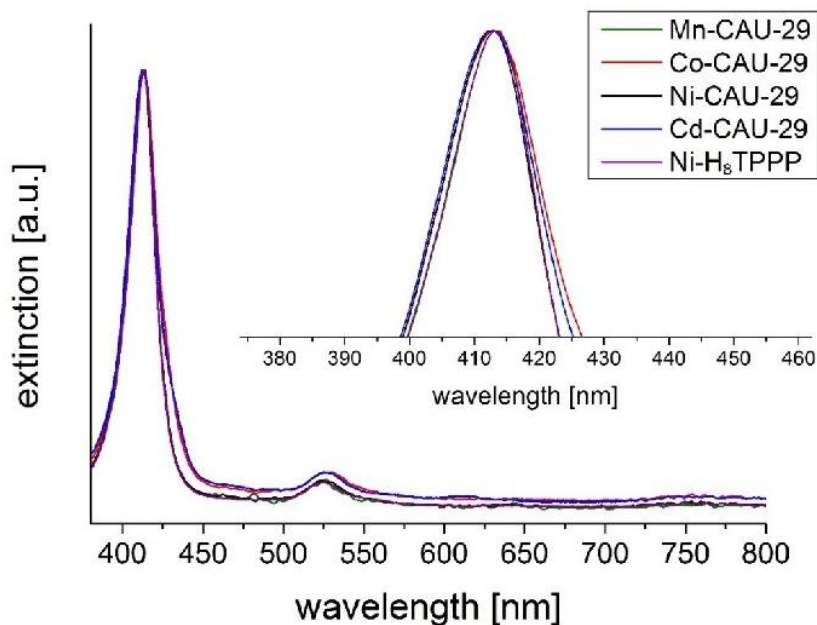


**Figure S28.** UV/vis spectra between 380 and 800 nm of M-CAU-29 (M= Mn, Co, Ni, Cd) compared with the spectrum of the free linker Ni-H<sub>8</sub>TPPP (for comparison all intensities were normalized). All spectra show the absorption maximum (Soret-band) of the Nickel complexed porphyrin at 412/ 413 nm. Furthermore the Q<sub>1</sub> band of the Ni complexed porphyrin is observed at 526/ 527 nm.

**8. References**

1. A. D. Adler, F. R. Longo, J. D. Finarelli, J. Goldmacher, J. Assour and L. Korsakoff, *The Journal of Organic Chemistry*, 1967, **32**, 476-476.
2. A. D. Adler, F. R. Longo, F. Kampas and J. Kim, *J. Inorg. Nucl. Chem.*, 1970, **32**, 2443-2445.
  3. P. Tavs, *Chem. Ber.*, 1970, **103**, 2428-2436.
4. Bruker, *SAINT V9.32B*, Bruker AXS Inc., Madison, Wisconsin, USA, 2012.
  5. G. Sheldrick, *Acta Crystallogr. Sect. A*, 2015, **71**, 3-8.
  6. G. Sheldrick, *Acta Crystallographica Section C*, 2015, **71**, 3-8.
  7. A. Coelho, *Journal*, 2007, DOI: citeulike-article-id:12635011.
  8. K. Brandenburg, *Diamond Version 3*, Crystal Impact GbR, Bonn, 2012.
  9. *Materials Studio Version 5.0*, Accelrys Inc., San Diego, CA, 2009.
10. G. G. Rajeshwaran, M. Nandakumar, R. Sureshbabu and A. K. Mohanakrishnan, *Org. Lett.*, 2011, **13**, 1270-1273.
11. R. A. Coxall, S. G. Harris, D. K. Henderson, S. Parsons, P. A. Tasker and R. E. P. Winpenny, *J. Chem. Soc., Dalton Trans.*, 2000, DOI: 10.1039/B001404O, 2349-2356.
12. M. Feyand, C. F. Seidler, C. Deiter, A. Rothkirch, A. Lieb, M. Wark and N. Stock, *Dalton Trans.*, 2013, **42**, 8761-8770.
13. A. L. Pomerantsev, *Progress in Chemometrics Research*, Nova Science Publishers, 2005.
14. G. Socrates, *Infrared and Raman Characteristic Group Frequencies: Tables and Charts*, Wiley, 2004.
15. M. Hesse, H. Meier and B. Zeeh, *Spektroskopische Methoden in der organischen Chemie*, Thieme, 2005.

**11 SI zu „A porous cobalt tetrakisphosphonates metal-organic framework: structure determination by fast continuous rotation electron diffraction”**  
Supporting Information

**A porous cobalt tetrakisphosphonate metal-organic framework:  
structure determination by fast continuous rotation electron  
diffraction**

Bin Wang,<sup>a†</sup> Timo Rhauderwiek,<sup>b†</sup> A. Ken Inge,<sup>a</sup> Hongyi Xu,<sup>a</sup> Taimin Yang,<sup>a</sup> Zhehao Huang,<sup>a</sup>  
Norbert Stock<sup>b</sup> and Xiaodong Zou<sup>\*a</sup>

<sup>a</sup>Berzelii Center EXSELENT on Porous Materials, Department of Materials and Environmental Chemistry, Stockholm University, SE-106 91 Stockholm, Sweden.

<sup>b</sup> Institute of Inorganic Chemistry, Christian-Albrechts-Universität, Max-Eyth Straße 2, D-24118 Kiel, Germany.

<b>1. Materials and Characterization.....</b>	<b>2</b>
<b>2. Synthesis of Ni-H<sub>8</sub>TPPP and Co-CAU-36.....</b>	<b>3</b>
<b>3. Crystal structure analysis.....</b>	<b>8</b>
<b>4. N<sub>2</sub> sorption properties.....</b>	<b>13</b>
<b>5. TGA and chemical stability tests.....</b>	<b>13</b>
<b>6. FT_IR and UV/vis spectroscopy.....</b>	<b>16</b>
<b>7. References.....</b>	<b>18</b>



## S1. Materials and Characterization

### Materials

CoCl<sub>2</sub> · 6 H<sub>2</sub>O (98 %, Fluka), acetone (99 %, Walther), HCl (2 M, VWR chemicals) and DABCO (1,4-Diazabicyclo[2.2.2]octane, 99 %, Sigma-Aldrich) were used without further purification. The linker Ni-4,4',4'',4'''-(5,10,15,20-porphyrinetetrayl)-tetraphosphonobenzoic acid Ni-(4-tetraphosphonophenylporphyrin, Ni-H<sub>8</sub>TPPP) was synthesized according to reported procedures<sup>1-3</sup> starting with 4-bromobenzaldehyd (99 %, Sigma Aldrich) and pyrrole (98 %, ABCR) in propionic acid (99 %, Grüssing) with following NiCl<sub>2</sub>-catalyzed (97 %, Merck) phosphorylation in 1,3-diisopropylbenzene (96 %, Sigma-Aldrich) using triethyl phosphite (98 %, Sigma-Aldrich) with following hydrolysis in conc. HCl (35 %, VWR chemicals).

### Characterization

High-resolution PXRD patterns were measured on a STOE Stadi-P combi powder diffractometer equipped with a Mythen detector (Cu K $\alpha$ <sub>1</sub> radiation). The Pawley-fit (Fig. 3a) was carried out for Co-CAU-36 to confirm the phase purity. The Pawley fit was performed with the program TOPAS academic V4.1.<sup>4</sup> The results of the refinement and crystallographic data of Co-CAU-36 are given in Table S1. The diameters of all pores were determined using DIAMOND V.3<sup>5</sup> taking the van-der-Waals radii of the atoms into account. The VT-PXRD measurement was recorded on a STOE Stadi-P combi powder diffractometer (Cu K $\alpha$ <sub>1</sub> radiation) equipped with a capillary furnace. For the measurement 0.5 mm quartz capillary was used. The sample was heated up in steps of 5 °C between 25 and 600 °C and measured for 10 minutes each.

IR-spectra were recorded using a Bruker ALPHA-FT-IR A220/D-01 spectrometer equipped with an ATR-unit. UV/vis spectra were recorded at a Spectroquant Pharo 300 M. Prior to the measurements all samples were dissolved in 2M NaOH and measured at once. The <sup>1</sup>H- and <sup>31</sup>P- NMR spectra of the Ni-H<sub>8</sub>TPPP linker were recorded on a Bruker DRX 500 spectrometer. Sorption experiments were performed with a BEL Japan Inc. BELSORP-max. Before the sorption measurement the sample was activated at 170 °C under reduced pressure (10<sup>-2</sup> kPa) for 16 h. The thermogravimetric measurement was performed on a NETZSCH STA 409 CD analyzer under a flow of air (75 ml min<sup>-1</sup>) with a heating rate of 4 °C min<sup>-1</sup> between 25 and 1000 °C in Al<sub>2</sub>O<sub>3</sub>-crucibles. The data was corrected for buoyancy and current effects.

Electron diffraction data was collected on a JEOL JEM-2100 LaB<sub>6</sub> transmission electron microscope. SEM images were taken on a JEOL JSM-7401F scanning electron microscope.

## S2. Synthesis of Ni-H<sub>8</sub>TPPP and Co-CAU-36

### Synthesis and <sup>1</sup>H-NMR spectroscopy of Ni-H<sub>8</sub>TPPP

The three step synthesis route of Ni-H<sub>8</sub>TCP (Fig. S1) was carried out employing the Adler method.<sup>1, 2</sup> The first step was the synthesis of 4-bromophenylporphyrin (H<sub>2</sub>TBrPP). In the second step, the phosphorylation of H<sub>2</sub>TBrPP was achieved by using a Ni-catalyzed variation of the Arbuzov reaction,<sup>3, 6</sup> with the following third step, the hydrolysis of the -PO(OEt)<sub>2</sub> groups in conc. HCl.

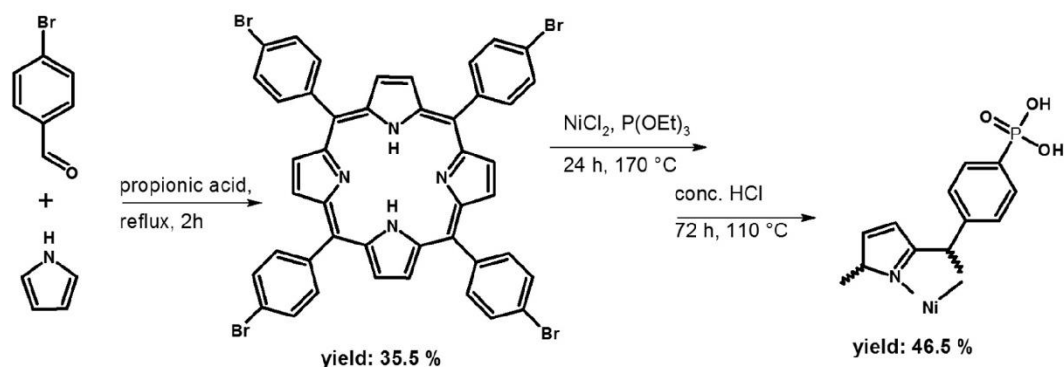


**Figure S1.** Schematic representation of the synthesis route of Ni-H<sub>8</sub>TPPP.

**H<sub>2</sub>TBrPP:** Pyrrole (7.47 mL, 108 mmol) and 4-bromobenzaldehyde (20.0 g, 108 mmol) in 400 mL propionic acid were heated under reflux for 2 h. Afterwards the reaction mixture was cooled down to room temperature and poured into 500 mL of MeOH and stirred for 30 min in an ice bath. The resulting precipitate was filtered off and washed several times with MeOH until the filtrate was clear. Subsequently, the product was washed with 100 mL warm distilled water and dried at 70 °C in a drying oven overnight. A blue powder of H<sub>2</sub>TBrPP (7.63 g, 8.2 mmol, 30.4 % yield) was obtained.

Elemental analysis of H<sub>2</sub>TBrPP (Br<sub>4</sub>C<sub>44</sub>H<sub>26</sub>N<sub>4</sub>): calc (%): C 56.8, H 2.6, N 6.0, found (%): C 59.7, H 3.2, N 6.2. The small differences between the calculated and observed values are due to impurities caused by propionic acid used in the synthesis. Propionic acid was also observed in the <sup>1</sup>H-NMR measurements, but not in the <sup>1</sup>H-NMR spectra of the products in the following synthesis steps. The low intensity peaks between 8.5 and 8.0 ppm are due to interactions of the H<sub>2</sub>TBrPP with propionic acid, indicated by the different chemical shift. This has no influence on the purity of the products in the following synthesis steps.

**<sup>1</sup>H-NMR (Fig. S2), H<sub>2</sub>TBrPP (500 MHz CDCl<sub>3</sub>):** δ = 8.76 (s, 8H, H-1); 7.99 (d, 8H, H-2); 7.82 (d, 8H, H-3); 7.18 (s, 1H, CDCl<sub>3</sub>); 2.30 (q, 2H, propionic acid); 1.08 (t, 3H, propionic acid) ppm. Additional peaks between 7 and 9 ppm are due to low impurities with higher condensed porphyrins.

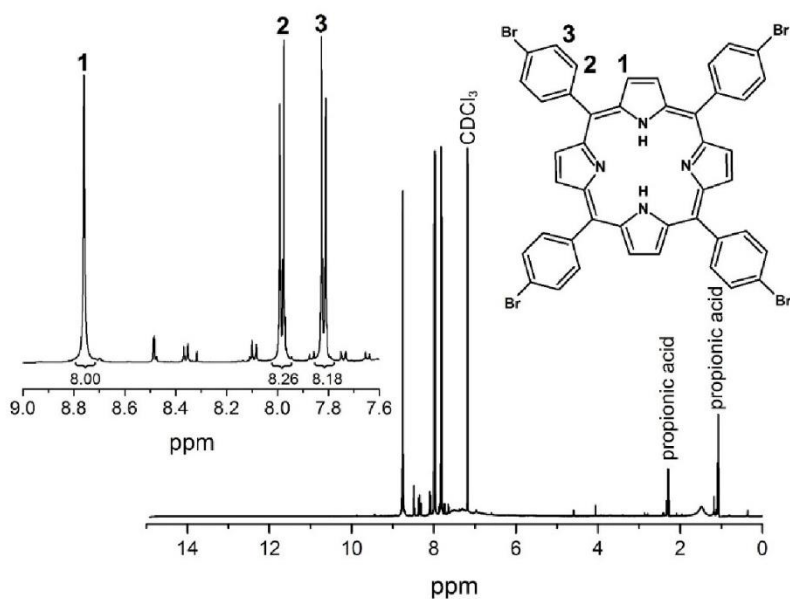


**Figure S2.**  $^1\text{H-NMR}$  spectrum of  $\text{H}_2\text{TBrPP}$  digested in  $\text{DMSO}$ .

**Ni- $\text{H}_8\text{TPPP}$ :**  $\text{H}_2\text{TBrPP}$  (3.42 g, 3.7 mmol) and anhydrous  $\text{NiCl}_2$  (1.79 g, 13.8 mmol) in 70 mL 1,3-diisopropylbenzene (prior the reaction for 30 min with  $\text{N}_2$  degassed) were heated up to exactly  $170^\circ\text{C}$  under  $\text{N}_2$  atmosphere. Afterwards triethylphosphite (7.05 mL, 43.7 mmol) was added slowly (30 min) and dropwise to the reaction mixture, which was heated further for 24 h at  $170^\circ\text{C}$ . The reaction mixture was cooled down to room temperature and the resulting precipitate was filtered off and washed with 250 mL  $\text{DCM}$ . The resulting organic phase was washed 2 times each with 100 mL  $\text{H}_2\text{O}$ . The organic solvents were evaporated under reduced pressure and the resulting precipitate was hydrolyzed with 80 mL conc.  $\text{HCl}$  at  $110^\circ\text{C}$  for 72 h. The resulting product was filtered off, washed with 100 mL cooled water and afterwards stirred in 100 mL  $\text{DCM}$  for 24 h. The resulting clean product was filtered off and dried at  $70^\circ\text{C}$  in a drying oven overnight. A red powder of  $\text{Ni-H}_8\text{TPPP}$  (2.74 g, 2.76 mmol, 75 % yield) was obtained.

Elemental analysis of  $\text{Ni-H}_8\text{TPPP}$  ( $\text{C}_{44}\text{H}_{32}\text{N}_4\text{NiO}_{12}$ ) $\cdot 4\text{H}_2\text{O}$ : calc (%): C 49.8, H 3.6, N 5.3, found (%): C 49.1, H 3.6, N 5.1.

**<sup>1</sup>H-NMR (Fig. S3), Ni-H<sub>8</sub>TPPP (500 MHz DMSO-d<sub>6</sub>):**  $\delta$ = 8.74 (s, 8H, H-1); 8.11 (dd, 8H, H-2); 8.06 (dd, 8H, H-3); 2.50 (s, 6H, DMSO-d<sub>6</sub>); 2.09 (s, 6H, acetone) ppm.

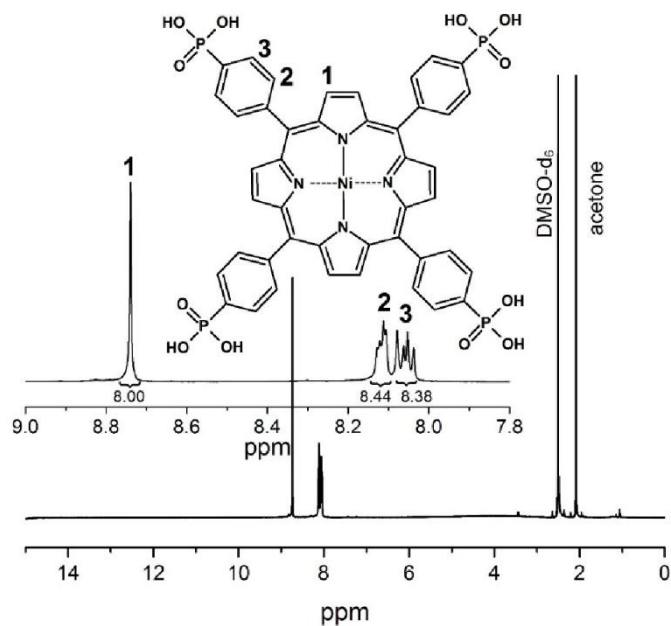


**Figure S3.** <sup>1</sup>H-NMR spectrum of Ni-H<sub>8</sub>TPPP digested in DMSO.

**<sup>31</sup>P-NMR (Fig. S4), Ni-H<sub>8</sub>TPPP (500 MHz DMSO-d<sub>6</sub>):**  $\delta$ = 12.04 (s, 4P, -PO(OH)<sub>2</sub>) ppm.

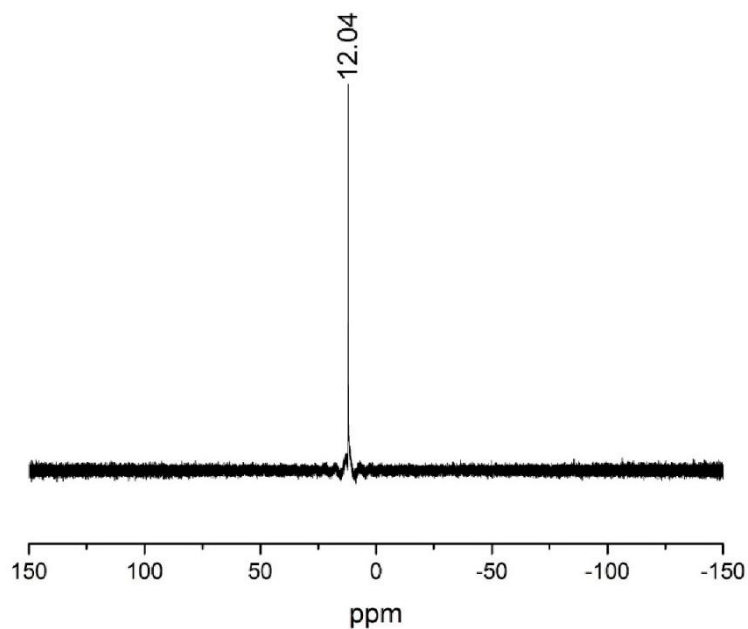


**Figure S4.** <sup>31</sup>P-NMR spectrum of Ni-H<sub>8</sub>TPPP digested in DMSO.

### Synthesis of Co-CAU-36 and high-throughput investigations

The synthesis of Co-CAU-36 was investigated using high-throughput methods ( $V_{\max}$  = 2.0 mL per Teflon insert) with H<sub>2</sub>O as a solvent. Using 160 °C as the reaction temperature, different reaction times between 6 and 48 h and different molar ratios of metal to linker to DABCO to 2M aqueous HCl solution in a range between 1 : 1 : 0 : 1 and 5 : 1 : 100 : 12 were employed. Different additives such as NaOH, HCl, DABCO, 4,4-bipyridine and organic acids (formic and acetic acid) were investigated, but only the use of DABCO in combination with 2 M aqueous HCl solution resulted in highly crystalline Co-CAU-36. Furthermore an upscaling of the synthesis of Co-CAU-36 in 30 mL reactors was successful by using the 12-fold amounts of all reactants. Optimized synthesis conditions could be obtained for Co-CAU-36 as described in the following paragraph for the synthesis in 2 mL Teflon inserts.

**Optimized synthesis of Co-CAU-36:** Ni-H<sub>8</sub>TPPP (5.0 mg,  $5.3 \times 10^{-3}$  mmol), CoCl<sub>2</sub> · 6 H<sub>2</sub>O (1.3 mg,  $5.3 \times 10^{-3}$  mmol), DABCO (30 mg,  $265.5 \times 10^{-3}$  mmol), H<sub>2</sub>O (1000 µL) and 2M aqueous HCl solution (10.7 µL,  $21.2 \times 10^{-3}$  mmol) were added to a 2 mL Teflon insert and placed in the high-throughput reactor. The reactor was heated for 12 h at 160 °C and cooled down to RT in 6 h. The resulting product was filtered off and washed with H<sub>2</sub>O and acetone. A yield of 6.0 mg (75 % based on Ni-H<sub>8</sub>TPPP) was obtained for Co-CAU-36, [Co<sub>2</sub>(Ni-TPPP)]·2DABCO·15H<sub>2</sub>O. Elemental analysis of Co-CAU-36: calc (%): C 43.7, H 5.5, N 7.3, found (%): C 43.9, H 5.2, N 8.6.

To remove unreacted DABCO molecules the sample was stirred in acetone for 24 h by following activation under reduced pressure of  $10^{-2}$  kPa at 170 °C for 16 h prior the sorption experiment.

The systematic study of the system Ni-H<sub>8</sub>TPPP/ Co<sup>2+</sup>/ DABCO/ HCl using high-throughput (HT) methods resulted in a highly porous and crystalline metal phosphonate. The product formation depends mainly on the amount of DABCO and the molar linker to metal ratio. The results of the high-throughput investigation are illustrated in Figure S5.

The HT-investigation resulted in optimized synthesis conditions of Co-CAU-36, resulting in molar metal : linker : DABCO : HCl ratios of 1 : 1 : 50 : 4 to give a highly crystalline product.

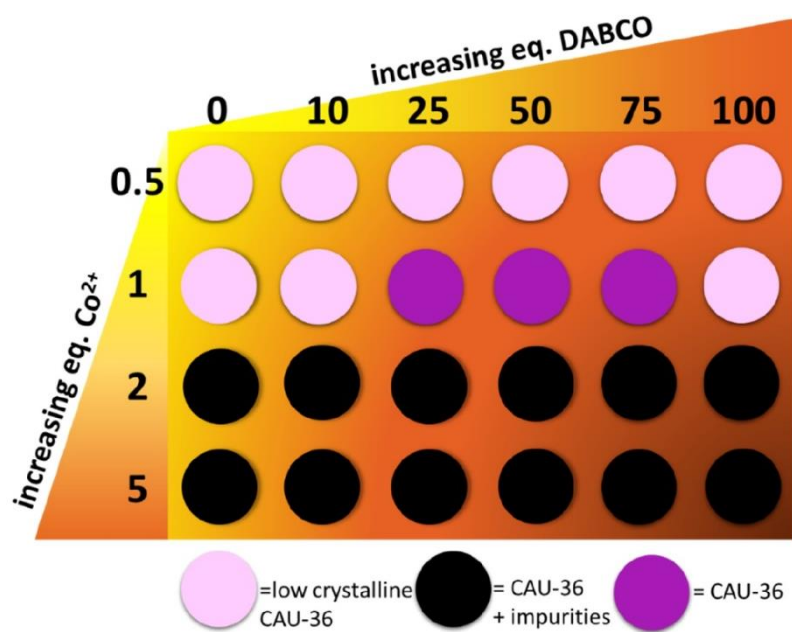


**Figure S5.** Results of the high-throughput investigation of Co-CAU-36 with the added amounts of  $\text{Co}^{2+}$  and DABCO as variables.

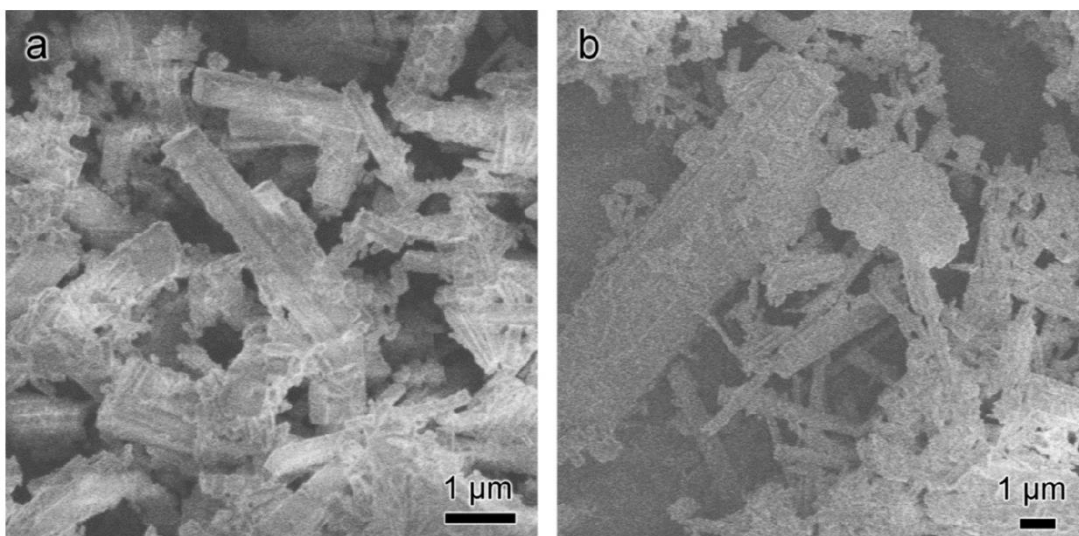


**Figure S6.** SEM images of Co-CAU-36.



### S3. Crystal structure analysis

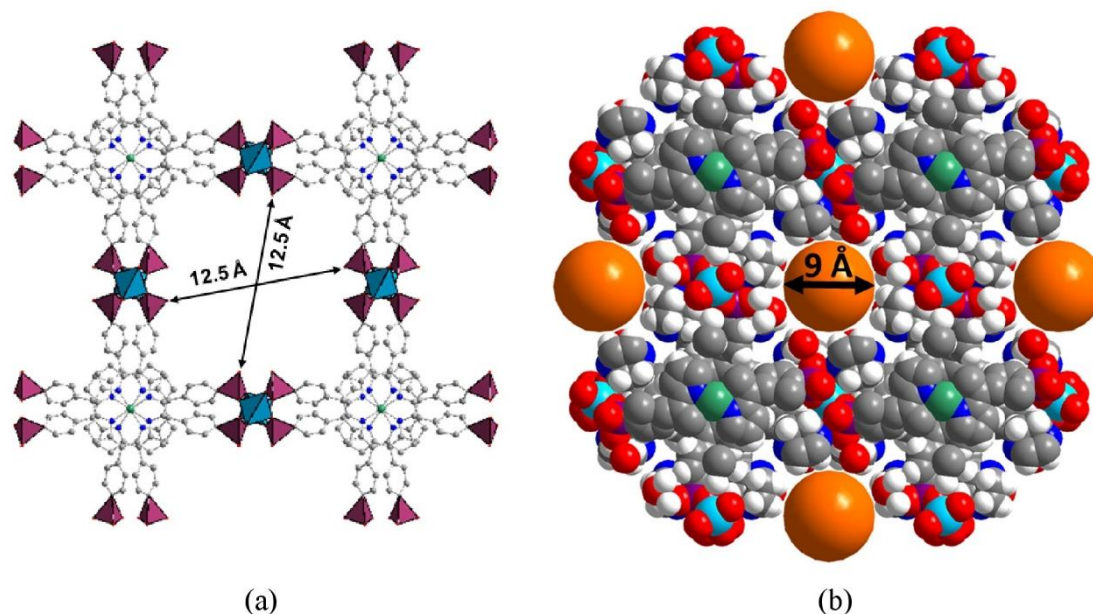
The continuous Rotation Electron Diffraction (cRED) technique was used for structure determination of Co-CAU-36. The data collection was conducted on a JEOL JEM-2100 LaB<sub>6</sub> TEM equipped a Timepix hybrid electron detector. The sample was cooled down to 96 K using a Gatan cryotransfer tomography holder in order to reduce the beam damage. Eight cRED datasets were collected from different crystals, with resolutions of 0.83 to 1.00 Å and angular tilt ranges of 71.8 to 110.6° (Table S1). Data processing was conducted using the software XDS<sup>7</sup> for the each of the eight datasets. Structure solution and refinement were conducted on each of the eight cRED datasets as well as on the merged dataset. The data statistics, refined unit cell parameters and structure refinement results are given in Table S1. The whole experimental processes, from TEM sample preparation (starting at 9 a.m.), data collection (10 a.m. to 1 p.m.), data reduction and initial structure solution (2 p.m. to 4 p.m.) to final structure refinement (4 p.m. to 6 p.m.) was finished within 8 hours.

Initial structural models were obtained by direct methods using the program SIR-2014<sup>8</sup>. Structure refinements against the cRED data were conducted by the program SHELXL<sup>9</sup> using atomic scattering factors for electrons and assuming kinematical intensities. The structure refinements were relatively straightforward, because the starting models were already close to the final ones. Only the atom types of a few atoms were wrongly assigned, which could be easily identified using chemical knowledge. Some missing atoms in the solvent molecules could be located from the difference Fourier maps during the refinements. Geometric restraints were only applied on a few atoms in the DABCO molecule, including the C-C and C-N distances and angles (DFIX, DANG). Other restraints were similar atomic displacement parameters (SIMU) for the C atoms in the linker Ni-H<sub>4</sub>TPPP<sup>4-</sup>, and isotropic approximation (ISOR) for ADPs of the O atoms on the phosphonate group.

**Table S1.** Refinement results and data quality for the eight datasets and a merged one.

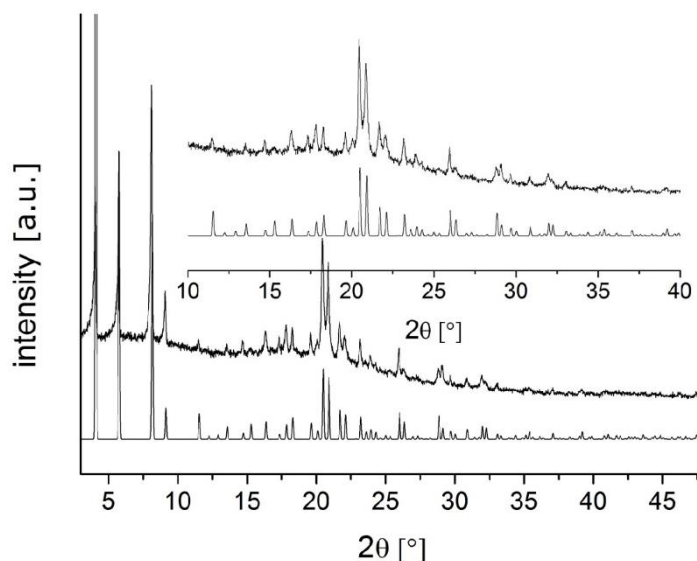
Dataset	R <sub>int</sub>	R <sub>1obs</sub>	R <sub>1all</sub>	Completeness/%	Resolution /Å	No. Refls	Average I/Sigma	Cell Dim/Å	Tilt range/°
1	0.3147	0.1891	0.2412	98.9	1.00	2247	3.39	22.126, 8.969	100.4
2	0.1642	0.1567	0.1781	90.6	0.90	2142	5.20	22.250, 8.770	75.4
3	0.2402	0.1587	0.2169	92.4	1.00	2041	3.66	21.696, 8.852	71.8
4	0.2050	0.1486	0.2010	98.9	0.90	3111	5.70	22.241, 8.924	91.6
5	0.2269	0.1356	0.2133	96.7	0.83	4008	3.70	21.980, 8.960	101.7
6	0.2542	0.1517	0.2188	79.0	0.95	1970	4.34	21.812, 8.704	92.4
7	0.2932	0.1530	0.1869	99.8	0.90	2290	3.97	22.240, 8.780	110.6
8	0.2084	0.1454	0.2052	99.1	0.90	3047	5.06	21.782, 9.012	81.5
Merged	0.2472	0.1444	0.1643	99.8	0.90	3103	9.00	21.980, 8.960	---

Figure S7 shows the pore diameters of Co-CAU-36 with and without the located solvent molecules in the pores. Without the solvent molecules, the free diameter of the pores is 12.5 Å taken into account the van-der-Waals radii of oxygen 1.35 Å (Fig. S7a). When the solvents are present, the remaining pore has a free diameter of ca. 9 Å (Fig. S7b).



**Figure S7.** The free diameter of the 1D channels in Co-CAU-36 without (a) and with (b) the solvent DABCO and H<sub>2</sub>O molecules, viewed along [001]. The van-der-Waals radii have been subtracted. Even with the presence of the solvents, the channel is still accessible and can accommodate a sphere of ca. 9 Å in diameter.

Figure S8 shows the comparison of experimental and simulated PXRD patterns. The similarity between them confirmed the structural model. The intensity differences for the low angle peaks are due to the presence of disordered solvent molecules in the pores, which were not included in the simulation. The presence of the extra solvent molecules makes it difficult for Rietveld refinement.



**Figure S8.** Comparison of experimental and simulated PXRD patterns for Co-CAU-36.

The structural model was further confirmed by comparing the atomic positions obtained from the refinements against each of the eight individual datasets, collected on several different crystals. Figure S9 shows a superposition of the eight refined structural models. The framework atoms including the metals and linker almost perfectly overlap and one can barely see any differences. There are slight differences in the atomic positions of the solvent DABCO and water molecules. The atomic positions refined from different datasets were compared with the corresponding averaged positions, and the deviations are listed in Table S2. The results show that atomic positions deviated on average by 0.031(17) Å for the framework atoms, with the max deviation of 0.083 Å (for O3, dataset 3). The average deviations are 0.098(65) Å for DABCO molecules, and 0.16(12) Å for the water molecules.

In addition, four datasets that had the lowest average deviations of the framework positions (No. 2, 4, 5, 8) were merged using the program XSCALE<sup>10</sup> to generate a merged dataset for structure solution and refinement. The data was cut to the same resolution (0.90 Å) common for all the four datasets, and the structure refinement was conducted on the merged dataset (Table S1). A comparison of refinement results from different data merging methods is presented in Table S3. It was worth mentioning that through data merging, the atomic displacement parameters became more isotropic.

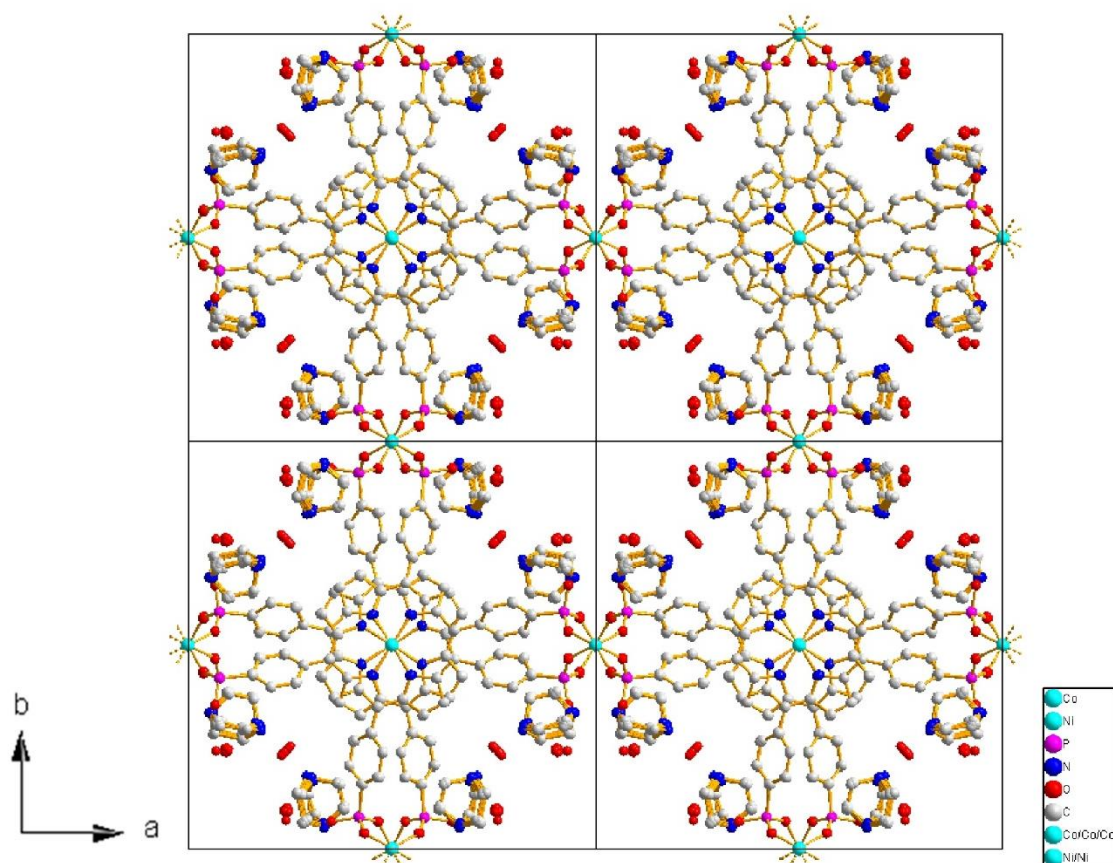


**Figure S9.** A superposition of eight refinement results. Largest uncertainty came from the positions of solvent molecules. The framework atom positions were very consistent. (See Table S3)



**Table S2** Deviations in atomic positions from individual refinements with regard to the average atomic positions (in Å). \*The atom Ni1 is at a special position (0.5 0.5 0) and has not been included in the calculation. The numbers in the parentheses are standard deviations.

<b>Atom/Dataset</b>	<b>1</b>	<b>2</b>	<b>3</b>	<b>4</b>	<b>5</b>	<b>6</b>	<b>7</b>	<b>8</b>	<b>Average</b>
<b>Framework/Å</b>									
Co1	0.035	0.005	0.016	0.022	0.006	0.011	0.008	0.001	<b>0.013</b>
Ni1*	0.000	0.000	0.000	0.000	0.000	0.000	0.000	0.000	<b>0.000</b>
P1	0.035	0.028	0.013	0.028	0.035	0.046	0.007	0.015	<b>0.027</b>
N1	0.048	0.027	0.048	0.011	0.009	0.023	0.032	0.019	<b>0.041</b>
O1	0.031	0.020	0.034	0.023	0.029	0.083	0.061	0.044	<b>0.038</b>
O2	0.023	0.036	0.031	0.055	0.037	0.042	0.033	0.044	<b>0.038</b>
O3	0.030	0.037	0.083	0.023	0.027	0.042	0.046	0.016	<b>0.036</b>
C1	0.073	0.028	0.020	0.055	0.015	0.029	0.041	0.028	<b>0.031</b>
C2	0.042	0.019	0.022	0.028	0.021	0.068	0.010	0.035	<b>0.029</b>
C3	0.050	0.024	0.043	0.020	0.030	0.012	0.021	0.031	<b>0.022</b>
C4	0.060	0.024	0.023	0.016	0.011	0.012	0.009	0.022	<b>0.031</b>
C5	0.056	0.031	0.030	0.036	0.020	0.032	0.028	0.016	<b>0.027</b>
C6	0.076	0.025	0.021	0.010	0.017	0.019	0.029	0.018	<b>0.032</b>
C7	0.078	0.010	0.014	0.027	0.030	0.042	0.027	0.028	<b>0.035</b>
C8	0.053	0.023	0.043	0.043	0.032	0.027	0.030	0.025	<b>0.042</b>
C9	0.042	0.024	0.067	0.014	0.029	0.060	0.040	0.059	<b>0.033</b>
C10	0.029	0.028	0.063	0.016	0.036	0.038	0.026	0.027	<b>0.031</b>
C11	0.029	0.036	0.063	0.029	0.017	0.037	0.026	0.012	<b>0.013</b>
<b>Average</b>	<b>0.046</b>	<b>0.025</b>	<b>0.037</b>	<b>0.027</b>	<b>0.024</b>	<b>0.037</b>	<b>0.028</b>	<b>0.026</b>	<b>0.031(17)</b>
<b>DABCO/Å</b>									
N2	0.108	0.287	0.069	0.118	0.111	0.095	0.109	0.058	<b>0.119</b>
N3	0.087	0.152	0.123	0.097	0.048	0.126	0.059	0.054	<b>0.093</b>
C12	0.179	0.051	0.075	0.130	0.078	0.110	0.035	0.064	<b>0.090</b>
C13	0.059	0.114	0.017	0.042	0.047	0.099	0.064	0.036	<b>0.060</b>
C14	0.048	0.400	0.062	0.148	0.058	0.135	0.117	0.087	<b>0.132</b>
C15	0.123	0.162	0.060	0.084	0.040	0.106	0.186	0.046	<b>0.101</b>
C16	0.259	0.139	0.050	0.038	0.074	0.027	0.153	0.044	<b>0.098</b>
C17	0.159	0.079	0.062	0.115	0.063	0.166	0.035	0.063	<b>0.093</b>
<b>Average</b>	<b>0.128</b>	<b>0.173</b>	<b>0.065</b>	<b>0.097</b>	<b>0.065</b>	<b>0.108</b>	<b>0.095</b>	<b>0.057</b>	<b>0.098(65)</b>
<b>Water/Å</b>									
O1 <sub>w</sub>	0.163	0.333	0.122	0.192	0.209	0.090	0.137	0.166	<b>0.177</b>
O2 <sub>w</sub>	0.063	0.448	0.073	0.324	0.014	0.079	0.149	0.073	<b>0.153</b>
<b>Average</b>	<b>0.113</b>	<b>0.391</b>	<b>0.098</b>	<b>0.258</b>	<b>0.112</b>	<b>0.085</b>	<b>0.143</b>	<b>0.120</b>	<b>0.165(116)</b>

**Table S3** Deviations in atomic positions (in Å) between averaged model from the four individual structures refined using datasets No. 2, 4, 5 and 8 (labeled AVG), and the refined structure against the merged dataset of the four datasets using XSCALE (labeled XMERG). \*The atom Ni1 is at a special position (0.5 0.5 0) and has not been included in the calculation. The numbers in the parentheses are standard deviations.

Atom	$\Delta(\text{AVG-XMERG})/\text{\AA}$
<b>Framework</b>	
Co1	0.016
Ni1*	0.000
P1	0.023
N1	0.011
O1	0.020
O2	0.017
O3	0.026
C1	0.036
C2	0.039
C3	0.016
C4	0.018
C5	0.019
C6	0.019
C7	0.028
C8	0.028
C9	0.022
C10	0.024
C11	0.019
<b>Average</b>	<b>0.022(7)</b>
<b>DABCO</b>	
N2	0.081
N3	0.060
C12	0.095
C13	0.083
C14	0.090
C15	0.071
C16	0.089
C17	0.059
<b>Average</b>	<b>0.078(14)</b>
<b>Water</b>	
O1 <sub>w</sub>	0.149
O2 <sub>w</sub>	0.122
<b>Average</b>	<b>0.136(19)</b>

#### S4. N<sub>2</sub> Sorption Properties.

Co-CAU-36 is porous to N<sub>2</sub> at 77 K. A specific surface area of  $a_{\text{BET}} = 700 \text{ m}^2 \text{ g}^{-1}$  ( $V_m = 0.31 \text{ cm}^3 \text{ g}^{-1}$ ) was obtained. Prior to the measurement the sample was activated at 170 °C under vacuum ( $10^{-2}$  kPa) for 16 h. Subsequently sorption experiments using N<sub>2</sub> at 77 K (Fig. 4) as the adsorbate was performed. The specific surface area was determined using the BET method recommended by IUPAC.<sup>11, 12</sup> The micropore volume  $V_m$  was determined by using the amount of adsorbed N<sub>2</sub> at the relative pressure  $p/p_0 = 0.5$ . Co-CAU-36 is stable towards activation and sorption measurements as proven by PXRD measurements (Fig. S12). The N<sub>2</sub> measurement leads to a Type-1a isotherm as expected for microporous materials with pore diameters of ca. 1 nm.<sup>12</sup>

#### S5. Thermal and Chemical stability

To investigate the thermal stability of Co-CAU-36 thermogravimetric analysis measurements (TGA) and variable temperature PXRD studies (VT-PXRD) were carried out.

The TGA curve (Fig. S10) show four characteristic steps of weight losses. The loss up to 120 °C (11.6 %) is assigned to the evaporation of 12 physisorbed water molecules. The weight loss between 200 and 360 °C (meas.: 13.3 %, calc.: 13.5 %) is assigned to two DABCO and the two crystal water molecules. From 360 °C a two-step decomposition of the compound took place corresponding to the decomposition of the linker and the loss of its organic part (meas.: 42.2 %, calc.: 44.9 %). The final products were identified by PXRD (Fig. S12) to be Co<sub>2</sub>P<sub>2</sub>O<sub>7</sub> and Ni<sub>2</sub>P<sub>4</sub>O<sub>12</sub> (meas.: 31.6 %, calc.: 28.5 %). The TGA result agrees well with the elemental analyses, and confirms the phase purity of the sample. The difference in the amount of occluded water molecules are due to the different water contents in the sample, which can vary depending on the sample environment prior to the measurements.

The results of the VT-PXRD study of Co-CAU-36 are shown in Figure S11. The decomposition of the framework took place at ca. 350 °C, which agrees with the decomposition of the linkers observed by TGA. No phase transformation was observable. Some changes of relative intensities for the low angle peaks at temperatures above 150 °C could be due to the loss of physisorbed water molecules in the pores, which was also observed in the TGA curve. The small temperature difference compared to the TG measurement (150 respective 120 °C) is attributed to the confinement of the sample in a capillary during the VT-PXRD measurement.

Co-CAU-36 shows limited stability in aqueous solutions. Stirring at RT for 24 h in H<sub>2</sub>O led to a decrease of the crystallinity (Fig. S12), hence no further solvents were tested. The comparison of the PXRD pattern of Co-CAU-36 stirred in acetone (see activation of the sample) and water is shown in Figure S12.



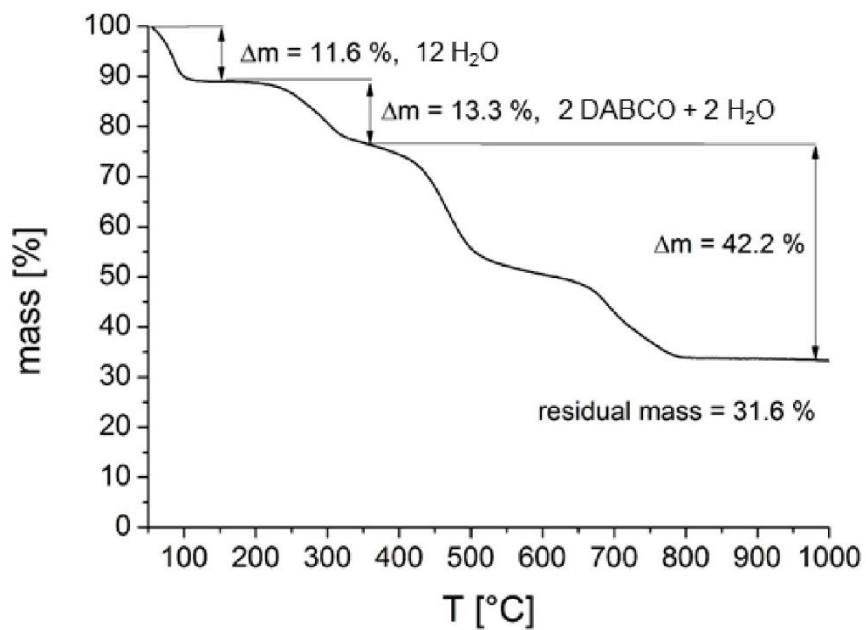


**Figure S10.** Thermogravimetric curve of Co-CAU-36 [Co<sub>2</sub>(Ni-H<sub>4</sub>TPPP)] · 2 DABCO · 12 H<sub>2</sub>O

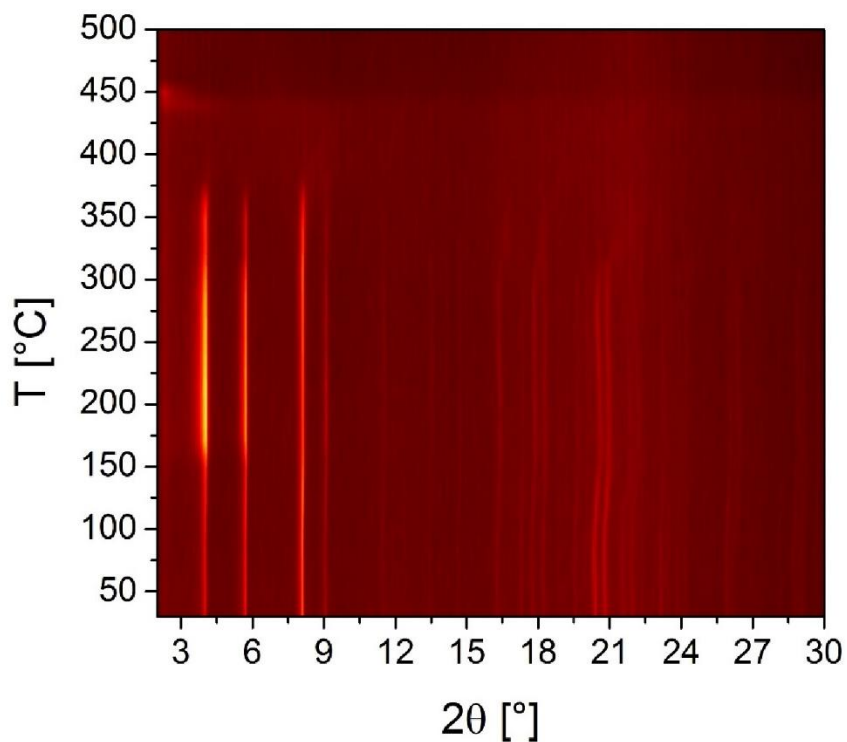


**Figure S11.** Results of the VT-PXRD study of Co-CAU-36 (Cu-K $\alpha_1$  radiation) measured in open quartz capillaries (0.5 mm) under atmospheric conditions.

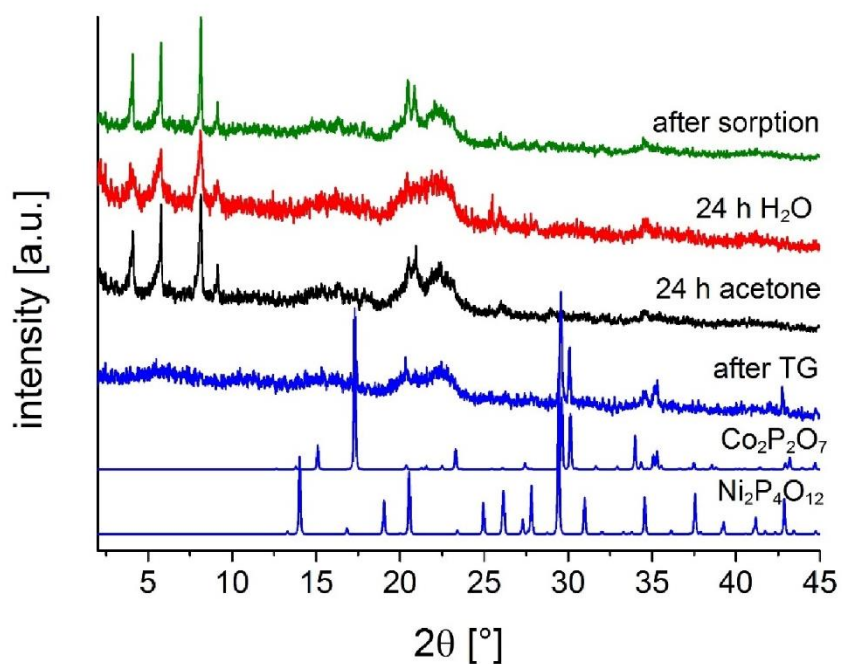
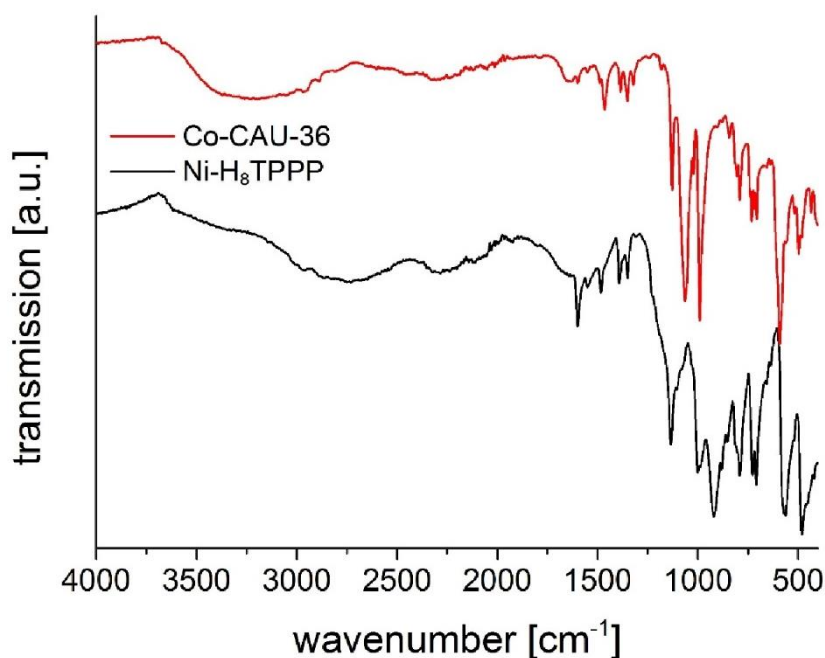


**Figure S12.** PXRD patterns of Co-CAU-36 after the N<sub>2</sub> sorption experiment (green), after 24 h stirring in H<sub>2</sub>O (red) and acetone (black), and after the TGA experiment (blue). The latter is compared with the theoretical PXRD pattern of Co-pyrophosphate and Ni-metaphosphate.

## S6. IR and UV/vis spectroscopy

IR spectra of Co-CAU-36 and the Ni-H<sub>8</sub>TPPP linker are shown in Figure S13. The assignment of the bands is presented in Table S4 in detail. The characteristic bands of Co-CAU-36 are compared with those of the free linker Ni-H<sub>8</sub>TPPP.

The positions of the bands of the free linker are shown in brackets, behind the ones of the partly deprotonated linker molecule. Vibrations of the porphyrin moiety like the  $\nu$  C=C,  $\delta$  C=C C=N,  $\nu$  C=N,  $\gamma$  C-H and  $\delta$  C-H N-H are observed at 1550, 1386, 1349, 791 and 728 cm<sup>-1</sup>, respectively. Characteristic bands of the phosphonic acid are for example the  $\nu$  P-O and  $\nu$  P-C vibrations at 1600 (1606) and 1465 (1480) cm<sup>-1</sup>.  $\nu$  P=O and  $\nu$  P-O bands are observed at 1185 (1223) and 1129 (1136) cm<sup>-1</sup>. Furthermore  $\delta$  P-C and  $\delta$  P(OR)<sub>3</sub> deformation vibrations are observed at 708 (704) and 592 (567) cm<sup>-1</sup>. Characteristic bands of the H-bonded DABCO molecules are found at 2894 ( $\nu$  CH), 1321 ( $\nu$  C-N) and 844 ( $\gamma$  C-H) cm<sup>-1</sup>. The  $\nu$  NH vibration at 3670 cm<sup>-1</sup> indicates the presence of H-DABCO species in the pores, which suggests that the proton is rather located at the DABCO molecule instead of at the phosphonate group.<sup>13,14,15</sup>

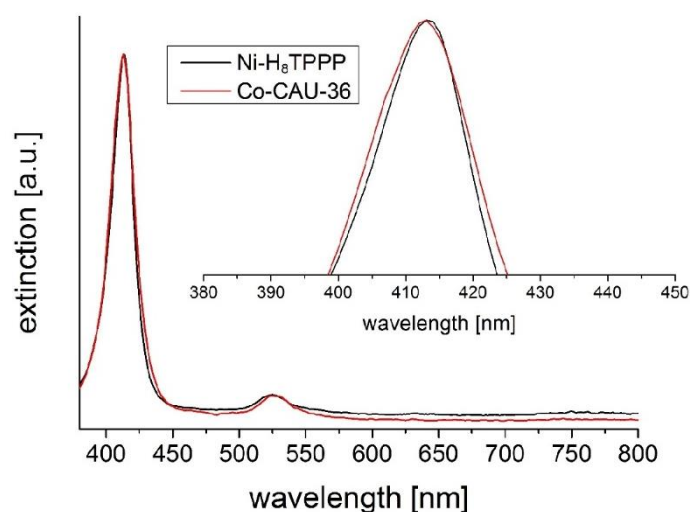


**Figure S13.** IR spectrum of Co-CAU-36 compared with the IR spectrum of the free linker Ni-H<sub>8</sub>TPPP.

**Table S4.** Assignment of the bands in Co-CAU-36 compared to those in the free linker H<sub>8</sub>TPPP.

Vibration $\tilde{\nu}$ IR [cm <sup>-1</sup> ]	Co-CAU-36	Ni-H <sub>8</sub> TPPP
$\nu$ NH (H-DABCO)	3670	
$\nu$ OH (H <sub>2</sub> O)	3386	
$\nu$ CH (DABCO)	2894	
$\nu$ P-O	1600	1606
$\nu$ C=C (arom.)	1550	1519
$\nu$ P-C (phenyl)	1465	1480
$\delta$ C=C, N=C (in plane)	1386	1389
$\nu$ C-N (pyrrole)	1349	1352
$\nu$ C-N (DABCO)	1321	
$\nu$ P=O (stretching)	1185	1223
$\nu$ P-O (stretching)	1129	1136
$\delta$ C-H, N-H (pyrrole)	1070	1100
$\delta$ C-H (in plane)	1020	1005
$\nu$ P=O (stretching)	989	921
$\gamma$ C-H (DABCO)	844	
$\gamma$ C-H (1,4-subst.)	791	793
$\delta$ C-H, N-H (pyrrole)	728	730
$\delta$ P-C	708	704
$\delta$ P(OR) <sub>3</sub>	592	567
$\delta$ C=C (skeleton)	496	484

UV/vis spectra were recorded to check the metalation of the porphyrin after the synthesis of the MOF (Fig. S14). For the measurement 0.1 mg of the Co-CAU-36 sample was dissolved in 1 mL 2 M aqueous NaOH solution and filled up with water to a total volume of 5 mL. Afterwards a 4 mL cuvette was filled with 3 mL water and 5 drops of the dissolved Co-CAU-36 solution was added to the cuvette. The solution containing the porphyrin linker was subsequently measured.

**Figure S14.** UV/vis spectrum of Co-CAU-36 compared with the UV/vis spectrum of the free linker Ni-H<sub>8</sub>TPPP. The absorption maximum (Soret-band) of the Ni-H<sub>8</sub>TPPP linker was found at 413 nm. Furthermore a Q<sub>1</sub>-band was found at 526 nm.

**S7. References**

1. A. D. Adler, F. R. Longo, F. Kampas and J. Kim, *J. Inorg. Nucl. Chem.*, 1970, **32**, 2443-2445.
2. A. D. Adler, F. R. Longo, J. D. Finarelli, J. Goldmacher, J. Assour and L. Korsakoff, *J. Organ. Chem.*, 1967, **32**, 476-476.
3. P. Tavs, *Chem. Ber.*, 1970, **103**, 2428-2436.
4. A. Coelho, *Journal*, 2007, DOI: citeulike-article-id:12635011.
5. K. Brandenburg, *Diamond Version 3*, Crystal Impact GbR, Bonn, 2012.
6. G. G. Rajeshwaran, M. Nandakumar, R. Sureshbabu and A. K. Mohanakrishnan, *Org. Lett.*, 2011, **13**, 1270-1273.
7. W. Kabsch, *Acta Cryst.* 2010, **D66**, 125–132.
8. M. C. Burla, R. Caliandro, B. Carrozzini, G. L. Cascarano, C. Cuocci, C. Giacovazzo, M. Mallamo, A. Mazzone and G. Polidori, *J. Appl. Cryst.*, 2015, **48**, 306–309.
9. G. M. Sheldrick, *Acta Cryst.* 2008, **A64**, 112–122.
10. W. Kabsch, *Acta Cryst.* 2010, **D66**, 133–144.
11. J. Rouquerol, D. Avnir, C. W. Fairbridge, D. H. Everett, J. M. Haynes, N. Pernicone, J. D. F. Ramsay, K. S. W. Sing and K. K. Unger, *Pure Appl. Chem.*, 1994, **66**, 1739–1758.
12. M. Thommes, K. Kaneko, V. Neimark Alexander, P. Olivier James, F. Rodriguez-Reinoso, J. Rouquerol and S. W. Sing Kenneth, *Pure Appl. Chem.*, 2015, **87**, 1051–1069.
13. K. M. Kadish, P. Chen, Y. Y. Enakieva, S. E. Nefedov, Y. G. Gorbunova, A. Y. Tsivadze, A. Bessmertnykh-Lemeune, C. Stern and R. Guilard, *J. Electroanal. Chem.*, 2011, **656**, 61–71.
14. Y. Fang, Y. G. Gorbunova, P. Chen, X. Jiang, M. Manowong, A. A. Sinelshchikova, Y. Y. Enakieva, A. G. Martynov, A. Y. Tsivadze, A. Bessmertnykh-Lemeune, C. Stern, R. Guilard and K. M. Kadish, *Inorg. Chem.*, 2015, **54**, 3501–3512.
15. L. D. Quin, *A Guide to Organophosphorus Chemistry*, Wiley, 2000.

## 12 SI zu „Highly stable and porous porphyrin-based zirconium and hafnium phosphonates - Electron crystallography as an important tool for structure elucidation“

Supporting Information

### Highly stable and porous porphyrin-based zirconium and hafnium phosphonates - Electron crystallography as an important tool for structure elucidation

*Timo Rhauderwiek,<sup>a</sup> Haishuang Zhao,<sup>b</sup> Patrick Hirschle,<sup>c</sup> Markus Döblinger<sup>c</sup>, Bart Bueken<sup>d</sup>, Helge Reinsch,<sup>a</sup> Dirk de Vos,<sup>d</sup> Stefan Wuttke,<sup>c</sup> Ute Kolb<sup>b</sup> and Norbert Stock<sup>a</sup>*

<sup>a</sup> Institute of Inorganic Chemistry, Christian-Albrechts-Universität, Max-Eyth Straße 2, D-24118 Kiel, Germany.

<sup>b</sup> Institute of Inorganic Chemistry and Analytical Chemistry, Johannes Gutenberg-University Mainz, Jakob-Welder-Weg 11, D-55128 Mainz, Germany

<sup>c</sup> Department of Chemistry and Center for NanoScience (CeNS), University of Munich (LMU), Butenandtstraße 5-13, D-81377 Munich, Germany.

<sup>d</sup> Centre for Surface Chemistry and Catalysis, KU Leuven, Celestijnenlaan 200f, B-3001 Leuven, Belgium.

1. <sup>1</sup> H-NMR spectroscopy of Ni-H <sub>8</sub> TPPP, list of known Zr-phosphonates and high-throughput investigations.....	2-7
2. Electron diffraction tomography and Pawley-/ Rietveld-refinements.....	8-13
3. H <sub>2</sub> O Sorption properties and PXRD patterns of the activated samples.....	14
4. TG investigations, PXRD patterns of the decomposition products, VT-PXRD studies and chemical stability.....	15-18
5. Spectroscopy .....	19-20
6. TEM and SEM measurements.....	21-27
7. Cyclic voltammetry.....	28
8. References.....	29



## 1. $^1\text{H-NMR}$ spectroscopy of Ni-H<sub>8</sub>TPPP, list of known Zr-phosphonates and high-throughput investigations

**Synthesis of Ni-H<sub>8</sub>TPPP.** The three step synthesis of Ni-H<sub>8</sub>TPPP (Fig. S1) was carried out employing in the first step the Adler method<sup>7, 8</sup> for the synthesis of 4-Bromophenylporphyrin (H<sub>2</sub>TBrPP). The second step, the phosphorylation of H<sub>2</sub>TBrPP was achieved by using a Ni-catalyzed variation of the Arbuzov reaction,<sup>9, 10</sup> with the following third step, the hydrolysis of the -PO(OEt)<sub>2</sub> groups in conc. HCl.

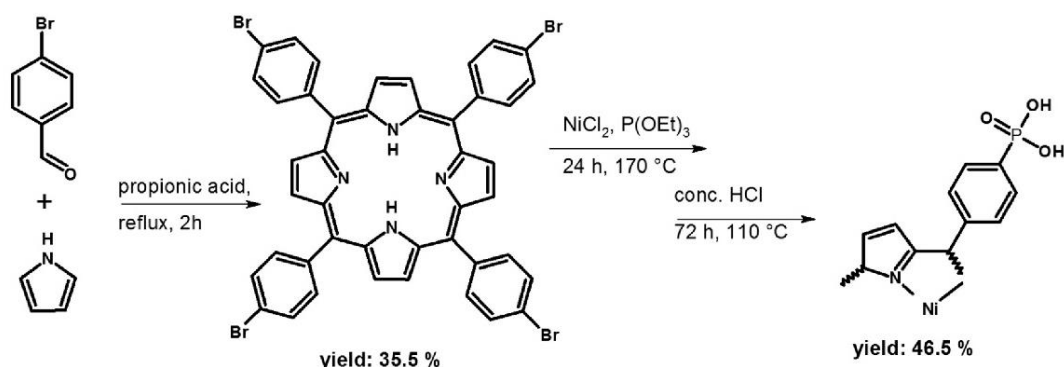


**Figure S1.** Schematic representation of the synthesis of Ni-H<sub>8</sub>TPPP.

**H<sub>2</sub>TBrPP:** Pyrrole (7.47 mL, 108 mmol) and 4-bromobenzaldehyde (20.0 g, 108 mmol) in 400 mL propionic acid were heated under reflux for 2 h. Afterwards the reaction mixture was cooled down to room temperature and poured into 500 mL of MeOH and stirred for 30 min in an ice bath. The resulting precipitate was filtered off and washed several times with MeOH until the filtrate was only slightly red. Subsequently, the product was washed with 100 mL warm distilled water and dried at 70 °C in a drying oven over night. A blue powder of H<sub>2</sub>TBrPP 7.63 g (8.2 mmol, 30.4 %) was obtained.

Elemental analysis of H<sub>2</sub>TBrPP (Br<sub>4</sub>C<sub>44</sub>H<sub>26</sub>N<sub>4</sub>): calc (%): C 56.8, H 2.6, N 6.0, found (%): C 59.7, H 3.2, N 6.2. The small difference between the calculated and observed values is due to impurities caused by solvent molecules used in the synthesis. These impurities were also observed in the  $^1\text{H-NMR}$  measurements.

**<sup>1</sup>H-NMR (Fig. S2), H<sub>2</sub>TBrPP (500 MHz CDCl<sub>3</sub>):** δ= 8.76 (s, 8H, H-1); 7.99 (d, 8H, H-2); 7.82 (d, 8H, H-3); 7.18 (s, 1H, CDCl<sub>3</sub>); 2.30 (q, 2H, propionic acid); 1.08 (t, 3H, propionic acid) ppm. Additional peaks between 7 and 9 ppm are due to small impurities with porphyrinic oligomers.

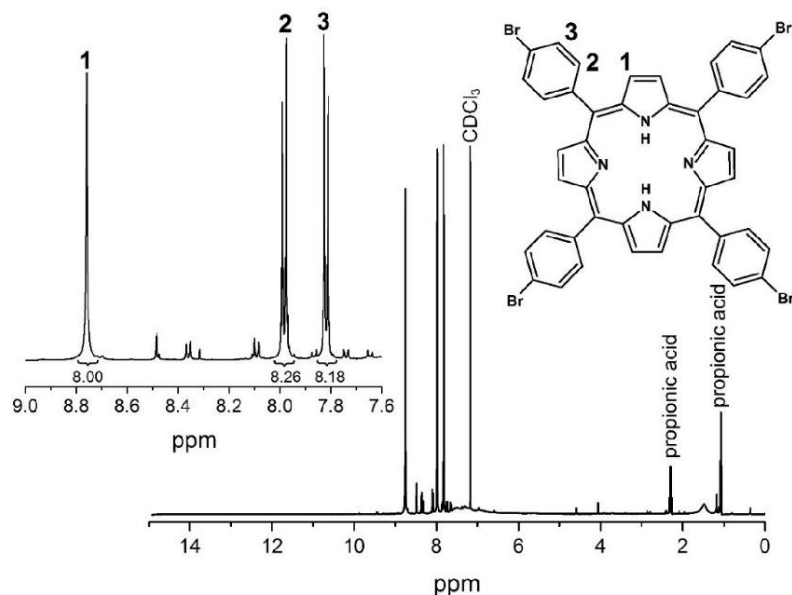


**Figure S2.** <sup>1</sup>H-NMR spectrum of H<sub>2</sub>TBrPP digested in DMSO.

**Ni-H<sub>8</sub>TPPP:** H<sub>2</sub>TBrPP (3.42 g, 3.7 mmol) and anhydrous NiCl<sub>2</sub> (1.79 g, 13.8 mmol) in 70 mL 1,3-diisopropylbenzene (prior the reaction for 30 min with N<sub>2</sub> degassed) were heated up to exactly 170 °C under N<sub>2</sub> atmosphere. Afterwards triethylphosphite (7.05 mL, 43.7 mmol) was added slowly (within 30 min) and dropwise to the reaction mixture and heated for further 24 h at 170 °C. The reaction mixture was cooled down to room temperature and the resulting precipitate was filtered off and washed with 250 mL CH<sub>2</sub>Cl<sub>2</sub>. The resulting organic phase was washed 2 times each with 100 mL H<sub>2</sub>O. The organic solvents were evaporated under reduced pressure and the precipitate was hydrolyzed with 80 mL conc. HCl at 110 °C in 72 h. The resulting product was filtered off, washed with 100 mL cold water and afterwards stirred in 100 mL CH<sub>2</sub>Cl<sub>2</sub> for 24 h. The clean product was filtered off and dried at 70 °C in a drying oven over night. A red powder of Ni-H<sub>8</sub>TPPP 2.74 g (2.76 mmol, 74.6 %) was obtained.

Elemental analysis of Ni-H<sub>8</sub>TPPP (C<sub>44</sub>H<sub>32</sub>N<sub>4</sub>NiO<sub>12</sub>) · 4H<sub>2</sub>O: calc (%): C 49.8, H 3.6, N 5.3, found (%): C 49.1, H 3.6, N 5.1.

**$^1\text{H-NMR}$  (Fig. S3), Ni-H<sub>8</sub>TPPP (500 MHz DMSO-d<sub>6</sub>):**  $\delta$ = 8.74 (s, 8H, H-1); 8.11 (dd, 8H, H-2); 8.06 (dd, 8H, H-3); 2.50 (s, 6H, DMSO-d<sub>6</sub>); 2.09 (s, 6H, acetone) ppm.

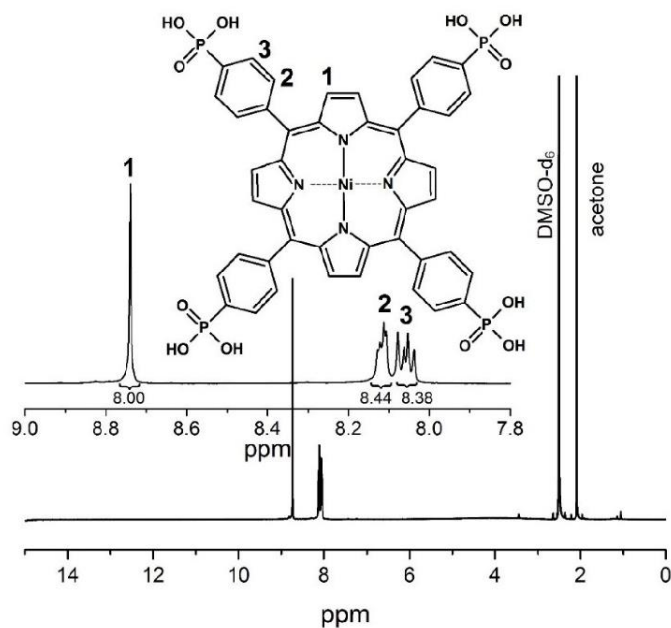


**Figure S3.**  $^1\text{H-NMR}$  spectrum of Ni-H<sub>8</sub>TPPP digested in DMSO.

**$^{31}\text{P-NMR}$  (Fig. S4), Ni-H<sub>8</sub>TPPP (500 MHz DMSO-d<sub>6</sub>):**  $\delta$ = 12.04 (s, 4P, -PO(OH)<sub>2</sub>) ppm.

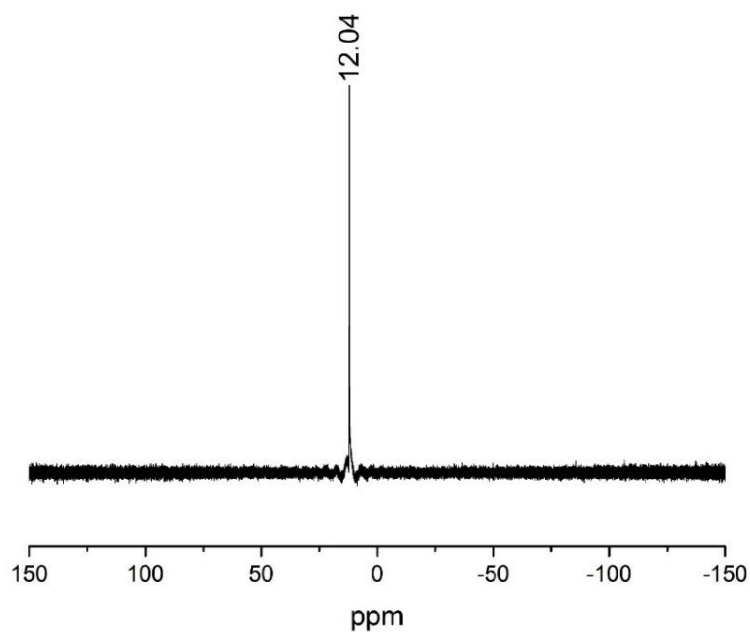


**Figure S4.**  $^{31}\text{P-NMR}$  spectrum of Ni-H<sub>8</sub>TPPP digested in DMSO.

**Table S1.** Overview of porous and crystalline Zr-phosphonates. In addition to the names the formula, the specific surface areas and the space group symmetry of the crystal structure are given.

name <sup>[Lit.]</sup>	formula	Specific surface area	SG
CALF-31 <sup>4</sup>	[Zr(H <sub>2</sub> PPB)] H <sub>6</sub> PPB= 1,3,5- <i>Tris</i> -(4-phosphonophenyl)benzene	793 m <sup>2</sup> g <sup>-1</sup>	model
ZrPPB <sup>3</sup>	[Zr <sub>3</sub> (H <sub>3</sub> PPB) <sub>4</sub> ]	10 m <sup>2</sup> g <sup>-1</sup>	<i>P</i> $\bar{3}$ <i>1c</i>
ZrPBMP <sup>1</sup>	[Zr <sub>2</sub> H <sub>4</sub> (PBMP) <sub>3</sub> ] H <sub>4</sub> PBMP= N,N'-piperazin <i>Bismethylenphosphonic acid</i>	-	<i>R</i> $\bar{3}$
UPG-1 <sup>2</sup>	[Zr(H <sub>4</sub> PMPT) <sub>2</sub> ] H <sub>6</sub> PMPT= 2,4,6- <i>Tris</i> (4-(phosphonomethyl)phenyl)-1,3,5-triazine	410 m <sup>2</sup> g <sup>-1</sup>	<i>R</i> $\bar{3}$
SZ-1 <sup>6</sup>	[C <sub>4</sub> mpyr][Zr <sub>2.5</sub> (H <sub>3</sub> TPPM)F <sub>6</sub> ] C <sub>4</sub> mpyr <sup>+</sup> = N-butyl-N-methylpyrrolidinium H <sub>8</sub> TPPM=Tetrakis(4-phosphonophenyl)methane	10 m <sup>2</sup> g <sup>-1</sup>	<i>Pbca</i>
SZ-2 <sup>6</sup>	[C <sub>4</sub> mpyr] <sub>2</sub> [Zr <sub>1.5</sub> (TPPM) <sub>0.5</sub> F <sub>4</sub> ]	225 m <sup>2</sup> g <sup>-1</sup>	<i>I4/m</i>
SZ-3 <sup>6</sup>	[C <sub>2</sub> py] <sub>2</sub> [Zr <sub>3.5</sub> (HTPPA)F <sub>9</sub> ] C <sub>2</sub> py <sup>+</sup> =N-ethylpyridinium H <sub>8</sub> TPPA= 1,3,5,7-Tetrakis(4-phosphonophenyl)adamantane	594 m <sup>2</sup> g <sup>-1</sup>	<i>P2</i> <sub>1</sub> / <i>n</i>

**High-throughput investigations**

High-throughput reactors (2 mL Teflon inserts) were employed in the screening of synthesis parameters such as molar ratio of metal to linker to NaF to NaOH, pH and reaction temperature and time (Fig. S5a). The use of 0 and 12 eq. NaOH resulted in X-ray amorphous products while 4 and 8 eq. NaOH resulted in CAU-30 (1 eq. corresponds to 5 mg Ni-H<sub>8</sub>TPPP ( $5.3 \cdot 10^{-3}$  mmol, Fig S5b)). A molar linker to metal ratio of 1 : 1 resulted in CAU-30 with low crystallinity, while a ratio of  $\geq 1 : 2$  led to highly crystalline CAU-30. Furthermore an upscaling of CAU-30 in 30 mL Teflon inserts was possible using the 12 fold amount of all reactants and solvents. By using 5 mL glass vials and stirring of the reaction mixture, the reaction temperature could be reduced from 48 to 3 h and the reaction temperature from 180 to 160 °C (Fig. S5b)

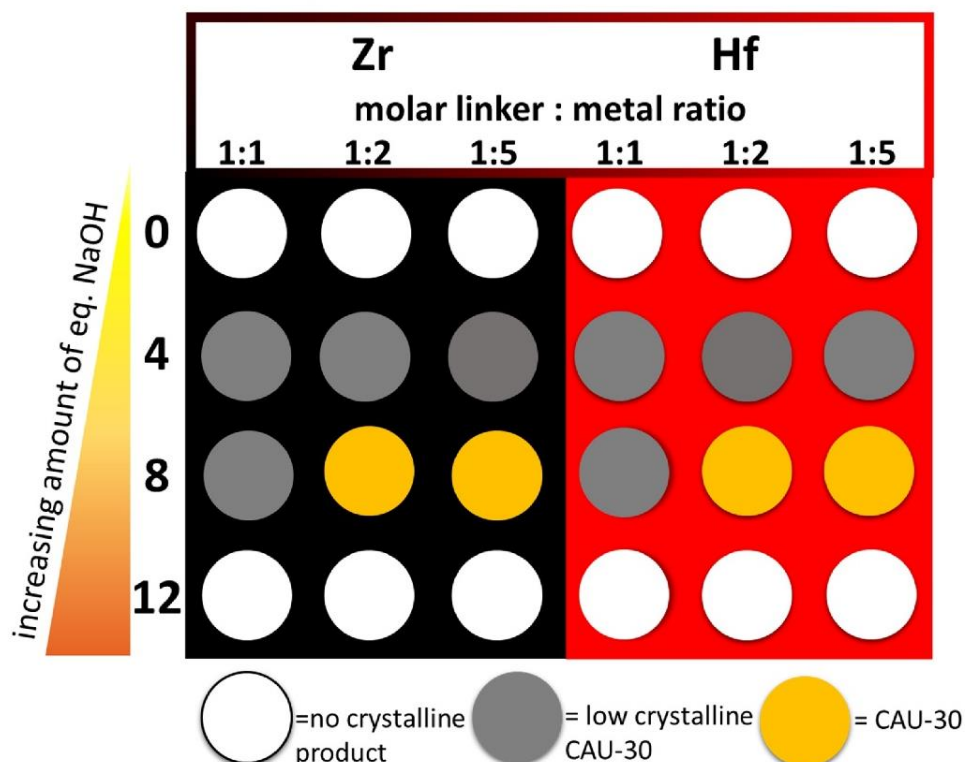


**Figure S5a.** Results of the high-throughput investigation of M-CAU-30 (M= Zr, Hf) varying the molar ratio linker to metal to NaOH. In all reactions 60 eq. of NaF (1 eq. corresponds to 5 mg Ni-H<sub>8</sub>TPPP ( $5.3 \cdot 10^{-3}$  mmol)) were used.

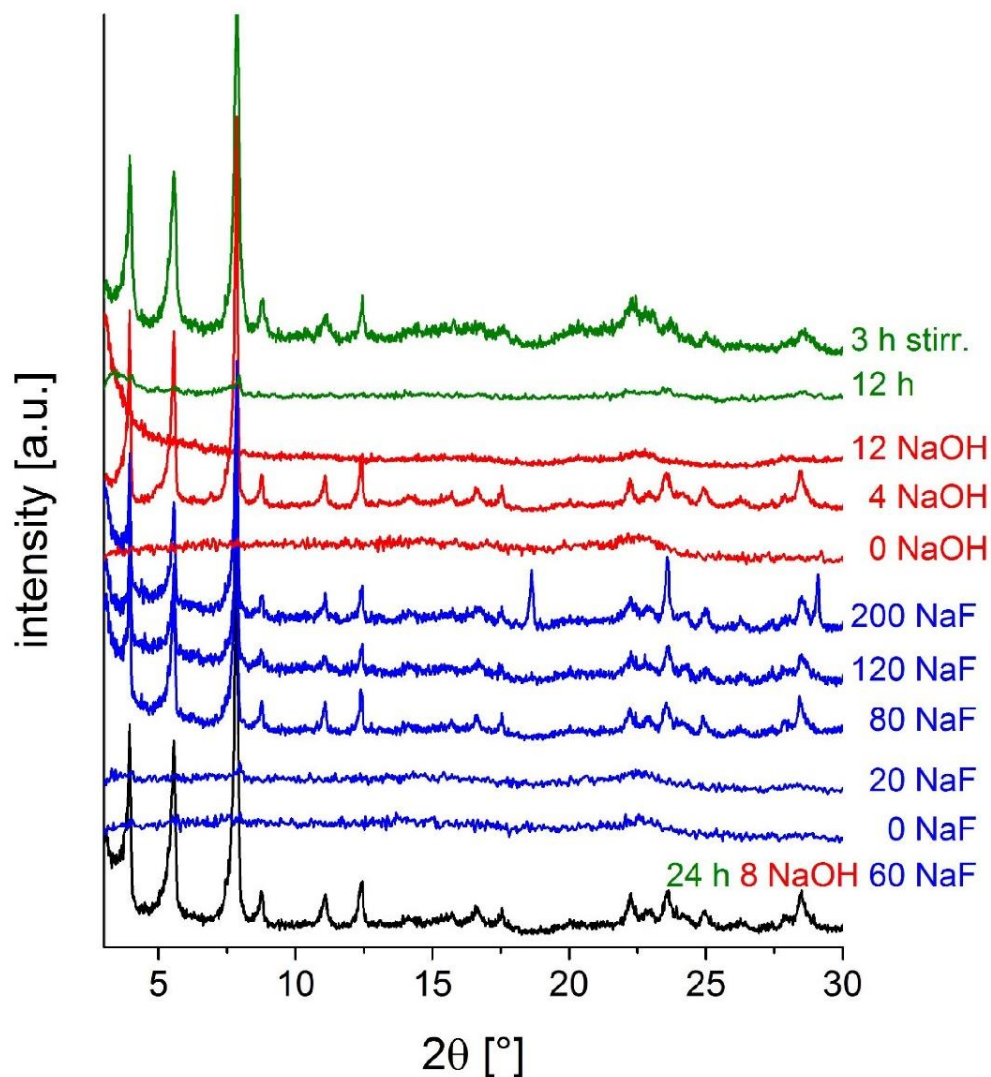


**Figure S5b.** PXRD patterns obtained from the reaction products of the high-throughput investigation of M-CAU-30 (M= Zr, Hf). The black pattern corresponds to the product obtained using the final optimized synthesis conditions (24 h without stirring, 8 eq. NaOH, 60 eq. NaF). The blue and the red patterns demonstrate the influence of the amount of NaF (24 h, 8 eq. NaOH) and NaOH (24 h, 60 eq. NaF), respectively, on the product formation. The influence of stirring and changing the reactor from a Teflon reactor to a glass vials is shown in the green PXRD patterns: the reduction of the reaction time (8 eq. NaOH, 60 eq. NaF) to 12 h without stirring and 3 h under stirring results in an X-ray amorphous and a crystalline product, respectively. A value of 1 eq. corresponds  $5.3 \cdot 10^{-3}$  mmol.



## 2. Electron diffraction tomography and Pawley / Rietveld refinements.

STEM images and 2D slices of the reciprocal lattice of Zr-CAU-30 are given in Figures S6a to S6d.

The crystallographic data of M-CAU-30 (M= Zr, Hf) obtained by Pawley- and Rietveld-refinements reveal very similar unit cell parameters and the resulting Rietveld- and Pawley-refinements prove that the two CAU-30 derivatives are isostructural and contain no further crystalline impurities (Fig. S7a – S7c, Tab.S2).

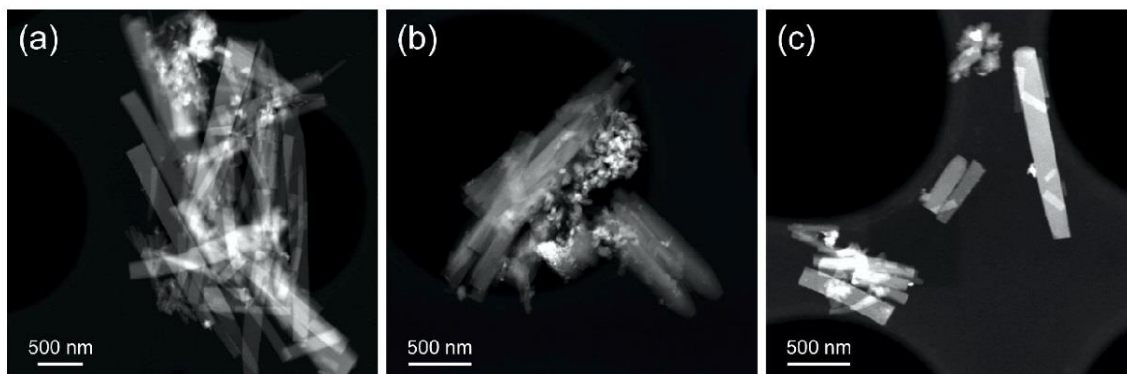


**Figure S6a:** STEM images of Zr-CAU-30: (a, b) overview of nanorods; (c) single separate nanorods.

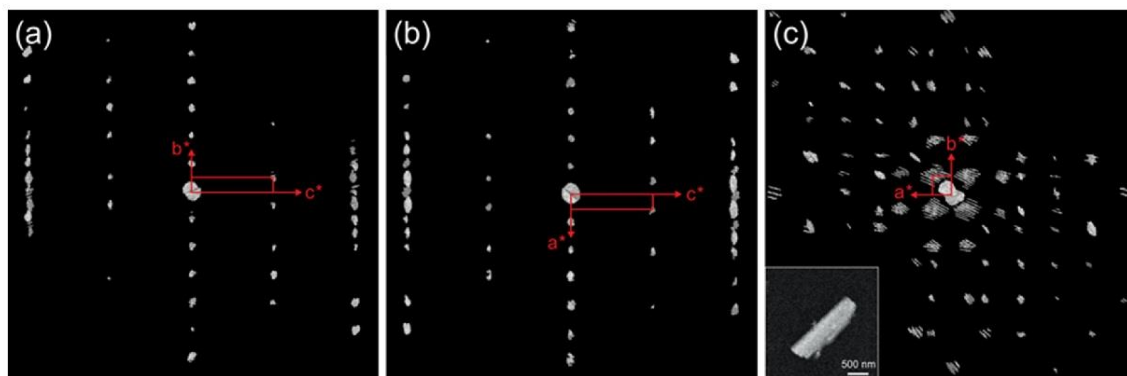


**Figure S6b.** Reconstructed three-dimensional reciprocal space obtained from ADT data viewed down the three main axes ( $a - c$ ), delivering  $a = 46.09 \text{ \AA}$ ,  $b = 45.74 \text{ \AA}$ ,  $c = 7.81 \text{ \AA}$ ,  $\alpha = 89.0^\circ$ ,  $\beta = 90.5^\circ$ ,  $\gamma = 91.1^\circ$ . The inset shows the STEM image of the selected crystal for acquisition of ADT data. The electron beam for data collection was shifted on the crystal at the ADT data acquisition to minimize beam damage.

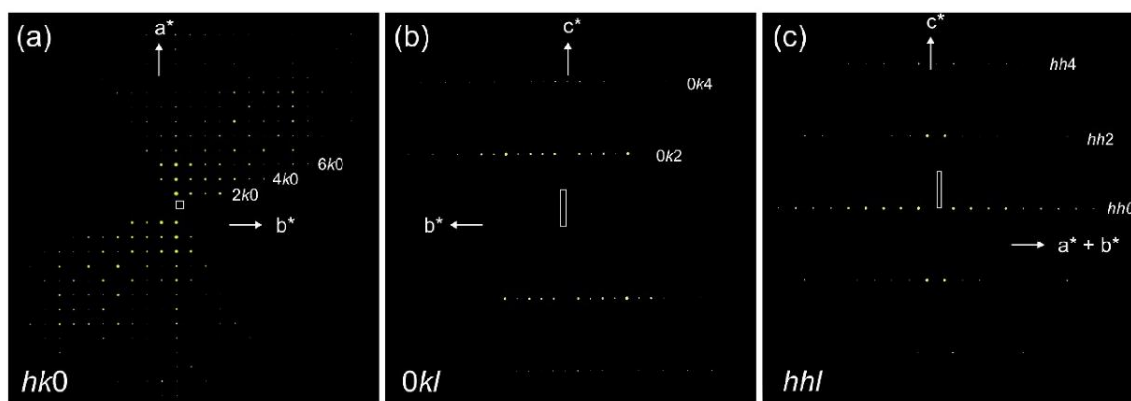


**Figure S6c:** Three 2D slices  $hk0$  (a),  $0kl$  (b) and  $hhl$  (c) cut from reconstructed 3D reciprocal lattice of Zr-CAU-30.

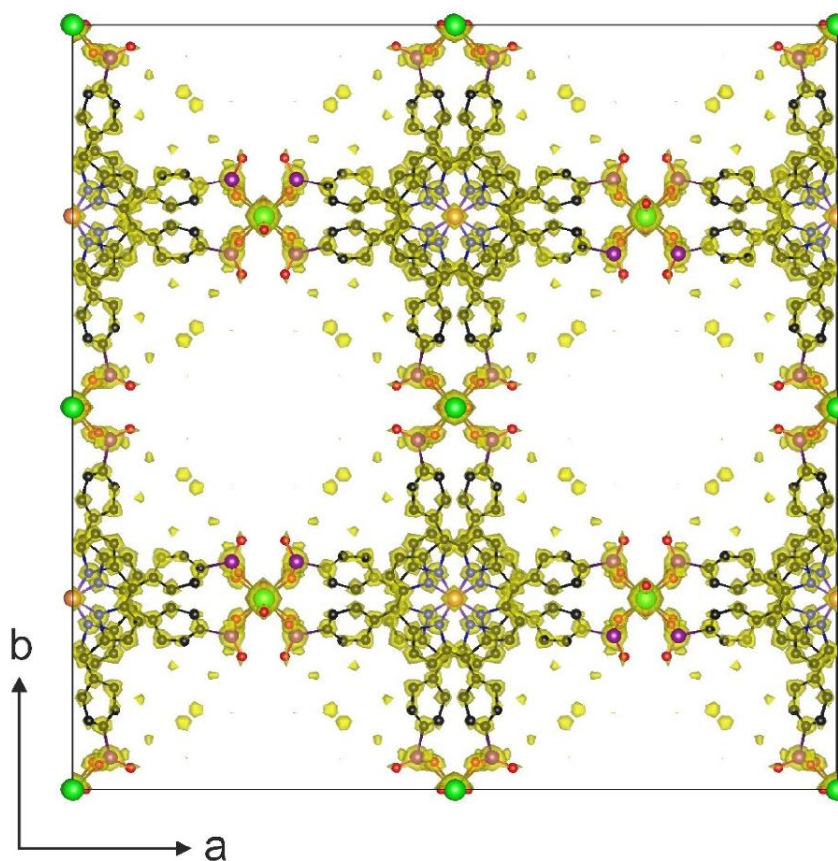


**Figure S6d.** Fourier potential map of Zr-CAU-30-as derived from the structure solution using ADT data and overlaid atomic framework model (view along  $[001]$ ). Atom color: green for Zr, yellow for Ni, violet for P, red for O, black for C, blue for N.

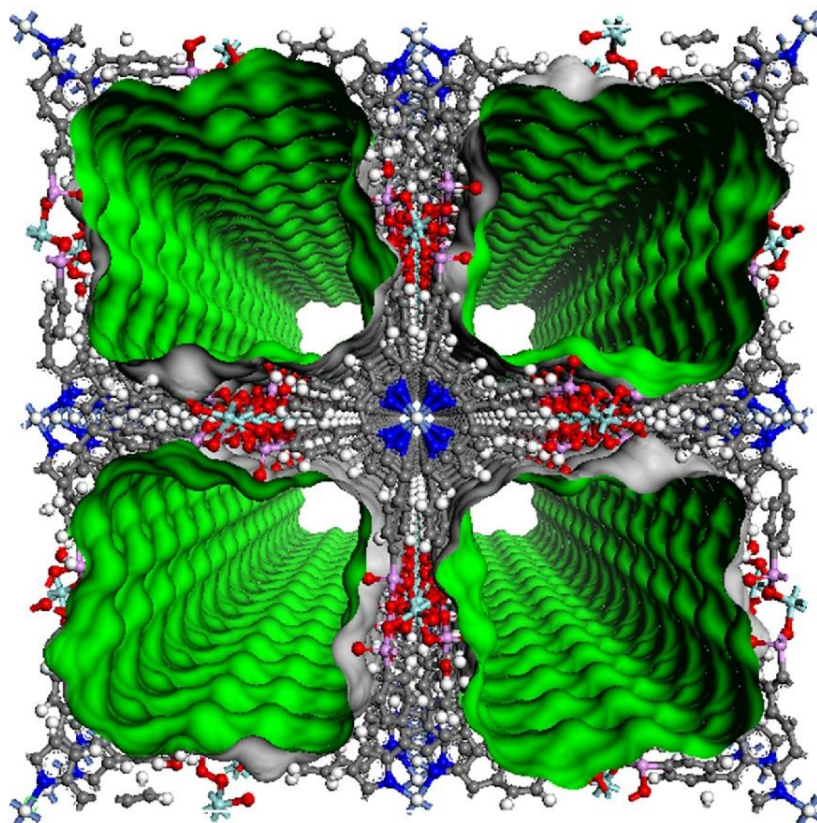


**Figure S6e.** Connolly Surface of the pores in Zr-CAU-30 along [001] (green, probe radius 1.8 Å).

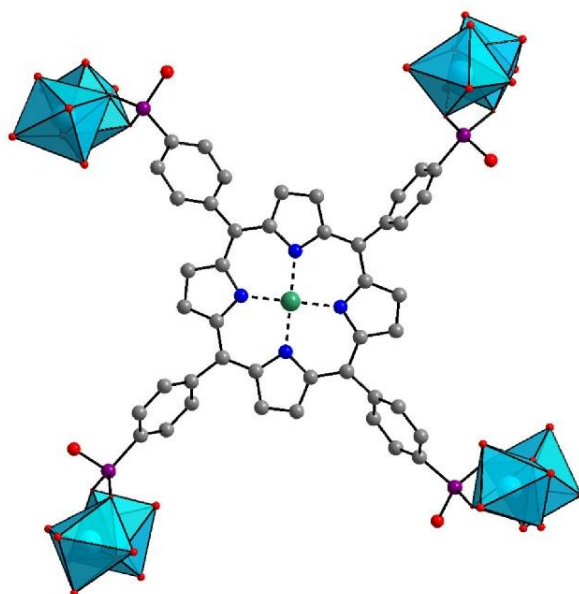


**Figure S6f.** Coordination mode of the linker molecule. Each linker molecule is coordinated to eight  $Zr^{4+}$  ions. Zirconium and  $ZrO_6$  polyhedra are represented in light blue, nickel in green phosphorous in purple, oxygen in red, nitrogen in blue and carbon in grey.

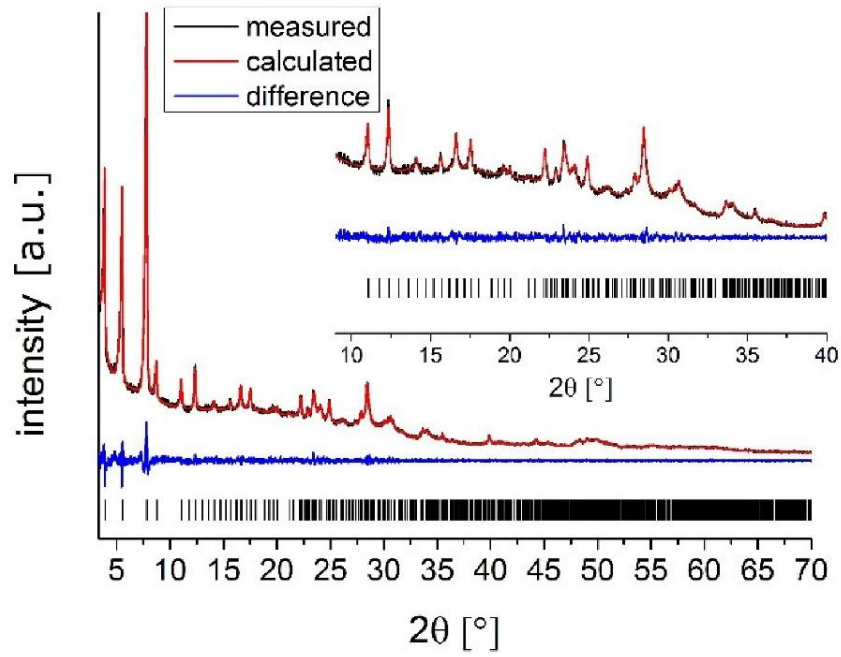


**Figure S7a.** Results of the Pawley-refinement of Zr-CAU-30-as.

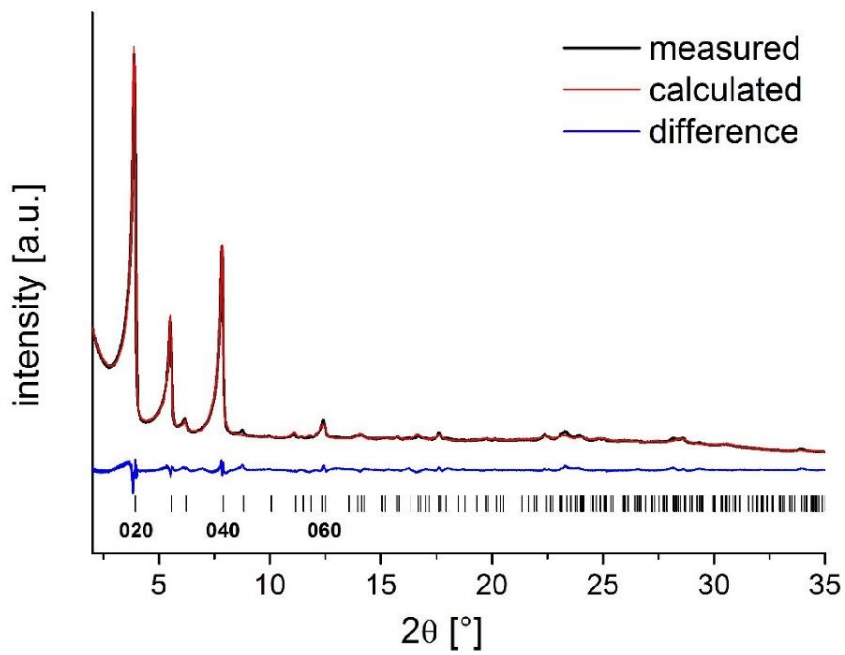


**Figure S7b.** Results of the Rietveld refinement of Zr-CAU-30-act (250 °C, reduced pressure of  $10^{-2}$  kPa) with mentioned reflections hkl as observed by TEM measurements.



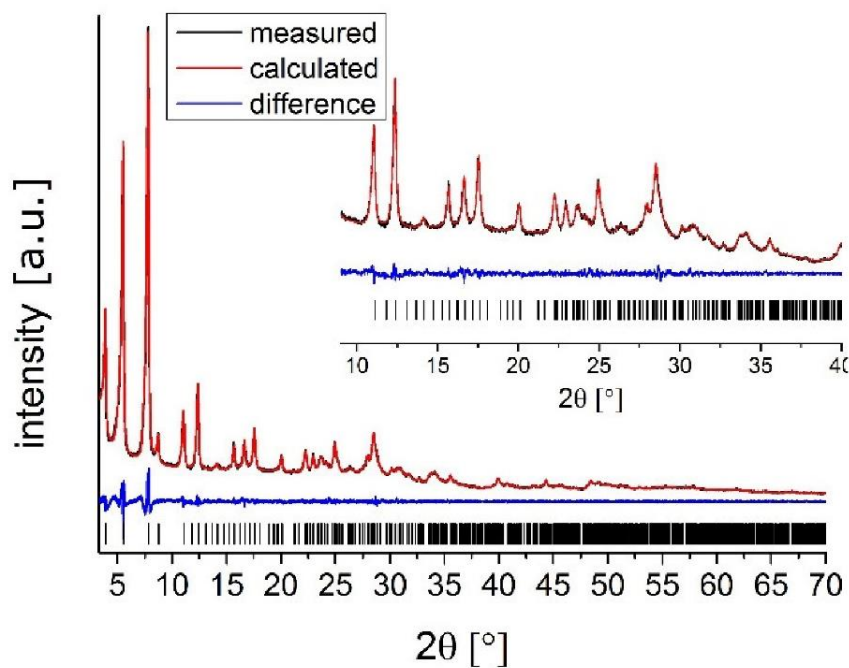


Figure S7c. Results of the Pawley-refinement of Hf-CAU-30-as.

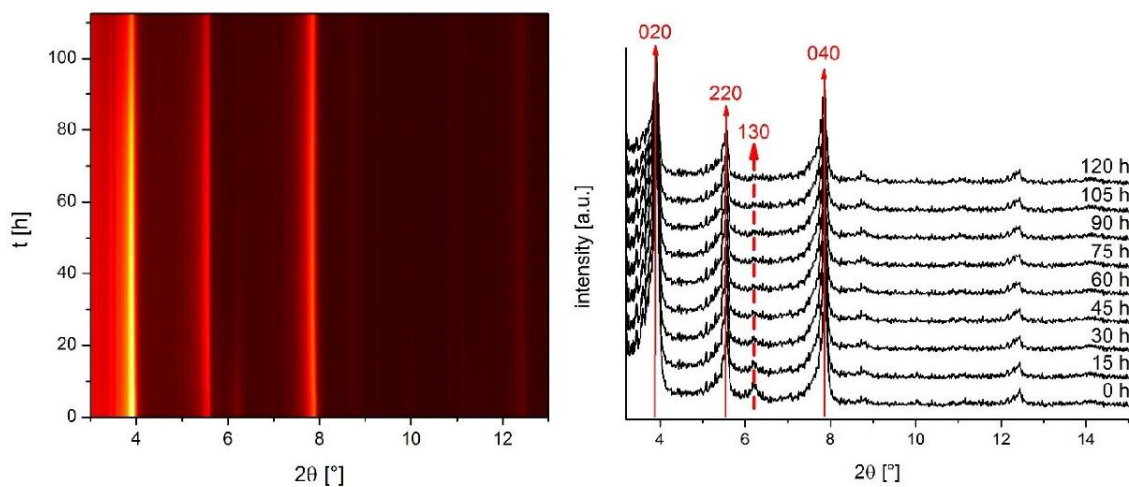


Figure S7d. PXRD patterns of Zr-CAU-30 measured every 5 minutes over 5 days to show the reversibility of the transformation from Zr-CAU-30-act ( $I4_1cd$ ) into Zr-CAU-30-as ( $I4_1acd$ ), indicated by the disappearance of the 130 reflection at  $6.2^\circ$   $2\theta$  and changes in the relative intensities. Contour-plot (left) and selected PXRD pattern between 0 and 120 h (right).

**Table S2.** Results of the Rietveld refinement of Zr-CAU-30-act (activated at 250 °C for 2h under reduced pressure of  $10^{-2}$  kPa) and the Pawley refinement of M-CAU-30-as (M= Zr, Hf, as synthesized).

	<b>Zr-act</b>	<b>Zr-as</b>	<b>Hf-as</b>
<b>determination method</b>	Rietveld	Pawley	Pawley
<b>crystal system</b>	tetragonal	tetragonal	tetragonal
<b>a</b> [Å]	44.778(6)	45.121(5)	45.040(5)
<b>b</b> [Å]	44.778(6)	45.121(5)	45.040(5)
<b>c</b> [Å]	7.658(4)	8.090(2)	8.049(3)
<b>α</b> [°]	90	90	90
<b>β</b> [°]	90	90	90
<b>γ</b> [°]	90	90	90
<b>V</b> [Å <sup>3</sup> ]	15354(8)	16470(5)	16329(8)
<b>space group</b>	<i>I4<sub>1</sub>cd</i>	<i>I4<sub>1</sub>/acd</i>	<i>I4<sub>1</sub>/acd</i>
<b>GoF</b>	2.0	0.72	0.94
<b>R<sub>wp</sub></b> [%]	3.8	3.3	3.8



### 3. H<sub>2</sub>O Sorption properties and PXRD patterns of the activated samples.

In the following figures the H<sub>2</sub>O sorption isotherms of M-CAU-30 (M= Zr, Hf) (Figure S8) and the PXRD patterns of the samples before and after the sorption experiments are shown (Figure S9).

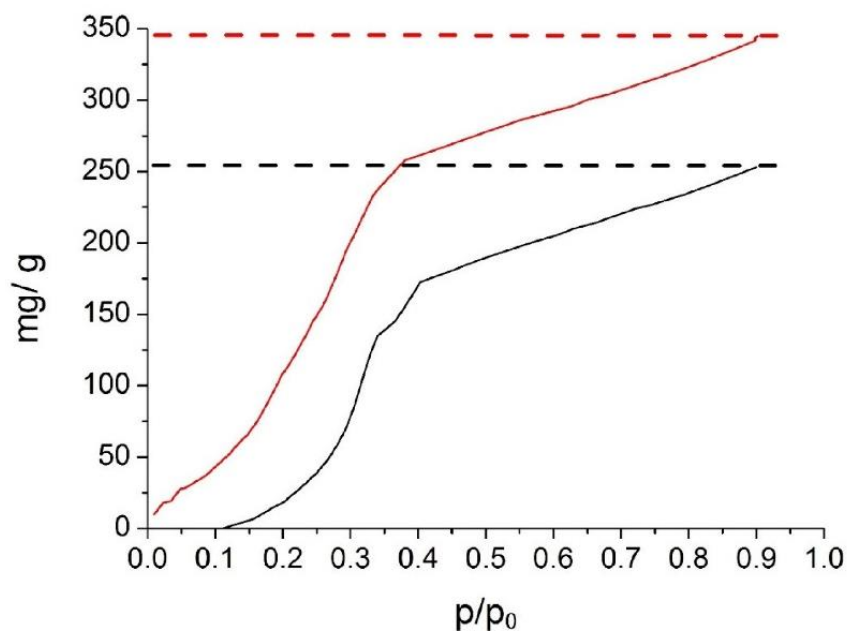


**Figure S8.** H<sub>2</sub>O-sorption isotherms of M-CAU-30 (M = Zr (black), Hf (red)) measured at 298 K.

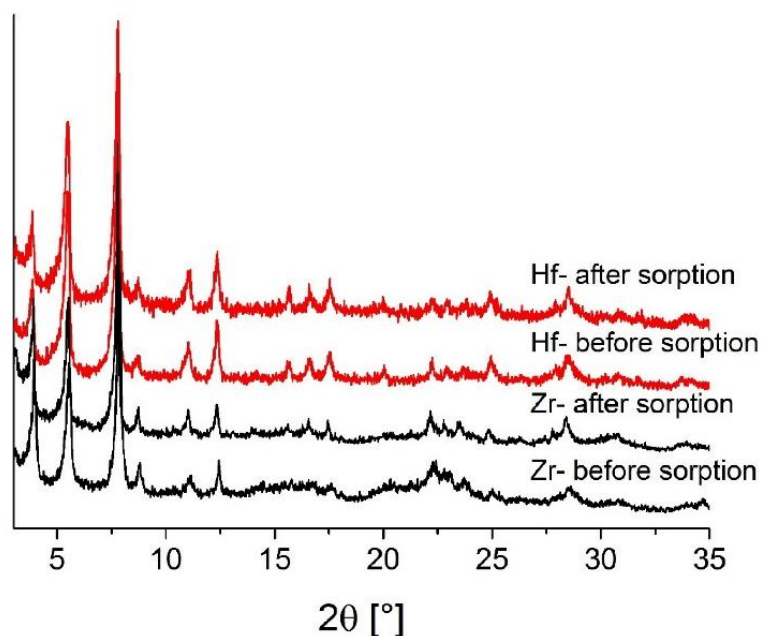


**Figure S9.** PXRD patterns of M-CAU-30 (M= Zr, Hf) after the sorption experiments (activation 120 °C, 10<sup>-2</sup> kPa). For comparison the patterns of M-CAU-30 before the sorption experiment are also presented.

#### 4. TG investigations, PXRD patterns of the decomposition products, VT-PXRD studies and chemical stability.

The results of the TG measurement of Hf-CAU-30 are shown in Fig. S10 and Tab. S3. The decomposition products of M-CAU-30 (M= Zr, Hf) mostly consists of Ni-M-phosphates and  $\text{MO}_2$  which was shown by PXRD measurements (Fig. S11). The results of VT-PXRD studies (Fig. S12) confirm the results obtained from the TG measurements. Complete collapse of the frameworks takes place above ca. 400 °C.

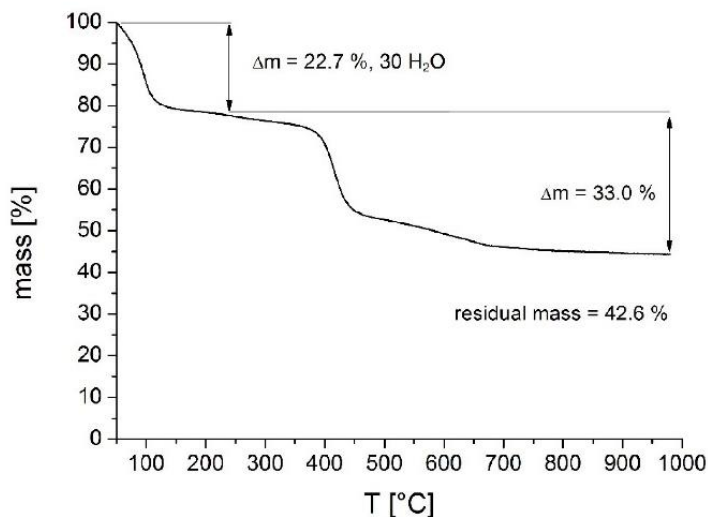


**Figure S10.** Thermogravimetric curve of Hf-CAU-30  $[\text{Hf}_2(\text{Ni-H}_2\text{TPPP})(\text{OH}/\text{F})_2] \cdot 30 \text{ H}_2\text{O}$  (Table S4).

**Table S3.** Results of the thermogravimetric measurements of M-CAU-30 (Zr, Hf) calculated for 0 and 1  $\text{MO}_2$  per formula unit.

sum formula	residual mass		mass loss 200-1000 °C linker decomposition		mass loss 25-200 °C $\text{H}_2\text{O}$	
	meas. [%]	calc. [%]	meas. [%]	calc. [%]	meas. [%]	calc. [%]
$[\text{Zr}_2(\text{Ni-H}_2\text{TPPP})(\text{OH}/\text{F})_2] \cdot 23 \text{ H}_2\text{O}$	38.2	33.2	39.6	44.0	20.5	20.5
$[\text{Zr}_2(\text{Ni-H}_2\text{TPPP})(\text{OH}/\text{F})_2] \cdot 23 \text{ H}_2\text{O} \cdot \text{ZrO}_2$	38.2	37.4	39.6	41.2	20.5	20.5
$[\text{Hf}_2(\text{Ni-H}_2\text{TPPP})(\text{OH}/\text{F})_2] \cdot 30 \text{ H}_2\text{O}$	42.6	36.5	33.0	37.6	22.7	22.7
$[\text{Hf}_2(\text{Ni-H}_2\text{TPPP})(\text{OH}/\text{F})_2] \cdot 30 \text{ H}_2\text{O} \cdot \text{HfO}_2$	42.6	42.2	33.0	34.2	22.7	22.7

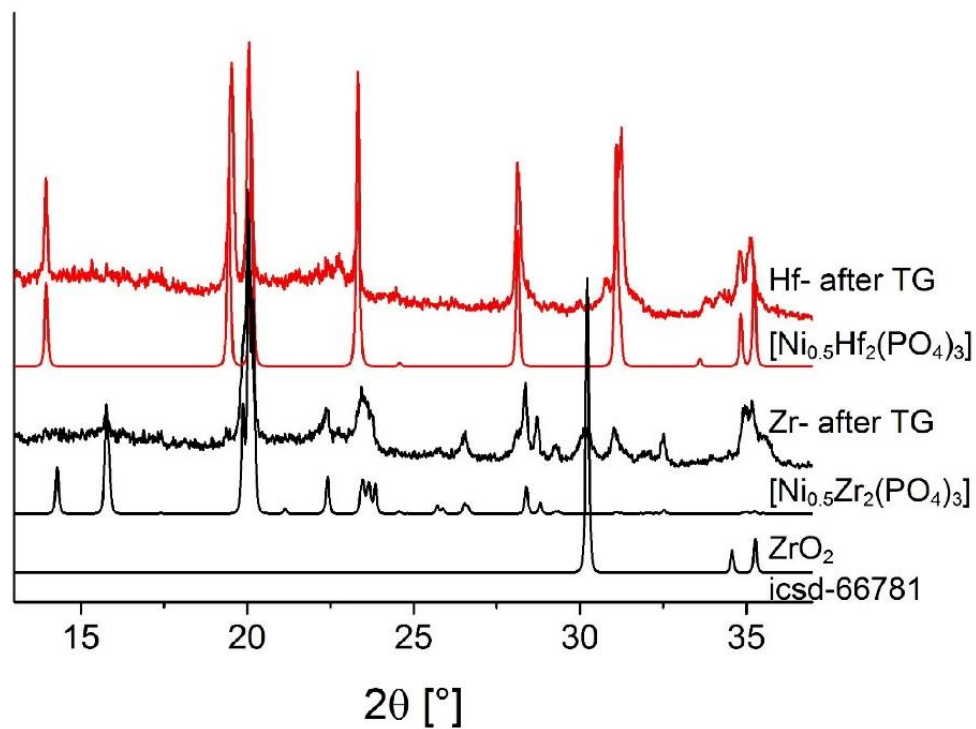


**Figure S11.** PXRD patterns of M-Ni-phosphates and oxides (M=Zr, Hf) compared with the residual products of the thermogravimetric experiments of M-CAU-30.

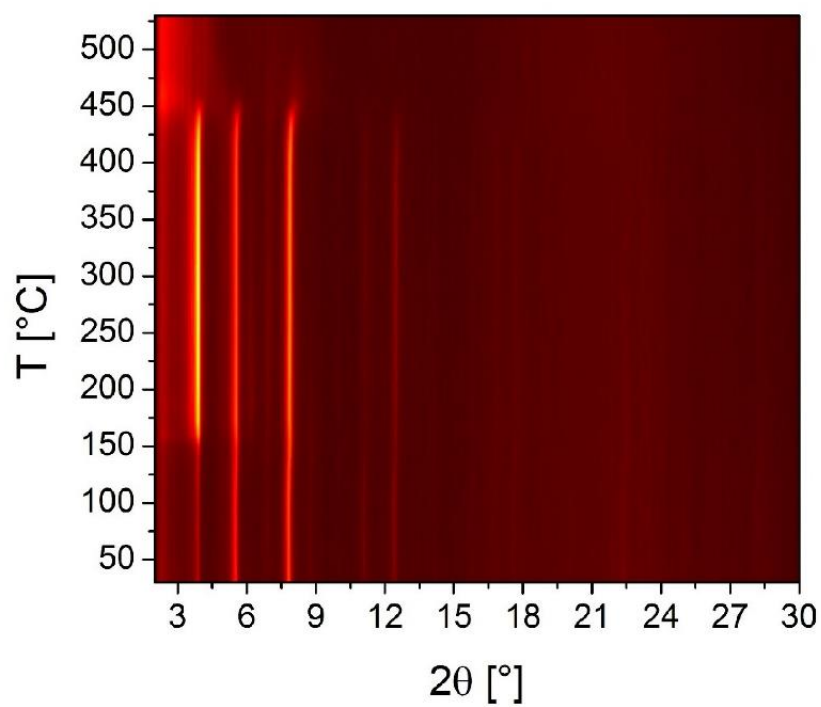


**Figure S12.** Results of the VT-PXRD studies of Hf-CAU-30 (Cu-K $\alpha_1$  radiation) measured in open quartz capillaries (0.5 mm).

To study the chemical stability M-CAU-30 were stirred in different solvents for 24 h and subsequently characterized by PXRD measurements (Fig. S13). Both MOFs are stable in all tested organic solvents as well as in a pH range between 0 and 12 (aqueous HCl/ NaOH solutions). Furthermore both MOFs are stable in 0.1 M phosphate buffer. Hf-CAU-30 shows a loss of the long range order by stirring in 100 % acetic acid, while Zr-CAU-30 is stable.

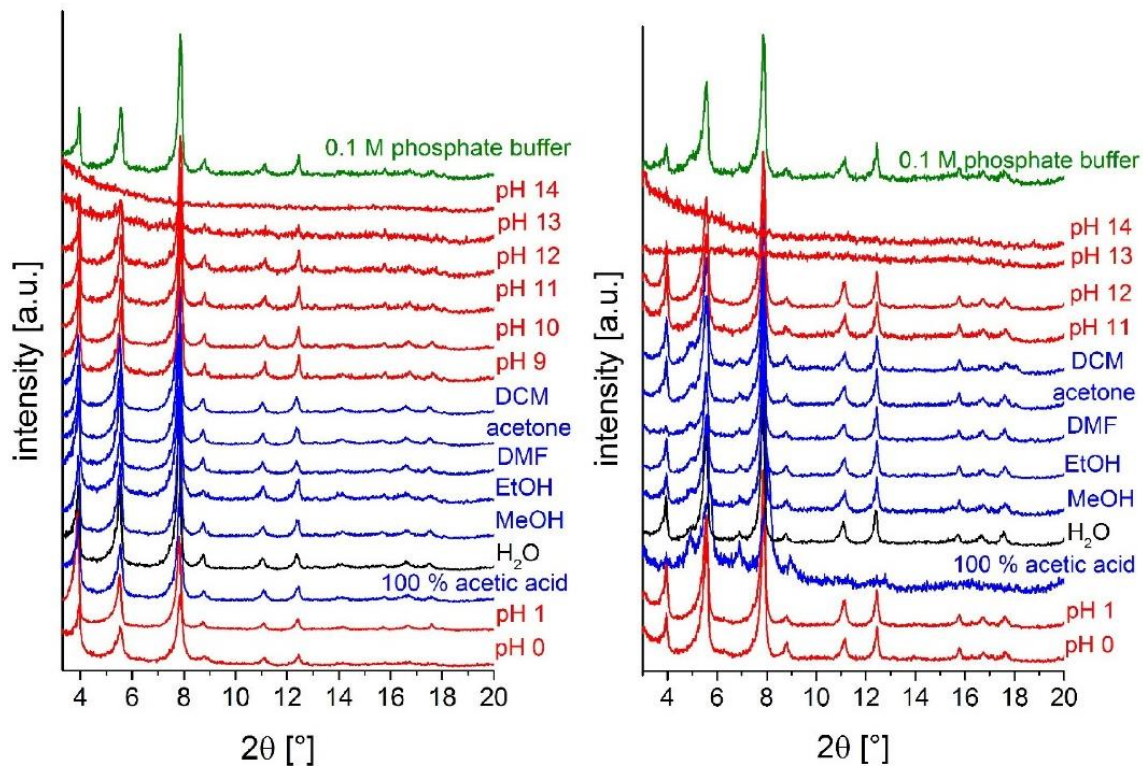


**Figure S13.** Chemical stability of Zr-CAU-30 (left) and Hf-CAU-30 (right) in different solvents (24 h, stirring at room temperature).

## 5. Spectroscopy

IR spectra of M-CAU-30 (M= Zr, Hf) and the Ni-H<sub>8</sub>TPPP linker are shown in Figure S14. The assignment of the bands are given in Table S4.

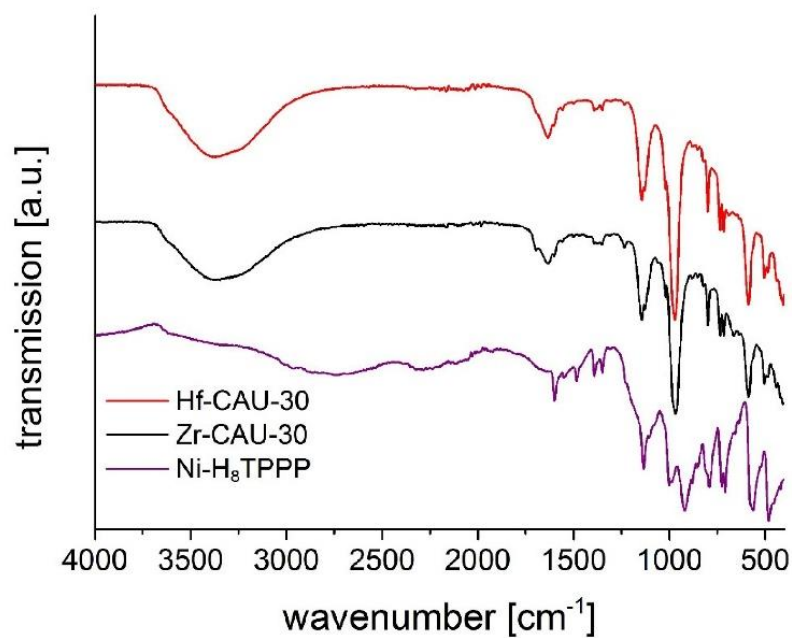


**Figure S14a.** IR spectra of M-CAU-30 (M=Zr, Hf) compared with the IR spectrum of the free linker Ni-H<sub>8</sub>TPPP.



**Table S4.** Assignment of the vibrations in the IR-spectra of M-CAU-30 (M= Zr, Hf) and the free linker Ni-H<sub>8</sub>TPPP.<sup>11, 12</sup>

<b>Vibration <math>\tilde{\nu}</math>IR [cm<sup>-1</sup>]</b>	<b>Zr</b>	<b>Hf</b>	<b>Ni-H<sub>8</sub>TPPP</b>
$\nu$ OH (H <sub>2</sub> O)	3389	3389	
$\nu$ P-OH	1634	1634	1606
$\nu$ C=C (arom.)	1562	1562	1519
$\nu$ P-C (phenyl)	1501	1501	1480
$\delta$ C=C, N=C (in plane)	1392	1392	1389
$\nu$ C-N (pyrrole)	1351	1351	1352
$\nu$ P=O (stretching)	1234	1234	1223
$\nu$ P-O (stretching)	1141	1141	1136
$\delta$ C-H, N-H (pyrrole)	over	layed	1100
$\delta$ C-H (in plane)	over	layed	1005
$\nu$ P=O (stretching)	966	966	921
$\gamma$ C-H (1,4-subst.)	800	800	793
$\delta$ C-H, N-H (pyrrole)	737	737	730
$\gamma$ P-C	717	717	704
$\delta$ P(OR) <sub>3</sub>	588	588	567
$\delta$ C=C (skeleton)	506	506	484

## 6. TEM and SEM measurements

### Scanning Electron Microscopy (SEM)

All SEM micrographs shown were acquired using a *Helios NanoLab G3UC (FEI)* electron microscope operating at 3 keV. Sample preparation was performed by dispersing both Zr-CAU-30 and Hf-CAU-30 in ethanol via sonication and subsequently drying respective aliquots on a carbon film placed on an aluminum sample holder. Before performing the actual measurements the samples were sputtered with carbon. For data evaluation the software *ImageJ v1.49* was used.

### Transmission Electron Microscopy

TEM micrographs and EDX investigations were recorded either on a *Tecnai G2 20 S-TWIN (FEI)* or a *Titan Themis 60-300 (FEI)* electron microscope that were operated at an acceleration voltage of 200 kV and 300 kV, respectively. For sample preparation, ethanolic dispersions of Zr-CAU-30 and Hf-CAU-30 were prepared and then dried on a carbon-coated copper grid. For data evaluation the software *ImageJ v1.49* was used.

### Zr-CAU-30

To further analyze the spherical secondary phase visible in the STEM images in Figure 5, electron diffraction was performed on the particles: Figure S15 (left) shows a typical area of the aggregated and intergrown nanoparticles along with a diffraction pattern in Figure S15 (right). Due the small domain sizes the reflections of the nanocrystals are broadened.

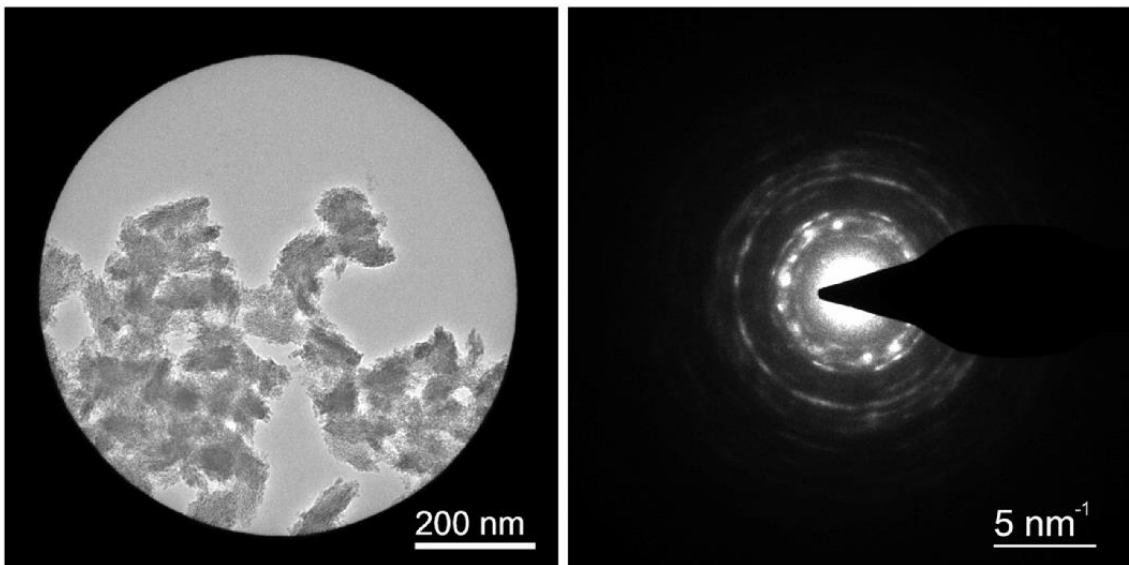


**Figure S15:** Secondary phase observed in the reaction produce that led to the formation of Zr-CAU-30 along with the respective electron diffraction pattern.

The most prominent lattice distances are listed in

<b>Bragg Ring (Inside to Outside)</b>	<b>Lattice distance</b>
1	0.36 nm
2	0.30 nm
3	0.26 nm
4	0.20 nm
5	0.18 nm
6	0.17 nm

5. They are in good agreement with the monoclinic phase of  $ZrO_2$ .<sup>13</sup>

**Table S5:** Lattice distances of secondary phase in Zr-CAU-30.<sup>13</sup>

<b>Bragg Ring (Inside to Outside)</b>	<b>Lattice distance</b>
1	0.36 nm
2	0.30 nm
3	0.26 nm
4	0.20 nm
5	0.18 nm
6	0.17 nm

To further identify the constituents of this phase, EDX measurements were performed on the nanoparticles. The area chosen for the measurements is shown in **Figure S1S16**. The results of these measurements are summarized in **Table S6**, excluding the support film material carbon. The two largest fractions are Zirconium and Oxygen while both nickel and phosphorus are absent. This shows that this secondary phase does not contain any linker molecules and is in agreement with the presence of zirconium oxide as determined by electron diffraction.

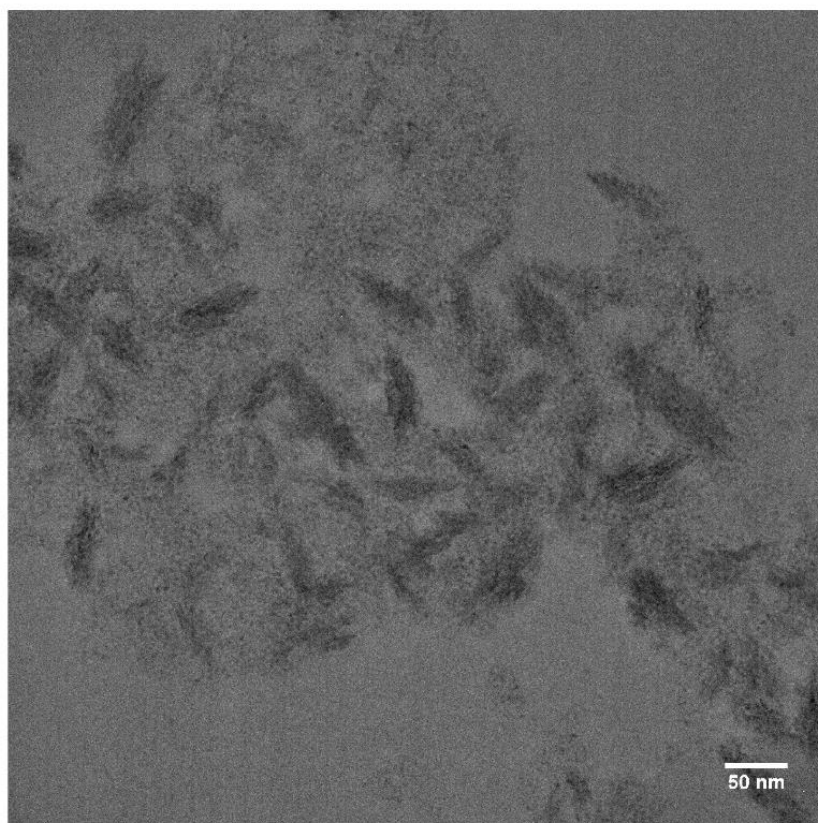


**Figure S16:** Secondary phase observed in the reaction produce that led to the formation of Zr-CAU-30.

**Table S6:** Composition of secondary phase observed in the reaction produce that led to the formation of Zr-CAU-30 derived from EDX measurement, excluding carbon. The first column refers to the element and the x-ray line used for quantification.

Element	Atomic %
Zr(L)	24.2
O(K)	69.2
Na(K)	3.0
F(K)	3.5

### Hf-CAU-30

In a similar manner to Zr-CAU-30, Hf-CAU-30 was also examined by TEM. An overview micrograph, depicting the morphology of the species is shown in Figure S17. Similar to Zr-CAU-30, the majority of Hf-CAU-30 consists of needles that are up to 700 nm long with a width of 30 - 60 nm. In addition to that two other morphologies are present in the sample as shown in **Fehler! Verweisquelle konnte nicht gefunden werden**. Next to the needles there are spherical aggregations of particles with a diameter between 2 – 5 nm and a cube-shaped crystalline species featuring particle diameter between 40 – 60 nm. Both needles and cube-shaped species are crystalline as can be seen on the periodic lattice planes visible in Figure S19.

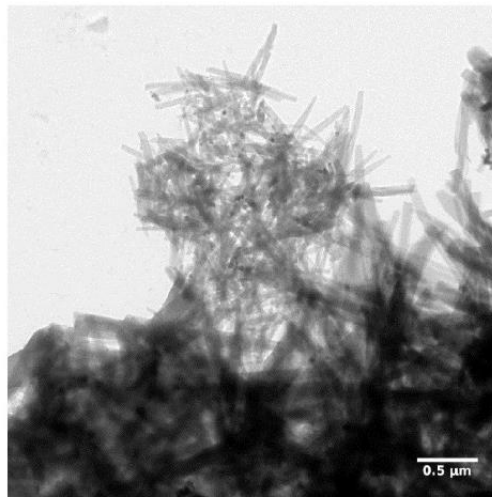


**Figure S17:** TEM micrograph of Hf-CAU-30.

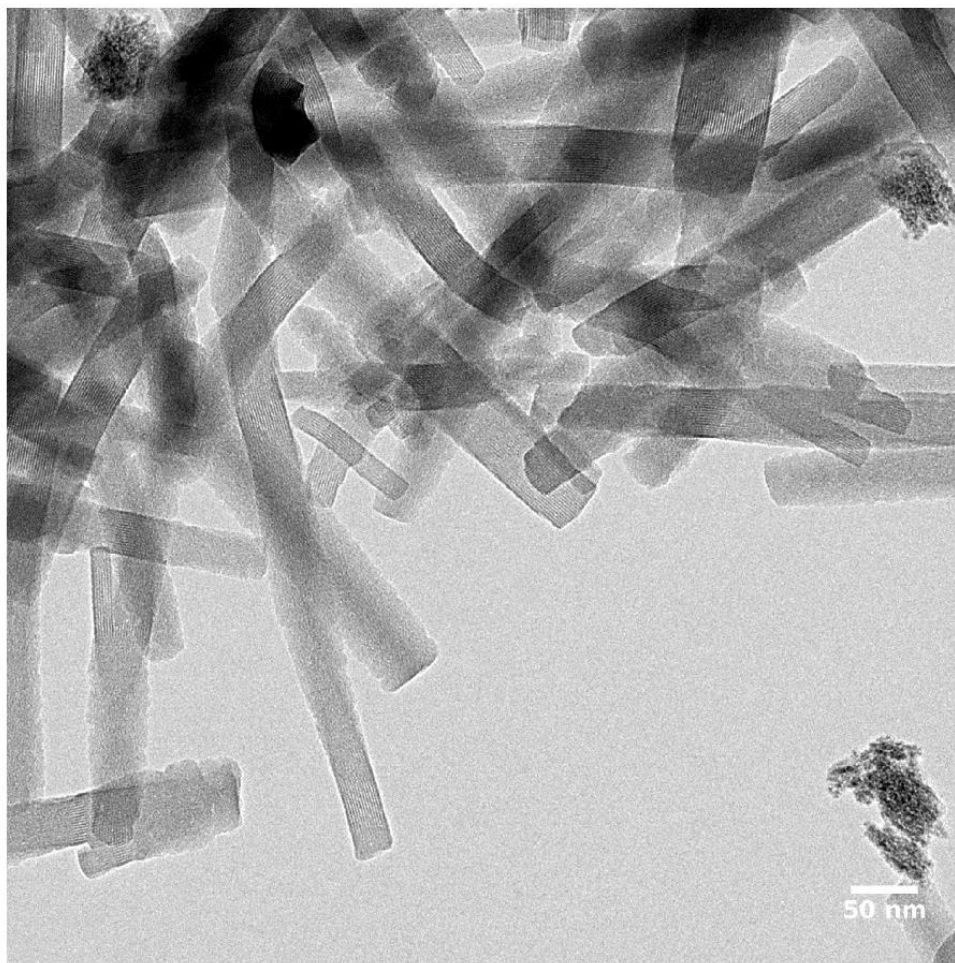


**Figure S19:** Crystalline Needles of Hf-CAU-30



Nanocrystalline aggregates in the Hf-CAU-30 sample

In addition to the needle-like and the cubic morphologies observed in this sample, nanocrystalline aggregates were observed as well, similar to the secondary phase in the Zr-CAU-30 sample. The particles with their corresponding diffraction pattern are shown in Figure S20. The observed lattice plane distances (Table S7) are very similar to those observed for the secondary phase in the Zr-CAU-30 sample, albeit slightly smaller. This is consistent with a HfO<sub>2</sub> phase isostructural to monoclinic ZrO<sub>2</sub> but having slightly smaller lattice parameters, as known from the literature.<sup>13</sup>

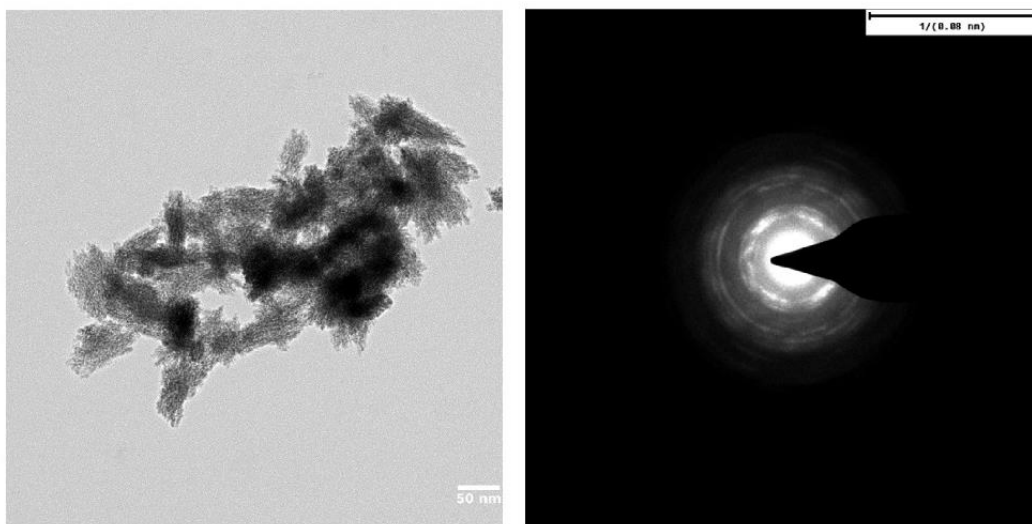


**Figure S20:** Secondary phase of sample Hf-CAU-30 along with electron diffraction pattern. (Bragg rings are marked with yellow lines)

**Table S7:** Lattice plane distances of secondary phase in Hf-CAU-30.<sup>13</sup>

Reflection	Lattice plane distance
1	0.35 nm
2	0.25 nm
3	0.18 nm
4	0.17 nm
5	0.13 nm

Evaluations of EDX spectra of Hf-CAU-30 and the secondary phase are shown in Table S8. The elemental quantifications confirm the expected respective compositions of Hf-CAU-30 and HfO<sub>2</sub>. The presence of sodium and fluorine is a result of the synthesis route employing NaOH and NaF.

**Table S8:** Results of EDX measurements of Hf-CAU-30. Both quantifications exclude carbon, the substrate film material. The first column refers to the element and the X-ray line used for quantification. The second and the third column respectively refer to the two phases observed, easily to distinguish by their morphologies.

	<b>Hf-CAU-30 [at %]</b>	<b>Secondary phase [at %]</b>
Hf (L)	7.0	28.0
O (K)	58.2	63.2
Ni (K)	2.7	1.0
N (K)	14.3	0.0
P (K)	11.3	4.3
Na (K)	5.5	2.6
F (K)	1.0	0.9

## 7. Cyclic voltammetry

Cyclic voltammograms (CVs) of Zr-CAU-30 were measured on a fluorine doped tin oxide (FTO) electrode in 0.1 M phosphate buffer (pH 7) with an Ag/AgCl type reference electrode and Pt as counter electrode. The cyclic stability was demonstrated by measuring 50 cycles; the first and the 50th CV is shown in Figure S22. Applying different scan rates between 50 and 1000  $\text{mV s}^{-1}$  reveals the expected behavior of increasing currents with the scan rate (Fig. S23).

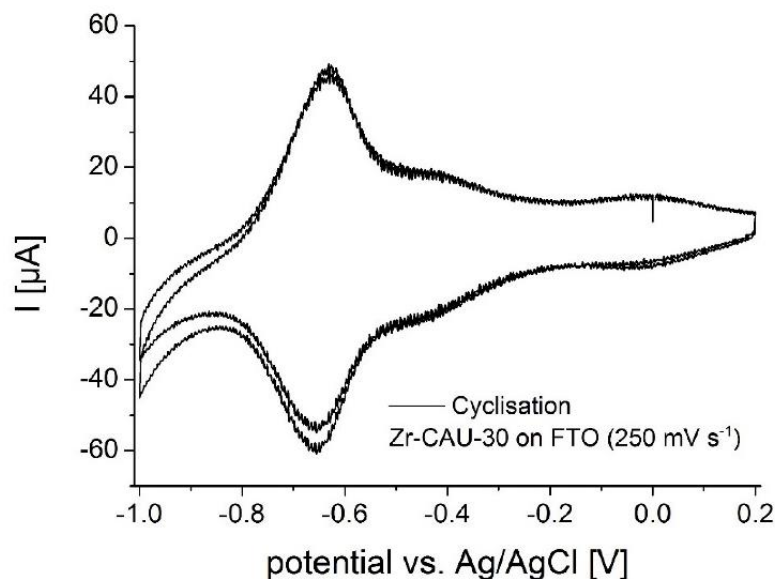


**Figure S22:** Results of the cyclic stability of Zr-CAU-30 on FTO. The CVs of the first and 50<sup>th</sup> cycle indicate no significant decrease in the measured current.

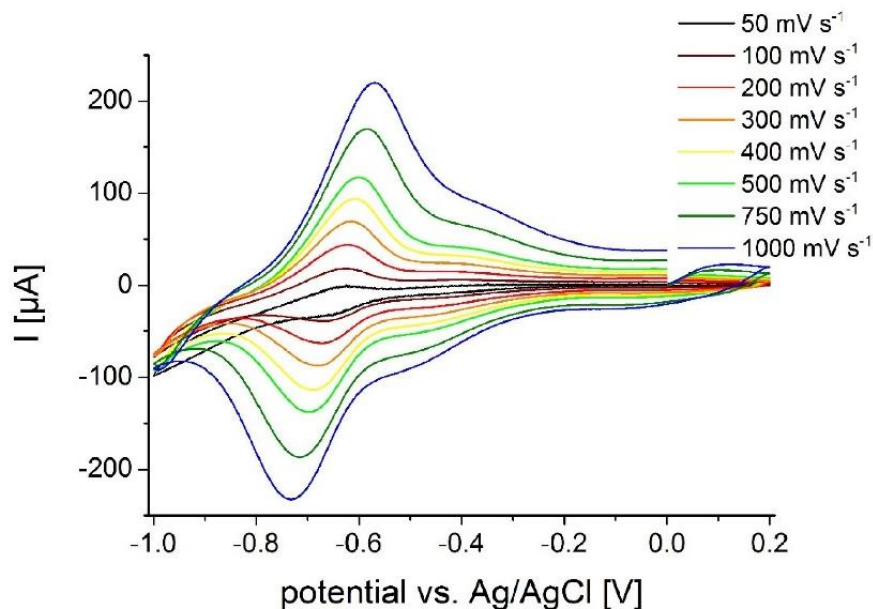


**Figure S23.** CVs of Zr-CAU-30 on FTO at different scan rates between 50 and 1000  $\text{mV s}^{-1}$ .

**8. References**

1. M. Taddei, F. Costantino and R. Vivani, *Inorg. Chem.*, 2010, **49**, 9664-9670.
2. M. Taddei, F. Costantino, F. Marmottini, A. Comotti, P. Sozzani and R. Vivani, *Chem. Commun.*, 2014, **50**, 14831-14834.
3. M. Taddei, F. Costantino, R. Vivani, S. Sabatini, S.-H. Lim and S. M. Cohen, *Chem. Commun.*, 2014, **50**, 5737-5740.
4. R. K. Mah, B. S. Gelfand, J. M. Taylor and G. K. H. Shimizu, *Inorganic Chemistry Frontiers*, 2015, **2**, 273-277.
5. C.-Y. Gao, J. Ai, H.-R. Tian, D. Wu and Z.-M. Sun, *Chem. Commun.*, 2017, **53**, 1293-1296.
6. T. Zheng, Z. Yang, D. Gui, Z. Liu, X. Wang, X. Dai, S. Liu, L. Zhang, Y. Gao, L. Chen, D. Sheng, Y. Wang, J. Diwu, J. Wang, R. Zhou, Z. Chai, T. E. Albrecht-Schmitt and S. Wang, *Nat Commun.*, 2017, **8**, 15369.
7. A. D. Adler, F. R. Longo, F. Kampas and J. Kim, *J. Inorg. Nucl. Chem.*, 1970, **32**, 2443-2445.
8. A. D. Adler, F. R. Longo, J. D. Finarelli, J. Goldmacher, J. Assour and L. Korsakoff, *The Journal of Organic Chemistry*, 1967, **32**, 476-476.
9. G. G. Rajeshwaran, M. Nandakumar, R. Sureshbabu and A. K. Mohanakrishnan, *Org. Lett.*, 2011, **13**, 1270-1273.
10. P. Tavs, *Chem. Ber.*, 1970, **103**, 2428-2436.
11. G. Socrates, *Infrared and Raman Characteristic Group Frequencies: Tables and Charts*, Wiley, 2004.
12. M. Hesse, H. Meier and B. Zeeh, *Spektroskopische Methoden in der organischen Chemie*, Thieme, 2005.
13. R. E. Hann, P. R. Suitch and J. L. Pentecost, *J. Am. Ceram. Soc.*, 1985, **68**, C-285-C-286.



## Curriculum Vitae

**Timo Rhauderwiek**

---

### Persönliche Daten

Geburtstag: 23.08.1988

Geburtsort: Leer (Ostfriesland)

Staatsangehörigkeit: deutsch

### Bildungsweg

---

- |                   |  |
|-------------------|--|
| 10/2014 – 06/2018 | Christian-Albrechts-Universität zu Kiel<br><b>Promotion</b> im Arbeitskreis von Prof. Dr. N. Stock am Institut für anorganische Chemie.<br><b>Promotionsthema:</b> „ <i>Porphyrin-basierte Metall-Organische Gerüstverbindungen: Von Metall-Carboxylaten zu Metall-Phosphonaten.</i> “ |
| 10/2012 – 08/2014 | Christian-Albrechts-Universität zu Kiel<br><b>Masterstudium Chemie 1-Fach</b> (Note: 1.6) und <b>Masterarbeit</b> im Arbeitskreis von Prof. Dr. N. Stock.<br>Thema: „ <i>Synthese und Charakterisierung Porphyrin-basierter MOFs mit dreiwertigen Kationen.</i> “                      |
| 10/2009 – 09/2012 | Christian-Albrechts-Universität zu Kiel<br><b>Bachelorstudium Chemie 1-Fach</b> (Note: 2.4) und <b>Bachelorarbeit</b> im Arbeitskreis von Prof. Dr. N. Stock.<br>Thema: „ <i>2,4,6-Pyridintricarbonsäure ein neuer Linker für MOFs?</i> “  |
| 04/2009 – 07/2009 | Justus-Liebig-Universität Gießen<br><b>Gasthörer Chemie 1-Fach</b>   |
| 09/2001 – 06/2008 | Ubbo-Emmius-Gymnasium Leer<br><b>Abitur</b> (Note: 2.9)  |



## Tagungsbeiträge

---

### Poster:

#### **Synthesis and Characterisation of Two Porphyrin-based Metal Organic Frameworks with Indium and Gallium**

Timo Rhauderwiek, Norbert Stock

- 27. *Deutsche Zeolith-Tagung 2015, Oldenburg*

#### **Co-ligand-dependent formation of three new porphyrin based Ce-MOFs**

Timo Rhauderwiek, Sigurd Øien-Ødegaard, Helge Reinsch, Karl-Petter Lillerud, Norbert Stock

- 28. *Deutsche Zeolith-Tagung 2016, Gießen*

- 19. *Norddeutsches Doktorandenkolloquium 2016, Hamburg*

#### **Tetra(4-phosphonophenyl)porphyrin –a new tetraphosphonic acid for the synthesis of MOFs**

Timo Rhauderwiek, Bin Wang, Ken Inge, Hongyi Xu, Taimin Yang, Sigurd Øien-Ødegaard, Haishuang Zhao, Helge Reinsch, Ute Kolb, Xiaodong Zou, Karl-Petter Lillerud and Norbert Stock

- 29. *Deutsche Zeolith-Tagung 2017, Frankfurt*

- 2. *EuroMOF-Tagung 2017, Delft, Niederlande*

- *Workshop on Bulk Scattering in Condensed Matter Physics and Chemistry (CMPC), DESY, Hamburg*

- 30. *Deutsche Zeolith-Tagung 2018, Kiel*

## Publikationen

---

### **Group 13 Metal Carboxylates: Using Molecular Clusters As Hybrid Building Units in a MIL-53 Type Framework**

*Michael T. Wharmby, Malte Snoyek, Timo Rhauderwiek, Knut Ritter, Norbert Stock*

*Cryst. Growth Des.*, **2014**, 14 (10), pp 5310–5317; DOI: 10.1021/cg501189n.

### **Nanoscale Synthesis of Two Porphyrin-Based MOFs with Gallium and Indium**

*Timo Rhauderwiek, Steve Waitschat, Stefan Wuttke, Helge Reinsch, Thomas Bein, Norbert Stock*

*Inorg. Chem.*, **2016**, 55 (11), pp 5312–5319; DOI: 10.1021/acs.inorgchem.6b00221.

### **Co-Ligand Dependent Formation and Phase Transformation of Four Porphyrin-Based Cerium Metal–Organic Frameworks**

*Timo Rhauderwiek, Niclas Heidenreich, Helge Reinsch, Sigurd Øien-Ødegaard, Kirill A. Lomachenko, Uta Rütt, Alexander V. Soldatov, Karl Petter Lillerud, Norbert Stock*

*Cryst. Growth Des.*, **2017**, 17 (6), pp 3462–3474; DOI: 10.1021/acs.cgd.7b00450.

### **Crystalline and permanently porous porphyrin-based metal tetraphosphonates**

*Timo Rhauderwiek, Konrad Wolkersdörfer, Sigurd Øien-Ødegaard, Karl-Petter Lillerud, Michael Wark, Norbert Stock*

*Chem. Commun.*, **2018**, 54, pp 389-392; DOI: 10.1039/C7CC07766A.

### **A precursor method for the synthesis of new Ce(IV) MOFs with reactive tetracarboxylate linkers**

*Simon Smolders, Aranud Struyf, Helge Reinsch, Bart Bueken, Timo Rhauderwiek, Luise Mintrop, Philipp Kurz, Norbert Stock und Dirk E. De Vos*

*Chem. Commun.*, **2018**, 54, pp 876; DOI: 10.1039/c7cc08200b.

### **Bismuth Coordination Polymers with 2,4,6-Pyridine Tricarboxylic Acid – High-Throughput Investigations, Crystal Structures and Luminescence Properties**

*Timo Rhauderwiek, César dos Santos Cunha, Huayna Terraschke, Norbert Stock*

*Eur. J. Inorg. Chem.*, **2018**, 10.1002/ejic.201800154.

### **A porous cobalt tetraphosphonates metal-organic framework: structure determination by fast continuous rotation electron diffraction**

*Bin Wang,<sup>†</sup> Timo Rhauderwiek,<sup>†</sup> A. Ken Inge, Hongyi Xu, Taimin Yang, Zhehao Huang, Norbert Stock, Xiaodong Zou*

*CrystEngComm*, **2018**, submitted.

### **Highly stable and porous porphyrin-based metal phosphonates - Electron crystallography as an important tool for structure elucidation**

*Timo Rhauderwiek, Haishuang Zhao, Patrick Hirschle, Markus Döblinger, Bart Bueken, Helge Reinsch, Dirk de Vos, Stefan Wuttke, Ute Kolb, Norbert Stock*

*Chem. Sci.*, **2018**, 10.1039/C8SC01533C.



## **Eidesstattliche Erklärung**

Hiermit versichere ich an Eides statt, dass ich die vorliegende Arbeit selbständig abgesehen von der wissenschaftlichen Betreuung durch meinen Betreuer Herrn Prof. Stock und nur unter Verwendung der angegebenen Hilfsmittel angefertigt habe. Die Dissertation wird ausschließlich an dieser Stelle zur Promotion vorgelegt. Teile der Arbeit wurden in den genannten Journalen als wissenschaftliche Beiträge bereits veröffentlicht oder wurden zur Veröffentlichung eingereicht. Ich erkläre hiermit, dass ich noch keinen Promotionsversuch unternommen habe und dass die Arbeit unter Einhaltung der Regeln guter wissenschaftlicher Praxis der Deutschen Forschungsgesellschaft entstanden ist.

Kiel, Juni 2018

---

(Timo Rhauderwiek)